OPTOGENETIC TOOLS IN THE MOLECULAR SPOTLIGHT

EDITED BY: Tilo Mathes and John T. M. Kennis
PUBLISHED IN: Frontiers in Molecular Biosciences

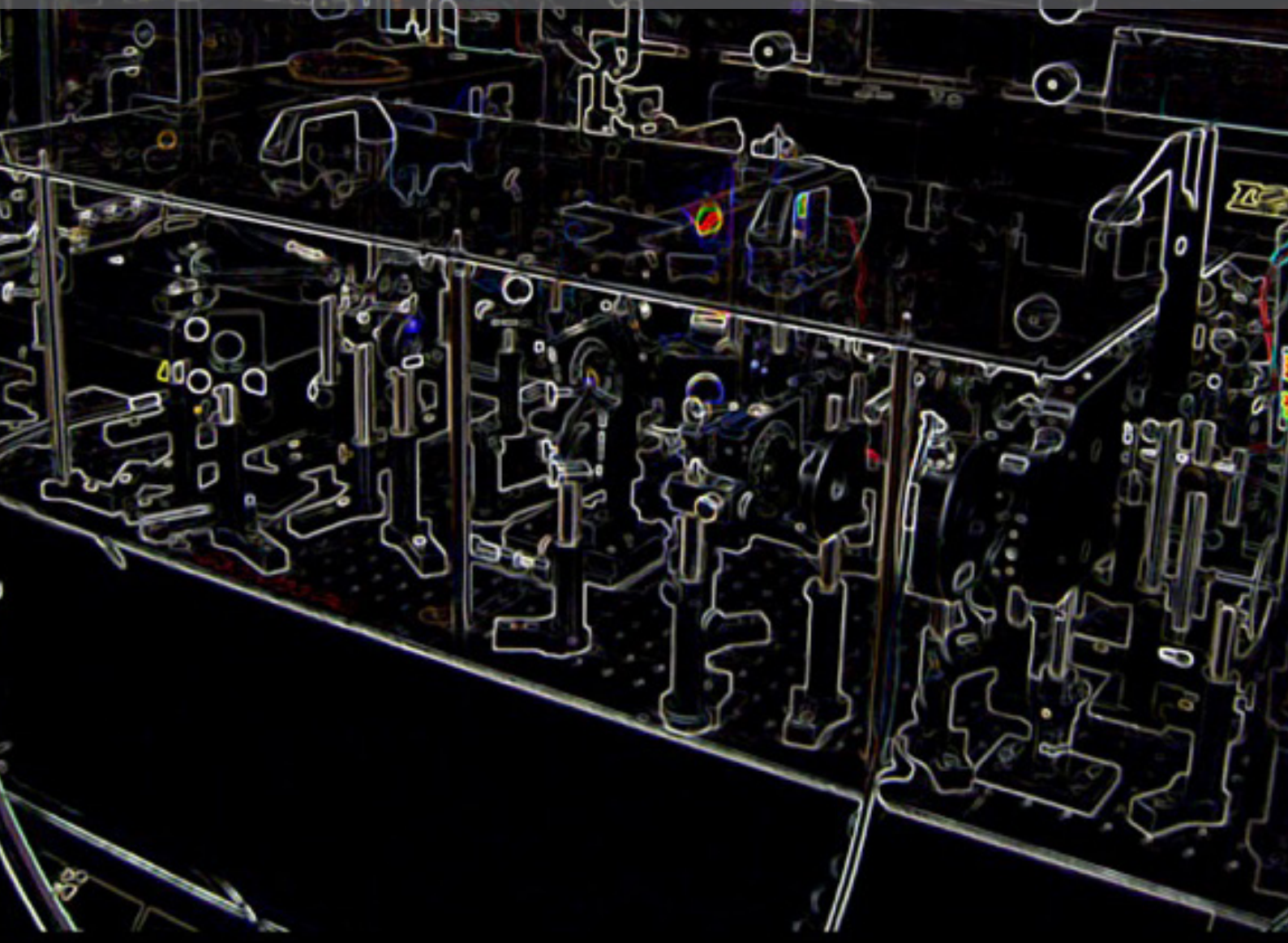

frontiers Research Topics

ISSN 1664-8714
ISBN 978-2-88919-899-3
DOI 10.3389/978-2-88919-899-3

About Frontiers

Frontiers is more than just an open-access publisher of scholarly articles: it is a pioneering approach to the world of academia, radically improving the way scholarly research is managed. The grand vision of Frontiers is a world where all people have an equal opportunity to seek, share and generate knowledge. Frontiers provides immediate and permanent online open access to all its publications, but this alone is not enough to realize our grand goals.

Frontiers Journal Series

The Frontiers Journal Series is a multi-tier and interdisciplinary set of open-access, online journals, promising a paradigm shift from the current review, selection and dissemination processes in academic publishing. All Frontiers journals are driven by researchers for researchers; therefore, they constitute a service to the scholarly community. At the same time, the Frontiers Journal Series operates on a revolutionary invention, the tiered publishing system, initially addressing specific communities of scholars, and gradually climbing up to broader public understanding, thus serving the interests of the lay society, too.

Dedication to quality

Each Frontiers article is a landmark of the highest quality, thanks to genuinely collaborative interactions between authors and review editors, who include some of the world's best academicians. Research must be certified by peers before entering a stream of knowledge that may eventually reach the public - and shape society; therefore, Frontiers only applies the most rigorous and unbiased reviews.
Frontiers revolutionizes research publishing by freely delivering the most outstanding research, evaluated with no bias from both the academic and social point of view.
By applying the most advanced information technologies, Frontiers is catapulting scholarly publishing into a new generation.

What are Frontiers Research Topics?

Frontiers Research Topics are very popular trademarks of the Frontiers Journals Series: they are collections of at least ten articles, all centered on a particular subject. With their unique mix of varied contributions from Original Research to Review Articles, Frontiers Research Topics unify the most influential researchers, the latest key findings and historical advances in a hot research area! Find out more on how to host your own Frontiers Research Topic or contribute to one as an author by contacting the Frontiers Editorial Office: **researchtopics@frontiersin.org**

OPTOGENETIC TOOLS IN THE MOLECULAR SPOTLIGHT

Topic Editors:
Tilo Mathes, Vrije Universiteit Amsterdam, Netherlands
John T. M. Kennis, Vrije Universiteit Amsterdam, Netherlands

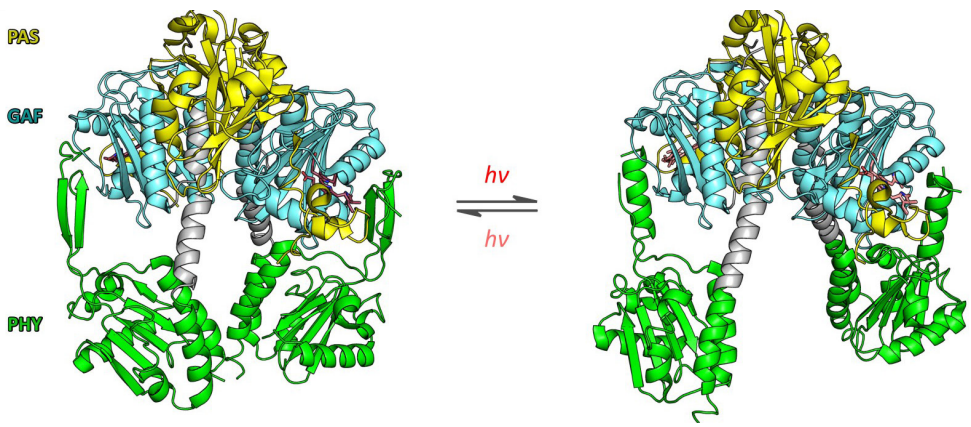

High-resolution structures of the photosensor module of Deinococcus radiodurans bacteriophytochrome, comprising PAS, GAF, and PHY domains, in its dark-adapted Pr state (left, 4O0P) and red-light-adapted Pfr state (right, 4O01, Takala et al., 2014) implicate a pivot motion and splaying apart of the PHY domains as the molecular mechanism for light-induced signal transduction.
Figure taken from: Ziegler T and Möglich A (2015) Photoreceptor engineering. Front. Mol. Biosci. 2:30. doi: 10.3389/fmolb.2015.00030

The rise of optogenetics as a standard technique to non-invasively probe and monitor biological function created an immense interest in the molecular function of photosensory proteins. These photoreceptors are usually protein/pigment complexes that translate light into biological information and have become essential tools in cell biology and neurobiology as their function is genetically encoded and can be conveniently delivered into a given cell. Like for fluorescent proteins that quickly became invaluable as genetically encodable reporters in microscopy and imaging, variants of photosensory proteins with customized sensitivity and functionality are nowadays in high demand.

In this ebook we feature reviews and original research on molecular approaches from synthetic biology and molecular spectroscopy to computational molecular modelling that all aspire to elucidate the molecular prerequisites for the photosensory function of the given proteins. The

principle property of changing activity of biological function simply by application of light is not only very attractive for cell biology, it also offers unique opportunities for molecular studies as excitation can be controlled with high time precision. Especially in spectroscopy the usually fully reversible photoactivation of photosensory proteins allows researchers to to perform time resolved studies with up to femtosecond resolution. In addition, functional variants can be investigated and quickly screened in common biochemical experiments.

The insights that are obtained by the here presented various yet complementary methods will ultimately allow us write the script for a molecular movie from excitation of the protein by a photon to activation of its biological function. Such deep understanding does not only provide unique insights into the dynamics of protein function, it will also ultimately enable us to rationally design novel optogenetic tools to be used in cell biology and therapy.

Citation: Mathes, T., Kennis, J. T. M., eds. (2016). Optogenetic Tools in the Molecular Spotlight. Lausanne: Frontiers Media. doi: 10.3389/978-2-88919-899-3

Table of Contents

frontiers in Molecular Biosciences

EDITORIAL
published: 28 April 2016
doi: 10.3389/fmolb.2016.00014

Editorial: Optogenetic Tools in the Molecular Spotlight

Tilo Mathes and John T. M. Kennis*

Department of Physics and Astronomy, Vrije Universiteit Amsterdam, Amsterdam, Netherlands

Keywords: photoreceptors, optogenetics, flavins, opsins, phytochrome, spectroscopy, computational modeling, protein engineering

The Editorial on the Research Topic

Optogenetic Tools in the Molecular Spotlight

Photosensory receptors have been in the center of vision research and photobiology since the discovery of rhodopsin in 1876 by Franz Boll. However, in the last 10 years the rise of optogenetics has placed them in a broader focus. The majority of these biological light-sensors consist of a protein/pigment complex that alters the activity of a cognate biological effector upon absorption of a photon. With the nowadays available information on the corresponding genes, proteins and the vast access to (meta-) genomic data as well as sophisticated methods in molecular biology and genome engineering the photoreceptor principle of transforming light into biological information is now exploited in many different fields of research.

Photosensory receptors therefore not only constitute the backbone of a major methodological breakthrough in cell and neurobiology but also offer bright perspectives for our understanding of dynamic biomolecular processes in general. The possibility to use photons as substrates enables researchers to induce and experimentally monitor biomolecular reactions with up to femtosecond resolution. Combined with techniques capable of molecular resolution such time-resolved experiments not only provide dynamic molecular information on the underlying mechanisms of photosensory and general signal transduction, but also will enable us to identify structure/function relations and design principles of biological sensor/effector complexes. Ultimately, this knowledge will allow us to rationally design novel light-responsive tools with customized properties for application in optogenetics and synthetic biology.

This ebook features research articles and reviews covering the most prominent photosensory modules applied in optogenetics, as represented by flavin based photoreceptors (LOV and BLUF), phytochromes and microbial opsins. The articles of this collection showcase state-of-the-art approaches to elucidate the molecular function of such photosensory modules from the initial event of photon absorption to the activation of a downstream effector.

Ritter et al. summarize recent advances in time resolved infrared absorption spectroscopy, which allows researchers to visualize structural changes involved in the activation of photosensory proteins by identifying changes in vibrational frequencies of individual chemical bonds. While infrared spectroscopic data may therefore become extremely complex in proteins, larger scale structural transformations like domain rearrangements in photosensor/effector complexes and their dynamics can be more efficiently mapped by discrete distance measurements between interacting paramagnetic centers using pulsed electron paramagnetic spectroscopy as illustrated by Nohr et al. Another elegant way of characterizing functionally relevant differences in signaling-active and inactive protein forms is presented by Lindner et al. Their review summarizes hydrogen/deuterium exchange mass spectrometry that provides information on solvent accessibility and domain flexibility, and thus important mechanistic insights on how protein dynamics determine signal transduction.

OPEN ACCESS

Edited and reviewed by:
Andrea Bassi,
Politecnico di Milano, Italy

****Correspondence:***
Tilo Mathes
t.mathes@vu.nl

Specialty section:
This article was submitted to Biophysics, a section of the journal Frontiers in Molecular Biosciences

Received: *07 February 2016*
Accepted: *08 April 2016*
Published: *28 April 2016*

Citation:
Mathes T and Kennis JTM (2016) Editorial: Optogenetic Tools in the Molecular Spotlight. Front. Mol. Biosci. 3:14. doi: 10.3389/fmolb.2016.00014

In their research article, Song and coworkers employ magic angle spinning solid state nuclear magnetic resonance spectroscopy to investigate the molecular and electronic structure of the protein-embedded tetrapyrrole cofactor (Song et al.). The chromophore and its dynamic interaction with the protein environment can be studied with extremely high molecular resolution using this technique and allowed the authors to determine aggregation and hydration effects induced by sample preparation on the local structure of the chromophore. Such insights are crucial to critically evaluate experimental results and their functional implications.

Lehtivuori et al. also investigate the molecular environment of the phytochrome chromophore and combine various methods to identify structural prerequisites and potential design guidelines for the fluorescence lifetime in phytochrome based infrared fluorescent proteins. Besides being used as optogenetic actuators phytochromes turned out to be highly attractive tools for deep tissue imaging due to the relatively high penetration of long wavelength light in tissue. Fluorescence spectroscopy and X-ray crystallography demonstrate that phytochrome fluorescence is strongly influenced by bulky residues proximal to the chromophore and by presence of water in the vicinity of the chromophore.

As photoinduced signal transduction is ultimately determined by the primary events following photoexcitation and their quantum efficiencies, ultrafast techniques with femtosecond resolution are essential. Ihalainen et al. summarize and compare the primary photochemistry of the red light absorbing phytochromes obtained by ultrafast absorption spectroscopy up to several nanoseconds. They show that the excited state dynamics are strongly affected by the length and subunit composition of the investigated proteins and suggest feedback mechanisms from the distal domains to the chromophore binding pocket, which are most likely of functional relevance.

Stensitzki et al. employ ultrafast time resolved visible absorption spectroscopy to investigate the photoactivation of the light-activated ion channel channelrhodopsin-1, a close relative of the most prominent optogenetic tool: channelrhodopsin-2. They identify a distinct ground state heterogeneity illustrated by a strong excitation wavelength dependence of the observed photodynamics that has not been observed for the well-studied channelrhodopsin-2 and discuss its implications for the activation of the protein.

Heterogeneity in receptor conformation is a recurring topic both in photoreceptor and signal transduction research and is crucial to understand dark noise of receptor proteins. Chromophore heterogenetity and its relation to signaling is also the focus of the study of Velazquez Escobar et al. on phytochromes (Velazquez Escobar et al.). They identify two far-red absorbing states in the cyanobacterial phytochrome Cph1 using a combination of steady state Raman spectroscopy, ultrafast time resolved infrared spectroscopy and quantum chemical calculations.

In addition to experimental methods as described in the articles above, computational methods are powerful approaches to calculate spectroscopic properties or molecular dynamics under selected conditions, which may not be accessible experimentally. In this collection computational methods are used to support experimental findings by calculating vibrational frequencies of chromophores (Velazquez Escobar et al.) and to simulate molecular structural dynamics of photoreceptor proteins. Bocola et al. employ molecular dynamics simulations to investigate light-induced structural changes in dimeric LOV domains and provide a novel mechanism for the photoactivation of dimeric LOV photoreceptors. Mathes and Götze review the currently available computational studies on the spectroscopic properties and vibrational frequencies of BLUF photoreceptors and explore an alternative mechanism of BLUF photoactivation using quantum chemical calculations.

Finally, the ebook contains concise reviews on opsin based optogenetic tools and modular photoreceptors that illustrate how the molecular insights that we obtained so far can be applied to rationally design novel photoswitches with customized activities. Ziegler and Möglich provide a thorough overview on modular photoreceptor function, architecture and design principles. The review of Pudasani et al. focuses on the structural prerequisites for tuning the LOV domain chemistry and signal transduction to ultimately allow for improved LOV-domain based optogenetic tools. Kandori summarizes structure/function relations in the extremely versatile microbial rhodopsin pumps that have been proven to be key optogenetic tools.

This ebook thus provides an exciting collection of various molecular approaches to elucidate the photochemistry and signal generation in a variety of photoreceptors from absorption of a photon to the biological output that will provide researchers with fundamental knowledge to create and customize novel optogenetic tools.

AUTHOR CONTRIBUTIONS

All authors listed, have made substantial, direct and intellectual contribution to the work, and approved it for publication.

FUNDING

JK and TM were supported by the Chemical Sciences Council of the Netherlands Organization for Scientific Research (NWO-CW) through a VICI grant to JK.

Conflict of Interest Statement: The authors declare that the research was conducted in the absence of any commercial or financial relationships that could be construed as a potential conflict of interest.

frontiers in Molecular Biosciences

HYPOTHESIS AND THEORY
published: 23 December 2015
doi: 10.3389/fmolb.2015.00075

Fast Photochemistry of Prototypical Phytochromes—A Species vs. Subunit Specific Comparison

Janne A. Ihalainen[1]*, *Heikki Takala*[1,2] and *Heli Lehtivuori*[1,3]

[1] Department of Biological and Environmental Sciences, Nanoscience Center, University of Jyväskylä, Jyväskylä, Finland, [2] Department of Anatomy, Institute of Biomedicine, University of Helsinki, Helsinki, Finland, [3] Department of Physics, Nanoscience Center, University of Jyväskylä, Jyväskylä, Finland

Phytochromes are multi-domain red light photosensor proteins, which convert red light photons to biological activity utilizing the multitude of structural and chemical reactions. The steady increase in structural information obtained from various bacteriophytochromes has increased understanding about the functional mechanism of the photochemical processes of the phytochromes. Furthermore, a number of spectroscopic studies have revealed kinetic information about the light-induced reactions. The spectroscopic changes are, however, challenging to connect with the structural changes of the chromophore and the protein environment, as the excited state properties of the chromophores are very sensitive to the small structural and chemical changes of their environment. In this article, we concentrate on the results of ultra-fast spectroscopic experiments which reveal information about the important initial steps of the photoreactions of the phytochromes. We survey the excited state properties obtained during the last few decades. The differences in kinetics between different research laboratories are traditionally related to the differences of the studied species. However, we notice that the variation in the excited state properties depends on the subunit composition of the protein as well. This observation illustrates a feedback mechanism from the other domains to the chromophore. We propose that two feedback routes exist in phytochromes between the chromophore and the remotely located effector domain. The well-known connection between the subunits is the so-called tongue region, which changes its secondary structure while changing the light-activated state of the system. The other feedback route which we suggest is less obvious, it is made up of several water molecules ranging from the dimer interface to the vicinity of the chromophore, allowing even proton transfer reactions nearby the chromophore.

Keywords: red photosensors, excited state dynamics, fluorescence, transient absorption, laser spectroscopy

OPEN ACCESS

Edited by:
Tilo Mathes,
Vrije Universiteit Amsterdam, Netherlands

Reviewed by:
Derren Heyes,
University of Manchester, UK
Rolf Diller,
University Kaiserslautern, Germany

***Correspondence:**
Janne A. Ihalainen
janne.ihalainen@jyu.fi

Specialty section:
This article was submitted to Biophysics, a section of the journal Frontiers in Molecular Biosciences

Received: *08 August 2015*
Accepted: *07 December 2015*
Published: *23 December 2015*

Citation:
Ihalainen JA, Takala H and Lehtivuori H (2015) Fast Photochemistry of Prototypical Phytochromes—A Species vs. Subunit Specific Comparison. Front. Mol. Biosci. 2:75. doi: 10.3389/fmolb.2015.00075

INTRODUCTION

Phytochromes are red light-sensing photosensory proteins that exist in plants, fungi, and bacteria. The incident light leads to several structural and chemical changes of the protein, and thus, controls its biological activity. The structural changes between the two (thermodynamically stable) light-switchable states are considerably large in the photosensory module of the bacteriophytochromes (Takala et al., 2014a). The far-red fluorescence emission

properties of phytochromes offer potential to tissue imaging (Fischer and Lagarias, 2004). Due to relatively low scattering, lower light absorption in living tissue, and good tissue penetration, the red light-sensing proteins provide an advantage over other photosensory proteins. The potential of phytochrome-based optogenetic switches have already been recognized by several laboratories (Shimizu-Sato et al., 2002; Möglich and Moffat, 2010; Piatkevich et al., 2013a,b; Gasser et al., 2014).

Phytochromes are widely found in the bacterial kingdom. A comprehensive description of various species, their occurrence, and function, is represented elsewhere (for example the review of Auldridge and Forest, 2011). On the other hand, the time-resolved spectroscopic studies of phytochromes have concentrated on a rather small set of phytochromes. We focus on phytochrome species which contain canonical domain architecture (**Figure 1**). We also concentrate on phytochromes whose light-activated reactions from Pr to Lumi-R have been studied on the ultra-fast time scales. These are the phytochromes from *Agrobacterium tumenfaciens* (*A. tumenfaciens*, Agp1), *Synechocystis sp.* PCC 6803 (cyanobacterial phytochrome, Cph1), *Deinococcus radiodurans* (*D. radiodurans*, *Dr*BphP), *Rhodopseudomonas palustris* (*R. palustris*, *Rp*BphP2 and *Rp*BphP3), and *Stigmatella aurantiaca*, *Sa*BphP1. The chromophore of the bacteriophytochrome is an open tetrapyrrole bilin molecule (**Figure 1**). In the case of Cph1, the chromophore is phycocyanobilin (PCB), The PCB differs from the BV by the lack of double bond character in the A ring and an ethyl-group in the C18 position. The plant phytochromes carry either PCB or phytochromobilin (PΦB) (Rockwell et al., 2006).

PROTEIN CONSTITUENTS AND THE PHOTOACTIVE STATES

A canonical bacteriophytochrome functions as a homodimer and consists of four different protein domains (**Figure 1**). The photosensory unit is made up of so-called PAS (PER, ARNT, SIM), GAF (cGMP phosphodiesterase, adenylate cyclase, FhlA), and PHY (Phytochrome-specific GAF related) domains. The PAS and GAF domains are together called a chromophore-binding domain (CBD). In prokaryotes, the bilin-binding residue resides in the PAS domain, whereas in cyanobacteria and plants the PCB and PΦB pigments are ligated with the GAF domain (Wagner et al., 2007). The fourth subunit, C-terminal of the PHY-domain, functions as biological effector and is often histidine kinase domain (HK). In addition to this canonical domain composition, a large set variation in the domain architecture exists in different phytochrome types. For example, *Synechocystis* Cph2 lacks the PAS domain, while cyanobacteriochromes lack both PAS and PHY domains and function as multi-subunit GAF domains (Rockwell et al., 2006).

The two photostable states of phytochromes are called Pr (red-absorbing state) and Pfr (far-red-absorbing state). The phytochromes with the Pr as dark resting state, like Agp1, Cph1, *Dr*BphP, *Rp*BphP2, and *Sa*BphP1, are called prototypical phytochromes. The bacteriophytochromes, like Agp2 from *A. tumenfaciens* and a phytochrome from *Pseudomonas aeruginosa* (*P. aeruginosa*, *Pa*BphP) thermally revert to the Pfr state and are called bathy phytochromes. In plants where a large variety of phytochrome isoforms exist, most of the phytochromes are prototypical.

The recent structural information has lifted the understanding about the phytochrome function considerably (Vierstra and Zhang, 2011; Burgie and Vierstra, 2014). The CBD fragment of *Dr*BphP was the first ever-published phytochrome structure in atomic resolution (Wagner et al., 2005, 2007). This structure confirmed the bilin-binding pocket and the conformation of BV as a ZZZ_{ssa} conformation (**Figure 1**) (Wagner et al., 2005). It revealed a peculiar figure-of-eight-knot structure which bridges the PAS and GAF domains. The refined CBD structure confirmed how $C3^2$ in the vinyl group in the A-ring of the BV binds via a thioether linkage to the protein. Higher resolution structures revealed a number of coordinated water molecules and buried contacts between the monomeric units as dimerization sites (Wagner et al., 2007). Later, Auldridge et al. utilized this information for the production of monomeric CBD protein (Auldridge et al., 2012). Comparison with the CBD structures of other species set an important basis in the understanding about the photoconversion mechanism of the bilin molecules in the binding pocket (Yang et al., 2007). The high-resolution structures of CBD proteins have naturally been highly beneficial in the design of phytochrome-based near-infrared fluorescent proteins (Shu et al., 2009; Filonov et al., 2011; Auldridge et al., 2012; Shcherbakova and Verkhusha, 2013; Bhattacharya et al., 2014; Yu et al., 2014).

The structures of the full photosensory module (CBD-PHY) of Cph1 (Essen et al., 2008), *Pa*BphP (Yang et al., 2008, 2009), *Dr*BhP (Burgie et al., 2014a; Takala et al., 2014a), and a PhyB isoform from *Arabidopsis thaliana* (Burgie et al., 2014b) have been reported. The structure of the photosensory module resembles a tandem-GAF arrangement with a long connecting helix backbone (Essen et al., 2008). The PHY domain extends near to the chromophore by a so-called tongue-region which has a β-hairpin structure or an α-helical structure in the prototypical and bathy phytochromes, respectively, in their resting state (Essen et al., 2008; Yang et al., 2008). This tongue region contains a conserved PRxSF motif that interacts with the GAF domain near the chromophore and blocks the solvent accessibility to the chromophore-binding pocket. In the Pr state, this tongue motif forms a salt bridge between residues Asp207 and Arg466. The structural studies confirmed the15Za and the 15Ea conformations of the biliverdin in the Pr state and Pfr state, respectively. The BV isomerization leads to changes in the PHY-GAF interaction matrix. The β-hairpin structure in the tongue region disappears and an α-helical structure is stabilized. In the same process, a separation of the sister PHY domains was observed (Takala et al., 2014a). At the moment, the high-resolution structural information of the full-length phytochrome is missing and we need to settle for electron microscopic information (Burgie et al., 2014a,b). Solid-state magic-angle spinning NMR spectroscopy has also revealed detailed information about the hydrogen bond network around the chromophore (Song et al., 2011). Most of the studies have been conducted with Cph1 and oat PhyA proteins, however.

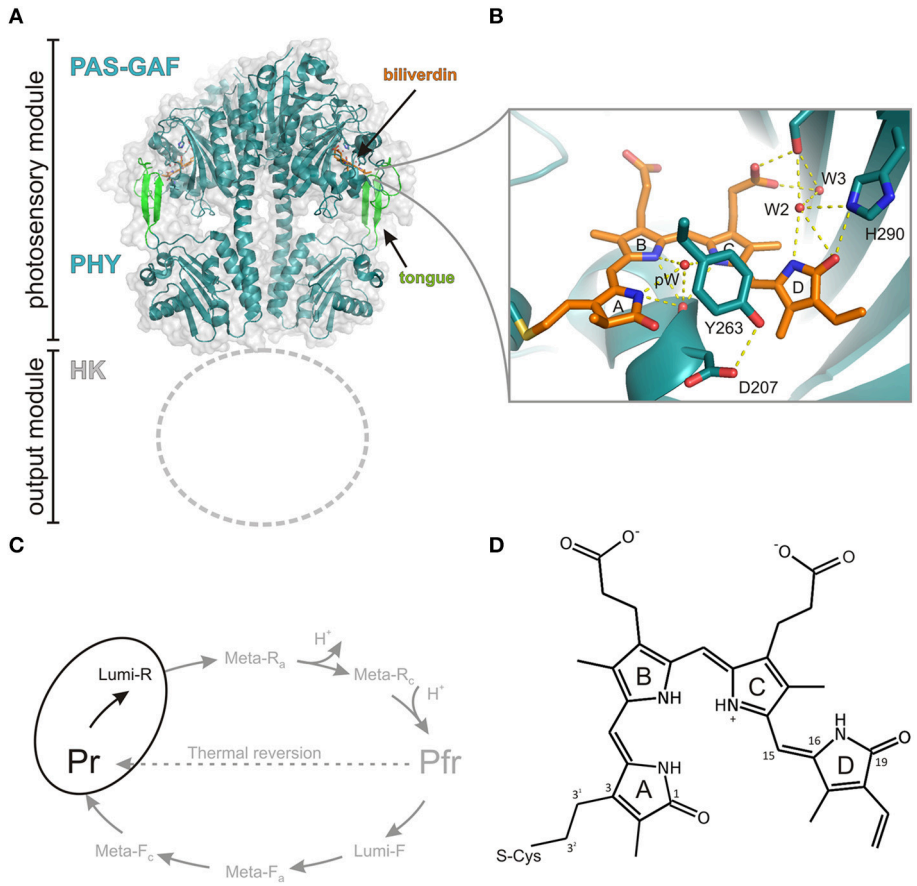

FIGURE 1 | Structure and photocycle of a canonical phytochrome from *Deinococcus radiodurans*. (A) The photosensory module of the phytochrome (PDB code 4O0P, Takala et al., 2014a) forms a parallel dimer that consists of chromophore-binding PAS and GAF domains, which are followed by a PHY domain. Due to the lack of structural information, the N-terminal histidine kinase (HK) domain is not shown. **(B)** A closed view of the biliverdin chromophore and its selected interactions to three water molecules pW (pyrrole water), W2, W3 and amino acids (Asp207, Tyr263, and His290). The panel is based on the high-resolution structure of the CBD fragment (PDB code 4Q0H, Burgie et al., 2014b). **(C)** Photocycle of the phytochrome with its intermediates. In this study, we concentrate on the first step of the forward reaction (Pr -> Lumi-R), highlighted in black. **(D)** The structure of the biliverdin molecule. The key atoms are numbered.

The kinetic information between the Pr and Pfr states relies on visible and vibrational spectroscopic results. The spectroscopic results are, however, difficult to link directly with the structural and chemical changes of the protein. The transition between Pr and Pfr state contains intermediate states (**Figure 1**), initially determined by UV-Vis absorption spectral changes at various temperatures (Eilfeld and Rüdiger, 1985). A similar method has also been used for the characterization of these states by the means of FTIR-spectroscopy (Foerstendorf et al., 2001; Schwinté et al., 2009; Piworski et al., 2010) and FT-Raman spectroscopy (Matysik et al., 1995). Due to the resonance-Raman conditions the signal assignment of the Raman spectra concentrates on the bilin vibrational modes. The FTIR-spectroscopy reveals information also from the protein and the assignment of IR-absorption spectrum is more challenging (Foerstendorf et al., 2001; Barth and Zscherp, 2002; Schwinté et al., 2009; Piworski et al., 2010; Stojkovicì et al., 2015; Velazquez Escobar et al., 2015). The clearest changes are in the 1730 cm^{-1} region, which reports the carbonyl vibrations of the chromophore. Several Amide I transitions have been indicated to the changes in the secondary structure of the protein during the reaction. The first intermediate, which is formed from the excited state bilin molecule is called Lumi-R state (**Figure 1**). It has a characteristic, slightly red-shifted absorption band. The transition between excited Pr* to Lumi-R takes place in ps-ns range as it occurs via the excited state of the bilin molecule. The Pr to Lumi-R reaction is the gateway reaction to the photocycle (**Figure 1**). The quantum yield of the total Pr to Pfr photo reaction is mainly determined by the Pr to Lumi-R-reaction although a back reaction channel from Lumi-R to Pr state has been observed with a time-scale of 100 ns (Mathes et al., 2015). Typically, the fast photo processes are studied by means of ultrafast transient absorption techniques, either in the visible region or in the mid-infrared region, but also fluorescence techniques have been used for determining the excited state lifetimes. The description of this transition will come later in the ultra-fast spectroscopy section. The Lumi-R state transfers to so-called Meta-R_a state in about 100 μs time scale and shows a further red-shifted absorption. The

next transition is Meta-R_a to Meta-R_c transition and it takes place in ms time scale, after which the protein undergoes the Meta-R_c to Pfr reaction. During these phases, kinetic proton transfer reactions take place (van Thor et al., 2001; Borucki et al., 2005). In the transition from Meta-R_a to Meta-R_c state a proton is released to the solvent which is again taken up by the protein in the Meta-Rc to Pfr reaction. The spectroscopic character during these reactions is a decrease of the extinction coefficient at most of the spectral region and a final far-red shift of the absorption. Thus, the decrease of the absorption intensity represents the proton release mechanism in the protein. The site(s) of the released and reclaiming site(s) of protons are unknown, however. A recent study suggests a model of the proton transfer pathway and a tautomeric system in bathy phytochromes (Velazquez Escobar et al., 2015), initially suggested by Lagarias and Rapoport (1980).

Probably due to crystal packing effects, the studies of intermediate states with crystallography-based techniques have been challenging. Up to present, the nature of the various intermediate states has been studied structurally by the means of cryotrapping X-ray crystallography (Yang et al., 2011). Detailed structural changes in the chromophore-binding pocket under illumination at the temperature range of -180°C to -120°C report the initial changes of the chromophore. Besides temperature-dependent experiments, rather extensive mutagenesis approaches have been linked to resonance Raman experiments. Several site-selective mutations in the vicinity of the chromophore (like in Asp207, Tyr263, His290, see **Figure 1**) or in the tongue region (e.g., Arg466) block the photocycle to a certain intermediate state, which can then be then probed by resonance Raman spectroscopy (Wagner et al., 2008).

ULTRA-FAST KINETICS OF THE PR* TO Lumi-R -TRANSITION

Plant phytochromes were the first phytochrome systems to be studied with ultra-fast spectroscopic methods (Sineshchekov, 1995). The initial photoprocesses of the oat phytochrome were determined to be around 30 ps. Similar photoactivated reaction times have been determined for cyanobacterial Cph1 (Heyne et al., 2002; van Thor et al., 2007; Kim et al., 2013). The time-resolved IR-spectroscopy (tr-IR) follows the most intimately of the structural changes of the chromophore and/or its protein environment in the Pr* to Lumi-R reaction. Recently, by using polarized tr-IR experiments (Yang et al., 2012, 2014) elegantly recorded the orientation of $C_{19} = O$ bond of the D-ring after photoexcitation and thus demonstrated the action of the Pr* to Lumi-R reaction. The time constant for the rotation of the D-ring was reported being about 30 ps in Cph1Δ2 (CBD-PHY). In addition, two different PCB orientations were detected in the resting Pr state with significantly different H-bond networks and different rotation yields for both starting orientations (Yang et al., 2014). Longer reaction lifetimes have been reported for bacteriophytochromes, where the excited-state reactions were slower, about 100–300 ps (Toh et al., 2011a,b; Lehtivuori et al., 2013; Mathes et al., 2015). The Agp1 shows a 30 ps photoproduct formation (Schumann et al., 2007; Linke et al., 2013), which would indicate more similar lifetimes with the plant and cyanobacterial phytochromes. However, the lifetime results from *Dr*BphP, *Pa*BphP, and *Sa*BphP, are from truncated systems. By plotting the kinetics of the full-length system with the truncated constructs in (**Figure 2**), we show clearly longer decay times in the transient absorption data and fluorescence data of the shorter constructs than in the full-length system, in line with (Toh et al., 2011a,b; Lehtivuori et al., 2013; Mathes et al., 2015).

In ultra-fast spectroscopic studies, it has become clear that the excited state decay is complex with multi-exponential kinetics (Sineshchekov, 1995). The multi-exponential decay profiles indicate the multiple pathways of the excited Pr* state, including sub-ps S1-relaxation processes, fluorescence, and (multiple) non-radiative (productive and non-productive) decay channels. By using two different excitation wavelengths and a rate distribution modeling, Heyne et al. observed a different type of excited-state kinetics for Cph1 (Heyne et al., 2002). Multi-pulse experiments in the transient absorption data have provided interesting details on the excited-state dynamics of the Pr* states (Kim et al., 2013, 2014). In these experiments a "fluorescing" pool, non-radiative decay pool, and a reactive pathway with the time constants of the reactions between each of the pools are identified (Kim et al., 2014).

All of the above-mentioned studies indicate that the phytochrome systems contain strong non-productive channels. This has a consequence that the photochemical yield of the Pr* to Lumi-R transition is low. In all studied species it has been shown to be between 0.1 and 0.2 for cyanobacterial phytochromes (Schumann et al., 2007; van Thor et al., 2007) and 0.05–0.15 for bacteriophytochromes (Toh et al., 2010; Mathes et al., 2015; Lehtivuori et al., unpublished).

In addition to the multiple decay pathways, the multi-exponential decay profile of the phytochromes may indicate the heterogeneity of the system. The heterogeneity vs. the homogeneity of the Pr state has been under debate the last decade. With NMR-studies (which probes solely the electronic ground states), Song et al. (2011) stated the presence of multiple Pr states in the Cph1 system, whereas the Pfr state is homogenous. Also low temperature single-molecule spectroscopic and site-specific fluorescence experiments indicate heterogeneity in the Pr state in several species (Nieder et al., 2009, 2013; Sineshchekov et al., 2014; Yang et al., 2014). In fact, Nieder et al. revealed, in addition to the heterogeneity between individual particles, spectral diffusion among single particles (Nieder et al., 2009). Thus, the phytochromes switch between the spectral forms even at very low temperatures. Room temperature Raman experiments with the Cph1 systems demonstrate the homogenous behavior of the absorption profile (Dasgupta et al., 2009; Spillane et al., 2009).

EXCITED STATE LIFETIMES—TIME-RESOLVED FLUORESCENCE STUDIES

As mentioned above, a fraction of the excitation in the phytochrome system is emitted as fluorescence and

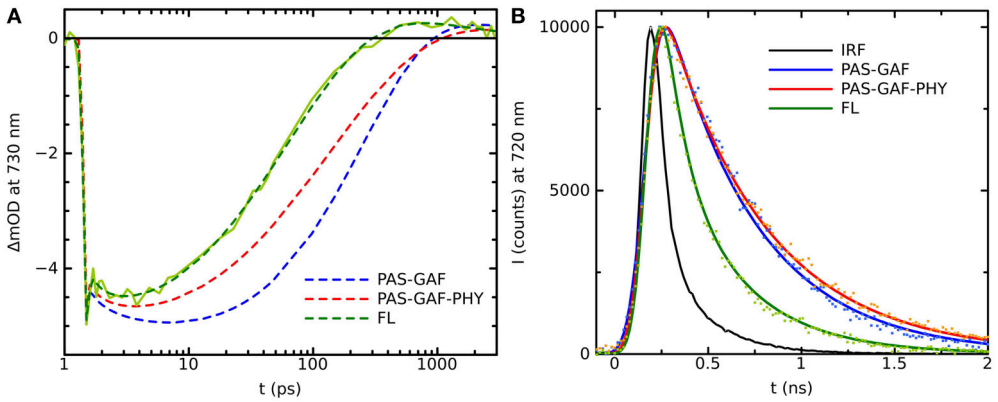

FIGURE 2 | (A) Transition absorption decay traces of PAS-GAF (blue), PAS-GAF-PHY (red), and FL (green) from *Deinococcus radiodurans* excited at 656 nm and monitored at 730 nm. Solid lines show the multiexponential fit of the data, which result in following characteristic lifetimes of each complexes are: 1.5, ps and 320 ps for CBD; 1.2 ps and 170 ps for CBD-PHY; 0.5 ps and 70 ps for FL. **(B)** Emission decays of PAS-GAF, PAS-GAF-PHY, and FL from *Deinococcus radiodurans* excited at 660 nm and monitored at 720 nm. IRF is the instrument response function. The corresponding average lifetimes are: 410 ps for CBD; 550 ps for CBD-PHY; 340 ps for FL. The fluorescence quantum yields are 0.034, 0.017, and 0.008 for CBD, CBD-PHY, and FL, respectively. The samples were prepared as described in Takala et al. (2014b). The pump–probe technique for time-resolved absorption was used to detect fast processes with a time resolution shorter than 0.2 ps. A laser setup with an integrated one-box femtosecond Ti:sapphire laser (Quantronix Integra C) was used to pump two home-built non-collinear optical parametric amplifiers (NOPAs) to produce the (656 ± 14) nm pump pulses. A white light continuum generated in a sapphire crystal was used for probing. After the sample, the probe and reference beams entered a monochromator (Acton), and the detection was set to (730 ± 8) nm. Fluorescence decays of the samples in the nanosecond time scales were measured using a time-correlated single photon counting (TCSPC) system (PicoQuant GmBH). The excitation wavelengths were 660 nm. The monochromator (Jobin Yvon) was used to detect the emission at 720 nm with a single photon avalanche photodiode (MPD). To avoid excessive sample degradation in both time-resolved measurements, the sample solution was cycled using a peristaltic pump (Ismatec). A far-red diode at (750 ± 5) nm (Leading-Tech Laser Co.) was used to transform the sample to the Pr state by constantly illuminating. More details in Lehtivuori et al. (2013).

phytochromes offer great potential for far-red fluorescent proteins (Fischer and Lagarias, 2004; Miller et al., 2006; Shu et al., 2009; Filonov et al., 2011; Auldridge et al., 2012; Shcherbakova and Verkhusha, 2013; Bhattacharya et al., 2014; Yu et al., 2014; Shcherbakova et al., 2015). However, regardless of the low photochemical yield, wild-type phytochromes are typically poorly fluorescent with fluorescence yields ranging from 0.01 to 0.04 (Fischer and Lagarias, 2004; Toh et al., 2010; Zienicke et al., 2011; Auldridge et al., 2012). Often, the low fluorescence yield is linked to photoisomerization activity (i.e., Pr* to Lumi-R production). This, however, is a misconception as the largest decay channel for phytochromes systems are typically the non-productive channels (neither fluorescent nor Lumi-R-forming channel). This can be rationalized from the results of the fluorescence lifetime experiments. As stated above, the initial photoreaction of the cyanobacterial Cph1 take place in about 30 ps, but their fluorescence lifetimes have been measured to be around 1 ns (Otto et al., 2003; Miller et al., 2006). The same is true for plant systems (Sineshchekov, 1995). In bacteriophytochromes the difference between transient absorption and the transient fluorescence experiments is smaller (**Figure 2**) although in the case of Agp1 the photochemical reaction, from Pr* to Lumi-R, is also around 30 ps (Schumann et al., 2007; Linke et al., 2013). The photoreaction times and fluorescence lifetimes of various species are gathered in the **Table 1**. At first glance, the difference between the reported photoreaction times and fluorescence lifetime, together with the low quantum yields, appear puzzling. In fact, fluoroproteins with excited-state lifetimes of about 2 ns and switching ability, would be good fluorescent proteins. For example, the excited state decay times of GFP are 2.8 and 3.3 ns (Striker et al., 1999) and the fluorescence yield can be as high as 0.8. In principle, the time-resolved fluorescence reflects the general lifetime of the excited state and reveals information about the initial photochemistry. There is, however, a caveat. By using ps laser pulses, which are typically used in single-photon counting set ups, only processes slower than about 100 ps are recorded. As fluorescence rates are considerably slower than the photochemical reactions of the phytochromes, only the fluorescence process is detected and other photo-activated processes remain underneath of the excitation pulse. In addition, other fluorescent channels, like the Lumi-R state (Sineshchekov, 1995), may influence to the lifetime experiments as the mixtures of Lumi-R and Pr fluorescent states are detected.

DISCUSSION

We have summarized the key observations of the excited state reactions of the phytochrome systems. In the case of plant and cyanobacterial systems the excited-state reactions take place in about 30 ps and the fluorescence lifetime is above 1 ns. If the photoisomerization is impaired, the excited-state lifetimes can be increased up to 3.2 ns. In the bacteriophytochrome systems the photoreaction and excited-state decay processes have similar photoreaction excited state lifetimes, between 100 and 300 ps, and with site-selective mutations the lifetime can be increased to 870 ps (Bhattacharya et al., 2014). As the plant and cyanobacterial systems bind PCB and PΦB chromophores and the bacteriophytochromes BV chromophore, it is clear that the type of the pigment has a role in the excited state lifetime.

TABLE 1 | Excited state lifetimes of phytochrome systems from various species.

Species	Construct	Cof	Pr lifetime	Yield (%)	References
Agp1	FL	BV	25 ps (ppf), 540 ps* (flt)	9	Schumann et al., 2007; Linke et al., 2013
*Dr*BphP	PAS-GAF	BV	300 ps, 410 (flt)		Lehtivuori et al., 2013; **Figure 2**
*Dr*BphP	PAS-GAF-PHY	BV	170 ps, 550 (flt)		**Figure 2**
*Dr*BphP	FL	BV	70 ps, 340 (flt)		**Figure 2**
*Rp*BphP2	PAS-GAF	BV	175 ps		Toh et al., 2011a,b
*Rp*BphP2	PAS-GAF-PHY	BV	58 ps	13	Toh et al., 2011a,b
*Rp*BphP3	PAS-GAF	BV	300 ps		Toh et al., 2011a,b
*Rp*BphP3	PAS-GAF-PHY	BV	330 ps		Toh et al., 2011a,b
*Sa*BphP1	PAS-GAF	BV	225 ps		Mathes et al., 2015
*Sa*BphP1	PAS-GAF-PHY	BV	85 ps		Mathes et al., 2015
Cph1	PAS-GAF	PCB	30 ps (ppf)	15	Heyne et al., 2002
Cph1	PAS-GAF-PHY	PCB	25 ps (ppf)	13	Heyne et al., 2002; Yang et al., 2014
Cph1	FL	PCB	60 ps (ppf), 1.2 ns (flt)		Otto et al., 2003; Kim et al., 2014
Cph1	FL	PEB	ND(ppf) 3.2 ns (flt)		Otto et al., 2003
PhyB, Oat	FL	PCB	24 ps	15	Andel et al., 1997
PhyA, Oat	FL	PCB	24 ps		Müller et al., 2008
PhyA, Oat	65kDa	PCB	24 ps		Müller et al., 2008

*In many cases the decay is not single exponential. In cases where the average lifetime has not given, the lifetime has been estimated from the given analysis of the paper. *Measured with locked BV, ppf, photoproduct formation; flt, fluorescence lifetime; Cof, Cofactor.*

We emphasize, however, that the excited state reactions of the phytochromes are complex. Three processes, photo-isomerization, fluorescence, and non-photochemical quenching, are competitive, and we still lack a comprehensive picture of these reactions. One of the main stumbling blocks is the description of the interaction lattice of the bilin molecule with its environment. In the highest resolution structural models, obtained from the CBD systems (Wagner et al., 2007; Auldridge et al., 2012; Burgie et al., 2014b) the amino acid positions as well as the oxygen atoms of the water molecules are well-described. Different species show a different amino acid arrangement in the chromophore binding pocket (Mathes et al., 2015). It is, however, too straightforward to link an effect of single amino acid change in the structure directly to the excited state reaction, such as isomerization process. For example, the protonation states of the chromophore and its nearby histidine-residues influence the photochemical behavior of the molecule. Moreover, a labile protonation state can lead to several different conformations of the amino acids around the chromophore, and thus, heterogeneity in the system. Such effects are invisible in the X-ray crystal structures of the protein complexes.

The great sensitivity of the excited state behavior of the chromophore makes possible for other subunits to influence the photochemical reactions of the chromophore from the larger distances. We have shown that on top of the variation in photo-excitation kinetics among different phytochrome species, each type of construct, i.e., the chromophore-binding domain (CBD), the photosensory core (CBD-PHY), or the full-length phytochrome, show differences in the excited state kinetics. We interpret this variation as the feedback mechanisms of the PHY and effector (HK) domains to the CBD domain. The first feedback route is the tongue of the PHY domain (**Figure 1**). In the Pr state, a salt bridge has formed between the Asp207 (from CBD) and Arg466 (in the PHY tongue) whereas in Pfr state the Asp207 coordinates with Ser468 of the tongue (Takala et al., 2014a). The Asp207, part of the conserved DIP motif, locates in the central position in the chromophore-binding pocket and locks the so-called pyrrole (pW in **Figure 1B**) water in its place. Furthermore, the interactions between the sister HK domains may stabilize the PHY domain orientation and further stabilize the chromophore binding pocket via tongue interactions. Moreover, the tongue controls solvent access to the chromophore-binding pocket. Thus, in the case of truncated CBD systems more water molecules occupy the chromophore binding pocket than in the CBD-PHY and FL-systems. The second feedback route could be a trail of water molecules from the protein interior to the nearby D-ring of the chromophore. In our opinion, the water lattices from the protein interior to the nearby chromophore have gained too little attention. The water molecule(s) nearby the NH-group and the CO group of the D-ring, marked as W2 and W3 in (**Figure 1**) and (**Figure 3**) certainly have H-bond character to the D-ring in the Pr-state and play role in the reaction to Lumi-R. These water molecules seem to be rather conserved in the structures of each species published to date and allow (water mediated) hydrogen-bonding network from deeper sites of the protein scaffold, and possibly, proton transfer pathways as well. Unfortunately, it is very demanding to perform a systematic study about the effect of the H-bond network of these water molecules. We propose that these differences are enough to build up slightly different micro-environment around the pigment in its ground and excited state so that it influences the excitation state kinetics of the systems.

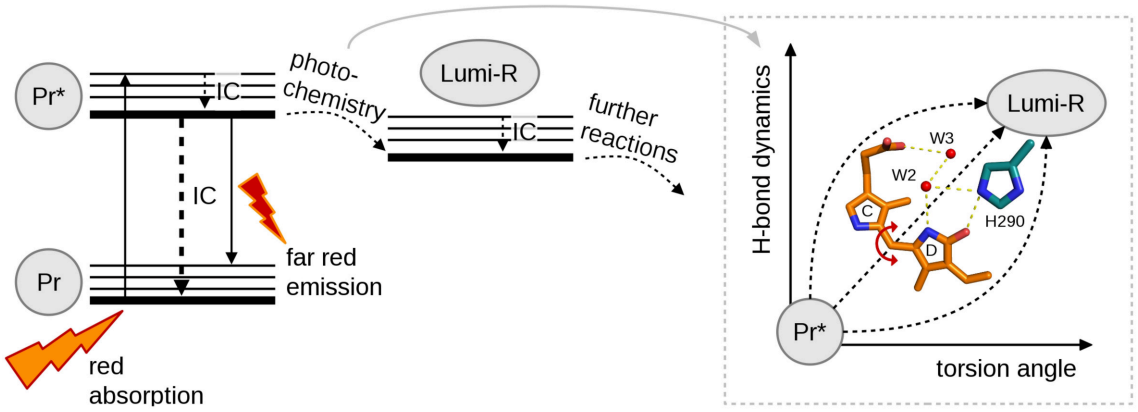

FIGURE 3 | A simplified reaction diagram showing the excitation of molecule with red light from Pr ground state to its singlet excited state (Pr*) followed by internal conversion (IC), fluorescence or photochemistry. Pr* relaxes back to the ground state by IC or far-red fluorescence. For photochemistry at least two coordinates are needed to describe the complete reaction, torsion angle and H-bond dynamics.

THE REACTION COORDINATES TOWARD PRODUCTIVE Lumi-R STATE

Full understanding about the photochemical reaction of phytochromes requires to reveal the most representative reaction coordinate along which the system proceeds from excited Pr* state to Lumi-R state. **Figure 3** summarizes the two main coordinates involved in reaction and how they are linked to structural changes. Temperature-dependent spectroscopic experiments have revealed a barrier along a reaction coordinate, with the activation energy of about 5 kJ/mol (Sineshchekov, 1995; Andel et al., 1996; Kim et al., 2013), which corresponds for example to the strength of one hydrogen bond in a system. By using temperature-dependent fluorescence measurements, a small barrier (2–3 kJ/mol) has been determined in a so-called Pre-Lumi-R to Lumi-R step in Cph1 (Sineshchekov et al., 2014). An obvious reaction coordinate would be the torsional rotation of the D-ring of the bilin chromophore. Rockwell et al. (2009) demonstrated by using circular dichroism spectroscopy that the C15 = C16 isomerization, or the rotation of the D-ring, occurs clockwise in the biliverdin phytochromes whereas the rotation is counter-clockwise in the phytobilin phytochromes (Rockwell et al., 2009). Just following the reaction coordinate of "torsion angle," however, is not sufficient for describing the complete reaction. The other coordinate, called "H-bond dynamics" in (**Figure 3**), has actually many dimensions. The hydrogen bond network can be described between the D-ring and several amino acids and water molecules in its vicinity (**Figure 3**). Actually, rather similar amino acid composition around the D-ring (His290 in case of *D. radiodurans* and in Cph1, with an additional H-bond network of Lys183 and Ser297 in case of *Rp*BphP3, and diminished H-bonding character in the case of *Sa*BphP1) has been reported. Still, these species show different excited-state lifetimes (**Table 1**).

The non-productive channels of excitation energy are very dominant in all phytochrome systems and they are challenging to describe. Kennis and co-workers have put forward one potential pathway for excited state decay, namely an excited-state proton transfer reaction, which is suggested to take place among the pyrrole nitrogens of the chromophore, the pyrrole waters and their coordinating amino acid, Asp207 (Toh et al., 2010; Nieder et al., 2013). Other non-productive channels are most likely related to the tumbling of the D-ring, as its stabilization of the D-ring by the hydrogen bond network leads to stronger fluorescent molecules.

To increase the quantum yield of the fluorescence, internal conversion and photochemistry channels are to be diminished, either by protein mutations or by inserting chromophores with impaired photoisomerization capability (Shcherbakova et al., 2015). By using site-selective mutations for the stabilization of the chromophore D-ring environment has been shown to lead higher fluorescence quantum yields in bacteriophytochromes (Shu et al., 2009; Auldridge et al., 2012; Bhattacharya et al., 2014; Yu et al., 2014). An additional increase in the fluorescence yield may be obtained by rigidifying of the protein scaffold part (Bhattacharya et al., 2014). The photoisomerization pathway can be blocked by incorporating the apoprotein with phycoerythrobilin, PEB, which lack the double bond at the C15 = C16 position of the chromophore (**Figure 1**). In this case, the strain for isomerization is lost and excitation does not lead to the isomerization process. Another way of blocking the isomerization process is to use a BV15Za chromophore where C and D-rings are bridged with an additional linker preventing the rotation of the D-ring (Inomata et al., 2005). In these cases, stronger fluorescence with longer excited state lifetimes, up to 3.2 ns, have been reported for cyanobacterial and bacterial phytochromes (Heyne et al., 2002; Otto et al., 2003; Miller et al., 2006; Zienicke et al., 2011; Kim et al., 2014).

Finally, we would like to point out that the low quantum yields of the photoproductive states are critical only in the

situations where low flux, or ultra-fast femtosecond pulses need to be used. For the studies of slower, thermally driven reactions, ns-laser pulses with sufficient excitation fluxes can be used. As the spectral shift of phytochrome is so large due to the light activated reaction, multiple excitation lead to full photo-conversion of the protein ensemble. With typical illumination systems with 5–20 nm spectral widths, photo-conversion yields of 0.6–0.7 are reached by constant illumination, which allows easily controlling the molecules for a large number of optogenetic purposes.

FUNDING

Finnish Cultural foundation (for JI and HT, 0131067) and Academy of Finland (for HT and HL, 285461 and 277194, respectively) are acknowledged.

ACKNOWLEDGMENTS

We thank G. Groenhof, S. Westenhoff, K. T. Forest, and T. Lamparter for insightful discussions of the topic.

REFERENCES

Andel, F., Lagarias, J. C., and Mathies, R. A. (1996). Resonance Raman analysis of chromophore structure in the lumi-R photoproduct of phytochrome. *Bochemistry* 35, 15997–16008. doi: 10.1021/bi962175k

Andel, F., Hasson, K. C., Gai, F., Anfinrud, P. A., and Mathies, R. A. (1997). Femtosecond time-resolved spectroscopy of the primary photochemistry of phytochrome. *Biospectroscopy* 3, 421–433.

Auldridge, M. E., and Forest, K. T. (2011). Bacterial phytochromes: more than meets the light. *Crit. Rev. Biochem. Mol. Biol.* 46, 67–88. doi: 10.3109/10409238.2010.546389

Auldridge, M. E., Satyshur, K. A., Anstrom, D. M., and Forest, K. T. (2012). Structure-guided engineering enhances a phytochrome-based infrared fluorescent protein. *J. Biol. Chem.* 287, 7000–7009. doi: 10.1074/jbc.M111.295121

Barth, A., and Zscherp, C. (2002). What vibrations tell us about proteins. *Q. Rev. Biophys.* 35, 369–430. doi: 10.1017/S0033583502003815

Bhattacharya, S., Auldridge, M. E., Lehtivuori, H., Ihalainen, J. A., and Forest, K. T. (2014). Origins of fluorescence in evolved bacteriophytochromes. *J. Biol. Chem.* 289, 32144–32152. doi: 10.1074/jbc.M114.589739

Borucki, B., von Stetten, D., Seibeck, S., Lamparter, T., Michael, N., Mroginski, M. A., et al. (2005). Light-induced proton release of phytochrome is coupled to the transient deprotonation of the tetrapyrrole chromophore. *J. Biol. Chem.* 280, 34358–34364. doi: 10.1074/jbc.M505493200

Burgie, E. S., Bussell, A. N., Walker, J. M., Dubiel, K., and Vierstra, R. D. (2014a). Crystal structure of the photosensing module from a red/far-red light-absorbing plant phytochrome. *Proc. Natl. Acad. Sci. U.S.A.* 111, 10176–10184. doi: 10.1073/pnas.1403096111

Burgie, E. S., and Vierstra, R. D. (2014). Phytochromes: an atomic perspective on photoactivation and signaling. *Plant Cell* 26, 4568–4583. doi: 10.1105/tpc.114.131623

Burgie, E. S., Wang, T., Bussell, A. N., Walker, J. M., Li, H., and Vierstra, R. D. (2014b). Crystallographic and electron microscopic analyses of a bacterial phytochrome reveal local and global rearrangements during photoconversion. *J. Biol. Chem.* 289, 24573–24587. doi: 10.1074/jbc.M114.571661

Dasgupta, J., Frontiera, R. R., Taylor, K. C., Lagarias, J. C., and Mathies, R. A. (2009). Ultrafast excited-state isomerization in phytochrome revealed by femtosecond stimulated Raman spectroscopy. *Proc. Natl. Acad. Sci. U.S.A.* 106, 1784–1789. doi: 10.1073/pnas.0812056106

Eilfeld, P., and Rüdiger, W. (1985). Absoprtion spectra of phytochrome intermediates. *Z Naturforsch C* 40, 109–114.

Essen, L. O., Mailliet, J., and Hughes, J. (2008). The structure of a complete phytochrome sensory module in the Pr ground state. *Proc. Natl. Acad. Sci. U.S.A.* 105, 14709–14714. doi: 10.1073/pnas.0806477105

Filonov, G. S., Piatkevich, K. D., Ting, L. M., Zhang, J., Kim, K., and Verkhusha, V. V. (2011). Bright and stable near-infrared fluorescent protein for *in vivo* imaging. *Nat. Biotechnol.* 29, 757–761. doi: 10.1038/nbt.1918

Fischer, A. J., and Lagarias, J. G. (2004). Harnessing phytochrome's glowing potential. *Proc. Natl. Acad. Sci. U.S.A.* 101, 17334–17339. doi: 10.1073/pnas.0407645101

Foerstendorf, H., Benda, C., Gärtner, W., Storf, M., Scheer, H., and Siebert, F. (2001). FTIR studies of phytochrome photoreactions reveal the C=O bands of the chromophore: consequences for its protonation states, conformation, and protein interaction. *Biochemistry* 40, 14952–14959. doi: 10.1021/bi0156916

Gasser, C., Taiber, S., Yeh, C.-M., Wittig, C. H., Hegemann, P., Ryu, S., et al. (2014). Engineering of red-light-activated human cAMP/cGMP-specific phosphodiesterase. *Proc. Natl. Acad. Sci. U.S.A.* 111, 8803–8808. doi: 10.1073/pnas.1321600111

Heyne, K., Herbst, J., Stehlik, D., Esteban, B., Lamparter, T., Hughes, J., et al. (2002). Ultrafast dynamics of phytochrome from the cyanobacterium synechocystis, reconstituted with phycocyanobilin and phycoerythrobilin. *Biophys. J.* 82, 1004–1016. doi: 10.1016/S0006-3495(02)75460-X

Inomata, K., Hammam, M. A., Kinoshita, H., Murata, Y., Khawn, H., Noack, S., et al. (2005). Sterically locked synthetic bilin derivatives ad phytochrome Agp1 from Agrobacterium tumenfacies form photosensitive Pr- and Pfr-like adducts. *J. Biol. Chem.* 280, 24491–24497. doi: 10.1074/jbc.M504710200

Kim, P. W., Rockwell, N. C., Freer, L. H., Chang, C.-W., Martin, S. S., Lagarias, J. C., et al. (2013). Unraveling the primary isomerization dynamics in Cyanobacterial Phytochrome Cph1 with multipulse manipulations. *J. Phys. Chem. Lett.* 4, 2605–2609. doi: 10.1021/jz401443q

Kim, P. W., Rockwell, N. C., Martin, S. S., Lagarias, J. C., and Larsen, D. S. (2014). Dynamic inhomogeneity in the Photodynamics of Cyanobacterial Phytochrome Cph1. *Biochemistry* 53, 2818–2826. doi: 10.1021/bi500108s

Lagarias, J. C., and Rapoport, H. (1980). Chromopeptides from phytochrome. the structure and linkage of the Pr form of the phytochrome chromophore. *J. Am. Chem. Soc.* 102, 4821–4828. doi: 10.1021/ja00534a042

Lehtivuori, H., Rissanen, I., Takala, H., Bamford, J., Tkachenko, N. V., and Ihalainen, J. A. (2013). Fluorescence properties of the chromophore-binding domain of bacteriophytochrome from Deinococcus radiodurans. *J. Phys. Chem. B* 117, 11049–11057. doi: 10.1021/jp312061b

Linke, M., Yang, Y., Zienicke, B., Hammam, M. A. S., von Haimberger, T., Zacarias, A., et al. (2013). Electronic transitions and heterogeneity of the bacteriophytochrome Pr absorption band: an angle balanced polarization resolved femtosecond VIS pump–IR probe study. *Biophys. J.* 105, 1756–1766. doi: 10.1016/j.bpj.2013.08.041

Mathes, T., Ravensbergen, J., Kloz, M., Gleichemann, T., Gallagher, K. D., Woitowich, N. C., et al. (2015). Femto- to microsecond photodynamics of an unusual bacteriophytochrome. *J. Phys. Chem. Lett.* 6, 239-243. doi: 10.1021/jz502408n

Matysik, J., Hildebrandt, P., Schlamann, W., Braslavsky, S. E., and Schaffner, K. (1995). Fourier-transform resonance raman spectroscopy of intermediates of the phytochrome photocycle. *Biochemistry* 34, 10497–10507. doi: 10.1021/bi00033a023

Miller, A. E., Fischer, A. J., Laurence, T., Hollars, C. W., Saykally, R. J., Lagarias, J. C., et al. (2006). Single-molecule dynamics of phytochrome-bound fluorophores probed by fluorescence correlation spectroscopy. *Proc. Natl. Acad. Sci. U.S.A.* 103, 11136–11141. doi: 10.1073/pnas.0604724103

Möglich, A., and Moffat, K. (2010). Engineered photoreceptors as novel optogenetic tools. *Photocehm. Photobiol. Sci.* 9, 1286–1300. doi: 10.1039/c0pp00167h

Müller, M. G., Lindner, I., Martin, I., Gärtner, W., and Holzwarth, A. R. (2008). Femtosecond kinetics of photoconversion of the highre plant photoreceptor phytochrome carrying native and modified chromophores. *Biophys. J.* 94, 4370–4382. doi: 10.1529/biophysj.106.091652

Nieder, J. B., Brecht, M., and Bittl, R. (2009). Dynamic intracomplex heterogeneity of phytochrome. *J. Am. Chem. Soc.* 131, 69–71. doi: 10.1021/ja8058292

Nieder, J. B., Stojkovic, E. A., Moffat, K., Forest, K. T., Lamparter, T., Bittl, R., et al. (2013). Pigment-protein interactions in phytochromes probed by fluorescence line narrowing spectroscopy. *J. Phys. Chem. B* 117, 14940 – 14950. doi: 10.1021/jp409110q

Otto, H., Lamparter, T., Borucki, B., Hughes, J., and Heyn, M. P. (2003). Dimerization and inter-chromophore distance of Cph1 phytochrome from synechocystis, as monitored by fluorescence homo and hetero energy transfer. *Biochemistry* 42, 5885–5895. doi: 10.1021/bi026946y

Piatkevich, K. D., Subach, F. V., and Verkhusha, V. V. (2013a). Far-red light photoactivable near-infrared fluorescent proteins engineered from a bacterial phytochrome. *Nat. Commun.* 4, 1–10. doi: 10.1038/ncomms3153

Piatkevich, K. D., Subach, F. V., and Verkhusha, V. V. (2013b). Engineering of bacterial phytochromes for near-infrared imaging, sensing, and light-control in mammals. *Chem. Soc. Rev.* 42, 3441–3452. doi: 10.1039/c3cs35458j

Piworski, P., Ritter, E., Hofmann, K.-P., Hildebrandt, P., von Stetten, D., Scheerer, P., et al. (2010). Light-induced activation of bacterial phytochrome agp1 monitored by static and time-resolved FTIR spectroscopy. *Chemphyschem* 11, 1207 – 1214. doi: 10.1002/cphc.200901008

Rockwell, N. C., Shang, L., Martin, S. S., and Lagarias, J. C. (2009). Distinct classes of red/far-red photochemistry within the phytochrome superfamily. *Proc. Natl. Acad. Sci. U.S.A.* 106, 6123–6127. doi: 10.1073/pnas.0902370106

Rockwell, N. C., Su, Y. S., and Lagarias, J. C. (2006). Phytochrome structure and signaling mechanisms. *Annu. Rev. Plant Biol.* 57, 837–858 doi: 10.1146/annurev.arplant.56.032604.144208

Schumann, C., Groß, R., Michael, N., Lamparter, T., and Diller, R. (2007). Sub-picosecond mid-infrared spectroscopy of phytochrome Agp1 from agrobacterium tumefaciens. *Chemphyschem* 8, 1657–1663. doi: 10.1002/cphc.200700210

Schwinté, P., Gärtner, W., Sharda, S., Mroginski, M.-A., Hildebrandt, P., and Siebert, F. (2009). The photoreactions of recombinant phytochrome CphA from the cyanobacterium *Calothrix* PCC7601: a low-temperature UV-Vis and FTIR study. *Photochem. Photobiol.* 85, 239–249. doi: 10.1111/j.1751-1097.2008.00426.x

Shcherbakova, D. M., Baloban, M., and Verkhusha, V. V. (2015). Near-infrared fluorescent proteins engineered from bacterial phytochromes. *Curr. Opin. Chem. Biol.* 27, 52–63. doi: 10.1016/j.cbpa.2015.06.005

Shcherbakova, D. M., and Verkhusha, V. V. (2013). Near-infrared fluorescent proteins for multicolor *in vivo* imaging. *Nat. Methods* 10, 751–754. doi: 10.1038/nmeth.2521

Shimizu-Sato, S., Huq, E., Tepperman, J. M., and Quail, P. H. (2002). A light-switchable gene promoter system. *Nat. Biotechnol.* 20, 1041–1044. doi: 10.1038/nbt734

Shu, X., Royant, A., Lin, M. Z., Aguilera, T. A., Lev-Ram, V., Steinbach, P. A., et al. (2009). Mammalian expression of infrared fluorescent proteins engineered from a bacterial phytochrome. *Science* 324, 804–807. doi: 10.1126/science.1168683

Sineshchekov, V. (1995). Photobiophysics and photobiochemistry of the heterogenous phytochrome system. *Biochim. Biophys. Acta* 1228, 125–164. doi: 10.1016/0005-2728(94)00173-3

Sineshchekov, V., Mailliet, J., Psakis, G., Feilke, K., Kopycki, J., Zeidler, M., et al. (2014). Tyrosine 263 in cyanobacterial phytochrome Cph1 optimizes photochemistry at the prelumi-R⟶lumi-R step. *Photochem. Photobiol.* 90, 786–795. doi: 10.1111/php.12263

Song, C., Psakis, G., Lang, C., Mailliet, J., Gärtner, W., Hughes, J., et al. (2011). Two ground state isoforms and a chromophore D-ring photoflip triggering extensive intramolecular changes in a canonical phytochrome. *Proc. Natl. Acad. Sci. U.S.A.* 108, 3842–3847. doi: 10.1073/pnas.1013377108

Spillane, K. M., Dasgupta, J., Lagarias, J. C., and Mathies, R. A. (2009). Homogeneity of Phytochrome Cph1 vibronic absorption revealed by resonance raman intensity analysis. *J. Am. Chem. Soc.* 131, 13946–13948. doi: 10.1021/ja905822m

Stojkovic, E. A., Toh, K. C., Alexandre, M. T. A., Baclayon, M., Moffat, K., and Kennis, J. T. M. (2015). FTIR spectroscopy revealing light-dependent refolding of the conserved tongue region of bacteriophytochrome. *J. Phys. Chem. Lett.* 5, 2512-2515. doi: 10.1021/jz501189t

Striker, G., Subramaniam, V., Seidel, C. A. M., and Volkmer, A. (1999). Photochromicity and fluorescence lifetimes of green fluorescent protein. *J. Phys. Chem. B* 40, 8612–8617. doi: 10.1021/jp991425e

Takala, H., Björling, A., Berntsson, O., Lehtivuori, H., Niebling, S., Hoernke, M., et al. (2014a). Signal amplification and transduction in phytochrome photosensors. *Nature* 509, 245–248. doi: 10.1038/nature13310

Takala, H., Lehtivuori, H., Hammarén, H., Hytönen, V. P., and Ihalainen, J. A. (2014b). Connection between absorption properties and conformational changes in deinococcus radiodurans phytochrome. *Biochemistry* 53, 7076–7085. doi: 10.1021/bi501180s

Toh, K. C., Stojkovic, E. A., Rupenyan, A. B., van Stokkum, I. H., Salumbides, M., Groot, M. L., et al. (2011b). Primary reactions of bacteriophytochrome observed with ultrafast mid-infrared spectroscopy. *J. Phys. Chem. A* 115, 3778–3786. doi: 10.1021/jp106891x

Toh, K. C., Stojkovic, E. A., van Stokkum, I. H., Moffat, K., and Kennis, J. T. (2010). Proton-transfer and hydrogen-bond interactions determine fluorescence quantum yield and photochemical efficiency of bacteriophytochrome. *Proc. Natl. Acad. Sci. U.S.A.* 107, 9170–9175. doi: 10.1073/pnas.0911535107

Toh, K. C., Stojkovic, E. A., van Stokkum, I. H., Moffat, K., and Kennis, J. T. (2011a). Fluorescence quantum yield and photochemistry of bacteriophytochrome constructs. *Phys. Chem. Chem. Phys.* 13, 11985–11997. doi: 10.1039/c1cp00050k

van Thor, J. J., Boruki, B., Crielaard, W., Otto, H., Lamparter, T., Hughes, J., et al. (2001). Light-induced proton release and proton uptake reactions in the cyanobacterial phytochrome Cph1. *Biochemistry* 82, 11460 –11471. doi: 10.1021/bi002651d

van Thor, J. J., Ronayne, K. L., and Towrie, M. (2007). Formation of the early photoproduct lumi-R of cyanobacterial phytochrome cph1 observed by ultra-fast mid-infrared spectroscopy. *J. Am. Chem. Soc.* 129, 126–132. doi: 10.1021/ja0660709

Velazquez Escobar, F., Piwowarski, P., Salewski, J., Michael, N., Fernandez Lopez, M., Rupp, A., et al. (2015). A protonation-coupled feedback mechanism controls the signalling process in bathy phytochromes. *Nat. Chem.* 7, 423–430. doi: 10.1038/nchem.2225

Vierstra, R. D., and Zhang, J. (2011). Phytochrome signaling: solving the Gordian knot with microbial relatives. *Trends Plant Sci.* 16, 417–426. doi: 10.1016/j.tplants.2011.05.011

Wagner, J. R., Brunzelle, J. S., Forest, K. T., and Vierstra, R. D. (2005). A light-sensing knot revealed by the structure of the chromophore-binding domain of phytochrome. *Nature* 438, 325–331. doi: 10.1038/nature04118

Wagner, J. R., Zhang, J., Brunzelle, J. S., Vierstra, R. D., and Forest, K. T. (2007). High resolution structure of Deinococcus bacteriophytochrome yields new insights into phytochrome architecture and evolution. *J. Biol. Chem.* 282, 12298–12309. doi: 10.1074/jbc.M611824200

Wagner, J. R., Zhang, J., von Stetten, D., Günther, M., Murgida, D. H., Mroginski, M. A., et al. (2008). Mutational analysis of Deinococcus radiodurans bacteriophytochrome reveals key amino acids necessary for the photochromicity and proton exchange cycle of phytochromes. *J. Biol. Chem.* 283, 12212–12226. doi: 10.1074/jbc.M709355200

Yang, X., Kuk, J., and Moffat, K. (2008). Crystal structure of *Pseudomonas aeruginosa* bacteriophytochrome: photoconversion and signal transduction. *Proc. Natl. Acad. Sci. U.S.A.* 105, 14715–14720. doi: 10.1073/pnas.0806718105

Yang, X., Kuk, J., and Moffat, K. (2009). Conformational differences between the Pfr and Pr states in *Pseudomonas aeruginosa* bacteriophytochrome. *Proc. Natl. Acad. Sci. U.S.A.* 106, 15639–15644. doi: 10.1073/pnas.0902178106

Yang, X., Ren, Z., Kuk, J., and Moffat, K. (2011). Temperature-scan cryocrystallography reveals reaction intermediates in bacteriophytochrome. *Nature* 479, 428–432. doi: 10.1038/nature10506

Yang, X., Stojkovic, E. A., and Moffat, K. (2007). Crystal structure of the chromophore binding domain of an unusual bacteriophytochrome, RpBphP3, reveals residues that modulate photoconversion. *Proc. Natl. Acad. Sci. U.S.A.* 104, 12571-12576. doi: 10.1073/pnas.0701737104

Yang, Y., Linke, M., von Haimberger, T., Hahn, J., Matute, R., Gonzaìlez, L., et al. (2012). Real-time tracking of phytochrome's orientational changes during Pr photoisomerization. *J. Am. Chem. Soc.* 134, 1408–1411. doi: 10.1021/ja209413d

Yang, Y., Linke, M., von Haimberger, T., Matute, R., Gonzaìlez, L., Schmieder, P., et al. (2014). Active and silent chromophore isoforms for phytochrome

Pr photoisomerization: an alternative evolutionary strategy to optimize photoreaction quantum yields. *Struct. Dyn.* 1, 014701. doi: 10.1063/1.4865233

Yu, D., Gustafson, W. C., Han, C., Lafaye, C., Noirclerc-Savoye, M., Ge, W. P., et al. (2014). An improved monomeric infrared fluorescent protein for neuronal and tumour brain imaging. *Nat. Commun.* 5, 3626. doi: 10.1038/ncomms4626

Zienicke, B., Chen, L.-Y., Khawn, H., Hammam, M. A. S., Kinoshita, H., Reichert, J., et al. (2011). Fluorescence of phytochrome adducts with synthetic locked chromophores. *J. Biol. Chem.* 286, 1103–1113. doi: 10.1074/jbc.M110.155143

Conflict of Interest Statement: The authors declare that the research was conducted in the absence of any commercial or financial relationships that could be construed as a potential conflict of interest.

frontiers in Molecular Biosciences

ORIGINAL RESEARCH
published: 25 November 2015
doi: 10.3389/fmolb.2015.00065

Removal of Chromophore-Proximal Polar Atoms Decreases Water Content and Increases Fluorescence in a Near Infrared Phytofluor

Heli Lehtivuori[1,2], Shyamosree Bhattacharya[1], Nicolaas M. Angenent-Mari[1], Kenneth A. Satyshur[1] and Katrina T. Forest[1]**

[1] Department of Bacteriology, University of Wisconsin-Madison, Madison, WI, USA, [2] Department of Physics, Nanoscience Center, University of Jyväskylä, Jyväskylä, Finland

OPEN ACCESS

Edited by:
Tilo Mathes,
Vrije Universiteit Amsterdam,
Netherlands

Reviewed by:
Petr Leiman,
Ecole Polytechnique Federale de Lausanne, Switzerland
Wolfgang Gärtner,
Max-Planck-Institut für Chemische Energiekonversion, Germany
Hernán Ruy Bonomi,
Fundación Instituto Leloir-CONICET, Argentina

***Correspondence:**
Heli Lehtivuori
heli.lehtivuori@jyu.fi;
Katrina T. Forest
forest@bact.wisc.edu

Specialty section:
This article was submitted to Biophysics, a section of the journal Frontiers in Molecular Biosciences

Received: 01 August 2015
Accepted: 02 November 2015
Published: 25 November 2015

Citation:
Lehtivuori H, Bhattacharya S, Angenent-Mari NM, Satyshur KA and Forest KT (2015) Removal of Chromophore-Proximal Polar Atoms Decreases Water Content and Increases Fluorescence in a Near Infrared Phytofluor. Front. Mol. Biosci. 2:65. doi: 10.3389/fmolb.2015.00065

Genetically encoded fluorescent markers have revolutionized cell and molecular biology due to their biological compatibility, controllable spatiotemporal expression, and photostability. To achieve *in vivo* imaging in whole animals, longer excitation wavelength probes are needed due to the superior ability of near infrared light to penetrate tissues unimpeded by absorbance from biomolecules or autofluorescence of water. Derived from near infrared-absorbing bacteriophytochromes, phytofluors are engineered to fluoresce in this region of the electromagnetic spectrum, although high quantum yield remains an elusive goal. An invariant aspartate residue is of utmost importance for photoconversion in native phytochromes, presumably due to the proximity of its backbone carbonyl to the pyrrole ring nitrogens of the biliverdin (BV) chromophore as well as the size and charge of the side chain. We hypothesized that the polar interaction network formed by the charged side chain may contribute to the decay of the excited state via proton transfer. Thus, we chose to further probe the role of this amino acid by removing all possibility for polar interactions with its carboxylate side chain by incorporating leucine instead. The resultant fluorescent protein, WiPhy2, maintains BV binding, monomeric status, and long maximum excitation wavelength while minimizing undesirable protoporphyrin IXα binding in cells. A crystal structure and time-resolved fluorescence spectroscopy reveal that water near the BV chromophore is excluded and thus validate our hypothesis that removal of polar interactions leads to enhanced fluorescence by increasing the lifetime of the excited state. This new phytofluor maintains its fluorescent properties over a broad pH range and does not suffer from photobleaching. WiPhy2 achieves the best compromise to date between high fluorescence quantum yield and long illumination wavelength in this class of fluorescent proteins.

Keywords: chromophore binding domain (CBD), *Deinococcus radiodurans*, Wisconsin infrared phytofluor (WiPhy2), tetrapyrrole, excitation-emission matrix (EEM)

INTRODUCTION

Fluorophores active in the near infrared (NIR) attract ongoing attention due to their diverse applications in biomedical research, materials science and related fields. They allow imaging with minimal autofluorescence and light scattering in animals, and deep tissue penetration (Weissleder, 2001). *In vivo*, real-time advanced imaging studies and vascular mapping of the heart and brain, the visualization of tumors and plaques, and guided surgery are aspects of fundamental research and translational applications that will benefit substantially from the creation of improved NIR fluorophores. The development of simple, stable, non-toxic, modular, and small molecular weight NIR platforms is thus of great interest to the biomedical community and has proceeded both in the realm of chemical biology and fluorescent proteins. In the former category, there are several classes of small molecule NIR dyes available including nanoparticles, cyanine dyes, phthalocyanine, and squaraine dyes (Escobedo et al., 2010; Hahn et al., 2011; Luo et al., 2011; Gibbs, 2012; Battistelli et al., 2015). The promise of genetically encoded NIR fluorescent proteins has, on the other hand, led to a renaissance in research of engineered fluorescent proteins, based both on Green Fluorescent Protein-like β-barrel folds and more recently on bacteriophytochromes (Zhang et al., 2002; Gibbs, 2012; Guo et al., 2014; Marx, 2014).

Bacteriophytochromes (BphPs) are promising design templates for NIR fluorescent proteins. Their covalent association with the linear tetrapyrrole biliverdin IXα (BV) allows BphPs to absorb light in the red and far-red region of the spectrum. As an intermediate of normal mammalian heme catabolism, BV does not necessarily need to be provided exogenously in order to achieve *in vivo* fluorescence. Thus, great effort has gone into improving the photophysical and chemical properties of microbial phytochrome-based dyes in the last decade (Marx, 2014). Fluorescence quantum yields have increased, molecular weight has decreased, and excitation wavelengths are both extended farther to the red (above 700 nm) while also being available in multiple colors (**Figure 1**). The use of these tools promises to extend fluorescence imaging to live animals. Further development in all of these areas will bring phytofluors into quotidian use.

The family of phytochromes shares a conserved photosensory protein core consisting of a PAS (Per/Arndt/Sim) domain, a GAF (GMP phospho-diesterase/adenyl cyclase/FhlA) domain and a PHY (phytochrome) domain. While full-length phytochromes are required for biological activity, fluorescence protein development is concentrated to PAS and GAF domains, which together form a chromophore-binding domain (CBD). Wild-type BphPs are dimers, but the strength of the dimerization interface varies among phytochromes (Takala et al., 2015). To increase BphP utility as a fluorophore, residues in this GAF dimer interface have been rationally mutated to create a monomer (Bhattacharya et al., 2014; Yu et al., 2014).

This initial monomeric CBD from *Deinococcus radiodurans* ($DrCBD_{mon}$) has a low fluorescence quantum yield (0.029 ± 0.001; Auldridge et al., 2012; Bhattacharya et al., 2014). In order to rationally improve this yield, one can imagine engineering the protein to affect changes in the kinetics of the competing processes that take place in the excited state, in particular internal conversion or isomerization in the BV C15 = C16 double bond leading to the first relatively stable photoproduct (Lumi-R). Much attention has been paid in particular to the Y263F and D207H substitutions, in large part because of the critical roles these positions play in the normal photocycle (Sineshchekov et al., 2014). Recently it has been shown that the H207 residue is not required for enhanced fluorescence of Infrared Fluorescent Protein (IFP)1.4 (Shu et al., 2009; Bhattacharya et al., 2014) and does not markedly increase fluorescence in Wisconsin Infrared Phytofluor (WiPhy = $DrCBD_{mon}$-Y263F/D207H) (Auldridge et al., 2012). Indeed in IFP2.0, this position is a Thr (Yu et al., 2014). The side chains introduced by these mutations change the hydrogen-bonding network of the binding pocket (Toh et al., 2010, 2011a,b; Zienicke et al., 2011, 2013; Auldridge et al., 2012; Bhattacharya et al., 2014; Yu et al., 2014).

Our motivation in this study has been to explore the effects of a nonpolar substitution of residue 207, which is in closest proximity to the four nitrogen atoms of BV and the ordered pyrrole water found interacting with three of them. We chose to substitute Leu because it is the nonpolar side chain whose structure most closely mimics that of the native Asp. The size of Leu should prevent adventitious binding of Protoporphyrin IXα (PPIXα), which interacts covalently with H207-carrying variants (Fischer and Lagarias, 2004; Wagner et al., 2008; Lehtivuori et al., 2013; Burgie et al., 2014). The

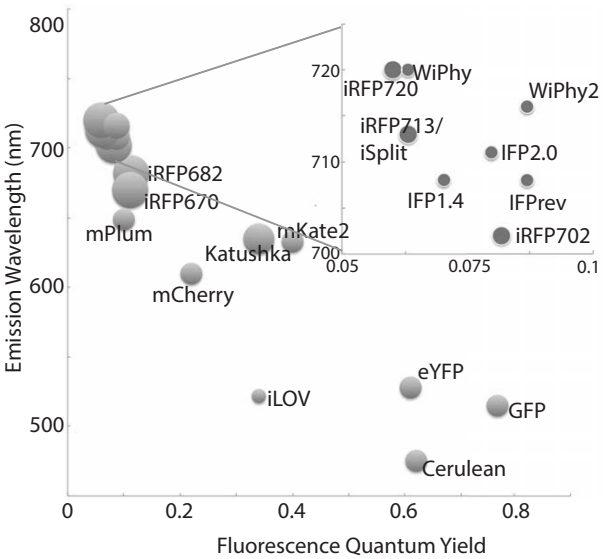

FIGURE 1 | A representative sampling of historical and currently favored genetically-encoded fluorescent probes are classified by excitation wavelength and fluorescence quantum yield. The relative size of each fluorophore, taking both polypeptide molecular mass and oligomeric status into account, is proportional to the diameter of its marker. Quantum yields and emission wavelengths are taken from the literature (Johnson et al., 1962; Ormö et al., 1996; Rizzo et al., 2004; Shaner et al., 2004; Shcherbo et al., 2007, 2009; Shu et al., 2009; Auldridge et al., 2012; Christie et al., 2012; Filonov and Verkhusha, 2013; Shcherbakova and Verkhusha, 2013; Yu et al., 2014) except for WiPhy2 (this work).

evidence for PPIXα binding includes the fact that fluorescence spectroscopy of the D207A apoprotein assembled with BV detected two fluorescent species, one matching the absorption and emission spectra of incorporated PPIXα, and a second matching those for BV (Fischer and Lagarias, 2004; Lehtivuori et al., 2013).

In this paper we engineered two $DrCBD_{mon}$ variants containing D207L; $DrCBD_{mon}$-D207L itself and $DrCBD_{mon}$-Y263F/D207L (WiPhy2). We present a detailed comparative analysis of the spectroscopic properties of these two variants, as well as the three-dimensional structure of WiPhy2. This structural and spectroscopic study improves the integrated understanding of the fluorescence properties of BphPs.

MATERIALS AND METHODS

Cloning

Unless otherwise indicated, all reagents and solvents were obtained from commercial suppliers and used without further purification. Novel constructs were made by QuickChange mutagenesis (Stratagene, La Jolla, CA) using an existing pET21a plasmid encoding $DrCBD_{mon}$ with N-terminal T7 and C-terminal hexahistidine tags (Auldridge et al., 2012). The following primers were used to introduce the appropriate mutations: D207L: 5′TTTCCCGCGTCGCTCATTCCGGCGC AGGCC3′; 5′TGCGCCGGAATGAGCGACGCGGGAAAAC GG3′ and Y263F: 5′CATGCACATGCAGTTCCTGCGGAAC A3′; 5′CATGTTCCGCAGGAACTGCATGTGCA3′. Correct sequences of clones were verified using DNA sequencing at the University of Wisconsin-Madison Biotechnology Center.

Protein Purification

Constructs encoding $DrCBD_{mon}$ variants were transformed into BL21 (DE3) expression cells and grown at 37°C in LB-amp (0.1 mg/ml ampicillin). At OD_{600} 0.5, cells were induced with isopropyl—β-D-1-thiogalactopyranoside at 28°C. Cells were harvested after 4 h by centrifugation at 5000 × g for 30 min, resuspended in lysis buffer (25 mM Tris buffer, pH 8.0, 50 mM NaCl, 5 mM imidazole), and lysed by sonication. After clarification by centrifugation at 40,000 × g for 30 min, the supernatant was incubated with a final concentration of 0.16 mM BV (Frontier Scientific Inc., Logan, UT) in the dark overnight. Proteins were affinity-purified under green light using nickel-nitrilotriacetic acid resin (Qiagen, Valencia, CA). Further purification was performed using hydrophobic interaction on a phenyl-Sepharose column (GE Healthcare) to separate apo- and holophytochrome. Ammonium sulfate was added to the protein at a final concentration of 0.35 M prior to loading. All buffers were filtered and degassed before use. Purified samples were dialyzed overnight against a 200-fold excess volume of (30 mM Tris·HCl, pH 8.0). Finally samples were concentrated to 20 mg/ml, flash-vitrified, and stored at −80°C. Unless otherwise indicated, the samples were kept in the dark before and during the experiments.

Structure Determination by X-Ray Crystallography

Purified WiPhy2 protein was crystallized by hanging drop vapor diffusion with drops containing a 1:1 mixture of protein and reservoir solution (20% PEG400 and 0.1 M phosphate citrate buffer at pH 4.0). The crystal used for data collection at LS-CAT was soaked for 5 min in a cryoprotectant of 20% glycerol in mother liquor before vitrification.

Data were collected at the Advanced Photon Source, beamline LSCAT 21-ID-D at a wavelength of 0.9787 Å on a Mar 300 CCD detector. The data were integrated and scaled using HKL2000 (**Table 1**).

The structure was solved in two stages. First, an initial data set collected on a Bruker Microstar rotating anode/R6000 Proteum CCD detector setup from a crystal from the same crystallization

TABLE 1 | WiPhy2 X-ray data collection and structure determination statistics.

	Rotating anode (PDB ID 4ZRR)	LS-CAT ID-D (PDB ID 4Z1W)
DATA COLLECTION		
Wavelength, Å	1.5418	0.9785
Resolution*, Å	47.60–1.50 (1.60–1.50)	23.8–1.30 (1.35–1.30)
Space Group	C2	C2
Unit Cell [a, b, c (Å), β (°)]	94.8, 55.1, 69.8, 91.9	94.4, 53.3, 65.7, 90.9
No. Unique Reflections	57,159	80,665
No. Unique Reflections Obs.	54,864	77,741
Completeness, %	96.0 (91.2)	96.5 (94.3)
Redundancy	2.9 (2.0)	7.7 (7.7)
<I/σI>	14.69 (4.83)	33.2 (4.0)
Wilson B value, $Å^2$	10.8	10.5
$R^{\dagger}_{sym}$, %	5.0 (17.9)	5.2 (35.3)
REFINEMENT		
Resolution, Å	25.0–1.50 (1.54–1.51)	23.22–1.30 (1.33–1.30)
R_{work}/R_{free}, ‡ %	16.0/19.5 (18.8/27.5)	14.4/16.0 (15.1/17.5)
Rms deviations Bonds, Å	0.007	0.006
Rms deviations Angles, °	1.39	1.31
Ramachandran Statistics		
Allowed	98.6	98.0
Generously allowed	1.4	2.0
No. Atoms		
Protein	2547	2551
Ligand	86	86
Water	288	231
<B factor>, $Å^2$		
Protein	18.5	16.5
Ligand	9.1	7.8
Water	28.4	26.1

*The highest resolution bin is indicated in parentheses.

†$R_{sym} = \Sigma\Sigma j|Ij - <I>|\Sigma Ij$, where Ij is the intensity measurement for reflection j and<I> is the mean intensity for multiply recorded reflections.

‡$R_{work}/R_{free} = \Sigma||F_{obs}|- |F_{calc}||/|F_{obs}|$, where the working and free R factors are calculated by using the working and free reflection sets, respectively. For the R_{free}, 5% of the total reflections were held aside throughout refinement.

experiment was phased by molecular replacement using 4O8G as a model, and refined. This structure was used to phase the higher resolution data set by molecular replacement using Phaser (McCoy et al., 2007). Those reflections assigned to the R_{free} bin were kept consistent.

For refinement, BV was linked to the Cys24 sulfur with a link entry in the input pdb. To create a library file for the ligand, BV was energy minimized using the Sybyl®-X Suite (Certara) employing the Tripos (Clark et al., 1989) Force Field after correct assignment of the atom types. The restraints for the two enantiomers of the chromophore (designated LBV and LBW) were generated using the Phenix (Adams et al., 2010) routine Elbow without energy minimization. Refinement and model building were carried out in iterative cycles using Refmac5.8.0107 and Coot V0.8.1 (Emsley et al., 2010; Murshudov et al., 2011). The BV chromophore is found with the A-ring C2

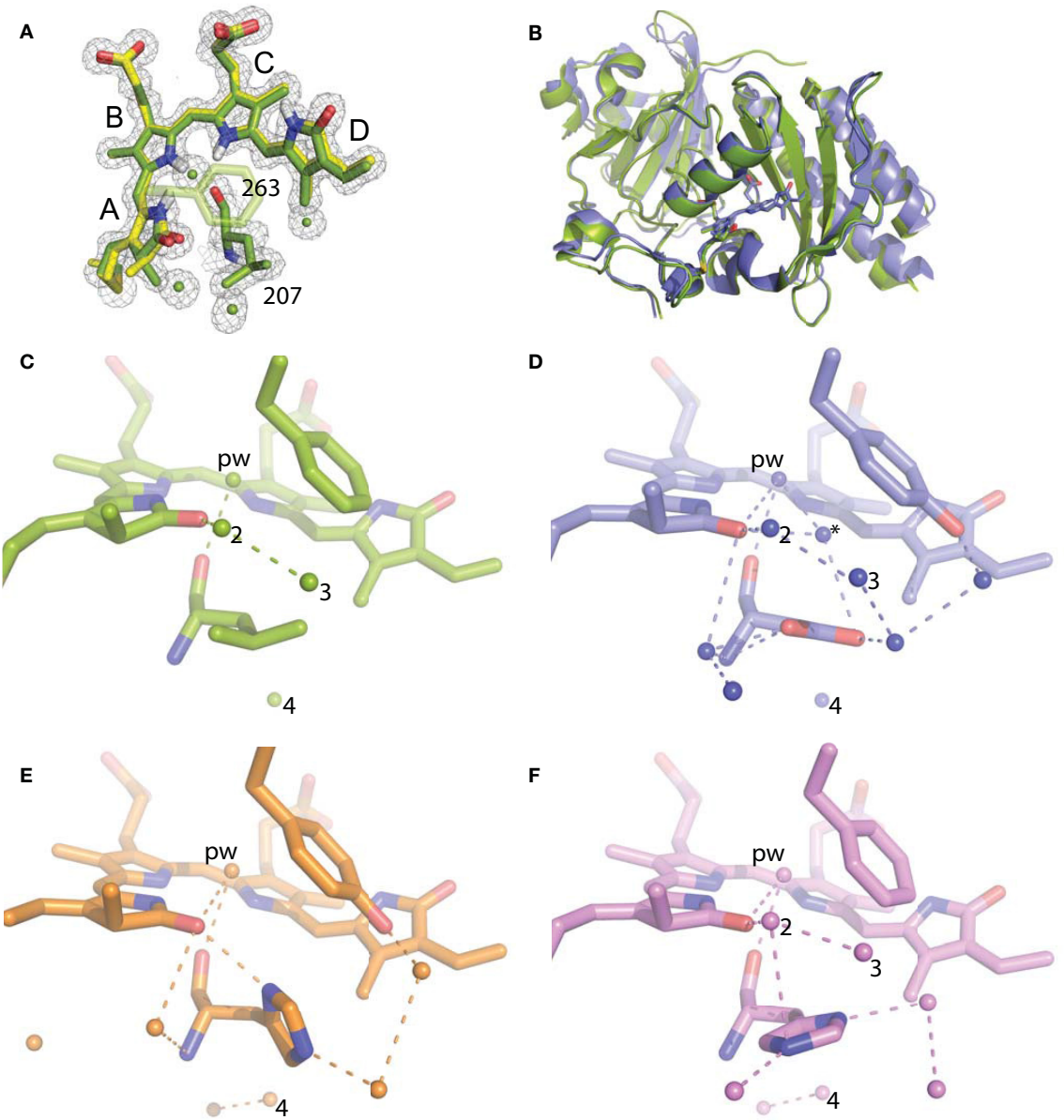

FIGURE 2 | Structural analysis of WiPhy2 and its water network. (A) BV A-ring methyl in both conformations (green and yellow) and adjacent waters in the WiPhy2 structure. Mesh corresponds to the 2_mF_o-DF_c electron density map contoured at 1.0 σ and displayed within a radius of 1.6 Å from the chromophore, the waters, or L207. **(B)** Overall structural alignment between $DrCBD_{mon}$ (PDB ID: 4IJG, blue) and WiPhy2 (green). **(C)** WiPhy2 H-bonding network loss in comparison to **(D)** the native sequence monomer (PDB ID: 4IJG), **(E)** the D207H variant (PDB ID: 3S7O, orange), and **(F)** the subsequent addition of the Y263 to create WiPhy (PDB ID: 3S7Q, violet). All waters within 5 Å of any atom within residue 207 are shown as spheres, and H-bonds of up to 3.8 Å are shown between any of the atoms in this set plus the –OH group of BV A-ring or Y263.

methyl occupying both up and down positions, consistent with previously published structures of DrCBD (**Figure 2A**).

Spectroscopic Measurements

All measurements were carried out at room temperature in complete darkness. Absorption wavelength scans in 1 nm steps from 250 to 850 nm were performed on a Beckman Coulter DU640B and Perkin Elmer LAMBDA 850 spectrophotometers. Sample illumination was as described previously (Auldridge et al., 2012). Briefly, samples were illuminated 15 min with red light or kept in the dark prior to each measurement. The 700 nm light was provided by a Fostec ACE light source fitted with a 700 ± 5 nm interference filter (Andover Corp., Salem, NH). The light source-to-sample distance was adjusted so that irradiances of 150 μmol m^{-2} s^{-1} were used for 700 nm light.

The samples used to record steady-state and time-resolved fluorescence were diluted in (30 mM Tris·HCl, pH 8.0) so that the absorption was sufficiently low (OD_{700} close to 0.1) to prevent an inner filter effect. Fluorescence spectra were measured on a Tecan Infinite M1000 Monochromator-based plate reader with a bandwidth of 5 nm. Emission scans were run in Greiner FLUOTRAC 200 96-well flat-bottom black microplates. The excitation wavelength was 630 nm. The excitation density was kept low to avoid photoconversion of the samples; its absence was confirmed by the identity of absorbance spectra immediately before and after the fluorescence experiments. The fluorescence quantum yields of $DrCBD_{mon}$-D207L and WiPhy2 were determined relative to two reference fluorophores with known quantum yields (Eaton, 1988). Cy5-N-hydroxysuccinimidyl ester ($\Phi_{Cy5} = 0.27$; Lumiprobe) dissolved in phosphate-buffered saline (PBS) and Nile Blue perchlorate ($\Phi_{NileBlue} = 0.27$; Sigma Aldrich) in acidic ethanol [0.5% (v/v) 0.1 M HCl in ethanol] were used as fluorescence quantum yield standards (Sens and Drexhage, 1981; Mujumdar et al., 1993). For pH titration experiments, the protein solution was diluted 50-fold into the appropriate buffer (pH 4-7, 30 mM citrate-phosphate buffer; pH 7-9, 30 mM Tris-HCl; and pH 9 and 10, 30 mM glycine). pH values of aqueous solutions were measured using a standard laboratory pH meter (Fisher Scientific™) calibrated prior to experiments using biotechnology grade standard buffer solutions (pH 4, 7, and 10, Amresco). For the photostability test for WiPhy2 the sample was continuously irradiated (696 ± 5 nm) within the Varian Cary Eclipse spectrophotometer. Power was 2.3 mW, which corresponds to a photon flux of 160 μmol $m^{-2}s^{-1}$. Fluorescence intensity was measured at 719 nm every 5 min.

The excitation-emission matrix (EEM) of $DrCBD_{mon}$-D207L and WiPhy2 were recorded on a Varian Cary Eclipse fluorescence spectrophotometer. The EEM fluorescence spectrum was obtained by concatenating emission spectra measured from 630 to 850 nm by using excitation wavelengths of 550-770 nm (5 nm intervals) with 0.1 s integration time and a 5 nm slit widths. The Raman scattering peaks in the EEM spectrum were corrected with a described method (Zepp et al., 2004). The sample resided in a vertically mounted glass capillary with an inner diameter close to 1.1 mm (VITREX, micro-haematocrit) with OD_{700} of about 0.1/mm. To avoid excessive sample degradation, the sample solution (volume 400 μL) was cycled using a peristaltic pump (Ismatec, Reglo Digital) at a flow rate of 0.1 mL min^{-1} through a glass reservoir, the capillary, and connecting Teflon tubing (1 mm inner diameter). A far-red laser diode (750 ± 5 nm, 3 mW, Leading-Tech Laser Co.) was used to transform the sample to the Pr state by constantly illuminating the sample through the Teflon tubing.

Fluorescence decays of the samples in the sub-nanosecond and nanosecond time scales were measured using a time-correlated single photon counting (TCSPC) system consisting of a HydraHarp 400 controller and a PDL 800-B driver (PicoQuant GmBH). The excitation wavelength was 660 nm from a pulsed diode laser head LDH-P-C-660. The repetition rate of the excitation pulses was set to 40 MHz in all measurements, and the output power of the laser was 0.98 mW for 660 nm excitation. The Jobin Yvon monochromator was used to detect the emission at 720 nm with a single photon avalanche photodiode (SPAD, MPD-1CTC). The time resolution was approximately 70 ps [full width at half-maximum of the instrument response function (IRF)]. The data were fitted with monoexponential functions to obtain fluorescence lifetimes (Lehtivuori et al., 2013). In addition to the fluorescence decay components, a fast rise component of about 20 ps was needed to obtain satisfactory fits at early time points.

RESULTS

Structural Properties

To gain insight into the fluorescent nature of WiPhy2, a 1.3 Å resolution crystal structure was obtained (**Table 1**). There were no significant changes to the overall structure of WiPhy2 compared to $DrCBD_{mon}$ (RMSD 0.82 Å over all 296 shared Cα atoms including mobile loop regions; **Figure 2B**). The BV chromophore is well-ordered with no evidence of a break in electron density for the cysteine connection to the A-ring (**Figure 2A**).

The most obvious result from this new structure is the confirmation of our hypothesis: waters are less abundant around the L207 side chain than has been seen in other high-resolution structures containing either Asp or His at this position. For D207L, within 5 Å of any Leu atom there are only four waters, including the pyrrole water with strong interactions to BV nitrogen atoms in A-, B-, and C-rings (**Figure 2C**). The closest of these waters to any Leu side chain atom is 3.8 Å. All four water positions are conserved in the water network of $DrCBD_{mon}$ (PDB ID: 4IJG, **Figure 2D**; Bhattacharya et al., 2014). The second and third form a path from the pyrrole water to the solvent, whereas the fourth is located under the residue 207 side chain and forms a H-bond with Y176. Of course, there are no H-bonds from any of these waters to the L207 side chain in WiPhy2.

This paucity of solvent molecules can be strongly contrasted with the native sequence found in the monomer structure, which holds nine waters (**Figure 2D**). These waters permit an extensive H-bonding network of 16 different pair wise interactions of 3.8 Å or less between any two atoms in the set containing all atoms in

residue 207, the –OH of Y263, the –OH of the A-ring, and these waters.

The introduction of His at position 207 (PDB ID: 3S7O; Auldridge et al., 2012) diminishes this H-bonding network somewhat, with seven waters and nine remaining H-bonds (**Figure 2E**). For WiPhy (PDB ID: 3S7Q; (Auldridge et al., 2012)), which also has the polar His at position 207 but introduces the nonpolar Phe263, there remain eight waters in the 5 Å cutoff window from the 207 side chain and 9 H-bonds (**Figure 2F**). Thus, we can conclude that the identity of the residue at position 207 and not at position 263 has the greatest effect on this water network near the "mouth" leading from BV to the solvent. Among the four structures compared here, it is notable that only in $DrCBD_{mon}$ which is known to weakly photoconvert (Auldridge et al., 2012) is there a second water located between the chromophore and this outlet (**Figure 2D**, asterisk).

Spectroscopic Properties

In the dark state (**Figure 3**), both of the D207L constructs show absorption spectra in the characteristic phytochrome region between 600 and 800 nm similar to other monomeric $DrCBD_{mon}$ variants (Auldridge et al., 2012; Bhattacharya et al., 2014; Takala et al., 2015). The D207L constructs have absorption maxima at 696 (WiPhy2) and 697 ($DrCBD_{mon}$D207L), respectively, with a pronounced shoulder at 650 nm. The slight shift (−2 nm relative to $DrCBD_{mon}$) in the maximum absorption wavelength is a hypsochromic shift caused by the decreased hydrogen-bond network around BV compared to $DrCBD_{mon}$ and WiPhy. The amplitude of the shoulder at 650 nm (**Figure 3**, inset) is higher in the case of the proteins containing Leu at position 207 compared to previously analyzed derivatives of $DrCBD_{mon}$.

The photoconversion potentials for both D207L variants were also tested (**Figure 4**). After illumination with red light, the Q band at 696 nm decreases (**Figure 4**, inset) in each. While native BphP and $DrCBD_{mon}$ as well as other studied variants show an increase in absorbance at 750 nm upon illumination (Auldridge et al., 2012), neither D207L sample has this behavior. Instead, in the two D207L-containing samples, there is a noticeable increase in absorbance in the photoproduct at 730 nm (**Figure 4**, inset). This difference implies an incomplete or a different type of photocycle than other $DrCBD_{mon}$ variants.

The fluorescence spectra of the D207L samples, when excited at the Q-band of BV at 630 nm, are presented in **Figure 5A**. The observed fluorescence emission originates from the BV chromophore, with the same spectral shape in $DrCBD_{mon}$D207L and WiPhy2, in keeping with their matching absorption spectra (**Figure 3**). The maxima of the emission spectra are located at 722 and 719 nm for $DrCBD_{mon}$D207L and WiPhy2, respectively. Their fluorescence quantum yields were determined to be 0.070 ± 0.005 ($DrCBD_{mon}$D207L) and 0.087 ± 0.005 (WiPhy2). The quantum yield of WiPhy2 is thus 24% higher than that of $DrCBD_{mon}$D207L.

A similar trend was observed for the time-resolved lifetime measurements (**Figure 5B**). Using excitation wavelength of 660 nm and monitoring wavelength of 720 nm, the excitation decay properties of BV molecules in the binding pocket can be studied. The excited state decay can be described by monoexponential components, with time constants of 650 ± 30 ps for $DrCBD_{mon}$D207L and 780 ± 30 ps for WiPhy2 (parameters summarized in **Table 2**).

The emission-excitation matrix (EEM) spectra for both D207L variants were measured to study with finer detail how fluorescence properties vary with excitation wavelength. We sought to determine whether WiPhy2 binds PPIXα present naturally in the cells it is expressed in. Given that the shape of the fluorescence spectra remains the same in every

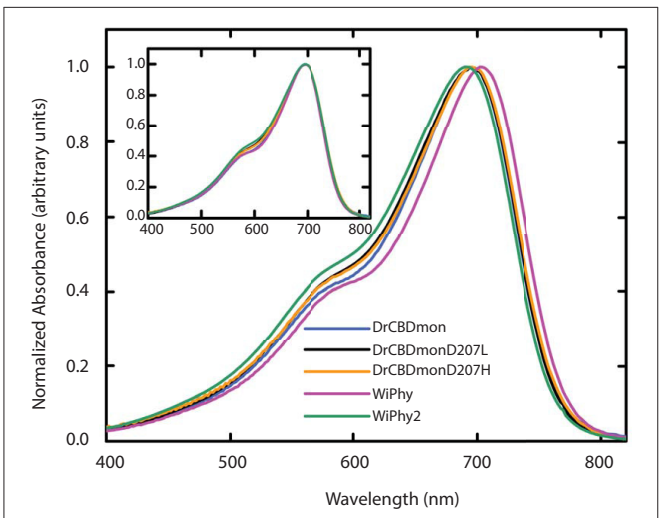

FIGURE 3 | UV-Vis absorption spectra of the five $DrCBD_{mon}$ variants in the Pr state immediately after sample thawing. All absorption spectra were normalized at their maxima. (Inset) Spectra are aligned at their absorbance maxima for better visualization of shoulder heights.

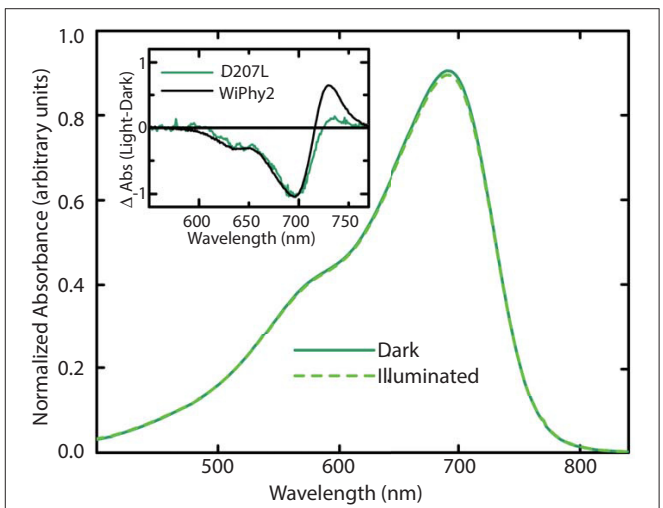

FIGURE 4 | Steady-state absorption spectra of purified WiPhy2 measured immediately upon thawing (dark) and after 15 min of 700 nm light illumination (illuminated). Inset shows absorption difference spectra of $DrCBD_{mon}$D207L and WiPhy2 (red irradiated spectrum has been subtracted from dark spectrum) absorption difference spectra were normalized at 698 nm.

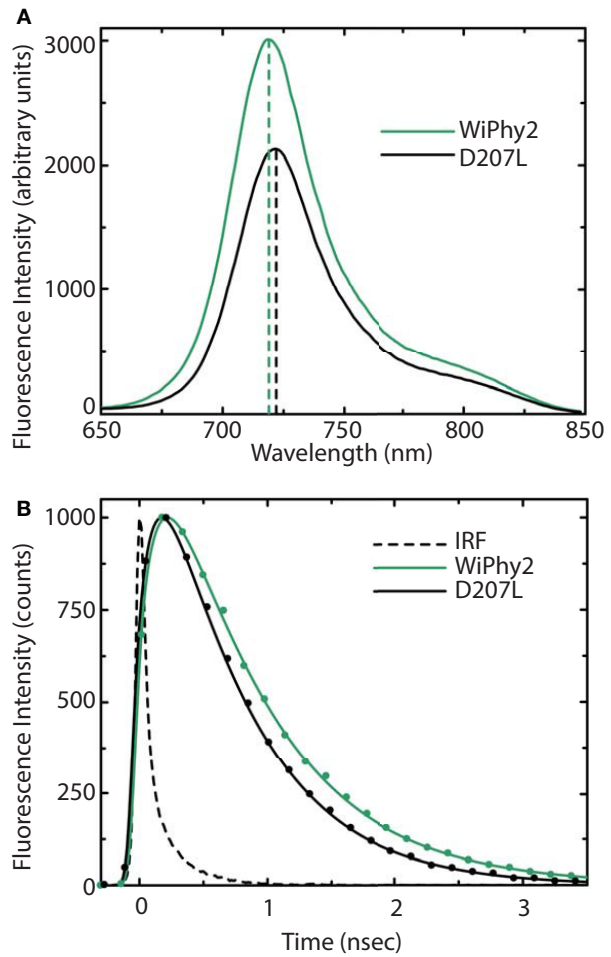

FIGURE 5 | (A) Steady-state emission spectra and **(B)** emission decays of purified DrCBD$_{mon}$-D207L and WiPhy2 variants. For steady-state measurements, samples were excited at 630 nm light and intensities were corrected for the number of absorbed photons. Emission decay samples were excited at 660 nm and monitored at 720 nm. IRF is the instrument response function. Solid lines show the multiexponential fit of the data.

TABLE 2 | Quantum yield measurements and fluorescence lifetimes.

Protein variant	Abs. max (nm)	Em. max(nm)	Φ (%)	Lifetime (ps)	Binding PPIXα
DrCBD$_{mon}$-D207L	697	722	7.0 ± 0.5	650 ± 30 ps	ND
WiPhy2 (DrCBD$_{mon}$-Y263F/D207L	696	719	8.7 ± 0.5	780 ± 30 ps	No

excitation wavelength (**Figures 6A,B**), in contrast, for example, to DrCBD$_{mon}$, we conclude that the fluorescence emission from WiPhy2 originates only from the BV chromophore. The composite EEM reveals the change in fluorescence intensity as a function of wavelength and shows a single maximum at ex = 696, em = 719 nm (**Figure 6A**).

We further investigated the effect of pH on absorption and fluorescence of WiPhy2 (**Figure 7A**). The fluorescence intensity of sample displayed linear responses to pH values in the range from 4 to 9. The sample was non-fluorescent with pH > 9. Correspondingly, the absorption spectra of WiPhy2 was unaffected by changes in pH ranging from 4.0 to 9.0 (**Figure 7A**, inset). Drop-off in fluorescence at low pH has been noted with some of the previously published fluorescent variants with His in the 207th position (Filonov et al., 2011) likely due to changes in the protonation state of His (pKa 6.1). This challenge is removed in the case of L207.

Photostability of the WiPhy2 variant was also tested. Samples were excited continuously at their optimal excitation wavelength (696 nm) and fluorescence intensity was measured at 719 nm every 5 min. Fluorescence dropped by only 2% after 60 min (**Figure 7B**).

DISCUSSION

Bacteriophytochromes are characterized by structural and spectroscopic variability. Intermediates in their light-driven forward and backward reactions have been trapped at low temperature and spectrally characterized (Eilfeld and Rüdiger, 1985). The first, formed from the excited state bilin molecule on a timescale of ps-ns, is the Lumi-R state. In BphPs, Lumi-R has a ground-state bleach at 700 nm and induced absorption at 730 nm (Toh et al., 2011b). None of the full-length DrBphP Asp207 substitutions stably photoconvert to Pfr upon photoexcitation with red light, although some do reach the Meta-R state, with a steady-state absorption peak between 740 and 750 nm (Borucki et al., 2005; Wagner et al., 2008). By reduction of polarity near the chromophore of WiPhy, we endeavored to limit photoconversion and excited state proton transfer and thus improve fluorescence yield. This goal was informed by the fact that for full-length dimeric DrBph-D207L there is essentially no steady state photoconversion even after extended irradiation (Wagner et al., 2008), and by the fact that two phytofluors in the iRFP series carry D207L substitutions among others.

Here we show that DrCBD$_{mon}$D207L and WiPhy2 respond to red light with miniscule decreases in absorption at 696 nm and induced absorption at 730 nm (**Figure 4**, inset). Logically, there is also no subsequent appearance of absorbance at 750 nm to indicate the Meta-R or Pfr photoproducts as seen in the parent DrCBD$_{mon}$. Formation of the Meta-R state must require the polar hydrogen-bonding network that is set up by the chromophore, charged residue at position 207, and associated waters (**Figure 2**). Thus, our study reinforces the major role of Asp207 in the photocycle, and demonstrates that Leu at this position leads to negligible Lumi-R photoproduct yield. Since only steady-state measurements were carried out, we are unable to draw conclusions about a particular reaction scheme for the excited state Pr to the Lumi-R-state. We demonstrate that WiPhy2 has a fluorescence quantum yield of nearly 9% and an excited state lifetime of 780 ps, both ∼20% higher than WiPhy (**Figure 5**), representing the effect of the Leu on the excited state decay of BV in the binding pocket.

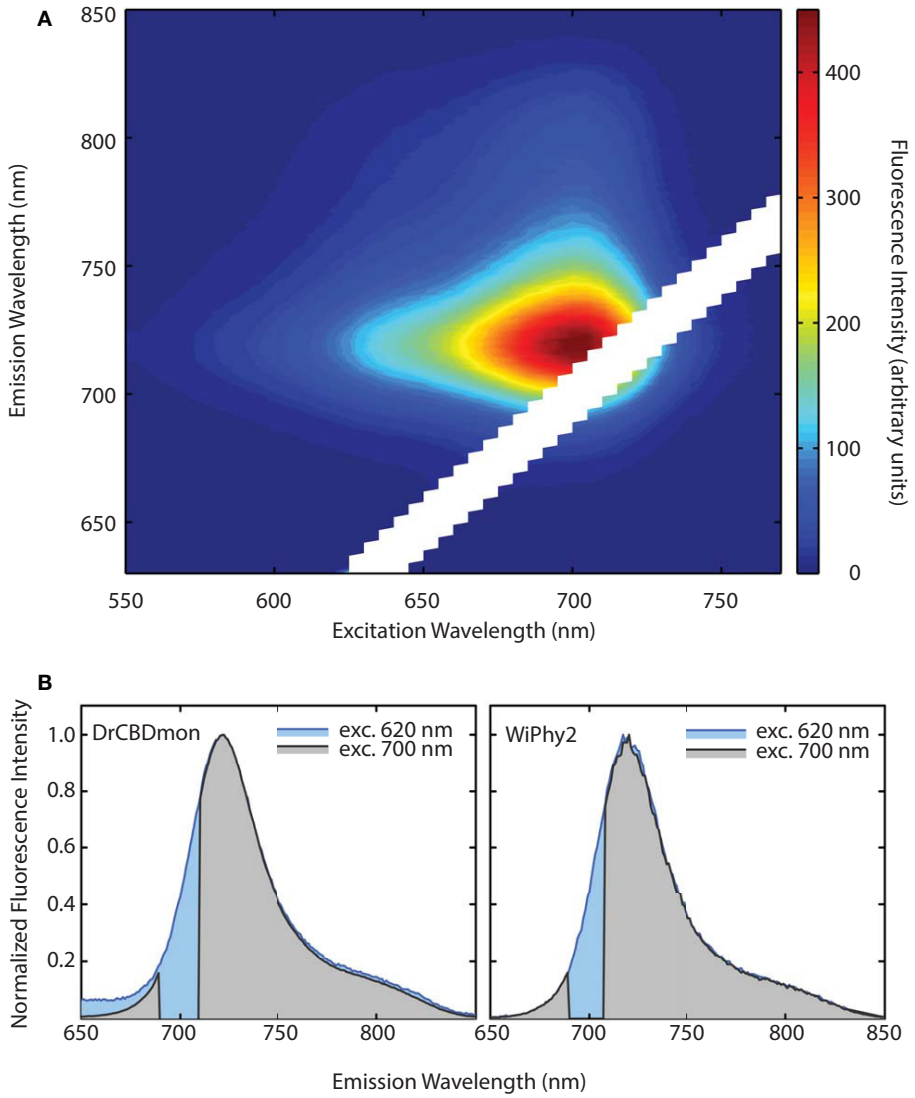

FIGURE 6 | (A) Excitation-Emission Matrix (EEM) for WiPhy2 represents fluorescence as a function of both excitation and emission wavelengths. Fluorescence intensities are corrected with the number of absorbed photons. **(B)** Two extracted excitation wavelengths (620 nm and 700 nm) are compared for $DrCBD_{mon}$ (left) and WiPhy2 (right).

The excited state lifetimes for both fluorescent L207 $DrCBD_{mon}$ variants (650 and 780 ps) are longer than for DrCBDmon (620 ps; Bhattacharya et al., 2014) or *Rhodopseudomonas palustris* BphP3 (362 ps; Toh et al., 2011b). Although WiPhy2 lifetime was increased compared to $DrCBD_{mon}$, cyanobacterial Cph1 variant lifetimes have been reported as long as 1.8 ns and IFP_{rev} has a lifetime of 815 ps at room temperature (Miller et al., 2006; Bhattacharya et al., 2014; Kim et al., 2014a). One key reason for variation in lifetimes, apart from the slightly different bilin in Cph1, is immobilization of the D-ring by H-bonding and/or hydrophobic packing (Toh et al., 2011b; Bhattacharya et al., 2014).

We now show that a second mechanism for achieving a longer decay lifetime is to decrease the number of waters near the chromophore, which in turn curtails the hydrogen-bonding network among BV, polar side chains and coordinating water molecules. Opportunities for photoconversion or excited state proton transfer are thus lost. DrCBD variants analyzed to date have clear interactions among solvent molecules (Auldridge et al., 2012; Bhattacharya et al., 2014) but in WiPhy2 there are fewer waters than in any other structurally characterized $DrCBD_{mon}$ variant (**Figure 2**). Thus, the change to Leu might be viewed as a "mutation" of waters away from the chromophore. We note that the crystals from which these data were obtained have the same C2 space group and are grown under similar solvent content and pH, lending validity to the comparisons. Nonetheless, because cryopreservation conditions may affect overall solvent distributions and because moreover for our spectroscopic studies solution water molecules can be expected to exchange rapidly, our conclusion focuses on this trend rather

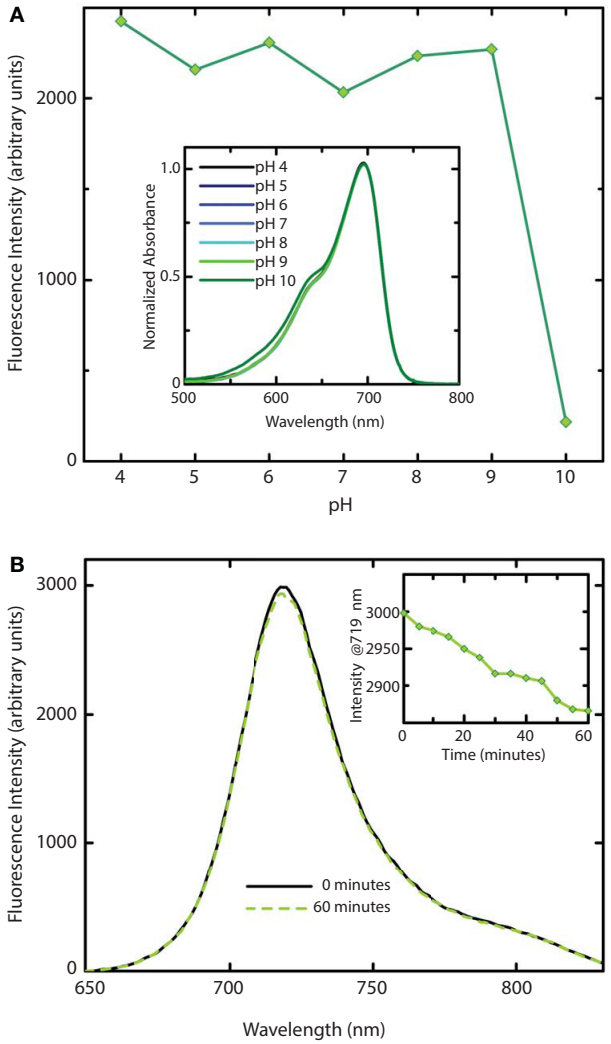

FIGURE 7 | Stability of WiPhy2 Fluorescence vs. pH and illumination time. (A) Dependency of WiPhy2 absorption (inset) and fluorescence on pH. **(B)** Steady-state emission spectra of WiPhy2 before and after a 1-h photostability test. Inset shows fluorescence intensity at peak over time.

than a particular water constellation. Following the same logic, our conclusions are not affected by the existence of heterogeneity in the ground or excited states (Samma et al., 2010; Song et al., 2011; Kim et al., 2014b). Thus, X-ray crystallography confirmed the spatial observations of spectroscopic studies; removing polar interactions in the vicinity of the chromophore shifts steady state absorption band location, photocycle yields and fluorescence properties.

Previously it has been demonstrated that phytochromes' absorbance shoulder around 650 nm is not due to a second chromophore species (such as PPIXα) but is instead a natural physical consequence of vibronic progressions in the absorption spectrum (Spillane et al., 2009, 2012). PPIXα binding to the CBD has been a noted disadvantage in several described phytofluors. In the case of *Dr*BphP D207H and as first described in cyanobacterial phytochrome variants (Cph1 Y176R in particular) by Lagarias and coworkers, not only the linear chromophore but also cyclized PPIXα is accommodated in the binding pocket (Fischer and Lagarias, 2004), as observed in emission spectra upon excitation at 600–650 nm. Lehtivuori et al. have shown these minor emission bands due to PPIXα at 660 nm in DrCBD-D207H as well as to some extent in DrCBD (Lehtivuori et al., 2013). Burgie et al. obtained the same result in the case of DrCBD and its D207A variant (Burgie et al., 2014). For both of our D207L variants this PPIXα binding disadvantage is alleviated, as seen in our EEM spectra. Indeed, regardless of the excitation maximum, we obtain same emission spectra of only BV (**Figure 7**).

We have used steady state and time-resolved spectroscopy as well as protein crystallography to test the hypothesis that the introduction of a nonpolar amino acid in place of the native charge in DrCBD would improve its fluorescence properties. Indeed, in WiPhy2 Leu at position 207 raises fluorescence quantum yield and lengthens excited state lifetime, maintaining an illumination wavelength of nearly 700 nm while avoiding PPIXα binding or a narrow pH window for efficacy (**Figure 1**).

FUNDING

The research was supported by the Academy of Finland grant 277194 (HL), University of Jyväskylä (HL), the Fulbright Center in Finland (HL), the National Science Foundation 1518160 (KTF), and the W. H. Peterson Fellowship (SB). Use of the Advanced Photon Source, an Office of Science User Facility operated for the U.S. Department of Energy (DOE) Office of Science by Argonne National Laboratory, was supported by the U.S. DOE under Contract No. DE-AC02-06CH11357. Use of the LS-CAT Sector 21 was supported by the Michigan Economic Development Corporation and the Michigan Technology Tri-Corridor (Grant 085P1000817).

ACKNOWLEDGMENTS

The high resolution WiPhy2 structure discussed here has been deposited in the Protein Data Bank with accession code PDB ID: 4Z1W. In addition the lower resolution structure solved with rotating anode data has been deposited with code PDB ID: 4ZRR.

REFERENCES

Adams, P. D., Afonine, P. V., Bunkóczi, G., Chen, V. B., Davis, I. W., Echols, N., et al. (2010). PHENIX: a comprehensive Python-based system for macromolecular structure solution. *Acta Crystallogr. D Biol. Crystallogr.* 66, 213–221. doi: 10.1107/S0907444909052925

Auldridge, M. E., Satyshur, K. A., Anstrom, D. M., and Forest, K. T. (2012). Structure-guided engineering enhances a phytochrome-based infrared fluorescent protein. *J. Biol. Chem.* 287, 7000–7009. doi: 10.1074/jbc.M111.295121

Battistelli, G., Cantelli, A., Guidetti, G., Manzi, J., and Montalti, M. (2015). Ultra-bright and stimuli-responsive fluorescent nanoparticles for bioimaging. *Wiley*

Interdiscip. Rev. Nanomed. Nanobiotechnol. doi: 10.1002/wnan.1351. [Epub ahead of print].

Bhattacharya, S., Auldridge, M. E., Lehtivuori, H., Ihalainen, J. A., and Forest, K. T. (2014). Origins of fluorescence in evolved bacteriophytochromes. *J. Biol. Chem.* 289, 32144–32152. doi: 10.1074/jbc.M114.589739

Borucki, B., von Stetten, D., Seibeck, S., Lamparter, T., Michael, N., Mroginski, M. A., et al. (2005). Light-induced proton release of phytochrome is coupled to the transient deprotonation of the tetrapyrrole chromophore. *J. Biol. Chem.* 280, 34358–34364. doi: 10.1074/jbc.M505493200

Burgie, E. S., Wang, T., Bussell, A. N., Walker, J. M., Li, H., and Vierstra, R. D. (2014). Crystallographic and electron microscopic analyses of a bacterial phytochrome reveal local and global rearrangements during photoconversion. *J. Biol. Chem.* 289, 24573–24587. doi: 10.1074/jbc.M114.571661

Christie, J. M., Hitomi, K., Andrew, A. S., Hartfield, K. A., Mettlen, M., Pratt, A. J., et al. (2012). Structural tuning of the fluorescent protein ilov for improved photostability. *J. Biol. Chem.* 287, 22295–22304. doi: 10.1074/jbc.M111.318881

Clark, M., Cramer, R. D. III, and Van Opdenbosch, N. (1989). Validation of the general purpose tripos 5.2 force field. *J. Comput. Chem.* 10, 982–1012. doi: 10.1002/jcc.540100804

Eaton, D. F. (1988). Reference materials for fluorescence measurements. *Pure Appl. Chem.* 60, 1107–1114.

Eilfeld, P., and Rüdiger, W. (1985). Absorption spectra of phytochrome intermediates. *Z. Naturforsch. C* 40, 109–113.

Emsley, P., Lohkamp, B., Scott, W. G., and Cowtan, K. (2010). Features and development of Coot. *Acta Crystallogr. D Biol. Crystallogr.* 66, 486–501. doi: 10.1107/S0907444910007493

Escobedo, J. O., Rusin, O., Lim, S., and Strongin, R. M. (2010). NIR dyes for bioimaging applications. *Curr. Opin. Chem. Biol.* 14, 64–70. doi: 10.1016/j.cbpa.2009.10.022

Filonov, G. S., and Verkhusha, V. V. (2013). A near-infrared bifc reporter for *in vivo* imaging of protein-protein interactions. *Chem. Biol.* 20, 1078–1086. doi: 10.1016/j.chembiol.2013.06.009

Filonov, G. S., Piatkevich, K. D., Ting, L., Zhang, J., Kim, K., and Verkhusha, V. V. (2011). Bright and stable near-infrared fluorescent protein for *in vivo* imaging. *Nat. Biotechnol.* 29, 757–761. doi: 10.1038/nbt.1918

Fischer, A. J., and Lagarias, J. C. (2004). Harnessing phytochrome's glowing potential. *Proc. Natl. Acad. Sci. U.S.A.* 101, 17334–17339. doi: 10.1073/pnas.0407645101

Gibbs, S. L. (2012). Near infrared fluorescence for image-guided surgery. *Quant. Imaging Med. Surg.* 2, 177–187. doi: 10.3978/j.issn.2223-4292.2012.09.04

Guo, Z., Park, S., Yoon, J., and Shin, I. (2014). Recent progress in the development of near-infrared fluorescent probes for bioimaging applications. *Chem. Soc. Rev.* 43, 16–29. doi: 10.1039/C3CS60271K

Hahn, M. A., Singh, A. K., Sharma, P., Brown, S. C., and Moudgil, B. M. (2011). Nanoparticles as contrast agents for *in-vivo* bioimaging: current status and future perspectives. *Anal. Bioanal. Chem.* 399, 3–27. doi: 10.1007/s00216-010-4207-5

Johnson, F. H., Shimomura, O., Saiga, Y., Gershman, L. C., Reynolds, G. T., and Waters, J. R. (1962). Quantum efficiency of Cypridina luminescence, with a note on that ofAequorea. *J. Cell. Comp. Physiol.* 60, 85–103. doi: 10.1002/jcp.1030600111

Kim, P. W., Rockwell, N. C., Martin, S. S., Lagarias, J. C., and Larsen, D. S. (2014a). Dynamic inhomogeneity in the photodynamics of cyanobacterial phytochrome Cph1. *Biochemistry* 53, 2818–2826. doi: 10.1021/bi500108s

Kim, P. W., Rockwell, N. C., Martin, S. S., Lagarias, J. C., and Larsen, D. S. (2014b). Heterogeneous photodynamics of the pfr state in the cyanobacterial phytochrome Cph1. *Biochemistry* 53, 4601–4611. doi: 10.1021/bi5005359

Lehtivuori, H., Rissanen, I., Takala, H., Bamford, J., Tkachenko, N. V., and Ihalainen, J. A. (2013). Fluorescence properties of the chromophore-binding domain of bacteriophytochrome from *Deinococcus radiodurans*. *J. Phys. Chem. B* 117, 11049–11057. doi: 10.1021/jp312061b

Luo, S., Zhang, E., Su, Y., Cheng, T., and Shi, C. (2011). A review of NIR dyes in cancer targeting and imaging. *Biomaterials* 32, 7127–7138. doi: 10.1016/j.biomaterials.2011.06.024

Marx, V. (2014). Probes: seeing in the near infrared. *Nat. Methods* 11, 717–720. doi: 10.1038/nmeth.3001

McCoy, A. J., Grosse-Kunstleve, R. W., Adams, P. D., Winn, M. D., Storoni, L. C., and Read, R. J. (2007). Phaser crystallographic software. *J. Appl. Crystallogr.* 40, 658–674. doi: 10.1107/S0021889807021206

Miller, A. E., Fischer, A. J., Laurence, T., Hollars, C. W., Saykally, R. J., Lagarias, J. C., et al. (2006). Single-molecule dynamics of phytochrome-bound fluorophores probed by fluorescence correlation spectroscopy. *Proc. Natl. Acad. Sci. U.S.A.* 103, 11136–11141. doi: 10.1073/pnas.0604724103

Mujumdar, R. B., Ernst, L. A., Mujumdar, S. R., Lewis, C. J., and Waggoner, A. S. (1993). Cyanine dye labeling reagents: sulfoindocyanine succinimidyl esters. *Bioconjug. Chem.* 4, 105–111. doi: 10.1021/bc00020a001

Murshudov, G. N., Skubák, P., Lebedev, A. A., Pannu, N. S., Steiner, R. A., Nicholls, R. A., et al. (2011). REFMAC5 for the refinement of macromolecular crystal structures. *Acta Crystallogr. D Biol. Crystallogr.* 67, 355–367. doi: 10.1107/S0907444911001314

Ormö, M., Cubitt, A. B., Kallio, K., Gross, L. A., Tsien, R. Y., and Remington, S. J. (1996). Crystal structure of the Aequorea victoria green fluorescent protein. *Science* 273, 1392–1395. doi: 10.1126/science.273.5280.1392

Rizzo, M. A., Springer, G. H., Granada, B., and Piston, D. W. (2004). An improved cyan fluorescent protein variant useful for FRET. *Nat. Biotechnol.* 22, 445–449. doi: 10.1038/nbt945

Samma, A. A., Johnson, C. K., Song, S., Alvarez, S., and Zimmer, M. (2010). On the origin of fluorescence in bacteriophytochrome infrared fluorescent proteins. *J. Phys. Chem. B* 114, 15362–15369. doi: 10.1021/jp107119q

Sens, R., and Drexhage, K. H. (1981). Fluorescence quantum yield of oxazine and carbazine laser dyes. *J. Lumin.* 24–25, 709–712. doi: 10.1016/0022-2313(81)90075-2

Shaner, N. C., Campbell, R. E., Steinbach, P. A., Giepmans, B. N. G., Palmer, A. E., and Tsien, R. Y. (2004). Improved monomeric red, orange and yellow fluorescent proteins derived from Discosoma sp. red fluorescent protein. *Nat. Biotechnol.* 22, 1567–1572. doi: 10.1038/nbt1037

Shcherbakova, D. M., and Verkhusha, V. V. (2013). Near-infrared fluorescent proteins for multicolor *in vivo* imaging. *Nat. Methods* 10, 751–754. doi: 10.1038/nmeth.2521

Shcherbo, D., Merzlyak, E. M., Chepurnykh, T. V., Fradkov, A. F., Ermakova, G. V., Solovieva, E. A., et al. (2007). Bright far-red fluorescent protein for whole-body imaging. *Nat. Methods* 4, 741–746. doi: 10.1038/nmeth1083

Shcherbo, D., Murphy, C. S., Ermakova, G. V., Solovieva, E. A., Chepurnykh, T. V., Shcheglov, A. S., et al. (2009). Far-red fluorescent tags for protein imaging in living tissues. *Biochem. J.* 418, 567–574. doi: 10.1042/BJ20081949

Shu, X., Royant, A., Lin, M. Z., Aguilera, T. A., Lev-Ram, V., Steinbach, P. A., et al. (2009). Mammalian expression of infrared fluorescent proteins engineered from a bacterial phytochrome. *Science* 324, 804–807. doi: 10.1126/science.1168683

Sineshchekov, V., Mailliet, J., Psakis, G., Feilke, K., Kopycki, J., Zeidler, M., et al. (2014). Tyrosine 263 in cyanobacterial phytochrome Cph1 optimizes photochemistry at the prelumi-R→lumi-R step. *Photochem. Photobiol.* 90, 786–795. doi: 10.1111/php.12263

Song, C., Psakis, G., Lang, C., Mailliet, J., Gärtner, W., Hughes, J., et al. (2011). Two ground state isoforms and a chromophore D-ring photoflip triggering extensive intramolecular changes in a canonical phytochrome. *Proc. Natl. Acad. Sci. U.S.A.* 108, 3842–3847. doi: 10.1073/pnas.1013377108

Spillane, K. M., Dasgupta, J., Lagarias, J. C., and Mathies, R. A. (2009). Homogeneity of phytochrome Cph1 vibronic absorption revealed by resonance Raman intensity analysis. *J. Am. Chem. Soc.* 131, 13946–13948. doi: 10.1021/ja905822m

Spillane, K. M., Dasgupta, J., and Mathies, R. A. (2012). Conformational homogeneity and excited-state isomerization dynamics of the bilin chromophore in phytochrome Cph1 from resonance Raman intensities. *Biophys. J.* 102, 709–717. doi: 10.1016/j.bpj.2011.11.4019

Takala, H., Björling, A., Linna, M., Westenhoff, S., and Ihalainen, J. A. (2015). Light-induced changes in the dimerization interface of bacteriophytochromes. *J. Biol. Chem.* 290, 16383–16392. doi: 10.1074/jbc.m115.650127

Toh, K. C., Stojković, E. A., Rupenyan, A. B., van Stokkum, I. H., Salumbides, M., Groot, M. L., et al. (2011a). Primary reactions of bacteriophytochrome observed with ultrafast mid-infrared spectroscopy. *J. Phys. Chem. A* 115, 3778–3786. doi: 10.1021/jp106891x

Toh, K. C., Stojković, E. A., van Stokkum, I. H., Moffat, K., and Kennis, J. T. (2010). Proton-transfer and hydrogen-bond interactions determine fluorescence

quantum yield and photochemical efficiency of bacteriophytochrome. *Proc. Natl. Acad. Sci. U.S.A.* 107, 9170–9175. doi: 10.1073/pnas.0911535107

Toh, K. C., Stojković, E. A., van Stokkum, I. H., Moffat, K., and Kennis, J. T. (2011b). Fluorescence quantum yield and photochemistry of bacteriophytochrome constructs. *Phys. Chem. Chem. Phys.* 13, 11985–11997. doi: 10.1039/c1cp00050k

Wagner, J. R., Zhang, J., von Stetten, D., Günther, M., Murgida, D. H., Mroginski, M. A., et al. (2008). Mutational analysis of *Deinococcus radiodurans* bacteriophytochrome reveals key amino acids necessary for the photochromicity and proton exchange cycle of phytochromes. *J. Biol. Chem.* 283, 12212–12226. doi: 10.1074/jbc.M709355200

Weissleder, R. (2001). A clearer vision for *in vivo* imaging. *Nat. Biotechnol.* 19, 316–317. doi: 10.1038/86684

Yu, D., Gustafson, W. C., Han, C., Lafaye, C., Noirclerc-Savoye, M., Ge, W.-P., et al. (2014). An improved monomeric infrared fluorescent protein for neuronal and tumour brain imaging. *Nat. Commun.* 5, 3626. doi: 10.1038/ncomms4626

Zepp, R. G., Sheldon, W. M., and Moran, M. A. (2004). Dissolved organic fluorophores in southeastern US coastal waters: correction method for eliminating Rayleigh and Raman scattering peaks in excitation–emission matrices. *Mar. Chem.* 89, 15–36. doi: 10.1016/j.marchem.2004.02.006

Zhang, J., Campbell, R. E., Ting, A. Y., and Tsien, R. Y. (2002). Creating new fluorescent probes for cell biology. *Nat. Rev. Mol. Cell Biol.* 3, 906–918. doi: 10.1038/nrm976

Zienicke, B., Chen, L. Y., Khawn, H., Hammam, M. A., Kinoshita, H., Reichert, J., et al. (2011). Fluorescence of phytochrome adducts with synthetic locked chromophores. *J. Biol. Chem.* 286, 1103–1113. doi: 10.1074/jbc.M110.155143

Zienicke, B., Molina, I., Glenz, R., Singer, P., Ehmer, D., Escobar, F. V., et al. (2013). Unusual spectral properties of bacteriophytochrome Agp2 result from a deprotonation of the chromophore in the red-absorbing form Pr. *J. Biol. Chem.* 288, 31738–31751. doi: 10.1074/jbc.M113.479535

Conflict of Interest Statement: The authors declare that the research was conducted in the absence of any commercial or financial relationships that could be construed as a potential conflict of interest.

frontiers in Molecular Biosciences

ORIGINAL RESEARCH
published: 28 July 2015
doi: 10.3389/fmolb.2015.00042

NMR chemical shift pattern changed by ammonium sulfate precipitation in cyanobacterial phytochrome Cph1

Chen Song[1,2], *Christina Lang*[3], *Jakub Kopycki*[3], *Jon Hughes*[3] *and Jörg Matysik*[1,2]*

[1] *Leids Instituut voor Chemisch Onderzoek, Universiteit Leiden, Leiden, Netherlands,* [2] *Institut für Analytische Chemie, Fakultät für Chemie and Mineralogie, Universität Leipzig, Leipzig, Germany,* [3] *Institut für Pflanzenphysiologie, Justus-Liebig-Universität Gießen, Gießen, Germany*

Phytochromes are dimeric biliprotein photoreceptors exhibiting characteristic red/far-red photocycles. Full-length cyanobacterial phytochrome Cph1 from *Synechocystis* 6803 is soluble initially but tends to aggregate in a concentration-dependent manner, hampering attempts to solve the structure using NMR and crystallization methods. Otherwise, the Cph1 sensory module (Cph1Δ2), photochemically indistinguishable from the native protein and used extensively in structural and other studies, can be purified to homogeneity in >10 mg amounts at mM concentrations quite easily. Bulk precipitation of full-length Cph1 by ammonium sulfate (AmS) was expected to allow us to produce samples for solid-state magic-angle spinning (MAS) NMR from dilute solutions before significant aggregation began. It was not clear, however, what effects the process of partial dehydration might have on the molecular structure. Here we test this by running solid-state MAS NMR experiments on AmS-precipitated Cph1Δ2 in its red-absorbing Pr state carrying uniformly $^{13}C/^{15}N$-labeled phycocyanobilin (PCB) chromophore. 2D ^{13}C–^{13}C correlation experiments allowed a complete assignment of ^{13}C responses of the chromophore. Upon precipitation, ^{13}C chemical shifts for most of PCB carbons move upfield, in which we found major changes for C4 and C6 atoms associated with the *A*-ring positioning. Further, the broad spectral lines seen in the AmS ^{13}C spectrum reflect primarily the extensive inhomogeneous broadening presumably due to an increase in the distribution of conformational states in the protein, in which less free water is available to partake in the hydration shells. Our data suggest that the effect of dehydration process indeed leads to changes of electronic structure of the bilin chromophore and a decrease in its mobility within the binding pocket, but not restricted to the protein surface. The extent of the changes induced differs from the freezing process of the solution samples routinely used in previous MAS NMR and crystallographic studies. AmS precipitation might nevertheless provide useful protein structure/functional information for full-length Cph1 in cases where neither X-ray crystallography nor conventional NMR methods are available.

Keywords: biliprotein, photoreceptor, phycocyanobilin, red-absorbing state, dehydration process, solid-state NMR

OPEN ACCESS

Edited by:
John T. M. Kennis, VU University Amsterdam, Netherlands

Reviewed by:
Litao Sun, The Scripps Research Institute, USA
Peter Hildebrandt, Technische Universität Berlin, Germany
Shimon Vega, Weizmann Institute of Science, Israel

***Correspondence:**
Jörg Matysik, Institut für Analytische Chemie, Universität Leipzig, Linnéstraße 3, D-04103 Leipzig, Germany
joerg.matysik@uni-leipzig.de

Specialty section:
This article was submitted to Biophysics, a section of the journal Frontiers in Molecular Biosciences

Received: *04 March 2015*
Accepted: *06 July 2015*
Published: *28 July 2015*

Citation:
Song C, Lang C, Kopycki J, Hughes J and Matysik J (2015) NMR chemical shift pattern changed by ammonium sulfate precipitation in cyanobacterial phytochrome Cph1. Front. Mol. Biosci. 2:42. doi: 10.3389/fmolb.2015.00042

Introduction

Phytochromes modulate various biological responses to light in almost all phases of plant development (Franklin and Quail, 2010). Plant phytochromes represent a paradigm for a large and diverse set of photochromic photoreceptors that are also known in many microorganisms (Kehoe and Grossman, 1996; Hughes et al., 1997; Yeh et al., 1997; Davis et al., 1999; Bhoo et al., 2001; Giraud et al., 2002; Froehlich et al., 2005; De Riso et al., 2009; Rockwell et al., 2014b). Phytochromes typically photoconvert between red-absorbing (Pr) and far-red-absorbing (Pfr) states via a C15-*Z*/*E* isomerization of their covalently bound linear tetrapyrrole (bilin) chromophores (Rockwell et al., 2006; Hughes, 2010; Rockwell and Lagarias, 2010; Song et al., 2011a; Yang et al., 2011). The bilin chromophore such as phycocyanobilin (PCB), phytochromobilin (PΦB), or biliverdin (BV) is buried in a conserved pocket formed in the GAF (c*G*MP phosphodiesterase, *a*denylate cyclase, *F*hlA) domain which is part of a knotted N-terminal photosensory module also comprising PAS (*P*eriod/*A*RNT/*S*ingle-minded) and PHY (*phy*tochrome-specific) domains. The tripartite sensory module is conserved in canonical phytochromes and bacteriophytochromes (Wagner et al., 2005; Essen et al., 2008; Yang et al., 2008; Nagatani, 2010; Auldridge and Forest, 2011; Burgie et al., 2014). Phytochromes as well as a large group of related photoswitchable biliproteins, the cyanobacteriochromes (CBCRs) (Rockwell et al., 2011, 2012, 2014a; Chen et al., 2012; Hirose et al., 2013; Narikawa et al., 2013) have attracted increasing attention as *in vivo* fluorophores, in optogenetics and in synthetic biology (Shimizu-Sato et al., 2002; Levskaya et al., 2005, 2009; Shu et al., 2009; Tabor et al., 2009; Möglich and Moffat, 2010; Zhang et al., 2010; Lee et al., 2013; Müller and Weber, 2013; Müller et al., 2013, 2014a,b; Piatkevich et al., 2013; Tischer and Weiner, 2014; Yu et al., 2014; Ziegler and Möglich, 2015). Phytochrome absorbance and fluorescence at red to near-infrared wavelengths makes the superfamily interesting for studies involving whole, living organisms whose tissues scatter light particularly strongly at short wavelengths. Even more valuable is their peculiar photochromicity whereby two (meta)stable ground states with different absorbance maxima and physiological activities exist, thereby allowing biological processes to be switched on or off by a brief pulse of red or far-red light (Borthwick et al., 1952). Neither the photochromic absorbance properties nor its mechanistic connection to signaling are well understood, however.

Cyanobacterial phytochrome Cph1 from *Synechocystis* 6803 (Hughes et al., 1997; Yeh et al., 1997) represents the evolutionary link between bacteriophytochromes and plant phytochromes. The complete chromophore-bearing sensory module (amino acids 1–515) of the full-length holoCph1 (termed Cph1Δ2) exhibits almost identical absorption spectra (van Thor et al., 2001) and photodynamics (Sineshchekov et al., 2002) to those of the native molecule. Cph1Δ2 has proven to be an especially useful model for basic studies of structure/function relationship in full-length protein because of its tractability for the recombinant expression in *Escherichia coli* cells (Lamparter et al., 1997) and availability for biophysical studies including X-ray crystallography (Essen et al., 2008; Mailliet et al., 2009) as well as both liquid-state (Strauss et al., 2005a; van Thor et al., 2006; Hahn et al., 2008) and solid-state (Rohmer et al., 2006, 2008, 2010a; Song et al., 2011a,b) NMR spectroscopy. These studies together with other physical and spectroscopic methods (van Thor et al., 2001, 2005; Dasgupta et al., 2009; Mroginski et al., 2009; Rockwell et al., 2009; Kim et al., 2012b, 2013, 2014a,b; Yang et al., 2012; Velazquez Escobar et al., 2015), and mutagenesis (Fischer and Lagarias, 2004; Strauss et al., 2005b; Hahn et al., 2006) have provided an improved mechanistic understanding of the phytochrome photosensor.

Cph1Δ2 lacks the C-terminal transmitter module, comprising an ATP-binding/kinase domain as well as an amphiphilic helix-loop-helix largely responsible for dimerization (Matsushita et al., 2003; Mateos et al., 2006) and a histidine phosphoacceptor proximal to the sensory module. Since there is no 3D structure of the complete structure of any phytochrome available (see Essen et al., 2008; Yang et al., 2008, 2009; Scheerer et al., 2010; Burgie et al., 2014; Takala et al., 2014), how the light signal is propagated from the bilin through the sensor module to affect the kinase/phosphotransferase activities of the transmitter module remains conjectural. Domain-swapping experiments with Cph1 and EnvZ, however, imply that the mechanism of intramolecular signaling in SHPK's (sensory histidine protein kinases) is conserved (Levskaya et al., 2005).

Attempts to solve the 3D structure of full-length holoCph1 have been impeded by concentration-dependent aggregation in solution. Psakis et al. (2011) found that glycerol/xylitol retards aggregation significantly, but does not prevent it. The problems associated with aggregation might be circumvented by precipitating the material using ammonium sulfate (AmS) before it begins to aggregate, i.e., by collecting the SEC (size-exclusion chromatography) fractions directly into AmS. This procedure seems not to disturb the structure greatly, as the relative proportions of Pr and Pfr remain the same before and after AmS precipitation. Moreover, as previously described in full-length phyA phytochrome from *Avena sativa*, the low-temperature FTRR (Fourier-transform resonance Raman) spectra of AmS precipitates displayed similar vibrational band patterns to those of the frozen solutions (Matysik et al., 1995), implying that the effect of AmS precipitation is restricted to the hydration shell of the protein molecule. These relatively old FTRR data, however, would be insufficiently accurate to detect subtle modifications of the electronic structure of the bilin as well as its interactions with the direct binding pocket upon dehydration.

Previous MAS NMR studies on phytochromes used frozen solutions of highly concentrated proteins routinely, e.g., the complete sensory modules of Cph1 from *Synechocystis* 6803 and phyA3 from *A. sativa* (Rohmer et al., 2008, 2010a; Song et al., 2011a, 2012) as well as an isolated GAF-domain fragment of Cph2 from *Synechococcus* OS-B' (Song et al., 2014). Holoproteins of these phytochromes were produced by *in vitro* assembly with a uniformly $^{13}C/^{15}N$-labeled PCB chromophore (*u*-[^{13}C,^{15}N]-PCB). Here, we use MAS NMR technique to assess whether the structure and immediate environment of the bilin in the *u*-[^{13}C,^{15}N]-PCB-holoCph1Δ2 are preserved in an AmS pellet using 2D ^{13}C–^{13}C dipolar correlation experiments which allow

for a complete and unambiguous ^{13}C assignment for the entire bilin. We find that almost all of bilin signals move upfield (smaller chemical shifts) in the precipitated sample relative to those obtained from the frozen solution. The global effect induced by the partial dehydration on the bilin electronic structure can be attributed predominantly to packing effects between the bilin and its binding pocket. It is, however, unlikely to arise from the local modification of bilin interaction with specific protein residues.

Material and Methods

AmS Precipitation of Cph1Δ2 as Pr

The *u*-[^{13}C,^{15}N]-PCB-holoCph1Δ2 was prepared and purified by Ni-affinity and SEC as described (Song et al., 2011a). Working in dim blue–green safelight (490 nm LED), 37.5 ml of cold AmS buffer (50 mM Tris; 3.3 M AmS; 1 mM IDA, pH 7.8) was added to 15 mg of this material in the Pr state (following saturating irradiation with 730 nm monochromatic red light) in 25 ml TESß (50 mM Tris; 5 mM EDTA; 300 mM NaCl; 1 mM β-mercaptoethanol, pH 7.8), gently mixed at 4 °C for >24 h. The precipitate was then pelleted at 10,000*g* for 10 min at 4 °C and most of the supernatant removed. Following centrifugation at 50,000*g*, the pellet was finally suspended in 600 µL of the original precipitant. This slurry was packed stepwise into a 4-mm zirconia MAS NMR rotor by centrifugation at 50,000*g*, the supernatant being removed after each spin. The final packed volume was 100 µL, comprising ca. 10 mg of holoprotein. The rotor was then snap-frozen in liquid nitrogen and kept at −80 °C.

MAS NMR Spectroscopy

Two-dimensional ^{13}C–^{13}C dipolar-assisted rotational resonance (DARR) experiments were used to assign ^{13}C chemical shifts of the *u*-[^{13}C,^{15}N]-PCB chromophore in Cph1Δ2 as an AmS pellet. The DARR spectra shown in **Figure 1** and Figure S1 were recorded by using a DMX-400 spectrometer equipped with a 4-mm CP/MAS probe (Bruker, Karlsruhe). The rotor containing the *in vitro* assembled holo-Cph1Δ2 was cooled to −50 °C in the magnet. The DARR spectra were acquired at a MAS rate of 13 kHz with two mixing times of 2 and 28 ms for ^{13}C homonuclear recoupling. During the mixing period, the ^{1}H–^{13}C dipolar interaction was recovered by ^{1}H continuous wave irradiation with the intensity satisfying the $n = 1$ rotary-resonance condition (Takegoshi et al., 2001). Two-pulse phase-modulated proton decoupling scheme (Bennett et al., 1995) was applied during free evolution and acquisition periods. The typical decoupling field strength was 84 kHz. The data were collected with an 8-ms evolution in the indirect dimension; 1434 complex t_2 and 128 real t_1 points with 2048 scans. A relaxation delay of 1.5 s was applied. Each spectrum was recorded over a period of ∼140 h. Prior to Fourier transformation, the data were zero-filled to 4096 points, and an exponential apodization of 25 Hz was applied. ^{13}C resonances were externally referenced with respect to backbone CO signal of solid glycine· HCl at 176.04 ppm on the TMS scale. The data were processed with Bruker Topspin 3.1 and further analyzed by using the Sparky 3.114 (Goddard and Kneller, 2008).

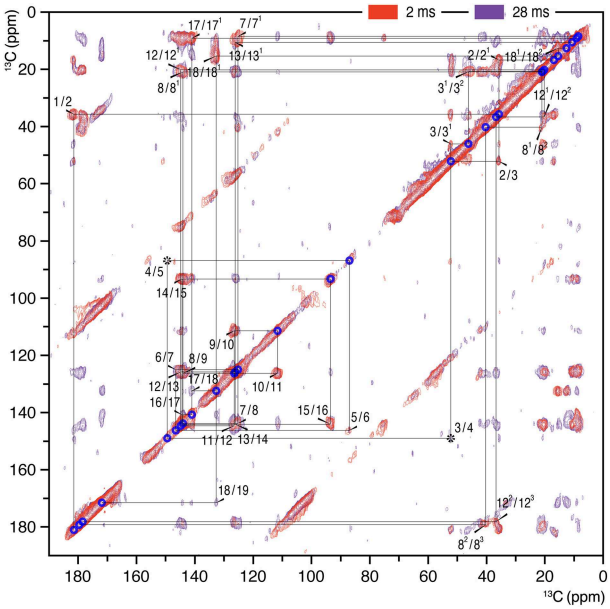

FIGURE 1 | 2D ^{13}C–^{13}C homonuclear dipolar correlation spectra of AmS precipitated Cph1Δ2 holoprotein assembled with *u*-[^{13}C,^{15}N]-PCB chromophore in the Pr dark state. Proton mixing times of 2 (red) and 28 ms (purple) were employed. The lines indicate sequences of nearest-neighbor correlations (for numbering, see **Figure 4**). The assignment of indirect-bonded correlation peaks is provided in Figure S1 (enlarged view of the DARR spectra with projections along both dimensions). The complete ^{13}C chromophore assignment as Pr is listed in Table S1 and illustrated in **Figure 4**.

Results

2D ^{13}C–^{13}C correlation spectra of the AmS-precipitated *u*-[^{13}C,^{15}N]-PCB-holoCph1Δ2 in its red-absorbing Pr form were recorded for ^{13}C chemical shifts (δ^C) of the bilin chromophore with two DARR mixing periods of 2 and 28 ms (**Figure 1**, red and purple, respectively; enlarged views of the spectra with external 1D projections along both dimensions shown in Figure S1). With a shorter mixing time of 2 ms, the DARR spectrum (red) is dominated by correlations occurring between strongly coupled (e.g., directly bonded) spins, whereas the data acquired with a 28-ms mixing time (purple) also reveal weak, through space ^{13}C–^{13}C couplings (e.g., long-range distances). It should be noted that the DARR experiments on this sample with mixing times beyond 40 ms yield much decreased overall signal intensity with many expected correlations only partially resolved (e.g., C1–C3 correlation build-up curve shown in **Figure 2**, red). Whereas, in the frozen solution states of canonical phytochromes a mixing time of 50 ms was found to be optimal for revealing the long-range ^{13}C–^{13}C correlations (Rohmer et al., 2008; Song et al., 2012). Thus, DARR mixing in the precipitated sample shows a much faster build-up behavior for long-range correlations relative to the frozen one, indicative of a more efficient spin-diffusion process between protons (Huster et al., 2002; Akbey et al., 2012).

The ^{13}C assignment of two Pr spectra of the precipitated Cph1Δ2 (**Figure 1**) is based on our previous DARR data from its frozen solution (Rohmer et al., 2008): preliminary assignment achieved by analysis of direct correlations between ^{13}C spins (red) and validated by indirect correlations originated from weak polarization transfers among isolated ^{13}C spins (purple). For example in the precipitated Cph1Δ2, the previously unambiguous assignment for the propionate side-chains of two inner rings *B* and *C* in the frozen solution because of the signal overlapping of C8/C8^1 and C12/C12^1 (Rohmer et al., 2008) can be assigned unequivocally. Well-defined correlation networks of both propionates, C8 (144.2 ppm)–C8^1 (21.0 ppm)–C8^2 (40.4 ppm)–C8^3 (179.8 ppm) and C12 (144.9 ppm)–C12^1 (20.2 ppm)–C12^2 (36.9 ppm)–C12^3 (178.5 ppm) are apparent in the spectrum recorded with a mixing period of 2 ms (**Figure 1**, red). These assignments are confirmed by multi-bond correlation peaks involving non-propionate carbons such as C7 (125.2 ppm)/C7^1 (8.7 ppm)–C8^1/C8^2/C8^3, C10 (111.8 ppm)/C11 (126.5 ppm)–C12^1, C13 (126.2 ppm)–C12^1/C12^2/C12^3, and C13^1 (10.7 ppm)–C12^2/C12^3 resolved in the 28-ms DARR mixing spectrum (**Figure 1**, purple). Intriguingly, for the *C*-ring propionate in the frozen solution state, two sets of chemical shifts were observed, indicative of local mobility of the chromophore and structural plasticity of the protein pocket (Song et al., 2011a), whereas only a single set was resolved for the precipitated Cph1Δ2. Similarly, no signal splitting in this sample was observed for its bilin ring *A* as a single correlation network for C1 (181. 5 ppm)–C2 (35.8 ppm)–[C2^1 (16.9 ppm)]–C3 (52.2 ppm)–[C3^1 (46.1 ppm)–C3^2 (20.9 ppm)]–C4 (149.5 ppm). In general, the ^{13}C MAS spectrum is better resolved in the solution state in terms of relatively narrow spectral lines which become broader on precipitation (see **Figure 3** for comparison and discussed below).

The complete ^{13}C bilin assignment in the precipitated Cph1Δ2 is summarized in Table S1, and the changes in its ^{13}C shifts ($\Delta\delta^C$) upon precipitation is illustrated in **Figure 4**. The main features are as follows:

(i) Almost all the bilin signals move upfield, as represented by blue circles in **Figure 4**, amongst which most ^{13}C atoms (27 of 33) exhibit moderate shifts of $-0.5 \leq \Delta\delta^C \leq -2.0$ ppm (Table S1). The global $\Delta\delta^C$ induced by the partial dehydration reflect changes of the electronic structure of the bilin chromophore as well as the modification of its interactions with the protein surrounding. One might doubt whether the ^{13}C chemical shift scale has shifted between these two experiments. However, in addition to standard external referencing procedure (see **Material and Methods**),

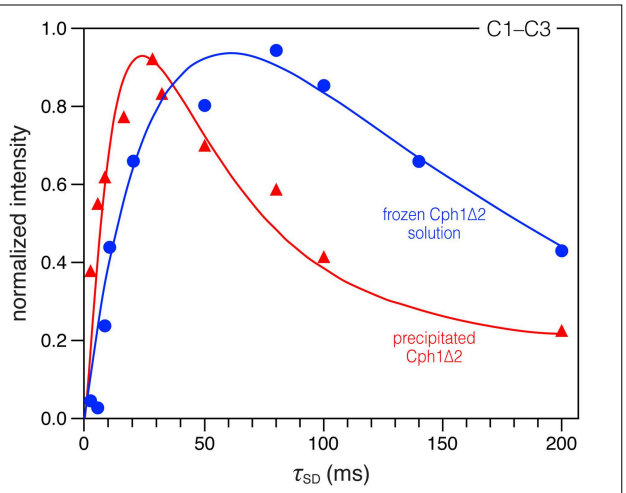

FIGURE 2 | Comparison of DARR build-up curves for the selected C1–C3 correlation in the precipitated and frozen solution states. Spin-diffusion mixing times (τ_{SD}) between 2 and 200 ms were used. All spectra were recorded under the similar conditions (with a MAS rate of 13 kHz at −50 °C, see Material and Methods for more details). The data were fitted by nonlinear least-square method (Ernst and Meier, 1998). For time evolution less than 200 ms, we expect the main contribution for the correlation intensities to be due to spin diffusion.

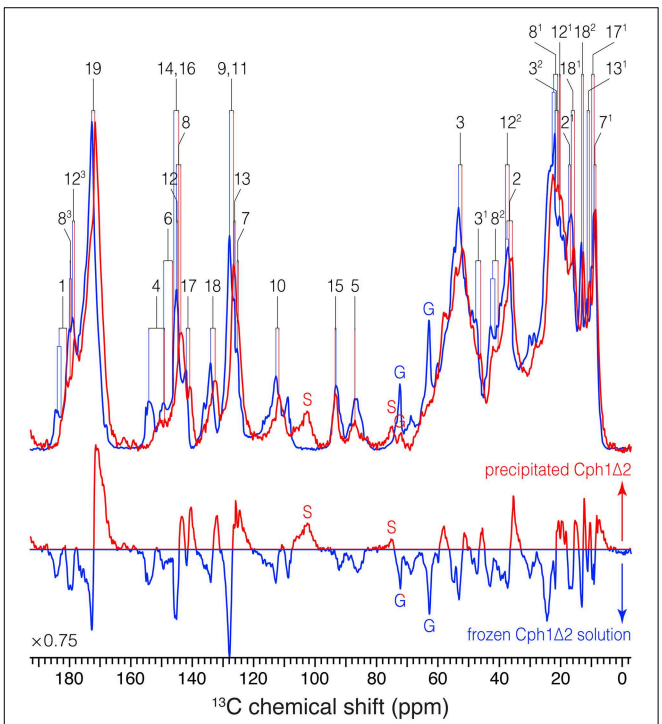

FIGURE 3 | 1D ^{13}C MAS spectra of *u*-[^{13}C,^{15}N]-PCB-Cph1Δ2 in the Pr state as an AmS pellet and as frozen solution. ^{13}C signals in the partial dehydrated (red) and frozen solution (blue) states are labeled. Signals of the natural abundance glycerol carbons at 62.8 and 72.1 ppm (Williamson et al., 2001; Rosay et al., 2002; Rohmer et al., 2008) are labeled as "G". The spinning sidebands are labeled as "S". Normalized difference spectrum (bottom) was calculated as spectrum from the precipitated sample minus that of frozen solution. The MAS rate of both experiments was maintained at 13 kHz. Typical ^{1}H $\pi/2$ and ^{13}C π pulses were 3.0 and 5.2 μs, respectively. ^{13}C transverse magnetization created by the ramped CP was transformed from ^{1}H with a contact time of 2.048 μs for both spectra. For ^{1}H decoupling, two-pulse phase modulation scheme with a pulse duration of 5.5–7 μs and a ^{1}H r.f. field strength of ~70 kHz were employed. Both spectra were recorded with 8 k scans with a recycle delay of 1.5 s. A Lorentzian apodization function with line broadening factors of 20 Hz was applied to the data processing.

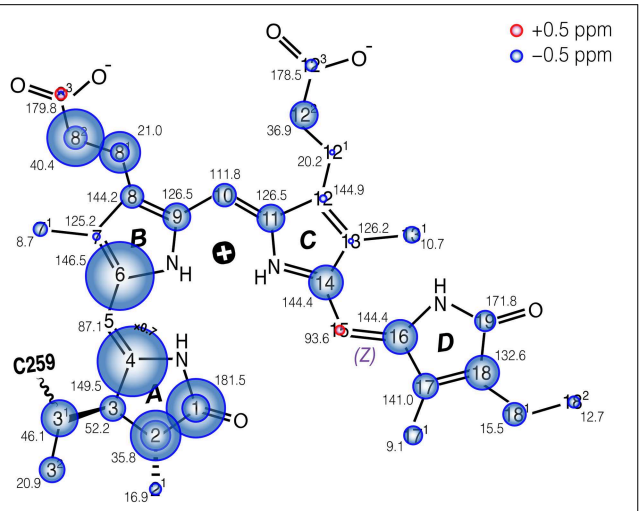

FIGURE 4 | Schematic of the changes in ^{13}C shifts of the *u*-[^{13}C,^{15}N]-PCB chromophore in Cph1Δ2 in the Pr state as an AmS pellet and as frozen solution. The size of the circles is proportional to the $\Delta\delta^C$ as AmS precipitate minus frozen solution. Carbons showing doublings as frozen solution (Rohmer et al., 2008) are labeled with two circles. δ^C values of AmS precipitate as Pr are labeled by black numbers. δ^C of both Cph1Δ2 Pr samples are summarized in Table S1.

both ^{13}C MAS spectra show the same positions of glycerol natural abundance signal as internal standard (labeled as "G", **Figure 3**). Also, the precision of ^{13}C chemical shift measurement was controlled by comparing the spectra of frozen Cph1Δ2 solution sample obtained before (shown in **Figure 3**, blue) and after (data not shown) a series of measurements of precipitated sample, only subtle variations of the ^{13}C chemical shifts were observed in the two spectra (before/after), and both are in line with the values reported ($|\Delta\delta^C| \leq 0.2$ ppm Rohmer et al., 2008). Hence, we conclude that the observed collective upfield shift is real and not an artifact that might have been occurred since wobbling of samples with high salt concentration is indeed difficult.

(ii) $\Delta\delta^C$ occurring in the region of pyrrole rings *A* and *B* are larger than those of rings *C* and *D*, in which C4 and C6 associated with the *A*–*B* methine bridge experience the largest upfield shifts of −4.4 and −3.0 ppm respectively. This likely reflects some conformational change of ring *A*, e.g., a different *A*-ring orientation relative to the *B*/*C*-ring plane. Also, the robust ^{13}C shifts localized at bilin ring *A* and the propionate side-chain of ring *B* imply the modification of bilin–protein interactions because of a tight packing around rings *A*–*C* seen in the structures of Cph1 and plant phytochromes (Essen et al., 2008; Burgie et al., 2014).

(iii) The subtle shifts found at C9 and C11 ($\Delta\delta^C = -1.2$ ppm) strongly suggest the bilin ring system in the precipitated sample retains the protonation state (Rohmer et al., 2010b), i.e., all four bilin nitrogens are fully protonated and thus positively charged, as in the frozen solution sample as both Pr and Pfr (Rohmer et al., 2008).

(iv) As can be seen from **Figure 3**, the ^{13}C line broadening of the bilin signals occurs when protein is precipitated (expressed as full-width at half maximum, $\nu_{1/2}$, summarized in Table S2). The broadening is most significant in the signals in/around *A*-ring region, for example, the ^{13}C linewidth of the ethylidene side-chain C3^1 increases from 342 Hz in the frozen solution to 489 Hz in the precipitated sample. A similar extent of line broadening is seen for C4 which broadens from 286 Hz (frozen solution) to 459 Hz (precipitate) and for C6 from 213 to 384 Hz. Also, a number of signals from rings *C* and *D* broaden dramatically like C12, C17, and C18 (Table S2). The observed increase in ^{13}C linewidth upon precipitation does not result from the interference between ^{1}H decoupling and methyl group motion at low temperatures (Maus et al., 1996). For optimal decoupling performance in the case of Cph1Δ2 precipitation, we scanned the ^{1}H r.f. field in a wide range at −50 °C, as for the spectra shown in **Figure 3** (red). Also, the proton exchange with water molecules seems unlikely to be relevant for the observed ^{13}C line broadening which occurs not only in the positions close to hydrogen-bonding functions but spreads over the entire bilin chromophore (Table S2).

Discussion

The Collective ^{13}C Upfield Shift of Bilin Carbons

The most striking finding is the upfield shift of almost the entire bilin chromophore (as shown in **Figure 4**). This shift implies stronger shielding, most likely due to a reduced paramagnetic shift of the bilin carbons. Paramagnetic chemical shifts are related to the spatially-extended and non-spherical π-orbital structures of the ^{13}C nuclei. Decay of ^{13}C shifts can be related to a dense packing of the bilin chromophore in its binding pocket. This effect occurs in particular at rings *A* and *B*, suggesting that the change of packing is especially pronounced in this region. For example, major bilin δ^C changes are seen at C1 (−2.6 ppm), C2 (−2.2 ppm), and C3^1 (−1.6 ppm) associated with the ring *A* (**Figure 4**). We suggest that these effects arise directly from a modification of the protein–chromophore linkage. Also, the C4 and C6 associated with the *A*–*B* methine bridge exhibit striking upfield shifts (−4.4 and −3.0 ppm respectively) on partial dehydration, reflecting a contortion of the thioether linkage which may also change the tilt of ring *A* in relation to the plane of rings *B* and *C*. Such deviations may arise from proximity of electrostatic charges and steric effects due to the tighter packing. This interpretation is also supported by the observed increase of spin-diffusion efficiency upon precipitation.

In presence of concentrated AmS, the effective size of the protein molecule decreases, together with increased hydrophobic protein–protein interactions resulting in a higher packing density in the partial dehydrated state primarily for the surface groups, and a shortening of the internuclear distances compared to those in the frozen solution (Kachalova et al., 1991). The strength of dipolar couplings (e.g., between ^{1}H–^{1}H and ^{1}H–^{13}C) in this state is thus increased because it is proportional to the inverse cube of

the distances between them (Huster et al., 2002; Reichert et al., 2004; Diakova et al., 2007). In this study, we observe that such difference in packing density between the partial dehydrated and frozen solution states affects not only surface groups but also the bilin and its hydrophobic binding pocket too.

A more compact protein environment of the bilin on precipitation is supported by the faster ^{13}C correlation build-up behavior observed in the DARR experiments. Taking C1–C3 correlation (181.5/52.2 ppm Figure S1) as an example, a sharp maximum is reached at mixing time of 28 ms (build-up curve shown in **Figure 2**, red), whereas in the solution state this correlation continues to increase up to 80 ms (**Figure 2**, blue). The build-up curve for C1–C3 correlation in **Figure 2** also reveals differences between the two states at short mixing times around 2 ms. In the partially-dehydrated state (red), the correlation is already intense, whereas the correlation in the solution state (blue) is just above the *S*/*N* level. Similar build-up behaviors are also seen for most correlations involving pyrrolic carbons: a maximum intensity is reached after a short mixing period of 8–32 ms (build-up curves not shown). The faster build-up rates observed in the precipitated state indicate a more efficient spin diffusion than in the frozen solution state, thus facilitating the cross-talk between protons. Also, local dynamics leads to a reduction of the spin-diffusion rates constants. For the Cph1Δ2 precipitate, larger spin-diffusion rate constants can reasonably be expected because of the faster build-up behavior of the bilin correlations, suggesting a decrease in mobility within the bilin-binding pocket. Finally, although faster correlation build-up rates are observed in this sample, the maximum intensity reached is slightly smaller compared to the frozen solution (**Figure 3**). This could arise from relaxation effects and conformational transitions between different protein subconformations (energy minima), both of which are hydration-dependent (Zanotti et al., 1999; Krushelnitsky et al., 2009; Akbey et al., 2012). These data thus demonstrate that the process of partial dehydration causes changes of electronic structure of the bilin as well as its mobility within the pocket.

An Increased Heterogeneous Bilin Environment

The Pr ground-state heterogeneity is common in Pr-state phytochromes including both canonical Cph1 (Sineshchekov et al., 2002; Rohmer et al., 2008; Mroginski et al., 2009; Mailliet et al., 2011; Song et al., 2011a, 2012; Kim et al., 2014a) and oat phyA3 (Schmidt et al., 1998; Song et al., 2012) as well as bacteriophytochromes from *Agrobacterium*, *D. radiodurans,* and *R. palustris* (von Stetten et al., 2008; Wagner et al., 2008; Toh et al., 2010). A heterogeneous ground-state population was also noted for phytochrome-related CBCRs such as NpR6012g4 (Kim et al., 2012a,b,c; Rockwell et al., 2012; Chang et al., 2013). Our previous NMR study on frozen Cph1Δ2 sample revealed the coexistence of two Pr isoforms in the solution, distinguished by their hydrogen-bonding networks and charge distribution patterns in the tetrapyrrole cavity (Song et al., 2011a). This idea has been extended by Kim et al. (2014a): they demonstrated using temperature-dependent pump–probe (PP) spectroscopy and singular-value decomposition (SVD) analysis that in solution the Pr subpopulations (fluorescent vs. photoactive) are in equilibrium at ambient temperatures and are associated with changes in the heat capacity (C_p) of the protein.

For the precipitated Cph1Δ2, however, the ^{13}C bilin signals are broader than those measured in frozen solution even for a number of peripheral carbons below ∼50 ppm (**Figure 3** and Table S2), suggesting a more heterogeneous protein environment of the bilin. Such a situation can arise from the amorphous character of the partial dehydrated sample (Kennedy and Bryant, 1990; Jia and Liu, 2006; Krushelnitsky et al., 2009), e.g., a broad distribution of protein subconformations with different interactions with the bilin (see below). The static disorder would be associated with the structural rearrangement of protein surface area because the addition of neutral salt like AmS constricts the hydration shells around the protein (Adamson and Gast, 1997) and thus results in increased hydrophobic protein–protein interactions. Although the possibility of structural distortions due to the formation of non-native electrostatic contacts between polar and charged groups in the partial dehydrated protein (Griebenow and Klibanov, 1995; Zanotti et al., 1999), the moderate ^{13}C shifts of $-0.5 \leq \Delta\delta^{C} \leq -2.0$ ppm for most bilin carbons on partial dehydration (Table S1) would rule out major rearrangement of key protein–chromophore interactions. Moreover, water percolation through the protein interior is unlikely because buried water molecules are mainly strategically placed and tightly bound, and also because their population (of full hydration) is too low for them to form interconnected threads.

Intriguingly, C4 and C6 associated with the *A*–*B* methine bridge show not only the largest ^{13}C chemical shift changes upon precipitation but also the greatest degree of line broadening (Tables S1,S2). A similar effect is also seen for other pyrrolic carbons associated with the ring *A* and its linkage to the protein. These obvious differences of direct protein environment of the ring *A* might reflect also changes of the water networks around the ring. Hence, under precipitation, the protein becomes more densely packed and its structural order is partially lost. These changes affect in particular rings *A* and *B*, here in addition also a conformational change of the chromophore, probably a change of the dihedral angle about the C4=C5 bond occurs. Since the less affected rings *C* and *D* are more hidden in the protein interior, i.e., the ring *D* is completely shielded from the solvent by the side-chains of several residues of the GAF domain and the tongue region (Essen et al., 2008), it is reasonable to assume that changes in the water environment, caused by the partial dehydration, are responsible for these changes. It appears that the lack of nearby water molecules do not modify photoprocess affects between rings *C* and *D* but rather result in a fixation of the conformations. That implies that a fully-hydrated protein does not have a single conformation but a range of conformations which appear to be averaged on NMR timescale. Water may act as "lubricant" in protein conformational changes. As the sample is precipitated, less free water molecules are available, so the ordered protein conformation collapses, and thus protein molecules in different subconformations become trapped. It has been proposed from the Cph1Δ2 Pr crystal structure (PDB code 2VEA) that the bilin is sealed off from the solvent (Essen et al., 2008), although the higher-resolution structure of the Y263F

mutant (PDB code 2ZQ5) implies that the seal is far from perfect (Mailliet et al., 2011). Future MAS NMR experiments might reveal which water molecules in the tetrapyrrole cavity (especially those in close contacts with the ring *A*) are affected in the process of partial dehydration, allowing their functional role in the reaction dynamics to be understood. It is evident from our MAS data that Cph1Δ2 precipitate as Pr shows increased heterogeneity of bilin environment.

Conclusion

AmS precipitation is a mild, reversibly treatment commonly used to purify and concentrate proteins. It acts by withdrawing water from the hydration shell surrounding proteins, thereby reducing their solubility. The precipitate is quite dense and can be compacted by centrifugation, thereby offering a potential new route to gaining 3D structural information via solid-state NMR which otherwise requires highly-concentrated frozen samples. On the other hand, AmS precipitation might have more extensive effects, blocking access to the native structure. Here we have investigated the structure of AmS-precipitated holo-Cph1Δ2 *in vitro* assembled with *u*-[^{13}C,^{15}N]-PCB in its Pr state using solid-state NMR. This represents a useful case study as earlier studies showed that not only is the phytochrome photochromic state unaffected by AmS precipitation, resonance Raman spectra differ only slightly between AmS precipitates and frozen solutions (Matysik et al., 1995). We have extensively studied frozen solutions of Cph1Δ2 phytochrome using solid-state NMR, thus we are in a good position to assay possible effects of the AmS technique with Cph1Δ2. Indeed, the bilin ^{13}C lines are broadened in the precipitated state, probably as a result of a more heterogeneous bilin environment. We identify a significant collective upfield ^{13}C chemical shift of the bilin compared to the ^{13}C data obtained from the frozen solution which reflect more dense sample packing around the bilin chromophore likely caused by the partial dehydration. Additionally, the MAS data reveal a dehydration-induced conformational change of the bilin chromophore, in particular for rings *A* and *B*. However, other key factors capable of modulating light absorption like protonation of the bilin and its direct hydrogen-bonding network seem to be unaffected by AmS precipitation. We conclude, therefore, that AmS precipitation can have significant effects throughout the protein and thus that the method, while perhaps useful in specific cases, might not provide *bona fide* structure/functional information. On the other hand, this method might allow for obtaining information on the local water pool and its exchange to the bulk. Future studies with AmS (or other salts) might elucidate how the salt-related dehydration process affects protein structure.

Acknowledgments

This work was supported by Deutsche Forschungsgemeinschaft (DFG) grant Hu702/8 and Nederlandse Organisatie voor Wetenschappelijk Onderzoek (NWO) grants DN 89-190 and ALW 822.02.007.

Supplementary Material

The Supplementary Material for this article can be found online at: http://journal.frontiersin.org/article/10.3389/fmolb.2015.00042

References

Adamson, A. W., and Gast, A. P. (1997). *Physical Chemistry of Surfaces 4th Edn.* New York, NY: John Wiley.

Akbey, Ü., van Rossum, B.-J., and Oschkinat, B.-J. (2012). Practical aspects of high-sensitivity multidimensional ^{13}C MAS NMR spectroscopy of perdeuterated proteins. *J. Magn. Reson.* 217, 77–85. doi: 10.1016/j.jmr.2012.02.015

Auldridge, M. E., and Forest, K. T. (2011). Bacterial phytochromes: more than meets the light. *Crit. Rev. Biochem. Mol. Biol.* 46, 67–88. doi: 10.3109/10409238.2010.546389

Bennett, A. E., Rienstra, C. M., Auger, M., Lakshmi, K. V., and Griffin, R. G. (1995). Heteronuclear decoupling in rotating solids. *J. Chem. Phys.* 103, 6951–6958. doi: 10.1063/1.470372

Bhoo, S. H., Davis, S. J., Walker, J., Karniol, B., and Vierstra, R. D. (2001). Bacteriophytochromes are photochromic histidine kinases using a biliverdin chromophore. *Nature* 414, 776–779. doi: 10.1038/414776a

Borthwick, H. A., Hendricks, S. B., Parker, M. W., Toole, E. H., and Toole, V. K. (1952). A reversible photoreaction controlling seed germination. *Proc. Natl. Acad. Sci. U.S.A.* 38, 662–666. doi: 10.1073/pnas.38.8.662

Burgie, E. S., Bussell, A. N., Walker, J. M., Dubiel, K., and Vierstra, R. D. (2014). Crystal structure of the photosensing module from a red/far-red light-absorbing plant phytochrome. *Proc. Natl. Acad. Sci. U.S.A.* 111, 10179–10184. doi: 10.1073/pnas.1403096111

Chang, C.-W., Gottlieb, S. M., Kim, P. W., Rockwell, N. C., Lagarias, J. C., and Larsen, D. S. (2013). Reactive ground-state pathways are not ubiquitous in red/green cyanobacteriochromes. *J. Phys. Chem. B* 117, 11229–11238. doi: 10.1021/jp402112u

Chen, Y., Zhang, J., Luo, J., Tu, J. M., Zeng, X. L., Xie, J., et al. (2012). Photophysical diversity of two novel cyanobacteriochromes with phycocyanobilin chromophores: photochemistry and dark reversion kinetics. *FEBS J.* 279, 40–54. doi: 10.1111/j.1742-4658.2011.08397.x

Dasgupta, J., Frontiera, R. R., Taylor, K. C., Lagarias, J. C., and Mathies, R. A. (2009). Ultrafast excited-state isomerization in phytochrome revealed by femtosecond stimulated Raman spectroscopy. *Proc. Natl. Acad. Sci. U.S.A.* 106, 1784–1789. doi: 10.1073/pnas.0812056106

Davis, S. J., Vener, A. V., and Vierstra, R. D. (1999). Bacteriophytochromes: phytochrome-like photoreceptors from nonphotosynthetic eubacteria. *Science* 286, 2517–2520. doi: 10.1126/science.286.5449.2517

De Riso, V., Raniello, R., Maumus, F., Rogato, A., Bowler, C., and Falciatore, A. (2009). Gene silencing in the marine diatom *Phaeodactylum tricornutum*. *Nucleic Acids Res.* 37:e96. doi: 10.1093/nar/gkp448

Diakova, G., Goddard, Y. A., Korb, J.-P., and Bryant, R. G. (2007). Changes in protein structure and dynamics as a function of hydration from ^{1}H second moments. *J. Magn. Reson.* 189, 166–172. doi: 10.1016/j.jmr.2007.09.005

Ernst, M., and Meier, B. H. (1998). "Spin diffusion in solids," in *Solid State NMR of Polymers*, eds I. Ando and T. Asakura (Amsterdam: Elsevier), 83–121. doi: 10.1016/S0167-6881(98)80007-4

Essen, L.-O., Mailliet, J., and Hughes, J. (2008). The structure of a complete phytochrome sensory module in the Pr ground state. *Proc. Natl. Acad. Sci. U.S.A.* 105, 14709–14714. doi: 10.1073/pnas.0806477105

Fischer, A. J., and Lagarias, J. C. (2004). Harnessing phytochrome's glowing potential. *Proc. Natl. Acad. Sci. U.S.A.* 101, 17334–17339. doi: 10.1073/pnas.0407645101

Franklin, K. A., and Quail, P. H. (2010). Phytochrome functions in *Arabidopsis* development. *J. Exp. Bot.* 61, 11–24. doi: 10.1093/jxb/erp304

Froehlich, A. C., Noh, B., Vierstra, R. D., Loros, J., and Dunlap, J. C. (2005). Genetic and molecular analysis of phytochromes from the filamentous fungus *Neurospora crassa*. *Eukaryot. Cell* 4, 2140–2152. doi: 10.1128/EC.4.12.2140-2152.2005

Giraud, E., Fardoux, J., Fourrier, N., Hannibal, L., Genty, B., Bouyer, P., et al. (2002). Bacteriophytochrome controls photosystem synthesis in anoxygenic bacteria. *Nature* 417, 202–205. doi: 10.1038/417202a

Goddard, T. D., and Kneller, D. G. (2008). *SPARKY, Version 3*. San Francisco, CA: University of California.

Griebenow, K., and Klibanov, A. M. (1995). Lyophilization-induced reversible changes in the secondary structure of proteins. *Proc. Natl. Acad. Sci. U.S.A.* 92, 10969–10976. doi: 10.1073/pnas.92.24.10969

Hahn, J., Strauss, H. M., Landgraf, F. T., Gimenèz, H. F., Lochnit, G., Schmieder, P., et al. (2006). Probing protein–chromophore interactions in Cph1 phytochrome by mutagenesis. *FEBS J.* 273, 1415–1429. doi: 10.1111/j.1742-4658.2006.05164.x

Hahn, J., Strauss, H. M., and Schmieder, P. (2008). Heteronuclear NMR investigation on the structure and dynamics of the chromophore binding pocket of the cyanobacterial phytochrome Cph1. *J. Am. Chem. Soc.* 130, 11170–11178. doi: 10.1021/ja8031086

Hirose, Y., Rockwell, N. C., Nishiyama, K., Narikawa, R., Ukaji, Y., Inomata, K., et al. (2013). Green/red cyanobacteriochromes regulate complementary chromatic acclimation via a protochromic photocycle. *Proc. Natl. Acad. Sci. U.S.A.* 110, 4974–4979. doi: 10.1073/pnas.1302909110

Hughes, J. (2010). Phytochrome three-dimensional structures and functions. *Biochem. Soc. Trans.* 38, 710–716. doi: 10.1042/BST0380710

Hughes, J., Lamparter, T., Mittmann, F., Hartmann, E., Gärtner, W., Wilde, A., et al. (1997). A prokaryotic phytochrome. *Nature* 386, 663. doi: 10.1038/386663a0

Huster, D., Yao, X., and Hong, M. (2002). Membrane protein topology probed by ^{1}H spin diffusion from lipids using solid-state NMR spectroscopy. *J. Am. Chem. Soc.* 124, 874–883. doi: 10.1021/ja017001r

Jia, Y., and Liu, X.-Y. (2006). From surface self-assembly to crystallization: prediction of protein crystallization conditions. *J. Phys. Chem. B* 110, 6949–6955. doi: 10.1021/jp0536089

Kachalova, G. S., Morozov, V. N., Morozova, T. Y., Myachin, E. T., Vagin, A. A., Strokopytov, B. V., et al. (1991). Comparison of structures of dry and wet hen egg-white lysozyme molecule at 1.8 Å resolution. *FEBS Lett.* 284, 91–94. doi: 10.1016/0014-5793(91)80769-Y

Kehoe, D. M., and Grossman, A. R. (1996). Similarity of a chromatic adaptation sensor to phytochrome and ethylene receptors. *Science* 273, 1409–1412. doi: 10.1126/science.273.5280.1409

Kennedy, S. D., and Bryant, R. G. (1990). Structural effects of hydration: studies of lysozyme by ^{13}C solids NMR. *Biopolymers* 29, 1801–1806. doi: 10.1002/bip.360291411

Kim, P. W., Freer, L. H., Rockwell, N. C., Martin, S. S., Lagarias, J. C., and Larsen, D. S. (2012a). Second-chance initiation dynamics of the cyanobacterial photocycle in the NpR6012 GAF4 domain of *Nostoc punctiforme*. *J. Am. Chem. Soc.* 134, 130–133. doi: 10.1021/ja209533x

Kim, P. W., Freer, L. H., Rockwell, N. C., Martin, S. S., Lagarias, J. C., and Larsen, D. S. (2012b). Femtosecond photodynamics of the red/green cyanobacteriochrome NpR6012g4 from *Nostoc punctiforme*. 1. Forward dynamics. *Biochemistry* 51, 608–618. doi: 10.1021/bi201507k

Kim, P. W., Freer, L. H., Rockwell, N. C., Martin, S. S., Lagarias, J. C., and Larsen, D. S. (2012c). Femtosecond photodynamics of the red/green cyanobacteriochrome NpR6012g4 from *Nostoc punctiforme*. 2. Reverse dynamics. *Biochemistry* 51, 619–630. doi: 10.1021/bi2017365

Kim, P. W., Rockwell, N. C., Freer, L. H., Chang, C.-W., Martin, S. S., Lagarias, J. C., et al. (2013). Unraveling the primary isomerization dynamics in cyanobacterial phytochrome Cph1 with multipulse manipulations. *J. Phys. Chem. Lett.* 4, 2605–2609. doi: 10.1021/jz401443q

Kim, P. W., Rockwell, N. C., Martin, S. S., Lagarias, J. C., and Larsen, D. S. (2014a). Dynamic inhomogeneity in the photodynamics of cyanobacterial phytochrome Cph1. *Biochemistry* 53, 2818–2826. doi: 10.1021/bi500108s

Kim, P. W., Rockwell, N. C., Martin, S. S., Lagarias, J. C., and Larsen, D. S. (2014b). Heterogeneous photodynamics of the P_{fr} state in the cyanobacterial phytochrome Cph1. *Biochemistry* 53, 4601–4611. doi: 10.1021/bi5005359

Krushelnitsky, A., Zinkevich, T., Mukhametshina, N., Tarasova, N., Gogolev, Y., Gnezdilov, O., et al. (2009). ^{13}C and ^{15}N NMR study of the hydration response of T4 lysozyme and αB-crystallin internal dynamics. *J. Phys. Chem. B* 113, 10022–10034. doi: 10.1021/jp900337x

Lamparter, T., Mittmann, F., Gärtner, W., Börner, T., Hartmann, E., and Hughes, J. (1997). Characterization of recombinant phytochrome from the cyanobacterium *Synechocystis*. *Proc. Natl. Acad. Sci. U.S.A.* 94, 11792–11797. doi: 10.1073/pnas.94.22.11792

Lee, J. M., Lee, J., Kim, T., and Lee, S. K. (2013). Switchable gene expression in *Escherichia coli* using a miniaturized photobioreactor. *PLoS ONE* 8:e52382. doi: 10.1371/journal.pone.0052382

Levskaya, A., Chevalier, A. A., Tabor, J. J., Simpson, Z. B., Lavery, L. A., Levy, M., et al. (2005). Synthetic biology: engineering *Escherichia coli* to see light. *Nature* 438, 441–442. doi: 10.1038/nature04405

Levskaya, A., Weiner, O. D., Lim, W. A., and Voigt, C. A. (2009). Spatiotemporal control of cell signalling using a light-switchable protein interaction. *Nature* 461, 997–1001. doi: 10.1038/nature08446

Mailliet, J., Psakis, G., Schroeder, C., Kaltofen, S., Dürrwang, U., Hughes, J., et al. (2009). Dwelling in the dark: procedures for the crystallography of phytochromes and other photochromic proteins. *Acta Cryst.* D65, 1232–1235. doi: 10.1107/S0907444909034106

Mailliet, J., Psakis, G., Sineshchekov, V., Essen, L.-O., and Hughes, J. (2011). Spectroscopy and a high-resolution crystal structure of Tyr-263 mutant of cyanobacterial phytochrome Cph1. *J. Mol. Biol.* 413, 115–127. doi: 10.1016/j.jmb.2011.08.023

Mateos, J. L., Luppi, J. B., Ogorodnikova, O. B., Sineshchekov, A. A., Yanovsky, M. J., and Braslavsky, S. E. (2006). Functional and biochemical analysis of the N-terminal domain of phytochrome A. *J. Biol. Chem.* 281, 34421–34429. doi: 10.1074/jbc.M603538200

Matsushita, T., Mochizuki, N., and Nagatani, A. (2003). Dimers of the N-terminal domain of phytochrome B are functional in the nucleus. *Nature* 424, 571–574. doi: 10.1038/nature01837

Matysik, J., Hildebrandt, P., Schlamann, W., Braslavsky, S. E., and Schaffner, K. (1995). Fourier-transform resonance Raman spectroscopy of intermediates of the phytochrome photocycle. *Biochemistry* 34, 10497–10507. doi: 10.1021/bi00033a023

Maus, D. C., Copié, V., Sun, B., Griffiths, J. M., Griffin, R. G., Luo, S., et al. (1996). A solid-state NMR study of tungsten methyl group dynamics in $[W(\eta^5\text{-}C_5Me_5)Me_4][PF_6]$. *J. Am. Chem. Soc.* 118, 5665–5671. doi: 10.1021/ja960248h

Möglich, A., and Moffat, K. (2010). Engineered photoreceptors as novel optogenetic tools. *Photochem. Photobiol. Sci.* 9, 1286–1300. doi: 10.1039/c0pp00167h

Mroginski, M. A., von Stetten, D., Velazquez Escobar, F., Strauss, H. M., Kaminski, S., Scheerer, P., et al. (2009). Chromophore structure of cyanobacterial phytochrome Cph1 in the Pr state: reconciling structural and spectroscopic data by QM/MM calculations. *Biophys. J.* 96, 4153–4163. doi: 10.1016/j.bpj.2009.02.029

Müller, K., Engesser, R., Schulz, S., Steinberg, T., Tomakidi, P., Weber, C. C., et al. (2013). Multi-chromatic control of mammalian gene expression and signalling. *Nucleic Acids Res.* 41, e124. doi: 10.1093/nar/gkt340

Müller, K., Engesser, R., Timmer, J., Zurbriggen, M. D., and Weber, W. (2014b). Orthogonal optogenetic triple-gene control in mammalian cells. *ACS Synth. Biol.* 3, 796–801. doi: 10.1021/sb500305v

Müller, K., and Weber, W. (2013). Optogenetic tools for mammalian systems. *Mol. BioSyst.* 9, 596–608. doi: 10.1039/c3mb25590e

Müller, K., Zurbriggen, M. D., and Weber, W. (2014a). Control of gene expression using a red- and far-red light–responsive bi-stable toggle switch. *Nat. Protoc.* 9, 622–632. doi: 10.1038/nprot.2014.038

Nagatani, A. (2010). Phytochrome: structural basis for its functions. *Curr. Opin. Plant Biol.* 13, 565–570. doi: 10.1016/j.pbi.2010.07.002

Narikawa, R., Ishizuka, T., Muraki, N., Shiba, T., Kurisu, G., and Ikeuchi, M. (2013). Structures of cyanobacteriochromes from phototaxis regulators AnPixJ and TePixJ reveal general and specific photoconversion mechanism. *Proc. Natl. Acad. Sci. U.S.A.* 110, 918–923. doi: 10.1073/pnas.1212098110

Piatkevich, K. D., Subach, F. V., and Verkhusha, V. V. (2013). Engineering of bacterial phytochromes for near-infrared imaging, sensing, and light-control in mammals. *Chem. Soc. Rev.* 42, 3441–3452. doi: 10.1039/c3cs35458j

Psakis, G., Mailliet, J., Lang, C., Teufel, L., Essen, L.-O., and Hughes, J. (2011). Signaling kinetics of cyanobacterial phytochrome Cph1, a light regulated histidine kinase. *Biochemistry* 50, 6178–6188. doi: 10.1021/bi200612d

Reichert, D., Pascui, O., deAzevedo, E. R., Bonagamba, T. J., Arnold, K., and Huster, D. (2004). A solid-state NMR study of the fast and slow dynamics of collagen fibrils at varying hydration levels. *Magn. Reson. Chem.* 42, 276–284. doi: 10.1002/mrc.1334

Rockwell, N. C., Duanmu, D., Martin, S. S., Bachy, C., Price, D. C., Bhattacharya, D., et al. (2014b). Eukaryotic algal phytochromes span the visible spectrum. *Proc. Natl. Acad. Sci. U.S.A.* 111, 3871–3876. doi: 10.1073/pnas.1401871111

Rockwell, N. C., and Lagarias, J. C. (2010). A brief history of phytochromes. *Chemphyschem* 11, 1172–1180. doi: 10.1002/cphc.200900894

Rockwell, N. C., Martin, S. S., Feoktistova, K., and Lagarias, J. C. (2011). Diverse two-cysteine photocycles in phytochromes and cyanobacteriochromes. *Proc. Natl. Acad. Sci. U.S.A.* 108, 11854–11859. doi: 10.1073/pnas.1107844108

Rockwell, N. C., Martin, S. S., Gulevich, A. G., and Lagarias, J. C. (2014a). Conserved phenylalanine residues are required for blue-shifting of cyanobacteriochrome photoproducts. *Biochemistry* 53, 3118–3130. doi: 10.1021/bi500037a

Rockwell, N. C., Martin, S. S., and Lagarias, J. C. (2012). Red/green cyanobacteriochromes: sensors of color and power. *Biochemistry* 51, 9667–9677. doi: 10.1021/bi3013565

Rockwell, N. C., Shang, L., Martin, S. S., and Lagarias, J. C. (2009). Distinct classes of red/far-red photochemistry within the phytochrome superfamily. *Proc. Natl. Acad. Sci. U.S.A.* 106, 6123–6127. doi: 10.1073/pnas.0902370106

Rockwell, N. C., Su, Y.-S., and Lagarias, J. C. (2006). Phytochrome structure and signaling mechanisms. *Annu. Rev. Plant Biol.* 57, 837–858. doi: 10.1146/annurev.arplant.56.032604.144208

Rohmer, T., Lang, C., Bongards, C., Gupta, K. B., Neugebauer, J., Hughes, J., et al. (2010a). Phytochrome as molecular machine: revealing chromophore action during the Pfr→Pr photoconversion by magic-angle spinning NMR spectroscopy. *J. Am. Chem. Soc.* 132, 4431–4437. doi: 10.1021/ja9108616

Rohmer, T., Lang, C., Gärtner, W., Hughes, J., and Matysik, J. (2010b). Role of the protein cavity in phytochrome chromoprotein assembly and double-bond isomerization: a comparison with model compounds. *Photochem. Photobiol.* 86, 856–861. doi: 10.1111/j.1751-1097.2010.00740.x

Rohmer, T., Lang, C., Hughes, J., Essen, L.-O., Gärtner, W., and Matysik, J. (2008). Light-induced chromophore activity and signal transduction in phytochromes observed by ^{13}C and ^{15}N magic-angle spinning NMR. *Proc. Natl. Acad. Sci. U.S.A.* 105, 15229–15234. doi: 10.1073/pnas.0805696105

Rohmer, T., Strauss, H., Hughes, J., de Groot, H., Gärtner, W., Schmieder, P., et al. (2006). ^{15}N MAS NMR studies of Cph1 phytochrome: chromophore dynamics and intramolecular signal transduction. *J. Phys. Chem. B* 110, 20580–20585. doi: 10.1021/jp062454+

Rosay, M., Weis, V., Kreischer, K. E., Temkin, R. J., and Griffin, R. G. (2002). Two-dimensional ^{13}C–^{13}C correlation spectroscopy with magic angle spinning and dynamic nuclear polarization. *J. Am. Chem. Soc.* 124, 3214–3215. doi: 10.1021/ja0176752

Scheerer, P., Michael, N., Park, J. H., Nagano, S., Choe, H.-W., Inomata, K., et al. (2010). Light-induced conformational changes of the chromophore and the protein in phytochromes: bacterial phytochromes as model systems. *Chemphyschem* 11, 1090–1105. doi: 10.1002/cphc.200900913

Schmidt, P., Gensch, T., Remberg, A., Gärtner, W., Braslavsky, S. E., and Schaffner, K. (1998). The complexity of the P_r to P_{fr} phototransformation kinetics is an intrinsic property of native phytochrome. *Photochem. Photobiol.* 68, 754–761.

Shimizu-Sato, S., Huq, E., Tepperman, J. M., and Quail, P. H. (2002). A light-switchable gene promoter system. *Nat. Biotechnol.* 20, 1041–1044. doi: 10.1038/nbt734

Shu, X., Royant, A., Lin, M. Z., Aguilera, T. A., Lev-Ram, V., Steinbach, P. A., et al. (2009). Mammalian expression of infrared fluorescent proteins engineered from a bacterial phytochrome *Science* 324, 804–807. doi: 10.1126/science.1168683

Sineshchekov, V., Koppel, L., Esteban, B., Hughes, J., and Lamparter, T. (2002). Fluorescence investigation of the recombinant cyanobacterial phytochrome (Cph1) and its C-terminally truncated monomeric species (Cph1Δ2): implication for holoprotein assembly, chromophore–apoprotein interaction and photochemistry. *J. Photochem. Photobiol. B* 67, 39–50. doi: 10.1016/S1011-1344(02)00282-8

Song, C., Essen, L.-O., Gärtner, W., Hughes, J., and Matysik, J. (2012). Solid-state NMR spectroscopic study of chromophore–protein interactions in the Pr ground state of plant phytochrome A. *Mol. Plant.* 5, 698–715. doi: 10.1093/mp/sss017

Song, C., Psakis, G., Kopycki, J., Lang, C., Matysik, J., and Hughes, J. (2014). The D-ring, not the A-ring, rotates in *Synechococcus* OS-B' phytochrome. *J. Biol. Chem.* 289, 2552–2562. doi: 10.1074/jbc.M113.520031

Song, C., Psakis, G., Lang, C., Mailliet, J., Gärtner, W., Hughes, J., et al. (2011a). Two ground state isoforms and a chromophore *D*-ring photoflip triggering extensive intramolecular changes in a canonical phytochrome. *Proc. Natl. Acad. Sci. U.S.A.* 108, 3842–3847. doi: 10.1073/pnas.1013377108

Song, C., Psakis, G., Lang, C., Mailliet, J., Zaanen, J., Gärtner, W., et al. (2011b). On the collective nature of phytochrome photoactivation. *Biochemistry* 50, 10987–10989. doi: 10.1021/bi201504a

Strauss, H. M., Hughes, J., and Schmieder, P. (2005a). Heteronuclear solution-state NMR studies of the chromophore in cyanobacterial phytochrome Cph1. *Biochemistry* 44, 8244–8250. doi: 10.1021/bi050457r

Strauss, H. M., Schmieder, P., and Hughes, J. (2005b). Light-dependent dimerisation in the N-terminal sensory module of cyanobacterial phytochrome 1. *FEBS Lett.* 579, 3970–3974. doi: 10.1016/j.febslet.2005.06.025

Tabor, J. J., Salis, H., Simpson, Z. B., Chevalier, A. A., Levskaya, A., Marcotte, E. M., et al. (2009). A synthetic genetic edge detection program. *Cell* 137, 1272–1281. doi: 10.1016/j.cell.2009.04.048

Takala, H., Björling, A., Berntsson, O., Lehtivuori, H., Niebling, S., Hoernke, M., et al. (2014). Signal amplification and transduction in phytochrome photosensors. *Nature* 509, 245–248. doi: 10.1038/nature13310

Takegoshi, K., Nakamura, S., and Terao, T. (2001). ^{13}C–^{1}H dipolar-assisted rotational resonance in magic-angle spinning NMR. *Chem. Phys. Lett.* 344, 631–637. doi: 10.1016/S0009-2614(01)00791-6

Tischer, D., and Weiner, O. D. (2014). Illuminating cell signalling with optogenetic tools. *Nat. Rev. Mol. Cell Biol.* 15, 551–558. doi: 10.1038/nrm3837

Toh, K. C., Stojković, E. A., van Stokkum, I. H. M., Moffat, K., and Kennis, J. T. M. (2010). Proton-transfer and hydrogen-bond interactions determine fluorescence quantum yield and photochemical efficiency of bacteriophytochrome. *Proc. Natl. Acad. Sci. U.S.A.* 107, 9170–9175. doi: 10.1073/pnas.0911535107

van Thor, J. J., Borucki, B., Crielaard, W., Otto, H., Lamparter, T., Hughes, J., et al. (2001). Light-induced proton release and proton uptake reactions in the cyanobacterial phytochrome Cph1. *Biochemistry* 40, 11460–11471. doi: 10.1021/bi002651d

van Thor, J. J., Fisher, N., and Rich, P. R. (2005). Assignments of the Pfr–Pr FTIR difference spectrum of cyanobacterial phytochrome Cph1 using ^{15}N and ^{13}C isotopically labeled phycocyanobilin chromophore. *J. Phys. Chem. B* 109, 20597–20604. doi: 10.1021/jp052323t

van Thor, J. J., Mackeen, M., Kuprov, I., Dwek, R. A., and Wormald, M. R. (2006). Chromophore structure in the photocycle of the cyanobacterial phytochrome Cph1. *Biophys. J.* 91, 1811–1822. doi: 10.1529/biophysj.106.084335

Velazquez Escobar, F., von Stetten, D., Günther-Lütkens, M., Keidel, A., Michael, N., Lamparter, T., et al. (2015). Conformational heterogeneity of the Pfr chromophore in plant and cyanobacterial phytochromes. *Front. Mol. Biosci.* 2:37. doi: 10.3389/fmolb.2015.00037

von Stetten, D., Günther, M., Scheerer, P., Murgida, D. H., Mroginski, M. A., Krauss, N., et al. (2008). Chromophore heterogeneity and photoconversion in phytochrome crystals and solution studied by resonance Raman spectroscopy. *Angew. Chem. Int. Ed. Engl.* 47, 4753–4755. doi: 10.1002/anie.200705716

Wagner, J. R., Brunzelle, J. S., Forest, K. T., and Vierstra, R. D. (2005). A light-sensing knot revealed by the structure of the chromophore-binding domain of phytochrome. *Nature* 438, 325–331. doi: 10.1038/nature04118

Wagner, J. R., Zhang, J., von Stetten, D., Günther, M., Murgida, D. H., Mroginski, M. A., et al. (2008). Mutational analysis of *Deinococcus radiodurans* bacteriophytochrome reveals key amino acids necessary for the phytochromicity and proton exchange cycle of phytochromes. *J. Biol. Chem.* 283, 12212–12226. doi: 10.1074/jbc.M709355200

Williamson, P. T. F., Bains, S., Chung, C., Cooke, R., Meier, B. H., and Watts, A. (2001). "Characterization and assignment of uniformly labeled NT(8-13) at the agonist binding site of the G-protein coupled neurotensin receptor," in *Perspectives on Solid State NMR in Biology*, eds S. R. Kiihne and H. J. M. de Groot (Dordrecht: Kluwer Academic Publishers), 191–202. doi: 10.1007/978-94-017-2579-8_17

Yang, X., Kuk, J., and Moffat, K. (2009). Conformational differences between the Pfr and Pr states in *Pseudomonas aeruginosa* bacteriophytochrome. *Proc. Natl. Acad. Sci. U.S.A.* 106, 15639–15644. doi: 10.1073/pnas.0902178106

Yang, X., Kuk, J., and Moffat, K. (2008). Crystal structure of *Pseudomonas aeruginosa* bacteriophytochrome: photoconversion and signal transduction. *Proc. Natl. Acad. Sci. U.S.A.* 105, 14715–14720. doi: 10.1073/pnas.0806718105

Yang, X., Ren, Z., Kuk, K., and Moffat, K. (2011). Temperature-scan cryocrystallography reveals reaction intermediates in bacteriophytochrome. *Nature* 479, 428–432. doi: 10.1038/nature10506

Yang, Y., Linke, M., von Haimberger, T., Hahn, J., Matute, R., González, L., et al. (2012). Real-time tracking of phytochrome's orientational changes during Pr photoisomerization. *J. Am. Chem. Soc.* 134, 1408–1411. doi: 10.1021/ja209413d

Yeh, K.-C., Wu, S.-H., Murphy, J. T., and Lagarias, J. C. (1997). A cyanobacterial phytochrome two-component light sensory system. *Science* 277, 1505–1508. doi: 10.1126/science.277.5331.1505

Yu, D., Gustafson, W. C., Han, C., Lafaye, C., Noirclerc-Savoye, M., Ge, W.-P., et al. (2014). An improved monomeric infrared fluorescent protein for neuronal and tumour brain imaging. *Nat. Commun.* 5:3626. doi: 10.1038/ncomms4626

Zanotti, J.-M., Bellissent-Funel, M. C., and Parello, J. (1999). Hydration-coupled dynamics in proteins studied by neutron scattering and NMR: the case of the typical EF-hand calcium-binding parvalbumin. *Biophys. J.* 76, 2390–2411. doi: 10.1016/S0006-3495(99)77395-9

Zhang, J. A., Wu, X. J., Wang, Z. B., Chen, Y., Wang, X., Zhou, M., et al. (2010). Fused-gene approach to photoswitchable and fluorescent biliproteins. *Angew. Chem. Int. Ed. Engl.* 49, 5456–5458. doi: 10.1002/anie.201001094

Ziegler, T., and Möglich, A. (2015). Photoreceptor engineering. *Front. Mol. Biosci.* 2:30. doi: 10.3389/fmolb.2015.00030

Conflict of Interest Statement: The authors declare that the research was conducted in the absence of any commercial or financial relationships that could be construed as a potential conflict of interest.

frontiers in Molecular Biosciences

ORIGINAL RESEARCH
published: 10 July 2015
doi: 10.3389/fmolb.2015.00037

Conformational heterogeneity of the Pfr chromophore in plant and cyanobacterial phytochromes

Francisco Velazquez Escobar[1‡], *David von Stetten*[1†‡], *Mina Günther-Lütkens*[1], *Anke Keidel*[1], *Norbert Michael*[1], *Tilman Lamparter*[2], *Lars-Oliver Essen*[3], *Jon Hughes*[4], *Wolfgang Gärtner*[5], *Yang Yang*[6], *Karsten Heyne*[6], *Maria A. Mroginski*[1] and *Peter Hildebrandt*[1*]

[1] Institut für Chemie, Technische Universität Berlin, Berlin, Germany, [2] Botanisches Institut, Karlsruher Institut für Technologie, Karlsruhe, Germany, [3] Fachbereich Chemie, Philipps-Universität Marburg, Marburg, Germany, [4] Institut für Pflanzenphysiologie, Justus Liebig University, Gießen, Germany, [5] Max-Planck-Institut für Chemische Energiekonversion, Mülheim, Germany, [6] Institut für Experimentalphysik, Freie Universität Berlin, Berlin, Germany

Phytochromes are biological photoreceptors that can be reversibly photoconverted between a dark and photoactivated state. The underlying reaction sequences are initiated by the photoisomerization of the tetrapyrrole cofactor, which in plant and cyanobacterial phytochromes are a phytochromobilin (PΦB) and a phycocyanobilin (PCB), respectively. The transition between the two states represents an on/off-switch of the output module activating or deactivating downstream physiological processes. In addition, the photoactivated state, i.e., Pfr in canonical phytochromes, can be thermally reverted to the dark state (Pr). The present study aimed to improve our understanding of the specific reactivity of various PΦB- and PCB-binding phytochromes in the Pfr state by analysing the cofactor structure by vibrational spectroscopic techniques. Resonance Raman (RR) spectroscopy revealed two Pfr conformers (Pfr-I and Pfr-II) forming a temperature-dependent conformational equilibrium. The two sub-states—found in all phytochromes studied, albeit with different relative contributions—differ in structural details of the *C-D* and *A-B* methine bridges. In the Pfr-I sub-state the torsion between the rings *C* and *D* is larger by ca. 10° compared to Pfr-II. This structural difference is presumably related to different hydrogen bonding interactions of ring *D* as revealed by time-resolved IR spectroscopic studies of the cyanobacterial phytochrome Cph1. The transitions between the two sub-states are evidently too fast (i.e., nanosecond time scale) to be resolved by NMR spectroscopy which could not detect a structural heterogeneity of the chromophore in Pfr. The implications of the present findings for the dark reversion of the Pfr state are discussed.

Keywords: phytochrome, tetrapyrrole, isomerization, structural heterogeneity, hydrogen bonding, resonance Raman spectroscopy, time-resolved IR spectroscopy, quantum chemical calculations

OPEN ACCESS

Edited by:
Tilo Mathes, Vrije Universiteit Amsterdam, Netherlands

Reviewed by:
Nathan C. Rockwell, University of California, Davis, USA
Delmar Larsen, University of California, Davis, USA

***Correspondence:**
Peter Hildebrandt, Institut für Chemie, Technische Universität Berlin, Sekr. PC14, Straße des 17. Juni 135, D-10623 Berlin, Germany
hildebrandt@chem.tu-berlin.de

†Present Address:
David von Stetten, Structural Biology Group, European Synchrotron Radiation Facility, Grenoble, France

‡*These authors have contributed equally to this work.*

Specialty section:
This article was submitted to Biophysics, a section of the journal Frontiers in Molecular Biosciences

Received: *29 April 2015*
Accepted: *22 June 2015*
Published: *10 July 2015*

Citation:
Velazquez Escobar F, von Stetten D, Günther-Lütkens M, Keidel A, Michael N, Lamparter T, Essen L-O, Hughes J, Gärtner W, Yang Y, Heyne K, Mroginski MA and Hildebrandt P (2015) Conformational heterogeneity of the Pfr chromophore in plant and cyanobacterial phytochromes. Front. Mol. Biosci. 2:37. doi: 10.3389/fmolb.2015.00037

Introduction

Phytochromes are ubiquitous photoreceptor in plants that utilize light as a source of information for controlling photomorphogenic processes (Quail, 1998; Schäfer and Nagy, 2006). Upon light excitation phytochromes are interconverted between the red-absorbing (Pr) and far-red absorbing state (Pfr), corresponding to a switch between physiologically inactive and active states, respectively. The light-absorbing cofactor is a linear methine-bridged tetrapyrrole, phytochromobilin (PΦB), that is covalently linked to a cysteine residue via a thioether bridge formed with the vinyl substituent of ring *A* (**Figure 1**) (Gärtner and Braslavsky, 2004; Rockwell et al., 2006; Rockwell and Lagarias, 2010). The primary photochemical step of the Pr → Pfr conversion is a double-bond isomerization (*Z*/*E*) of the *C-D* methine bridge (Rockwell et al., 2006; Rockwell and Lagarias, 2010). Subsequent steps include protein motions which eventually induce the functional relevant structural changes leading to the physiological signal. Phytochrome can therefore be regarded as a bimodal photoswitch which is based on the photoinduced conversion between the *ZZZssa* (Pr) and *ZZEssa* (Pfr) tetrapyrrole configuration. In addition to photoconversion, a unidirectional thermal pathway allowing dark reversion of Pfr to Pr is often apparent. Amongst the prokaryotic bacteriophytochromes, the resting state of the small "bathy"-type group is Pfr rather than Pr. Here dark reversion from Pr to Pfr takes place, corresponding to a thermal *E* → *Z* double bond isomerization that is initiated by a keto/enol tautomerization (Velazquez Escobar et al., 2015). It might well be that an analogous mechanism also holds for Pfr → Pr dark reversion in canonical phytochromes as suggested earlier (Lagarias and Rapoport, 1980).

Most of the knowledge in molecular phytochrome research was obtained from cyanobacterial phytochromes and bacteriophytochromes which employ phycocyanobilin (PCB) and biliverdin (BV) as chromophores, respectively (Rockwell and Lagarias, 2010). These phytochromes are more tractable than plant phytochromes and thus, the first three-dimensional (3D) structures at atomic resolution were obtained from these representatives of the superfamily (Wagner et al., 2005, 2007; Yang et al., 2007, 2008, 2009, 2011; Essen et al., 2008; Malliet et al., 2011; Bellini and Papiz, 2012; Anders et al., 2013, 2014; Takala et al., 2014). Crystallographic studies of a bacteriophytochrome also revealed the protein structural changes implicated in regulating the output module (Takala et al., 2014) that is typically a histidine kinase-like region. Only recently 3D structural data have been obtained for plant phytochromes (Song et al., 2012; Burgie et al., 2014). Otherwise, structural investigations of plant phytochromes were largely restricted to spectroscopic approaches, including nuclear magnetic resonance (NMR), transient absorption, resonance Raman (RR), and infrared (IR) spectroscopy (Fodor et al., 1988, 1990; Mizutani et al., 1994; Matysik et al., 1995; Kneip et al., 1997, 1999; Andel et al., 2000; Gärtner and Braslavsky, 2004; Mroginski et al., 2004, 2011a,b; Murgida et al., 2007; Rohmer et al., 2008; Schwinté et al., 2008; Dasgupta et al., 2009; Song et al., 2012, 2013). These results together with spectroscopic data and molecular modeling studies (Mroginski et al., 2011b) demonstrated extensive similarities in the overall fold and the chromophore structure in the parent states of plant, cyanobacterial, and bacteriophytochromes, although the different chromophores (PΦB vs. BV) attach to different Cys residues (Lamparter et al., 2002; Rockwell et al., 2006).

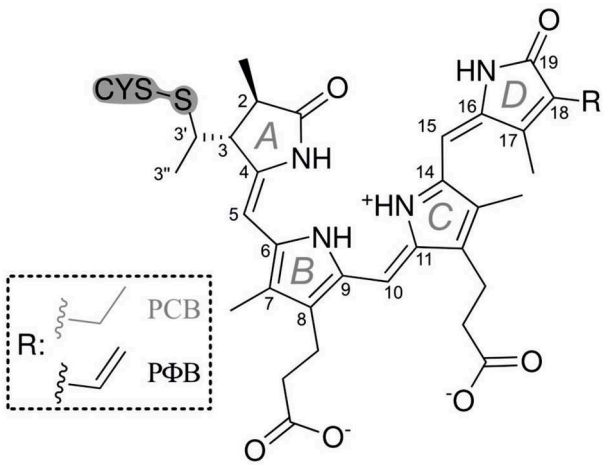

FIGURE 1 | Structural formulae of the PCB and PΦB chromophores in the *ZZEssa* configuration of Pfr.

Although most spectroscopic studies on canonical phytochromes have focused on the thermally stable Pr state (Rockwell et al., 2006; Rockwell and Lagarias, 2010), important structural insight has also been obtained for the Pfr state albeit with partly conflicting conclusions. Based on NMR spectroscopy on the canonical cyanobacterial phytochrome Cph1 as well as plant phytochrome A, Matysik and co-workers demonstrated that the chromophore was held rigidly in the binding pocket of Pfr, whereas in the Pr state the chromophore was much more flexible—indeed showing two distinct substates (Song et al., 2011, 2012, 2013), as implied by fluorescence spectroscopy (Sineshchekov et al., 1998). However, time-resolved optical spectroscopies of plant phytochrome A provided evidence for a conformational heterogeneity in both the Pr and Pfr states, corresponding to two parallel photo-induced reaction pathways (Schmidt et al., 1998; Sineshchekov, 2004). Essentially, the same conclusions were derived from transient absorption spectroscopy of Cph1, covering a wide dynamic range (Kim et al., 2013, 2014a,b). A heterogeneous chromophore structure has also been demonstrated for the Pfr state of algal phytochromes on the basis of circular dichroism (CD) spectroscopy (Rockwell et al., 2014). Furthermore, a recent RR spectroscopic study on BV-binding bacteriophytochromes revealed a homogeneous chromophore structure in the Pfr state only for representatives

Abbreviations: BV, biliverdin; PCB, phycocyanobilin; PΦB, phytochromobilin; Agp1, Cph1, Cph2, CphA, and phyA refer to the photosensor modules of the various phytochromes studied in this work; Pr and Pfr denote the red- and far-red-absorbing states, respectively; *A-B*, *B-C*, and *C-D* denote the methine bridges between the respective pyrrole rings; CD, circular dichroism; RR, resonance Raman; IR, infrared; HOOP, hydrogen out-of-plane; NH ip, N-H in-plane bending.

of the bathy-phytochromes family, whereas a temperature-dependent equilibrium between two Pfr conformers was also observed for prototypical phytochromes (Salewski et al., 2013). This structural heterogeneity was suggested to be associated with the thermal double bond isomerization preceding the Pfr → Pr dark reversion.

In this work, we have extended these studies to the Pfr state of various phytochromes that bind PΦB or PCB. We have employed RR spectroscopy that selectively probes the vibrational spectrum of the cofactor representing a characteristic fingerprint of the structure of the tetrapyrrole and its interactions with the protein environment (Mroginski et al., 2011a). To support the vibrational assignment and thus the structural analysis of the chromophore, we have used phyA adducts including different tetrapyrroles (PΦB vs. PCB) and selectively ^{13}C-labeled isotopomers of PCB. These static RR experiments were complemented by time-resolved IR spectroscopy to determine conformational distributions specifically of ring *D*. The main goal of this work is to explore possible structural heterogeneities of the chromophore in the Pfr state that might provide insights into the role of conformational dynamics in the thermal isomerization of the tetrapyrrole.

Materials and Methods

Protein Expression, Purification, and Reconstitution

PCB (and its isotopomers) and PΦB were assembled in a 5:1 molar ratio with the recombinant His-tagged 65 kDa (residues 1–595) N-terminal photosensory module of oat phyA3 apoprotein as described previously (Mozley et al., 1997; Song et al., 2012). The adduct showed absorption maxima at 650 and 715 nm for Pr and Pfr, respectively. The isotopic labeling affected neither the absorption maxima, the photochemical behavior, nor the thermal stability. Production, purification, and chromophore assembly of Cph1, Cph2, CphA, and Agp1-V249C have been described elsewhere (Landgraf et al., 2001; Essen et al., 2008; Borucki et al., 2009; Schwinté et al., 2009; Anders et al., 2011). In each case, the experiments were carried out with the photosensory module of the proteins, i.e., N-terminal PAS, GAF, and PHY domains. For the sake of simplicity, the deletion of the output module is not specifically indicated here, e.g., the notation Cph1 corresponds to the commonly used abbreviation Cph1Δ2. As long as no further modifications are specified such as Agp1-V249C, these photosensor modules are referred to as wild-type (WT) variants. RR experiments were carried out in 50 mM Tris, 300 mM NaCl, 5 mM EDTA in H_2O (D_2O) at pH (pD) of 7.8. Protein samples were concentrated by ultrafiltration to an optical density of ca. 50 at 280 nm. Typical protein concentrations for the RR experiments were between 400 and 600 μM.

Syntheses

^{13}C(5)-PCB and ^{13}C(15)-PCB were synthesized according to Makhynya et al. (2007). The synthesis followed the convergent strategy by generating the right and the left half of PCB separately (**Figure 1**), followed by condensation of both compounds at the central C(10) position as described previously (Mroginski et al., 2011b). Isotope content at the labeled position of the target PCB was >95% as determined by mass spectrometry.

Resonance Raman Spectroscopy

RR spectra of the Pr state of phyA were obtained with 1064-nm excitation (Nd-YAG cw laser, line width <1 cm^{-1}) with a Bruker RFS 100/S Fourier-transform Raman spectrometer (4 cm^{-1} spectral resolution). All spectra were measured at −140°C using a liquid-nitrogen cooled cryostat (Linkam). The laser power was ca. 0.4 W at the sample which does not cause any laser-induced damage of the protein samples as checked by comparing the spectra obtained before and after a series of measurements. Data was accumulated for ca. 2 h for each spectrum. In all RR spectra shown in this work, the background as well as contributions from the Pr state were subtracted. For the band fitting analysis of selected spectral regions, the contribution of the apoprotein was also subtracted (see also Salewski et al., 2013; Zienicke et al., 2013).

Time-resolved VIS Pump IR Probe Spectroscopy

Pump and probe pulses were generated using non-linear optical methods. By difference frequency mixing in various steps, we obtained mid-IR pulses of 200 fs (FWHM) or shorter at a repetition rate of 1.088 kHz. Simultaneously, 200 fs laser pulses at 710 nm were used to photoexcite the sample at the absorption maximum of the Pfr state, thus initiating the photoreaction. Photoselection experiments were performed using focal pump pulse diameters of 300 μm, sample thickness of 50 μm, focal probe pulse diameters of 150 μm, pulse energies of <100 nJ. This results in excitation efficiencies below 8%. The transient absorptions for parallel A_p and perpendicular A_s polarization were simultaneously probed by two mid-IR pulses with polarizations oriented parallel and perpendicular to the pump pulse polarization at various delay times. The isotropic polarized absorption A_{iso} was calculated by $A_{iso} = (A_p + 2A_s)/3$ at each delay time. The time-resolved data presented show isotropic polarized absorption. Probe pulses were dispersed with an imaging spectrograph at a resolution of 1.5 cm^{-1} and recorded with a 2 × 32 element MCT array detector, resulting in transient spectra with high spectral resolution (Linke et al., 2013). The high repetition rate requires that the sample be moved across the focused laser beams with a Lissajous sample cell in order to avoid multiple excitation of a specific sample volume. The ^{13}C/^{15}N labeled Cph1 phytochrome apoprotein, to which non-labeled PCB chromophore was added) was prepared in D_2O solution at an optical density of 0.15–0.2 OD at 710 nm, as described previously (Hahn et al., 2008; Robben et al., 2010). Background illumination at wavelengths of ∼640 nm ensured that the sample remained in the Pfr form.

Quantum Chemical Calculations

Vibrational spectra of tetrapyrroles in the *ZZEssa* configuration were calculated by density functional theory (DFT) using the B3LYP functional and the 6–31G* basis set. All spectra refer to protonated (cationic) tetrapyrroles with a chloride ion in the vicinity of the pyrrole N-H groups serving as a counterion. Further details of the computational methods are given elsewhere

(Schwinté et al., 2008). Due to the lack of a complete atomic model for a canonical phytochrome in the Pfr state, the calculations in this case refer to the chromophore *in vacuo*, thus ruling out structural interpretation (Mroginski et al., 2009). However, as shown by comparison with previous theoretical analyses of phytochromes with known 3D structures (Mroginski et al., 2011b; Salewski et al., 2013), the calculations can be used to determine the number of normal modes in specific spectral regions and to assess the character of these modes including the expected isotopic shifts. Calculated frequencies, intensities, and normal mode compositions for PΦB and the different PCB isotopomers are given in the Supplementary Material.

Results

The 1064 nm excitation line is ideally suited for selectively probing the vibrational spectrum of the chromophore in the Pfr state of phytochromes. Due to its red-shift compared to the absorption maximum of the chromophore (ca. 700 nm), interference of the Raman spectrum with the chromophore fluorescence as well as unwanted photochemical reactions are avoided, whereas the energy of the excitation line is still sufficient for selective resonance enhancement of the Raman bands of the chromophore (Mroginski et al., 2011a). The only contribution of protein Raman bands refers to the Phe mode at ca. 1004 cm^{-1} which, however, is only of very low intensity (**Figure 2**). Besides, the RR spectra exclusively display the chromophore bands of the Pfr state.

Figure 2 shows a collection of Pfr spectra obtained from various PCB-binding canonical phytochromes, including those in which PCB is the natural chromophore, i.e., Cph1, CphA, and the WT and the Y47H variant of Cph2, as well as plant phytochrome phyA which in planta binds PΦB. Furthermore, we have studied a variant of the bacterial phytochrome Agp1, Agp1-V249C, in which the natural BV attachment site was by one at position 249 to allow for binding of PCB (or PΦB, *vide infra*) (Borucki et al., 2009). In each case, the characteristic overall band pattern of Pfr is clearly visible, including two regions with prominent bands around 800 and 1600 cm^{-1} originating from modes that are dominated by hydrogen-out-plane (HOOP) (orange rectangle) and C = C stretching coordinates (blue rectangle) of the methine bridges, respectively. The modes in these regions are largely localized in specific parts of the tetrapyrrole and dominated by a single internal coordinate (Mroginski et al., 2011b; Salewski et al., 2013). Thus, spectral changes of these modes in the spectra of the various phytochromes can be more easily related to specific structural changes as compared to variations of the bands in other parts of the spectra, such as between 1200 and 1400 cm^{-1} where the individual modes contain comparable contributions of a large number of coordinates. We therefore restrict a more detailed analysis to the HOOP and C = C stretching regions.

Vibrational Analysis: Hoop Region

The Pfr states of all phytochromes display strong RR activity around 800 cm^{-1} attributed to the HOOP mode of the *C-D* methine bridge (Fodor et al., 1988; Mroginski et al., 2011b; Salewski et al., 2013). The high RR intensity was proposed to be related to the torsion of ring *D* with respect to the remainder of the tetrapyrrole (Fodor et al., 1988). However, the present spectra demonstrate two closely-spaced bands with different relative intensities in the various phytochromes (**Figure 3**). The intensity ratio of the high- to the low-frequency component varies by more than a factor of three among the different species, accompanied by frequency shifts between 5 and 10 cm^{-1}. In principle, these bands might originate from two modes of the same chromophore conformer or of the same mode of two conformers. To distinguish between these possibilities we compare the RR spectra of phyA assembled with ^{13}C-labeled and non-labeled PCB (**Figure 4**), which shows the shift of the 804/814 cm^{-1} band pair to 797/807 cm^{-1} when the C(15) (*C-D* methine bridge) position is labeled. Neither labeling at the C(5) (*A-B* methine bridge) position nor D/H exchange at the pyrrole nitrogens has a significant effect on the spectrum (data not shown), ruling out the assignment of one of these bands to a HOOP mode of the *A-B* methine bridge or a N-H out-of-plane

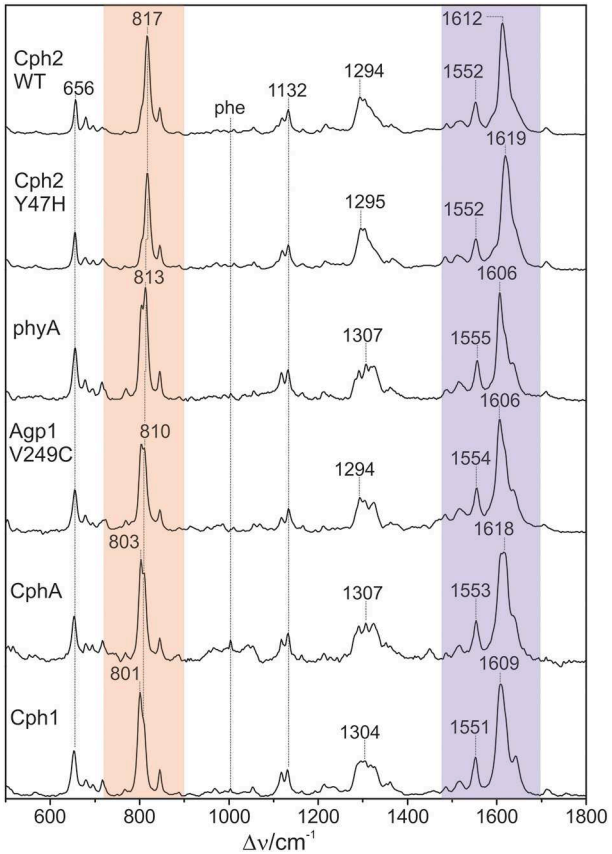

FIGURE 2 | Overview RR spectra of the Pfr states of various PCB-binding phytochromes. The HOOP and C = C stretching regions are colored in pale red and violet, respectively. The spectra were measured from buffered H_2O solutions (pH 7.8) with 1064 nm excitation at −140°C. Further details are given in the text (Sections Resonance Raman Spectroscopy and Results).

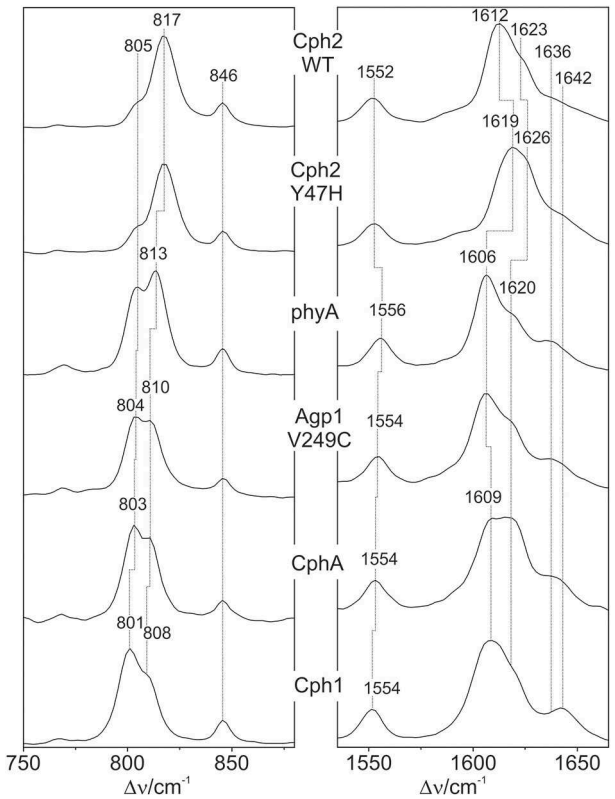

FIGURE 3 | Expanded view of the HOOP (left) and C = C stretching region (right) of the RR spectra of the Pfr states of various phytochromes including the PCB chromophore (see Figure 2). The spectra were measured from buffered H_2O solutions (pH 7.8) with 1064 nm excitation at −140°C. Further details are given in the text (Sections Resonance Raman Spectroscopy and Results).

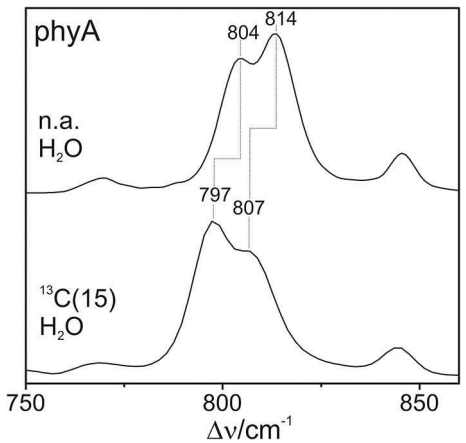

FIGURE 4 | Expanded view of the HOOP region of the RR spectra of the Pfr state of phyA including the non-labeled (natural abundance, n.a.) PCB and the PCB chromophore ^{13}C labeled at C(15). The spectra were measured from buffered H_2O solutions (pH 7.8) with 1064 nm excitation at −140°C. Further details are given in the text (Sections Resonance Raman Spectroscopy and Results).

deformation mode. Thus, we conclude that both bands are due to HOOP modes of the *C-D* methine bridge but originating from two different conformers. This interpretation is supported by quantum chemical calculations of the free PCB which predict only one mode of strong RR intensity in this region (820 cm^{-1}) (Supplementary Material). This mode is dominated by the HOOP mode of the *C-D* methine bridge which is predicted to show a $^{13}C/^{12}C$ isotopic shift at position C(15) of −8 cm^{-1}, similar to the experimentally determined shifts of −7 cm^{-1}.

Vibrational Analysis: C = C Stretching Region

Also in the C = C stretching region we note remarkable changes between the spectra of the various PCB-binding phytochromes (**Figure 3**). However, the C = C stretching region is considerably more complex than the HOOP region as shown exemplarily for phyA (**Figure 5**). Band fitting analysis of the spectrum of the phyA adduct with non-labeled PCB required a minimum number of 7 bands in the region between 1540 and 1650 cm^{-1} (**Figure 5B**; **Table 1**). In contrast, quantum chemical calculations predict only five fundamentals in this region, which are dominated by the C = C stretching coordinates of the *A-B*, *B-C*, and *C-D* methine bridges, the C = C stretching of ring *D*, and the in-plane N-H bending coordinates of rings *B* and *C* (NH ip) (Supplementary Material). Thus, we expect distinct isotopic shifts upon comparing the RR spectra of non-labeled phyA-PCB with the PCB-adducts including specific ^{13}C-labeling at the *A-B* and *C-D* methine bridges [^{13}C(5), ^{13}C(15), see **Figure 1**] and deuteration at the pyrrole nitrogens (**Figure 5**). Accordingly, the band at 1556 cm^{-1} is readily assigned to the NH ip mode (**Figure 5B**) since it remains nearly unchanged upon ^{13}C-labeling at C(5) and C(15) (**Figures 5A,C**) but disappears upon H/D exchange of the N-H groups (**Figures 5D–F**). In agreement with previous experimental and theoretical studies (Mroginski et al., 2011b; Salewski et al., 2013), the most intense RR band at 1606 cm^{-1} (**Figure 5B**) of phyA-PCB is attributed to the C = C stretching of the *C-D* methine bridge. This band is accompanied by a somewhat weaker band on the high frequency side originating from the C = C stretching of ring *D*. This mode is insensitive to ^{13}C-labeling at C(15) and C(5) whereas the *C-D* stretching should display a ca. −25 cm^{-1} shift upon ^{13}C-labeling at C(15) as predicted by the calculations. Consequently, the invariant band at 1620 cm^{-1} is attributed to the C = C stretching of ring *D* whereas—in view of the ca. −20 cm^{-1} shifts in phyA-PCB-^{13}C(15)—both the 1606 and the 1611 cm^{-1} appear to correspond to *C-D* stretching (**Figures 5A,B**). This assignment implies that these two modes originate from two PCB conformers that differ with respect to the structure of the *C-D* methine bridge, in line with the conclusions drawn from the analysis of the HOOP region (*vide supra*).

Above 1620 cm^{-1}, the band-fitting analysis of the spectrum of non-labeled phyA-PCB (**Figure 5B**) reveals two further bands at 1640 cm^{-1} and, with rather low intensity, at 1635 cm^{-1}. Both are marginally affected by ^{13}C-labeling at C (15) but shift down in the PCB-^{13}C(5) adduct (**Figures 5A,C**) such that they coincide with the C = C stretching of ring *D* to give a band envelope centered at 1620 cm^{-1}.

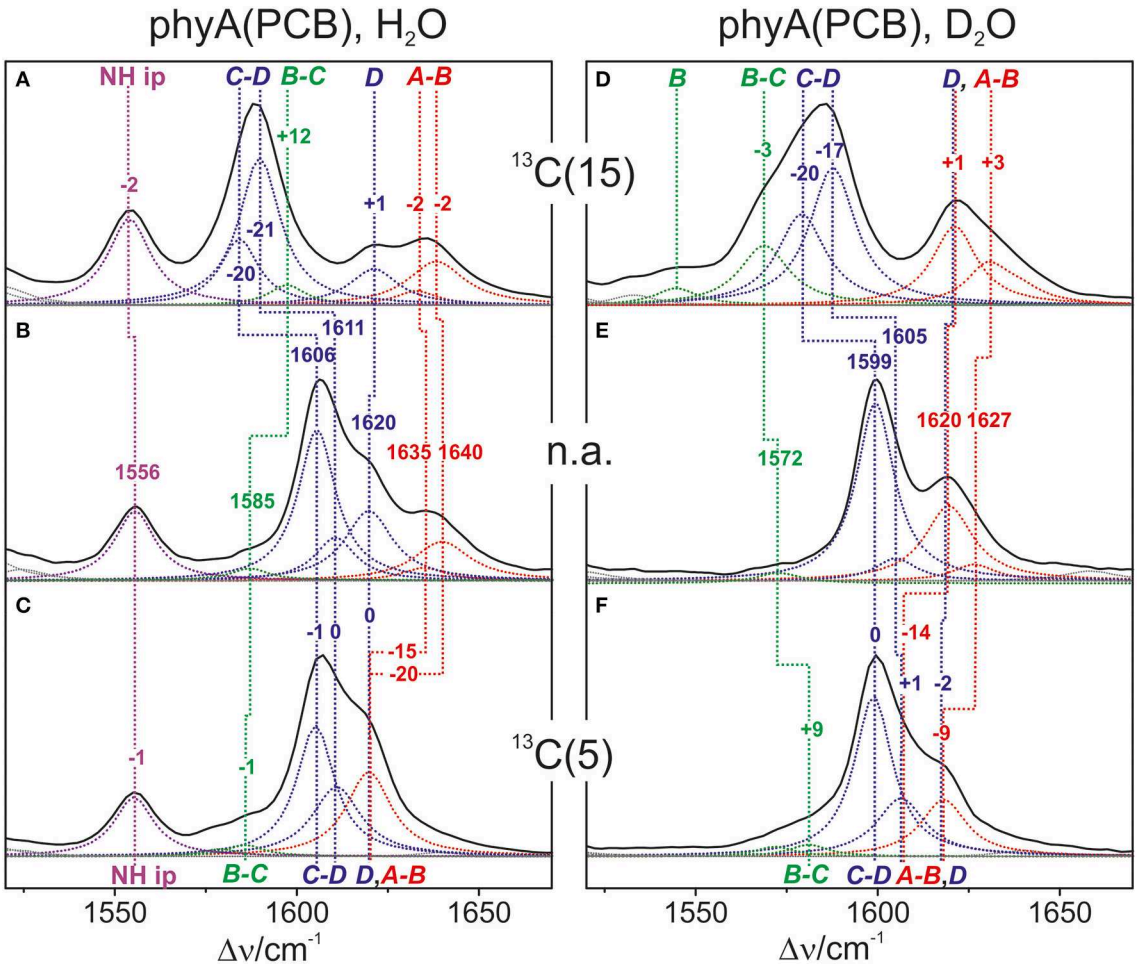

FIGURE 5 | Expanded view of the C = C stretching region of the RR spectra of the Pfr state of phyA(PCB), including the fitted band components. The left **(A–C)** and right panel (**D–F**) refer to the spectra measured from samples in H_2O and D_2O, respectively. The spectra were obtained from phyA-PCB adducts including the non-labeled PCB (**B**,**E**; n.a., natural abundance) and the PCB chromophores ^{13}C-labeled at position C(15) **(A,D)** and C(5) **(C,F)**. The main character of the individual modes is indicated by colored Lorentzian functions and abbreviations, i.e., *A-B* stretching (red); *C-D* and ring *D* C = C stretching (blue); *B-C* and ring *B* C = C stretching (green); N-H ip bending of rings *B* and *C* (magenta). The spectra were measured from buffered H_2O or D_2O solutions (pH 7.8 or pD 7.8) with 1064 nm excitation at −140°C. Further details are given in the text (Sections Resonance Raman Spectroscopy and Results). For the quality of the fits, see Supplementary Material Figure S1.

H/D exchange at the pyrrole nitrogens affects not only the NH ip mode but also the methine bridge modes due to the admixture of small contributions of the N-H ip coordinates of the neighboring pyrrole rings. These shifts are expected to be $<10\,cm^{-1}$ for the *C-D* stretching but 10—15 cm^{-1} for the *A-B* and *B-C* stretching, as predicted by the present QM calculations (Supplementary Material) and observed in previous studies on the Pfr state of BV-binding phytochromes (Salewski et al., 2013). Indeed, our experimental findings accord with this (**Figures 5D–F**). Since the C = C stretching of ring D is not affected by D/H exchange, this band overlaps with those originating from the downshifted *A-B* stretchings in the spectra of the deuterated sample (**Figures 5D,E**). The additional downshift of the *A-B* stretchings upon ^{13}C-labeling at C(5) then leads to the overlap with the non-shifted *C-D* stretching (**Figure 5F**). A summary of the assignments of the C = C stretching region is given in **Table 1**. Note that the correlation between modes of the non-labeled and labeled chromophore is an approximation. Each change of atomic masses (^{13}C/^{12}C; D/H) affects *all* solutions of the vibrational eigenvalue problem and thus frequencies, intensities and character (i.e., the potential energy distribution—PED) of *all* modes. Although the effects are particularly strong for modes dominated by coordinates of the label site, notable changes may also be observed for other modes that cannot be predicted by intuition. One instructive example refers to the B-C stretching which is known to be IR active but exhibits only low Raman activity (Schwinté et al., 2008) such that it can hardly be identified in the RR spectra. Previous IR studies have assigned this mode to a band between 1580 and 1590 cm^{-1} (Schwinté et al., 2008) and thus is attributed

TABLE 1 | Band components in the C = C stretching region of the RR spectra of the Pfr state of phyA-PCB obtained by the fitting analysis[a].

Mode[b]	n.a. H_2O		$^{13}C(5)$ H_2O		$^{13}C(15)$ H_2O		n.a. D_2O		$^{13}C(5)$ D_2O		$^{13}C(15)$ D_2O	
	ν/cm^{-1}	I_{rel}	ν/cm^{-1}	I_{rel}	ν/cm^{-1}	I_{rel}	ν/cm^{-1}	I_{rel}	ν/cm^{-1}	I_{rel}	ν/cm^{-1}	I_{rel}
AB	1639.9	18			1638.4	21	1626.5[d]	8			1630.2[d]	11
	1635.0	6	1619.8[c]	40	1632.9	7			1618.1[c]	27		
D[c]	1619.8	33			1621.1	17	1619.5	35			1621.1	28
CD	1610.5	20	1610.9	33	1584.2	32	1605.0	11	1598.8	76	1568.8	28
	1605.5	71	1605.1	62	1589.8	70	1599.4	84	1606.3	28	1587.7	48
BC			1585.7	5	1597.3	10			1581.1	6	1579.1	32
			1578.9	4					1571.9	5		
N-H ip	1555.5	33	1555.3	28	1554.0	41	–	–	–	–	–	–

[a]*Data refer to the unlabeled (n.a.) and ^{13}C-labeled PCB bound to phyA in H_2O and D_2O.*
[b]*The main coordinate of the modes is indicated by AB, CD, BC, and D referring to the C = C stretching of the respective methane bridges and of ring D, and by NH ip, denoting the N-H in-plane bending of the rings B and C.*
[c]*Not resolved in terms of the two AB and the D band components.*
[d]*Not resolved in terms of the two AB band components.*

to the weak band at 1585 cm^{-1} in the spectrum of phyA-PCB (**Figure 5B**). In the spectrum of the deuterated PCB adduct ^{13}C-labeled at position C(15) a distinct band at 1569 cm^{-1} is observed (**Figure 5D**) for which the *B-C* stretching is the only plausible assignment. Most likely, the intensity increase is due to an altered PED, presumably by a stronger contribution of the ring *B* C = C stretching coordinate.

Altogether the analysis of the C = C stretching region (**Figure 5**; **Table 1**) indicates a conformational heterogeneity of the PCB chromophore associated with sub-states differing with respect to the *C-D* and *A-B* methine bridges.

Correlated Spectral Changes

The band-fitting analyses of the RR spectra in the C = C stretching region was extended to the Pfr states of all phytochromes studied in this work reflecting different distributions among the sub-states. Due to the strong overlap with the ring *D* C = C stretching, the intensity determination of the two conjugate *C-D* stretching modes is uncertain. Thus, we will restrict the discussion to the *A-B* stretching modes which are somewhat separated from the other modes in this region. As already shown by the spectra in **Figure 3** (right panel), the intensity ratio of the high- and low-frequency *A-B* stretching component is different for the Pfr states of the various phytochromes, in analogy to the changes in the HOOP region (**Figure 3**, left panel). In fact, the intensity ratios R_i of the HOOP and *A-B* stretching mode components as implied by band fitting are correlated (**Figure 6**), suggesting a coupling of the conformational differences at the *C-D* methine bridge (HOOP mode) and the *A-B* methine bridge (*A-B* stretching) that characterize the two apparent sub-states. Interestingly, a distinct coupling correlation is observed for the HOOP and C = C mode for Cph2 and its Y47H mutant compared to the other phytochromes. This is likely to be a result of the solvent exposure of the A-B ring moiety of the PCB chromophore that is caused by the lack of a shielding PAS domain present in the other studied phytochromes (Anders et al., 2013).

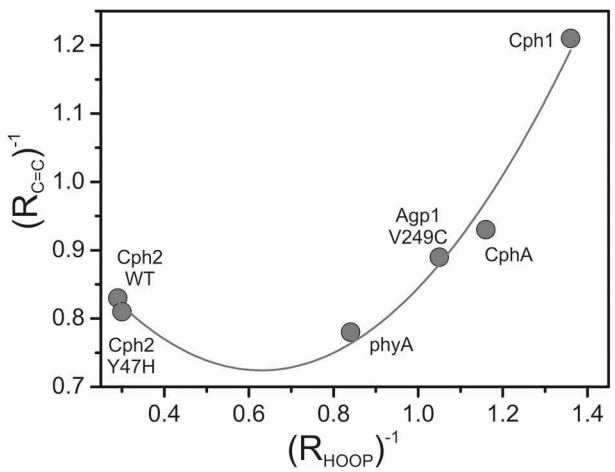

FIGURE 6 | Plot of the reciprocal intensity ratios of the high- to low-frequency components of the *A-B* stretching mode ($R_{C=C}$) and the HOOP mode (*C-D* methine bridge; R_{HOOP}), determined from the RR spectra of the Pfr states of various phytochromes by band fitting analyses. The solid line represents the fit of a parabolic function to the data points.

To determine the energetic difference between the two sub-states we analyzed the temperature-dependence of the sub-state distribution on the basis of the HOOP mode components. Indeed, temperature-dependent measurements in the range between 293 and 233 K reveal small spectral changes, particularly in the HOOP region. However, in many cases spectral analysis was aggravated by the interference of temperature-dependent contributions of the Pr state. Thus, we have restricted the quantitative analysis to the spectra of Agp1-V249C which included the lowest and largely temperature-independent Pr

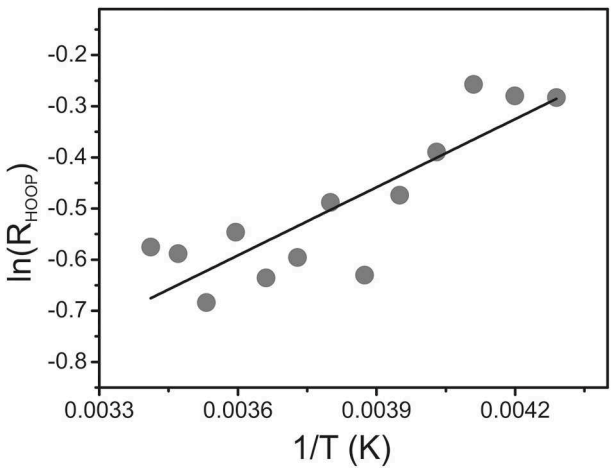

FIGURE 7 | van't Hoff plot of the intensity ratio of the high- to low-frequency components of the HOOP mode (R_{HOOP}) of the Pfr state of Agp1-V249C determined from a band fitting of the spectra measured as a function of the temperature. The solid line represents a linear fit to the experimental data.

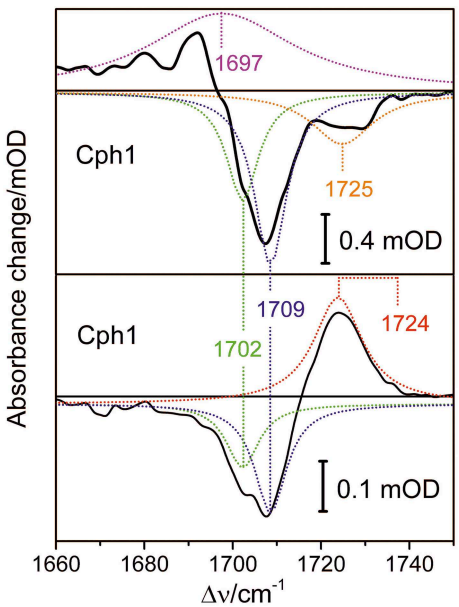

FIGURE 8 | Transient spectra of femtosecond time-resolved Vis pump IR probe experiments of the Pfr form of Cph1 upon excitation at 710 nm. Upper panel: Decay associated spectrum calculated for delay time zero (black line), and simulated Lorentzian profiles (dotted lines); excited state contribution at 1697 cm^{-1} (magenta), bleaching signals at 1702 cm^{-1} (green), 1709 cm^{-1} (blue), and 1725 cm^{-1} (orange). **Lower panel:** Absorbance spectrum at 100 ps delay time, and simulated Lorentzian profiles (dotted lines); Lumi-F contribution at 1724 cm^{-1} (red), bleaching signals at 1702 cm^{-1} (green), and 1709 cm^{-1} (blue).

contributions because the quantum efficiency of the Pfr to Pr photoconversion is extraordinarily low (Lamparter et al., 2002; Schumann et al., 2008). The intensity ratio of the HOOP modes of Pfr (R_{HOOP}, high- to low-frequency), proportional to the equilibrium constant between the two sub-states, can be described by the van't Hoff equation (**Figure 7**) leading to an enthalpy difference between the two sub-states of 3.6 $kJ.M^{-1}$.

Time-resolved Vibrational Analysis: C = O Stretching Region

Conformational heterogeneity of the PCB chromophore with respect to the *C-D* and *A-B* methine bridges could be reflected by carbonyl stretching absorptions of ring *D* and ring *A*. We used femtosecond time-resolved IR spectroscopy to study the carbonyl bleaching bands of the unlabeled PCB chromophore upon Pfr photoexcitation within a $^{13}C/^{15}N$-labeled Cph1 apoprotein. Upon excitation at 710 nm ultrafast absorption dynamics are displayed in the spectral range from 1660 cm^{-1} to 1750 cm^{-1} (**Figure 8**). Positive signals belong to excited state absorption, while negative (bleaching) signals around 1708 cm^{-1}, and 1724 cm^{-1} are due to C(19) = O stretching vibrations, and C(1) = O stretching vibrations, respectively (**Figure 8**, upper panel) (Yang et al., 2012). The C(19) = O stretching vibration bleaching signal around 1708 cm^{-1} consists of two contributions at 1702 cm^{-1} and 1709 cm^{-1} simulated with band integrals of −12, and −20, respectively (**Figure 8**, upper panel). The C(1) = O stretching vibration bleaching signal exhibits a double peak feature with maxima at 1724 cm^{-1}, and 1729 cm^{-1}. However, due to low signal strength this feature is simulated with a single bleaching band at 1725 cm^{-1}. At 100 ps delay time the initial Pfr photoreaction is finished and the remaining signals only consist of the negative bleaching signals and the positive photoproduct absorption signal of Lumi-F (**Figure 8**, lower panel). Since ring *A* is not involved in the primary photochemical process, no signals of the C(1) = O stretching vibration remain after photoisomerization. The C(19) = O stretching vibration signals around 1708 cm^{-1} can be assigned to two contributions at 1702 cm^{-1} and at 1709 cm^{-1} with simulated band integrals of −1.8, and −3.1, respectively. The positive Lumi-F signal is at 1724 cm^{-1}.

The bleaching bands provide information on the ground state. The transient spectra demonstrate two closely-spaced bleaching bands of the C(19) = O stretching vibration at 1702 cm^{-1} and at 1709 cm^{-1} with relative intensity ratio of I_{1702}/I_{1709} = 0.6. This assignment implies two modes originating from two PCB conformers in the Pfr state that differ with respect to the structure of the ring *D* carbonyl mode, in agreement with the conclusions drawn from the analysis of the HOOP and C = C stretching regions (*vide supra*).

Phytochromobilin-binding Phytochromes

All phytochromes studied in this work are able to attach PΦB at the same site as used for PCB. Previous comparative studies of oat phyA3 already demonstrated that the different ring *D* substituents (**Figure 1**) are associated with few spectral changes (Kneip et al., 1997; Remberg et al., 1997). It was of interest to determine whether the substituent affects the conformational heterogeneity of the chromophore. Focusing on the PΦB adducts of phyA, Cph1, and Agp1-V249C (**Figure 9**), spectral differences between the three phytochromes are noted in the entire spectral

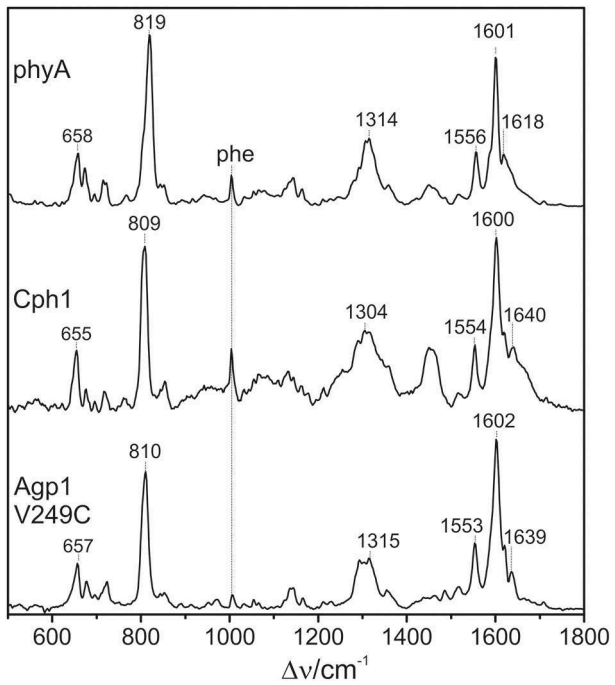

FIGURE 9 | Overview RR spectra of the Pfr states of phytochromes studied here including the PΦB chromophore. The spectra were measured from buffered H_2O solutions (pH 7.8) with 1064 nm excitation at −140°C. Further details are given in the text (Sections Resonance Raman Spectroscopy and Results).

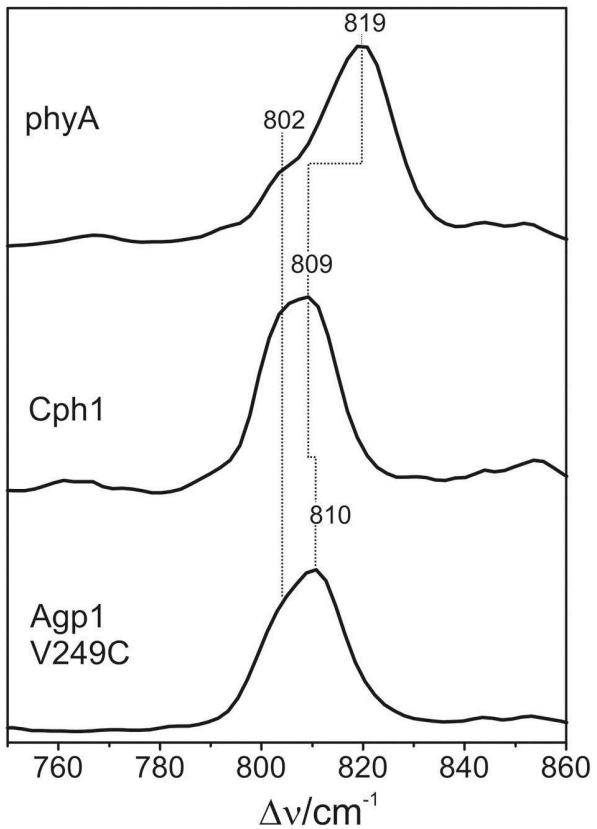

FIGURE 10 | Expanded view of the HOOP region of the RR spectra of the Pfr states of phytochromes studied here including the PΦB chromophore (see Figure 8). The spectra were measured from buffered H_2O solutions (pH 7.8) with 1064 nm excitation at −140°C. Further details are given in the text (Sections Resonance Raman Spectroscopy and Results).

range including the HOOP and the C = C stretching region, as for PCB adducts.

The HOOP region displays two overlapping bands with different relative intensities in the three spectra (**Figure 10**). These intensity variations are accompanied by shifts predominantly of the high-frequency component. In phyA(PΦB), the latter band clearly dominates, whereas both components are of similar intensities in the spectra of Cph1(PΦB) and Agp1-V249C(PΦB). As for PCB, quantum chemical calculations predict only one Raman-active mode in this region at 825 cm^{-1} that originates from the HOOP coordinate of the *C-D* methine bridge (Supplementary Material).

In the high-frequency region (**Figure 11**), the calculations predict again five modes between 1550 and 1650 cm^{-1} with similar mode composition as for PCB, except for the C = C stretching mode of ring *D* (Supplementary Material). For PΦB, this mode up-shifts to higher frequencies compared to the *C-D* stretching mode due to the admixture of the C = C stretching coordinate of the vinyl substituent. The assignment of the individual bands in this region otherwise follows the same scheme as that for the PCB adducts (**Table 1**). Accordingly, the *C-D* stretching corresponds to the strongest band which is found at essentially the same frequency in all three proteins (ca. 1600 cm^{-1}; **Figure 11**). The band at ca. 1555 cm^{-1} is attributed to the N-H ip as it disappears upon H/D exchange (Kneip et al., 1999), whereas the weak band on the low frequency side of the *C-D* stretching is due to the *B-C* stretching, in line with previous IR spectroscopic data (Schwinté et al., 2008). On the high-frequency side of the *C-D* stretching, the number of bands that are resolved by band fitting differs for the three phytochromes. In phyA and Cph1 the two bands between 1634 and 1644 cm^{-1} are assigned to the A-B stretching in analogy to the spectra analysis of the PCB adducts (**Figure 5**), pointing to two sub-states with slightly different conformations of the *A-B* methine bridge. Thus, the remaining bands at 1620 and 1626 cm^{-1} in phyA and at 1605, 1609, and 1621 cm^{-1} in Cph1 (**Figure 11**) can in principle only be assigned to a second *C-D* stretching mode (in addition to the band at ca. 1600 cm^{-1}) and to one or two ring *D* modes, pointing to conformational heterogeneity at the *C-D* bridge or ring *D*. In contrast, the spectrum of Agp1-V249C(PΦB) displays a different picture inasmuch as the total number of bands identified by the band-fitting analysis just agrees with the theoretically-predicted number of modes. Thus, the evident structural heterogeneity of the *C-D* methine bridge conformation as mirrored by the HOOP modes (**Figure 10**) has only marginally affects the C = C stretching region.

Discussion

The present study has demonstrated that the Pfr states of a number of PCB- and PΦB-binding phytochromes display a

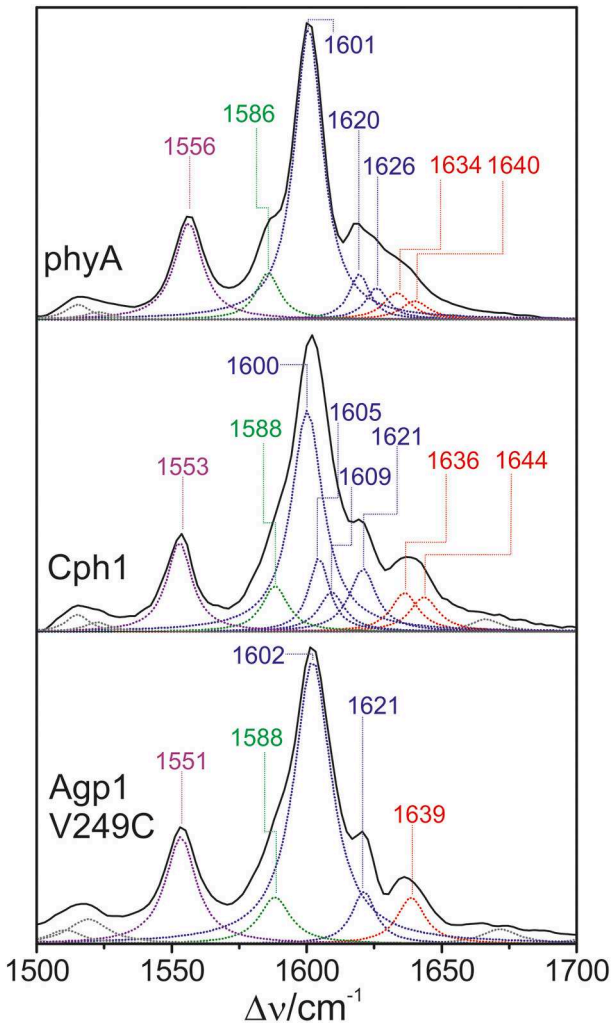

FIGURE 11 | Expanded view of the C = C stretching region (including fitted band components) of the RR spectra of the Pfr state of phytochromes studied here carrying the PΦB chromophore. The main character of the individual modes is indicated by colored Lorentzian functions and abbreviations, i.e., *A-B* stretching (red); *C-D* and ring *D* C = C stretching (blue); *B-C* and ring *B* C = C stretching (green); N-H ip bending of rings *B* and *C* (magenta). The spectra were measured from buffered H_2O solutions (pH 7.8) with 1064 nm excitation at −140°C. Further details are given in the text (Sections Resonance Raman Spectroscopy and Results). For the quality of the fits, see Supplementary Material Figure S1.

structural heterogeneity of the chromophore involving two main sub-states, differing at the *A-B* and *C-D* methine bridges. The sub-states are populated to different extents in the phytochromes studied. The underlying structural differences are probably small since they affect only a few marker bands whereas most of the conjugate modes coincide.

Structural Differences between the Sub-states

The structural differences associated with the *C-D* methine bridge are reflected by the HOOP, and the C = C stretching, and the C = O stretching mode. Inspection of **Figure 3** shows that the intensity ratio of the high- to low-frequency HOOP component decreases in the order Cph2-WT < Cph2-Y47H < phyA < Agp1-V249C < CphA < Cph1. Unfortunately, the overlap of the C = C stretching mode of the ring *D* with those of the *C-D* methine bridge hampers reliable determination of the relative intensities of the latter modes even by band-fitting analyses. This uncertainty is particularly large for the two Cph2 variants in which the PAS domain is missing and the chromophores are partially exposed to the solvent as well as for Cph1. However, the remaining phytochromes display a tendency that can even be seen in **Figure 3** inasmuch as the high frequency component of the *C-D* stretching increases in intensity according to phyA < Agp1-V249C < CphA. For these phytochromes, the low-frequency HOOP and the high-frequency *C-D* stretching component can readily be ascribed to one conformer, Pfr-I, whereas the high-frequency HOOP and the low-frequency *C-D* stretching component are attributed to the second conformer, Pfr-II. In view of the strong spectral similarities between phyA(PCB) and phyA(PΦB), this conclusion also holds for plant phytochrome A carrying its natural chromophore.

The coexistence of two conformers differing with respect to the HOOP and methine bridge modes is reminiscent of the results obtained for the Pfr states of BV-binding bacterial phytochromes shown previously (Salewski et al., 2013). In that case, quantum-mechanics/molecular-mechanics (QMMM) hybrid methods could be employed for a more profound analysis of spectra-structure relationships due to the availability of a well-resolved 3D structure of the bathy phytochrome PaBphP from *Pseudomonas aeruginosa* (Yang et al., 2008). The study demonstrated an inverse correlation of the HOOP frequency with the C(14)-C(15)-C(16)-N(*D*) dihedral angle, whereas the C = C stretching frequency was directly correlated with the N(*C*)-C(14)-C(15)-C(16) dihedral angle and inversely correlated with the C(15)-C(*D*) bond length (Salewski et al., 2013). An increase of both dihedral angles, as reflected by a downshift of the HOOP and an upshift of the C = C stretching mode, thus corresponds to an increased torsion of ring *D* with respect to ring *C*. Adopting the approximately linear relationship between the C = C stretching frequency and the dihedral angle with a slope of 0.65 degree/cm^{-1}, as previously determined for the Pr state of phyA and Cph1 (Mroginski et al., 2011b), the torsional angle between rings *C* and *D* should be >10° larger in Pfr-I than in Pfr-II in the case of phyA.

An increased torsion of ring *D* with respect to ring *C* by about 10° permits formation of an additional hydrogen bond to ring *D*. Structural investigations on Cph1 demonstrated two possible hydrogen bonds on ring *D* between C(19) = O and Tyr263, and between N(*D*)-H and Asp207 (Song et al., 2013). Structural flexibility of the chromophore and ring *D* makes formation of one hydrogen bond more likely. Hydrogen bonds to carbonyl groups induce a red-shift of the frequency, as well as formation of hydrogen bonds to adjacent N-H groups. Thus, the conformer Pfr-I with a more twisted ring *D* is related with two hydrogen bonds on ring *D*, and conformer Pfr-II with one hydrogen bond on ring *D* in Cph1. This is supported by the intensity ratio Pfr-II / Pfr-I of 0.6 of the C(19) = O stretching vibrations at

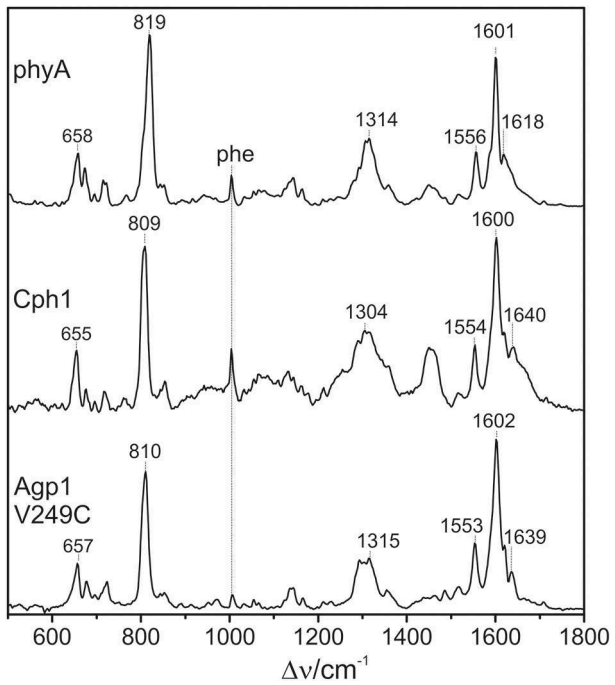

FIGURE 9 | Overview RR spectra of the Pfr states of phytochromes studied here including the PΦB chromophore. The spectra were measured from buffered H_2O solutions (pH 7.8) with 1064 nm excitation at −140°C. Further details are given in the text (Sections Resonance Raman Spectroscopy and Results).

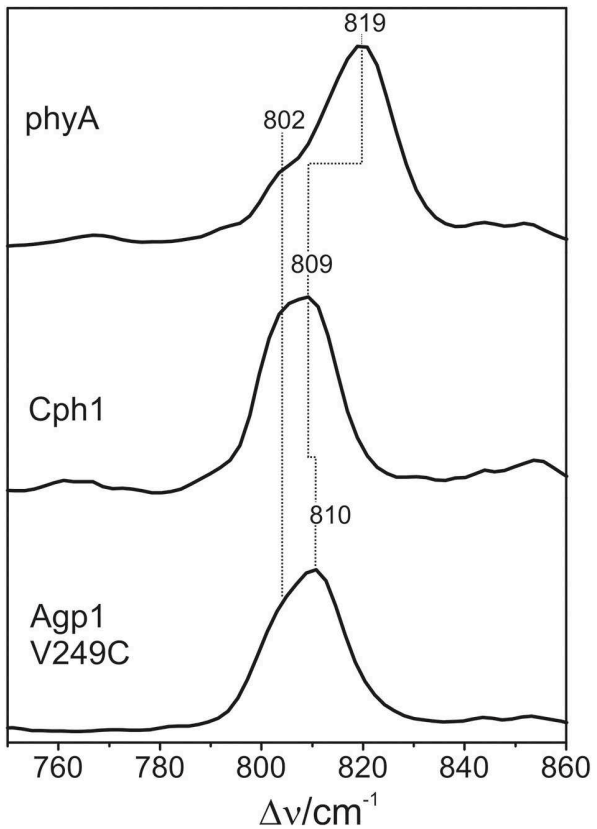

FIGURE 10 | Expanded view of the HOOP region of the RR spectra of the Pfr states of phytochromes studied here including the PΦB chromophore (see Figure 8). The spectra were measured from buffered H_2O solutions (pH 7.8) with 1064 nm excitation at −140°C. Further details are given in the text (Sections Resonance Raman Spectroscopy and Results).

range including the HOOP and the C = C stretching region, as for PCB adducts.

The HOOP region displays two overlapping bands with different relative intensities in the three spectra (**Figure 10**). These intensity variations are accompanied by shifts predominantly of the high-frequency component. In phyA(PΦB), the latter band clearly dominates, whereas both components are of similar intensities in the spectra of Cph1(PΦB) and Agp1-V249C(PΦB). As for PCB, quantum chemical calculations predict only one Raman-active mode in this region at 825 cm^{-1} that originates from the HOOP coordinate of the *C-D* methine bridge (Supplementary Material).

In the high-frequency region (**Figure 11**), the calculations predict again five modes between 1550 and 1650 cm^{-1} with similar mode composition as for PCB, except for the C = C stretching mode of ring *D* (Supplementary Material). For PΦB, this mode up-shifts to higher frequencies compared to the *C-D* stretching mode due to the admixture of the C = C stretching coordinate of the vinyl substituent. The assignment of the individual bands in this region otherwise follows the same scheme as that for the PCB adducts (**Table 1**). Accordingly, the *C-D* stretching corresponds to the strongest band which is found at essentially the same frequency in all three proteins (ca. 1600 cm^{-1}; **Figure 11**). The band at ca. 1555 cm^{-1} is attributed to the N-H ip as it disappears upon H/D exchange (Kneip et al., 1999), whereas the weak band on the low frequency side of the *C-D* stretching is due to the *B-C* stretching, in line with previous IR spectroscopic data (Schwinté et al., 2008). On the high-frequency side of the *C-D* stretching, the number of bands that are resolved by band fitting differs for the three phytochromes. In phyA and Cph1 the two bands between 1634 and 1644 cm^{-1} are assigned to the A-B stretching in analogy to the spectra analysis of the PCB adducts (**Figure 5**), pointing to two sub-states with slightly different conformations of the *A-B* methine bridge. Thus, the remaining bands at 1620 and 1626 cm^{-1} in phyA and at 1605, 1609, and 1621 cm^{-1} in Cph1 (**Figure 11**) can in principle only be assigned to a second *C-D* stretching mode (in addition to the band at ca. 1600 cm^{-1}) and to one or two ring *D* modes, pointing to conformational heterogeneity at the *C-D* bridge or ring *D*. In contrast, the spectrum of Agp1-V249C(PΦB) displays a different picture inasmuch as the total number of bands identified by the band-fitting analysis just agrees with the theoretically-predicted number of modes. Thus, the evident structural heterogeneity of the *C-D* methine bridge conformation as mirrored by the HOOP modes (**Figure 10**) has only marginally affects the C = C stretching region.

Discussion

The present study has demonstrated that the Pfr states of a number of PCB- and PΦB-binding phytochromes display a

functional for the thermal decay of the photoactivated state of the photosensor.

Acknowledgments

The work was supported by the Deutsche Forschungsgemeinschaft (SFB1078 (B6, C3, B3), Hu702/9; Es152/9). WG is grateful for the financial support by the Max-Planck-Gesellschaft.

Supplementary Material

The Supplementary Material for this article can be found online at: http://journal.frontiersin.org/article/10.3389/fmolb.2015.00037

Supplementary materials include a list of the DFT-based normal mode analyses of PCB and PΦB isotopomers (frequencies, Raman, and IR intensities, normal mode compositions) and a figure illustrating the goodness of the band fitting analyses (residuals).

References

Andel, F. III., Murphy, J. T., Haas, J. A., McDowell, M. T., van der Hoef, I., Lugtenburg, J., et al. (2000). Probing the photoreaction mechanism of phytochrome through the vibrational analysis of resonance raman spectra of recombinant analogs. *Biochemistry* 39, 2667–2676. doi: 10.1021/bi991688z

Anders, K., Daminelli-Widany, G., Mroginski, M. A., von Stetten, D., and Essen, L. O. (2013). Structure of the cyanobacterial phytochrome 2 photosensor implies a tryptophan switch for phytochrome signaling. *J. Biol. Chem.* 288, 35714–35725. doi: 10.1074/jbc.M113.510461

Anders, K., Gutt, A., Gärtner, W., and Essen, L. O. (2014). Phototransformation of the red light sensor cyanobacterial phytochrome 2 from synechocystis species depends on its tongue motifs. *J. Biol. Chem.* 289, 25590–25600. doi: 10.1074/jbc.M114.562082

Anders, K., von Stetten, D., Mailliet, J., Kiontke, S., Sineshchekov, V. A., Hildebrandt, P., et al. (2011). Spectroscopic characterisation of the red light sensitive photosensory module of Cph2 from Synechocystis sp. PCC 6803. *Photochem. Photobiol.* 87, 160–173. doi: 10.1111/j.1751-1097.2010.00845.x

Bellini, D., and Papiz, M. Z. (2012). Dimerization properties of the RpBphP2 chromophore-binding domain crystallized by homologue-directed mutagenesis. *Acta Cryst. D* 68, 1058–1066. doi: 10.1107/S0907444912020537

Borucki, B., Otoo, H., Rottwinkel, G., Hughes, J., Heyn, M. P., and Lamparter, T. (2003). Mechanism of Cph1 phytochrome assembly from stopped-flow kinetics and circular dichroism. *Biochemistry* 48, 6305–6317. doi: 10.1021/bi900436v

Borucki, B., Seibeck, S., Heyn, M. P., and Lamparter, T. (2009). Characterization of the covalent and noncovalent adducts of Agp1 phytochrome assembled with biliverdin and phycocyanobilin by circular dichroism and flash photolysis. *Biochemistry* 42, 13684–13697. doi: 10.1021/bi035511n

Burgie, E. S., Bussell, A. N., Walker, J. M., Dubiel, K., and Vierstra, R. D. (2014). Crystal structure of the photosensing module from a red/far-red light-absorbing plant phytochrome, *Proc. Natl. Acad. Sci. U.S.A.* 111, 10179–10184. doi: 10.1073/pnas.1403096111

Dasgupta, Y. J., Frontiera, R. R., Taylor, K. C., Lagarias, J. C., and Mathies, R. A. (2009). Ultrafast excited state isomerization in phytochrome revealed by femtosecond stimulated raman spectroscopy. *Proc. Natl. Acad. Sci. U.S.A.* 106, 1784–1789. doi: 10.1073/pnas.0812056106

Essen, L. O., Hughes, J., and Mailliet, J. (2008). The structure of a complete phytochrome sensory module in the Pr ground state. *Proc. Natl. Acad. Sci. U.S.A.* 105, 14709–14714. doi: 10.1073/pnas.0806477105

Fodor, S. P. A., Lagarias, J. C., and Mathies, R. A. (1988). Resonance raman spectra of the pr-form of phytochrome. *Photochem. Photobiol.* 48, 129–136. doi: 10.1111/j.1751-1097.1988.tb02797.x

Fodor, S. P. A., Lagarias, J. C., and Mathies, R. A. (1990). Resonance raman analysis of the Pr and Pfr forms of phytochrome. *Biochemistry* 29, 11141–11146. doi: 10.1021/bi00502a018

Gärtner, W., and Braslavsky, S. E. (2004). "The phytochromes: spectroscopy and function," in *Photoreceptors and Light Signalling,* ed A. Batschauer (Cambridge: Royal Society of Chemistry), 136–180.

Hahn, J., Strauss, H. M., and Schmieder, P. (2008). Heteronuclear NMR investigation on the structure and dynamics of the chromophore binding pocket of the cyanobacterial phytochrome Cph1. *J. Am. Chem. Soc.* 130, 11170–11178. doi: 10.1021/ja8031086

Kim, P. W., Rockwell, N. C., Freer, L. H., Chung, C. W., Martin, S. S., Lagarias, J. V., et al. (2013). Unraveling the primary isomerization dynamics in cyanobacterial phytochrome Cph1 with multipulse manipulations. *J. Phys. Chem. Lett.* 4, 2605–2609. doi: 10.1021/jz401443q

Kim, P. W., Rockwell, N. C., Martin, S. S., Lagarias, J. V., and Larsen, D. S. (2014a). Heterogeneous photodynamics of the Pfr state in the cyanobacterial phytochrome Cph1. *Biochemistry* 53, 4601-4611. doi: 10.1021/bi5005359

Kim, P. W., Rockwell, N. C., Martin, S. S., Lagarias, J. V., and Larsen, D. S. (2014b). Dynamic inhomogeneity in the photodynamics of cyanobacterial phytochrome Cph1. *Biochemistry* 53, 2818-2826. doi: 10.1021/bi500108s

Kneip, C., Hildebrandt, P., Schlamann, W., Braslavsky, S. E., Mark, F., and Schaffner, K. (1999). Protonation state and structural changes of the tetrapyrrole chromophore during the Pr → Pfr phototransformation of phytochrome. A resonance raman spectroscopic study. *Biochemistry* 38, 15185–15192. doi: 10.1021/bi990688w

Kneip, C., Mozley, D., Hildebrandt, P., Gärtner, W., Braslavsky, S. E., and Schaffner, K. (1997). Effect of chromophore exchange on the resonance raman spectra of recombinant phytochromes. *FEBS Lett.* 414, 23–26. doi: 10.1016/S0014-5793(97)00969-1

Lagarias, J. C., and Rapoport, H.,(1980). Chromopeptides from phytochrome. The structure and linkage of the Pr form of the phytochrome chromophore. *J. Am. Chem. Soc.* 102, 4821–4828. doi: 10.1021/ja00534a042

Lamparter, T., Michael, N., Mittmann, F., and Esteban, B. (2002). Phytochrome from Agrobacterium tumefaciens has unusual spectral properties and reveals an N-terminal chromophore attachment site. *Proc. Natl. Acad. Sci. U.S.A.* 99, 11628–11633. doi: 10.1073/pnas.152263999

Landgraf, F. T., Forreiter, C., Hurtado Pico, A., Lamparter, T., and Hughes, J. (2001). Recombinant holopyhtochrome in *Escherichia coli*. *FEBS Lett.* 508, 459–462. doi: 10.1016/S0014-5793(01)02988-X

Linke, M., Yang, Y., Zienicke, B., Hammam, M. A., von Haimberger, T., Zacarias, A., et al. (2013). Electronic transitions and heterogeneity of the bacteriophytochrome Pr absorption band: an angle balanced polarization resolved femtosecond VIS pump-IR probe study. *Biophys. J.* 105, 1756–1766. doi: 10.1016/j.bpj.2013.08.041

Makhynya, Y., Hussain, Z., Bauschlicher, T., Schwinte, P., Siebert, F., and Gärtner, W. (2007). Synthesis of selectively ^{13}C-labelled bilin compounds. *Eur. J. Org. Chem.* 2007, 1287–1293. doi: 10.1002/ejoc.200600677

Malliet, J., Psakis, G., Sineshchekov, V., Essen, L. O., and Hughes, J. (2011). Spectroscopy and a high-resolution crystal structure of Tyr-263 mutants of cyanobacterial phytochrome Cph1. *J. Mol. Biol.* 413, 115–127. doi: 10.1016/j.jmb.2011.08.023

Matysik, J., Hildebrandt, P., Schlamann, W., Braslavsky, S. E., and Schaffner, K. (1995). Fourier-Transform resonance raman spectroscopic study of the intermediate states of phytochrome. *Biochemistry* 34, 10497–10507. doi: 10.1021/bi00033a023

Mizutani, Y., Tokutomi, S., and Kitagawa, T. (1994). Resonance Raman spectra of the intermediates in phototransformation of large phytochrome: deprotonation of the chromophore in the bleached intermediate. *Biochemistry* 33, 153–158. doi: 10.1021/bi00167a020

Mozley, D., Remberg, A., and Gärtner, W. (1997). Large-scale generation of affinity-purified recombinant phytochrome chromopeptide. *Photochem. Photobiol.* 686, 710–715. doi: 10.1111/j.1751-1097.1997.tb03211.x

Mroginski, M. A., Kaminski, S., von Stetten, D., Ringsdorf, S., Gärtner, W., Essen, L. O., et al. (2011b). The structure of the chromophore binding pocket in the Pr state of plant phytochrome phyA. *J. Phys. Chem. B* 115, 1220–1231. doi: 10.1021/jp108265h

Mroginski, M. A., Murgida, D. H., von Stetten, D., Kneip, C., Mark, F., and Hildebrandt, P. (2004). Determination of the chromophore structures in the photoinduced reaction cycle of phytochrome. *J. Am. Chem. Soc.* 126, 16734–16735. doi: 10.1021/ja043959l

Mroginski, M. A., von Stetten, D., Velazquez Escobar, F., Strauss, H. M., Kaminski, S., Scheerer, P., et al. (2009). Chromophore structure of cyanobacterial phytochrome Cph1 in the Pr state: reconciling structural and spectroscopic data by QM/MM calculations. *Biophys. J.* 96, 4153–4163. doi: 10.1016/j.bpj.2009.02.029

Mroginski, M. A., von Stetten, D., Kaminski, S., Velazquez Escobar, F., Michael, N., Daminelli-Widany, G., et al. (2011a). Elucidating photoinduced structural changes in phytochromes by the combined application of resonance Raman spectroscopy and theoretical methods. *J. Mol. Struct.* 993, 15–25. doi: 10.1016/j.molstruc.2011.02.038

Murgida, D. H., von Stetten, D., Hildebrandt, P., Schwinté, P., Siebert, F., Sharda, S., et al. (2007). The chromophore structures of the Pr state in plant and bacterial phytochromes. *Biophys. J.* 93, 2410–2417. doi: 10.1529/biophysj.107.108092

Quail, P. H. (1998). The phytochrome family: dissection of functional roles and signalling pathways among family members. *Philos. Trans. R. Soc. B Biol. Sci.* 353, 1399–1403.

Remberg, A., Lindner, I., Lamparter, T., Hughes, J., Kneip, C., Hildebrandt, P., et al. (1997). Spectral and light-induced kinetic characterization of a recombinant phytochrome of the cyanobacterium *Synechocystis*. *Biochemistry* 36, 13389–13395. doi: 10.1021/bi971563z

Ren, Z., Chan, P. W. Y., Moffat, K., Pai, E. F., Royer, W. E. Jr., Srajera, V., et al. (2013). Resolution of structural heterogeneity in dynamic crystallography. *Acta Cryst. D* 69, 946–959. doi: 10.1107/S0907444913003454

Robben, M., Hahn, J., Klein, E., Lamparter, T., Psakis, G., Hughes, J., et al. (2010). NMR spectroscopic investigation of mobility and hydrogen bonding of the chromophore in the binding pocket of phytochrome proteins. *Chem. Phys. Chem.* 11, 1248–1257. doi: 10.1002/cphc.200900897

Rockwell, N. C., Duanmu, D., Martin, S. S., Bachy, C., Price, D. C., Bhattacharya, D., et al. (2014). Eukaryotic algal phytochromes span the visible spectrum. *Proc. Natl. Acad. Sci. U.S.A.* 111, 3871–3876. doi: 10.1073/pnas.1401871111

Rockwell, N. C., and Lagarias, J. C. (2010). A brief history of phytochromes. *Chem. Phys. Chem* 11, 1172–1180. doi: 10.1002/cphc.200900894

Rockwell, N. C., Shang, L., Martin, S. S., and Lagarias, J. C. (2009). Distinct classes of red/far-red photochemistry within the phytochrome superfamily. *Proc. Natl. Acad. Sci. U.S.A.* 106, 6123–6127. doi: 10.1073/pnas.0902370106

Rockwell, N. C., Su, Y., and Lagarias, J. C. (2006). Phytochrome structure and signaling mechanisms. *Annu. Rev. Plant. Biol.* 57, 837–858. doi: 10.1146/annurev.arplant.56.032604.144208

Rohmer, T., Lang, C., Hughes, J., Essen, L. O., Gärtner, W., and Matysik, J. (2008). Light-induced chromophore activity and signal transduction in phytochromes observed by 13C and 15N magic angle spinning NMR. *Proc. Natl. Acad. Sci. U.S.A.* 105, 15229–15234. doi: 10.1073/pnas.0805696105

Salewski, J., Velazquez, F., Kaminski, S., von Stetten, D., Keidel, A., Rippers, Y., et al. (2013). The structure of the biliverdin cofactor in the Pfr state of bathy and prototypical phytochromes. *J. Biol. Chem.* 288, 16800–16814. doi: 10.1074/jbc.M113.457531

Schäfer, E., and Nagy, F. (2006). *Photomorphogenesis in Plants and Bacteria*. Dordrecht: Springer.

Schmidt, P., Gensch, T., Remberg, A., Gärtner, W., Braslavsky, S. E., and Schaffner, K. (1998). The complexity of the Pr to Pfr phototransformation kinetics is an intrinsic property of native phytochrome. *Photochem. Photobiol.* 68, 754–761.

Schumann, C., Groß, R., Wolf, M. M. N., Michael, N., Lamparter, T., and Diller, R. (2008). Sub-picosecond mid-infrared spectroscopy of the Pfr reaction of phytochrome Agp1 from Agrobacterium tumefaciens. *Biophys. J.* 94, 3189–3197. doi: 10.1529/biophysj.107.119297

Schwinté, P., Foerstendorf, H., Gärtner, W., Mroginski, M. A., Hildebrandt, P., and Siebert, F. (2008). Fourier transform infrared studies of the photoinduced processes of phytochrome phyA using isotopically labelled chromophores and density functional theory calculations. *Biophys. J.* 95, 1256–1267. doi: 10.1529/biophysj.108.131441

Schwinté, P., Gärtner, W., Sharda, S., Mroginski, M. A., Hildebrandt, P., and Siebert, F. (2009). The photoreactions of recombinant phytochrome CphA from the cyanobacterium Calothrix. A low temperature UV-vis and FTIR study. *Photochem. Photobiol.* 85, 239–249. doi: 10.1111/j.1751-1097.2008.00426.x

Sineshchekov, V. (2004). Phytochrome A: functional diversity and polymorphism. *Photochem. Photobiol. Sci.*3, 596–607. doi: 10.1039/b315430k

Sineshchekov, V., Hughes, J., Hartmann, E., and Lamparter, T. (1998). Fluorescence and photochemistry of recombinant phytochrome from the cyanobacterium *Synechocystis*. *Photochem. Photobiol.* 67, 263–267.

Song, C., Essen, L. O., Gärtner, W., Hughes, J., and Matysik, J. (2012). Solid-state NMR spectroscopic study of chromophore–protein interactions in the Pr ground state of plant Phytochrome A. *Mol. Plant* 5, 698–715. doi: 10.1093/mp/sss017

Song, C., Psakis, G., Lang, C., Mailliet, J., Zaanen, J., Gärtner, W., et al. (2011). Cooperative nature of phytochrome photoactivation. *Biochemistry* 50, 10987–10989.

Song, C., Rohmer, T., Tiersch, M., Zaanen, J., Hughes, J., and Matysik, J. (2013). Solid-state NMR spectroscopy to probe photoactivation in canonical phytochromes. *Photochem. Photobiol.* 89, 259–273. doi: 10.1111/php.12029

Takala, H., Björling, A., Berntsson, O., Lehtivuori, H., Niebling, S., Hoernke, M., et al. (2014). Signal amplification and transduction in phytochrome photosensors. *Nature* 509, 245–248. doi: 10.1038/nature13310

Velazquez Escobar, F., Piwowarski, P., Salewski, J., Michael, N., Fernandez Lopez, M., Rupp, A., et al. (2015). A protonation-coupled feedback mechanism controls the signaling process in bathy phytochromes. *Nat. Chem.* 7, 423–430. doi: 10.1038/nchem.2225

Wagner, J. R., Brunzelle, J. S., Forest, K. T., and Vierstra, R. D. (2005). A light-sensing knot revealed by the structure of the chromophore-binding domain of phytochrome. *Nature* 438, 325–331. doi: 10.1038/nature04118

Wagner, J. R., Zhang, J. R., Brunzelle, J. S., Vierstra, R. D., and Forest, K. T. (2007). High resolution structure of *Deinococcus bacteriophytochrome* yields new insights into phytochrome architecture and evolution. *J. Biol. Chem.* 282, 12298–12309. doi: 10.1074/jbc.M611824200

Yang, X. J., Kuk, J., and Moffat, K. (2008). Crystal structure of Pseudomonas aeruginosa bacteriophyrochrome: photoconversion and signal transduction. *Proc. Natl. Acad. Sci. U.S.A.* 105, 14715–14720. doi: 10.1073/pnas.0806718105

Yang, X. J., Kuk, J., and Moffat, K. (2009). Conformational differences between the Pfr and Pr states in Pseudomonas aeruginosa bacteriophytochrome. *Proc. Natl. Acad. Sci. U.S.A.* 106, 15639–15644. doi: 10.1073/pnas.0902178106

Yang, X. J., Ren, Z., Kuk, J., and Moffat, K. (2011). Temperature-scan cryocrystallography reveals reaction intermediates in bacteriophytochrome. *Nature* 479, 428–432. doi: 10.1038/nature10506

Yang, X. J., Stojkovic, E. A., Kuk, J., and Moffatt, K. (2007). Crystal structure of the chromophore binding domain of an unusual bacteriophytochrome, RpBphP3, reveals residues that modulate photoconversion. *Proc. Natl. Acad. Sci. U.S.A.* 104, 12571–12576. doi: 10.1073/pnas.0701737104

Yang, Y., Linke, M., von Haimberger, T., Hahn, J., Matute, R., Gonzalez, L., et al. (2012). Real-time tracking of phytochrome's orientational changes during Pr photoisomerization. *J. Am. Chem. Soc.* 134, 1408–1411. doi: 10.1021/ja209413d

Zhang, J., Stankey, R. J., and Vierstra, R. D. (2013). Structure-guided engineering of plant Phytochrome B with altered photochemistry and light signaling. *Plant Physiol.* 161, 1454–1457. doi: 10.1104/pp.112.208892

Zienicke, B., Molina, I., Glenz, R., Singer, P., Ehmer, D., Velazquez Escobar, F., et al. (2013). Unusual spectral properties of bacteriophytochrome Agp2 result from a deprotonation of the chromophore in the red-absorbing form Pr. *J. Biol. Chem.* 288, 31738–31751. doi: 10.1074/jbc.M113.479535

Conflict of Interest Statement: The authors declare that the research was conducted in the absence of any commercial or financial relationships that could be construed as a potential conflict of interest.

frontiers in Molecular Biosciences

REVIEW
published: 22 September 2015
doi: 10.3389/fmolb.2015.00052

Ion-pumping microbial rhodopsins

Hideki Kandori *

Department of Frontier Materials and OptoBioTechnology Research Center, Nagoya Institute of Technology, Nagoya, Japan

Rhodopsins are light-sensing proteins used in optogenetics. The word "rhodopsin" originates from the Greek words "rhodo" and "opsis," indicating rose and sight, respectively. Although the classical meaning of rhodopsin is the red-colored pigment in our eyes, the modern meaning of rhodopsin encompasses photoactive proteins containing a retinal chromophore in animals and microbes. Animal and microbial rhodopsins possess 11-*cis* and all-*trans* retinal, respectively, to capture light in seven transmembrane α-helices, and photoisomerizations into all-*trans* and 13-*cis* forms, respectively, initiate each function. Ion-transporting proteins can be found in microbial rhodopsins, such as light-gated channels and light-driven pumps, which are the main tools in optogenetics. Light-driven pumps, such as archaeal H^+ pump bacteriorhodopsin (BR) and Cl^- pump halorhodopsin (HR), were discovered in the 1970s, and their mechanism has been extensively studied. On the other hand, different kinds of H^+ and Cl^- pumps have been found in marine bacteria, such as proteorhodopsin (PR) and *Fulvimarina pelagi* rhodopsin (FR), respectively. In addition, a light-driven Na^+ pump was found, *Krokinobacter eikastus* rhodopsin 2 (KR2). These light-driven ion-pumping microbial rhodopsins are classified as DTD, TSA, DTE, NTQ, and NDQ rhodopsins for BR, HR, PR, FR, and KR2, respectively. Recent understanding of ion-pumping microbial rhodopsins is reviewed in this paper.

Keywords: light-driven pump, retinal, photoisomerizatoin, photocycle, H^+ transfer, hydrogen bond, structural change

OPEN ACCESS

Edited by:
Tilo Mathes,
Vrije Universiteit Amsterdam, Netherlands

Reviewed by:
Christian Bamann,
Max Planck Insitute of Biophysics, Germany
Klaus Gerwert,
Ruhr-University Bochum, Germany

***Correspondence:**
Hideki Kandori,
Department of Frontier Materials and OptoBioTechnology Research Center, Nagoya Institute of Technology, Showa-ku, Nagoya 466-8555, Japan
kandori@nitech.ac.jp

Specialty section:
This article was submitted to Biophysics, a section of the journal Frontiers in Molecular Biosciences

Received: *06 May 2015*
Accepted: *31 August 2015*
Published: *22 September 2015*

Citation:
Kandori H (2015) Ion-pumping microbial rhodopsins. Front. Mol. Biosci. 2:52. doi: 10.3389/fmolb.2015.00052

Rhodopsins and Light-driven Ion Pumps

The word "rhodopsin" originates from the Greek words "rhodo" and "opsis," which indicate rose and sight, respectively. Thus, the classical meaning of rhodopsin is the red-colored pigment in the retinal rods of eyes. The chromophore molecule to absorb light is retinal, which is the origin of red color. Then, similar colored retinal-binding proteins were found in microbes, largely expanding the definition of the word rhodopsin. The modern meaning of rhodopsin encompasses photoactive proteins containing a retinal chromophore in animals and microbes (Ernst et al., 2014; Kandori, 2015). Rhodopsins are now found in all domains of life and are classified into two groups, animal and microbial rhodopsins. While animal rhodopsins are exclusively photosensory receptors as a specialized subset of G-protein coupled receptors, microbial rhodopsins have various functions, including as photosensory receptors, a light-switch for gene expression, photoactivatable enzymes, light-driven ion pumps and light-gated ion channels (**Figure 1**) (Ernst et al., 2014).

Microbial and animal rhodopsins share a common architecture of seven transmembrane α-helices with the N- and C-termini located extracellularly and intracellularly, respectively, but have almost no sequence homology and differ largely in their functions. Retinal, the aldehyde of vitamin A, is derived from β-carotene and is bound to the protein in the shape of all-*trans* and 11-*cis* forms in microbial and animal rhodopsins, respectively (**Figure 2**). Retinal is attached by a Schiff base

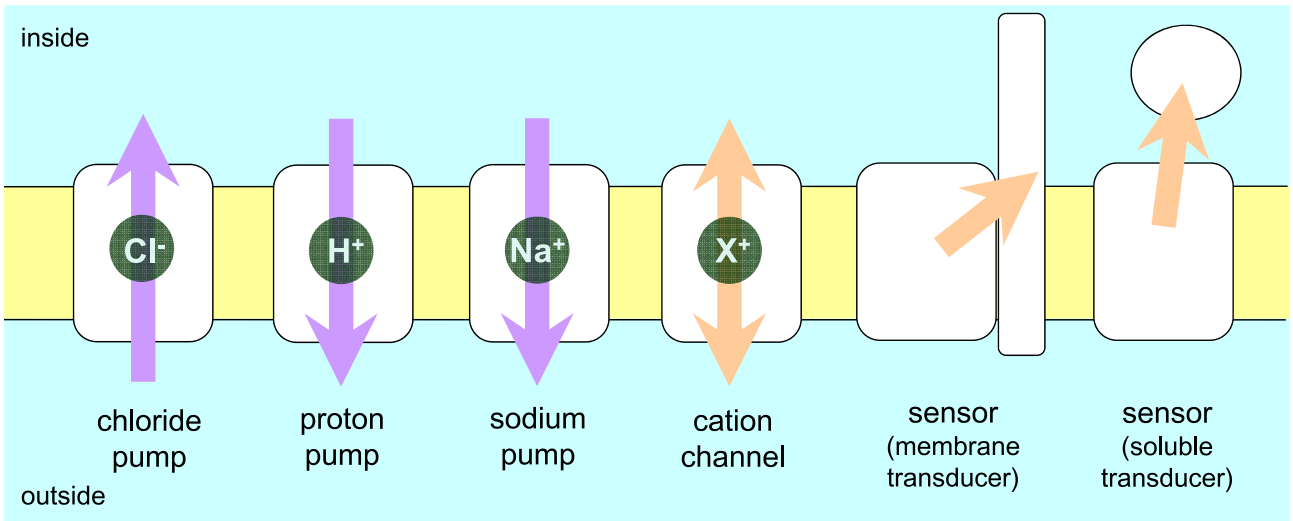

FIGURE 1 | Function of rhodopsins. Animal rhodopsins are G-protein coupled receptors, which are categorized as sensors activating a soluble transducer. On the other hand, microbial rhodopsins can act as pumps, channel, and light-sensors. Arrows indicate the direction of transport or flow of a signal. Purple and orange arrows represent energy conversion and signal transduction, respectively.

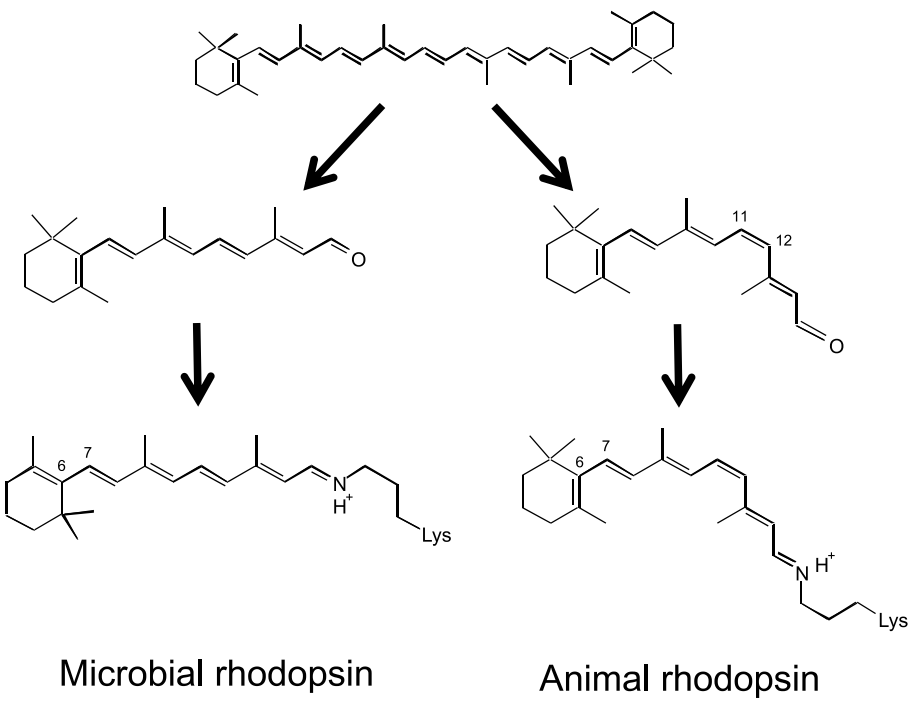

FIGURE 2 | Chromophore molecules of microbial (left) and animal (right) rhodopsins. β-carotene (top) is the source of the chromophore, and all-*trans* and 11-*cis* retinal is bound to protein through the Schiff base linkage.

linkage to the ε-amino group of a Lysine side chain in the middle of the 7th helix, and the retinal Schiff base is protonated in most cases (**Figure 2**).

Microbial rhodopsins were first found in the Archaea (*Halobacterium salinarum*) (Oesterhelt and Stoeckenius, 1971) and were therefore initially termed archaeal rhodopsins. *H. salinarum* contains bacteriorhodopsin (BR) (Oesterhelt and Stoeckenius, 1971) and halorhodopsin (HR) (Matsuno-Yagi and Mukohata, 1977; Schobert and Lanyi, 1982) that act as a light-driven outward H^+-pump or an inward Cl^- ion

pump, respectively (**Figure 1**). BR and HR contribute to the formation of a membrane potential and thus function in light-energy conversion. The two other *H. salinarum* rhodopsins are sensory rhodopsin I and II (SRI and SRII) (Spudich and Bogomolni, 1984; Jung et al., 2003), which act as positive and negative phototaxis sensors, respectively, by activating transmembrane transducers (**Figure 1**). For the first 30 years since the early 1970's, microbial rhodopsins were epitomized by haloarchaeal proteins, the first-discovered and best-studied light-driven H^+ pump BR and its close relatives (HR, SRI, and SRII). However, over the past 15 years, so many related photoactive proteins with similar or different functions were identified in *Archaea*, *Eubacteria,* and *Eukaryota*, and are now collectively called microbial rhodopsins (Brown, 2013; Grote et al., 2014). Channelrhodopsin (ChR), a microbial rhodopsin found in green algae, functions as a light-gated cation channel (Nagel et al., 2002, 2003) (**Figure 1**). Discovery of ChR led to the emergence of optogenetics (Miesenböck, 2011), in which light-gated ion channels and light-driven ion pumps are used to depolarize and hyperpolarize selected cells of neuronal networks, respectively. There are high expectations that this new method can be used to understand the circuitry of the brain (Deisseroth, 2011; Diester et al., 2011).

In optogenetics, animal brain functions are studied by incorporating microbial rhodopsins, but not animal rhodopsins, into the animal brain. There are two reasons for this. One is the isomeric structure of the chromophore (**Figure 2**). An 11-*cis* retinal, the chromophore molecule of animal rhodopsins, is not generally abundant in animal cells. In contrast, endogenous all-*trans* retinal, the chromophore molecule of microbial rhodopsins, is sufficient for optogenetics in animal cells, and there is no need to add the chromophore. The second reason is "bleaching." Upon light absorption, animal and microbial rhodopsins exhibit retinal isomerization from the 11-*cis* to all-*trans*, and all-*trans* to 13-*cis* forms, respectively (Ernst et al., 2014). Such an isomerization reaction is common, but the end of the photoreaction differs between animal and microbial rhodopsins. The isomerized all-*trans* retinal does not return to the 11-*cis* form in animal rhodopsins, and is thus called "photobleaching." This is not a problem in human visual cells because enzymatically isomerized 11-*cis* retinal is newly supplied, but this is not the case in other animal cells. In contrast, the 13-*cis* form is thermally isomerized into the all-*trans* form, and the spontaneous return is termed the "photocycle" in microbial rhodopsins. Due to the existence of naturally abundant all-*trans* retinal and its photocycle feature, microbial rhodopsins have become a tool in optogenetics.

In optogenetics, light-gated ion channels and light-driven ion pumps are used to depolarize and hyperpolarize selected cells of neuronal networks (Boyden et al., 2005; Zhang et al., 2007; Chow et al., 2010). It is interesting that two different ion-transporting functions, channel and pump, take place in microbial rhodopsins, even though their structures are similar. In pumps, the transport pathways between the two sides of the membrane cannot be fully connected because the gradient formed by active transport will collapse. This is an important aspect when distinguishing pumps from channels. The former needs energy input, which ensures the uni-directionality of transport across the membrane. To achieve this, alternative access for both sides and a switch in pumps, which are controlled spatially and temporally, is considered to take place. In contrast, a channel needs a fully connected ion pathway for passive transport of ions upon opening.

In this paper, I review recent understanding of light-driven ion-pumping rhodopsins, which are expected to be used as neural silencers in optogenetics. A light-driven H^+ pump was the first microbial rhodopsin discovered (BR), and metagenomic research identified thousands of new microbial rhodopsins from marine bacteria. The new rhodopsin is called proteorhodopsin (PR), and it is estimated that 50% of microbes in the photic zone possess PR genes (Béjà et al., 2000; de la Torre et al., 2003; Venter et al., 2004; Finkel et al., 2013). In addition to many PRs (H^+ pump), light-driven inward Cl^- pumps that differ from HR have recently been reported (Inoue et al., 2014; Yoshizawa et al., 2014). In contrast to light-driven outward H^+ and inward Cl^- pumps, no cation pumps are known, except for the H^+ pump. This is a reasonable possibility, as retinal chromophore is positively charged in rhodopsins, and thus non-H^+ cation-pumping rhodopsins are impossible because of electrostatic repulsion. However, an outward Na^+ pump has already been naturally created in the ocean (Inoue et al., 2013), and can be used as a novel neural silencer.

We now know that nature uses three different ion pump rhodopsins (H^+, Na^+, and Cl^- pumps). They can be distinguished by characteristic sequences (**Figure 3**). BR has two aspartic acid residues, D85 and D96, in helix C which function as the H^+ acceptor and donor, respectively, for the retinal Schiff base during its H^+ pumping photocycle (**Figure 4**). In addition, the former forms a hydrogen bond with T89. The DTD motif in BR (D85, T89, and D96) is well conserved for other archaeal H^+-pumping rhodopsins. At the corresponding position, most PRs have a DTE motif in which the H^+ donor is Glu instead of D96 in BR. However, there are some exceptions. *Exiguobacterium sibiricum* rhodopsin (ESR) has Lys instead of Glu (Petrovskaya et al., 2010), and the DTX motif may be more accurate for the marine bacterial H^+ pump. Light-driven Cl^- pump HR is a TSA rhodopsin, and light-driven Na^+ and Cl^- pumps have NDQ and NTQ motifs, respectively at the same position (**Figure 3**) (Inoue et al., 2013; Béjà and Lanyi, 2014; Yoshizawa et al., 2014). Thus, these three residues, which correspond to position 85, 89, and 96 of BR, are important for categorizing ion pump rhodopsins. The next section summarizes structural features of these light-driven pumps, followed by a mechanistic explanation on H^+, Cl^-, and Na^+ pumps, one by one.

Structural Features of Ion-pumping Microbial Rhodopsins

Despite a variety of sequences and functions, the structural and mechanistic principles of microbial rhodopsin architecture have one common structure, a tight alpha-helical bundle of seven transmembrane helices surrounding the retinal chromophore (Klare et al., 2008; Zhang et al., 2011; Brown, 2013; Ernst et al., 2014). **Figure 5** illustrates the overall structure of BR, which highlights the conserved aromatic amino acids. The retinal

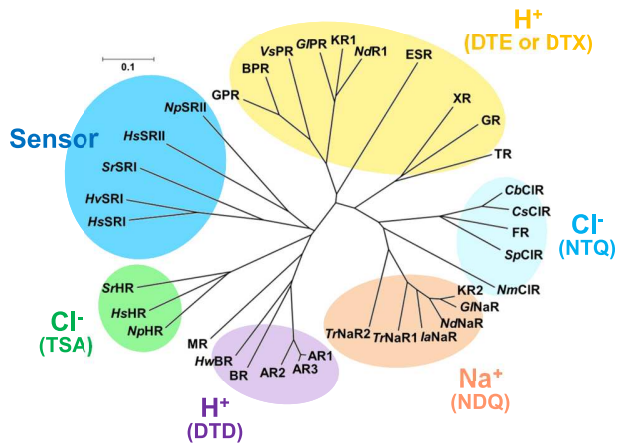

FIGURE 3 | Phylogenic tree of microbial rhodopsins. This figure is modified from Inoue et al. (2015). The scale bar represents the number of substitutions per site (0.1 indicates 10 nucleotides substitutions per 100 nucleotides). Marine bacterial H^+ (yellow), Na^+ (orange) and Cl^- (cyan) pumps have the DTE (or DTX), NDQ, and NTQ motifs, respectively, while archaeal H^+ and Cl^- pumps have the DTD and TSA motifs, respectively. Sensory rhodopsins from halophilic archaea and eubacteria are also shown. AR1, Archaerhodopsin-1; AR2, Archaerhodopsin-2; AR3, Archaerhodopsin-3; *Hw*BR, BR from *Haloquadratum walsbyi*; MR, Middle rhodopsin; *Np*HR, *Hs*HR, *Sr*HR, HR from *Natronomonas pharaonis*; *H. salinarum* and *Salinibacter ruber*; *Hs*SRI, *Hv*SRI, *Sr*SRI, sensory rhodopsin I from *H. salinarum*, *Haloarcula vallismortis* and *S. ruber*; *Hs*SRI, *Np*SRI, sensory rhodopsin I from *H. salinarum* and *N. pharaonis*; *Vs*PR, *Gl*PR, *Nd*R1. proteorhodopsins from *Vibrio* sp. AND4, *Gillisia limnaea* DSM 15749, *Nonlabens dokdonensis* DSW-6; XR, xanthorhodopsin, TR, proteorhodopsin from *Thermus thermophilus*; *Cb*ClR, *Cs*ClR, *Sp*ClR, NmClR, ClR from *Citromicrobium bathyomarinum*, *Citromicrobium* sp. JLT1363, *Sphingopyxis baekryungensis* DSM 16222 and *N. marinus*; *Gl*NaR, *Nd*NaR, *Ia*NaR, *Tr*NaR1, *Tr*NaR2, NaR from *G. limnaea*, *Nonlabens dokdonensis*, *Indibacter alkaliphilus*, and two NaRs from *Truepera radiovictrix*, respectively.

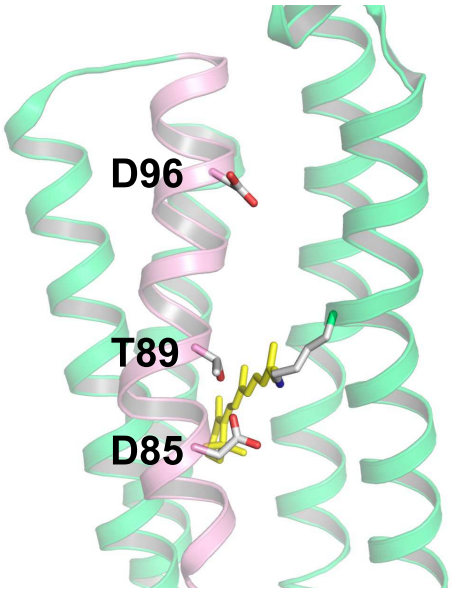

FIGURE 4 | Structure of bacteriorhodopsin (BR) with the DTD motif (PDB: 1QM8, Takeda et al., 1998). The three amino acid residues of the motif (D85, T89, and D96) are located in the C-helix (pink), while other helices are shown in green. Among the seven helices, the A-helix and B-helix are removed to provide a clear view. In BR, D85, and D96 act as the H^+ acceptor and donor to the Schiff base, respectively, and T89 forms a hydrogen bond with D85.

binding pocket is the most conserved element of the structure. W86, W182, and Y185, which constitute an important part of the chromophore binding site, are perfectly conserved among ion-pumping microbial rhodopsins (**Figure 6**). The presence of these bulky groups possibly determines the isomerization pathway from the all-*trans* to the 13-*cis* form after light absorption. Moreover, the interaction of photoisomerized retinal with W182 may serve as a mechanical transducer for passing the energy stored in retinal deformation into functionally important changes of the helical tilts necessary for function (Luecke et al., 2000). Y185 in BR (**Figure 6**) participates in hydrogen-bonding stabilization of the Schiff base counterion for many rhodopsins.

In addition to the aromatic sidechain rings, electrostatic and hydrogen-bonding interactions in the proximal region of retinal are crucial in defining the functionality of microbial rhodopsins (Ernst et al., 2014). The sidechain of K216 in BR (or its homologs in other microbial rhodopsins) forms a covalent linkage with the retinal molecule through the Schiff base (**Figure 7**). As the Schiff base is usually protonated, K216 and super-conserved R82 of helix C in BR provide two positive charges within the protein (**Figure 7**), which requires two negative charges for electrostatic stabilization. This dictates the most common configuration of the Schiff base counterion, which includes two perfectly conserved carboxylic acids (D85 and D212 in BR) for H^+-pumping microbial rhodopsins (**Figure 7**).

Other functions in microbial rhodopsins originate from deviation from this arrangement. For example, the negatively charged Asp at position 85 is replaced by Thr in Cl^--pumping HR, which requires a negative charge for electrostatic stabilization. This is the driving force of Cl^- binding near the retinal chromophore in Cl^- pumps. In ChR, the corresponding amino acid of D85 is Glu, and Tyr at position 185 of BR is replaced by Phe, which is possibly linked to the channel function. Ii should be emphasized that all microbial rhodopsins contain protein-bound water molecules near the Schiff base (**Figure 7**), probably contributing to the stabilization of the protonated Schiff base in the hydrophobic protein interior (Kandori, 2000; Heberle, 2004; Wolf et al., 2008). These water molecules play a key role in protein function, and have been extensively studied by X-ray crystallography of photointermediates, Fourier transform infrared spectroscopy (FTIR) spectroscopy and computational methods (Gerwert et al., 2014). The electrostatic quadrupole in the Schiff base region is characteristic of most microbial rhodopsins, and light-induced retinal isomerization causes a hydrogen-bonding alteration of this region as well as steric effects, leading to various functions of microbial rhodopsins.

Light-driven Proton Pumps

BR from *H. salinarum* is the first discovered microbial rhodopsin (Oesterhelt and Stoeckenius, 1971) and the first membrane

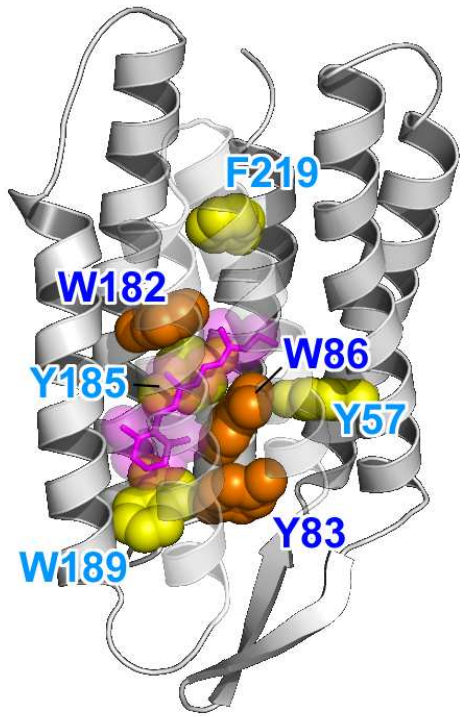

FIGURE 5 | Highlighted BR structure with the retinal chromophore, W86, W182, and Y185 (PDB: 1QM8). Y83, W86, and W182 are strongly conserved among the microbial rhodopsins (orange). Aromatic residues are strongly conserved at the Y185, W189, and F219 positions (yellow). In BR, W86, W182, Y185, and W189 constitute the chromophore binding pocket for all-*trans* retinal (red).

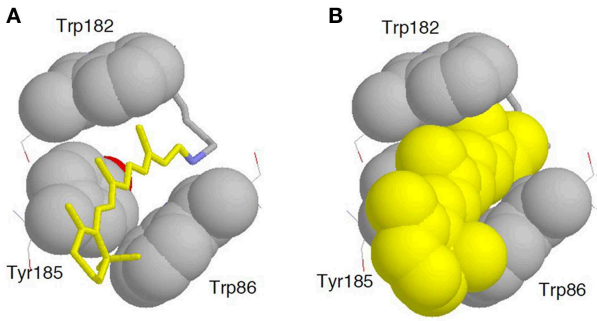

FIGURE 6 | Enlarged structure of BR with the retinal chromophore, W86, W182, and Y185 (PDB: 1QM8). All-*trans* retinal (**A**, yellow stick drawing; **B**, yellow space-filling drawing) is embedded in the binding pocket comprised of these aromatic amino acids.

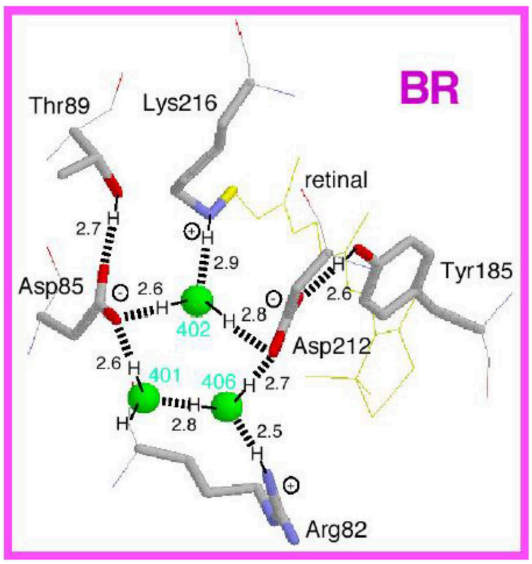

FIGURE 7 | Structure of the Schiff base region in bacteriorhodopsin (BR). This is the side view of the Protein Data Bank structure 1C3W, which has a resolution of 1.55 Å (Luecke et al., 1999). The membrane normal is approximately in the vertical direction of this figure. Hydrogen atoms and hydrogen bonds (dashed lines) are supposed from the structure, while the numbers indicate hydrogen-bonding distances in Å.

protein whose structure was found to be composed of seven helices by electron microscopy (Henderson and Unwin, 1975). BR is also the first membrane protein to have its amino acid sequence determined (Khorana et al., 1979). As the best studied microbial rhodopsin, it serves as a paradigm of a light-driven retinal-binding ion pump and aids in studies of novel rhodopsins. Archaerhodopsin 3 (Arch), the best used protein in optogenetics as a neural silencer (Chow et al., 2010), has a DTD motif, and its molecular mechanism is similar to that of BR (58% amino acid identity).

The H^+ pathway across the membrane from the cytoplasmic to the extracellular side in BR is shown in **Figure 8**, together with protonatable groups and the order of respective H^+ transfers. A summary of the photocycle is shown in **Figure 9**, which illustrates key intermediate states for most microbial rhodopsins. Although the photocycle of BR contains six intermediates, namely J, K, L, M, N, and O states that are named alphabetically, only three states (K, M, and N) are shown in **Figure 7** to demonstrate the mechanism clearly. After light absorption, photoisomerization occurs from the all-*trans*- to 13-*cis*-form in 10^{-13} second. This ultrafast retinal isomerization yields the formation of red-shifted J and K intermediates, in which J is the precursor of the K state. The protein cavity, which accommodates retinal, cannot change its shape promptly, and the K intermediate contains twisted 13-*cis* retinal. An altered hydrogen-bonding network in the Schiff base region also contributes to higher free energy in K than in the original state, and such energy storage in the primary intermediate structure leads to subsequent protein structural changes upon relaxation.

In the case of BR, relaxation of the K intermediate leads to the formation of the blue-shifted L intermediate. For H^+-pumping rhodopsins, as well as some photosensory rhodopsins, the L intermediate serves as the precursor of the H^+ transfer reaction from the Schiff base to its primary carboxylic H^+ acceptor, by which the M intermediate is formed. This is a key step in H^+ transport. Since the M intermediate has a deprotonated 13-*cis* chromophore, it exhibits a characteristically strong blue-shifted absorption (λ_{max} at 360–410 nm), and is well isolated from other

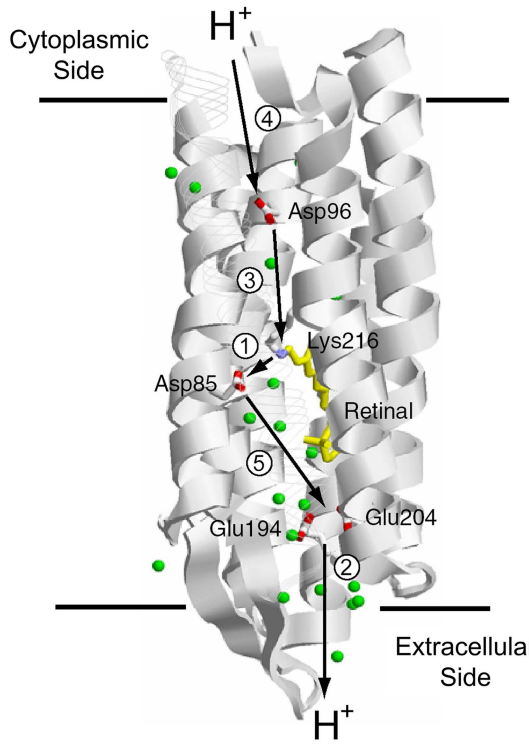

FIGURE 8 | H^+ transport pathway in bacteriorhodopsin (BR). Arrows indicate each H^+ transfer, and the numbers indicate a temporal order; (1) Schiff base to D85, (2) H^+ release, (3) D96 to Schiff base, (4) uptake, and (5) D85 to the H^+ release group.

intermediates. In BR, the H^+ acceptor (X^- in **Figure 9**) is D85, so that the primary H^+ transfer takes place from the Schiff base to D85. T89 in the DTD motif forms a hydrogen bond with D85, which is also persistent even after formation of the M intermediate (Kandori et al., 2001).

If the Schiff base of M is reprotonated from D85 in BR (the first D in DTD), no H^+ transport occurs. In reality, the Schiff base is reprotonated from D96 (the last D in DTD) in the cytoplasmic region (**Figures 6**, **8**), by which the N intermediate is formed (Gerwert et al., 1989). The molecular mechanism of unidirectional transport of H^+s in BR has attracted the attention of many researchers, and it is believed that the primary H^+ transfer from the Schiff base to D85, and the subsequent H^+ transfer from D96 to the Schiff base determine the unidirectionality from the cytoplasmic to the extracellular region. The crystal structure of BR exhibits an asymmetric pattern of hydration: while seven internal water molecules are found in the extracellular half, only two are observed in the cytoplasmic half (**Figure 10**). Such asymmetry makes sense in view of BR's function, as the water molecules build a hydrogen-bonding network on the extracellular side for fast H^+ release while the cytoplasmic side is likely inaccessible in the dark and allows H^+ uptake only after the light-induced accessibility switch. Such asymmetric access (EC open and CP closed) is not only the case for the unphotolyzed state, but is also the case for the K and M intermediates, as shown in **Figure 9**.

To make H^+ conduction in the cytoplasmic region possible (CP open), an additional conformational alteration should occur to allow the entrance of water into the vicinity of D96. Such a conformational change is realized mainly by outward motion of the cytoplasmic half of helix F and the N intermediate is often characterized as the largest changes in the protein backbone conformation. Such helical motions are functionally significant both for ion transport and interactions with transducers of sensory rhodopsins (Klare et al., 2008; Spudich et al., 2014). In fact, this is also the case for animal rhodopsins (Scheerer et al., 2008; Rasmussen et al., 2011), and in addition, such helix opening is believed to be the general mechanism of activation for G-protein coupled receptors. The photocycle usually ends with another red-shifted intermediate, the O intermediate, resetting the original unphotolyzed conformation. Thermal isomerization, which distinguishes "photocycling" microbial rhodopsins from "bleaching" animal rhodopsins, takes place in the transition from N to O. Large conformational alterations in N possibly act as an isomerase in the transition from 13-*cis* to all-*trans*. Thus, light-induced retinal isomerization drives protein structural changes at the beginning, while protein drives thermal isomerization of retinal at the end.

The photocycle of PR, a rhodopsin of the DTE motif, has many similarities to that of BR (Inoue et al., 2015). Five intermediates, K, M_1, M_2, N, and PR′, have been identified in the photocycle of PR, where PR′ represents the transient intermediate with identical absorption spectra as the initial state. Unlike BR, no significant accumulation of the L intermediate is observed in the photocycle of PR, probably for kinetic reasons. Another difference with BR is the red-shifted absorption of N. The red-shifted intermediates should be termed O, analogous to BR, but time-resolved FTIR spectroscopy suggested that the late red-shifted intermediate of PR has a 13-*cis* form, similar to the N of BR (Dioumaev et al., 2002). It is noted that the isomeric form is explicitly identified using C_{12} and C_{14} deuterated retinal, as was reported previously (Curry et al., 1984). Some marine bacteria possess an H^+ pump with the DTX motif, where X is neither Asp nor Glu, which are convenient amino acids to alter pKa, and are thus largely involved in the intramolecular H^+ transfer of proteins. The molecular mechanism of H^+ transfer for DTX rhodopsins such as ESR (DTK in this case) is intriguing (Balashov et al., 2013).

Light-driven Chloride Ion Pumps

The first identified light-driven inward Cl^- pump was HR in 1977 (Matsuno-Yagi and Mukohata, 1977). Interestingly, it was first believed to be an outward Na^+ pump, whereas clear anion dependence revealed that HR is an inward Cl^- pump (Schobert and Lanyi, 1982). While the overall architecture of HRs is BR-like, the crystal structures of two Cl^- pumps from *Halobacterium salinarum* (*Hs*HR; Kolbe et al., 2000) and from *Natronomonas pharaonis* (*Np*HR; Kouyama et al., 2010) clearly show the presence of a Cl^- in the Schiff base region. HR has the TSA motif in which D85 in BR is replaced by Thr. This suggests that the electric quadrupole of the Schiff base with its counterion complex (D85, D212, and R82 in BR) lacks a negative charge

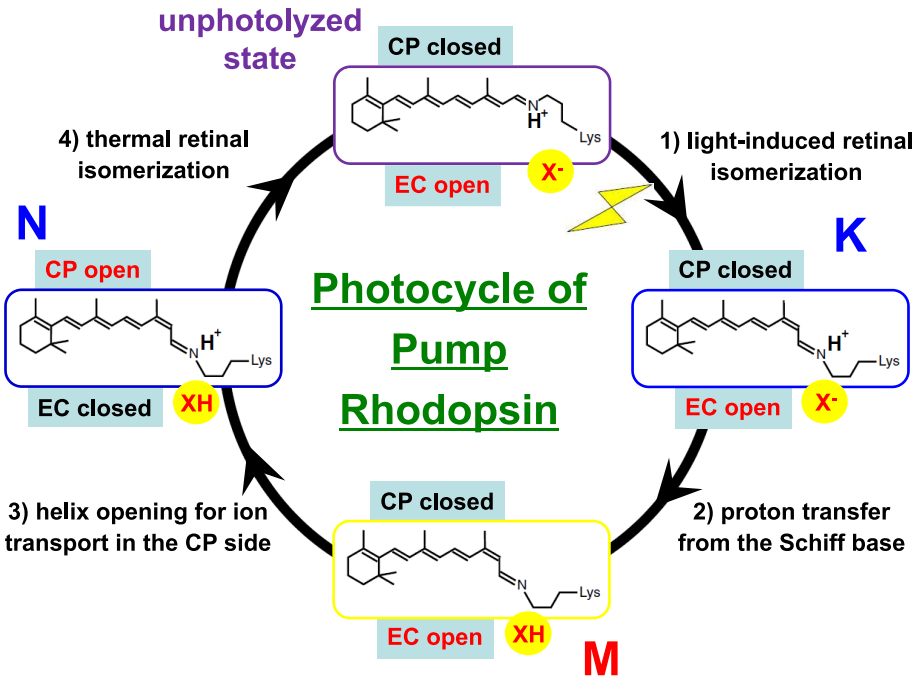

FIGURE 9 | Typical photocycle of microbial rhodopsins showing isomeric and protonation state of retinal. X^- represents the Schiff base counterion, and D85 in BR also acts as the H^+ acceptor from the Schiff base. In a Cl^- pump such as HR and FR, X^- is a Cl^-, so that the M intermediate is not formed because the Schiff base is not deprotonated. Instead, the Cl^- is transported upwards (in this figure). In KR2, a Na^+ pump, X^- is a D116 acting as the Schiff base counterion and H^+ acceptor from the Schiff base. CP and EC indicate cytoplasmic and extracellular domains, respectively. In the unphotolyzed state of microbial rhodopsins, the EC side is generally open through a hydrogen-bonding network but the CP side is closed. While this is persistent in the K and M states, the CP side is open in the N state. When the EC side is closed (black), the CP side is open, as is the case for an ion pump, as occurs in the N intermediate of BR. Such alternative access must work for all H^+, Cl^-, and Na^+ pumps.

and that the charge balance is compensated for by the binding of the negatively charged Cl^-. This is also the case for NTQ rhodopsins such as Fulvimarina rhodopsin (FR), where D85 is replaced by Asn (**Figure 11A**). FR clearly shows Cl^--dependent color changes, indicating direct binding near the Schiff base as well as HR (Inoue et al., 2014).

In HR, hydrogen bonds of the Schiff base and of protein-bound water molecules are weak (Shibata et al., 2005), suggesting that the transported Cl^- is not involved in strong hydrogen-bonding, in contrast to H^+ transport in BR. After light absorption, photoisomerization occurs from the all-*trans* to the 13-*cis* form in an ultrafast timescale, yielding the formation of the primary K intermediate. Relaxation of the K intermediate in HR leads to the formation of the blue-shifted L intermediate. In BR, the primary H^+ transfer takes place from the Schiff base to D85. In the case of Cl^- pump HR, the Schiff base does not deprotonate during the photocycle, because Asp85 in BR is replaced by Thr. In HR and FR, X^- in **Figure 9** is a Cl^-, and the accessibility of Cl^- in the unphotolyzed state must be the EC side, being supported by a CP closed structure of HR (Kolbe et al., 2000; Kouyama et al., 2010). During the photocycle, Cl^- is directly translocated upon decay of the L intermediate (Essen, 2002). Two L intermediates (L_1 and L_2, sometimes called L and N) were observed by various methods, suggesting an extracellular to intracellular change in accessibility during their interconversion, analogous to the M_1 and M_2 intermediates of BR (Ernst et al., 2014). Photoisomerization causes changes in the electric and hydrogen-bonding environment of the Cl^- binding site, which drives its movement to the cytoplasmic side of the protonated Schiff base (Shibata et al., 2005). To make Cl^- conduction in the cytoplasmic region possible, a conformational change is needed on the CP side (CP open) while the EC side should be closed when the Cl^- conduction channel is open on the cytoplasmic side. The hydrogen bond of the Schiff base is strengthened in the L intermediate, but the hydrogen-bonding acceptor of the Schiff base is not Cl^-. It is most likely a water molecule. Water-containing hydrogen-bonding network is rearranged, which probably opens the valve to the cytoplasmic region, and Cl^- is released to the cytoplasmic side during the transition to the O intermediate (Gruia et al., 2005; Kanada et al., 2011).

Interestingly, BR can be converted into an HR-like Cl^- pump by a single D-to-T amino acid replacement at D85 (Sasaki et al., 1995; Tittor et al., 1997). This suggests that the amino acid at position 85 being a determinant for ion specificity. Nevertheless, the reverse T-to-D mutations of HR, such as T108D of *Hs*HR and T126D of *Np*HR, does not convert HR into a BR-like outward H^+ pump (Havelka et al., 1995; Váró et al., 1996). These observations may imply that the molecular determinants of an H^+ pump are more demanding than those of a Cl^- pump. Indeed, *Np*HR mutated to contain 10 key BR-like amino

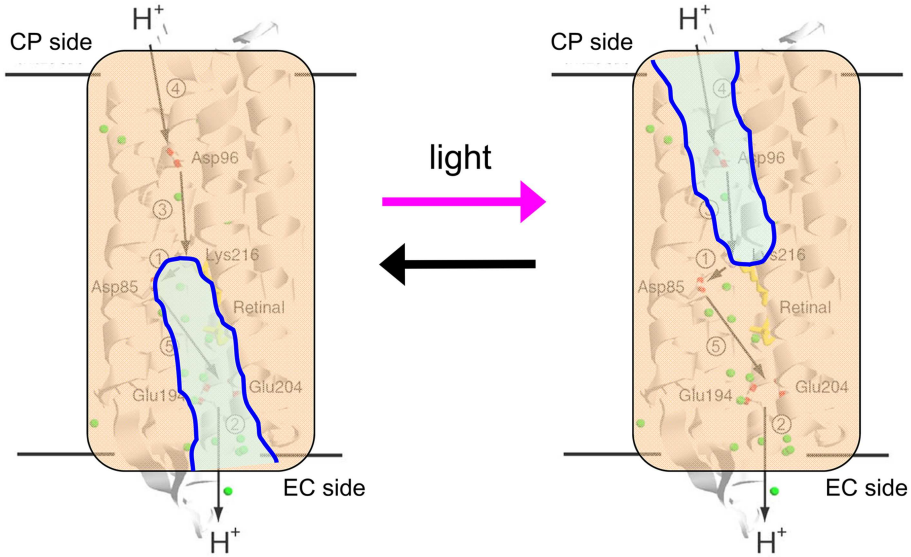

FIGURE 10 | Schematic drawing of alternative access in BR.

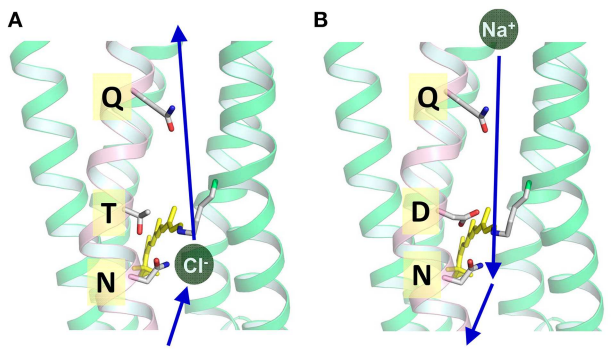

FIGURE 11 | (A) Cl^- transport pathway in HR and FR (NTQ rhodopsin). Cl^- binds near the Schiff base region, as is seen from the Cl^--dependent color change. The KR2 structure is used in which T is replaced by D116. **(B)** Na^+ transport pathway in KR2 (NDQ rhodopsin). Na^+ does not bind near the chromophore in the dark, while a light-induced structural alteration accompanies the uptake of Na^+ upon formation of the O intermediate. This is the structure of KR2 (PDB: 3X3C, Kato et al., 2015).

acids but lacking strongly hydrogen-bonded water, the functional determinant of the H^+ pump (Muroda et al., 2012). Although it is not easy by mutation, HR can be converted into an H^+ pump by the simple addition of sodium azide. Azide probably serves as an artificial H^+ shuttle, suggesting common elements in the transport mechanism of H^+ and Cl^- pumps (Hegemann et al., 1985; Váró et al., 1996). The restoration of strongly hydrogen-bonded water for the azide-bound HR is completely consistent with these results (Muneda et al., 2006).

About 15 years ago, an interesting hypothesis was proposed that BR might not be an outward H^+ pump, but instead an inward OH^- pump. The idea was gained from intermediate structures of BR and a Cl^--pumping BR mutant (D85S) (Luecke, 2000; Facciotti et al., 2004), which raised an important question about the H^+ pump. In the case of Na^+ and Cl^- pumps, proteins transport Na^+ and Cl^-, respectively. What then does the H^+ pump transport? An outward H^+ pump can be achieved by transporting (i) H^+ outwardly, (ii) H_3O^+ outwardly, or (iii) OH^- inwardly. The easy conversion of BR into a Cl^- pump by a point mutation was interpreted as supporting evidence of BR being an inward OH^- pump. However, H^+ transport is also possible by (iv) the Grotthuss mechanism (concerted H^+ transfer through water chains) (Agmon, 1995), and this most likely takes place in light-driven H^+ pumping rhodopsins (Freier et al., 2011). It should be noted that the hypothesis of BR as an inward OH^- pump has been never denied experimentally.

A spectroscopic study of FR, an NTQ rhodopsin, revealed a surprising similarity between two different Cl^- pumps of NTQ and TSA rhodopsins, even though they are evolutionarily distant (Inoue et al., 2014). A common mechanism of binding and transport of Cl^-s suggests the importance of the local structure in the Schiff base region. In an NTQ rhodopsin like FR, two positive charges and a negative charge (R82, protonated Schiff base and D212 in BR) are conserved, and binding of Cl^- satisfies the charge balance near the Schiff base.

Light-driven Sodium Ion Pumps

For more than 40 years after the first report of BR, Na^+-pumping rhodopsin was not discovered. This absence was thought to likely be because the protonated Schiff base, a positive charge, exists on the ion conductive pathway and must inhibit the transport of non-H^+ cations. However, a light-driven Na^+ pump rhodopsin (NaR) was found in the flavobacterium *K. eikastus* (Inoue et al., 2013). *K. eikastus* has two rhodopsin genes (KR1 and KR2). The former has a typical PR-like sequence with a DTE-motif, and shows an outward H^+ pump function. On the other hand, KR2,

possessing the NDQ motif, was shown to be a new outward Na^+ pump rhodopsin, based on its light-induced alkalization of a cell suspension. Since the residues in helix C form an ion conduction pathway, three residues in the NDQ motif are important for the transport of Na^+, as was revealed by a mutation study (Inoue et al., 2013). More than 10 rhodopsin genes with an NDQ-motif have been identified to date, indicating that Na^+ pump rhodopsins are diversely used among various species in nature (**Figure 3**).

Light absorption generates the red-shifted K-intermediate with 13-*cis* retinal (Ono et al., 2014), leading to the photocyclic reaction which recovers to the initial state in 100 ms. Following the K-intermediate, the L ⇄ M and O intermediates appear in this order of accumulation (Inoue et al., 2013; Balashov et al., 2014). The nomenclature of these intermediates is according to that of BR based on their absorption spectra and the time-scale in which each intermediate appears. While the K and O intermediates have red-shifted absorption, the spectrum of L ⇄ M is blue-shifted compared with the initial state. In particular, M (λ_{max} = 400 nm) has a more than 100-nm shorter absorption wavelength than KR2 (λ_{max} = 526 nm), as the retinal Schiff based is deprotonated in this state. In the D116N mutant, the M intermediate does not accumulate, supporting the notion that the H^+ acceptor of KR2 is D116, making up an NDQ-motif. The rate of O-accumulation is accelerated by an increase in Na^+ concentration, suggesting that Na^+ uptake occurs in the L ⇄ M-to-O process.

These findings explain how Na^+ is transported to the extracellular region across the protonated Schiff base of retinal. In the case of H^+ transport by H^+ pump rhodopsin, the H^+ bound to the Schiff base itself is transported. In contrast, the transfer of H^+ to the counterion (D116) upon M formation of KR2 transiently eliminates the positive charge in the Schiff base region, enabling the conduction of Na^+ beside the Schiff base during the (L ⇄ M)-to-O process (**Figure 11B**). This scenario is strongly supported by recent crystal structures of KR2, which were determined at acidic and neutral pHs (Kato et al., 2015). Although there were few structural differences at different pHs, a change in the orientation of D116 was observed (**Figure 12**). Therefore, it is likely that D116 interacts with the protonated Schiff base in the unphotolyzed state, while protonated D116 newly interacts with N112 (and S70), allowing Na^+ uptake from the cytoplasmic side by electrostatic neutralization (Kato et al., 2015). Upon formation of the red-shifted O intermediate, the Schiff base gains H^+ again presumably from D116, and the ion-pair between the Schiff base and D116 inhibits the backward flow of transported Na^+.

KR2 is a light-driven Na^+ pump that can also pump Li^+. On the other hand, KR2 pumps H^+ in K^+, Rb^+, and Cs^+. Thus, KR2 is a compatible Na^+-H^+ pump, although it functions as a light-driven Na^+ pump under physiological conditions in the ocean. A light-driven Na^+ pump from *Gillisia limnaea* does not pump H^+ (Balashov et al., 2014), suggesting a variety of Na^+ pumping rhodopsins. A mutation study revealed important residues for each pump function (Inoue et al., 2013). Both Na^+ and H^+ pump functions were completely lost for R109A, D251A, D251N, and D251E, indicating the important role of R109 and D251, which correspond to R82 and D212, respectively, in BR

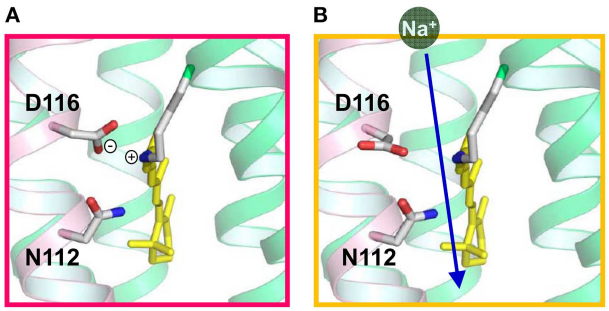

FIGURE 12 | Proposed local structures of KR2 in the dark (A) and in the M intermediate (B), suggested from crystal structures of KR2 at different pHs.

(**Figure 7**). Both functions were lost for D116A and D116N, while D116E pumps only H^+. Similarly, N112A pumps only H^+, though N112D pumps both Na^+ and H^+. D116 and N112 in the NDQ motif correspond to T89 and D85, respectively, in BR (**Figures 4**, **7**, **11B**, **12**). S70A pumps only H^+, while S70T pumps both Na^+ and H^+. These results demonstrate the importance of charged residues such as R109, D116, and D251, and the hydrogen-bonding interaction involving S70 and N112. The lack of a Na^+ pump for S70A, N112A, and D116E may originate from a narrowed Na^+ pathway by mutation and/or less stabilization of Na^+ binding in the O intermediate.

H^+ and Cl^- pump rhodopsins bind the substrate ions near the active center in the dark. In the case of H^+ pumps (BR, PR, etc.), substrate H^+ is bound to the retinal Schiff base and acidic amino acid residues constitute the H^+-transfer pathway. The binding site of Cl^- in HR was identified by X-ray crystallography in the vicinity of the protonated Schiff base. While the binding of ions affects the colors of H^+ pumps and HRs, KR2 does not show any change in color between the presence and absence of Na^+ (Inoue et al., 2013). This implies that the Na^+ binding site of KR2 is distant from retinal. Thus, the binding of Na^+ to KR2 cannot be studied by conventional UV-visible absorption spectroscopy. However, a conformational change of KR2 upon Na^+-binding (K_d of 11.4 mM) was clearly observed by using attenuated total reflection-Fourier transform infrared (ATR-FTIR) spectroscopy, and a mutation study showed that Na^+ binds to the extracellular surface (Inoue et al., 2013). The Na^+ binding site was directly recently visualized by its crystal structure (Gushchin et al., 2015). It is intriguing that several mutants do not bind Na^+ but can transport Na^+, indicating that Na^+ binding is not a prerequisite for pump function (Inoue et al., 2013). The role of Na^+ binding to KR2 is likely to increase thermal stability of the protein (Gushchin et al., 2015; Kato et al., 2015).

The H^+ pump mechanism by KR2 is the least understood to date. The efficiency of the H^+ pump is much lower than that of other H^+ pumps, and the H^+ pumping photocycle is >10 times slower than the Na^+ pumping photocycle (Inoue et al., 2013). As KR2 functions as a Na^+ pump in the ocean, it is plausible that the H^+ pump is never important for KR2. It should be noted, however, that the concentration of Na^+ in the ocean is 0.4 M and that of H^+ is 10^{-8} M (pH 8), a difference of more than seven orders of magnitude. Therefore, Na^+ and H^+ transport

needs to be compared under similar conditions for a better understanding of the mechanism. In the absence of Na^+ and Li^+ in the intracellular medium, it is likely that H^+ is taken up from the cytoplasmic side to the Schiff base, when the Schiff base proton is transferred to D116. Then, H^+ attached to D116 is released to the extracellular aqueous phase. This is a reasonable hypothesis based on current knowledge of natural H^+ pumps. However, the molecular mechanism of the H^+ pump by KR2 needs to be examined in detail.

Perspectives

This review provides a recent understanding of ion-pumping rhodopsins. Our knowledge has changed dramatically following the emergence of new classes of microbial rhodopsins. As the metagenomic analysis of the ocean environment is still ongoing, newly identifying rhodopsin genes, it is expected that additional functional rhodopsins will still be found (Venter et al., 2004; Finkel et al., 2013). As H^+ and Cl^- pump rhodopsins are now used as optogenetic tools for optical silencing of neurons (Zhang et al., 2007; Chow et al., 2010), it can be expected that new rhodopsins from marine bacteria will provide a molecular basis for developing novel optogenetic tools. In particular, Na^+ pump rhodopsin would be a potentially useful tool (Kato et al., 2015), because its outward Na^+-transport evokes hyperpolarization of membrane potential without unphysiological intracellular pH change and Cl^- accumulation. In addition, based on the structure of KR2, a light-driven K^+ pump has been created (Gushchin et al., 2015; Kato et al., 2015). This fact clearly shows that an understanding of the structure-function relationship in microbial rhodopsins is a prerequisite for novel molecular design.

Acknowledgments

I thank Dr. Keiichi Inoue for help in preparing figures. This work was supported by grants from the Japanese Ministry of Education, Culture, Sports, Science and Technology.

References

Agmon, N. (1995). The Grotthuss mechanism. *Chem. Phys. Lett.* 244, 456–462. doi: 10.1016/0009-2614(95)00905-J

Balashov, S. P., Imasheva, E. S., Dioumaev, A. K., Wang, J. M., Jung, K. H., and Lanyi, J. K. (2014). Light-driven Na^+ pump from *Gillisia limnaea*: a high-affinity Na^+ binding site is formed transiently in the photocycle. *Biochemistry* 53, 7549–7561. doi: 10.1021/bi501064n

Balashov, S. P., Petrovskaya, L. E., Imasheva, E. S., Lukashev, E. P., Dioumaev, A. K., Wang, J. M., et al. (2013). Breaking the carboxyl rule. Lysine96 facilitates protonation of the Schifff base in the photocycle of a retinal protein from *Exiguobacterium sibiricum*. *J. Biol. Chem.* 288, 21254–21265. doi: 10.1074/jbc.M113.465138

Béjà, O., Aravind, L., Koonin, E. V., Suzuki, M. T., Hadd, A., Nguyen, L. P., et al. (2000). Bacterial rhodopsin: evidence for a new type of phototrophy in the sea. *Science* 289, 1902–1906. doi: 10.1126/science.289.5486.1902

Béjà, O., and Lanyi, J. K. (2014). Nature's toolkit for microbial rhodopsin ion pumps. *Proc. Natl. Acad. Sci. U.S.A.* 111, 6538–6539. doi: 10.1073/pnas.1405093111

Boyden, E. S., Zhang, F., Bamberg, E., Nagel, G., and Deisseroth, K. (2005). Millisecond-timescale, genetically targeted optical control of neural activity. *Nat. Neurosci.* 8, 1263–1268. doi: 10.1038/nn1525

Brown, L. S. (2013). Eubacterial rhodopsins - unique photosensors and diverse ion pumps. *Biochim. Biophys. Acta* 1837, 553–561. doi: 10.1016/j.bbabio.2013.05.006

Chow, B. Y., Han, X., Dobry, A. S., Qian, X., Chuong, A. S., Li, M, et al. (2010). High-performance genetically targetable optical neural silencing by light-driven proton pumps. *Nature* 463, 98–102. doi: 10.1038/nature08652

Curry, B., Palings, I., Broeck, A., Pardoen, J. A., Lugtenburg, J., and Mathies, R. A. (1984). Vibrational analysis of 13-cis-retinal. *J. Phys. Chem.* 88, 688–702. doi: 10.1021/j150648a015

Deisseroth, K. (2011). Optogenetics. *Nat. Methods* 8, 26–29. doi: 10.1038/nmeth.f.324

de la Torre, J. R., Christianson, L. M., Béjà, O., Suzuki, M. T., Karl, D. M., Heidelberg, J., et al. (2003). Proteorhodopsin genes are distributed among divergent marine bacterial taxa. *Proc. Natl. Acad. Sci. U.S.A.* 100, 12830–12835. doi: 10.1073/pnas.2133554100

Diester, I., Kaufman, M. T., Mogri, M., Pashaie, R., Goo, W., Yizhar, O., et al. (2011). An optogenetic toolbox designed for primates. *Nat. Neurosci.* 14, 387–397. doi: 10.1038/nn.2749

Dioumaev, A. K., Brown, L. S., Shih, J., Spudich, E. N., Spudich, J. L., and Lanyi, J. K. (2002). Proton transfers in the photochemical reaction cycle of proteorhodopsin. *Biochemistry* 41, 5348–5358. doi: 10.1021/bi025563x

Ernst, O. P., Lodowski, D. T., Elstner, M., Hegemann, P., Brown, L. S., and Kandori, H. (2014). Microbial and animal rhodopsins: structures, functions, and molecular mechanisms. *Chem. Rev.* 114, 126–163. doi: 10.1021/cr4003769

Essen, L. O. (2002). Halorhodopsin: light-driven ion pumping made simple? *Curr. Opn. Struct. Biol.* 12, 516–522. doi: 10.1016/S0959-440X(02)00356-1

Facciotti, M. T., Rouhani, S., and Glaeser, R. M. (2004). Crystal structures of bR(D85S) favor a model of bacteriorhodopsin as a hydroxyl-ion pump. *FEBS Lett.* 564, 301–306. doi: 10.1016/S0014-5793(04)00208-X

Finkel, O. M., Béjà, O., and Belkin, S. (2013). Global abundance of microbial rhodopsins. *ISME J.* 7, 448–451. doi: 10.1038/ismej.2012.112

Freier, E., Wolf, S., and Gerwert, K. (2011). Proton transfer via a transient linear water-molecule chain in a membrane protein. *Proc. Natl. Acad. Sci. U.S.A.* 108, 11435–11439. doi: 10.1073/pnas.1104735108

Gerwert, K., Freier, E., and Wolf, S. (2014). The role of protein-bound water molecules in microbial rhodopsins. *Biochim. Biophys. Acta.* 1837, 606–613. doi: 10.1016/j.bbabio.2013.09.006

Gerwert, K., Hess, B., Soppa, J., and Oesterhelt, D. (1989). Role of aspartate-96 in proton translocation by bacteriorhodopsin. *Proc. Natil. Acad. Sci. U.S.A.* 86, 4943–4947. doi: 10.1073/pnas.86.13.4943

Grote, M., Engelhard, M., and Hegemann, P. (2014). Of ion pumps, sensors and channels - perspectives on microbial rhodopsins between science and history. *Biochim. Biophys. Acta* 1837, 533–545. doi: 10.1016/j.bbabio.2013.08.006

Gruia, A. D., Bondar, A. N., Smith, J. C., and Fischer, S. (2005). Mechanism of a molecular valve in the halorhodopsin chloride pump. *Structure* 13, 617–627. doi: 10.1016/j.str.2005.01.021

Gushchin, I., Shevchenko, V., Polovinkin, V., Kovalev, K., Alekseev, A., Round, E., et al. (2015). Crystal structure of a light-driven sodium pump. *Nat. Struct. Mol. Biol.* 22, 390–395. doi: 10.1038/nsmb.3002

Havelka, W. A., Henderson, R., and Oesterhelt, D. (1995). Three-dimensional structure of halorhodopsin at 7 Å resolution. *J. Mol. Biol.* 247, 726–738. doi: 10.1016/S0022-2836(05)80151-2

Heberle, J. (2004). A local area network of protonated water molecules. *Biophys. J.* 87, 2105–2106. doi: 10.1529/biophysj.104.050054

Hegemann, P., Oesterhelt, D., and Steiner, M. (1985). The photocycle of the chloride pump halorhodopsin. I: Azide-catalyzed deprotonation of the chromophore is a side reaction of photocycle intermediates inactivating the pump. *EMBO J.* 4, 2347–2350.

Henderson, R., and Unwin, P. N. (1975). Three-dimensional model of purple membrane obtained by electron microscopy. *Nature* 257, 28–32. doi: 10.1038/257028a0

Inoue, K., Kato, Y., and Kandori, H. (2015). Light-driven ion-translocating rhodopsins in marine bacteria. *Trends. Microbiol.* 23, 91–98. doi: 10.1016/j.tim.2014.10.009

Inoue, K., Koua, F. H., Kato, Y., Abe-Yoshizumi, R., and Kandori, H. (2014). Spectroscopic study of a light-driven chloride ion pump from marine bacteria. *J. Phys. Chem. B* 118, 11190–11199. doi: 10.1021/jp507219q

Inoue, K., Ono, H., Abe-Yoshizumi, R., Yoshizawa, S., Ito, H., Kogure, K., et al. (2013). A light-driven sodium ion pump in marine bacteria. *Nat. Commun.* 4, 1678. doi: 10.1038/ncomms2689

Jung, K. H., Trivedi, V. D., and Spudich, J. L. (2003). Demonstration of a sensory rhodopsin in eubacteria. *Mol. Microbiol.* 47, 1513–1522. doi: 10.1046/j.1365-2958.2003.03395.x

Kanada, S., Takeguchi, Y., Murakami, M., Ihara, K., and Kouyama, T. (2011). Crystal structures of an O-like blue form and an anion-free yellow form of pharaonis halorhodopsin. *J. Mol. Biol.* 413, 162–176. doi: 10.1016/j.jmb.2011.08.021

Kandori, H. (2000). Role of internal water molecules in bacteriorhodopsin. *Biochim. Biophys. Acta* 1460, 177–191. doi: 10.1016/S0005-2728(00)00138-9

Kandori, H (2015). "History and perspectives of light-sensing proteins," in *Optogenetics*, eds H. Yawo, H. Kandori, and A. Koizumi (Tokyo: Springer), 3–16.

Kandori, H., Yamazaki, Y., Shichida, Y., Raap, J., Lugtenburg, J., Belenky, M., et al. (2001). Tight Asp85-Thr89 association during the pump switch of bacteriorhodopsin. *Proc. Natl. Acad. Sci. U.S.A.* 98, 1571–1576. doi: 10.1073/pnas.98.4.1571

Kato, H. E., Inoue, K., Abe-Yoshizumi, R., Kato, Y., Ono, H., Konno, M., et al. (2015). Structural basis for Na^+ transport mechanism by a light-driven Na^+ pump. *Nature* 521, 48–53. doi: 10.1038/nature14322

Khorana, H. G., Gerber, G. E., Herlihy, W. C., Gray, C. P., Anderegg, R. J., Nihei, K., et al. (1979). Amino acid sequence of bacteriorhodopsin. *Proc. Natl. Acad. Sci. U.S.A.* 76, 5046–5050. doi: 10.1073/pnas.76.10.5046

Klare, J. P., Chizhov, I., and Engelhard, M. (2008). Microbial rhodopsins: scaffolds for ion pumps, channels, and sensors. *Results Probl. Cell Differ.* 45, 73–122. doi: 10.1007/400_2007_041

Kolbe, M., Besir, H., Essen, L. O., and Oesterhelt, D. (2000). Structure of the light-driven chloride pump halorhodopsin at 1.8 Å resolution. *Science* 288, 1390–1396. doi: 10.1126/science.288.5470.1390

Kouyama, T., Kanada, S., Takeguchi, Y., Narusawa, A., Murakami, M., and Ihara, K. (2010). Crystal structure of the light-driven chloride pump halorhodopsin from *Natronomonas pharaonis*. *J. Mol. Biol.* 396, 564–579. doi: 10.1016/j.jmb.2009.11.061

Luecke, H. (2000). Atomic resolution structures of bacteriorhodopsin photocycle intermediates: the role of discrete water molecules in the function of this light-driven ion pump. *Biochim. Biophys. Acta* 1460, 133–156. doi: 10.1016/S0005-2728(00)00135-3

Luecke, H., Schobert, B., Cartailler, J. P., Richter, H. T., Rosengarth, A., Needleman, R., et al. (2000). coupling photoisomerization of retinal to directional transport in bacteriorhodopsin. *J. Mol. Biol.* 300, 1237–1255. doi: 10.1006/jmbi.2000.3884

Luecke, H., Schobert, B., Richter, H. T., Cartailler, J. P., and Lanyi, J. K. (1999). Structure of bacteriorhodopsin at 1.55 Å resolution. *J. Mol. Biol.* 291, 899–911. doi: 10.1006/jmbi.1999.3027

Matsuno-Yagi, A., and Mukohata, Y. (1977). Two possible roles of bacteriorhodopsin; a comparative study of strains of *Halobacterium halobium* differing in pigmentation. *Biochem. Biophys. Res. Commun.* 78, 237–243. doi: 10.1016/0006-291X(77)91245-1

Miesenböck, G. (2011). Optogenetic control of cells and circuits. *Annu. Rev. Cell Dev. Biol.* 27, 731–758. doi: 10.1146/annurev-cellbio-100109-104051

Muneda, N., Shibata, M., Demura, M., and Kandori, H. (2006). Internal water molecules of the proton-pumping halorhodopsin in the presence of azide. *J. Am. Chem. Soc.* 128, 6294–6295. doi: 10.1021/ja060253d

Muroda, K., Nakashima, K., Shibata, M., Demura, M., and Kandori, H. (2012). Protein-bound water as the determinant of asymmetric functional conversion between light-driven proton and chloride pumps. *Biochemistry* 51, 4677–4684. doi: 10.1021/bi300485r

Nagel, G., Ollig, D., Fuhrmann, M., Kateriya, S., Musti, A. M., Bamberg, E., et al. (2002). Channelrhodopsin-1: a light-gated proton channel in green algae. *Science* 296, 2395–2398. doi: 10.1126/science.1072068

Nagel, G., Szellas, T., Huhn, W., Kateriya, S., Adeishvili, N., Berthold, P., et al. (2003). Channelrhodopsin-2, a directly light-gated cation-selective membrane channel. *Proc. Natl. Acad. Sci. U.S.A.* 100, 13940–13945. doi: 10.1073/pnas.1936192100

Oesterhelt, D., and Stoeckenius, W. (1971). Rhodopsin-like protein from the purple membrane of *Halobacterium halobium*. *Nat. New Biol.* 233, 149–152. doi: 10.1038/newbio233149a0

Ono, H., Inoue, K., Abe-Yoshizumi, R., and Kandori, H. (2014). FTIR spectroscopy of a light-driven compatible sodium ion-proton pumping rhodopsin at 77 K. *J. Phys. Chem. B* 118, 4784–4792. doi: 10.1021/jp500756f

Petrovskaya, L. E., Lukashev, E. P., Chupin, V. V., Sychev, S. V., Lyukmanova, E. N., Kryukova, E. A., et al. (2010). Predicted bacteriorhodopsin from *Exiguobacterium sibiricum* is a functional proton pump. *FEBS Lett.* 584, 4193–4196. doi: 10.1016/j.febslet.2010.09.005

Rasmussen, S. G., DeVree, B. T., Zou, Y., Kruse, A. C., Chung, K. Y., Kobilka, T. S., et al. (2011). Crystal structure of the β2 adrenergic receptor-Gs protein complex. *Nature* 477, 549–555. doi: 10.1038/nature10361

Sasaki, J., Brown, L. S., Chon, Y. S., Kandori, H., Maeda, A., Needleman, R., et al. (1995). Conversion of bacteriorhodopsin into a chloride ion pump. *Science* 269, 73–75. doi: 10.1126/science.7604281

Scheerer, P., Park, J. H., Hildebrand, P. W., Kim, Y. J., Krauss, N., Choe, H.-W., et al. (2008). Crystal structure of opsin in its G-protein-interacting conformation. *Nature* 455, 497–502. doi: 10.1038/nature07330

Schobert, B., and Lanyi, J. K. (1982). Halorhodopsin is a light-driven chloride pump. *J. Biol. Chem.* 257, 10306–10313.

Shibata, M, Muneda, N., Sasaki, T., Shimono, K., Kamo, N., Demura, M., et al. (2005). Hydrogen-bonding alterations of the protonated Schiff base and water molecule in the chloride pump of *Natronobacterium pharaonis*. *Biochemistry* 44, 12279–12286. doi: 10.1021/bi050726d

Spudich, J. L., and Bogomolni, R. A. (1984). Mechanism of colour discrimination by a bacterial sensory rhodopsin. *Nature* 312, 509–513. doi: 10.1038/312509a0

Spudich, J. L., Sineshchekov, O. A., and Govorunosa, E. G. (2014). Mechanism divergence in microbial rhodopsins. *Biochim. Biophys. Acta* 1837, 546–552. doi: 10.1016/j.bbabio.2013.06.006

Takeda, K., Sato, H., Hino, T., Kono, M., Fukuda, K., Sakurai, I., et al. (1998). A novel three-dimensional crystal of bacteriorhodopsin obtained by successive fusion of the vesicular assemblies. *J. Mol. Biol.* 283, 463–474. doi: 10.1006/jmbi.1998.2103

Tittor, J., Haupts, U., Haupts, C., Oesterhelt, D., Becker, A., and Bamberg, E. (1997). Chloride and proton transport in bacteriorhodopsin mutant D85T: different modes of ion translocation in a retinal protein. *J. Mol. Biol.* 271, 405–416, doi: 10.1006/jmbi.1997.1204

Váró, G., Brown, L. S., Needleman, R., and Lanyi, J. K. (1996). Proton transport by halorhodopsin. *Biochemistry* 35, 6604–6611. doi: 10.1021/bi9601159

Venter, J. C., Remington, K., Heidelberg, J. F., Halpern, A. L., Rusch, D., Eisen, J. A., et al. (2004). Environmental genome shotgun sequencing of the Sargasso Sea. *Science* 304, 66–74. doi: 10.1126/science.1093857

Wolf, S., Freier, E., and Gerwert, K. (2008). How does a membrane protein achieve a vectorial proton transfer via water molecules? *ChemPhysChem* 9, 2772–2778. doi: 10.1002/cphc.200800703

Yoshizawa, S., Kumagai, Y., Kim, H., Ogura, Y., Hayashi, T., Iwasaki, W., et al. (2014). Functional characterization of flavobacteria rhodopsins reveals a unique class of light-driven chloride pump in bacteria. *Proc. Natl. Acad. Sci. U.S.A.* 111, 6732–6737. doi: 10.1073/pnas.1403051111

Zhang, F., Vierock, J., Yizhar, O., Fenno, L. E., Tsunoda, S., Kianianmomeni, A., et al. (2011). The microbial opsin family of optogenetic tools. *Cell* 147, 1446–1457. doi: 10.1016/j.cell.2011.12.004

Zhang, F., Wang, L. P., Brauner, M., Liewald, J. F., Kay, K., Watzke, N., et al. (2007). Multimodal fast optical interrogation of neural circuitry. *Nature* 446, 633–639. doi: 10.1038/nature05744

Conflict of Interest Statement: The author declares that the research was conducted in the absence of any commercial or financial relationships that could be construed as a potential conflict of interest.

frontiers in Molecular Biosciences

ORIGINAL RESEARCH
published: 22 July 2015
doi: 10.3389/fmolb.2015.00041

The primary photoreaction of channelrhodopsin-1: wavelength dependent photoreactions induced by ground-state heterogeneity

Till Stensitzki, Vera Muders, Ramona Schlesinger, Joachim Heberle and Karsten Heyne *

Institute of Experimental Physics, Free University Berlin, Berlin, Germany

The primary photodynamics of channelrhodopsin-1 from *Chlamydomonas augustae* (*Ca*ChR1) was investigated by VIS-pump supercontinuum probe experiments from femtoseconds to 100 picoseconds. In contrast to reported experiments on channelrhodopsin-2 from *Chlamydomonas reinhardtii* (*Cr*ChR2), we found a clear dependence of the photoreaction dynamics on varying the excitation wavelength. Upon excitation at 500 and at 550 nm we detected different bleaching bands, and spectrally distinct photoproduct absorptions in the first picoseconds. We assign the former to the ground-state heterogeneity of a mixture of 13-*cis* and all-*trans* retinal maximally absorbing around 480 and 540 nm, respectively. At 550 nm, all-*trans* retinal of the ground state is almost exclusively excited. Here, we found a fast all-*trans* to 13-*cis* isomerization process to a hot and spectrally broad P_1 photoproduct with a time constant of (100 ± 50) fs, followed by photoproduct relaxation with time constants of (500 ± 100) fs and (5 ± 1) ps. The remaining fraction relaxes back to the parent ground state with time constants of (500 ± 100) fs and (5 ± 1) ps. Upon excitation at 500 nm a mixture of both chromophore conformations is excited, resulting in overlapping reaction dynamics with additional time constants of <300 fs, (1.8 ± 0.3) ps and (90 ± 25) ps. A new photoproduct Q is formed absorbing at around 600 nm. Strong coherent oscillatory signals were found pertaining up to several picoseconds. We determined low frequency modes around 200 cm^{-1}, similar to those reported for bacteriorhodopsin.

Keywords: *Ca*ChR1, retinal, isomerization, femtosecond pump-probe spectroscopy, reaction model, ground-state heterogeneity

OPEN ACCESS

Edited by:
Tilo Mathes, Vrije Universiteit Amsterdam, Netherlands

Reviewed by:
Josef Wachtveitl, Goethe-University Frankfurt, Germany
Jose Luis Perez Lustres, University of Santiago de Compostela, Spain

***Correspondence:**
Karsten Heyne, Institute of Experimental Physics, Free University Berlin, Arnimallee 14, 14195 Berlin, Germany
karsten.heyne@fu-berlin.de

Specialty section:
This article was submitted to Biophysics, a section of the journal Frontiers in Molecular Biosciences

Received: *31 March 2015*
Accepted: *06 July 2015*
Published: *22 July 2015*

Citation:
Stensitzki T, Muders V, Schlesinger R, Heberle J and Heyne K (2015) The primary photoreaction of channelrhodopsin-1: wavelength dependent photoreactions induced by ground-state heterogeneity. Front. Mol. Biosci. 2:41. doi: 10.3389/fmolb.2015.00041

Introduction

Microbial rhodopsins comprise a large family of light-driven ion pumps and sensors. In 2002, a new functionality of microbial rhodopsins was introduced by the discovery of a light-gated ion channel (named channelrhodopsin) in the eyespot of the green algae *Chlamydomonas reinhardtii* (Nagel et al., 2002). A year later, a second channelrhodopsin (*Cr*ChR2) was characterized, Nagel et al. (2003) which paved the way for the new field of optogenetics where action potentials are elicited in neurons simply by remote illumination (Fenno et al., 2011).

Common to all rhodopsins, the polypeptide folds into the membrane in the form of a seven-helical bundle with the retinal chromophore covalently attached to a conserved lysine to form

a protonated Schiff base (SB). Electron microscopy provided the first structural information on *Cr*ChR2 and resolved the arrangement of the seven transmembrane helices (Muller et al., 2011). X-ray crystallography provided a high-resolution three-dimensional structural model of C1C2, a chimera of channelrhodopsin derived from *Cr*ChR1 (helices A–E) and *Cr*ChR2 (helices F, G) (Kato et al., 2012). It was shown by PELDOR spectroscopy that helices B and F move to open the cation channel under illumination (Krause et al., 2013; Sattig et al., 2013). Electron microscopy of the open state confirmed these helical movements among others (Muller et al., 2015).

All native channelrhodopsins (ChRs) are cation channels which share sequence homology and similar functionalities but differ in spectral sensitivity, photocurrent, and desensitization. The visible absorption of retinal in ChR1 from *Chlamydomonas augustae* (*Ca*ChR1) is red-shifted by 50 nm as compared to the widely employed *Cr*ChR2 (Hou et al., 2012). This spectral feature renders *Ca*ChR1 advantageous in optogenetic applications where an increased penetration depth of the excitation light is required.

Illumination of ChRs induces a cyclic reaction (Ritter et al., 2008; Lorenz-Fonfria and Heberle, 2014). Up to now, the photocycle of *Ca*ChR1 has been recorded only at ns time resolution. Akin to the photoreaction of *Cr*ChR2 (Bamann et al., 2008; Ernst et al., 2008) an early red-shifted P_1^{590} intermediate with absorption maximum at ∼590 nm appears, which decays into the P_2^{380} intermediate with absorption peak at 380 nm. The long lifetime of the P_2^{380} state in *Ca*ChR1 is the most striking difference to *Cr*ChR2 (Sineshchekov et al., 2013) (our unpublished observations). As the lifetime of P_2^{380} correlates with the lifetime of the passive channel current, the P_2^{380} intermediate represents the conductive state of *Ca*ChR1. A P_3 intermediate is not observed in *Ca*ChR1 but minor contributions from an O-like intermediate at 600 nm appear (Sineshchekov et al., 2013). Intramolecular proton transfer occurs in *Ca*ChR1 (Sineshchekov et al., 2013; Ogren et al., 2015a) but with distinct differences to *Cr*ChR2 (Lorenz-Fonfria et al., 2013; Ogren et al., 2015b).

UV/VIS pump-probe spectroscopy shows *Cr*ChR2 relaxation on the S_1 potential energy surface by 150 fs, followed by a decay with a time constant of 400 fs into a hot ground state P_1 and the parent ground state. The hot P_1 relaxes with a time constant of 2.7 ps to a thermally equilibrated P_1, the first intermediate state of the photocycle (Verhoefen et al., 2010). This intermediate state is characterized by retinal in a 13-*cis* conformation and accompanied by conformational changes in the protein backbone (Neumann-Verhoefen et al., 2013). A slow relaxation pathway of 200 ps was observed (Verhoefen et al., 2010).

The configuration of retinal in the ground state of *Ca*ChR1 was identified by retinal extraction followed by isomer separation with high-performance liquid chromatography (HPLC). Similar to *Cr*ChR2, the retinal isomer composition of the ground state result in a mixture of ∼70:30 all-*trans* to 13-*cis* retinal (Nack et al., 2009; Muders et al., 2014). Resonance Raman experiments showed that the vibrational bands in the C = C stretching region derive from a mixture of retinals, which were assigned to mostly all-*trans* and partially 13-*cis* retinal. The band assignment in the C–C stretching region to contributions of 13-*cis* retinal was inexplicit, therefore also 100% all-*trans* retinal in the ground state was discussed (Ogren et al., 2014).

Here, we present the first femtosecond VIS pump supercontinuum probe spectroscopic experiments on *Ca*ChR1. Blue-shifted and red-shifted excitations with respect to the visible absorption maximum were applied to resolve the early photoreactions of 13-*cis* and all-*trans* retinal containing populations of *Ca*ChR1.

Materials and Methods

*Ca*ChR1 was prepared as described (Lorenz-Fonfria et al., 2014; Muders et al., 2014). Briefly, the truncated *Ca*ChR1 gene (1–352 aa) was fused with a 10 × His-tag (GeneArt, Life Technologies) and was heterologously expressed in *Pichia pastoris* cells. The solubilized protein was purified on a Ni-NTA column (Macherey-Nagel, Germany) and concentrated to 46 mg/mL in buffer containing 20 mM Hepes, 100 mM NaCl, 0.05% DDM at pH 7.4. Two times 150 µL of the *Ca*ChR1 solution was placed between two CaF_2 windows. The sample cell thickness was 100 µm, and the sample was rapidly moved perpendicular to the beam direction by a Lissajous scanner to provide a fresh sample at every shot. The spectral shape of the two selected femtosecond excitation pulses are plotted with the absorption spectrum of *Ca*ChR1 in **Figure 1**. Femtosecond laser pulses were generated starting from a fundamental femtosecond laser pulse delivered by a 1 kHz Ti:Sa laser system (Coherent Legend USP, 80 fs pulses at 800 nm). The fundamental beam was split into two parts for pump and probe pulse generation. The pump pulses were generated in a non-collinear optical parametric amplifier (NOPA). A sapphire white light supercontiuum was used as seed, amplified in a BBO crystal by frequency doubled pulses at 400 nm. We selected energies to excite the sample of about 0.4–0.5 µJ per pulse with a pump focus diameter of about 300 µm.

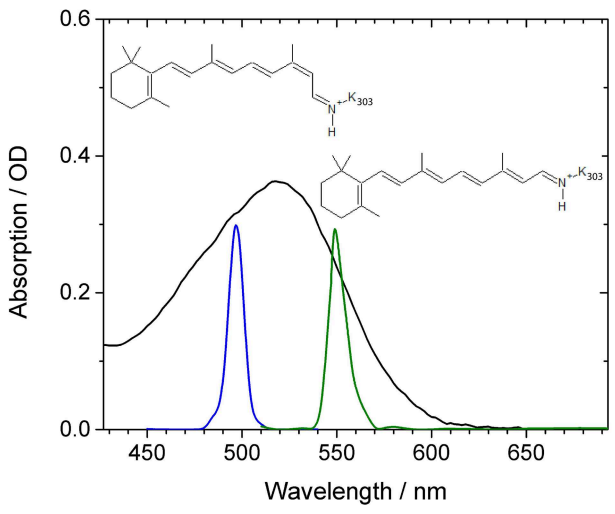

FIGURE 1 | Absorption spectrum of *Ca*ChR1 (black line) as a function of wavelength. Blue and green lines indicate the shape of the excitation pulses used in our experiments. The reported chromophore isomer structures of 13-*cis* retinal and all-*trans* retinal are inserted.

At an optical density of 0.25 OD in the absorption maximum we excite about 10% of the sample. The fundamental for the probe pulses were first directed over an optical delay line, then focused into a 1 cm water cell generating the broadband white light supercontinuum from ∼400 to ∼1100 nm for probing. We selected probe wavelengths from 427 to 693 nm. We achieved fluctuations of below 1% standard deviation with a properly aligned water white light setup. Both beams were focused into the sample cell by a curved mirror. Behind the cell, the probe beam is collimated and passed through a short-pass filter (<750 nm) and a polarizer. The beam is than focused into a fiber connected with a grating spectrometer (Andor Shamrock 303i, 600 l/cm) equipped with a CCD camera system (2000 × 5 pixel, 0.35 nm/pixel, Stresing GmbH Berlin). The spectral resolution was below 0.5 nm. We used step sizes of 30 fs from −1 to 5 ps, and step sizes of $\log_{10}$ for longer delay times, and 8000 averages per data point. Every second pump beam was blocked by a chopper to record excited and not excited sample volumes alternatively. Since we found negligible polarization effects, we selected perpendicular polarization between pump and probe beam to reduce stray light. The time-zero was determined by recording the signal in pure CaF_2 of the sample window. The delay with a maximal signal for each pixel was found and the resulting wavelength-delay curve was fitted with a 3rd order polynomial. For better visibility, the data shown in the contour plots in **Figure 2** were smoothed in the time domain with Gaussian windows with a width of 4 points of 30 fs step size (corresponding to FWHM of 200 fs). This strongly reduces the oscillatory features. The unfiltered dataset is available in Figure S2. The instrument response function (IRF) determined to be 90 fs is governed by the pump pulse length (see Figure S6) (Kovalenko et al., 1999). The chirped water white light supercontinuum has negligible influence on the IRF after mathematical chirp correction Hence, the low frequency mode at 316 cm^{-1} with an oscillation period of 104 fs of our CaF2 windows could be well-resolved, and was used as an internal standard.

Results

In **Figure 1** the absorption spectrum of *Ca*ChR1 is presented with two spectrally different excitation pulse positions, and the two retinal chromophore conformations. The absorption spectrum peaks at 518 nm, exhibits a steeper decline at longer wavelengths compared to shorter wavelengths, and has a shoulder at around 470 nm. Raman studies showed that the retinal chromophore in ground-state *Ca*ChR1 adopts a mixture of 13-*cis* and all-*trans* conformations with a fraction of ∼30 and ∼70%, respectively (Muders et al., 2014).

Thus, different absorptions are expected for *Ca*ChR1 harboring 13-*cis* and all-*trans* retinal (Muders et al., 2014). The displayed absorption profile is broad and covers about 100 nm similarly as it was reported for dark-adapted bacteriorhodopsin and some bacteriorhodopsin mutants (Mowery et al., 1979; Harbison et al., 1984; Heyne et al., 2000). Assuming the same protein surrounding, and a simple particle in a box approach for the direction of the electronic transition dipole moment, the 13-*cis* retinal is expected to absorb at lower wavelengths due to a reduced length in one direction of its bent conjugated π-electron system of the ethylenic moiety compared to all-*trans* retinal (Aton et al., 1977; Fodor et al., 1989). Therefore, we expect complex photoreaction dynamics of *Ca*ChR1 with 13-*cis* retinal and with all-*trans* retinal upon excitation at 500 nm, while upon excitation at 550 nm at the low energy side of the absorption

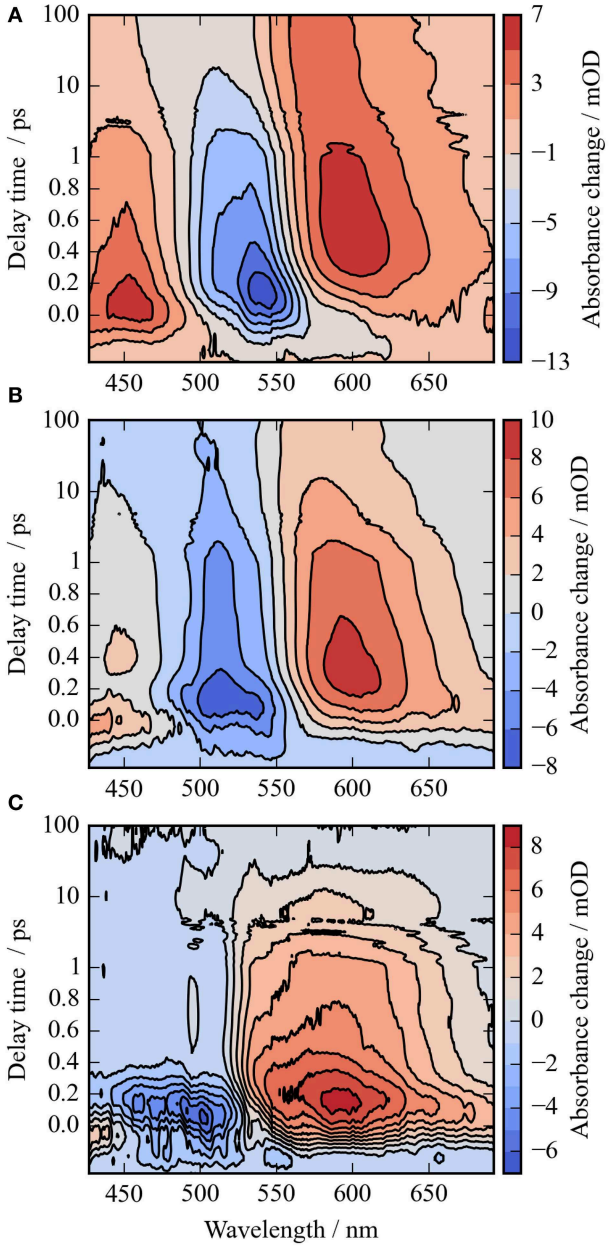

FIGURE 2 | Contour plots of the photoreaction dynamics of *Ca*ChR1 upon excitation at 550 nm (A), 500 nm (B), and the difference of both datasets (C). Blue colors indicate negative signals, red colors positive signals. The contour plots display the absorbance difference in mOD upon excitation as a function of delay time and wavelength. The contour plots were smoothed in the time domain with Gaussian windows with a width of 4 points (FWHM of ∼200 fs), the unfiltered dataset is depicted in Figure S2. The difference contour plot **(C)** is calculated by the direct difference of **(B)** and **(A)**.

spectrum the photoreaction dynamics of *Ca*ChR1 containing all-*trans* retinal will dominate.

In **Figure 2A** the absorbance change of *Ca*ChR1 upon excitation at 550 nm is presented as a function of probe wavelength from 427 to 693 nm for different pump probe delay times. In this contour plot positive signals are found in the spectral region around 450 and 600 nm, while negative signals are visible around 540 nm. Upon excitation the initial absorption increase of excited state absorption (ESA) is found around 450 nm. The transient at 450 nm is plotted in **Figure 3** (blue dots). The major part of the ESA signal exhibits a fast decay with time constant τ_1 of 100 fs accompanied with a spectral narrowing displayed in **Figure 2A**, in conflict with a blue shift of the ESA. This points to relaxation or isomerization on the electronic excited state potential energy surface. The negative signal in **Figure 2A** exhibits a blue shift and decays at longer wavelengths on the same time scale. The major fraction of the transient at 550 nm (**Figure 3**, green dots) decays with τ_1, a smaller fraction exhibits time constants of $\tau_2 = (0.5 \pm 0.1)$ and $\tau_3 = (5 \pm 1)$ ps. Decay associated spectra (DAS) representing decaying spectral features with a given time constant are displayed in **Figure 4**. The DAS of the time constant $\tau_1 = 100$ fs exhibits a positive signal from 427 to 490 nm, and a negative signal for longer wavelengths. At short wavelengths the positive signal shows the instantaneous ESA, while the negative signal represents stimulated emission decay and the rise of the first photoproduct. Note, there is no contribution matching the bleaching signal, indicating no back reaction to the parent ground state on this ultrafast time scale. We assign the time constant $\tau_1 = (100 \pm 50)$ fs to excited state decay accompanied by stimulated emission decay, and 13-*cis* photoproduct formation. The DAS for time constants of 500 fs and 5 ps exhibit very similar spectral features with a stronger signal for long and short wavelengths of the 500 fs component. This could be interpreted by involvement of the same electronic ground state showing broader spectral features of a hotter ground state at early delay times. A hot ground state is characterized by population of excited vibrations not relaxed to their thermal equilibrium. These populated non-thermal vibrations relax via intra- and intermolecular vibrational redistribution pathways on a picosecond time scale (Heyne et al., 2004a,b; Rey et al., 2004; Kozich et al., 2006; Shigeto et al., 2008). The positive signal contributions around 450 nm occur instantaneously upon excitation and persist up to 100 ps, as visible by the vanishing negative signal at 430 nm at 100 ps delay time (**Figures 4**, **5A**). Since the bleaching signal has negative contribution at this spectral position, a positive band is also contributing there. Thus, the first thermally relaxed photoproduct P_1 exhibits a broad spectral absorption from 427 to 693 nm with a maximum at about 560 nm (see Figure S1).

The rise of the vibrational excited (hot) photoproduct P_1 within 100 femtoseconds is visible at 600 nm, and at 650 nm in **Figures 2A**, **3**. After formation of the hot photoproduct P_1 a relaxation occurs on the low energy and high energy side of the absorption on a time scale of $\tau_2 = (500 \pm 100)$ fs to a more cooled, but still hot photoproduct, which relaxes further with a time constant of $\tau_2 = (5 \pm 1)$ ps to the thermally relaxed P_1. As a result of the cooling processes the positive absorption shifts to smaller wavelengths and the spectral feature narrows as displayed in **Figure 2A**. No stimulated emission signals were observed after 200 fs, corroborating the excited state decay with <100 fs.

The spectral integrated transient upon excitation at 550 nm is depicted in **Figure 7**. The spectral integrated transient provides information on the overall change in extinction coefficient. This assumption holds for integrated spectral ranges covering the whole contributing absorption band. This is fulfilled to a high extend in our measurements. Upon excitation at 550 nm a strong coherent contribution of the CaF_2 sample cell window is clearly

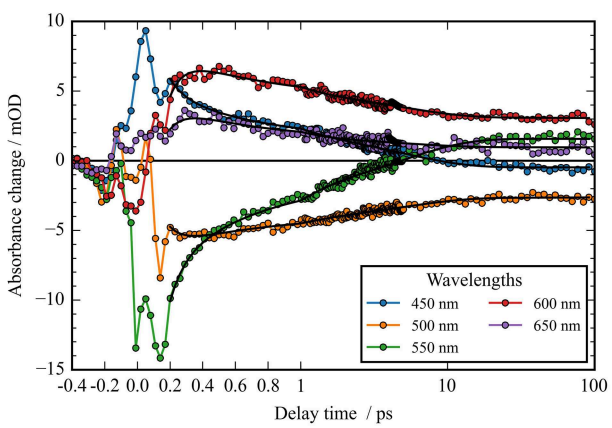

FIGURE 3 | Transients (dots) and simulated transients (black lines) upon excitation at 550 nm: the temporal change in absorption of *Ca*ChR1 is plotted as a function of delay time after excitation. Transient changes on the 100 femtosecond, sub picosecond, and picosecond time scales are directly visible.

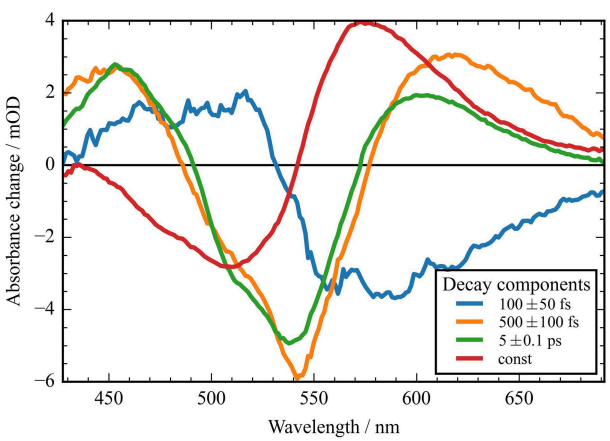

FIGURE 4 | Decay associated spectra (DAS) of the transient data upon excitation at 550 nm of *Ca*ChR1. Positive signals indicate decaying excited state and photoproduct absorption; negative signals indicate decaying bleaching absorption, rising photoproduct absorption, and stimulated emission decay. The fast component (blue line) exhibits no signature of the bleaching signal. The two components at 500 fs and 5 ps decay time exhibit similar spectral shapes with deviations at the high and low energy side. The red line displays the spectral difference between the bleaching signal and the photoproduct P_1.

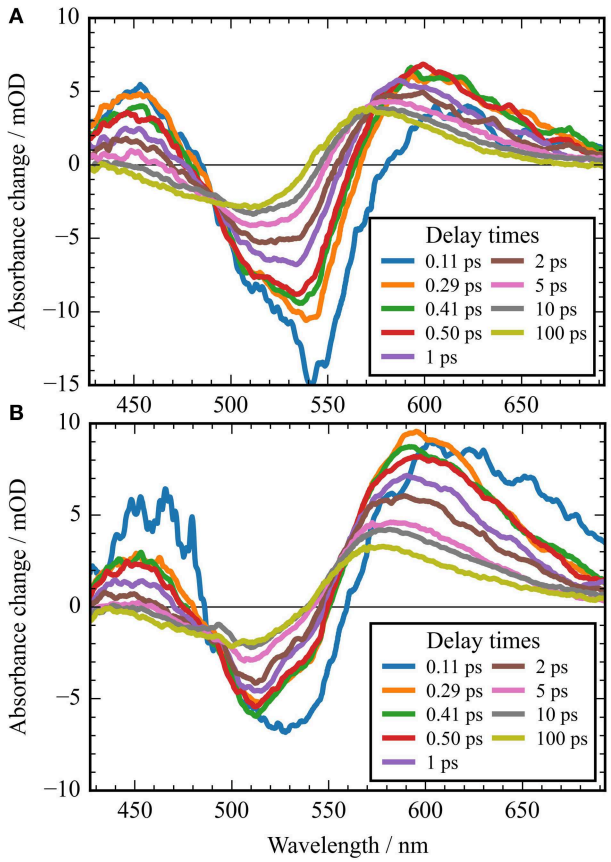

FIGURE 5 | Absorbance difference spectra of *Ca*ChR1 upon excitation at 550 nm (A), and upon excitation at 500 nm (B). The first spectra at 0.11 ps could still be influenced by the instrument response function. Comparison of both spectra displays striking differences in the photoproduct region around 600 nm at picosecond delay times.

visible in **Figure 7** around time zero. We observe coherent oscillations in the first picoseconds with a period of ∼100 fs. As shown in **Figure 7** the overall integrated transient rises within 100 femtoseconds to positive values, and stays nearly constant for picoseconds. Spectral integrated transients are not affected by spectral shifting, but are sensitive to new emerging species with different extinction coefficients. We see no significant signal change after 300 fs. Therefore, we assign the time constants of 500 fs and 5 ps to cooling processes of the photoproduct. As presented in **Figure 4**, the stimulated emission decays with a time constant of 100 fs. Since, the only detectable transition from the electronic excited state to another state is connected with the time constant of 100 fs, we assign this process to the all-*trans* to 13-*cis* isomerization.

It was reported that the initial photoreaction is independent of the excitation wavelength in *Cr*ChR2 (Verhoefen et al., 2010). For *Ca*ChR1, we see significant changes upon changing the excitation wavelength from the low energy side of the absorption band at 550 nm to the high energy side of the absorption band at 500 nm. The differences are best visible by comparing **Figures 5A,B**, as well as by comparing **Figures 2A,B**.

In **Figure 2B** the contour plot of the photoreaction dynamics upon 500 nm excitation is plotted. Again, there are instantaneous positive signals around 450 nm, instantaneous negative signals around 510 nm, and positive signals around 600 nm showing a delayed emergence. The negative signal exhibits features of a fast decaying fraction around 560 nm, pointing to a very small stimulated emission as compared to excitation at 550 nm. In addition, the bleaching signal peaks clearly at 510 nm continuing in position. The positive signal around 600 nm is much stronger compared to excitation at 550 nm. Since we expect to excite *Ca*ChR1 with 13-*cis* retinal as well as *Ca*ChR1 with all-*trans* retinal upon excitation at 500 nm, the photoreaction dynamics should consist of two parts. One part describes the photoreaction of *Ca*ChR1 with all-*trans* retinal, the other part the photoreaction of *Ca*ChR1 containing 13-*cis* retinal. Since the bleaching signals at 100 ps, where the primary photoreaction is nearly finished, shows identical spectral shape from 430 to 510 nm for excitation at 550 and 500 nm, we have a handle to compare both photoreactions directly. Therefore, the dataset excited at 500 nm was scaled by 1.4 to match the bleaching signals of both datasets at 100 ps delay time. Then, we subtracted the dataset upon excitation at 500 nm from the dataset upon excitation at 550 nm. The resulting difference is plotted as a contour plot in **Figure 2C**. The difference dataset has negative signals below ∼520 nm with a maximum around 480 nm, and positive signals above 520 nm. Within the first 100 femtoseconds ($\tau_1 < 300$ fs) the negative signal exhibits a strong decay, while the positive signal decays with a blue shift on this time scale (**Figure 2C**).

The remaining positive signal decays with time constants of $\tau_2 = (1.8 \pm 0.3)$ and $\tau_3 = (90 \pm 25)$ ps to zero. The corresponding decay associated spectra (DAS) and transients are presented in Figure S7. The positive signal corresponding to τ_2 exhibits a maximum at 590 nm and a broad absorption from 520 nm to wavelengths longer than 690 nm. A small negative contribution is found around 500 nm. The DAS corresponding to τ_3 (DAS_3) has a smaller amplitude with a maximum at 570 nm and positive signals from 490 to 690 nm. Small negative contributions are found around 450 nm. The spectral integrated signal in Figure S4 exhibits an instantaneous positive feature masked by oscillations, decaying with time constants <300 fs, 1.8 ps, and ∼90 ps. Since spectral integrated signals are insensitive to spectral shifts, three time constants indicate three transitions of electronic states. Thus, we assign the significant DAS_2 signal not to a cooling effect, but to a change of the electronic state properties.

The back reaction of the excited *Ca*ChR1 with 13-*cis* retinal to the parent ground state is nearly complete within 100 ps. This explains the nearly identical negative shapes of the absorption difference signals upon excitation at 500 and 550 nm.

At 100 ps delay time the spectral shape of the negative bleaching band signals are nearly identical for excitation at 500 and 550 nm (see Figure S5). Upon scaling of the bleaching bands for both excitations the photoproduct bands are rather similar, with band integrals differing by about 1.4, and absorption at longer wavelengths upon excitation at 500 nm. The intensity and spectral differences point to the existence of different photoproducts depending on the excitation energy. Increasing

the excitation energy by shorter wavelengths introduce a higher amount of excess energy into the *Ca*ChR1 protein allowing for formation of photoproducts with higher ground-state energy and consequently red-shifted absorption. Ground-state heterogeneity of chromophore structures were reported for several photoreceptors (Gervasio et al., 1998; Sineshchekov, 2004; von Stetten et al., 2008; Mailliet et al., 2011; Kim et al., 2012; Ritter et al., 2013).

Examination of the photoreaction quantum yield is difficult and can only be roughly estimated by our data.

We estimated a quantum yield for the *Ca*ChR1 with all-*trans* retinal upon excitation at 550 nm to be higher than 0.25 and lower than 0.7. Excitation of the *Ca*ChR1 at 500 nm is lower compared to excitation at 550 nm.

A striking property of the *Ca*ChR1 dynamics are the coherent oscillations visible in the transients (**Figure 3**), as well as in the contour plots (Figure S2). We obtained coherent oscillations up to 3 ps delay time by subtracting the simulated exponential dynamics from the dataset. The remaining residues were Fourier transformed and the amplitudes were plotted in **Figure 6A**. **Figure 6B** presents the spectral distribution of the Fourier components. Upon excitation at 550 nm we were able to identify oscillatory signals at about 80, 100, 150, 200, and 225 cm^{-1}. The vibrations around 100, 150, 200, and 225 cm^{-1} occur at spectral positions connected to the electronic excited state, and also to the photoproduct absorption at long wavelengths. This could be interpreted in a way that these four vibrations constitute a part of the reaction coordinate in *Ca*ChR1, transferring the electronic excited state population to the first hot photoproduct P_1. These vibrations at 100, 155, 200, and 225 cm^{-1} were assigned for all-*trans* retinal in solution to a ring torsion vibration, a chain methyl and ring torsion vibration, a methyl ring torsion vibration, and a chain bending and methyl ring torsion vibration, respectively (Prokhorenko et al., 2006). Two similar coherent vibrations at 195 and 226 cm^{-1} were reported to be crucial to optimize the photoisomerization reaction, while the coherent vibration of 155 cm^{-1} were reported to reduce the photoreaction quantum yield in bacteriorhodopsin (Polli et al., 2010; Johnson et al., 2014).

Discussion

Our model for the photoreaction of *Ca*ChR1 with all-*trans* retinal is presented in **Figure 8**:

Upon photoexcitation the all-*trans* retinal relaxes on the electronic excited state surface followed by an excited state decay and isomerization with a time constant of $\tau_1 = (100 \pm 50)$ fs via a conical intersection to the very hot photoproduct P_1. Our decay associated spectrum (DAS_1) in **Figure 4** with a time constant of $\tau_1 = (100 \pm 50)$ fs is the only signature explaining the rise of the delayed positive signal around 600 nm. The excess energy is located in retinal and protein vibrations strongly coupled to the reaction coordinate. We propose a reaction coordinate consisting of several vibrations including the low-frequency vibrations at 205 and 225 cm^{-1}. From the vibrational excited electronic hot P_1 the *Ca*ChR1 with 13-*cis* retinal relaxes via cascaded energy redistribution processes (Heyne et al., 2004a) to the relaxed photoproduct P_1 on a time scale of 500 fs and 5 ps. The initial P_1 photoproduct absorption band exhibits a very broad absorption ranging from 427 to 690 nm. A significant narrowing of the spectrum especially at the low-energy side of the photoproduct absorption is observed on a time scale of 500 fs, followed by a narrowing of the spectrum at the high-energy side of the photoproduct absorption on a time scale of 5 ps. These spectral shifts without a change of extinction coefficient are visible in the spectrally resolved data (**Figure 4**), but not in the spectral integrated transient (**Figure 7**). These processes are indicated by the change of the potential energy surface shapes of P_1 in **Figure 8**. Narrowing of P_1 absorption upon vibrational relaxation is accompanied with the narrowing of the photoproduct potential well. Despite the fact, that we cannot directly detect the photoisomerization process as by time-resolved infrared spectroscopy, we were able to identify the excited state decay with a time constant of 100 fs and the emerged absorption of the photoproduct within 200 fs (**Figure 2A**). Thus, we conclude that the photoisomerization process is an ultrafast process with a time constant of (100 ± 50) fs. The strong red-shift of P_1 absorption with 13-*cis* retinal can be explained by

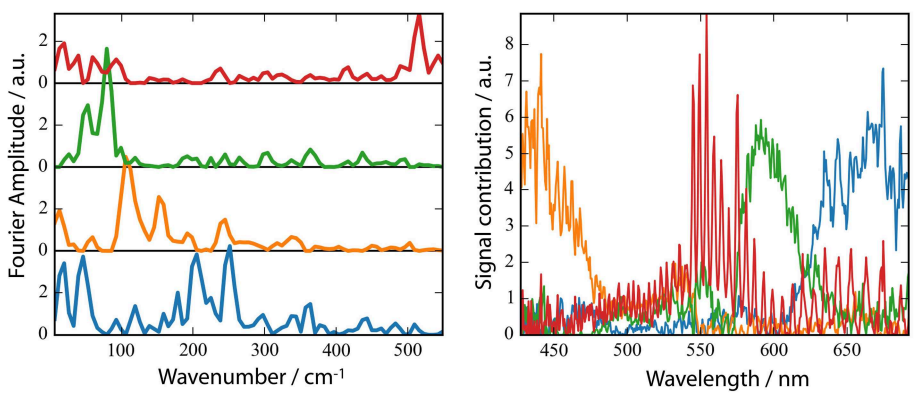

FIGURE 6 | Fast Fourier Transform (FFT) amplitudes of the residuals (A) and the spectral distribution of the components (B). (B) non-negative matrix factorization (NMF) of the 2D matrix presented in Figure S3 of the FFT amplitudes mapped to 4 components. The number of components was inferred from the singular values of the matrix.

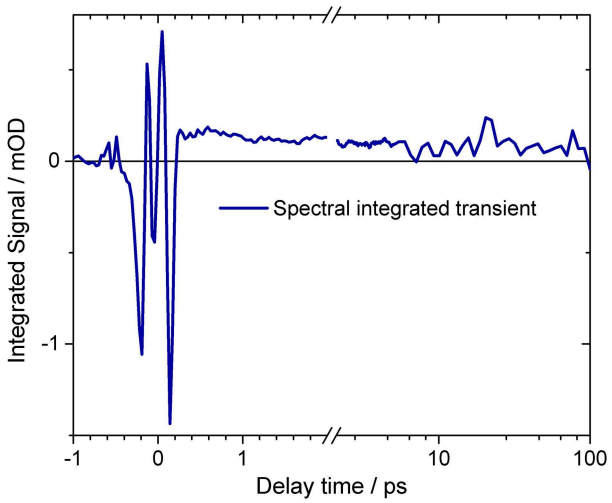

FIGURE 7 | Spectral integrated transient of the complete dataset upon excitation at 550 nm. At delay times around time zero and before 200 fs strong oscillatory signals are visible. The mean signal directly after excitation is negative, rising to about 500 fs. On a picosecond time scale the signal stays nearly constant. The transient is plotted on a logarithmic scale for long delay times. A small signal decrease is observed. Small oscillatory signals are also visible for delay times after 200 fs.

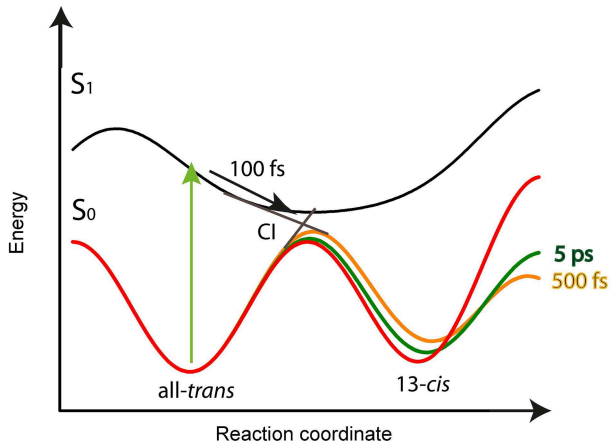

FIGURE 8 | Schematic potential energy surface as a function of the reaction coordinate for the *Ca*ChR1 with all-*trans* retinal. After excitation (green arrow) the molecules relax within 100 fs on the S_1 potential energy surface (black arrow) to the conical intersection (CI), indicated as straight lines from S_1 to S_0. Transition from S_1 to S_0 is accompanied with all-*trans* to 13-*cis* retinal photoisomerization. The excess energy excites vibrations of the chromophore and protein resulting in a softer ground-state potential energy surface (solid orange line) for the photoproduct P_1 with 13-*cis* retinal. Upon vibrational energy relaxation the ground-state potential energy surface becomes stiffer and more harmonic, thereby stabilizing the photoproduct (green line) until the fast relaxation process equilibrates (red curve). This process is connected with the same time constants as for parent ground-state recovery of 500 fs, and 5 ps.

protein surrounding that is not equilibrated. The structural change of the chromophore, change of electric fields around the chromophore, and redistribution of the excess energy into the protein surrounding promotes the energy of *Ca*ChR1 ground state, resulting in a red-shifted absorption. These changes lead to an energetically elevated photoproduct ground-state P_1 initiating the photocycle.

This early photoreaction mechanism is nearly identical to the photoreaction of rhodopsin (Schapiro and Ruhman, 2014). The chromophore relaxes from the Franck-Condon region within 100 fs and reaches the conical intersection. Within this time scale the stimulated emission vanishes completely in rhodopsin, as well as in *Ca*ChR1. In contrast, we see no ultrafast red-shift of the stimulated emission in *Ca*ChR1, probably due to a smaller extinction coefficient in *Ca*ChR1. With the disappearance of the stimulated emission the photoproduct absorption appears and shifts to higher energies in rhodopsin and in *Ca*ChR1.

The thermally equilibrated photoproduct P_1 in *Ca*ChR1 absorbs maximally around 560 nm (Figure S1). The quantum yield of the forward reaction is roughly estimated to be between 0.25 and 0.7, as expected for retinal proteins. The photoproduct P_1 is the first activated protein state of the photocycle of *Ca*ChR1.

The photoreaction is strongly influenced by coherent oscillations. Due to limited time resolution with an IRF of at least 90 fs we are able to identify strong coherent signals up to $\sim$320 cm^{-1}. We found oscillations resulted from low-frequency vibrations coupled to the photodynamics of *Ca*ChR1 with all-*trans* retinal at 205, 225, and 320 cm^{-1}. We assign the vibration around 320 cm^{-1} to Raman vibrations of the CaF_2 windows. The other low-frequency modes could be assigned to all-*trans* retinal vibrations (Prokhorenko et al., 2006) but further experiments with higher time resolution have to be performed to allow a precise assignment of frequency and phase of the involved vibrational oscillations.

In bacteriorhodopsin constructive and destructive interference effects of coherent vibrations drives the ultrafast isomerization process (Polli et al., 2010; Johnson et al., 2014). We expect a similar photoreaction mechanism for *Ca*ChR1 with all-*trans* retinal. Whether the quantum yield of the *Ca*ChR1 photoreaction can be optimized by coherent pulse shaping, has to be investigated in the future. As a result of the very fast isomerization process and formation of the hot electronic ground-state photoproduct, the chromophore and protein surrounding cannot follow this fast reaction speed. Thus, intra- and intermolecular energy redistribution processes on the sub picosecond and picosecond time scale transforms the system to the thermally equilibrated first photoproduct P_1. Whether the different time scales can be assigned to intramolecular redistribution within the 13-*cis* chromophore and intermolecular redistribution between chromophore and protein has to be investigated by time-resolved infrared spectroscopy.

Comparison with reported photoreaction of *Cr*ChR2 reveals several similarities and differences. The photoproduct absorbs red-shifted to the bleaching band in *Ca*ChR1, and in *Cr*ChR2. In *Cr*ChR2 the excited state relaxes with 150 fs similar to the fast time constant in *Ca*ChR1 of 100 fs, but decays with a longer time constant of 400 fs to the photoproduct. The photoproduct cooling was determined to 2.7 ps, in contrast to *Ca*ChR1, where

we observed two cooling processes with 500 fs and 5 ps. As visible in **Figure 2A** the spectral shifting in *Ca*ChR1 has not stopped completely at long delay times. In *Cr*ChR2 a similar spectral shift with a time constant of 200 ps was assigned to protein relaxation. For both systems the primary photoreaction process is assigned to all-*trans* to 13-*cis* retinal isomerization. Due to the blue-shifted absorption of *Cr*ChR2 with absorption maximum around 450 nm no positive signals from the ESA could be observed on the high energy side of the bleaching signal. In *Ca*ChR1, we detected the ESA on the high energy side of the bleaching signal, allowing for a direct separation of electronic excited state and photoproduct absorption. In contrast to *Cr*ChR2 we found strong oscillatory signals in *Ca*ChR1 and a dependence of the photoreaction dynamics on the excitation wavelength (Verhoefen et al., 2010).

Upon excitation at 550 nm we observe the expected photoisomerization of *Ca*ChR1 with all-*trans* retinal to the first photoproduct P_1 cooling down on the picosecond time scale. Changing the excitation energy to 500 nm, results in significantly different photoreaction dynamics. The initial bleaching band is blue-shifted with respect to excitation at 550 nm, demonstrating heterogeneity of the *Ca*ChR1 ground state. Whether the origin of heterogeneity is due to differences in the chromophore structure or differences in the protein strongly interacting with the chromophore can be assessed by electronic or vibrational dynamics. The dynamics of the electronic states show distinct differences in band positions, time scales, and extinction coefficients upon excitation at 500 nm and 550 nm. It was reported that two chromophore conformations appear with all-*trans* and 13-*cis* retinal of 70 and 30% abundance, respectively. Raman stretching vibrations of the C = C were determined at 1533 cm^{-1} for *Ca*ChR1 with all-*trans* retinal and at 1550 cm^{-1} for *Ca*ChR1 with 13-*cis* retinal (Muders et al., 2014). Thus, the differences in the photoreaction dynamics can be explained by ground-state heterogeneity of the *Ca*ChR1 retinal chromophore.

We determined the absorption maxima of *Ca*ChR1 with all-*trans* retinal, and 13-*cis* retinal to be at 540, and ~480 nm, respectively. This is in accordance with the reported linear correlation between the frequency of the retinal C = C stretching vibration ν(C = C) and the maximum of the visible absorption spectrum λ_{max} for equilibrated ground-state structures (Aton et al., 1977; Fodor et al., 1989).

Excitation at 500 nm triggers the photoreaction of *Ca*ChR1 with all-*trans* retinal, and of *Ca*ChR1 with 13-*cis* retinal. After subtraction of the *Ca*ChR1 with all-*trans* retinal dynamics we observed the *Ca*ChR1 with 13-*cis* retinal. We found an ultrafast photoreaction with a positive signal around 600 nm, which decays on a time scale of <300 fs. This is indicated by the decay of the negative and positive signals in **Figure 2C**, S7A at early delay times around 480 and 600 nm, respectively. A significant positive signal of the photoproduct Q with a maximum around 590 nm indicates absorption, decaying with a time constant $\tau_2 = (1.8 \pm 0.3)$ ps. The remaining positive absorption Q' with maximum around 570 nm decays with $\tau_3 = (90 \pm 25)$ ps. The bleaching signals around 480 nm are weak compared to the strong positive signals around 600 nm, indicating a smaller extinction coefficient for the bleaching signals. This explains the poor dynamics of the bleaching signal that might overlap with the high-energy part of the Q spectrum of similar strength. Hence, bleaching recovery of the Q population result in negligible changes of the bleaching signal. The dynamics of *Ca*ChR1 with 13-*cis* retinal show three time constants also visible in the spectral integrated transient in Figure S4A. Thus, we expect all time constants to be connected with changes of electronic state properties.

Since the bleaching signals are the same for excitation at 550 and 500 nm after 100 ps, we expect the photoreaction of *Ca*ChR1 with 13-*cis* retinal to be recovered to its parent state at this time. Thus, several photoreaction mechanism can be discussed:

A photoreaction without isomerization would promote the *Ca*ChR1 13-*cis* ground state (*cis*) to its electronic excited state *cis**, followed by a fast relaxation in the electronic excited state, decays to *cis*' ground state with vibrational excited protein surrounding, and relaxed back to its parent state *cis*. The first time constant of 200 fs (see Figure S7C) would correspond to the relaxation process, the second time constant $\tau_2 = (1.8 \pm 0.3)$ ps to the *cis** → *cis*' transition, and the 90 ps time constant to the recovery of the parent state. The only remaining question is why is the extinction coefficient so different in *cis** and *cis*' compared to *cis*. It seems to be more plausible that the difference of extinction coefficient is due to different chromophore structures induces by isomerization.

Possible photoreactions with two isomerizations start with the promotion of the *Ca*ChR1 13-*cis* ground state (*cis*) to its electronic excited state *cis**, followed by a fast relaxation in the electronic excited state. The first isomerization can occur either in the electronic excited state (*cis** → *trans**), or can be accompanied by the transition from the excited to the ground state *cis** → *trans** or *trans** → *cis*'. If a ground state with *trans*' is formed, an isomerization to *cis* has to take place in the ground state. The first time constant of 200 fs can be connected with an excited state relaxation or a *cis** → *trans** isomerization. The second time constant of 1.8 ps can be due to transitions from *cis** → *trans*' or *trans** → *cis*'. The third time constant of 90 ps reflects the recovery to the parent *Ca*ChR1 13-*cis* ground state from *trans*' → *cis* or *cis*' → *cis*.

Since isomerization processes in the electronic ground state are seldom, we prefer the photoreaction with a *cis** → *trans** isomerization in the electronic excited state on a time scale of <300 fs inducing a strong signal change (Q), followed by a back-isomerization (*trans** → *cis*') with 1.8 ps accompanied with the transition from the electronic excited to the ground state cis' (Q'), that recovers to its parent state by 90 ps. A small fraction can also decay to a *trans*' ground state (*trans** → *trans*').

This would explain the positive signal above 520 nm, upon excitation at 500 nm, with a significantly higher extinction coefficient than upon excitation at 550 nm for long delay times. We tentatively assign this positive signal to a photoproduct *Ca*ChR1 with all-*trans* retinal. For Anabaena Sensory Rhodopsin, it was reported that excitation of the ground state with 13-*cis* retinal, leads to formation of a first K-like photoproduct with all-*trans* retinal, decaying back to ground state with all-*trans* retinal (Anderson et al., 2004). The photoreaction of *Ca*ChR1 with 13-*cis* retinal is completed after some 100 picoseconds. Whether this photoreaction induces dynamics and structural changes of the

protein with possible biological function remains unclear, and has to be clarified in other studies.

In summary, we determined the primary photoreaction of *Ca*ChR1 for the first time. Ground-state heterogeneity of two isomers of the chromophore, all-*trans* retinal and 13-*cis* retinal leads to deviating photoreaction upon changing the excitation wavelength. Shorter wavelengths result in an increase of *Ca*ChR1 with 13-*cis* retinal dynamics, while excitation at longer wavelength increase the photoreaction of *Ca*ChR1 with all-*trans* retinal. Our data for *Ca*ChR1 with all-*trans* retinal are best explained by an all-*trans* to 13-*cis* retinal isomerization and hot photoproduct P_1 formation with a time constant of ∼100 fs. The photoreaction of *Ca*ChR1 with all-*trans* retinal turns out to be faster than in *Cr*ChR2, and exhibit strong oscillatory signals as reported for bacteriorhodopsin. Our data demonstrate a heterogeneity of isomers in the ground state with different photodynamics, but only one reaction pathway seems to be relevant for biological function.

Acknowledgments

We thank the Deutsche Forschungsgemeinschaft (SFB-1078, projects B3 to JH and KH and B4 to RS) for financial support and Dorothea Heinrich and Kirsten Hoffmann for excellent technical assistance. We also thank Yang Yang for sample preparation and setup alignment.

Supplementary Material

The Supplementary Material for this article can be found online at: http://journal.frontiersin.org/article/10.3389/fmolb.2015.00041

References

Anderson, S., Srajer, V., and Moffat, K. (2004). Structural heterogeneity of cryotrapped intermediates in the bacterial blue light photoreceptor, photoactive yellow protein. *Photochem. Photobiol.* 80, 7–14. doi: 10.1562/2004-03-15-RA-115.1

Aton, B., Callender, R. H., Becher, B., and Ebrey, T. G. (1977). Resonance raman studies of purple membrane. *Biochemistry* 16, 2995–2999. doi: 10.1021/bi00632a029

Bamann, C., Kirsch, T., Nagel, G., and Bamberg, E. (2008). Spectral characteristics of the photocycle of channelrhodopsin-2 and its implication for channel function. *J. Mol. Biol.* 375, 686–694. doi: 10.1016/j.jmb.2007.10.072

Ernst, O. P., Sanchez Murcia, P. A., Daldrop, P., Tsunoda, S. P., Kateriya, S., and Hegemann, P. (2008). Photoactivation of channelrhodopsin. *J. Biol. Chem.* 283, 1637–1643. doi: 10.1074/jbc.M708039200

Fenno, L., Yizhar, O., and Deisseroth, K. (2011). The development and application of optogenetics. *Annu. Rev. Neurosci.* 34, 389–412. doi: 10.1146/annurev-neuro-061010-113817

Fodor, S. P. A., Gebhard, R., Lugtenburg, J., Bogomolni, R. A., and Mathies, R. A. (1989). Structure of the retinal chromophore in sensory rhodopsin-I from resonance Raman-spectroscopy. *J. Biol. Chem.* 264, 18280–18283.

Gervasio, F. L., Cardini, G., Salvi, P. R., and Schettino, V. (1998). Low-frequency vibrations of all-trans-retinal: far-infrared and Raman spectra and density functional calculations. *J. Phys. Chem. A* 102, 2131–2136. doi: 10.1021/jp9724636

Harbison, G. S., Smith, S. O., Pardoen, J. A., Winkel, C., Lugtenburg, J., Herzfeld, J., et al. (1984). Dark-adapted bacteriorhodopsin contains 13-cis, 15-syn and all-trans, 15-anti retinal Schiff bases. *Proc. Natl. Acad. Sci. U.S.A.* 81, 1706–1709. doi: 10.1073/pnas.81.6.1706

Heyne, K., Herbst, J., Dominguez-Herradon, B., Alexiev, U., and Diller, R. (2000). Reaction control in bacteriorhodopsin: impact of arg82 and asp85 on the fast retinal isomerization, studied in the second site revertant arg82ala/gly231cys and various purple and blue forms of bacteriorhodopsin. *J. Phys. Chem. B* 104, 6053–6058. doi: 10.1021/jp992877u

Heyne, K., Huse, N., Dreyer, J., Nibbering, E. T. J., Elsaesser, T., and Mukamel, S. (2004b). Coherent low-frequency motions of hydrogen bonded acetic acid dimers in the liquid phase. *J. Chem. Phys.* 121, 902–913. doi: 10.1063/1.1762873

Heyne, K., Nibbering, E. T. J., Elsaesser, T., Petkovic, M., and Kuhn, O. (2004a). Cascaded energy redistribution upon O-H stretching excitation in an intramolecular hydrogen bond. *J. Phys. Chem. A* 108, 6083–6086. doi: 10.1021/jp048653f

Hou, S. Y., Govorunova, E. G., Ntefidou, M., Lane, C. E., Spudich, E. N., Sineshchekov, O. A., et al. (2012). Diversity of chlamydomonas channelrhodopsins. *Photochem. Photobiol.* 88, 119–128. doi: 10.1111/j.1751-1097.2011.01027.x

Johnson, P. J. M., Halpin, A., Morizumi, T., Brown, L. S., Prokhorenko, V. I., Ernst, O. P., et al. (2014). The photocycle and ultrafast vibrational dynamics of bacteriorhodopsin in lipid nanodiscs. *Phys. Chem. Chem. Phys.* 16, 21310–21320. doi: 10.1039/C4CP01826E

Kato, H. E., Zhang, F., Yizhar, O., Ramakrishnan, C., Nishizawa, T., Hirata, K., et al. (2012). Crystal structure of the channelrhodopsin light-gated cation channel. *Nature* 482, 369–374. doi: 10.1038/nature10870

Kim, P. W., Freer, L. H., Rockwell, N. C., Martin, S. S., Lagarias, J. C., and Larsen, D. S. (2012). Femtosecond photodynamics of the red/green cyanobacteriochrome NpR6012g4 from Nostoc punctiforme. 1. Forward dynamics. *Biochemistry* 51, 608–618. doi: 10.1021/bi201507k

Kovalenko, S. A., Dobryakov, A. L., Ruthmann, J., and Ernsting, N. P. (1999). Femtosecond spectroscopy of condensed phases with chirped supercontinuum probing. *Phys. Rev. A* 59, 2369–2384. doi: 10.1103/PhysRevA.59.2369

Kozich, V., Dreyer, J., Ashihara, S., Werncke, W., and Elsaesser, T. (2006). Mode-selective O-H stretching relaxation in a hydrogen bond studied by ultrafast vibrational spectroscopy. *J. Chem. Phys.* 125, 074504-1–074504-9. doi: 10.1063/1.2219111

Krause, N., Engelhard, C., Heberle, J., Schlesinger, R., and Bittl, R. (2013). Structural differences between the closed and open states of channelrhodopsin-2 as observed by EPR spectroscopy. *FEBS Lett.* 587, 3309–3313. doi: 10.1016/j.febslet.2013.08.043

Lorenz-Fonfria, V. A., and Heberle, J. (2014). Channelrhodopsin unchained: structure and mechanism of a light-gated cation channel. *Biochim. Biophys. Acta* 1837, 626–642. doi: 10.1016/j.bbabio.2013.10.014

Lorenz-Fonfria, V. A., Muders, V., Schlesinger, R., and Heberle, J. (2014). Changes in the hydrogen-bonding strength of internal water molecules and cysteine residues in the conductive state of channelrhodopsin-1. *J. Chem. Phys.* 141, 22D507. doi: 10.1063/1.4895796

Lorenz-Fonfria, V. A., Resler, T., Krause, N., Nack, M., Gossing, M., Fischer von Mollard, G., et al. (2013). Transient protonation changes in channelrhodopsin-2 and their relevance to channel gating. *Proc. Natl. Acad. Sci. U.S.A.* 110, E1273–E1281. doi: 10.1073/pnas.1219502110

Mailliet, J., Psakis, G., Feilke, K., Sineshchekov, V., Essen, L. O., and Hughes, J. (2011). Spectroscopy and a high-resolution crystal structure of Tyr263 mutants of cyanobacterial phytochrome Cph1. *J. Mol. Biol.* 413, 115–127. doi: 10.1016/j.jmb.2011.08.023

Mowery, P. C., Lozier, R. H., Chae, Q., Tseng, Y. W., Taylor, M., and Stoeckenius, W. (1979). Effect of acid pH on the absorption spectra and photoreactions of bacteriorhodopsin. *Biochemistry* 18, 4100–4107. doi: 10.1021/bi00586a007

Muders, V., Kerruth, S., Lorenz-Fonfria, V. A., Bamann, C., Heberle, J., and Schlesinger, R. (2014). Resonance Raman and FTIR spectroscopic characterization of the closed and open states of channelrhodopsin-1. *FEBS Lett.* 588, 2301–2306. doi: 10.1016/j.febslet.2014.05.019

Muller, M., Bamann, C., Bamberg, E., and Kuhlbrandt, W. (2011). Projection structure of channelrhodopsin-2 at 6 angstrom resolution by electron crystallography. *J. Mol. Biol.* 414, 86–95. doi: 10.1016/j.jmb.2011.09.049

Muller, M., Bamann, C., Bamberg, E., and Kuhlbrandt, W. (2015). Light-induced helix movements in channelrhodopsin-2. *J. Mol. Biol.* 427, 341–349. doi: 10.1016/j.jmb.2014.11.004

Nack, M., Radu, I., Bamann, C., Bamberg, E., and Heberle, J. (2009). The retinal structure of channelrhodopsin-2 assessed by resonance Raman spectroscopy. *FEBS Lett.* 583, 3676–3680. doi: 10.1016/j.febslet.2009.10.052

Nagel, G., Ollig, D., Fuhrmann, M., Kateriya, S., Musti, A. M., Bamberg, E., et al. (2002). Channelrhodopsin-1: a light-gated proton channel in green algae. *Science* 296, 2395–2398. doi: 10.1126/science.1072068

Nagel, G., Szellas, T., Huhn, W., Kateriya, S., Adeishvili, N., Berthold, P., et al. (2003). Channelrhodopsin-2, a directly light-gated cation-selective membrane channel. *Proc. Natl. Acad. Sci. U.S.A.* 100, 13940–13945. doi: 10.1073/pnas.1936192100

Neumann-Verhoefen, M. K., Neumann, K., Bamann, C., Radu, I., Heberle, J., Bamberg, E., et al. (2013). Ultrafast infrared spectroscopy on channelrhodopsin-2 reveals efficient energy transfer from the retinal chromophore to the protein. *J. Am. Chem. Soc.* 135, 6968–6976. doi: 10.1021/ja400554y

Ogren, J. I., Mamaev, S., Russano, D., Li, H., Spudich, J. L., and Rothschild, K. J. (2014). Retinal chromophore structure and Schiff base interactions in red-shifted channelrhodopsin-1 from *Chlamydomonas augustae*. *Biochemistry* 53, 3961–3970. doi: 10.1021/bi500445c

Ogren, J. I., Yi, A., Mamaev, S., Li, H., Spudich, J. L., and Rothschild, K. J. (2015a). Proton transfers in a channelrhodopsin-1 studied by Fourier transform infrared (FTIR) difference spectroscopy and site-directed mutagenesis. *J. Biol. Chem.* 290, 12719–12730. doi: 10.1074/jbc.M114.634840

Ogren, J. I., Yi, A., Mamaev, S., Li, H., Lugtenburg, J., DeGrip, W. J., et al. (2015b). Comparison of the structural changes occurring during the primary phototransition of two different channelrhodopsins from *Chlamydomonas algae*. *Biochemistry* 54, 377–388. doi: 10.1021/bi501243y

Polli, D., Altoe, P., Weingart, O., Spillane, K. M., Manzoni, C., Brida, D., et al. (2010). Conical intersection dynamics of the primary photoisomerization event in vision. *Nature* 467, 440–443. doi: 10.1038/nature09346

Prokhorenko, V. I., Nagy, A. M., Waschuk, S. A., Brown, L. S., Birge, R. R., and Miller, R. J. D. (2006). Coherent control of retinal isomerization in bacteriorhodopsin. *Science* 313, 1257–1261. doi: 10.1126/science.1130747

Rey, R., Moller, K. B., and Hynes, J. T. (2004). Ultrafast vibrational population dynamics of water and related systems: a theoretical perspective. *Chem. Rev.* 104, 1915–1928. doi: 10.1021/cr020675f

Ritter, E., Piwowarski, P., Hegemann, P., and Bartl, F. J. (2013). Light-dark adaptation of channelrhodopsin C128T mutant. *J. Biol. Chem.* 288, 10451–10458. doi: 10.1074/jbc.M112.446427

Ritter, E., Stehfest, K., Berndt, A., Hegemann, P., and Bartl, F. J. (2008). Monitoring light-induced structural changes of channelrhodopsin-2 by UV-visible and fourier transform infrared spectroscopy. *J. Biol. Chem.* 283, 35033–35041. doi: 10.1074/jbc.M806353200

Sattig, T., Rickert, C., Bamberg, E., Steinhoff, H. J., and Bamann, C. (2013). Light-induced movement of the transmembrane HelixB in channelrhodopsin-2. *Angew. Chem. Int. Ed. Engl.* 52, 9705–9708. doi: 10.1002/anie.201301698

Schapiro, I., and Ruhman, S. (2014). Ultrafast photochemistry of anabaena sensory rhodopsin: experiment and theory. *Biochim. Biophys. Acta* 1837, 589–597. doi: 10.1016/j.bbabio.2013.09.014

Shigeto, S., Pang, Y., Fang, Y., and Dlott, D. D. (2008). Vibrational relaxation of normal and deuterated liquid nitromethane. *J. Phys. Chem. B* 112, 232–241. doi: 10.1021/jp074082q

Sineshchekov, O. A., Govorunova, E. G., Wang, J., Li, H., and Spudich, J. L. (2013). Intramolecular proton transfer in channelrhodopsins. *Biophys. J.* 104, 807–817. doi: 10.1016/j.bpj.2013.01.002

Sineshchekov, V. A. (2004). Phytochrome A: functional diversity and polymorphism. *Photochem. Photobiol. Sci.* 3, 596–607. doi: 10.1039/b315430k

Verhoefen, M. K., Bamann, C., Blocher, R., Forster, U., Bamberg, E., and Wachtveitl, J. (2010). The photocycle of channelrhodopsin-2: ultrafast reaction dynamics and subsequent reaction steps. *Chemphyschem* 11, 3113–3122. doi: 10.1002/cphc.201000181

von Stetten, D., Gunther, M., Scheerer, P., Murgida, D. H., Mroginski, M. A., Krauss, N., et al. (2008). Chromophore heterogeneity and photoconversion in phytochrome crystals and solution studied by resonance Raman spectroscopy. *Angew. Chem. Int. Ed. Engl.* 47, 4753–4755. doi: 10.1002/anie.200705716

Conflict of Interest Statement: The authors declare that the research was conducted in the absence of any commercial or financial relationships that could be construed as a potential conflict of interest.

frontiers in Molecular Biosciences

MINI REVIEW
published: 07 July 2015
doi: 10.3389/fmolb.2015.00038

Time-resolved infrared spectroscopic techniques as applied to channelrhodopsin

Eglof Ritter[1]*, *Ljiljana Puskar*[2], *Franz J. Bartl*[3], *Emad F. Aziz*[2,4], *Peter Hegemann*[1] and *Ulrich Schade*[2]

[1] Experimentelle Biophysik, Institut für Biologie, Humboldt-Universität zu Berlin, Berlin, Germany, [2] Methods for Material Development, Helmholtz-Zentrum für Materialien und Energie GmbH, Berlin, Germany, [3] Institut für medizinische Physik und Biophysik, Charité – Universitätsmedizin Berlin, Berlin, Germany, [4] Fachbereich Physik, Freie Universität Berlin, Berlin, Germany

Among optogenetic tools, channelrhodopsins, the light gated ion channels of the plasma membrane from green algae, play the most important role. Properties like channel selectivity, timing parameters or color can be influenced by the exchange of selected amino acids. Although widely used, in the field of neurosciences for example, there is still little known about their photocycles and the mechanism of ion channel gating and conductance. One of the preferred methods for these studies is infrared spectroscopy since it allows observation of proteins and their function at a molecular level and in near-native environment. The absorption of a photon in channelrhodopsin leads to retinal isomerization within femtoseconds, the conductive states are reached in the microsecond time scale and the return into the fully dark-adapted state may take more than minutes. To be able to cover all these time regimes, a range of different spectroscopical approaches are necessary. This mini-review focuses on time-resolved applications of the infrared technique to study channelrhodopsins and other light triggered proteins. We will discuss the approaches with respect to their suitability to the investigation of channelrhodopsin and related proteins.

Keywords: infrared spectroscopy, time-resolved spectroscopy, FTIR, IR-spectrometer, retinal proteins, channelrhodopsin

OPEN ACCESS

Edited by:
Tilo Mathes, Vrije Universiteit Amsterdam, Netherlands

Reviewed by:
Andreas Barth, Stockholm University, Sweden
Carsten Kötting, Ruhr-University Bochum, Germany

***Correspondence:**
Eglof Ritter, Experimentelle Biophysik, Institute of Biology, Humboldt-Universität zu Berlin, Invalidenstr. 42, Berlin 10115, Germany
eglof.ritter@hu-berlin.de

Specialty section:
This article was submitted to Biophysics, a section of the journal Frontiers in Molecular Biosciences

Received: *30 April 2015*
Accepted: *22 June 2015*
Published: *07 July 2015*

Citation:
Ritter E, Puskar L, Bartl FJ, Aziz EF, Hegemann P and Schade U (2015) Time-resolved infrared spectroscopic techniques as applied to channelrhodopsin. Front. Mol. Biosci. 2:38. doi: 10.3389/fmolb.2015.00038

Introduction

Marked with the first description of channelrhodopsin as a light-gated ion channel in 2002 (Nagel et al., 2002) the new field of optogenetics emerged and has since gone through rapid development. It utilizes light sensitive proteins like channelrhodopsins, bacteriorhodopsin, rhodopsin, blue light receptors (BLUF) (Kennis and Mathes, 2013), phytochromes (Yang et al., 2013), or engineered proteins (Möglich and Moffat, 2010) as tools to control some defined events in living cells by light (Zhang et al., 2006).

The most commonly used channelrhodopsin is composed of the 7-helical apoprotein opsin and a retinal chromophore, covalently attached by a protonated Schiff base. Light causes retinal isomerization which in turn triggers conformational changes of opsin then forming the ion conductive pore. First information on the channelrhodopsin photocycle came from electrical measurements and from time-resolved UV-visible spectroscopy (Stehfest and Hegemann, 2010). Further structural information was revealed by the X-ray structure (Kato et al., 2012).

However, still to date a little is known about its exact gating mechanisms and photocycles.

Providing information on a molecular level, infrared (IR) spectroscopy has become an important tool for investigation of structure/function relationships in proteins. An overview of its applications in biophysics is given in (Siebert and Hildebrandt, 2008). The most commonly used spectral region is between ~800 and ~2500 cm^{-1} (4–12.5 μm) (Barth, 2007) and a resolution better than 8 cm^{-1} is usually desired. One advantage over other commonly used methods, EPR, NMR, or X-ray crystallography for instance, is that IR investigates systems in their native environment. However, a drawback of this technique is that the extinction coefficients of most functional groups are low (see Barth, 2007). To compare, in the UV-visible region, the protonated Schiff base absorbs near 500 nm with an extinction coefficient of ~40,000 M^{-1} cm^{-1} (Bridges, 1971) whereas in the IR-spectrum, the Schiff base protonation can be indirectly assigned by the strong protonated carboxylate C=O stretching mode of the corresponding counter ions. For a glutamate or aspartate, the extinction coefficient (~200–300 M^{-1} cm^{-1}) is over 100 times lower. This mini-review focuses on current IR-spectroscopic techniques and their applications to the study of proteins like channelrhodopsin.

IR-spectroscopy of Channelrhodopsin

IR-spectroscopy was among the first techniques used to obtain structural information on the channelrhodopsin photocycle (Ritter et al., 2008; Radu et al., 2009). Since 2008, several bands have been assigned by biophysical methods such as site-directed mutagenesis, $H_2O/^2H_2O$ exchange or isotopic labeling. **Figure 1** (*light gray*) shows the IR-spectrum of Channelrhodopsin-2 with some important bands marked. For example, its overall helical structure is typically discerned from the amide I and II bands (~1660 and ~1550 cm^{-1}) (Bandekar and Krimm, 1979; Byler and Susi, 1986; Goormaghtigh, 1990). However, when only the modes that undergo a change during conformational alterations of the protein are of interest, the difference spectrum calculated by subtracting the spectrum of the functional (illuminated) state from the spectrum of the resting (dark) state is used (**Figure 1**, *black line*). Hereby structural changes connected with the pre-formation, opening or closing of the pore become visible. The band at 1661 cm^{-1} indicates conformational changes of the protein, the band pattern between 1100 and 1300 cm^{-1} reflects the all-*trans*/13-*cis* chromophore isomerization (Nack et al., 2009; Bruun et al., 2011), whereas changes in hydrogen bonding and proton transfers of functional aspartates and glutamates are seen between 1700 and 1800 cm^{-1}. The protonation states and hydrogen bonding of the Schiff base counter ions E123 and D253 (1760 cm^{-1}) and the proton donor D156 (1737 and 1760 cm^{-1}) can be directly observed as well as the protonation state of E90 which, as a part of the central gate, plays a role in channel selectivity. For further band assignments see for instance (Kuhne et al., 2015; Lórenz-Fonfría et al., 2015) and citations therein.

The conductive state of channelrhodopsin arises within ~200 μs and decays within ~20 ms (Ernst et al., 2008). In contrast, the retinal isomerization occurs within femtoseconds

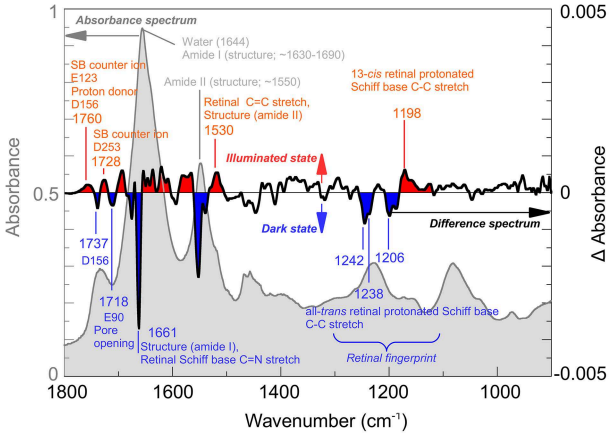

FIGURE 1 | Infrared spectroscopy of Channelrhodopsin. The absorption spectrum (*gray*) of retinal proteins like Channelrhodopsin-2 reconstituted in lipid vesicles shows bands associated with the lipid environment and protonated carboxyl groups (~1700–1800 cm^{-1}), water (1644 cm^{-1}) and the overall helical structure of the protein (amide I ~1650 cm^{-1}; amide II ~1550 cm^{-1}). Note, that the lipid vesicles allow a very dense packing of the protein in the cuvette thus reducing the water content. Light induced alterations are represented by the difference spectrum (*black*), where negative bands (*blue*) occur due to the dark state while positive bands (*red*) are due to the illuminated state, achieved by illumination with blue (480 nm) light. The spectrum was recorded at cryogenic conditions where a mixture of species, including the Schiff base deprotonated state and the conducting state is observed. Note that, while total absorbance is in the order of 0.9 OD (*left scale, gray*), largest changes in the difference spectrum are within 0.004 OD (*right scale, black*). In the picture, some bands assigned so far to their structural counterparts are marked. For details of the band assignments, see (Eisenhauer et al., 2012; Lórenz-Fonfría et al., 2013, 2015; Kuhne et al., 2015).

(Neumann-Verhoefen et al., 2013), de- and re-protonation of the Schiff base is faster than 1 ms (Ernst et al., 2008), and the recovery of the fully dark-adapted state, thereby closing the photocycle, is accomplished within minutes (Ritter et al., 2008). In addition, multiple photocycles with different reaction kinetics exist in parallel (Hegemann et al., 2005), and depending on the illumination conditions, additional side-ways can be populated (Ritter et al., 2013). Therefore time-resolved methods covering time-regimes from femtoseconds to minutes are necessary to understand the structure-function relationships. In the following chapters, we review IR-spectroscopic methods with focus on temporal resolution, sample and technical requirements, as applied to the study of proteins like channelrhodopsin.

Fourier-transform IR-spectroscopy

Rapid-scan Spectroscopy

In Fourier-transform infrared (FTIR) spectrometers the light from a broadband IR-source passes an interferometer where the incident beam is split by a beam splitter. The partial beams are back-reflected to the beam splitter by two mirrors one of which is a sliding mirror introducing a position-dependent phase-shift. The beam splitter allows the partial transmission of the reflected beams to the detector, where an interference signal is

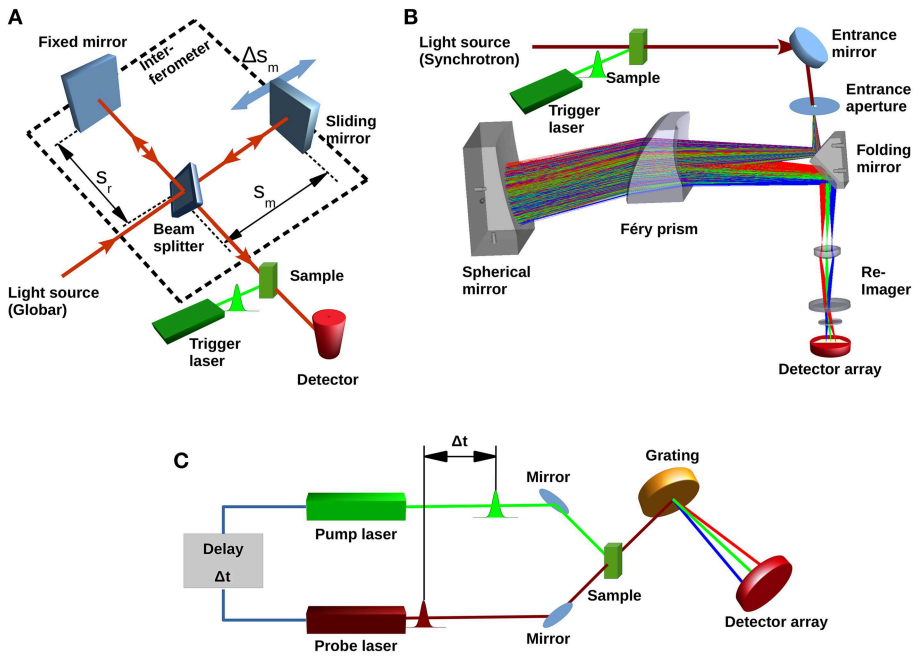

FIGURE 2 | Different types of IR spectrometers. (A) Basic concept of a typical Fourier-transform infrared spectrometer showing light source (Globar), beam splitter, fixed and movable mirrors and single element infrared detector. Conformational changes in the sample are initiated by the trigger laser. The conversion of the sample can then be followed with a time resolution either determined by the sliding mirror movement (rapid-scan) or by the rise-time of the detector (step-scan). **(B)** Concept of a recently proposed dispersive device (Schade et al., 2014) with Synchrotron light source, dispersive prism and focal-plane array detector. **(C)** Laser based pump-probe setup. A first pulse from the pump laser starts the photoreaction. A subsequent short pulse from the probe laser probes the system. The probe pulse can be dispersed to obtain spectra; however, spectral bandwidth is determined by the duration of the probe pulse.

recorded as a function of the optical path difference (Griffiths and De Haseth, 2007) (**Figure 2A**). This so-called interferogram is converted into a spectrum by a Fourier transformation (Herres and Gronholz, 1984). FTIR spectrometers benefit from high-throughput (Jacquinot), multiplex (Fellgett), and high registration precision (Connes) advantages (Perkins, 1987). The temporal resolution is only limited by the speed, sliding pathlength (corresponding to the resolution of the spectrum) and reversal-time of the movable mirror. For a spectrum of 4 cm^{-1} resolution, 40 ms time-resolution can be achieved (Smith and Palmer, 2002). Due to the symmetry of the interferogram around the position of equal optical path length ($\Delta s = 0$), one movement of the mirror yields two spectra by splitting the interferogram at ($\Delta s = 0$). Utilizing both forward- and backward movement of the mirror for data acquisition, a time-resolution of 10 ms is achieved. Further improvement to 5 ms (8 cm^{-1} resolution) was reported with the rapid-sweep method (Braiman et al., 1987). However, using sliding mechanisms means that after data acquisition the mirror has to be stopped and its direction reversed. This time-consuming process becomes significant when fast processes are investigated and the mirror is moved with high speed over a short distance. To avoid this, different types of interferometers have been utilized. For instance, a continuous rotary motion of a tilted mirror was used to measure an interferogram in less than 1 ms (4 cm^{-1} resolution) (Griffiths et al., 1999). However, difficulties in maintaining the alignment made an optical tilt-compensation necessary (Manning, 2002). Due to the limited time-resolution, rapid-scan FTIR is only suited to investigate the late stages of the channelrhodopsin photocycle. The conducting state can only be observed by this technique in exceptional cases, for example by cryotrapping or when slow-cycling mutants (i.e., ChR2-C128T, Berndt et al., 2009) are used (Stehfest et al., 2010).

Step-scan Spectroscopy

Here, time-courses at the particular interferogram data points corresponding to distinct mirror positions are recorded separately (Murphy et al., 1975). This is achieved by stopping the movable mirror, initiating the reaction to be followed and recording the time-trace while the mirror is at rest. The mirror is then moved to the next position ("step"). This process is repeated for each sampling point of the interferogram. Finally, the interferograms corresponding to given times after light flash are reconstructed using the intensities from the time-traces. This means that the experiment has to be repeated at least as often as the number of digital points of the interferogram which is usually more than 1000 times. The time-resolution is then only limited by the detector and the analog-digital converter of the acquisition system. Additional noise sources that potentially influence the experiments, for example instrument vibrations or slow source drifts are described by Andrews and Boxer (2001). To ensure sharp triggering (required for high time-resolution)

and to minimize multi-photon processes, the reaction is triggered by a laser flash usually shorter than the desired time-resolution. Several techniques avoid the complicated process of stopping the mirror by utilizing the time delay between the subsequent digitized interferogram points. In these synchronized continuous-scan measurements, the experiment also has to be triggered for each interferogram data point (see Fleischmann et al., 2003 and citations therein).

Siebert and coworkers described the set-up of a step-scan device based on a commercial interferometer designed to study the photoreaction of bacteriorhodopsin with μs time resolution (Uhmann et al., 1991). With current set-ups, fast detectors and electronics, time-resolutions down to nanoseconds have been achieved (Garczarek and Gerwert, 2006). The step-scan technique is ideal for investigation of fast cycling non-degrading systems like bacteriorhodopsin, however its application to many other light-sensitive proteins can be difficult. For instance, the long recovery kinetics of most channelrhodopsins requires a prolonged delay between two subsequent light flashes. The recording time of a spectral data set with a resolution of 4–8 cm^{-1}, a spectral width of ∼1000 cm^{-1} and appropriate signal-to-noise ratio (∼1000 experiment repetitions) can be in the order of days. For example, first results on channelrhodopsin activation, with 6 μs time-resolution took 5 days of accumulation time (Lórenz-Fonfría et al., 2013). Later the time-resolution was improved to the nanosecond range (Kuhne et al., 2015; Lórenz-Fonfría et al., 2015), however long measuring times are still an issue.

Non-cyclic systems can only be investigated using this technique when each point of the interferogram is recorded from a fresh sample. For liquid samples a flow-through cell is advantageous (Kaun et al., 2006), however for non-liquid ones, the sample has to be replaced once the time-course of a single data point of the interferogram has been measured. Set-ups utilizing rotating discs (Rödig and Siebert, 1999) or translational stages (Rammelsberg et al., 1999) have been developed for such cases. However, homogeneity of the samples is important here. For a more detailed review of the step-scan and other FTIR techniques, see (Kötting and Gerwert, 2005; Radu et al., 2011).

Synchrotron Based Dispersive Techniques

Dispersive spectrometer approaches have long been considered outdated since they typically suffer from low light intensity due to losses at the entrance slit and the dispersive grating and also from low data acquisition speed limited by the grating movement. Modern focal-plane-array (FPA) detectors allow simultaneous measurements of all data points. The light from the entrance slit, after passing through the grating, is imaged to the FPA where each detector element is used to record its own spectral interval.

To achieve sufficient spectral resolution, echelle gratings with higher diffraction orders are commonly used, particularly in astronomical sciences (Lacy et al., 1989). The low light intensity, and consequently the low signal-to-noise ratio makes them rather unsuitable for time-resolved IR-studies of proteins. Another drawback of gratings in combination with planar arrays is the significant curvature of the recorded spectral image (Pelletier et al., 2005), a problem which has to be addressed to avoid artifacts. Furthermore, array detectors require precise imaging of the entrance aperture at the detector elements and thus a highly brilliant light source such as that provided, for example by synchrotron radiation is particularly attractive. A conceptual design of a combined dispersive IR/X-ray spectroscopy set-up for simultaneous time resolved measurements using synchrotron light was proposed by (Marcelli et al., 2010). The high brilliance of the synchrotron IR-light allows optimal utilization of the spectrometer entrance aperture. Marcelli et al. calculated a signal-to-noise ratio of >1000 for integration times >0.3 μs using a time-resolved grating spectrometer in combination with a focal plane array and cooling all optical elements to 77 K.

A prism-based infrared spectrometer with synchrotron source, designed for single-shot measurements of photosensitive proteins like channelrhodopsin and enzyme rhodopsins is currently being developed (Schade et al., 2014). Design goals are microsecond time-resolution and a spectral resolution of 4–8 cm^{-1} in the 2000–950 cm^{-1} range while maintaining a signal-to-noise ratio of 1000 in single-shot mode. The concept is based on a Féry-spectrograph (Féry, 1911), where a prism consisting of two spherical surfaces is used. A spherical mirror behind the prism facilitates a second pass of the light (**Figure 2B**), and all spherical surfaces follow aplanatic conditions (Warren, 1997). This arrangement guarantees a coma and aberration free, non-tilted flat image of the entrance aperture in the image plane, and a high spectral resolution (Wilson, 1969). The usage of a prism rather than a grating has the advantage of higher optical transmission and the absence of interferences caused by order effects or stray light. The ray aberrations of this set-up were calculated to be less than 15 μm and therefore much smaller than the corresponding Airy disk, demonstrating the diffraction-limited operation over the whole spectral range. The expected signal-to-noise ratio calculation was based on parameters suitable for the IRIS Beamline at BESSY II (Peatman and Schade, 2001). For 1 μs accumulation time, a signal-to-noise ratio of ∼600 was calculated for an operation temperature of 300 K, which improves to ∼1000 when a cold-stop (77 K, f/1.5) in front of the detector array is introduced. This however requires a re-imaging system to map the image to the linear FPA through the cold-shield of the detector housing.

A direct comparison of the signal-to-noise ratio to other time-resolved methods like FTIR is rather complicated, since either the time-resolution is not achieved (rapid-scan methods are only applicable down to milliseconds), or the method is conceptually based on thousands of repetitions of the same experiment (step-scan). Using the data of (Schade et al., 2014) and neglecting other sources of noise in the setup, a signal-to-noise ratio of 10,000 is theoretically achievable by accumulating 100 measurements, corresponding to 100 μs accumulation time. This is comparable to the signal-to-noise ratio of rapid-scan FTIR experiments in the millisecond time range (for example-spectra of single-shot experiments, see Elgeti et al., 2008). The combination of synchrotron light with FPA detectors is largely compensating for the loss of FTIR advantages. This setup will allow for the direct observation of the formation and decay of the channelrhodopsin conductive state as well as crucial proton transfer reactions.

For example, de- and re-protonation of the Schiff base, under native environmental conditions can be observed in single-shot mode thus avoiding possible sample degradation due to the long recovery period necessary for repetition-based methods like step-scan FTIR.

Spectroscopy with Lasers

Time-resolved infrared spectroscopy takes advantage of laser light sources. For example, a PbS diode laser has been used to record conformational changes of the Ras protein in the nanosecond time regime with a flash-photolysis set-up (Lin et al., 2014). The intensity of the laser beam was measured, after passing through the sample, by an infrared detector. In this case, the photoreaction was initiated by photolysis of caged compounds through a UV laser flash. Such setups however only allow the acquisition of signals at fixed wavelength. Quantum cascade lasers (QCLs) emitting in the mid- and far-infrared range are currently under heavy development. Their tunability and high output intensity, while maintaining a narrow bandwidth, make them ideal light sources for infrared spectroscopy. Intrinsic temperature fluctuations however introduce noise that has to be considered (Borri et al., 2011; Liu and Wang, 2011). Current developments in laser absorption spectroscopy based on QCLs are reviewed elsewhere (Zhang et al., 2014). They are becoming more frequently used in spectrochemical imaging (Clemens et al., 2014) and nanospectroscopy (Amenabar et al., 2013). A QCL-based spectrometer has been applied to study the first steps of the channelrhodopsin activation process (Lórenz-Fonfría et al., 2015). The authors used a tunable QCL in a flash-photolysis setup, where the laser is tuned to the desired wavelength, the photoreaction then initiated by a VIS flash and the time-dependent signal change recorded by an infrared detector. This procedure has to be repeated for each desired wavelength. A time-dependent dataset of channelrhodopsin in the range 1610 and 1680, and 1700 and 1780 cm^{-1} at a resolution of 1 and 0.5 cm^{-1} could thus be acquired with a repetition rate of 0.33 Hz by using a fast-cycling channelrhodopsin mutant (ChR2-E123T, Gunaydin et al., 2010).

For time-resolutions of nanoseconds or better, pump-probe technologies can be used. The photoreaction of a protein is started by a first laser pulse, usually in the fs time regime. A second pulse with a certain time delay probes the protein's response. For each pump-probe cycle, a difference spectrum can be obtained when the probe pulse, after passing the sample, is fed through a dispersive element and measured at an infrared detector array (Hamm and Zinth, 1995) (**Figure 2C**). An overview on how this is applied to dynamics of light-triggered proteins is given in Groot et al. (2007). This technique has been used to investigate ultrafast dynamics of bacteriorhodopsin, photoactive yellow protein (see for example, Van Wilderen et al., 2006), and LOV domains (Alexandre et al., 2009). Channelrhodopsin-2 was also studied by Vis-pump/IR-probe spectroscopy (Neumann et al., 2008) in the fs-timescale. The experiments showed amide-I vibrational modes occurring within ∼500 fs thus demonstrating a very strong protein-chromophore coupling (Neumann-Verhoefen et al., 2013).

An alternative method to measure mid-infrared pulses is to optically convert them into the UV-visible range where a broad variety of array detectors is available. Zhu et al. (2012) used chirped pulse upconversion facilitated by a non-linear optical crystal. The authors investigated the photoreaction of BLUF photoreceptors on a picosecond time scale and demonstrated the method is suited for investigation of signal changes down to the mOD range.

Summary/Outlook

While the time regime of milliseconds and slower can be accessed by the rapid-scan FTIR technique for most biological samples, for faster systems special considerations have to be taken into account. Ultrafast alterations can be observed by pump-probe spectroscopy. Step-scan FTIR facilitates a good signal-to-noise ratio and a time-resolution down to nanoseconds but requires perfectly cyclic systems under investigations. For non-cyclic or slow cycling systems, fast time-resolved investigations are challenging. However, developments addressing this problem by QCL-based setups or dispersive spectroscopy in combination with highly brilliant light sources are in progress.

Acknowledgments

This work was supported by the German Federal Ministry of Education and Research (Bundesministerium für Bildung und Forschung) Grant 05K13KH1 to PH.

References

Alexandre, M. T., Domratcheva, T., Bonetti, C., Van Wilderen, L. J., Van Grondelle, R., Groot, M. L., et al. (2009). Primary reactions of the LOV2 domain of phototropin studied with ultrafast mid-infrared spectroscopy and quantum chemistry. *Biophys. J.* 97, 227–237. doi: 10.1016/j.bpj.2009.01.066

Amenabar, I., Poly, S., Nuansing, W., Hubrich, E. H., Govyadinov, A. A., Huth, F., et al. (2013). Structural analysis and mapping of individual protein complexes by infrared nanospectroscopy. *Nat. Commun.* 4, 2890. doi: 10.1038/ncomms3890

Andrews, S. S., and Boxer, S. G. (2001). Analysis of noise for rapid-scan and step-scan methods of FT-IR difference spectroscopy. *Appl. Spectrosc.* 55, 1161–1165. doi: 10.1366/0003702011953414

Bandekar, J., and Krimm, S. (1979). Vibrational analysis of peptides, polypeptides, and proteins: characteristic amide bands of ß-turns. *Proc. Natl. Acad. Sci. U.S.A.* 76, 774–777.

Barth, A. (2007). Infrared spectroscopy of proteins. *Biochim. Biophys. Acta* 1767, 1073–1101. doi: 10.1016/j.bbabio.2007.06.004

Berndt, A., Yizhar, O., Gunaydin, L. A., Hegemann, P., and Deisseroth, K. (2009). Bi-stable neural state switches. *Nat. Neurosci.* 12, 229–234. doi: 10.1038/nn.2247

Borri, S., Bartalini, S., Pastor, P. C., Galli, I., Giusfredi, G., Mazzotti, D., et al. (2011). Frequency-noise dynamics of mid-infrared quantum cascade lasers. *IEEE J. Quantum Electron.* 47, 984–988. doi: 10.1109/JQE.2011.2147760

Braiman, M. S., Ahl, P. L., and Rothschild, K. J. (1987). Millisecond Fourier-transform infrared difference spectra of bacteriorhodopsin's M412 photoproduct. *Proc. Natl. Acad. Sci. U.S.A.* 84, 5221–5225.

Bridges, C. D. B. (1971). The molar absorbance coefficient of rhodopsin. *Vision Res.* 11, 841–848. doi: 10.1016/0042-6989(71)90006-X

Bruun, S., Naumann, H., Kuhlmann, U., Schulz, C., Stehfest, K., Hegemann, P., et al. (2011). The chromophore structure of the long-lived intermediate of the C128T channelrhodopsin-2 variant. *FEBS Lett.* 585, 3998–4001. doi: 10.1016/j.febslet.2011.11.007

Byler, D. M., and Susi, H. (1986). Examination of the secondary structure of proteins by deconvolved FTIR spectra. *Biopolymers* 25, 469–487. doi: 10.1002/bip.360250307 ET - 1986/03/01

Clemens, G., Bird, B., Weida, M., Rowlette, J., and Baker, M. J. (2014). Quantum cascade laser-based mid-infrared spectrochemical imaging of tissues and biofluids. *Spectroscopyeurope* 26, 14–19.

Eisenhauer, K., Kuhne, J., Ritter, E., Berndt, A., Wolf, S., Freier, E., et al. (2012). In channelrhodopsin-2 Glu-90 is crucial for ion selectivity and is deprotonated during the photocycle. *J. Biol. Chem.* 287, 6904–6911. doi: 10.1074/jbc.M111.327700

Elgeti, M., Ritter, E., and Bartl, F. J. (2008). New insights into light-induced deactivation of active rhodopsin by SVD and global analysis of time-resolved UV/Vis- and FTIR-Data. *Zeitschrift Phys. Chem.* 222, 1117–1129. doi: 10.1524/zpch.2008.5392

Ernst, O. P., Sánchez Murcia, P. A., Daldrop, P., Tsunoda, S. P., Kateriya, S., Hegemann, P., et al. (2008). Photoactivation of channelrhodopsin. *J. Biol. Chem.* 283, 1637–1643. doi: 10.1074/jbc.M708039200

Féry, C. (1911). A prism with curved faces, for spectrograph or spectroscope. *Astrophys. J.* 34, 79–87.

Fleischmann, O. C., Burrows, J. P., and Orphal, J. (2003). Time-windowing Fourier transform absorption spectroscopy for flash photolysis investigations. *J. Photochem. Photobiol. A Chem.* 157, 127–136. doi: 10.1016/S1010-6030(03)00069-8

Garczarek, F., and Gerwert, K. (2006). Functional waters in intraprotein proton transfer monitored by FTIR difference spectroscopy. *Nature* 439, 109–112. doi: 10.1038/nature04231

Goormaghtigh, E. (1990). Secondary structure and dosage of soluble and membrane proteins by attenuated total reflection Fourier−transform infrared spectroscopy on hydrated films. *Eur. J. Biochem.* 193, 409–420.

Griffiths, P. R., and De Haseth, J. A. (2007). *Fourier Transform Infrared Spectrometry*. Hoboken, NJ: John Wiley & Sons, Inc.

Griffiths, P. R., Hirsche, B. L., and Manning, C. J. (1999). Ultra-rapid-scanning Fourier transform infrared spectrometry. *Vib. Spectrosc.* 19, 165–176.

Groot, M. L., van Wilderen, L. J., and Di Donato, M. (2007). Time-resolved methods in biophysics. 5. Femtosecond time-resolved and dispersed infrared spectroscopy on proteins. *Photochem. Photobiol. Sci.* 6, 501–507. doi: 10.1039/b613023b

Gunaydin, L. A., Yizhar, O., Berndt, A., Sohal, V. S., Deisseroth, K., and Hegemann, P. (2010). Ultrafast optogenetic control. *Nat. Neurosci.* 13, 387–392. doi: 10.1038/nn.2495

Hamm, P., and Zinth, W. (1995). Ultrafast initial reaction in bacterial photosynthesis revealed by femtosecond infrared spectroscopy. *J. Phys. Chem.* 99, 13537–13544. doi: 10.1021/j100036a034

Hegemann, P., Ehlenbeck, S., and Gradmann, D. (2005). Multiple photocycles of channelrhodopsin. *Biophys. J.* 89, 3911–3918. doi: 10.1529/biophysj.105.069716

Herres, W., and Gronholz, J. (1984). Understanding FT-IR Data Processing. 1, 352–356.

Kato, H. E., Zhang, F., Yizhar, O., Ramakrishnan, C., Nishizawa, T., Hirata, K., et al. (2012). Crystal structure of the channelrhodopsin light-gated cation channel. *Nature* 482, 369–374. doi: 10.1038/nature10870

Kaun, N., Kulka, S., Frank, J., Schade, U., Vellekoop, M. J., Harasek, M., et al. (2006). Towards biochemical reaction monitoring using FT-IR synchrotron radiation. *Analyst* 131, 489–494. doi: 10.1039/b514102h

Kennis, J. T. M., and Mathes, T. (2013). Molecular eyes: proteins that transform light into biological information. *Interface Focus* 3:20130005. doi: 10.1098/rsfs.2013.0005

Kötting, C., and Gerwert, K. (2005). Proteins in action monitored by time-resolved FTIR spectroscopy. *ChemPhysChem* 6, 881–888. doi: 10.1002/cphc.200400504

Kuhne, J., Eisenhauer, K., Ritter, E., Hegemann, P., Gerwert, K., and Bartl, F. (2015). Early formation of the ion-conducting pore in Channelrhodopsin-2. *Angew. Chemie Int. Ed.* 54, 4953–4957. doi: 10.1002/anie.201410180

Lacy, J. H., Achtermann, J. M., Bruce, D. E., Lester, D. F., Arens, J. F., Peck, M. C., et al. (1989). IRSHELL: a mid-infrared cryogenic echelle spectrograph. *Publ. Astron. Soc. Pacific* 101, 1166. doi: 10.1086/132593

Lin, J., Gerwert, K., and Kötting, C. (2014). A modified infrared spectrometer with high time resolution and its application for investigating fast conformational changes of the GTPase Ras. *Appl. Spectrosc.* 68, 531–535. doi: 10.1366/13-07320

Liu, T., and Wang, Q. J. (2011). Fundamental frequency noise and linewidth broadening caused by intrinsic temperature fluctuations in quantum cascade lasers. *Phys. Rev. B Condens. Matter Mater. Phys.* 84, 1–14. doi: 10.1103/PhysRevB.84.125322

Lórenz-Fonfría, V. A., Resler, T., Krause, N., Nack, M., Gossing, M., Fischer von Mollard, G., et al. (2013). Transient protonation changes in channelrhodopsin-2 and their relevance to channel gating. *Proc. Natl. Acad. Sci. U.S.A.* 110, E1273–E1281. doi: 10.1073/pnas.1219502110

Lórenz-Fonfría, V. A., Schultz, B.-J., Resler, T., Schlesinger, R., Bamann, C., Bamberg, E., et al. (2015). Pre-gating conformational changes in the ChETA variant of Channelrhodopsin-2 monitored by nanosecond IR spectroscopy. *J. Am. Chem. Soc.* 137, 1850–1861. doi: 10.1021/ja5108595

Manning, C. J. (2002). *Tilt-Compensated Interferometers*. U.S. Patent 6,469,790 B1.

Marcelli, A., Xu, W., Hampai, D., Malfatti, L., Innocenzi, P., Schade, U., et al. (2010). Infrared and X-ray simultaneous spectroscopy: a novel conceptual beamline design for time resolved experiments. *Anal. Bioanal. Chem.* 397, 2095–2108. doi: 10.1007/s00216-010-3745-1

Möglich, A., and Moffat, K. (2010). Engineered photoreceptors as novel optogenetic tools. *Photochem. Photobiol. Sci.* 9, 1286–1300. doi: 10.1039/c0pp00167h

Murphy, R. E., Cook, F. H., and Sakai, H. (1975). Time-resolved Fourier spectroscopy. *J. Opt. Soc. Am.* 65, 600–604.

Nack, M., Radu, I., Bamann, C., Bamberg, E., and Heberle, J. (2009). The retinal structure of channelrhodopsin-2 assessed by resonance Raman spectroscopy. *FEBS Lett.* 583, 3676–3680. doi: 10.1016/j.febslet.2009.10.052

Nagel, G., Ollig, D., Fuhrmann, M., Kateriya, S., Musti, A. M., Bamberg, E., et al. (2002). Channelrhodopsin-1: a light-gated proton channel in green algae. *Science* 296, 2395–2398. doi: 10.1126/science.1072068

Neumann, K., Verhoefen, M.-K., Weber, I., Glaubitz, C., and Wachtveitl, J. (2008). Initial reaction dynamics of proteorhodopsin observed by femtosecond infrared and visible spectroscopy. *Biophys. J.* 94, 4796–4807. doi: 10.1529/biophysj.107.125484

Neumann-Verhoefen, M.-K., Neumann, K., Bamann, C., Radu, I., Heberle, J., Bamberg, E., et al. (2013). Ultrafast infrared spectroscopy on channelrhodopsin-2 reveals efficient energy transfer from the retinal chromophore to the protein. *J. Am. Chem. Soc.* 135, 6968–6976. doi: 10.1021/ja400554y

Peatman, W. B., and Schade, U. (2001). A brilliant infrared light source at BESSY. *Rev. Sci. Instrum.* 72, 1620–1624. doi: 10.1063/1.1347976

Pelletier, I., Pellerin, C., Chase, D. B., and Rabolt, J. F. (2005). New developments in planar array infrared spectroscopy. *Appl. Spectrosc.* 59, 156–163. doi: 10.1366/0003702053085043

Perkins, W. (1987). Fourier transform infrared spectroscopy. Part II. Advantages of FT-IR. *J. Chem. Educ.* 64, 269–271. doi: 10.1021/ed064pA269

Radu, I., Bamann, C., Nack, M., Nagel, G., Bamberg, E., and Heberle, J. (2009). Conformational changes of channelrhodopsin-2. *J. Am. Chem. Soc.* 131, 7313–7319. doi: 10.1021/ja8084274

Radu, I., Schleeger, M., Nack, M., and Heberle, J. (2011). Time-resolved FT-IR spectroscopy of membrane proteins. *Aust. J. Chem.* 64, 9–15. doi: 10.1071/CH10286

Rammelsberg, R., Boulas, S., Chorongiewski, H., and Gerwert, K. (1999). Set-up for time-resolved step-scan FTIR spectroscopy of noncyclic reactions. *Vib. Spectrosc.* 19, 143–149. doi: 10.1016/S0924-2031(99)00013-2

Ritter, E., Piwowarski, P., Hegemann, P., and Bartl, F. J. (2013). Light-dark adaptation of channelrhodopsin C128T mutant. *J. Biol. Chem.* 288, 10451–10458. doi: 10.1074/jbc.M112.446427

Ritter, E., Stehfest, K., Berndt, A., Hegemann, P., and Bartl, F. J. (2008). Monitoring light-induced structural changes of Channelrhodopsin-2 by UV-visible and Fourier transform infrared spectroscopy. *J. Biol. Chem.* 283, 35033–35041. doi: 10.1074/jbc.M806353200

Rödig, C., and Siebert, F. (1999). Distortion of the L→M transition in the photocycle of the bacteriorhodopsin mutant D96N: a time-resolved step-scan FTIR investigation. *FEBS Lett.* 445, 14–18. doi: 10.1016/S0014-5793(99)00088-5

Schade, U., Ritter, E., Hegemann, P., Aziz, E. F., and Hofmann, K. P. (2014). Concept for a single-shot mid-infrared spectrometer using synchrotron radiation. *Vib. Spectrosc.* 75, 190–195. doi: 10.1016/j.vibspec.2014.07.004

Siebert, F., and Hildebrandt, P. (2008). *Vibrational Spectroscopy in Life Science*. Berlin: Wiley-VCH.

Smith, G., and Palmer, R. (2002). Fast time-resolved mid-infrared spectroscopy using an interferometer. *Handb. Vib. Spectrosc.* 653–668. doi: 10.1002/0470027320.s0217

Stehfest, K., and Hegemann, P. (2010). Evolution of the channelrhodopsin photocycle model. *ChemPhysChem* 11, 1120–1126. doi: 10.1002/cphc.200900980

Stehfest, K., Ritter, E., Berndt, A., Bartl, F., and Hegemann, P. (2010). The branched photocycle of the slow-cycling channelrhodopsin-2 mutant C128T. *J. Mol. Biol.* 398, 690–702. doi: 10.1016/j.jmb.2010.03.031

Uhmann, W., Becker, A., Taran, C., and Siebert, F. (1991). Time-resolved FT-IR absorption spectroscopy using a step-scan interferometer. *Appl. Spectrosc.* 45, 390–397.

Warren, D. W. (1997). Compact prism spectrographs based on aplanatic principles. *Opt. Eng.* 36, 1174. doi: 10.1117/1.601237

Van Wilderen, L. J., van der Horst, M. A., van Stokkum, I. H., Hellingwerf, K. J., van Grondelle, R., and Groot, M. L. (2006). Ultrafast infrared spectroscopy reveals a key step for successful entry into the photocycle for photoactive yellow protein. *Proc. Natl. Acad. Sci. U.S.A.* 103, 15050–15055. doi: 10.1073/pnas.0603476103

Wilson, R. N. (1969). *Die Anwendung von Aplanatischen Prismen in Monochromatoren und Spektrographen*, Vol. 29. Stuttgart: Optik.

Yang, X., Jost, A. P.-T., Weiner, O. D., and Tang, C. (2013). A light-inducible organelle-targeting system for dynamically activating and inactivating signaling in budding yeast. *Mol. Biol. Cell* 24, 2419–2430. doi: 10.1091/mbc.E13-03-0126

Zhang, F., Wang, L. P., Boyden, E. S., and Deisseroth, K. (2006). Channelrhodopsin-2 and optical control of excitable cells. *Nat. Methods* 3, 785–792. doi: 10.1038/nmeth936

Zhang, L., Tian, G., Li, J., and Yu, B. (2014). Applications of absorption spectroscopy using quantum cascade lasers. *Appl. Spectrosc.* 68, 1095–1107. doi: 10.1366/14-00001

Zhu, J., Mathes, T., Stahl, A. D., Kennis, J. T. M., and Groot, M. L. (2012). Ultrafast mid-infrared spectroscopy by chirped pulse upconversion in 1800-1000cm^{-1} region. *Opt. Express* 20:10562. doi: 10.1364/OE.20.010562

Conflict of Interest Statement: The Guest Associate Editor, Tilo Mathes, declares that, despite having recently collaborated with the author PH, the review process was handled objectively. The authors declare that the research was conducted in the absence of any commercial or financial relationships that could be construed as a potential conflict of interest.

frontiers in Molecular Biosciences

REVIEW
published: 17 June 2015
doi: 10.3389/fmolb.2015.00030

Photoreceptor engineering

Thea Ziegler[1,2] *and Andreas Möglich*[1,2]*

[1] Biophysikalische Chemie, Institut für Biologie, Humboldt-Universität zu Berlin, Berlin, Germany, [2] Lehrstuhl für Biochemie, Universität Bayreuth, Bayreuth, Germany

Sensory photoreceptors not only control diverse adaptive responses in Nature, but as light-regulated actuators they also provide the foundation for optogenetics, the non-invasive and spatiotemporally precise manipulation of cellular events by light. Novel photoreceptors have been engineered that establish control by light over manifold biological processes previously inaccessible to optogenetic intervention. Recently, photoreceptor engineering has witnessed a rapid development, and light-regulated actuators for the perturbation of a plethora of cellular events are now available. Here, we review fundamental principles of photoreceptors and light-regulated allostery. Photoreceptors dichotomize into associating receptors that alter their oligomeric state as part of light-regulated allostery and non-associating receptors that do not. A survey of engineered photoreceptors pinpoints light-regulated association reactions and order-disorder transitions as particularly powerful and versatile design principles. Photochromic photoreceptors that are bidirectionally toggled by two light colors augur enhanced spatiotemporal resolution and use as photoactivatable fluorophores. By identifying desirable traits in engineered photoreceptors, we provide pointers for the design of future, light-regulated actuators.

Keywords: allostery, light, optogenetics, protein engineering, sensory photoreceptor, signal transduction

OPEN ACCESS

Edited by:
Tilo Mathes,
Vrije Universiteit
Amsterdam, Netherlands

Reviewed by:
John Clark Lagarias,
University of California, USA
Welivitiya K. Ajith Karunarathne,
The University of Toledo, USA
Christof Taxis,
Philipps-Universität
Marburg, Germany

***Correspondence:**
Andreas Möglich,
Lehrstuhl für Biochemie, Fakultät für Biologie, Chemie und Geowissenschaften, Universität Bayreuth, Universitätsstraße 30, Gebäude NW III, 95447 Bayreuth, Germany
andreas.moeglich@uni-bayreuth.de

Specialty section:
This article was submitted to Biophysics, a section of the journal Frontiers in Molecular Biosciences

Received: *17 April 2015*
Accepted: *28 May 2015*
Published: *17 June 2015*

Citation:
Ziegler T and Möglich A (2015) Photoreceptor engineering. Front. Mol. Biosci. 2:30. doi: 10.3389/fmolb.2015.00030

Introduction

Ever since the original description of algal channelrhodopsins as light-gated ion channels (Nagel et al., 2002, 2003), various sensory photoreceptors have been widely deployed across biology as light-regulated actuators for precise perturbation and probing of cellular events. The underlying approach, dubbed optogenetics (Deisseroth et al., 2006), derives its power and versatility from several key properties of sensory photoreceptors: first, they can be genetically encoded and functionally expressed *in situ*, thus affording exquisite molecular targeting and superior spatial resolution compared to conventional perturbation, e.g., by electrical or chemical means; second, they can be triggered by light that penetrates living matter to certain depth, thus affording non-invasive control and superior temporal resolution; and third, they operate reversibly, thus affording transient and repeat perturbation. While initial optogenetic applications were restricted to the neurosciences and exclusively

Abbreviations: BLUF, sensors of blue light using flavin adenine dinucleotide; BV, biliverdin; cAMP, 3′,5′-cyclic adenosine monophosphate; CBCR, cyanobacteriochrome; cGMP, 3′,5′-cyclic guanosine monophosphate; FAD, flavin adenine dinucleotide; FMN, flavin mononucleotide; FP, fluorescent protein; GAF, cGMP-specific phosphodiesterases, adenylate cyclases and FhlA; GPCR, G-protein-coupled receptor; LOV, light-oxygen-voltage; MAP kinase, mitogen-activated protein kinase; MTHF, methenyltetrahydrofolate; PAS, Per-ARNT-Sim; pCA, p-coumaric acid; PCB, phycocyanobilin; PΦB, phytochromobilin; Phy, phytochrome; PHY, phytochrome-specific domain; PYP, photoactive yellow protein (xanthopsin); RTK, receptor tyrosine kinase; STED, stimulated emission depletion.

relied on light-gated ion channels and light-driven ion pumps, the concept clearly transcends ion transport and applies to a plethora of biologically relevant processes. Early on, optogenetics solely utilized naturally occurring sensory photoreceptors, but customized photoreceptors have since been engineered that achieve light perturbation of numerous cellular events of interest as diverse as transcription, enzyme catalysis, protein degradation, and cell motility.

Here, we survey the engineering and optogenetic application of sensory photoreceptors. The sheer number of engineered photoreceptors testifies to the vigor of the field, but it effectively precludes a detailed discussion of each and every example. Rather than providing a mere enumeration, which—given the pace of current developments—would be outdated fairly soon, we discuss general aspects and strategies by means of particularly illustrative examples. By identifying recurring and overarching features, we aspire to provide a guide for the selection of photoreceptors for optogenetic applications as well as for their engineering. By necessity, this treatise emphasizes certain areas less than others, and we refer the reader to review articles for coverage of natural photoreceptors (Möglich et al., 2010b), protein engineering (Moffat et al., 2013; Pudasaini et al., 2015; Schmidt and Cho, 2015; Shcherbakova et al., 2015), and applications in cell biology (Beyer et al., 2015b; Fan and Lin, 2015; Zhang and Cui, 2015) and neuroscience (Pashaie et al., 2014).

Photoreceptor Fundamentals

To convert light signals, i.e., electromagnetic waves, into cellular signals, i.e., "jiggling and wiggling of atoms and molecules" (Feynman, 1963), sensory photoreceptors harbor two principal functions in dedicated modules: first, a photosensor module absorbs light; second, an effector module exerts biological activity (e.g., ion transport, catalysis, protein interaction). The engineering of photoreceptors with emergent properties encompasses the modification of photosensors and/or effectors as well as the modular recombination/rewiring of photosensors and effectors. Depending upon whether these modules are realized as distinct proteins, distinct protein domains or fragments of a single protein domain, physical separation and subsequent recombination of photosensors and effectors may be more or less challenging (cf. Section Allostery of Photoreceptors). Each photosensor bears an organic chromophore that contains a conjugated π electron system, that is either covalently or non-covalently bound, and that derives from either amino-acid side chains or small-molecule metabolites. Based on identity and photochemistry of their chromophores, photoreceptors distribute into several classes with different spectral sensitivities as indicated in **Figure 1**. For example, plant UV-B receptors, exemplified by *Arabidopsis thaliana* UVR8, use tryptophan side chains to sense UV-B light; the flavin-nucleotide-binding cryptochromes, LOV (light-oxygen-voltage) and BLUF

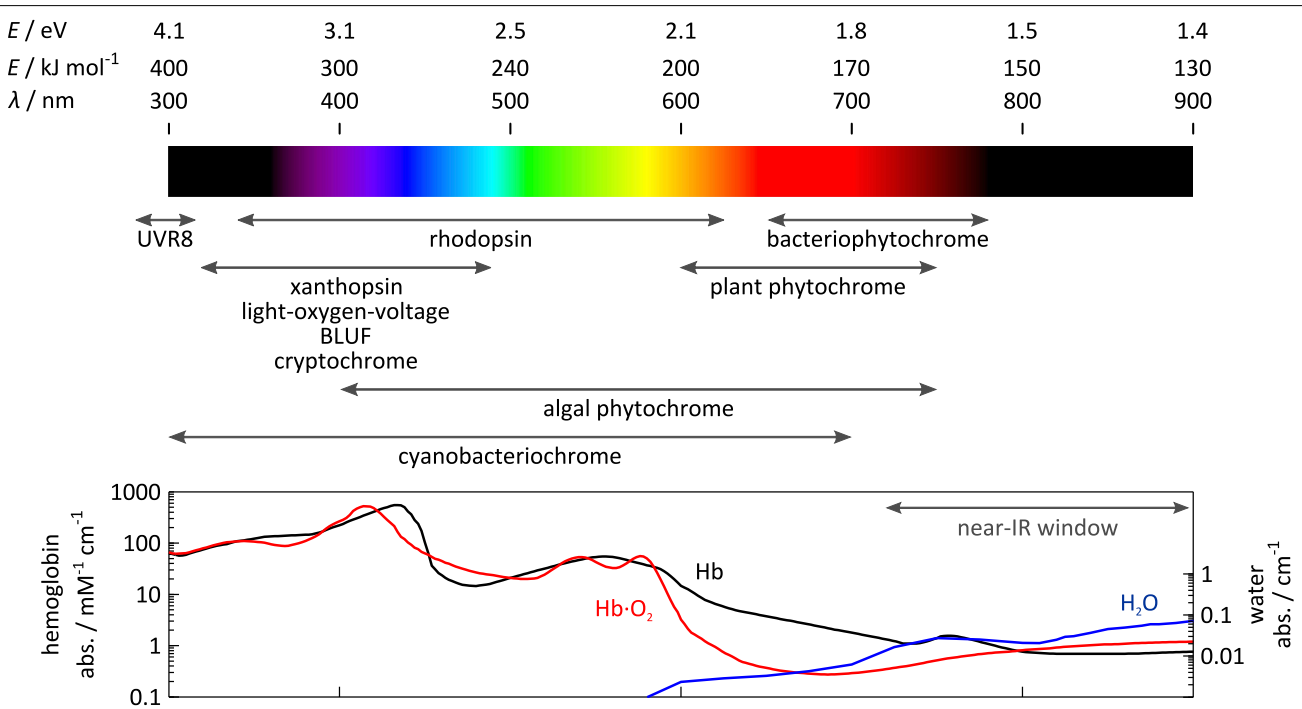

FIGURE 1 | Spectral sensitivity of photoreceptors. The spectral sensitivity of sensory photoreceptors ranges from the UV to the near-infrared region of the electromagnetic spectrum. Visible light is strongly absorbed or scattered by opaque biological tissue owing to the presence of lipids, heme-containing proteins, e.g., hemoglobin (Hb), and other pigments. Above 700 nm within the so-called near-infrared window, scattering and absorption by pigments are lower, and light penetrates biological tissue more deeply.

(blue-light sensors using flavin-adenine dinucleotide) proteins are sensitive to blue light; within the rhodopsins, individual representatives use retinal to respond to different light bands in the UV to red spectral region; phytochromes (Phys) from terrestrial plants employ linear tetrapyrroles (bilins) to achieve sensitivity toward red and near-infrared light, but a recently characterized lineage of algal phytochromes essentially covers the entire visible and near-infrared spectrum (Rockwell et al., 2014); similarly, cyanobacteriochromes (CBCRs) use bilins as well and display increased spectral diversity covering the electromagnetic spectrum from UV to near-infrared wavelengths.

The choice of photoreceptor for optogenetic application is dictated by at least two principal considerations (also cf. Section Guidelines for Photoreceptor Engineering), namely chromophore availability and tissue penetration of light. First, to achieve true genetic encoding, not only must a photoreceptor fold autonomously and incorporate its chromophore, but also the chromophore must be available in the target tissue to sufficient extent. While the former is generally true, the latter is only the case for certain chromophores. Due to their role as core cofactors in diverse metabolic proteins and enzymes, flavin nucleotides universally occur in different cells and organisms. Moreover, the widespread, successful deployment of rhodopsin-based ion channels and pumps in diverse contexts testifies that this also pertains to retinal in many tissues (Deisseroth et al., 2006; Karunarathne et al., 2013). Several recent studies indicate that the oxidized linear tetrapyrrole biliverdin (BV) also recurs in commonly used model systems (Piatkevich et al., 2013a; Gasser et al., 2014; Ryu et al., 2014), presumably as a degradation product of heme. By contrast, reduced tetrapyrroles, such as phycocyanobilin (PCB), that plant Phys and CBCRs depend on, are not generally available in most systems of optogenetic interest. Second, for efficient optical perturbation *in situ*, light of the required wavelength must penetrate tissue to sufficient depth. While light penetration often is of little concern for studies in microorganisms or cell culture where the relevant dimensions are small, it may become limiting in applications in deep tissue or whole animals. Due to light scattering in opaque tissues, in particular by lipids (Chung et al., 2013), and absorption by heme-containing proteins and other pigments, tissue penetration is severely limited across essentially the entire visible spectrum; however, within the spectral region above 700 nm, often denoted the "near-infrared spectral window," high penetration depths are achieved. The spectral sensitivity of certain photoreceptor classes, e.g., LOV, BLUF, cryptochrome, and UVR8, is largely invariant between representatives, essentially owing to the rigid scaffold of their chromophores. By contrast, individual representatives of the rhodopsins (Ernst et al., 2014), phytochromes (Rockwell et al., 2014), and cyanobacteriochromes (Ikeuchi and Ishizuka, 2008; Rockwell and Lagarias, 2010) considerably differ in their spectral sensitivities which can be accounted for by the structural malleability and varying protonation of their chromophores, as well as by electrostatic interactions with residues lining the chromophore-binding pocket. As a corollary, these photoreceptors are amenable to so-called color tuning, the variation of spectral sensitivity via mutagenesis. However, color tuning is often fraught with problems of limited predictability and inadvertent effects on signal transduction (cf., e.g., Ernst et al., 2014).

In the absence of light, photoreceptors adopt their thermodynamically most stable, dark-adapted state, denoted D (cf. Section Thermodynamics of Photoreceptors). Upon light absorption, they undergo a so-called photocycle, a series of photochemical reactions within the chromophore and accompanying structural and dynamic transitions within the surrounding protein scaffold (**Figure 2A**). In addition to D, the photocycle minimally comprises the signaling state S which persists for milliseconds to many hours depending upon photoreceptor and which differs from D in structure, dynamics and function. For an in-depth treatise of photochemistry we refer to pertinent review articles (Hegemann, 2008; Möglich et al., 2010b). While the molecular aspects widely differ across classes, in all photoreceptors the initial photochemical reaction toward formation of the signaling state S is very fast, e.g., bond isomerization or inter-system crossing, so as to achieve high quantum yields for photoreception, at the same time minimizing competing reactions, i.e., chiefly fluorescence and internal conversion. The initial reaction may be succeeded by additional, slower steps, e.g., formation of a covalent bond in LOV proteins (Conrad et al., 2014), but in all cases the signaling state S is formed after photon absorption within at most microseconds which is faster than the timescale of most physiological responses. For the purpose of this overview article, we thus resort to a grossly simplified, operational model of the photocycle in which the light-driven reaction to the signaling state is considered unimolecular and single-step with rate constant $k_1(I)$ depending upon light intensity I. A thermally driven, spontaneous reaction, denoted dark reversion, closes the photocycle and reverts S back to D; for simplicity, we consider this reversion as unimolecular and single-step with rate constant k_{-1}.

The absolute light sensitivity of a photoreceptor is determined by its absorption cross section and its overall quantum yield for formation of the signaling state, lumped together in the rate constant $k_1(I)$. However, optogenetic experiments are often conducted under constant illumination at photostationary state where there is no net change in the populations of D and S, i.e., where the velocities of the reverse reaction v_{-1} and the light-driven forward reaction v_1 equal. The balance between D and S at photostationary state is governed by the effective light sensitivity of the photoreceptor, i.e., the ratio between the forward and reverse rate constants $k_1(I)$ and k_{-1}, the former of which is a function of applied light intensity I. In optogenetic applications, the response kinetics of light-sensitive systems are often of key relevance, i.e., how soon after onset of illumination the desired biological effect manifests (*on*-kinetics), and how long after stop of illumination the effect persists (*off*-kinetics). With the exception of fast events in the neurosciences, the intrinsic photochemical response of photoreceptors after initial photon absorption is near-instantaneous on most biologically relevant time scales and thus not limiting; rather, *on*-kinetics are often limited by the light dose that can be delivered per unit of time to the system under study which is subject to instrumental (e.g., maximum output of light sources, tissue

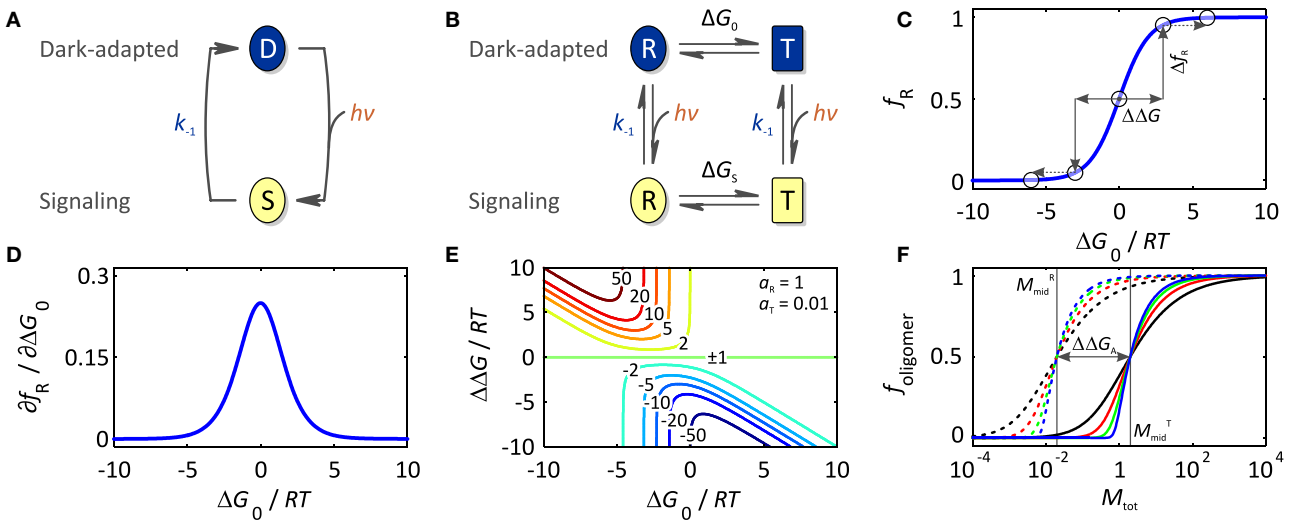

FIGURE 2 | Thermodynamics of photoreceptors. (A) Absorption of light drives the transition from the dark-adapted state D to the signaling state S, which depending upon photoreceptor, may involve reaction intermediates. As the life time of these intermediates is usually much smaller than the time scale of optogenetic applications, operationally the reaction is considered unimolecular and single-step even though mechanistically it may not be. Once in the signaling state, the photoreceptor thermally reverts to the dark-adapted state which again is assumed to be unimolecular, single-step with rate constant k_{-1}. **(B)** In the framework of an allosteric model, signal receptors exist in dynamic equilibrium between states R (relaxed) of higher biological activity a_R and T (tense) of lower biological activity a_T. In the dark, the equilibrium between R and T is governed by the free energy difference, ΔG_0, between these states. Introduction of a signal, light in case of sensory photoreceptors, (de)stabilizes the R and T states, and thus shifts the equilibrium to ΔG_S. **(C)** The fractional population of the R state, f_R, is a function of ΔG_0. Significant populations of R and T coexist close to equilibrium, i.e., $\Delta G_0 = 0$. Free energy perturbations $\Delta\Delta G$, e.g., introduced by signal or mutation, shift the equilibrium to a new value (arrows), where positive values of $\Delta\Delta G$ increase f_R, and negative values of $\Delta\Delta G$ decrease f_R. **(D)** f_R is maximally sensitive to free energy perturbations near $\Delta G_0 = 0$ but essentially invariant if $|\Delta G_0| >> 0$. **(E)** The dynamic range d for the signal response, i.e., the ratio of the biological activities in the absence and presence of signal, depends on the initial equilibrium between R and T (ΔG_0), the magnitude of the perturbation ($\Delta\Delta G$), and the intrinsic activities of R and T, a_R and a_T. Contour lines denote the magnitude of d for the parameter set $a_R = 1$ and $a_T = 0.01$, where positive values of d refer to light-activated and negative values to light-repressed photoreceptors. **(F)** Isotherms for homo-association of photoreceptors where $f_{oligomer}$ denotes the protein fraction in oligomeric form and M_{tot} the total monomer concentration. Black, red, green and blue curves refer to dimeric, trimeric, pentameric and decameric complexes, respectively, bold lines correspond to the low-affinity T state and dashed lines to the high-affinity R state. For photoassociating systems, $\Delta\Delta G_A$ is positive, and light promotes a transition from the low-affinity (solid) to the high-affinity (dashed) isotherms. *Vice versa*, for photodissociating systems, $\Delta\Delta G_A$ is negative, and light promotes a transition from high-affinity to low-affinity isotherms.

penetration of light) and biological constraints (e.g., radiation damage, phototoxicity). Moreover, biological steps subsequent to photochemical events may be rate-limiting; in particular, certain cellular responses, notably gene expression, are inherently slow. *Off*-kinetics are governed by the rate constant for dark recovery k_{-1} at physiological conditions as well as by slow biological processes. Note that dark-recovery reactions are often associated with large activation energies and can hence be strongly temperature-dependent. Photochromic photoreceptors, which we discuss in detail in Section Photochromic Photoreceptors, offer potentially much faster *off*-kinetics via active, light-driven reversion of the signaling state to the dark-adapted state. For some photoreceptor classes, specifically LOV proteins, certain rhodopsins and phytochromes, mutations have been identified that greatly accelerate or decelerate the dark-recovery reaction and that could hence be used to modulate *off*-kinetics (Yang et al., 2007; Berndt et al., 2009; Zoltowski et al., 2009). Less is known on mutations that would modify the forward kinetics (k_1); however, to achieve sensitive signal reception, photoreceptors generally possess high quantum yields for formation of the signaling state and hence there is little, if any, scope for further enhancement. Further, any variation of forward or reverse kinetics will invariably affect the effective light sensitivity at photostationary state (cf. above). Finally, mutations introduced with the intent of modulating photocycle kinetics may have inadvertent, often deleterious effects on signal transduction, even to the extent of completely abolishing any downstream response (Diensthuber et al., 2014).

Thermodynamics of Photoreceptors

Before regarding specific case studies, it is illuminating to consider the general thermodynamics that govern signaling processes and set energetic limits on both natural and engineered photoreceptors. Adapting concepts from classic models of allostery (Monod et al., 1965; Wyman and Gill, 1990; Motlagh et al., 2014), we previously introduced a simple framework for stimulus perception in signal receptors (Möglich et al., 2009b; Möglich and Moffat, 2010) (**Figure 2A**). Within this model, signal receptors are assumed to be in dynamic equilibrium between states of lower (T, tense) and higher (R, relaxed) biological activity. In the dark-adapted state D, the equilibrium

$L_0 = [T]_0/[R]_0$ is determined by the free energy difference $\Delta G_0 = -RT \ln L_0$ between these states. Introduction of signal (de)stabilizes T and R to different extents, thus alters the free energy difference by $\Delta\Delta G$ to ΔG_S, and shifts the equilibrium to the new value $L_S = [T]_S/[R]_S$ in the signaling state S. Consequently, signal does not alter the pre-existing, intrinsic states themselves but shifts the dynamic equilibrium between them. Evidence in support of co-existing states of different biological activity has been obtained for both signal receptors in general, e.g., (Volkman et al., 2001), and photoreceptors in specific (e.g., Yao et al., 2008). In particular, the widely deployed LOV2 domain from *Avena sativa* phototropin 1 (*As*LOV2, **Figure 3A**) possesses a C-terminal extension, denoted Jα, that exists in conformational equilibrium between an α-helical state docked against the LOV core (T state) and an unfolded, undocked state (R state) (Harper et al., 2003; Halavaty and Moffat, 2007). In the dark, the equilibrium between the coexisting states is shifted toward the folded, helical state, but under blue light the unfolded, undocked state predominates (Yao et al., 2008). An N-terminal helical extension, denoted A′α, also contributes to the light-promoted unfolding reaction (Zayner et al., 2012). In general, if the absolute free energy

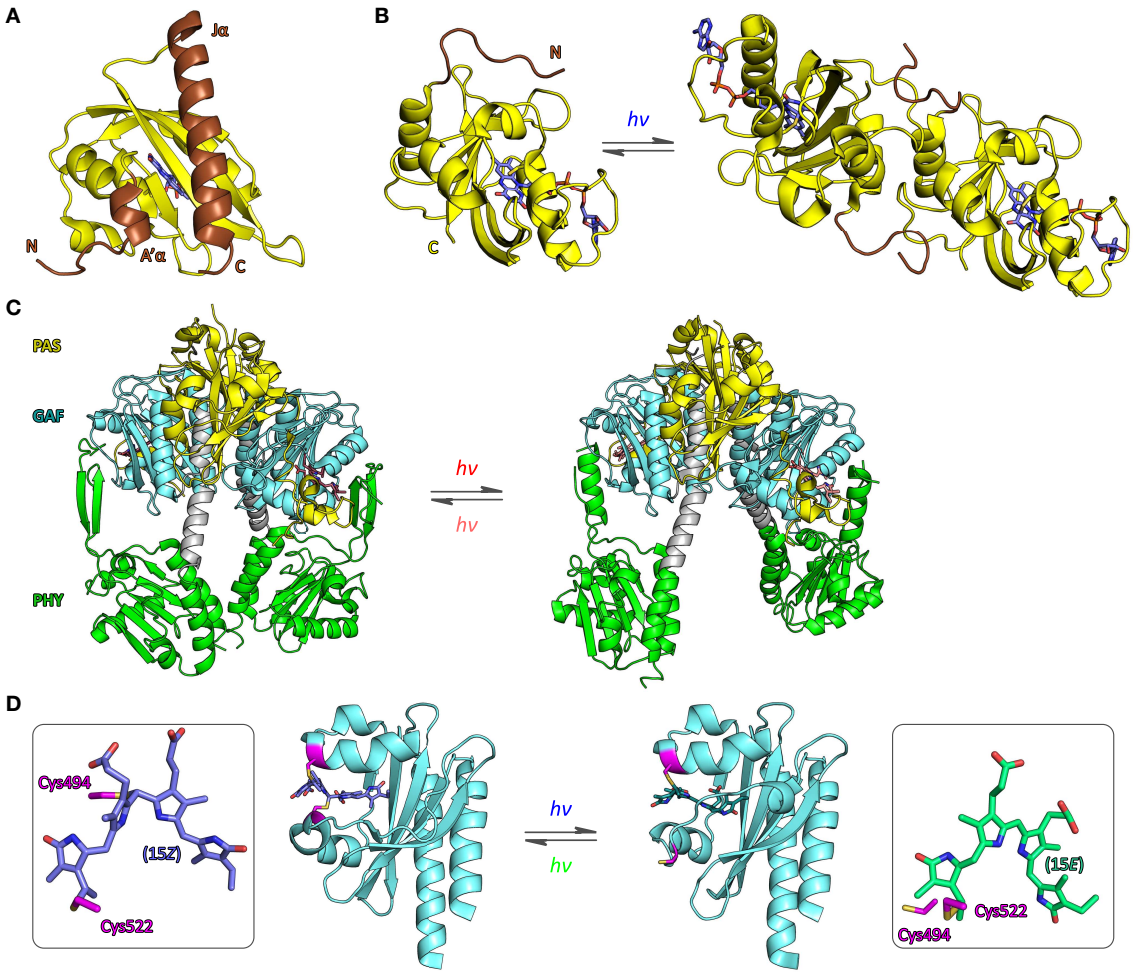

FIGURE 3 | Structure of photoreceptors. (A) The LOV2 domain of *Avena sativa* phototropin 1 (*As*LOV2) adopts the canonical PAS fold (Möglich et al., 2009b) with N-terminal and C-terminal helices, denoted A′α and Jα (brown), packed onto the outer face of a five-stranded antiparallel β sheet (PDB entry 2V0U, Halavaty and Moffat, 2007). Light absorption promotes unfolding and concomitant dissociation of Jα from the LOV core domain (Harper et al., 2003). **(B)** The structures of the *Neurospora crassa* LOV protein Vivid in its dark-adapted state (left, 2PD8, Zoltowski et al., 2007) and in its signaling state (right, 3RH8, Vaidya et al., 2011) provide an atomic perspective on refolding of an N-terminal extension to the LOV core domain (brown) and concomitant dimerization. **(C)** High-resolution structures of the photosensor module of *Deinococcus radiodurans* bacteriophytochrome, comprising PAS, GAF, and PHY domains, in its dark-adapted Pr state (left, 4O0P) and red-light-adapted Pfr state (right, 4O01, Takala et al., 2014) implicate a pivot motion and splaying apart of the PHY domains as the molecular mechanism for light-induced signal transduction. **(D)** The structure of a cyanobacteriochrome photosensor from the PixJ protein of *Thermosynecchococcus elongatus* BP-1 has been determined in the dark-adapted, blue-light-absorbing 15*Z* state (left, 4FOF, Burgie et al., 2013) and the light-adapted, green-light-absorbing 15*E* state (right, 3VV4, Narikawa et al., 2013), where *Z* and *E* refer to isomers of the C15=C16 double bond of the PCB chromophore that is covalently bound to cysteine 522 (see boxes). In the 15*Z* state cysteine 494 (magenta) forms a second thioether bridge to the C10 atom of the chromophore.

difference between states T and R is large, the equilibrium is almost entirely shifted to one side, and the minority state may not be detectable at all (**Figure 2B**). When applied to photoreceptors, the allosteric model can elegantly account for both light-activated and light-repressed phenomena. For light-activated proteins, $\Delta\Delta G$ is positive, and the fraction of the more active R state, f_R, increases in the signaling state relative to that in the dark-adapted receptor; for light-repressed proteins, $\Delta\Delta G$ is negative, and f_R is diminished in the signaling state (**Figure 2C**). The fraction of R state is maximally sensitive to signal-induced free energy perturbations near equilibrium, i.e., $\Delta G_0 = 0$ (**Figures 2C,D**); by contrast, if $|\Delta G_0| >> 0$, free energy perturbations will have less effect on f_R. However, as also noted by Schmidt and Cho (2015), applications of sensory photoreceptors more often do not demand maximum sensitivity of f_R but rather maximum dynamic range d, here defined as the ratio of biological activities in the dark-adapted and in the signaling states, where positive values of d denote light activation and negative values denote light repression. The activities in the dark-adapted and signaling states in turn are given by the relative fractions f_T and f_R in the D and S states as well as by the elementary activities a_T and a_R of the T and R states, respectively. The ratio a_R/a_T defines an upper limit of the maximum dynamic range that can be achieved. Furthermore, high dynamic ranges of light activation ($d >> 1$) can only be realized if the dark-adapted photoreceptor predominantly assumes the T state (**Figure 2E**), i.e., $\Delta G_0 < 0$. Likewise, high dynamic ranges for light repression ($d << -1$) can only be achieved if the photoreceptor in its signaling state predominantly populates T, i.e., $\Delta G_S < 0$. Put another way, the magnitude of d is mainly dependent upon how well biological activity can be shut off in the low-activity state, i.e., in the dark-adapted state for light-activated receptors and in the signaling state for light-repressed receptors. Notably, these considerations directly bear on signal transduction and the engineering of photoreceptors: although it may be challenging to much alter $\Delta\Delta G$, i.e., the amount of free energy that can be derived from light perception, it is well documented that ΔG_0 can deliberately be changed, e.g., via site-directed mutagenesis, so as to achieve improved dynamic range (Strickland et al., 2010).

Dating back to the original implementation by Quail and coworkers (Shimizu-Sato et al., 2002), photoreceptors that undergo association/dissociation reactions in response to light absorption have been widely deployed in the engineering of light-responsive systems and in optogenetics. Their widespread prevalence, their undisputed success in optogenetics, and the often fairly predictable engineering strategies warrant a specific spotlight on these associating photoreceptors (cf. Section Associating Photoreceptors and Optogenetic Applications). Signal-dependent oligomerization reactions can be rationalized by a lower dissociation constant K_D^R in the R state, i.e., higher affinity, than in the T state, K_D^T (**Figure 2F**). Of key importance, the transition between dark-adapted and signaling states hence involves changes in oligomeric state, meaning that the system response to light strongly depends upon the concentration of photoreceptor molecules. As determined by the magnitude of K_D, at a total photoreceptor concentration M_{tot}, a fraction of molecules $f_{oligomer}$ will be in oligomeric complex, and the remaining fraction of 1-$f_{oligomer}$ will be present as monomers. A number of fundamental insights can be gleaned from inspection of the corresponding association isotherms (**Figure 2F**). First, with increasing number n of monomers in the oligomeric complex, the association reaction becomes increasingly cooperative, and the isotherm between monomeric and oligomeric state becomes steeper. Second, the total photoreceptor concentration M_{tot} needs to be matched to the affinities in both the T and R states; notably, the midpoint of the isotherms, where the fraction of molecules in monomeric form equals that in oligomeric complex, occurs at $M_{mid} = 2 \cdot \sqrt[n-1]{K_D/n}$. As a consequence, significant light-dependent changes in oligomeric state can only be induced if M_{tot} ranges between M_{mid}^R and M_{mid}^T. By contrast, if $M_{tot} << M_{mid}^R$, no oligomeric complex will be formed, even in the higher-affinity state R; if $M_{tot} >> M_{mid}^T$, photoreceptor molecules will be largely present in oligomeric complex in both the T and R states. Third, variations of M_{tot} near either M_{mid}^T or M_{mid}^R can have disproportionate effect on the degree of oligomerization and extent of regulation by light. For example, such variations may arise from differing protein levels across expression systems and/or mutant variants of photoreceptors. Fourth, the extent of photoreceptor activation can have immense influence on the cooperative association reaction. Drastic changes in oligomerization occur for concentrations of light-activated molecules in the signaling state around the threshold defined by M_{mid}^R; the degree of oligomerization and the system response can thus depend on applied light dose in highly non-linear manner. Fifth, to induce by signal a change in M_{mid} of a factor x, a total free energy perturbation of $\Delta\Delta G_A = (n-1) \cdot \mathrm{RT} \ln x$ is required, or $(n-1)/n \cdot RT \ln x$ per monomer. In the example in **Figure 2F**, M_{mid}^T and M_{mid}^R differ by a 100-fold, corresponding to about 11.4 kJ mol^{-1} per monomer for large n.

Due to space constraints, we only consider fully cooperative homo-association reactions, i.e., cases where the Hill coefficient amounts to n. Equations can also be obtained for less cooperative reactions and hetero-association reactions; fundamentally similar considerations hold for these scenarios as well.

Allostery of Photoreceptors

Numerous studies of natural photoreceptors have unveiled ingenious allosteric strategies by which light signals are translated into changes of biological activity. Many of these strategies have subsequently been co-opted for photoreceptor engineering. Invariably, initial light-induced changes within the chromophore-binding pocket of the photosensor have to be propagated and allosterically coupled to associated, often distal effector modules. When present as isolated modules, photosensors and effectors usually retain their elementary functions of absorbing light and exerting biological activity, respectively. By contrast, the desired property of light-regulated biological activity is only accomplished in composite photoreceptors where photosensor and effector are linked in a manner conducive to thermodynamic coupling between these modules. Consequently, the physical nature of

the linker (topology, length, sequence, structure, dynamics) between photosensor and effector modules clearly is of central importance for light-regulated allostery. In fact, successful photoreceptor engineering has often amounted to optimizing the inter-module linker, whereas photosensor and effector have been minimally modified or left untouched altogether (cf. below). We categorize the plethora of engineering examples to date (**Figure 4**) based on whether photoreception involves light-regulated association (Section Associating Photoreceptors and Optogenetic Applications, **Table 2**) or not (Section Non-associating Photoreceptors and Optogenetic Applications, **Table 1**). It should be noted that the below strategies mostly represent specific manifestations of more general design concepts that have proven successful in the engineering of allosterically regulated, mostly light-inert proteins (Makhlynets et al., 2015; Stein and Alexandrov, 2015).

Non-associating Photoreceptors and Optogenetic Applications

This section treats non-associating photoreceptors where formation of the signaling state is not accompanied by changes in oligomeric state. Within this diverse class, linkers are either non-existent, in particular where sensor and effector modules are integrated into a single protein domain, as in rhodopsins, or they are of defined structure, usually of α-helical conformation. Due to their rigid structure, α helices and α-helical coiled coils are well-suited for transmitting conformational and dynamic changes over long distances between spatially distant sensors and effectors (Wolgemuth and Sun, 2006). Indeed, many natural signal receptors display sequence signatures indicative of helical and coiled-coil linkers (Anantharaman et al., 2006; Möglich et al., 2009a,b, 2010a; Rockwell et al., 2013). Furthermore, since α helices are self-contained structural elements stabilized by short-range contacts, locally confined order-disorder transitions, i.e., unfolding of helices, are enabled. Despite their disparity, non-associating photoreceptors can be further divided into two subcategories based on whether they chiefly capitalize on local unfolding (Section Light-regulated Order-disorder Transitions) or use other allosteric mechanisms involving tertiary and quaternary (apart from association) structural transitions (Section Light-regulated Tertiary and Quaternary Structural Transitions).

Light-regulated Tertiary and Quaternary Structural Transitions

The first subcategory of non-associating photoreceptors comprises a diverse group in which photoreception is not (primarily) accomplished by order-disorder transitions but by other tertiary and quaternary structural transitions, many of which are not yet understood in full molecular detail. Tracing back to seminal work by the Khorana group (Kim et al., 2005), the engineering of animal (type II) rhodopsin photoreceptors

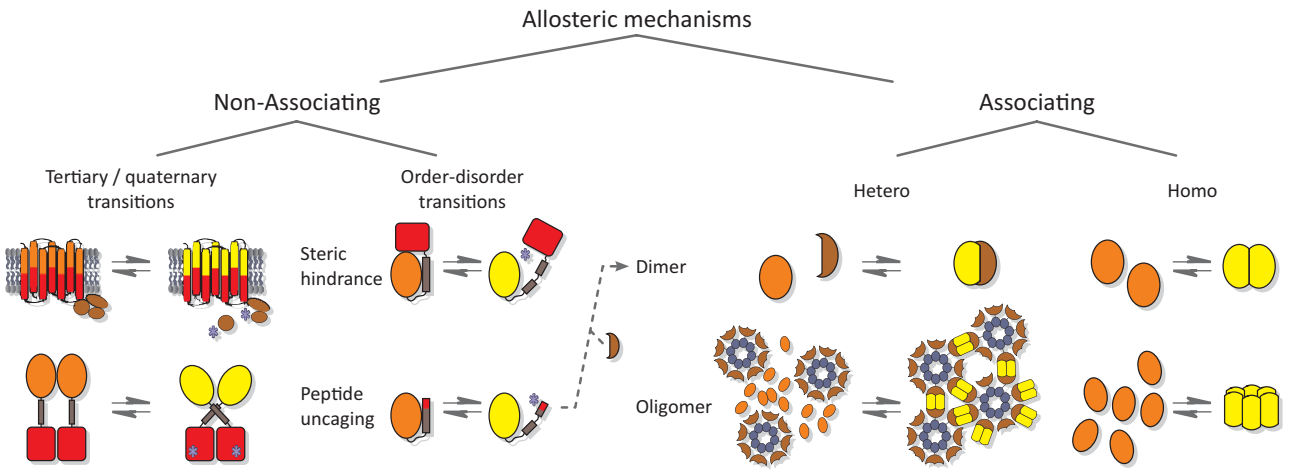

FIGURE 4 | Allostery of photoreceptors. Allosteric signal transduction mechanisms realized in natural and engineered photoreceptors are grouped into non-associating and associating categories. Within the category of non-associating photoreceptors (Section Non-associating Photoreceptors and Optogenetic Applications), a disparate subclass of receptors relies on light-induced transitions of tertiary and quaternary (other than association) structure to regulate biological activity (Section Light-regulated Tertiary and Quaternary Structural Transitions). A second subclass capitalizes on light-induced order-disorder transitions, epitomized by Jα helix unfolding in *As*LOV2 (Harper et al., 2003), most often to restrict access to either an effector active site or to a peptide epitope in light-regulated manner (Section Light-regulated Order-disorder Transitions). Within the category of associating photoreceptors (Section Associating Photoreceptors and Optogenetic Applications), light-induced signal transduction goes along with a change in oligomeric state. Association can be either light-promoted or light-repressed; can be between alike (homo) or different (hetero) partners; and can be of dimeric or higher stoichiometry. Note that other categorization schemes are conceivable as well; in particular, several photoreceptors based on light-induced Jα unfolding subsequently undergo heteroassociation (Lungu et al., 2012; Strickland et al., 2012; Guntas et al., 2015) (indicated by dashed arrow). Orange and yellow symbols denote T and R states, respectively, of photosensor modules; red symbols denote effector modules; and blue stars indicate effectors in their high-activity state.

TABLE 1 | Non-associating engineered photoreceptors.

Class	Protein architecture[a]	Trade name	Cofactor	Size (aa)[b]	Activation/Deactivation λ_{max} (nm)	Dark recovery[c]	Optogenetic application
LOV	*As*LOV2-*Ec*TrpR	LOV-TAP	FMN	240	450/dark	Seconds	DNA binding (Strickland et al., 2008)
	*As*LOV2 inserted into *Ec*DHFR	–	FMN	300	450/dark	Seconds	Enzymatic activity (Lee et al., 2008)
	*As*LOV2-*Hs*Rac1	PA-Rac1	FMN	320	450/dark	Seconds	GTPase signaling (Wu et al., 2009)
	*As*LOV2-*Hs*Stim1	LOVS1K	FMN	360	450/dark	Seconds	Ion channel activation (Pham et al., 2011)
	*As*LOV2-*Hs*Caspase 7	L57V	FMN	400	450/dark	Seconds	Caspase/apoptosis (Mills et al., 2012)
	*Da*αDTX-*As*LOV2	Lumitoxin	FMN	300	450/dark	Seconds	Ion channel inhibition (Schmidt et al., 2014)
	*At*LOV2-*Mm*Odc1 peptide	PSD	FMN	160	450/dark	Seconds	Protein degradation (Renicke et al., 2013)
	*As*LOV2-peptide	B-LID	FMN	150	450/dark	Seconds	Protein degradation (Bonger et al., 2014)
	*As*LOV2-*Hs*PKI	PA-PKI	FMN	160	450/dark	Seconds	Inhibition of endogenous Ser/Thr kinases (Yi et al., 2014)
	*As*LOV2-peptide	PA-MKI					
	*As*LOV2-peptides	LINuS	FMN	150	450/dark	Seconds	Nuclear transport (Niopek et al., 2014)
	*Bs*YtvA-*Bj*FixL	YF1, YHF	FMN	390	Dark/450	Minutes to hours	Prokaryotic gene expression (Möglich et al., 2009a, 2010a; Ohlendorf et al., 2012)
PYP	*Sc*GCN4-*Hh*PYP	–	pCA	160	450/dark	Seconds	DNA binding (Fan et al., 2011)
rhodopsin	*Bt*Rhodopsin-*Cg*β_2AR	–	Retinal	350	500/dark	Seconds to minutes	cNMP signaling (Kim et al., 2005)
	*Bt*Rhodopsin-*Hs*α_{1a}AR *Bt*Rhodopsin-*Cg*β_2AR	OptoXR	Retinal	400 350	500 /dark	Seconds to minutes	cNMP and PLC signaling (Airan et al., 2009)
	*Mm*Melanopsin *Cr*Opsin	–	Retinal	500 330	480/light[d] 500	Seconds Seconds	cNMP and PLC signaling (Karunarathne et al., 2013)
	*Mm*Melanopsin-*Mm*mGluR6	Opto-mGluR6	Retinal	500	480/light[d]	Seconds	vision restoration (Van Wyk et al., 2015)
	*Rr*Rhodopsin-*Hs*5-HT_{1A}	Rh-$CT_{5\text{-}HT1A}$	Retinal	350	485/dark	Seconds to minutes	Ion-channel activation (Oh et al., 2010)
bacterio-phytochrome	*Sp*Cph1-*Ec*EnvZ	Cph8	PCB	750	660/720	Minutes	Prokaryotic gene expression (Levskaya et al., 2005)
	*Dr*BPhy-*Hs*PDE2A	LAPD	BV	890	700/750	Minutes	cNMP hydrolysis (Gasser et al., 2014)
	*Rs*BPhG-*Ns*CyaB1	IlaC	BV	800	710/760	Minutes	cAMP formation (Ryu et al., 2014)

[a] *Species abbreviations as follows: As, Avena sativa; At, Arabidopsis thaliana; Bj, Bradyrhizobium japonicum; Bs, Bacillus subtilis; Bt, Bos taurus; Cg, Cricetulus griseus; Cr, Carybdea rastonii; Dr, Deinococcus radiodurans; Da, Dendroaspis angusticeps; Ec, Escherichia coli; Hh, Halorhodospira halophila; Hs, Homo sapiens; Mm, Mus musculus; Ns, Nostoc sp.; Rr, Rattus rattus; Rs, Rhodobacter sphaeroides; Sc, Saccharomyces cerevisiae; Sp, Synechocystis PCC6803; "peptide" refers to a short, synthetic sequence.*

[b] *Sizes are approximate.*

[c] *Time scales refer to intrinsic dark-recovery reaction; note that this is temperature-dependent and may be followed by slow biological processes.*

[d] *Melanopsin has been reported to be photochromic but the spectrum for deactivation has not been thoroughly determined (Ernst et al., 2014).*

has been particularly successful (Airan et al., 2009; Karunarathne et al., 2013; Van Wyk et al., 2015). Type-II rhodopsins belong to the superfamily of G-protein-coupled receptors (GPCR) and consist of a retinal-binding seven-helix transmembrane photosensor module and an effector module formed by several intracellular loops; that is, both modules are integrated into a single protein domain (Ernst et al., 2014; Terakita and Nagata, 2014). Downstream signaling is mediated by heterotrimeric G proteins which specifically interact with the effector loops in signal-dependent manner. By exchanging these intracellular

effector loops between type-II rhodopsins and other GPCRs, cellular signaling pathways can be rewired and put under light control. Following the initial demonstration (Kim et al., 2005), this engineering concept has later been popularized as "optoXR" (Airan et al., 2009). Replacement of the effector loops in bovine visual rhodopsin that originally mediate interactions with transducin (G_t) by corresponding loops of the α_1- and β_2-adrenergic receptors yielded chimeric rhodopsins that achieve light control over G_s- and G_q-coupled signal pathways, i.e., control over cAMP (3′,5′-cyclic adenine monophosphate) production and phospholipase-C activity (Kim et al., 2005; Airan et al., 2009). However, a big drawback of this approach is the requirement for enzymatic regeneration of the 11-*cis* retinal chromophore of bovine rhodopsin once it underwent photoiosmerization to its all-*trans* form. This bottleneck can be overcome by resorting to rhodopsins that undergo reversible photoisomerization, as, e.g., melanopsin; in this way, G_i, G_q, and G_s signaling pathways have been put under light control (Karunarathne et al., 2013). In a very recent application of the optoXR concept, the activity of the metabotropic glutamate receptor mGluR6 could be controlled by light, thus yielding a promising tool for vision restoration (Van Wyk et al., 2015). Certain rhodopsins intrinsically mediate the desired type of G protein signaling and could hence immediately be used as optogenetic tools. As a prerequisite, correct expression and trafficking in heterologous hosts need to be ensured, for example by appending C-terminal localization signals to otherwise intact rhodopsins (Oh et al., 2010; Spoida et al., 2014).

For several homodimeric photoreceptors, engineering is based on the exchange of light-inert chemosensors for structurally and functionally homologous LOV (Möglich et al., 2009a, 2010a) or bacteriophytochrome (Levskaya et al., 2005; Gasser et al., 2014; Ryu et al., 2014) photosensors. For example, we replaced the oxygen-sensitive PAS B domain of the histidine kinase FixL from *Bradyrhizobium japonicum* with the LOV domain of *Bacillus subtilis* YtvA to obtain the photoreceptor YF1. Net histidine kinase activity of YF1 is repressed by more than 1000-fold under blue light (Möglich et al., 2009a) which underpins two systems for light-regulated gene expression in prokaryotes (Ohlendorf et al., 2012). YF1 variants differing in the linker connecting the LOV photosensor and histidine kinase effector modules displayed a striking heptad periodicity of activity and light regulation on linker length. Based on these observations, we posited (Möglich et al., 2009a) that these modules of the homodimeric photoreceptor are connected by a parallel α-helical coiled coil which has been borne out in the full-length crystal structure of YF1 (Diensthuber et al., 2013). Signals originating in the LOV photosensor could be transmitted to the distal effector via torque motions (supertwisting) of the coiled coil. In a derivative photoreceptor, denoted YHF, in which the PAS B domain is retained and combined with the *Bs*YtvA LOV domain, net kinase activity is regulated by oxygen and blue light in a positive cooperative manner (Möglich et al., 2010a). A conceptually similar, prior study yielded the red-light-repressed photoreceptor Cph8 which consists of a cyanobacterial phytochrome photosenor module, that comprises PAS, GAF, and PHY domains and uses a phycocyanobilin chromophore, and the *E. coli* histidine kinase EnvZ (Levskaya et al., 2005). Recently, bacteriophytochrome photosensors have also been used in the engineering of red-light-activated, far-red-light-reversible actuators of cyclic-nucleotide metabolism (Gasser et al., 2014; Ryu et al., 2014). For one, we substituted the two GAF sensor domains of the human phosphodiesterase 2A for the biliverdin-binding PAS-GAF-PHY tandem of *Deinococcus radiodurans* bacteriophytochrome to engineer the photoreceptor LAPD (Gasser et al., 2014). Hydrolysis of cAMP and cGMP (3′,5′-cyclic guanosine monophosphate) by LAPD could be enhanced by up to seven-fold by red light and could be attenuated by far-red light. Studies in cell culture and zebrafish confirmed *in vivo* functionality and revealed that biliverdin is sufficiently available endogenously and hence needs not be added exogenously. The implementation of a closely related design concept yielded the red-light-regulated adenylate cyclase IlaC that recombines the PAS-GAF-PHY photosensory module of the *Rhodobacter sphaeroides* bacteriophytochrome BphG1 with the catalytic domain of *Nostoc* sp. CyaB1 (Ryu et al., 2014). The cyclase activity of IlaC could be enhanced by around six-fold under red light, and functionality in nematodes was demonstrated. For both LAPD and IlaC, a strong dependence of catalytic activity and regulation on the length of the linker between photosensor and effector modules has been observed. Although these dependencies were less pronounced than for YF1, it is nonetheless conceivable that similar mechanisms for signal propagation are at play in YF1, LAPD, and IlaC. While the verdict is still out, future bacteriophytochrome engineering efforts will doubtless benefit from a ground-breaking recent study which revealed that the isolated PAS-GAF-PHY tandem of *D. radiodurans* bacteriophytochrome undergoes a pivot motion upon red-light absorption (**Figure 3C**) (Takala et al., 2014); recent findings imply a similar mechanism in plant phytochromes, too (Burgie et al., 2014; Burgie and Vierstra, 2014).

Light-regulated Order-disorder Transitions

Within the second subcategory of non-associating photoreceptors, several studies have exploited the light-regulated unfolding of the C-terminal Jα helix of phototropin LOV domains, chiefly the *As*LOV2 domain (Harper et al., 2003), in one of essentially three ways: mutually exclusive folding (Strickland et al., 2008), steric restriction of effector active sites (Lee et al., 2008; Wu et al., 2009; Pham et al., 2011; Mills et al., 2012; Schmidt et al., 2014), or uncaging of peptide epitopes (Lungu et al., 2012; Strickland et al., 2012; Renicke et al., 2013; Bonger et al., 2014; Niopek et al., 2014; Yi et al., 2014; Guntas et al., 2015). As explained in Section Thermodynamics of Photoreceptors, in the dark the Jα helix is predominantly folded and docked against the LOV core domain, but upon blue-light absorption it predominantly dissociates and unfolds. In the LOV-TAP protein (Strickland et al., 2008), the C-terminal Jα helix of *As*LOV2 is fused with an N-terminal helix of the *E. coli* TrpR repressor such that steric interference between the two modules results in mutually exclusive folding: the joint helix can either fold unto the *As*LOV2 or the TrpR domain but not unto both simultaneously; correct folding and DNA affinity of TrpR could thus be modestly regulated by blue light.

The *As*LOV2 domain has also been inserted into surface loops of an effector domain to put biological activity under light control, albeit yielding poor overall activity and dynamic range for light regulation in the initial implementation (Lee et al., 2008). However, the successful design of several light-inert receptors by domain insertion (Makhlynets et al., 2015; Stein and Alexandrov, 2015) strongly suggests that the basic concept is viable and suitable for the regulation of diverse effectors. In a related strategy, the *As*LOV2 domain is connected via its Jα helix to selected effector domains such that their active site is occluded (Wu et al., 2009). Once Jα unfolds, the effector domain dissociates from *As*LOV2, steric restriction to the active site is relieved, and biological activity is enhanced. This concept was pioneered in the regulation of the small GTPase Rac1 which afforded blue-light control over cell motility (Wu et al., 2009). Crystallographic analysis revealed an adventitious structural contact in the resultant PA-Rac1 construct between the *As*LOV2 and Rac1 domains which was not rationally planned but is apparently necessary for light regulation. The requirement for such, highly specific interactions may be the reason why the successful design strategy could not readily be transferred to homologous GTPases, e.g., Cdc42 (Wu et al., 2009). Later on, the concept of steric restriction to active sites has also been applied to the regulation of Ca^{2+} ion channels (Pham et al., 2011) and caspases (Mills et al., 2012). In the related lumitoxin approach, peptide toxins are appended N-terminally to a membrane-tethered *As*LOV2 domain such that the toxins are sequestered from their inhibitory sites on endogenous potassium channels (Schmidt et al., 2014). Light-induced unfolding of the Jα helix grants the *As*LOV2 domain enhanced mobility and allows the associated toxin to reach and inhibit the ion channel.

In the particularly versatile "peptide uncaging" strategy, a peptide epitope is interleaved with or appended to the Jα helix such that its folding and solvent exposure become subject to light control. Once the peptide epitope is undocked from the LOV core domain following light absorption, it can trigger downstream signaling events. This principle has been implemented to achieve light-regulated protein degradation (Renicke et al., 2013; Bonger et al., 2014), inhibition of endogenous serine/threonine kinases (Yi et al., 2014), and nuclear transport (Niopek et al., 2014). Unfolding of peptide epitopes interleaved with Jα also forms the basis for several associating photoreceptors (cf. Section Associating Photoreceptors and Optogenetic Applications) (Lungu et al., 2012; Strickland et al., 2012; Guntas et al., 2015). Note that the incorporation of peptide epitopes may significantly alter the stabilities of the α-helical (T) and unfolded (R) states of Jα and thereby affect the equilibrium between these states (cf. Section Thermodynamics of Photoreceptors and **Figures 2C–E**). To compensate for such effects and to optimize dynamic range as dictated by application, several mutations within the *As*LOV2 core domain and the Jα helix can be deployed that deliberately (de)stabilize the α-helical vs. the unfolded states (Strickland et al., 2010, 2012; Lungu et al., 2012; Zayner et al., 2012; Guntas et al., 2015).

Notably, light-regulated unfolding is by no means exclusive to *As*LOV2 but also occurs in other photoreceptors; as a case in point, the light-induced unfolding of an N-terminal segment of the photoactive yellow protein (PYP) has been exploited in subjecting the DNA affinity of an N-terminally appended GCN4 leucine-zipper protein under light control (Fan et al., 2011).

Associating Photoreceptors and Optogenetic Applications

Since many biological processes involve protein oligomerization, often dimerization (Klemm et al., 1998), it should come as no surprise that (i) many sensory photoreceptors exist in Nature that undergo light-dependent association reactions; and (ii) that these photoreceptors have proven particularly powerful in optogenetic engineering. Associating photoreceptors can be further subdivided into homo- vs. heteroassociation, reactions of different stoichiometry (dimer, oligomer), and into light-triggered association vs. dissociation (cf. Section Thermodynamics of Photoreceptors). Regulation of biological activity in this class amounts to co-localization of interacting proteins and/or recruitment to subcellular compartments; notably, this concept extends to the control of split proteins, well established for chemically induced dimerization (Pollock and Clackson, 2002). For this engineering concept, photosensor and effector modules need to be physically connected but they generally need not directly interact with one another (in fact, it is often preferable, they do not). Constraints on linker identity are hence less demanding than for non-associating photoreceptors (cf. Section Non-associating Photoreceptors and Optogenetic Applications), and engineering ideally becomes less challenging and more predictive. Notably, the engineering of associating photoreceptors shares aspects with the labeling with fluorescent proteins (Tsien, 2009), in that linkers are often short, flexible and predominantly hydrophilic. Various associating photoreceptors with sensitivity to different portions of the visible electromagnetic spectrum (cf. **Figure 1**) have been used in engineering, and we provide an overview in **Table 2** and in the following.

The plant photoreceptor UVR8 (Brown et al., 2005) does not require any cofactors but utilizes tryptophan chromophores to sense UV-B light. Photon absorption induces disruption of the homodimeric UVR8 receptor and enables the constituent monomers to associate with COP1 (Christie et al., 2012; Wu et al., 2012). In the absence of additional plant proteins, the dark-recovery reaction of UVR8 is exceedingly slow (hours to days), thus rendering pertinent optogenetic applications effectively irreversible on most biologically relevant time scales. The dissociation reaction of UVR8 has been exploited in subjecting protein secretion under UV-light control (Chen et al., 2013), and the interaction with COP1 provides the basis for two closely similar systems for UV-light-regulated expression of transgenes in eukaryotic cells (Crefcoeur et al., 2013; Müller et al., 2013b).

Several optogenetic applications resort to associating photoreceptors of the flavin-binding light-oxygen-voltage (LOV) family (Conrad et al., 2014). Certain LOV domains, e.g., those of *Neurospora crassa* Vivid (*Nc*VVD, Lamb et al., 2008, **Figure 3B**), stramenopile aureochromes (Takahashi et al., 2007) and *Erythrobacter litoralis* EL222 (Nash et al., 2011), assemble into homodimers upon blue-light absorption. While mechanistic details often remain to be elucidated, in all cases flanking, mostly α-helical extensions N- and C-terminal to the LOV core domain

effector loops between type-II rhodopsins and other GPCRs, cellular signaling pathways can be rewired and put under light control. Following the initial demonstration (Kim et al., 2005), this engineering concept has later been popularized as "optoXR" (Airan et al., 2009). Replacement of the effector loops in bovine visual rhodopsin that originally mediate interactions with transducin (G_t) by corresponding loops of the α_1- and β_2-adrenergic receptors yielded chimeric rhodopsins that achieve light control over G_s- and G_q-coupled signal pathways, i.e., control over cAMP (3′,5′-cyclic adenine monophosphate) production and phospholipase-C activity (Kim et al., 2005; Airan et al., 2009). However, a big drawback of this approach is the requirement for enzymatic regeneration of the 11-*cis* retinal chromophore of bovine rhodopsin once it underwent photoiosmerization to its all-*trans* form. This bottleneck can be overcome by resorting to rhodopsins that undergo reversible photoisomerization, as, e.g., melanopsin; in this way, G_i, G_q, and G_s signaling pathways have been put under light control (Karunarathne et al., 2013). In a very recent application of the optoXR concept, the activity of the metabotropic glutamate receptor mGluR6 could be controlled by light, thus yielding a promising tool for vision restoration (Van Wyk et al., 2015). Certain rhodopsins intrinsically mediate the desired type of G protein signaling and could hence immediately be used as optogenetic tools. As a prerequisite, correct expression and trafficking in heterologous hosts need to be ensured, for example by appending C-terminal localization signals to otherwise intact rhodopsins (Oh et al., 2010; Spoida et al., 2014).

For several homodimeric photoreceptors, engineering is based on the exchange of light-inert chemosensors for structurally and functionally homologous LOV (Möglich et al., 2009a, 2010a) or bacteriophytochrome (Levskaya et al., 2005; Gasser et al., 2014; Ryu et al., 2014) photosensors. For example, we replaced the oxygen-sensitive PAS B domain of the histidine kinase FixL from *Bradyrhizobium japonicum* with the LOV domain of *Bacillus subtilis* YtvA to obtain the photoreceptor YF1. Net histidine kinase activity of YF1 is repressed by more than 1000-fold under blue light (Möglich et al., 2009a) which underpins two systems for light-regulated gene expression in prokaryotes (Ohlendorf et al., 2012). YF1 variants differing in the linker connecting the LOV photosensor and histidine kinase effector modules displayed a striking heptad periodicity of activity and light regulation on linker length. Based on these observations, we posited (Möglich et al., 2009a) that these modules of the homodimeric photoreceptor are connected by a parallel α-helical coiled coil which has been borne out in the full-length crystal structure of YF1 (Diensthuber et al., 2013). Signals originating in the LOV photosensor could be transmitted to the distal effector via torque motions (supertwisting) of the coiled coil. In a derivative photoreceptor, denoted YHF, in which the PAS B domain is retained and combined with the *Bs*YtvA LOV domain, net kinase activity is regulated by oxygen and blue light in a positive cooperative manner (Möglich et al., 2010a). A conceptually similar, prior study yielded the red-light-repressed photoreceptor Cph8 which consists of a cyanobacterial phytochrome photosenor module, that comprises PAS, GAF, and PHY domains and uses a phycocyanobilin chromophore, and the *E. coli* histidine kinase EnvZ (Levskaya et al., 2005). Recently, bacteriophytochrome photosensors have also been used in the engineering of red-light-activated, far-red-light-reversible actuators of cyclic-nucleotide metabolism (Gasser et al., 2014; Ryu et al., 2014). For one, we substituted the two GAF sensor domains of the human phosphodiesterase 2A for the biliverdin-binding PAS-GAF-PHY tandem of *Deinococcus radiodurans* bacteriophytochrome to engineer the photoreceptor LAPD (Gasser et al., 2014). Hydrolysis of cAMP and cGMP (3′,5′-cyclic guanosine monophosphate) by LAPD could be enhanced by up to seven-fold by red light and could be attenuated by far-red light. Studies in cell culture and zebrafish confirmed *in vivo* functionality and revealed that biliverdin is sufficiently available endogenously and hence needs not be added exogenously. The implementation of a closely related design concept yielded the red-light-regulated adenylate cyclase IlaC that recombines the PAS-GAF-PHY photosensory module of the *Rhodobacter sphaeroides* bacteriophytochrome BphG1 with the catalytic domain of *Nostoc* sp. CyaB1 (Ryu et al., 2014). The cyclase activity of IlaC could be enhanced by around six-fold under red light, and functionality in nematodes was demonstrated. For both LAPD and IlaC, a strong dependence of catalytic activity and regulation on the length of the linker between photosensor and effector modules has been observed. Although these dependencies were less pronounced than for YF1, it is nonetheless conceivable that similar mechanisms for signal propagation are at play in YF1, LAPD, and IlaC. While the verdict is still out, future bacteriophytochrome engineering efforts will doubtless benefit from a ground-breaking recent study which revealed that the isolated PAS-GAF-PHY tandem of *D. radiodurans* bacteriophytochrome undergoes a pivot motion upon red-light absorption (**Figure 3C**) (Takala et al., 2014); recent findings imply a similar mechanism in plant phytochromes, too (Burgie et al., 2014; Burgie and Vierstra, 2014).

Light-regulated Order-disorder Transitions

Within the second subcategory of non-associating photoreceptors, several studies have exploited the light-regulated unfolding of the C-terminal Jα helix of phototropin LOV domains, chiefly the *As*LOV2 domain (Harper et al., 2003), in one of essentially three ways: mutually exclusive folding (Strickland et al., 2008), steric restriction of effector active sites (Lee et al., 2008; Wu et al., 2009; Pham et al., 2011; Mills et al., 2012; Schmidt et al., 2014), or uncaging of peptide epitopes (Lungu et al., 2012; Strickland et al., 2012; Renicke et al., 2013; Bonger et al., 2014; Niopek et al., 2014; Yi et al., 2014; Guntas et al., 2015). As explained in Section Thermodynamics of Photoreceptors, in the dark the Jα helix is predominantly folded and docked against the LOV core domain, but upon blue-light absorption it predominantly dissociates and unfolds. In the LOV-TAP protein (Strickland et al., 2008), the C-terminal Jα helix of *As*LOV2 is fused with an N-terminal helix of the *E. coli* TrpR repressor such that steric interference between the two modules results in mutually exclusive folding: the joint helix can either fold unto the *As*LOV2 or the TrpR domain but not unto both simultaneously; correct folding and DNA affinity of TrpR could thus be modestly regulated by blue light.

(Möglich et al., 2009b; Conrad et al., 2014) apparently play key roles in mediating the association reactions; mutations that (de)stabilize these regions, e.g., I52C (Nihongaki et al., 2014) and N56K (Wang et al., 2012), C71V (Zoltowski and Crane, 2008) in *Nc*VVD, can be applied for optimization of the dynamic range of the photoresponse. The *Nc*VVD LOV domain provides the basis for both the "LightON" system for light-induced expression of transgenes in eukaryotic hosts (Wang et al., 2012; Nihongaki et al., 2014) and for the engineering of a light-inducible caspase that elicits apoptosis (Nihongaki et al., 2014). Aureochrome proteins, originally discovered in the stramenopile alga *Vaucheria frigida* (Takahashi et al., 2007), are basic-zipper transcription factors that harbor a LOV domain at their C terminus, thus diverging from the more common topology of N-terminally situated LOV photosensors (Möglich et al., 2010b). By appending aureochrome LOV domains to the intracellular C terminus of receptor tyrosine kinases (RTK), these RTKs could be dimerized upon blue-light exposure, and MAP kinase signaling could be triggered (Grusch et al., 2014). Notably, the natural C-terminal topology of aureochrome LOV domains had to be recapitulated in the engineered RTKs to achieve efficient light regulation; by contrast, use of other associating LOV domains with N-terminal topology failed to yield light-regulated RTKs. EL222 is a bacterial LOV transcription factor that undergoes dimerization and DNA binding to cognate promoters under blue light (Nash et al., 2011). By connecting eukaryotic transactivation domains to EL222, a system for blue-light-induced transgene expression in eukaryotic cell culture and zebrafish larvae was furnished (Motta-Mena et al., 2014).

Although not yet used in photoreceptor engineering, a LOV protein from *Rhodobacter sphaeroides* (*Rs*LOV, Conrad et al., 2013) should be an attractive building block as this homodimeric photoreceptor dissociates into monomers upon blue-light absorption, i.e., it displays the opposite signal polarity than the above LOV systems. A functionally similar system has been engineered on the basis of a circularly permuted PYP protein; a domain-swapped dimer of this modified PYP dissociates into monomers under blue light (Reis et al., 2014).

Several LOV-based systems are available that mediate light-regulated heteroassociation. The plant FKF1 LOV protein associates with the GIGANTEA (GI) protein in blue-light-stimulated manner, and the FKF1:GI pair has been used in the engineering of systems for light regulation of transgene expression in eukaryotic hosts (Yazawa et al., 2009; Polstein and Gersbach, 2012) and ion-channel gating (Dixon et al., 2012). However, wider adoption has been hampered by the large size of GI and the very slow dark recovery of FKF1, lasting several hours to days. Given these shortcomings, several engineered systems for light-regulated heteroassociation based on the *As*LOV2 domain fill a niche not yet fully covered by naturally occurring, associating photoreceptors (Lungu et al., 2012; Strickland et al., 2012). These systems capitalize on the light-induced unfolding of the C-terminal Jα helix of *As*LOV2 and interleaved or appended peptide eptiopes (cf. Section Light-regulated Order-disorder Transitions). Once the peptide epitope is liberated upon light absorption, it can enter intermolecular interactions with a specific binding protein. Ideally, both the modified *As*LOV2 domain and the cognate binding protein are small in size and usable in different modular contexts, e.g., appended N- or C-terminally to target proteins. The TULIP system uses a modified PDZ domain as the binding protein and has been applied to subject MAP kinase signaling (Strickland et al., 2012) and intracellular transport under light control (Van Bergeijk et al., 2015). Two other systems rely on interactions of peptide epitopes with the vinculin and SsrB proteins, respectively (Lungu et al., 2012); a recently improved version of the SsrB-based system appears to outperform both the TULIP and the vinculin-based systems and has been applied to the regulation of GTPase signaling (Guntas et al., 2015). Very recently, the *Nc*VVD photoreceptor, which naturally assembles into a homodimer upon blue-light absorption (cf. above), has been re-engineered into a system for blue-light-induced heterodimerization (Kawano et al., 2015).

The currently most commonly applied photoreceptor systems for light-activated association reactions are based on *A. thaliana* cryptochrome 2 (*At*Cry2) which binds a FAD chromophore and a MTHF (methenyltetrahydrofolate) antenna pigment to respond to blue light (Conrad et al., 2014). Motivated by the initial demonstration that the blue-light-induced dimerization of *At*Cry2 with its partner protein *At*CIB1 (Liu et al., 2008) can be functionally reconstituted in heterologous hosts (Kennedy et al., 2010), the *At*Cry2:*At*CIB1 pair has been used for light control of various biological processes, including expression of transgenes (Kennedy et al., 2010; Liu et al., 2012) and endogenous genes (Konermann et al., 2013; Nihongaki et al., 2015; Polstein and Gersbach, 2015) in eukaryotic cells, DNA recombination (Kennedy et al., 2010), phosphoinositide metabolism (Idevall-Hagren et al., 2012; Kakumoto and Nakata, 2013) and MAP kinase signaling (Aoki et al., 2013; Zhang et al., 2014). A creative and potentially versatile approach is provided by the LARIAT strategy which combines the *At*Cry2:*At*CIB1 pair with multivalent adapter proteins. In this way, diverse target proteins can be recruited in light-triggered manner to larger protein agglomerates with commensurate inhibition of their biological activity (Lee et al., 2014). Studies by Tucker and coworkers showed that N-terminally truncated versions of both *At*Cry2 (residues 1–498) and *At*CIB1 (1–170) suffice for mediating light-induced heteroassociation (Kennedy et al., 2010).

*At*Cry2 is known to reversibly assemble into oligomers under blue light, as for example evident as punctae formation in plant cell nuclei (Yu et al., 2009). Light-dependent clustering of *At*Cry2 can be reconstituted in heterologous hosts and has been exploited in the regulation of GTPase signaling (Bugaj et al., 2013), expression of eukaryotic transgenes (Bugaj et al., 2013), MAP kinase signaling (Wend et al., 2014), RTK signaling (Chang et al., 2014; Kim et al., 2014), SH3 signaling (Taslimi et al., 2014) and clathrin-mediated endocytosis (Taslimi et al., 2014). As discussed in Section Thermodynamics of Photoreceptors, higher-order oligomerization reactions strongly depend on the total monomer concentration: if concentrations are too low, light-induced clustering will be inefficient; if concentrations are too high, clusters will exist under both dark and light conditions. Moreover, the efficiency of *At*Cry2 cluster formation strongly depends upon applied light dose and cell type under

investigation (Taslimi et al., 2014). Recently, the E490G variant of *At*Cry2, denoted "Cry2olig," has been reported as having increased propensity for light-induced oligomerization (Taslimi et al., 2014). While the great utility of Cry2olig is beyond doubt, it is not clear whether improved clustering is entirely due to a higher affinity (K_D^R), or there is a contribution of enhanced expression (cf. Section Thermodynamics of Photoreceptors).

The photoswitchable, fluorescent protein Dronpa has also been converted into a photoreceptor for optogenetics (Zhou et al., 2012). While the K145N mutant of Dronpa undergoes a weak homotetramerization reaction, it can also form a heterodimer with the wild-type protein. In both cases, association is triggered by violet light (400 nm) and can actively be reversed by cyan light (500 nm). Using these Dronpa variants, GTPase signaling and protease activity could be controlled by light. Of key advantage, the chromophore of Dronpa is formed autocatalytically from three residues, and thus no cofactor is required.

At the red end of the visible spectrum, the *A. thaliana* phytochrome *At*PhyB and its interacting proteins *At*PIF3 and *At*PIF6 provide commonly used systems for light-regulated heteroassociation reactions. Note that in the initial implementation of the Phy:PIF system *At*PhyA was used (Shimizu-Sato et al., 2002), but later applications instead employed *At*PhyB. A key advantage of *At*Phys is their photochromic nature (cf. Section Photochromic Photoreceptors): red light (of around 650 nm) promotes association, far-red light (above 700 nm) promotes dissociation. However, plant Phys require either their natural cofactor phytochromobilin (PΦB) or the cyanobacterial phycocyanobilin (PCB) as a surrogate, neither of which occur naturally in most tissues that are targeted by optogenetics. As a consequence, chromophore has to be added exogenously, or additional genes for endogenous production of PCB have to be introduced to target tissues as well (Müller et al., 2013c). Despite this limitation, *At*Phy:*At*PIF-based systems have been successfully used for regulating by light gene expression of eukaryotic transgenes (Shimizu-Sato et al., 2002; Müller et al., 2013b), protein splicing (Tyszkiewicz and Muir, 2008), GTPase signaling (Levskaya et al., 2009), MAP kinase signaling (Toettcher et al., 2013), nuclear transport (Beyer et al., 2015a), as well as sequestration to subcellular compartments (Yang et al., 2013). Similar to the cryptochrome case above, N-terminal fragments of *At*PhyA/B (either residues 1–650 or 1–910) and *At*PIF3/6 (residues 1–100) suffice to elicit red-light-activated, far-red-light-reversible heteroassociation (Levskaya et al., 2009; Müller et al., 2013a,b), with the caveat that a recent study implies that in a yeast transcriptional assay full-length PIF3 supports a higher dynamic range of light activation than the N-terminally truncated version (Pathak et al., 2014). Lastly, the PAS-GAF-PHY tandem of the cyanobacterial phytochrome Cph1 has been shown to associate into a homodimer upon red-light exposure which could be capitalized on in photoreceptor engineering (Strauss et al., 2005).

In summary, a variety of photoreceptor systems exist that achieve different light sensitivity and stoichiometries for association/dissociation reactions. Based on the number of successful engineering examples, the *At*Cry2:*At*CIB1 system currently appears to have the edge; key benefits of this system are low dark activity, reasonably compact tag size, use of widely occurring chromophores, and excitability with widespread illumination sources. By contrast, the *At*Phy:*At*PIF systems suffer from larger tag size, dependence on exogenous chromophore addition (or endogenous heterologous production, Müller et al., 2013c), and requirement for less common light sources. However, the photochromic nature of the Phy:PIF system and the very high dynamic range in at least some applications (Shimizu-Sato et al., 2002) certainly speak strongly in favor of this system. A palpable dearth of side-by-side comparisons between systems has recently been addressed in a laudable study that investigates the performance of several associating photoreceptors under comparable test conditions (Pathak et al., 2014). At least under the specific assay settings tested, *At*PhyB:*At*PIF3 displayed a higher dynamic range for light-regulated gene expression in yeast than *At*Cry2:*At*CIB1 did. While not included in the performance comparison, the recently improved LOV-SsrB system appears an attractive option for light-regulated heteroassociation (Guntas et al., 2015). However, we caution that the performance of associating photoreceptor systems apparently depends on the context in which they are used and tested (Pathak et al., 2014). As a consequence, for some applications a given associating photoreceptor may be the best choice, while in other applications it may be an altogether different one.

Photochromic Photoreceptors

Bacterial and plant phytochromes, cyanobacteriochromes and many rhodopsins are so-called photochromic photoreceptors (**Table 3**) in which the metastable signaling state S, formed after absorption of one photon, can be actively converted back to the dark-adapted state D by absorption of another photon (mostly of different color) (**Figure 5A**). To discriminate between these two light-driven reactions, in the following we denote them as activating and deactivating processes, respectively.

Classes of Photochromic Photoreceptors

Rhodopsins divide into microbial-type proteins (type I), which are exemplified by bacteriorhodopsin, and animal-type proteins (type II), which form a subclass of GPCRs (Ernst et al., 2014). Whereas in microbial rhodopsins the retinal chromophore undergoes an all-*trans* to 13-*cis* isomerization upon light absorption, in animal rhodopsins the retinal isomerizes from 11-*cis* to all-*trans* or *vice versa* (Ernst et al., 2014; Terakita and Nagata, 2014). In vertebrate visual opsins the chromophore is consumed after one isomerization event and the all-*trans* photoproduct needs to be recycled enzymatically to the 11-*cis* educt. By contrast, most microbial and non-visual animal rhodopsins are bistable, i.e., the signaling state thermally reverts to the dark-adapted state or it can be actively reverted by light absorption (Terakita and Nagata, 2014). In some rhodopsins, e.g., in channelrhodopsins (Berndt et al., 2009), mutations have been identified that greatly stabilize photocycle intermediates. As detailed above, originally bovine visual rhodopsins have been employed in the engineering of light-regulated GPCRs, but the design principle (Kim et al., 2005) also extends to other

TABLE 3 | Photochromic photoreceptors.

Class	Subclass/Family	Representative/Paradigm[a]	Cofactor	Activation λ_{max} (nm)	Deactivation λ_{max} (nm)	References
Rhodopsin	Type-I (microbial)	*Cr*HKR1	All-*trans*↔13-*cis* retinal	380	400	Luck et al., 2012
		*Cr*ChR2 C128A	All-*trans*↔13-*cis* retinal	470	530	Berndt et al., 2009
	Type-II (animal)	*Mm*Melanopsin	11-*cis*↔all-*trans* retinal	465	475	Freedman et al., 1999
		*Lj*Parapinopsin	11-*cis*↔all-*trans* retinal	370	515	Koyanagi et al., 2004
Phytochrome	Plant	*At*PhyB	PΦB orPCB	650–670	700–730	Rockwell et al., 2006; Rockwell and Lagarias, 2010
	Bacterial and fungal	*Dr*BphP	BV	700	750	Hughes et al., 1997; Rockwell et al., 2006; Rockwell and Lagarias, 2010
	Cyanobacterial	*Sy*Cph1	PCB	660	705	Rockwell et al., 2006; Rockwell and Lagarias, 2010
	Algal	*Dt*Phy1	PCB	595	725	Rockwell et al., 2014
		*Cp*GPS1	PCB	440	635	Rockwell et al., 2014
		*Es*PHL1	PϕB	690	565	Rockwell et al., 2014
Cyanobacteriochrome	Green/red CBCRs	*Sy*CcaS	PCB	535	670	Hirose et al., 2008
	Red/green CBCRs	*An*PixJ	PCB	650	545	Ikeuchi and Ishizuka, 2008; Rockwell and Lagarias, 2010; Narikawa et al., 2015
		*Am*AM1_1557	PCB (or BV)	650 (700)	545 (620)	
	DXCF CBCRs	*Te*PixJ	PCB→PVB	430	530	Ikeuchi and Ishizuka, 2008; Rockwell and Lagarias, 2010
		*Np*F4973	PCB	435	600	
	Insert-Cys CBCRs	*Np*F2164	PCB→PVB	400	590	Ikeuchi and Ishizuka, 2008; Rockwell and Lagarias, 2010
	Novel dual-Cys CBCR	*Am*AM1_1186	PCB	640	415	Ikeuchi and Ishizuka, 2008; Rockwell and Lagarias, 2010
Other	LOV	*Bs*YtvA	FMN	450	355	Losi et al., 2013
	Cryptochrome	*Cr*Cry	FAD	450	635	Beel et al., 2012
	Dronpa	*Pe*Dronpa	–	400	500	Zhou et al., 2012

[a]*Species abbreviations cf.* ***Tables 1***, ***2*** *and as follows: Am, Acaryochloris marina; An, Anabaena sp.; Cp, Cyanophora paradoxa; Cr, Chlamydomonas reinhardtii; Dt, Dolichomastix tenuilepis; Es, Ectocarpus siliculosus; Lj, Lethenteron japonica; Np, Nostoc punctiforme; Te, Thermosynechococcus elongates.*

animal rhodopsins which offer bistable switching, e.g., vertebrate melanopsin (Freedman et al., 1999) or certain catfish and lamprey rhodopsins (Blackshaw and Snyder, 1997; Koyanagi et al., 2004). In addition, rhodopsin photosensors covalently linked to enzymatic effectors are of interest: the so-called HKR1 rhodopsin from *C. reinhardtii* bears a histidine-kinase effector and can be bidirectionally switched by UV-A and blue light, respectively (Luck et al., 2012); furthermore, a rhodopsin photosensor connected to a guanylate-cyclase effector was recently reported (Avelar et al., 2014).

Phytochromes and cyanobacteriochromes all share a canonical photochemical mechanism in which the primary event is *Z*/*E* isomerization around the C15=C16 double bond of a linear tetrapyrrole (bilin) chromophore covalently attached to a conserved cysteine residue (Rockwell et al., 2006; Rockwell and Lagarias, 2010). As both the 15*Z*→15*E* and the 15*E*→15*Z* isomerization reactions can be driven by light, photochromicity is an inherent property of all bilin-based photoreceptors. The 15*Z* form commonly absorbs light at somewhat shorter wavelengths than the 15*E* form, but there are notable exceptions among the CBCRs (Ikeuchi and Ishizuka, 2008; Rockwell and Lagarias, 2010). Plant and cyanobacterial phytochromes employ the reduced bilin chromophores phycocyanobilin (PCB) and phytochromobilin (PΦB) and transition between red-light-absorbing 15*Z* ($\lambda_{max} \approx$ 650–670 nm) and far-red-light-absorbing 15*E* states ($\lambda_{max} \approx$ 700–730 nm). Bacterial phytochromes instead use the more oxidized biliverdin which gives rise to a red shift of about 30 nm for both states (Rockwell et al., 2006). In conventional Phys the 15*Z* state is the thermally most stable form predominating in the dark; by contrast, in the so-called bathyphytochromes, the 15*E* state is more stable (Rockwell et al., 2006; Rockwell and Lagarias, 2010). In an unexpected twist,

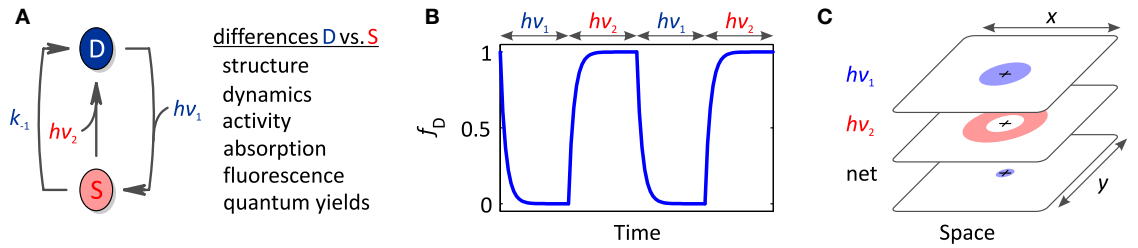

FIGURE 5 | Photochromic photoreceptors. (A) Photochromic photoreceptors derive added versatility from the ability to actively and bidirectionally interconvert dark-adapted and signaling states via absorption of photons of the activating (hv_1) and deactivating wavelengths (hv_2). As these states generally differ in their structure, dynamics, biological activity and spectral properties, light can be used to reversibly toggle these properties. **(B)** Light-driven, bidirectional interconversion enables better time resolution than for non-photochromic photoreceptors. **(C)** Likewise, superior local control is achievable by spatially interleaving different light colors. A setup akin to STED super-resolution microscopy might be implemented to achieve photoreceptor stimulation volumes with supreme spatial resolution.

certain marine alga were recently found to possess phytochromes with absorption maxima for their 15*Z* and 15*E* states that are not in the red/far-red region but essentially cover the entire visible spectrum (Rockwell et al., 2014) and that thus rival cyanobacteriochromes in their spectral diversity. Whereas the photosensor of canonical Phys is composed of PAS, GAF and PHY domains, CBCR photosensors simply consist of a sole GAF domain and thereby offer a much smaller footprint (Ikeuchi and Ishizuka, 2008; Rockwell and Lagarias, 2010). CBCRs distribute into at least four distinct categories, namely red/green, green/red, DXCF and insert-Cys types; as a group, CBCRs display a bewildering spectral and mechanistic diversity and cover the entire UV-A/B and visible spectrum (Ikeuchi and Ishizuka, 2008; Rockwell and Lagarias, 2010). The photocycle of red/green and green/red CBCRs resembles that of traditional red/far-red-responsive plant phytochromes, with 15*Z*↔15*E* isomerization around the C15=C16 double bond of the chromophore as the principal event (Ikeuchi and Ishizuka, 2008; Rockwell and Lagarias, 2010). By contrast, in the DXCF and insert-Cys classes which together form the dual-cysteine CBCRs, the 15*Z*/15*E* isomerization is accompanied by the reversible formation of a covalent thioether bond between a second conserved cysteine and atom C10 of the bilin (Rockwell et al., 2011; Burgie et al., 2013; Narikawa et al., 2013) (**Figure 3D**). Note that in certain DXCF CBCRs the PCB chromophore is autocatalytically isomerized to phycoviolobilin (PVB) which absorbs at shorter wavelengths than PCB (Ishizuka et al., 2011). Intriguingly, the CBCR family may even be more diverse than the above four categories capture: a recently discovered dual-cysteine CBCR fits in neither the DXCF or insert-Cys categories and displays the largest spectral shift observed in CBCRs to date, between a red-absorbing 15*Z* state and a blue-absorbing 15*E* state (Narikawa et al., 2014). Cyanobacteriochromes commonly use the reduced bilins phycocyanobilin and phycoviolobilin as chromophores which generally do not occur in most organisms and cells targeted by optogenetics. However, a recent report (Narikawa et al., 2015) describes a CBCR that binds biliverdin, which widely occurs in many tissues (Shu et al., 2009; Filonov et al., 2011; Gasser et al., 2014), with similar affinity as phycocyanobilin. If biliverdin binding can be extended to other CBCRs and plant Phys, optogenetic deployment of these photoreceptors would be greatly facilitated.

Beyond rhodopsins and the bilin-dependent families, several other photoreceptors also offer photochromic, bidirectional switching. As discussed above, the fluorescent protein Dronpa has been configured into a sensory photoreceptor while retaining its spectral properties including bidirectional switching by violet and cyan light, respectively (Zhou et al., 2012). Furthermore, the signaling state in plant cryptochromes is formed via photoreduction of oxidized FAD to the partially reduced, neutral semiquinone radical form FADH• (Conrad et al., 2014); as shown for a cryptochrome from *C. reinhardtii* (Beel et al., 2012), absorption of a second photon of longer wavelength can drive full reduction to the hydroquinone state $FADH_2$ with concomitant impact on downstream signaling. Finally, in LOV proteins the blue-light-induced adduct between a flavin-nucleotide chromophore and a cysteine residue can be disrupted by UV light to regenerate the dark-adapted state, albeit with low quantum yield (Losi et al., 2013).

Properties of Photochromic Photoreceptors

Owing to bidirectional and reversible switching between the dark-adapted and signaling states, photochromic photoreceptors afford a number of unique advantages. By applying defined mixtures of the activating and deactivating wavelengths, precise ratios of the states D and S can be set and maintained over long times (Toettcher et al., 2013). Furthermore, the bidirectional photoswitching allows the precise confining of the signaling state in both time and space, thus potentially offering higher spatiotemporal resolution than otherwise feasible (**Figures 5B,C**). As detailed in Section Photoreceptor Fundamentals (also cf. **Figure 2A**), *off*-kinetics of light responses are strongly determined by the rate constant for dark recovery k_{-1}. As one remedy, mutations can be introduced that accelerate the dark recovery; however, such mutations concomitantly increase the light intensities required at photostationary conditions for significant population of the signaling state (cf. Section Photoreceptor Fundamentals). A direct, active means of depleting the signaling state is afforded in photochromic photoreceptors via illumination with the "deactivating"

wavelength. Formation of the signaling state and downstream signaling events can hence be controlled with superior temporal precision (**Figure 5B**). If activating and deactivating wavelengths are interleaved in space rather than time, enhanced spatial resolution of formation of the signaling state and elicited physiological responses may be obtained (**Figure 5C**). The ultimate in spatial resolution can arguably be achieved by implementing an illumination scheme corresponding to that underpinning stimulated-emission-depletion (STED) super-resolution microscopy (Hell and Wichmann, 1994), which banks on the fact that individual light waves are subject to the diffraction limit but the spatial superposition of several light waves need not be. Briefly, a spherical illumination profile of the activating wavelength could be superposed with a dough-nut-shaped illumination profile of the deactivating wavelength. In the spatial region where these profiles overlap, a photochromic photoreceptor would be continuously toggled between the dark-adapted and signaling states. The net result of this tug-of-war would be determined by the intensities of activating and deactivating wavelengths as a function of space as well as the quantum yields for the activating and deactivating reactions. Whereas in STED the deactivating wavelength promotes an emissive transition originating from a short-lived, electronically excited state, the corresponding application to photochromic photoreceptors would involve light-driven transitions between comparatively long-lived electronic ground states; hence, we expect that much less light power for both the activating and the deactivating light pulses will be needed than in STED. To our knowledge experiments along these lines have not been realized yet, but if they prove feasible, they may well enable "super-resolution optogenetics."

Light-driven, bidirectional and reversible toggling between dark-adapted and signaling states makes photochromic photoreceptors also attractive for applications beyond their use as light-regulated actuators. Crucially, the two states not only differ in their biological activity but also in several other parameters including absorption and fluorescence properties. Photochromic photoreceptors might hence be developed into photoswitchable or photoactivatable fluorescent proteins.

Fluorescent Photoreceptors

Sensory photoreceptors are generally geared toward efficient photochemistry so as to achieve high sensitivity for light perception, cf. Section Photoreceptor Fundamentals; by contrast, the quantum yield for competing fluorescence processes is generally low. If, however, canonical photochemistry is impaired, e.g., via mutagenesis or protein truncation, fluorescence quantum yields can be greatly increased, and photoreceptors can thus be turned into efficient fluorescent proteins (FP), as demonstrated for LOV proteins (Drepper et al., 2007; Chapman et al., 2008) and bacterial phytochromes (Piatkevich et al., 2013a; Shcherbakova et al., 2015). Notably, the opposite route of converting FPs into sensory photoreceptors has been taken for the Dronpa protein (cf. Section Associating Photoreceptors and Optogenetic Applications) (Zhou et al., 2012). Since photoreceptor-derived FPs share with natural ones the key property of genetic encoding, they can be used as versatile reporters in much the same way as conventional FPs, provided their chromophores are available to sufficient extent. A broad palette of naturally occurring FPs notwithstanding, there are several use cases where FPs derived from sensory photoreceptors offer particular benefits.

First, LOV domains, which are rendered fluorescent by removal of a conserved cysteine residue required for canonical photochemistry (Drepper et al., 2007; Chapman et al., 2008), have a size of about 120 residues and are thus significantly smaller than the GFP-type jellyfish FPs (∼220 residues). This size difference can be decisive in certain biological applications, e.g., those relying on transfection with viruses that have stringent limits on their genome size (Chapman et al., 2008; Konermann et al., 2013). Second, in contrast to jellyfish FPs, photoreceptor-derived FPs do not undergo slow maturation processes but become fluorescent once they incorporate their chromophore. Moreover, maturation of conventional FPs depends on molecular oxygen, making them less suited for studies under anoxic or low-oxygen conditions than photoreceptor-derived FPs which readily incorporate their chromophores in the absence of oxygen (Chapman et al., 2008). However, we caution that both the flavin-nucleotide and linear-tetrapyrrole chromophores used by LOV domains and bacteriophytochromes, respectively, are oxidized compounds and may hence not be present in sufficient amounts at very low oxygen concentrations. Further note that in the presence of oxygen, LOV domains lacking the conserved cysteine residue not only show increased fluorescence, but also they become efficient photosensitizers for generation of singlet-oxygen species. Although this property can deliberately be exploited, e.g., for blue-light-driven cell ablation (Qi et al., 2012), it may cause inadvertent effects in LOV fluorescence applications. Third, fluorescent reporters derived from bacteriophytochromes provide excitation and emission at longer wavelengths than can be achieved with conventional FPs (Shu et al., 2009; Filonov et al., 2011; Piatkevich et al., 2013a; Shcherbakova et al., 2015). Of particular relevance, bacteriophytochromes have been engineered that absorb and fluoresce within the near-infrared window of the electromagnetic spectrum (cf. **Figure 1**). In this wavelength regime, high penetration depths of light are afforded, and applications in deep tissue are enabled (cf. Section Photoreceptor Fundamentals). Fourth, photoreceptor-derived FPs not only serve as static markers but also as dynamic sensors for protein-protein interactions and certain cellular parameters (Shcherbakova et al., 2015). Specifically, the pumping activity in light-driven rhodopsin proton pumps has been disrupted by mutagenesis to yield weakly fluorescent proteins that report on membrane potential (Kralj et al., 2011, 2012). The resultant fully genetically encodable, voltage sensors have been used to visualize spontaneous membrane-voltage fluctuations in *E. coli* (Kralj et al., 2011) as well as action potentials in neuronal cells (Kralj et al., 2012). Fifth, sensory photoreceptors could prove particularly useful in the design of photoactivatable/photoswitchable FPs (Patterson and Lippincott-Schwartz, 2002). Notably, photoswitching is an inherent property of all photoreceptors, since light absorption drives transitions between dark-adapted and signaling states (plus additional states that may occur in

the photocycle). In case of photochromic photoreceptors (cf. Section Photochromic Photoreceptors), state transitions can even be triggered in both directions by different colors of light. Since these states can considerably differ in their fluorescence properties (absorption and emission spectra, quantum yields), photochromic photoreceptors may be confectioned into versatile and efficient photoswitchable fluorescent probes. This has strikingly been demonstrated for certain bacteriophytochrome variants that serve as photoactivated, near-infrared fluorescent proteins (Piatkevich et al., 2013b).

For space constraints, we can but skim the engineering and fascinating applications of fluorescent photoreceptors; for in-depth coverage we recommend two recent review articles (Piatkevich et al., 2013a; Shcherbakova et al., 2015). The combination of sensory photoreceptors with fluorescent proteins, be it natural proteins, be it re-engineered proteins, augurs all-optical experiments in which both perturbation and readout are conducted optically. Since light-regulated actuators and fluorescent sensors are genetically encoded agents, such experiments can be conducted with the same level of reversibility, non-invasiveness and spatiotemporal definition as conventional optogenetic experiments. All-optical approaches should be particularly useful for closed-loop optogenetics where the behavior of a system is continuously monitored over time, and a measurable quantity, e.g., reporter fluorescence, is converted online into appropriate light pulses for optogenetic conditioning of said system (Paz et al., 2013). A particular impressive demonstration of the all-optical concept is provided by the combination of rhodopsin-based voltage sensors and light-gated ion channels that allow the simultaneous triggering and interrogation of action potentials in neurons (Hochbaum et al., 2014). Other biological processes, in particular cyclic-nucleotide metabolism, should also be amenable to all-optical approaches (Richter et al., 2015).

Guidelines for Photoreceptor Engineering

The multitude of nifty applications in optogenetics impressively demonstrates the broad usefulness and general applicability of engineered photoreceptors. Although design presently proceeds on a case-by-case basis and often requires repeat trials before eventual success, powerful principles and recipes emerge that have proven particularly versatile and that may expedite future engineering efforts. In this chapter, we hence strive to distill insight gleaned from numerous specific examples into general guidelines for photoreceptor engineering. Of course, no single approach provides a panacea succeeding in each and every instance, but we hope the reader will find the below discussion illuminating. We subdivide this chapter into several interlinked, desirable traits in light-responsive systems and outline how they may be realized in photoreceptor engineering and optogenetic applications (**Table 4**).

Design Strategy

Arguably, the foremost consideration in photoreceptor engineering is that of eventual success: will arduous work finally bear fruit, and which is the most promising strategy to establish the desired light-responsive system? The sheer diversity of the above case studies strikingly illustrates that the choice of the most appropriate strategy is intricately linked to the identities of the desired sensor input and effector output. As a corollary, there is no single solution that guarantees success in each and every scenario; in this section, we hence draw general inferences from current examples, rather than treating individual cases for which we refer to Section Allostery of Photoreceptors and literature cited therein. In the following, we present recurring strategies that have been particularly successful in photoreceptor engineering and optogenetics (also cf. **Table 4**).

By and large, the further one departs from natural systems (or previously engineered ones), the more challenging engineering and optogenetic applications become. By that token, in an ideal scenario, a natural photoreceptor exists that already exerts the demanded light-regulated biological activity and that can hence be used in optogenetics without any modification. Notable representatives are the light-gated channelrhodopsins (Nagel et al., 2002, 2003), certain animal rhodopsins (Oh et al., 2010; Spoida et al., 2014) and several light-activated nucleotide cyclases based on BLUF, LOV and rhodopsin photosensors (Schröder-Lang et al., 2007; Ryu et al., 2010; Stierl et al., 2011; Raffelberg et al., 2013; Avelar et al., 2014). Given the vast amounts of genome data (becoming) available, additional protein architectures of immediate optogenetic utility may be discovered in future (**Figure 6**).

In the absence of suitable natural photoreceptors, the most predictable and successful strategies in engineering light-responsive systems are based on light-dependent association reactions (cf. Section Associating Photoreceptors and Optogenetic Applications). Crucially, light-dependent recruitment and colocalization provide clear design rationales, especially when the target effector modules are naturally regulated via oligomerization processes. Strategies based on light-dependent association readily extend to split proteins where biological activity is only regained once the two halves are brought into proximity. Structural requirements of the linker between photosensor and effector modules are minimal, greatly facilitating photoreceptor engineering (cf. Section Associating Photoreceptors and Optogenetic Applications). Moreover, concrete design templates are provided by an ample body of literature on regulation of biological processes via chemically induced association. On the downside, light-regulated association reactions strongly depend on photoreceptor concentration which needs to be taken into account in applications (cf. Section Thermodynamics of Photoreceptors and Genetic Encoding). The relative performance of different associating photoreceptors may vary depending upon application context, and ideally several should be tested to achieve optimal optogenetic response.

Another class of highly versatile strategies for photoreceptor engineering capitalize on the light-triggered unfolding of the helical Jα appendage in the *As*LOV2 domain (Harper et al., 2003), where, again, a relatively clear design rationale is given (cf. Section Light-regulated Order-disorder Transitions). Interestingly, light-regulated Jα unfolding has been tapped in quite different, creative ways, e.g., to control the folding of

TABLE 4 | Desiderata in photoreceptor engineering.

Aspect	Challenges and measures
Design strategy	Most promising strategy to pursue? I. natural photoreceptor available II. associating photoreceptors (Section Associating Photoreceptors and Optogenetic Applications) III. order-disorder transitions (Section Light-regulated Order-disorder Transitions) IV. homologous exchange of sensor modules (Section Light-regulated Tertiary and Quaternary Structural Transitions)
Dynamic range	Maximum activity difference dark vs. light? (Section Photoreceptor Fundamentals.) I. maximize free energy perturbation $\Delta\Delta G$ by choice of photosensor/effector, by linker optimization, by mutagenesis, by use of oligomeric photoreceptors II. minimize specific activity of T state and maximize specific activity of R state, e.g., by choice of effector, by mutagenesis III. embed photoreceptor in signaling networks that amplify response
Genetic encoding	Functional expression *in situ*? I. codon optimization II. cell-type-specific promoters III. intracellular trafficking signals IV. ensure chromophore supply, e.g., by resorting to photoreceptors that use retinal, flavin-nucleotide and biliverdin chromophores
In situ activity	Appropriate activity levels *in situ*? I. adjust expression levels, especially for associating photoreceptors (Section Photoreceptor Fundamentals) II. vary specific activity by choice of effector module, by mutagenesis (e.g., attenuation of activity) III. embed photoreceptors in signaling networks for amplification of response
Light sensitivity	Can photoreceptor be activated to sufficient extent *in situ*? I. increase light power, improve light delivery II. use photoreceptors sensitive to long wavelengths at which light penetrates tissue more deeply III. embed photoreceptor in signaling networks for response amplification IV. modulate effective light sensitivity at photostationary state by variation of dark-recovery kinetics (Section Photoreceptor Fundamentals)
Temporal resolution	Are the response kinetics sufficiently fast? I. accelerate *on*-kinetics by increasing light power, by signal amplification (so that activation of fewer photoreceptors suffices), by speeding up downstream biological processes II. accelerate *off*-kinetics by choice of photosensor, by speeding up dark-recovery reaction via mutagenesis, by speeding up downstream biological processes III. use photochromic photoreceptors for temporal depletion of signaling state (Section Photochromic Photoreceptors)
Spatial resolution	How can spatial resolution be improved? I. cell-type-specific expression and subcellular trafficking (Section Genetic Encoding) II. spatially restricted illumination III. use photochromic photoreceptors for spatial depletion of signaling state (Section Photochromic Photoreceptors)
Orthogonality	Parallel use of several photoreceptors and fluorescent proteins? I. selective excitation via spectral separation II. selective excitation via different light sensitivities III. selective excitation via different recovery kinetics IV. use photochromic photoreceptors to counteract inadvertent cross-talk between excitation channels

covalently linked effector domains (Strickland et al., 2008), to control conformation and accessibility of peptide epitopes (Renicke et al., 2013; Bonger et al., 2014), or to control protein association (Lungu et al., 2012; Strickland et al., 2012). Often, the precise linker length and sequence have to be optimized to achieve efficient light regulation (e.g., Strickland et al., 2008; Wu et al., 2009). Moreover, several mutations have been identified that modulate the order-disorder equilibrium and that can thus be used to optimize the dynamic range of the light response (cf. Section Light-regulated Order-disorder Transitions). In general, light-regulated unfolding reactions are not specific to *As*LOV2 but represent a more general aspect of sensory photoreceptors as for example manifest in PYP. Consequently, similar engineering approaches may be implemented on the basis of photosensors other than *As*LOV2 and related phototropin LOV domains.

A last class of reasonably successful engineering strategies involve the recombination of homologous (photo)sensor and

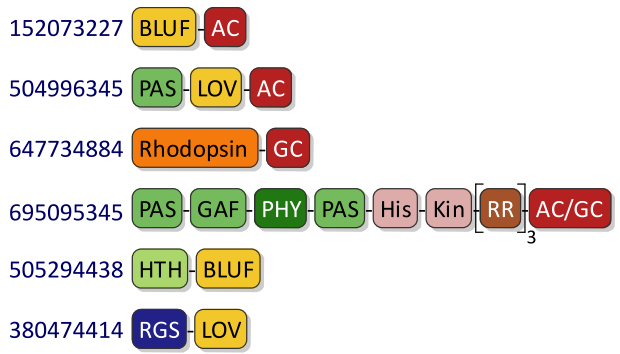

FIGURE 6 | Natural photoreceptors as optogenetic tools. Certain naturally occurring photoreceptors can serve as powerful light-regulated actuators in optogenetics without any need for re-engineering. The diagram shows domain architectures of select sensory photoreceptors that have been deployed for optogenetics or that could be used to that effect; exemplary Genbank accession numbers are provided that possess certain architectures. Abbreviations as in main text and as follows: AC, adenylate cyclase; GC, guanlyate cyclase; HTH, helix-turn-helix; RGS, regulator of G-protein signaling; RR, response regulator.

effector modules (e.g., Kim et al., 2005; Möglich et al., 2009a; Gasser et al., 2014) (cf. Section Light-regulated Tertiary and Quaternary Structural Transitions). As a design rationale, one exploits that sequence and structural homology between these modules often entails functional and mechanistic correspondence. However, this correspondence may not necessarily be a given, and several modules and design architectures may have to be tested to ensure eventual success. Moreover, in the first place, this engineering strategy depends on the availability of suitable homologous signal receptors and therefore appears less versatile than the above approaches based on light-dependent association and order-disorder transitions. Within this class, requirements on linker sequence and length are more demanding, as the linker often adopts defined structure and plays a critical role in governing overall activity, signal polarity and dynamic range (cf. Section Light-regulated Tertiary and Quaternary Structural Transitions).

At the end of this section, we reiterate that the selection of the best engineering strategy is tightly correlated with the identities of sensor and effector. Regardless of the precise strategy, all approaches benefit from efficient functional assays that allow the construction and screening of many candidate designs as well as the incremental improvement of functional designs. In particular, several studies demonstrate that the combination of random mutagenesis and high-throughput screening, often *in vivo*, can efficiently identify photoreceptor variants with altered and improved properties (e.g., Christie et al., 2007; Gleichmann et al., 2013; Ryu et al., 2014; Taslimi et al., 2014). These and related screening setups will doubtless be instrumental in photoreceptor engineering approaches that depart from the three categories listed above.

Dynamic Range

A key characteristic of sensory photoreceptors is their dynamic range for light regulation, i.e., the factor difference in activity between the dark-adapted and signaling states (cf. Section Thermodynamics of Photoreceptors). As illustrated in **Figure 2**, dynamic range is governed by both the amount of free energy that can be derived from incident light and the intrinsic activities a_R and a_T of the R and T states of the receptor. Notably, the maximum dynamic range that can be achieved is limited by the ratio of a_R/a_T and by how well activity can be shut down in the low-activity state T, i.e., in the dark state for light-activated photoreceptors. Visible light has an energy content of a few hundred kJ per mol of absorbed photons which in principle would suffice to shift the equilibrium between T and R by many orders of magnitude. However, the amount of this energy that can be translated into relevant free energy changes is actually far less, for example about 16 kJ mol^{-1} for *As*LOV2 (Yao et al., 2008). Due to a pervasive lack of detailed biophysical data, neither is it known which value this parameter assumes in other photoreceptors nor how it could be modified (improved). Depending on the specific photoreceptor system, the intrinsic activities of T and R might be modulated via variation of photosensor and effector. For example, biological activity may be attenuated by homologous exchange of one effector module for another with different specific activity or by mutagenesis near the active site. Moreover, dynamic range can be improved by embedding (engineered) photoreceptors in downstream cellular signaling networks such that the light response is enhanced. Notably, amplification mechanisms of this kind are integral parts of cellular signaling, e.g., in gene-expression networks or in pathways involving second messengers (Stierl et al., 2011; Gasser et al., 2014; Jansen et al., 2015), and can be co-opted for optogenetic intervention. Furthermore, for oligomeric photoreceptors formation of the R state may be cooperative and may require the concomitant population of the signaling state in several photosensor domains, as illustrated in **Figure 2F** for associating photoreceptors and experimentally observed in the dimeric histidine kinase YF1 where both LOV subunits need to reside in their dark-adapted states to obtain full effector output (Möglich et al., 2009a). By this means, a larger free energy difference could be derived from light than achievable for a sole photosensor module. Finally, a more specific mechanism for amplification is realized in histidine kinases, like YF1, which catalyze opposing elementary phosphorylation and phosphatase reactions; since the biological response is governed by the net balance of these reactions, relatively small changes in the respective individual velocities may elicit disproportionally large net effects.

Genetic Encoding

To enable optogenetic perturbation of cells and tissues, photoreceptors have to be functionally expressed *in situ*. In many organisms, cell-specific promoters are known that restrict gene expression to a select set of cells or even to individual cells. In addition, it is desirable to direct photoreceptors to specific cellular compartments and organelles which could be accomplished via targeting sequences or fusion with (inert) proteins that normally reside at these sites (Zalocusky et al., 2013). As another necessary requirement, the chromophore cofactor of photoreceptors has to be available in sufficient

quantities in the target tissue, and it has to be incorporated autonomously. Although the latter is generally true, the former is not necessarily given. Apparently, flavin nucleotides, retinal and the linear tetrapyrrole biliverdin widely occur across different cells and organisms (cf. Section Photoreceptor Fundamentals). By contrast, the tetrapyrrole phycocyanobilin utilized by plant phytochromes and cyanobacteriochromes is generally not available in most cells; it either needs to be added exogenously or produced endogenously by additionally introduced heterologous enzymes.

In Situ Activity

Another important consideration is the overall activity levels of sensory photoreceptors *in situ* which are determined by expression levels and specific activity. Depending upon application, overall activity has to be adjusted to certain ranges to achieve relevant light-induced effects. If several photoreceptor systems with congruent functionality are available, as for light-activated adenylate cyclases (Schröder-Lang et al., 2007; Ryu et al., 2010; Stierl et al., 2011; Raffelberg et al., 2013; Avelar et al., 2014), one may select according to the specific activity of these systems. As outlined above, photoreceptors can be integrated into downstream signaling cascades so as to modulate or amplify the light effect. Expression and activity levels are of particular relevance for associating photoreceptors since their behavior and light response can vastly differ between concentration regimes (cf. Section Thermodynamics of Photoreceptors and Associating Photoreceptors and Optogenetic Applications and **Figure 2F**).

Light Sensitivity

Light delivery and light sensitivity are closely linked aspects in optogenetic applications. Depending upon the quality (color) and quantity (dose) required, light delivery to target sites *in situ* can be challenging, especially where opaque tissues and entire organs or animals are concerned. Short of increasing light power which is subject to demanding technical and biological limitations, light sensitivity may be optimized regarding both color and dose. Certain photoreceptors, namely phytochromes and cyanobacteriochromes, can be sensitive to red and infra-red light which penetrates tissue more deeply than light of shorter wavelengths. Especially within the "near-infra-red window," lower light powers may hence suffice in optogenetic experiments (cf. **Figure 1**). To further decrease required light powers, the light response could be amplified in downstream signaling networks (cf. Section Dynamic Range), or the light sensitivity could be increased. Many optogenetic experiments are conducted at photostationary conditions, where individual photoreceptors repeatedly shuttle between their dark-adapted and signaling states, D and S, respectively. As discussed in Section Photoreceptor Fundamentals, in this regime, the effective light sensitivity is not only governed by the absolute sensitivity, i.e., the kinetics of going from D to S, but also by the reverse kinetics of going from S to D (cf. **Figure 2A**). The absolute light sensitivity can at best be modulated within rather narrow ranges; in particular, there is very limited scope for further enhancement since the quantum yields for photoreception are intrinsically high and cannot be increased beyond unity. By contrast, at least for some photoreceptor classes (phytochromes, LOV and rhodopsins) the reverse reaction and hence the effective light sensitivity can be varied by mutation across many orders of magnitude, cf., e.g., (Berndt et al., 2009), albeit at the cost of simultaneously affecting *off*-kinetics.

Temporal Resolution

Many optogenetic applications necessitate high temporal precision of both the *on*- and *off*-kinetics of the light response. As discussed in Section Photoreceptor Fundamentals, formation of the signaling state of photoreceptors after photon absorption occurs on the microseconds or faster timescale and hence is not rate-limiting for most biological scenarios. Rather, *on*-kinetics are limited by light delivery *in situ*, by the number of photoreceptors that need to assume their signaling state for triggering downstream signaling, and by ensuing biological processes that may be slow, e.g., gene expression. Accordingly, to accelerate *on*-kinetics, light power could be increased, the biological response could be amplified so that fewer photoreceptors need to assume their signaling state, and, in some cases, downstream biological processes could conceivably be accelerated. By contrast, *off*-kinetics are limited by the intrinsic dark-recovery reaction that returns the photoreceptor to its resting state, and by biological processes that may be inherently slow. Often, dark-recovery rates are strongly temperature-dependent and may hence become limiting if temperature is lowered. At least for LOV, rhodopsin and phytochrome photoreceptors, mutations are documented that can be introduced to deliberately modulate the recovery kinetics, although with two caveats: first, a change in dark-recovery kinetics will invariably affect the effective light sensitivity at photostationary state (cf. Section Photoreceptor Fundamentals and Light Sensitivity); second, these mutations should not be used indiscriminately as they could impair signal transduction (Diensthuber et al., 2014). Photochromic photoreceptors offer clear advantages in achieving fast *off*-kinetics since the return of the signaling state to the dark-adapted state of the photoreceptor can actively be driven by light (cf. Section Photochromic Photoreceptors).

Spatial Resolution

As another key advantage, optogenetics grants superior spatial resolution over competing perturbational approaches. One layer of spatial control is commonly achieved by cell-specific expression of sensory photoreceptors so that light sensitivity is confined to desired areas (cf. Section Genetic Encoding). Another layer is provided by spatially confined illumination so that photoreceptor activation is locally restricted, as impressively shown for, e.g., PA-Rac1 (Wu et al., 2009). Photochromic photoreceptors should be well-suited for achieving high spatial resolution in optogenetics since they can be bidirectionally toggled between states of different biological activity (e.g., Levskaya et al., 2009, and cf. Section Properties of Photochromic Photoreceptors). Crucially, not only can illumination thus be used to define areas of photoreceptor activation, but also areas of photoreceptor deactivation can be specified. For example, enhanced spatial resolution could benefit the optical targeting

of subcellular compartments and of individual cells within eukaryotic tissues or microbial agglomerates.

Orthogonality

If several sensory photoreceptors are deployed in parallel or in conjunction with fluorescent reporters (cf. Section Fluorescent Photoreceptors), it is imperative that light activation occur in an orthogonal manner, i.e., without inadvertent activation of other processes. Such orthogonality can be accomplished by spectral separation of light-responsive systems, e.g., by combining photoreceptors that are activated by blue light with fluorescent reporters that are monitored using red light. Generally, it appears favorable to resort to FPs sensitive to longer wavelengths than used for photoreceptor activation; notably, photoreceptors may be maximally sensitive to a relatively long wavelength, e.g., to red light in case of phytochromes, but to some extent they will be excited by all shorter wavelengths as well, e.g., by blue light. Again, photochromic photoreceptors offer unique advantages in that both formation and depletion of the signaling state can be controlled by light of different colors (cf. Section Photochromic Photoreceptors). If spectral separation is not feasible, orthogonality may still be achieved by resorting to systems that significantly differ in their light sensitivity, at the level of either the sensory photoreceptor or the associated downstream biological response. In a similar vein, separation may be possible in the kinetic domain; if two light-responsive systems strongly differ in dark-recovery kinetics, selective activation of the system with the slower recovery could be effected by pulsed illumination. These concepts are exemplified by the recently discovered channelrhodopsin variants Chronos and Chrimson (Klapoetke et al., 2014; Schmidt and Cho, 2015): Chrimson can be selectively excited with red light which Chronos does not respond to; *vice versa*, Chronos can be selectively excited with defined intensities of blue light as it is much more sensitive (in terms of photocurrents) than Chrimson which also responds to blue light, albeit to much lower extent. Moreover, Chronos has much faster response kinetics than Chrimson which allows kinetic separation (Schmidt and Cho, 2015). Given the continuing success of optogenetics and the emergence of all-optical approaches (Hochbaum et al., 2014; Richter et al., 2015), we expect orthogonal activation of sensory photoreceptors to become increasingly relevant.

Conclusion

Owing to tremendous advances over the recent past, optogenetics now constitutes a general, highly versatile and readily implementable approach for the perturbation and quantitative analysis of diverse cellular processes across the neurosciences and biology. Whereas initially optogenetics and photoreceptor engineering had been the province of specialists, by now they have well moved into the domain of applicants interrogating specific cellular and neural circuits. This welcome development is doubtless aided by the availability of a rich and continuously expanding toolkit of natural and engineered light-regulated actuators. At the same time, the emergence of particularly successful and reusable templates for photoreceptor engineering reviewed here (cf. Section Allostery of Photoreceptors and Guidelines for Photoreceptor Engineering) further promotes the wider adoption of optogenetics. Currently deployed optogenetic actuators mostly target general, broad-range processes as gene expression, membrane potential changes, protein-protein interactions, protein degradation or second-messenger metabolism. If, however, photoreceptor engineering further improves and simplifies to the extent where it becomes essentially predictable, more specific, narrow-range processes, e.g., the activity of particular protein kinases with just a few substrates, become worthwhile targets for optogenetic intervention. Beyond optogenetics, we note the recent emergence of conceptually similar techniques for the spatiotemporally defined, non-invasive and reversible perturbation of cellular events that rely on application of radio waves and alternating magnetic fields instead of light (Stanley et al., 2012, 2015; Leibiger and Berggren, 2015). These so-called radiogenetic and magnetogenetic strategies (Leibiger and Berggren, 2015) could well supplement existing and future optogenetic approaches.

Acknowledgments

Discussions with Dr. Keith Moffat and members of our group are greatly appreciated. Our laboratory is generously supported through a Sofja-Kovalevskaya Award by the Alexander-von-Humboldt Foundation (to AM).

References

Airan, R. D., Thompson, K. R., Fenno, L. E., Bernstein, H., and Deisseroth, K. (2009). Temporally precise *in vivo* control of intracellular signalling. *Nature* 458, 1025–1029. doi: 10.1038/nature 07926

Anantharaman, V., Balaji, S., and Aravind, L. (2006). The signaling helix: a common functional theme in diverse signaling proteins. *Biol. Direct* 1:25. doi: 10.1186/1745-6150-1-25

Aoki, K., Kumagai, Y., Sakurai, A., Komatsu, N., Fujita, Y., Shionyu, C., et al. (2013). Stochastic ERK activation induced by noise and cell-to-cell propagation regulates cell density-dependent proliferation. *Mol. Cell* 52, 529–540. doi: 10.1016/j.molcel.2013.09.015

Avelar, G. M., Schumacher, R. I., Zaini, P. A., Leonard, G., Richards, T. A., and Gomes, S. L. (2014). A rhodopsin-guanylyl cyclase gene fusion functions in visual perception in a fungus. *Curr. Biol.* 24, 1234–1240. doi: 10.1016/j.cub.2014.04.009

Beel, B., Prager, K., Spexard, M., Sasso, S., Weiss, D., Müller, N., Heinnickel, M., et al. (2012). A flavin binding cryptochrome photoreceptor responds to both blue and red light in Chlamydomonas reinhardtii. *Plant Cell* 24, 2992–3008. doi: 10.1105/tpc.112.098947

Berndt, A., Yizhar, O., Gunaydin, L. A., Hegemann, P., and Deisseroth, K. (2009). Bi-stable neural state switches. *Nat. Neurosci.* 12, 229–234. doi: 10.1038/nn.2247

Beyer, H. M., Juillot, S., Herbst, K., Samodelov, S. L., Müller, K., Schamel, W. W., et al. (2015a). Red light-regulated reversible nuclear localization

of proteins in mammalian cells and zebrafish. *ACS Synth. Biol.* doi: 10.1021/acssynbio.5b00004

Beyer, H. M., Naumann, S., Weber, W., and Radziwill, G. (2015b). Optogenetic control of signaling in mammalian cells. *Biotechnol. J.* 10, 273–283. doi: 10.1002/biot.201400077

Blackshaw, S., and Snyder, S. H. (1997). Parapinopsin, a novel catfish opsin localized to the parapineal organ, defines a new gene family. *J. Neurosci.* 17, 8083–8092.

Bonger, K. M., Rakhit, R., Payumo, A. Y., Chen, J. K., and Wandless, T. J. (2014). General method for regulating protein stability with light. *ACS Chem. Biol.* 9, 111–115. doi: 10.1021/cb400755b

Brown, B. A., Cloix, C., Jiang, G. H., Kaiserli, E., Herzyk, P., Kliebenstein, D. J., et al. (2005). A UV-B-specific signaling component orchestrates plant UV protection. *Proc. Natl. Acad. Sci. U.S.A.* 102, 18225–18230. doi: 10.1073/pnas.0507187102

Bugaj, L. J., Choksi, A. T., Mesuda, C. K., Kane, R. S., and Schaffer, D. V. (2013). Optogenetic protein clustering and signaling activation in mammalian cells. *Nat. Methods* 10, 249–252. doi: 10.1038/nmeth.2360

Burgie, E. S., Bussell, A. N., Walker, J. M., Dubiel, K., and Vierstra, R. D. (2014). Crystal structure of the photosensing module from a red/far-red light-absorbing plant phytochrome. *Proc. Natl. Acad. Sci. U.S.A.* 111, 10179–10184. doi: 10.1073/pnas.1403096111

Burgie, E. S., and Vierstra, R. D. (2014). Phytochromes: an atomic perspective on photoactivation and signaling. *Plant Cell* 26, 4568–4583. doi: 10.1105/tpc.114.131623

Burgie, E. S., Walker, J. M., Phillips, G. N. Jr., and Vierstra, R. D. (2013). A photolabile thioether linkage to phycoviolobilin provides the foundation for the blue/green photocycles in DXCF-cyanobacteriochromes. *Structure* 21, 88–97. doi: 10.1016/j.str.2012.11.001

Chang, K.-Y., Woo, D., Jung, H., Lee, S., Kim, S., Won, J., et al. (2014). Light-inducible receptor tyrosine kinases that regulate neurotrophin signalling. *Nat. Commun.* 5, 4057. doi: 10.1038/ncomms5057

Chapman, S., Faulkner, C., Kaiserli, E., Garcia-Mata, C., Savenkov, E. I., Roberts, A. G., et al. (2008). The photoreversible fluorescent protein iLOV outperforms GFP as a reporter of plant virus infection. *Proc. Natl. Acad. Sci. U.S.A.* 105, 20038–20043. doi: 10.1073/pnas.0807551105

Chen, D., Gibson, E. S., and Kennedy, M. J. (2013). A light-triggered protein secretion system. *J. Cell Biol.* 201, 631–640. doi: 10.1083/jcb.201210119

Christie, J. M., Arvai, A. S., Baxter, K. J., Heilmann, M., Pratt, A. J., O'Hara, A., et al. (2012). Plant UVR8 photoreceptor senses UV-B by tryptophan-mediated disruption of cross-dimer salt bridges. *Science* 335, 1492–1496. doi: 10.1126/science.1218091

Christie, J. M., Corchnoy, S. B., Swartz, T. E., Hokenson, M., Han, I.-S., Briggs, W. R., et al. (2007). Steric interactions stabilize the signaling state of the LOV2 domain of phototropin 1. *Biochemistry* 46, 9310–9319. doi: 10.1021/bi700852w

Chung, K., Wallace, J., Kim, S.-Y., Kalyanasundaram, S., Andalman, A. S., Davidson, T. J., et al. (2013). Structural and molecular interrogation of intact biological systems. *Nature* 497, 332–337. doi: 10.1038/nature12107

Conrad, K. S., Bilwes, A. M., and Crane, B. R. (2013). Light-induced subunit dissociation by a light-oxygen-voltage domain photoreceptor from *Rhodobacter sphaeroides*. *Biochemistry* 52, 378–391. doi: 10.1021/bi3015373

Conrad, K. S., Manahan, C. C., and Crane, B. R. (2014). Photochemistry of flavoprotein light sensors. *Nat. Chem. Biol.* 10, 801–809. doi: 10.1038/nchembio.1633

Crefcoeur, R. P., Yin, R., Ulm, R., and Halazonetis, T. D. (2013). Ultraviolet-B-mediated induction of protein-protein interactions in mammalian cells. *Nat. Commun.* 4, 1779. doi: 10.1038/ncomms2800

Deisseroth, K., Feng, G., Majewska, A. K., Miesenböck, G., Ting, A., and Schnitzer, M. J. (2006). Next-generation optical technologies for illuminating genetically targeted brain circuits. *J. Neurosci.* 26, 10380–10386. doi: 10.1523/JNEUROSCI.3863-06.2006

Diensthuber, R. P., Bommer, M., Gleichmann, T., and Möglich, A. (2013). Full-length structure of a sensor histidine kinase pinpoints coaxial coiled coils as signal transducers and modulators. *Structure* 21, 1127–1136. doi: 10.1016/j.str.2013.04.024

Diensthuber, R. P., Engelhard, C., Lemke, N., Gleichmann, T., Ohlendorf, R., Bittl, R., et al. (2014). Biophysical, mutational, and functional investigation of the chromophore-binding pocket of light-oxygen-voltage photoreceptors. *ACS Synth. Biol.* 3, 811–819. doi: 10.1021/sb400205x

Dixon, R. E., Yuan, C., Cheng, E. P., Navedo, M. F., and Santana, L. F. (2012). Ca^{2+} signaling amplification by oligomerization of L-type Cav1.2 channels. *Proc. Natl. Acad. Sci. U.S.A.* 109, 1749–1754. doi: 10.1073/pnas.1116731109

Drepper, T., Eggert, T., Circolone, F., Heck, A., Krauss, U., Guterl, J.-K., et al. (2007). Reporter proteins for *in vivo* fluorescence without oxygen. *Nat. Biotechnol.* 25, 443–445. doi: 10.1038/nbt1293

Ernst, O. P., Lodowski, D. T., Elstner, M., Hegemann, P., Brown, L. S., and Kandori, H. (2014). Microbial and animal rhodopsins: structures, functions, and molecular mechanisms. *Chem. Rev.* 114, 126–163. doi: 10.1021/cr4003769

Fan, H. Y., Morgan, S.-A., Brechun, K. E., Chen, Y.-Y., Jaikaran, A. S. I., and Woolley, G. A. (2011). Improving a designed photocontrolled DNA-binding protein. *Biochemistry* 50, 1226–1237. doi: 10.1021/bi101432p

Fan, L. Z., and Lin, M. Z. (2015). Optical control of biological processes by light-switchable proteins. *Wiley Interdiscip. Rev. Dev. Biol.* doi: 10.1002/wdev.188. [Epub ahead of print].

Feynman, R. P. (1963). *The Feynman Lectures on Physics*. Menlo-Park, CA: Addison-Wesley.

Filonov, G. S., Piatkevich, K. D., Ting, L.-M., Zhang, J., Kim, K., and Verkhusha, V. V. (2011). Bright and stable near-infrared fluorescent protein for *in vivo* imaging. *Nat. Biotechnol.* 29, 757–761. doi: 10.1038/nbt.1918

Freedman, M. S., Lucas, R. J., Soni, B., von Schantz, M., Muñoz, M., David-Gray, Z., et al. (1999). Regulation of mammalian circadian behavior by non-rod, non-cone, ocular photoreceptors. *Science* 284, 502–504.

Gasser, C., Taiber, S., Yeh, C.-M., Wittig, C. H., Hegemann, P., Ryu, S., et al. (2014). Engineering of a red-light-activated human cAMP/cGMP-specific phosphodiesterase. *Proc. Natl. Acad. Sci. U.S.A.* 111, 8803–8808. doi: 10.1073/pnas.1321600111

Gleichmann, T., Diensthuber, R. P., and Möglich, A. (2013). Charting the signal trajectory in a light-oxygen-voltage photoreceptor by random mutagenesis and covariance analysis. *J. Biol. Chem.* 288, 29345–29355. doi: 10.1074/jbc.M113.506139

Grusch, M., Schelch, K., Riedler, R., Reichhart, E., Differ, C., Berger, W., et al. (2014). Spatio-temporally precise activation of engineered receptor tyrosine kinases by light. *EMBO J.* 33, 1713–1726. doi: 10.15252/embj.201387695

Guntas, G., Hallett, R. A., Zimmerman, S. P., Williams, T., Yumerefendi, H., Bear, J. E., et al. (2015). Engineering an improved light-induced dimer (iLID) for controlling the localization and activity of signaling proteins. *Proc. Natl. Acad. Sci. U.S.A.* 112, 112–117. doi: 10.1073/pnas.1417910112

Halavaty, A. S., and Moffat, K. (2007). N- and C-terminal flanking regions modulate light-induced signal transduction in the LOV2 domain of the blue light sensor phototropin 1 from Avena sativa. *Biochemistry* 46, 14001–14009. doi: 10.1021/bi701543e

Harper, S. M., Neil, L. C., and Gardner, K. H. (2003). Structural basis of a phototropin light switch. *Science* 301, 1541–1544. doi: 10.1126/science.1086810

Hegemann, P. (2008). Algal sensory photoreceptors. *Annu. Rev. Plant Biol.* 59, 167–189. doi: 10.1146/annurev.arplant.59.032607.092847

Hell, S. W., and Wichmann, J. (1994). Breaking the diffraction resolution limit by stimulated emission: stimulated-emission-depletion fluorescence microscopy. *Opt. Lett.* 19, 780–782. doi: 10.1364/OL.19.000780

Hirose, Y., Shimada, T., Narikawa, R., Katayama, M., and Ikeuchi, M. (2008). Cyanobacteriochrome CcaS is the green light receptor that induces the expression of phycobilisome linker protein. *Proc. Natl. Acad. Sci. U.S.A.* 105, 9528–9533. doi: 10.1073/pnas.0801826105

Hochbaum, D. R., Zhao, Y., Farhi, S. L., Klapoetke, N., Werley, C. A., Kapoor, V., et al. (2014). All-optical electrophysiology in mammalian neurons using engineered microbial rhodopsins. *Nat. Methods* 11, 825–833. doi: 10.1038/nmeth.3000

Hughes, J., Lamparter, T., Mittmann, F., Hartmann, E., Gärtner, W., Wilde, A., et al. (1997). A prokaryotic phytochrome. *Nature* 386, 663. doi: 10.1038/386663a0

Idevall-Hagren, O., Dickson, E. J., Hille, B., Toomre, D. K., and De Camilli, P. (2012). Optogenetic control of phosphoinositide metabolism. *Proc. Natl. Acad. Sci. U.S.A.* 109, E2316–E2323. doi: 10.1073/pnas.1211305109

Ikeuchi, M., and Ishizuka, T. (2008). Cyanobacteriochromes: a new superfamily of tetrapyrrole-binding photoreceptors in cyanobacteria. *Photochem. Photobiol. Sci.* 7, 1159–1167. doi: 10.1039/b802660m

Ishizuka, T., Kamiya, A., Suzuki, H., Narikawa, R., Noguchi, T., Kohchi, T., et al. (2011). The cyanobacteriochrome, TePixJ, isomerizes its own chromophore by converting phycocyanobilin to phycoviolobilin. *Biochemistry* 50, 953–961. doi: 10.1021/bi101626t

Jansen, V., Alvarez, L., Balbach, M., Strünker, T., Hegemann, P., Kaupp, U. B., et al. (2015). Controlling fertilization and cAMP signaling in sperm by optogenetics. *Elife* 4:e05161. doi: 10.7554/eLife.05161

Kakumoto, T., and Nakata, T. (2013). Optogenetic control of PIP3: PIP3 is sufficient to induce the actin-based active part of growth cones and is regulated via endocytosis. *PLoS ONE* 8:e70861. doi: 10.1371/journal.pone.0070861

Karunarathne, W. K. A., Giri, L., Kalyanaraman, V., and Gautam, N. (2013). Optically triggering spatiotemporally confined GPCR activity in a cell and programming neurite initiation and extension. *Proc. Natl. Acad. Sci. U.S.A.* 110, E1565–E1574. doi: 10.1073/pnas.1220697110

Kawano, F., Suzuki, H., Furuya, A., and Sato, M. (2015). Engineered pairs of distinct photoswitches for optogenetic control of cellular proteins. *Nat. Commun.* 6:6256. doi: 10.1038/ncomms7256

Kennedy, M. J., Hughes, R. M., Peteya, L. A., Schwartz, J. W., Ehlers, M. D., and Tucker, C. L. (2010). Rapid blue-light-mediated induction of protein interactions in living cells. *Nat. Methods* 7, 973–975. doi: 10.1038/nmeth.1524

Kim, J.-M., Hwa, J., Garriga, P., Reeves, P. J., RajBhandary, U. L., and Khorana, H. G. (2005). Light-driven activation of beta 2-adrenergic receptor signaling by a chimeric rhodopsin containing the beta 2-adrenergic receptor cytoplasmic loops. *Biochemistry* 44, 2284–2292. doi: 10.1021/bi048328i

Kim, N., Kim, J. M., Lee, M., Kim, C. Y., Chang, K.-Y., and Heo, W. D. (2014). Spatiotemporal control of fibroblast growth factor receptor signals by blue light. *Chem. Biol.* 21, 903–912. doi: 10.1016/j.chembiol.2014.05.013

Klapoetke, N. C., Murata, Y., Kim, S. S., Pulver, S. R., Birdsey-Benson, A., Cho, Y. K., et al. (2014). Independent optical excitation of distinct neural populations. *Nat. Methods* 11, 338–346. doi: 10.1038/nmeth.2836

Klemm, J. D., Schreiber, S. L., and Crabtree, G. R. (1998). Dimerization as a regulatory mechanism in signal transduction. *Annu. Rev. Immunol.* 16, 569–592. doi: 10.1146/annurev.immunol.16.1.569

Konermann, S., Brigham, M. D., Trevino, A. E., Hsu, P. D., Heidenreich, M., Cong, L., et al. (2013). Optical control of mammalian endogenous transcription and epigenetic states. *Nature* 500, 472–476. doi: 10.1038/nature12466

Koyanagi, M., Kawano, E., Kinugawa, Y., Oishi, T., Shichida, Y., Tamotsu, S., et al. (2004). Bistable UV pigment in the lamprey pineal. *Proc. Natl. Acad. Sci. U.S.A.* 101, 6687–6691. doi: 10.1073/pnas.0400819101

Kralj, J. M., Douglass, A. D., Hochbaum, D. R., Maclaurin, D., and Cohen, A. E. (2012). Optical recording of action potentials in mammalian neurons using a microbial rhodopsin. *Nat. Methods* 9, 90–95. doi: 10.1038/nmeth.1782

Kralj, J. M., Hochbaum, D. R., Douglass, A. D., and Cohen, A. E. (2011). Electrical spiking in Escherichia coli probed with a fluorescent voltage-indicating protein. *Science* 333, 345–348. doi: 10.1126/science.1204763

Lamb, J. S., Zoltowski, B. D., Pabit, S. A., Crane, B. R., and Pollack, L. (2008). Time-resolved dimerization of a PAS-LOV protein measured with photocoupled small angle X-ray scattering. *J. Am. Chem. Soc.* 130, 12226–12227. doi: 10.1021/ja804236f

Lee, J., Natarajan, M., Nashine, V. C., Socolich, M., Vo, T., Russ, W. P., et al. (2008). Surface sites for engineering allosteric control in proteins. *Science* 322, 438–442. doi: 10.1126/science.1159052

Lee, S., Park, H., Kyung, T., Kim, N. Y., Kim, S., Kim, J., et al. (2014). Reversible protein inactivation by optogenetic trapping in cells. *Nat. Methods* 11, 633–636. doi: 10.1038/nmeth.2940

Leibiger, I. B., and Berggren, P.-O. (2015). Regulation of glucose homeostasis using radiogenetics and magnetogenetics in mice. *Nat. Med.* 21, 14–16. doi: 10.1038/nm.3782

Levskaya, A., Chevalier, A. A., Tabor, J. J., Simpson, Z. B., Lavery, L. A., Levy, M., et al. (2005). Synthetic biology: engineering *Escherichia coli* to see light. *Nature* 438, 441–442. doi: 10.1038/nature04405

Levskaya, A., Weiner, O. D., Lim, W. A., and Voigt, C. A. (2009). Spatiotemporal control of cell signalling using a light-switchable protein interaction. *Nature* 461, 997–1001. doi: 10.1038/nature08446

Liu, H., Gomez, G., Lin, S., Lin, S., and Lin, C. (2012). Optogenetic control of transcription in zebrafish. *PLoS ONE* 7:e50738. doi: 10.1371/journal.pone.0050738

Liu, H., Yu, X., Li, K., Klejnot, J., Yang, H., Lisiero, D., et al. (2008). Photoexcited CRY2 interacts with CIB1 to regulate transcription and floral initiation in Arabidopsis. *Science* 322, 1535–1539. doi: 10.1126/science.1163927

Losi, A., Gärtner, W., Raffelberg, S., Cella Zanacchi, F., Bianchini, P., Diaspro, A., et al. (2013). A photochromic bacterial photoreceptor with potential for super-resolution microscopy. *Photochem. Photobiol. Sci.* 12, 231–235. doi: 10.1039/C2PP25254F

Luck, M., Mathes, T., Bruun, S., Fudim, R., Hagedorn, R., Tran Nguyen, T. M., et al. (2012). A photochromic histidine kinase rhodopsin (HKR1) that is bimodally switched by ultraviolet and blue light. *J. Biol. Chem.* 287, 40083–40090. doi: 10.1074/jbc.M112.401604

Lungu, O. I., Hallett, R. A., Choi, E. J., Aiken, M. J., Hahn, K. M., and Kuhlman, B. (2012). Designing photoswitchable peptides using the AsLOV2 domain. *Chem. Biol.* 19, 507–517. doi: 10.1016/j.chembiol.2012.02.006

Makhlynets, O. V., Raymond, E. A., and Korendovych, I. V. (2015). Design of allosterically regulated protein catalysts. *Biochemistry* 54, 1444–1456. doi: 10.1021/bi5015248

Mills, E., Chen, X., Pham, E., Wong, S., and Truong, K. (2012). Engineering a photoactivated caspase-7 for rapid induction of apoptosis. *ACS Synth. Biol.* 1, 75–82. doi: 10.1021/sb200008j

Moffat, K., Zhang, F., Hahn, K. M., and Möglich, A. (2013). "The biophysics and engineering of signaling photoreceptors," in *Optogenetics*, eds P. Hegemann and S. Sigrist (Berlin: Walter de Gruyter), 7–22.

Möglich, A., Ayers, R. A., and Moffat, K. (2009a). Design and signaling mechanism of light-regulated histidine kinases. *J. Mol. Biol.* 385, 1433–1444. doi: 10.1016/j.jmb.2008.12.017

Möglich, A., Ayers, R. A., and Moffat, K. (2009b). Structure and signaling mechanism of Per-ARNT-Sim domains. *Structure* 17, 1282–1294. doi: 10.1016/j.str.2009.08.011

Möglich, A., Ayers, R. A., and Moffat, K. (2010a). Addition at the molecular level: signal integration in designed Per-ARNT-Sim receptor proteins. *J. Mol. Biol.* 400, 477–486. doi: 10.1016/j.jmb.2010.05.019

Möglich, A., and Moffat, K. (2010). Engineered photoreceptors as novel optogenetic tools. *Photochem. Photobiol. Sci.* 9, 1286–1300. doi: 10.1039/c0pp00167h

Möglich, A., Yang, X., Ayers, R. A., and Moffat, K. (2010b). Structure and function of plant photoreceptors. *Annu. Rev. Plant Biol.* 61, 21–47. doi: 10.1146/annurev-arplant-042809-112259

Monod, J., Wyman, J., and Changeux, J. P. (1965). On the nature of allosteric transitions: a plausible model. *J. Mol. Biol.* 12, 88–118. doi: 10.1016/S0022-2836(65)80285-6

Motlagh, H. N., Wrabl, J. O., Li, J., and Hilser, V. J. (2014). The ensemble nature of allostery. *Nature* 508, 331–339. doi: 10.1038/nature13001

Motta-Mena, L. B., Reade, A., Mallory, M. J., Glantz, S., Weiner, O. D., Lynch, K. W., et al. (2014). An optogenetic gene expression system with rapid activation and deactivation kinetics. *Nat. Chem. Biol.* 10, 196–202. doi: 10.1038/nchembio.1430

Müller, K., Engesser, R., Metzger, S., Schulz, S., Kämpf, M. M., Busacker, M., et al. (2013a). A red/far-red light-responsive bi-stable toggle switch to control gene expression in mammalian cells. *Nucleic Acids Res.* 41, e77. doi: 10.1093/nar/gkt002

Müller, K., Engesser, R., Schulz, S., Steinberg, T., Tomakidi, P., Weber, C. C., et al. (2013b). Multi-chromatic control of mammalian gene expression and signaling. *Nucleic Acids Res.* 41, e124. doi: 10.1093/nar/gkt340

Müller, K., Engesser, R., Timmer, J., Nagy, F., Zurbriggen, M. D., and Weber, W. (2013c). Synthesis of phycocyanobilin in mammalian cells. *Chem. Commun. (Camb.)* 49, 8970–8972. doi: 10.1039/c3cc45065a

Nagel, G., Ollig, D., Fuhrmann, M., Kateriya, S., Musti, A. M., Bamberg, E., et al. (2002). Channelrhodopsin-1: a light-gated proton channel in green algae. *Science* 296, 2395–2398. doi: 10.1126/science.1072068

Nagel, G., Szellas, T., Huhn, W., Kateriya, S., Adeishvili, N., Berthold, P., et al. (2003). Channelrhodopsin-2, a directly light-gated cation-selective membrane channel. *Proc. Natl. Acad. Sci. U.S.A.* 100, 13940–13945. doi: 10.1073/pnas.1936192100

Narikawa, R., Enomoto, G., Ni-Ni-Win, Fushimi, K., and Ikeuchi, M. (2014). A new type of dual-Cys cyanobacteriochrome GAF domain found in cyanobacterium Acaryochloris marina, which has an unusual

red/blue reversible photoconversion cycle. *Biochemistry* 53, 5051–5059. doi: 10.1021/bi500376b

Narikawa, R., Ishizuka, T., Muraki, N., Shiba, T., Kurisu, G., and Ikeuchi, M. (2013). Structures of cyanobacteriochromes from phototaxis regulators AnPixJ and TePixJ reveal general and specific photoconversion mechanism. *Proc. Natl. Acad. Sci. U.S.A.* 110, 918–923. doi: 10.1073/pnas.1212098110

Narikawa, R., Nakajima, T., Aono, Y., Fushimi, K., Enomoto, G., Ni-Ni-Win, et al. (2015). A biliverdin-binding cyanobacteriochrome from the chlorophyll d-bearing cyanobacterium Acaryochloris marina. *Sci. Rep.* 5:7950. doi: 10.1038/srep07950

Nash, A. I., McNulty, R., Shillito, M. E., Swartz, T. E., Bogomolni, R. A., Luecke, H., et al. (2011). Structural basis of photosensitivity in a bacterial light-oxygen-voltage/helix-turn-helix (LOV-HTH) DNA-binding protein. *Proc. Natl. Acad. Sci. U.S.A.* 108, 9449–9454. doi: 10.1073/pnas.1100262108

Nihongaki, Y., Suzuki, H., Kawano, F., and Sato, M. (2014). Genetically engineered photoinducible homodimerization system with improved dimer-forming efficiency. *ACS Chem. Biol.* 9, 617–621. doi: 10.1021/cb400836k

Nihongaki, Y., Yamamoto, S., Kawano, F., Suzuki, H., and Sato, M. (2015). CRISPR-Cas9-based photoactivatable transcription system. *Chem. Biol.* 22, 169–174. doi: 10.1016/j.chembiol.2014.12.011

Niopek, D., Benzinger, D., Roensch, J., Draebing, T., Wehler, P., Eils, R., et al. (2014). Engineering light-inducible nuclear localization signals for precise spatiotemporal control of protein dynamics in living cells. *Nat. Commun.* 5, 4404. doi: 10.1038/ncomms5404

Oh, E., Maejima, T., Liu, C., Deneris, E., and Herlitze, S. (2010). Substitution of 5-HT1A receptor signaling by a light-activated G protein-coupled receptor. *J. Biol. Chem.* 285, 30825–30836. doi: 10.1074/jbc.M110.147298

Ohlendorf, R., Vidavski, R. R., Eldar, A., Moffat, K., and Möglich, A. (2012). From dusk till dawn: one-plasmid systems for light-regulated gene expression. *J. Mol. Biol.* 416, 534–542. doi: 10.1016/j.jmb.2012.01.001

Pashaie, R., Anikeeva, P., Lee, J. H., Prakash, R., Yizhar, O., Prigge, M., et al. (2014). Optogenetic brain interfaces. *IEEE Rev. Biomed. Eng.* 7, 3–30. doi: 10.1109/RBME.2013.2294796

Pathak, G. P., Strickland, D., Vrana, J. D., and Tucker, C. L. (2014). Benchmarking of optical dimerizer systems. *ACS Synth. Biol.* 3, 832–838. doi: 10.1021/sb500291r

Patterson, G. H., and Lippincott-Schwartz, J. (2002). A photoactivatable GFP for selective photolabeling of proteins and cells. *Science* 297, 1873–1877. doi: 10.1126/science.1074952

Paz, J. T., Davidson, T. J., Frechette, E. S., Delord, B., Parada, I., Peng, K., et al. (2013). Closed-loop optogenetic control of thalamus as a tool for interrupting seizures after cortical injury. *Nat. Neurosci.* 16, 64–70. doi: 10.1038/nn.3269

Pham, E., Mills, E., and Truong, K. (2011). A synthetic photoactivated protein to generate local or global $Ca^{(2+)}$ signals. *Chem. Biol.* 18, 880–890. doi: 10.1016/j.chembiol.2011.04.014

Piatkevich, K. D., Subach, F. V., and Verkhusha, V. V. (2013a). Engineering of bacterial phytochromes for near-infrared imaging, sensing, and light-control in mammals. *Chem. Soc. Rev.* 42, 3441–3452. doi: 10.1039/c3cs35458j

Piatkevich, K. D., Subach, F. V., and Verkhusha, V. V. (2013b). Far-red light photoactivatable near-infrared fluorescent proteins engineered from a bacterial phytochrome. *Nat. Commun.* 4, 2153. doi: 10.1038/ncomms3153

Pollock, R., and Clackson, T. (2002). Dimerizer-regulated gene expression. *Curr. Opin. Biotechnol.* 13, 459–467. doi: 10.1016/S0958-1669(02)00373-7

Polstein, L. R., and Gersbach, C. A. (2012). Light-inducible spatiotemporal control of gene activation by customizable zinc finger transcription factors. *J. Am. Chem. Soc.* 134, 16480–16483. doi: 10.1021/ja3065667

Polstein, L. R., and Gersbach, C. A. (2015). A light-inducible CRISPR-Cas9 system for control of endogenous gene activation. *Nat. Chem. Biol.* 11, 198–200. doi: 10.1038/nchembio.1753

Pudasaini, A., El-Arab, K. K., and Zoltowski, B. D. (2015). LOV-based optogenetic devices: light-driven modules to impart photoregulated control of cellular signaling. *Front. Mol. Biosci* 2:18. doi: 10.3389/fmolb.2015.00018

Qi, Y. B., Garren, E. J., Shu, X., Tsien, R. Y., and Jin, Y. (2012). Photo-inducible cell ablation in Caenorhabditis elegans using the genetically encoded singlet oxygen generating protein miniSOG. *Proc. Natl. Acad. Sci. U.S.A.* 109, 7499–7504. doi: 10.1073/pnas.1204096109

Raffelberg, S., Wang, L., Gao, S., Losi, A., Gärtner, W., and Nagel, G. (2013). A LOV-domain-mediated blue-light-activated adenylate (adenylyl) cyclase from the cyanobacterium Microcoleus chthonoplastes PCC 7420. *Biochem. J.* 455, 359–365. doi: 10.1042/BJ20130637

Reis, J. M., Burns, D. C., and Woolley, G. A. (2014). Optical control of protein-protein interactions via blue light-induced domain swapping. *Biochemistry* 53, 5008–5016. doi: 10.1021/bi500622x

Renicke, C., Schuster, D., Usherenko, S., Essen, L.-O., and Taxis, C. (2013). A LOV2 domain-based optogenetic tool to control protein degradation and cellular function. *Chem. Biol.* 20, 619–626. doi: 10.1016/j.chembiol.2013.03.005

Richter, F., Scheib, U. S., Mehlhorn, J., Schubert, R., Wietek, J., Gernetzki, O., et al. (2015). Upgrading a microplate reader for photobiology and all-optical experiments. *Photochem. Photobiol. Sci.* 14, 270–279. doi: 10.1039/C4PP00361F

Rockwell, N. C., Duanmu, D., Martin, S. S., Bachy, C., Price, D. C., Bhattacharya, D., et al. (2014). Eukaryotic algal phytochromes span the visible spectrum. *Proc. Natl. Acad. Sci. U.S.A.* 111, 3871–3876. doi: 10.1073/pnas.1401871111

Rockwell, N. C., and Lagarias, J. C. (2010). A brief history of phytochromes. *Chemphyschem* 11, 1172–1180. doi: 10.1002/cphc.200900894

Rockwell, N. C., Martin, S. S., Feoktistova, K., and Lagarias, J. C. (2011). Diverse two-cysteine photocycles in phytochromes and cyanobacteriochromes. *Proc. Natl. Acad. Sci. U.S.A.* 108, 11854–11859. doi: 10.1073/pnas.1107844108

Rockwell, N. C., Ohlendorf, R., and Möglich, A. (2013). Cyanobacteriochromes in full color and three dimensions. *Proc. Natl. Acad. Sci. U.S.A.* 110, 806–807. doi: 10.1073/pnas.1220690110

Rockwell, N. C., Su, Y.-S., and Lagarias, J. C. (2006). Phytochrome structure and signaling mechanisms. *Annu. Rev. Plant Biol.* 57, 837–858. doi: 10.1146/annurev.arplant.56.032604.144208

Ryu, M.-H., Kang, I.-H., Nelson, M. D., Jensen, T. M., Lyuksyutova, A. I., Siltberg-Liberles, J., et al. (2014). Engineering adenylate cyclases regulated by near-infrared window light. *Proc. Natl. Acad. Sci. U.S.A.* 111, 10167–10172. doi: 10.1073/pnas.1324301111

Ryu, M.-H., Moskvin, O. V., Siltberg-Liberles, J., and Gomelsky, M. (2010). Natural and engineered photoactivated nucleotidyl cyclases for optogenetic applications. *J. Biol. Chem.* 285, 41501–41508. doi: 10.1074/jbc.M110.177600

Schmidt, D., and Cho, Y. K. (2015). Natural photoreceptors and their application to synthetic biology. *Trends Biotechnol.* 33, 80–91. doi: 10.1016/j.tibtech.2014.10.007

Schmidt, D., Tillberg, P. W., Chen, F., and Boyden, E. S. (2014). A fully genetically encoded protein architecture for optical control of peptide ligand concentration. *Nat. Commun.* 5, 3019. doi: 10.1038/ncomms4019

Schröder-Lang, S., Schwärzel, M., Seifert, R., Strünker, T., Kateriya, S., Looser, J., et al. (2007). Fast manipulation of cellular cAMP level by light *in vivo*. *Nat. Methods* 4, 39–42. doi: 10.1038/nmeth975

Shcherbakova, D. M., Shemetov, A. A., Kaberniuk, A. A., and Verkhusha, V. V. (2015). Natural photoreceptors as a source of fluorescent proteins, biosensors, and optogenetic tools. *Annu. Rev. Biochem.* 5, 519–550. doi: 10.1146/annurev-biochem-060614-034411

Shimizu-Sato, S., Huq, E., Tepperman, J. M., and Quail, P. H. (2002). A light-switchable gene promoter system. *Nat. Biotechnol.* 20, 1041–1044. doi: 10.1038/nbt734

Shu, X., Royant, A., Lin, M. Z., Aguilera, T. A., Lev-Ram, V., Steinbach, P. A., et al. (2009). Mammalian expression of infrared fluorescent proteins engineered from a bacterial phytochrome. *Science* 324, 804–807. doi: 10.1126/science.1168683

Spoida, K., Masseck, O. A., Deneris, E. S., and Herlitze, S. (2014). Gq/5-HT2c receptor signals activate a local GABAergic inhibitory feedback circuit to modulate serotonergic firing and anxiety in mice. *Proc. Natl. Acad. Sci. U.S.A.* 111, 6479–6484. doi: 10.1073/pnas.1321576111

Stanley, S. A., Gagner, J. E., Damanpour, S., Yoshida, M., Dordick, J. S., and Friedman, J. M. (2012). Radio-wave heating of iron oxide nanoparticles can regulate plasma glucose in mice. *Science* 336, 604–608. doi: 10.1126/science.1216753

Stanley, S. A., Sauer, J., Kane, R. S., Dordick, J. S., and Friedman, J. M. (2015). Remote regulation of glucose homeostasis in mice using genetically encoded nanoparticles. *Nat. Med.* 21, 92–98. doi: 10.1038/nm.3730

Stein, V., and Alexandrov, K. (2015). Synthetic protein switches: design principles and applications. *Trends Biotechnol.* 33, 101–110. doi: 10.1016/j.tibtech.2014.11.010

Stierl, M., Stumpf, P., Udwari, D., Gueta, R., Hagedorn, R., Losi, A., et al. (2011). Light-modulation of cellular cAMP by a small bacterial photoactivated adenylyl

cyclase, bPAC, of the soil bacterium beggiatoa. *J. Biol. Chem.* 286, 1181–1188. doi: 10.1074/jbc.M110.185496

Strauss, H. M., Schmieder, P., and Hughes, J. (2005). Light-dependent dimerisation in the N-terminal sensory module of cyanobacterial phytochrome 1. *FEBS Lett.* 579, 3970–3974. doi: 10.1016/j.febslet.2005.06.025

Strickland, D., Lin, Y., Wagner, E., Hope, C. M., Zayner, J., Antoniou, C., et al. (2012). TULIPs: tunable, light-controlled interacting protein tags for cell biology. *Nat. Methods* 9, 379–384. doi: 10.1038/nmeth.1904

Strickland, D., Moffat, K., and Sosnick, T. R. (2008). Light-activated DNA binding in a designed allosteric protein. *Proc. Natl. Acad. Sci. U.S.A.* 105, 10709–10714. doi: 10.1073/pnas.0709610105

Strickland, D., Yao, X., Gawlak, G., Rosen, M. K., Gardner, K. H., and Sosnick, T. R. (2010). Rationally improving LOV domain-based photoswitches. *Nat. Methods* 7, 623–626. doi: 10.1038/nmeth.1473

Takahashi, F., Yamagata, D., Ishikawa, M., Fukamatsu, Y., Ogura, Y., Kasahara, M., et al. (2007). AUREOCHROME, a photoreceptor required for photomorphogenesis in stramenopiles. *Proc. Natl. Acad. Sci. U.S.A.* 104, 19625–19630. doi: 10.1073/pnas.0707692104

Takala, H., Björling, A., Berntsson, O., Lehtivuori, H., Niebling, S., Hoernke, M., et al. (2014). Signal amplification and transduction in phytochrome photosensors. *Nature* 509, 245–248. doi: 10.1038/nature13310

Taslimi, A., Vrana, J. D., Chen, D., Borinskaya, S., Mayer, B. J., Kennedy, M. J., et al. (2014). An optimized optogenetic clustering tool for probing protein interaction and function. *Nat. Commun.* 5, 4925. doi: 10.1038/ncomms5925

Terakita, A., and Nagata, T. (2014). Functional properties of opsins and their contribution to light-sensing physiology. *Zool. Sci.* 31, 653–659. doi: 10.2108/zs140094

Toettcher, J. E., Weiner, O. D., and Lim, W. A. (2013). Using optogenetics to interrogate the dynamic control of signal transmission by the Ras/Erk module. *Cell* 155, 1422–1434. doi: 10.1016/j.cell.2013.11.004

Tsien, R. Y. (2009). Constructing and exploiting the fluorescent protein paintbox (Nobel Lecture). *Angew. Chem. Int. Ed. Engl.* 48, 5612–5626. doi: 10.1002/anie.200901916

Tyszkiewicz, A. B., and Muir, T. W. (2008). Activation of protein splicing with light in yeast. *Nat. Methods* 5, 303–305. doi: 10.1038/nmeth.1189

Vaidya, A. T., Chen, C.-H., Dunlap, J. C., Loros, J. J., and Crane, B. R. (2011). Structure of a light-activated LOV protein dimer that regulates transcription. *Sci. Signal.* 4, ra50. doi: 10.1126/scisignal.2001945

Van Bergeijk, P., Adrian, M., Hoogenraad, C. C., and Kapitein, L. C. (2015). Optogenetic control of organelle transport and positioning. *Nature* 518, 111–114. doi: 10.1038/nature14128

Van Wyk, M., Pielecka-Fortuna, J., Löwel, S., and Kleinlogel, S. (2015). Restoring the ON switch in blind retinas: opto-mGluR6, a next-generation, cell-tailored optogenetic tool. *PLoS Biol.* 13:e1002143. doi: 10.1371/journal.pbio.1002143

Volkman, B. F., Lipson, D., Wemmer, D. E., and Kern, D. (2001). Two-state allosteric behavior in a single-domain signaling protein. *Science* 291, 2429–2433. doi: 10.1126/science.291.5512.2429

Wang, X., Chen, X., and Yang, Y. (2012). Spatiotemporal control of gene expression by a light-switchable transgene system. *Nat. Methods* 9, 266–269. doi: 10.1038/nmeth.1892

Wend, S., Wagner, H. J., Müller, K., Zurbriggen, M. D., Weber, W., and Radziwill, G. (2014). Optogenetic control of protein kinase activity in mammalian cells. *ACS Synth. Biol.* 3, 280–285. doi: 10.1021/sb400090s

Wolgemuth, C. W., and Sun, S. X. (2006). Elasticity of alpha-helical coiled coils. *Phys. Rev. Lett.* 97, 248101. doi: 10.1103/PhysRevLett.97.248101

Wu, D., Hu, Q., Yan, Z., Chen, W., Yan, C., Huang, X., et al. (2012). Structural basis of ultraviolet-B perception by UVR8. *Nature* 484, 214–219. doi: 10.1038/nature10931

Wu, Y. I., Frey, D., Lungu, O. I., Jaehrig, A., Schlichting, I., Kuhlman, B., et al. (2009). A genetically encoded photoactivatable Rac controls the motility of living cells. *Nature* 461, 104–108. doi: 10.1038/nature08241

Wyman, J., and Gill, S. J. (1990). *Binding and Linkage: Functional Chemistry of Biological Macromolecules*. Mill Valley, CA: University Science Books.

Yang, X., Jost, A. P.-T., Weiner, O. D., and Tang, C. (2013). A light-inducible organelle-targeting system for dynamically activating and inactivating signaling in budding yeast. *Mol. Biol. Cell* 24, 2419–2430. doi: 10.1091/mbc.E13-03-0126

Yang, X., Stojkovic, E. A., Kuk, J., and Moffat, K. (2007). Crystal structure of the chromophore binding domain of an unusual bacteriophytochrome, RpBphP3, reveals residues that modulate photoconversion. *Proc. Natl. Acad. Sci. U.S.A.* 104, 12571–12576. doi: 10.1073/pnas.0701737104

Yao, X., Rosen, M. K., and Gardner, K. H. (2008). Estimation of the available free energy in a LOV2-J alpha photoswitch. *Nat. Chem. Biol.* 4, 491–497. doi: 10.1038/nchembio.99

Yazawa, M., Sadaghiani, A. M., Hsueh, B., and Dolmetsch, R. E. (2009). Induction of protein-protein interactions in live cells using light. *Nat. Biotechnol.* 27, 941–945. doi: 10.1038/nbt.1569

Yi, J. J., Wang, H., Vilela, M., Danuser, G., and Hahn, K. M. (2014). Manipulation of endogenous kinase activity in living cells using photoswitchable inhibitory peptides. *ACS Synth. Biol.* 3, 788–795. doi: 10.1021/sb5001356

Yu, X., Sayegh, R., Maymon, M., Warpeha, K., Klejnot, J., Yang, H., et al. (2009). Formation of nuclear bodies of Arabidopsis CRY2 in response to blue light is associated with its blue light-dependent degradation. *Plant Cell* 21, 118–130. doi: 10.1105/tpc.108.061663

Zalocusky, K. A., Fenno, L. E., and Deisseroth, K. (2013). "Current challenges in optogenetics," in *Optogenetics*, eds P. Hegemann and S. Sigrist (Berlin: Walter de Gruyter), 23–33.

Zayner, J. P., Antoniou, C., and Sosnick, T. R. (2012). The amino-terminal helix modulates light-activated conformational changes in AsLOV2. *J. Mol. Biol.* 419, 61–74. doi: 10.1016/j.jmb.2012.02.037

Zhang, K., and Cui, B. (2015). Optogenetic control of intracellular signaling pathways. *Trends Biotechnol.* 33, 92–100. doi: 10.1016/j.tibtech.2014.11.007

Zhang, K., Duan, L., Ong, Q., Lin, Z., Varman, P. M., Sung, K., et al. (2014). Light-mediated kinetic control reveals the temporal effect of the Raf/MEK/ERK pathway in PC12 cell neurite outgrowth. *PLoS ONE* 9:e92917. doi: 10.1371/journal.pone.0092917

Zhou, X. X., Chung, H. K., Lam, A. J., and Lin, M. Z. (2012). Optical control of protein activity by fluorescent protein domains. *Science* 338, 810–814. doi: 10.1126/science.1226854

Zoltowski, B. D., and Crane, B. R. (2008). Light activation of the LOV protein vivid generates a rapidly exchanging dimer. *Biochemistry* 47, 7012–7019. doi: 10.1021/bi8007017

Zoltowski, B. D., Schwerdtfeger, C., Widom, J., Loros, J. J., Bilwes, A. M., Dunlap, J. C., et al. (2007). Conformational switching in the fungal light sensor vivid. *Science* 316, 1054–1057. doi: 10.1126/science.1137128

Zoltowski, B. D., Vaccaro, B., and Crane, B. R. (2009). Mechanism-based tuning of a LOV domain photoreceptor. *Nat. Chem. Biol.* 5, 827–834. doi: 10.1038/nchembio.210

Conflict of Interest Statement: The authors declare that the research was conducted in the absence of any commercial or financial relationships that could be construed as a potential conflict of interest.

frontiers in Molecular Biosciences

REVIEW
published: 12 May 2015
doi: 10.3389/fmolb.2015.00018

LOV-based optogenetic devices: light-driven modules to impart photoregulated control of cellular signaling

*Ashutosh Pudasaini, Kaley K. El-Arab and Brian D. Zoltowski**

Department of Chemistry, Center for Drug Discovery, Design and Delivery at Dedman College, Southern Methodist University, Dallas, TX, USA

The Light-Oxygen-Voltage domain family of proteins is widespread in biology where they impart sensory responses to signal transduction domains. The small, light responsive LOV modules offer a novel platform for the construction of optogenetic tools. Currently, the design and implementation of these devices is partially hindered by a lack of understanding of how light drives allosteric changes in protein conformation to activate diverse signal transduction domains. Further, divergent photocycle properties amongst LOV family members complicate construction of highly sensitive devices with fast on/off kinetics. In the present review we discuss the history of LOV domain research with primary emphasis on tuning LOV domain chemistry and signal transduction to allow for improved optogenetic tools.

Keywords: LOV domain, optogenetics, protein engineering, photobiology, photosensors

OPEN ACCESS

Edited by:
Tilo Mathes, Vrije Universiteit Amsterdam, Netherlands

Reviewed by:
Aba Losi, University of Parma, Italy
John Christie, University of Glasgow, UK

****Correspondence:***
Brian D. Zoltowski, Department of Chemistry, Southern Methodist University, Fondren Science Building Rm. 231, Dallas, TX 75275-0314, USA
bzoltowski@smu.edu

Specialty section:
This article was submitted to Biophysics, a section of the journal Frontiers in Molecular Biosciences

Received: *31 March 2015*
Accepted: *27 April 2015*
Published: *12 May 2015*

Citation:
Pudasaini A, El-Arab KK and Zoltowski BD (2015) LOV-based optogenetic devices: light-driven modules to impart photoregulated control of cellular signaling. Front. Mol. Biosci. 2:18. doi: 10.3389/fmolb.2015.00018

Introduction

Over the past 10 years, advancements in our understanding of photoactivated proteins have enabled genetic control of cellular events through light. These optogenetic approaches allow researchers to dictate biological signaling with exquisite spatial and temporal precision. The ability to remotely and non-invasively trigger signal transduction has led to unparalleled breakthroughs in neuroscience, cardiology and cell biology (Moglich and Moffat, 2010; Boyden, 2011; Fenno et al., 2011; Deisseroth, 2012). Whereas, initially most research focused on the use of light-controlled opsins to affect neurobiology, more recent research has employed a host of photoactivatable proteins from the Light-Oxygen-Voltage (LOV), Cryptochrome (CRYs), Blue-light-using FAD (BLUF), Phytochrome (PHY), and UVR8 families of proteins (Moglich and Moffat, 2010; Fenno et al., 2011; Christie et al., 2012a). A central goal of these efforts has been to identify a protein module that can, in an efficient and robust manner, be coupled to any signaling domain to elicit photoregulated control. Despite a wide range of functional devices that have been developed, several key limitations exist in developing the ideal optogenetic tool. Given the breadth of the field and diverse reviews in the subject matter, the present review will focus on LOV-based optogenetic devices. Specific focus will be on existing tools, their limitations, and current efforts to improve them for widespread usage in cell biology and medicine.

LOV domains were first identified as the photoreactive module regulating plant phototropism (Huala et al., 1997; Salomon et al., 2000). Since their initial discovery, they have been found in bacterial, algal, fungal and plant species, where they impart blue-light sensitivity to myriad signal

transduction domains (Crosson et al., 2003). Structurally, LOV domains are a subclass to the wider Period-ARNT-Singleminded (PAS) domain family that is distinguished by the presence of a flavin (FMN, FAD, or riboflavin) cofactor and the presence of a consensus GXNCRFLQ motif (Taylor and Zhulin, 1999; Zoltowski and Gardner, 2011).

The LOV module is defined by a core domain of ∼110 amino acids forms a PAS fold composed of a central 5-stranded antiparallel β-sheet and a helical face that bind the photoreactive flavin (Zoltowski and Gardner, 2011). Current research indicates that in nearly all cases, the core domain signals to effector elements through highly variable N-terminal (Ncap) or C-terminal (Ccap) extensions to the LOV core (Halavaty and Moffat, 2007; Zoltowski et al., 2007; Zoltowski and Crane, 2008; Nash et al., 2011; Diensthuber et al., 2013; Lokhandwala et al., 2015). These extensions are typically helical and couple LOV-photochemistry to allosteric control of effector domains. In optogenetic devices allosteric regulation of effector elements has been harnessed through three general methods that are detailed further below: (1) Light-driven protein-protein interaction modules that drive transcription or cellular localization (Strickland et al., 2008; Yazawa et al., 2009; Lungu et al., 2012; Polstein and Gersbach, 2012; Chen et al., 2013; Motta-Mena et al., 2014). (2) Light-driven activators of signaling (e.g., histidine kinases, phosphodiesterases, cell mobility) (Wu et al., 2009; Ohlendorf et al., 2012; Grusch et al., 2014; Yi et al., 2014; Yin and Wu, 2015) and (3) Fluorescent reporter molecules (Chapman et al., 2008; Mukherjee and Schroeder, 2015). Currently, these devices are still limited in the degree of activation, residual dark state function and non-ideal photochemical cycles.

Herein we focus on five platforms that are commonly exploited as optogenetic devices; these are the LOV2 domain of *Avena sativa* phototropin 1 (AsLOV2), a fungal circadian clock photoreceptor Vivid (VVD), a *Bacillus subtilis* stress response protein (YtvA), a FLAVIN-BINDING, KELCH REPEAT, F-BOX 1 essential to plant flowering (FKF1), and a 222 amino acid LOV-transcription factor present in *Erythrobacter litoralis* (EL222) (**Figure 1**). These are summarized in **Table 1**. However, before going into detailed accounts of signal transduction mechanisms in existing LOV-based optogenetic tools, we briefly outline the current state of LOV photochemistry.

LOV Photocycles and Kinetics

All LOV proteins are defined by equivalent chemistry centered on the active site flavin and the Cysteine in the GXNCRFLQ motif (Salomon et al., 2000; Swartz et al., 2001; Crosson et al., 2003; Harper et al., 2003). Dark-state LOV proteins (ground state:LOV_{450}) contain an oxidized flavin cofactor that maximally absorbs blue-light at 450 nm (**Figure 1A**). Upon blue-light absorption, LOV proteins rapidly form a covalent linkage between the C4a position of the flavin cofactor and the thiol moiety of the active site cysteine (**Figure 1B**). Although some debates remain in regards to the nature of reactive intermediates, a consensus mechanism can be described as outlined in **Figure 1** (Holzer et al., 2002; Iwata et al., 2002; Bittl et al., 2003; Corchnoy et al., 2003; Kennis et al., 2003, 2004a; Schleicher et al., 2004; Dittrich et al., 2005; Sato et al., 2005; Alexandre et al., 2009a). Briefly, blue-light promotes LOV_{450} into a singlet-excited state that rapidly undergoes intersystem crossing. The triplet state then induces electron and proton transfer from the active site cysteine. Finally, the resulting radical species recombine to form the C4a adduct signaling state (S390) that is defined by a single broad absorption band centered at 390 nm. The photocycle is thermally reversible in the dark, decaying to the ground state on a timescale of seconds to days (see **Table 2**) (Zoltowski et al., 2009). The widely varying photocycle lifetimes have been of keen interest to researchers and their biological relevance is still weakly explored.

Currently, most research into the LOV photocycle centers on the large range in adduct decay kinetics. For the purpose of this review we will break down LOV photocycles as falling within three regimes: fast cycling ($\tau < 1000$ s), intermediate cycling ($1000 < \tau < 10000$ s), and slow cycling ($10000 < \tau$ s). Thus, existing optogenetic tools are either fast cycling (AsLOV2; ∼80 s, EL222; ∼30 s), intermediate (YtvA∼6000 s) or slow cycling (VVD;∼18000 s, FKF1; $100000 < \tau$. As noted below, the different photocycle lifetimes have significant impact on the sensitivity of optogenetic tools to different environmental light intensities as well as the dynamic reversibility of the systems (Zoltowski et al., 2009; Pudasaini and Zoltowski, 2013; Diensthuber et al., 2014).

Although, research into the *in vivo* effects of LOV photocycles is limited, recent studies of plant LOV photoreceptors indicate that the widely varying kinetics of adduct decay are important to dictating sensitivity to the intensity of environmental light (Okajima et al., 2012; Pudasaini and Zoltowski, 2013). Specifically, a UV-A light stimulated adduct decay pathway competes with blue-light activated formation of the C4a adduct (Kottke et al., 2003; Kennis et al., 2004b). These combine with thermal decay of the light-state species to generate a photodynamic equilibrium sensitive to environmental fluence (Pudasaini and Zoltowski, 2013). In this equilibrium, the rate of adduct decay specifies three regimes that differ in regards to their sensitivity to environmental light. The fast cycling LOV domains generate a dynamic equilibrium sensitive to all environmentally observed light-intensities. In contrast, intermediate LOV domains are completely saturated at moderate light intensities (greater than 20 $\mu mole/m^2 * s$), but retain peak sensitivity under low light conditions consistent with dusk/dawn (5–20 $\mu mole/m^2 * s$) (Pudasaini and Zoltowski, 2013). The third class of slow cycling LOV domains is exquisitely sensitive to even very low light intensities, where under natural lighting conditions the light/dark ratio is saturated. Although the biological relevance of these effects is still weakly explored, they have significant effects on the design of LOV based optogenetic tools. Namely, we are often forced into one of two regimes. Either we have a fast cycling LOV protein (AsLOV2/EL222) that requires high-intensity blue-light to saturate optogenetic signals, but affords rapid on/off kinetics, or one has a slow cycling protein (VVD/FKF1) that requires minimal light, but is limited in its on/off kinetics. For these reasons much research has gone into tuning these protein photocycles to afford a wide-ranging platform with diverse kinetic parameters.

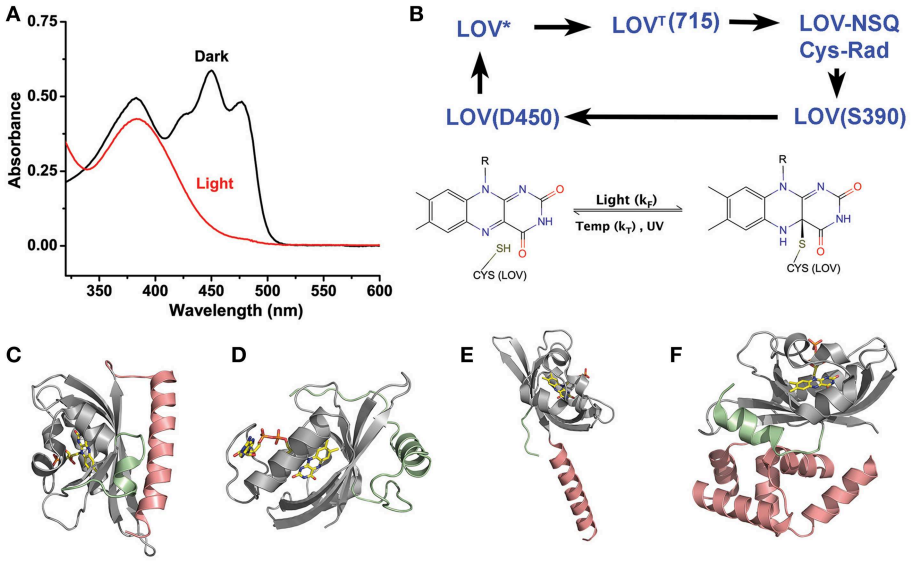

FIGURE 1 | LOV chemistry and structure. (A) Typical photocycle spectra of LOV containing proteins. Dark state proteins (black) demonstrate spectra consistent with oxidized flavin. Light activation (red) bleaches the 450 nm absorbing bands leaving a single 390 nm peak indicative of a C4a adduct. **(B)** LOV photocycles are characterized by a ground state oxidize flavin that form a flavin-cysteine C4a adduct following blue-light treatment. Adduct formation proceeds through an excited singlet state (LOV*) that rapidly forms a Triplet species (LOV^T). The triplet abstracts an electron from C38 generating a radical pair. Radical recombination forms the C4a adduct (LOV390). The adduct decays to the ground state by either thermal decay (k_T) or UV-scission. **(C–F)** Structures of LOV proteins involved in optogenetic tools, AsLOV2 **(C)**, VVD **(D)**, YtvA **(E)**, and EL222 **(F)**. The LOV core is depicted in gray, with associated N-terminal caps (green) and C-terminal caps (salmon).

Tuning of LOV Photochemistry Lifetime

Tuning of LOV photocycles has focused on three primary aspects of flavin chemistry and LOV structure (Christie et al., 2007; Nash et al., 2008; Zoltowski et al., 2009, 2011, 2013; Raffelberg et al., 2011; Song et al., 2011). First, dark-state LOV structures demonstrate two ground state conformations of the active site Cysteine (Fedorov et al., 2003; Christie et al., 2007; Sato et al., 2007; Zoltowski et al., 2009). Only one of these situates the Cysteine above the C4a position, where it is ideally poised for adduct formation (**Figure 2B**). Several studies have concluded that steric factors favoring an orientation away from the C4a position can destabilize the light-state adduct (Christie et al., 2007; Zoltowski et al., 2009; Kawano et al., 2013).

Second, adduct formation couples electron transfer and protonation of the N5 position of the isoalloxazine ring. These factors of LOV chemistry provide two practical means of attenuating adduct stability. (1) Factors that can stabilize increased electron density within the flavin system can stabilize the light state adduct. Thus, an increase in hydrogen bonding near the pyrimidine ring can stabilize the light-state species (Raffelberg et al., 2011; Zoltowski et al., 2011) (**Figure 2C**). (2) Factors that favor deprotonation of the N5 position of the isoalloxazine ring contribute to a faster decay pathway (Zoltowski et al., 2009, 2011; Raffelberg et al., 2011). This second factor is consistent with several reports indicating a single proton transfer event as being rate limiting in adduct decay (Corchnoy et al., 2003; Zoltowski et al., 2009, 2011; Pudasaini and Zoltowski, 2013). Further, adduct decay is readily base catalyzed by either increased solvent access to the active site, or the presence of exogenous bases such as imidazole (Kottke et al., 2003; Alexandre et al., 2007; Zoltowski et al., 2009, 2011; Purcell et al., 2010; Pudasaini and Zoltowski, 2013).

A third element of LOV photochemistry affecting adduct stability involves conformational changes within the isoalloxazine ring following adduct formation. The C4a adduct results in sp^3 hybridization of the C4a position as well as a tilt in the planarity of the flavin ring (Zoltowski and Gardner, 2011). These alter local steric constraints, particularly in residues occupying a position directly below the isoalloxazine ring (re-face) (**Figure 2D**). In turn, these combine to enable the re-face of the flavin ring to attenuate adduct stability through alterations in steric and electronic properties of residues at these sites (Zoltowski et al., 2009). Below we focus on residues affecting each of these parameters in model optogenetic systems. Due to different numbering for amino acids in LOV proteins, multiple reports of the same amino acid affecting adduct decay rates exists. To highlight the equivalence of sites in affecting adduct decay, we devised a numbering system for the LOV core, where residue 1 is the first non-PAS core residue in LOV proteins (C71 in VVD; K413 in AsLOV2). Numbering is then based in relation to the most widely studied system, AsLOV2. An alignment of LOV proteins according to the universal system is provided in **Figure 2A**. To avoid complications caused by insertions or deletions, these regions are not included in the numbering, rather all residue numbers reflect the equivalent residue in AsLOV2

TABLE 1 | Selected LOV-based optogenetic tools.

LOV-system	Effectors	Fold activation	Purpose	Lifetime (s)	References
AsLOV2	**Phototropism**			**2–4300 s (*WT* = 55 – 81)**	**a**
LINuSs1	NLS	3–7	Nuclear localization[20]	240 s (4 min)	Yazawa et al., 2009
LOV-TAP	TrpR	6, 70	DNA-binding/Tryptophan repressor	NA	Strickland et al., 2008; Wu et al., 2011
LOV-Rac	Rac1 (GTPase)	10	Control actin cytoskeletal dynamics	43 s	Wu et al., 2009
Tulips	ePDZ	2–49	Peptide caging		Strickland et al., 2012
LOV-TetR	TetR	NA	Tetracycline/DNA-binding	30 s	Moon et al., 2014
YtvA	**Stress**			**72–16000 (*WT* = 6240)**	**a**
Dusk/Dawn	FixL/FixJ	460	Transcription	NA	Ohlendorf et al., 2012
YF1	FixL	68	Kinase activity	~5900	Moglich et al., 2009
TetR	TetR	NA	Tetracycline/DNA-binding	2700	(100)
EL222	**Transcription**			**2.7–2000 (*WT* = 29)**	**a**
EL222-TF	HTH	>108	Transcription	~30 s	Motta-Mena et al., 2014
VVD	**Circadian clock**			**18000 s (WT)**	**a**
Caspase-9	Homo-dimerization	7.6–21	Caspase9 activation to regulate apoptosis	NA	Nihongaki et al., 2014
GAVPO	Gal4	200–300	Light induced transactivation of Gal4	7200 s	Chen et al., 2013; Ma et al., 2013
Magnets	Selective Dimerization of VVD	40-fold estimate	Create VVD heterodimers of two components	25 s–17000 h	Kawano et al., 2015
FKF1	**Flowering**			**>100000 s (WT)**	**a**
LITEZ	2-hybrid	53	Transcriptional control	NA	Polstein and Gersbach, 2012
LAD	Light induced dimerization	5	Rac1 induction of lamellipodia	62 h	Yazawa et al., 2009

*a, refer to **Table 2** for more details on range of photocycle lifetimes.*

as shown in **Figure 2A**. In **Table 2** we summarize rate-altering variants in four optogenetic systems, the corresponding residues in each protein as well as the generalized numbering system. Here forward we refer to residues by the generalized numbering system unless otherwise noted.

Steric Contacts at Active Site Cysteine

The active site cysteine (C38) adopts two possible configurations within the active site (Fedorov et al., 2003; Kottke et al., 2006; Sato et al., 2007; Zoltowski et al., 2009). Conformation 1 (Conf1) orients the thiol group toward the dimethyl-benzene ring of the active site flavin and away from the C4a position (**Figure 2B**). Such a conformation is stabilized by interactions with ordered water at the terminal end of a conserved solvent channel. Conformation 2 (Conf2) involves rotation of the C38 side chain, positioning the reactive thiol directly above the C4a position. Computational studies indicate that rotation of C38 is required for adduct formation, leading to a higher quantum yield for Conf2 (Fedorov et al., 2003; Sato et al., 2007). Initial searches for residues affecting adduct decay in LOV proteins identified a residue directly above C38 that attenuated adduct decay by up to an order of magnitude (Christie et al., 2007). Such data led to a proposed model, whereby steric factors favoring Conf1, could promote accelerated adduct decay in LOV proteins (Christie et al., 2007).

An alternative mechanism based approach to tuning LOV photocycles further solidified a role of the C38 conformation in altering decay kinetics. Studies of the fungal photoreceptor VVD identified two residues contacting C38 that can select for Conf1/2 (Zoltowski et al., 2009). Consistent with a steric model of regulating LOV kinetics, isoleucine residues that sterically constrain C38 favor Conf2 and a stable adduct. In contrast, decreased sterics through valine variants favor Conf1 and acceleration in adduct decay (Zoltowski et al., 2009). Combined, these two studies identified two key residues that can alter adduct decay pathways in VVD, AsLOV2, EL222 and YtvA in a predicable manner, namely V/I4 and V/I15 (Zoltowski et al., 2009, 2013). However, these sites do not only affect the conformation of C38. The close proximity to a solvent channel also attenuates adduct decay through alteration of the stability of the N5 protonation state and H-bonding to the active site flavin (Christie et al., 2007; Zoltowski et al., 2009; Kawano et al., 2013).

Hydrogen Bonding and the N5 Position

C4a adduct formation is coupled to an electron and proton transfer event. Detailed computational studies of LOV-type

TABLE 2 | Kinetics of thermal reversion for LOV constructs and variants at 296 K.

Protein	Time constant (s)	References
AsLOV2	**55, 68.3, 80, 81**	Nash et al., 2008; Zoltowski et al., 2009; Kawano et al., 2013; Zayner and Sosnick, 2014
N2A (N414A)	1427	
N2D (N414D)	69	
N2G (N414G)	615	
N2L (N414L)	1847	
N2Q (N414Q)	280	
N2S (N414S)	685	
N2T (N414T)	892	
V4I (V416I)	821	
V4T (V416T)	2.6	
V4L (V416L)	4300	
I15L (I427L)	19	
I15V (I427V)	4	
L41V (L453V)	160	
N80A (N492A)	54	
F82C (F494C)	282	
F82L (F494L)	206	
Q101A (Q513A)	261	
Q101D (Q513D)	5	
Q101H (Q513H)	30	
Q101L (Q513L)	1793	
Q101N (Q513N)	37.3	
N2A:Q101H	2	
N2A:Q101A	1900	
N2L:Q101A	2081	
V4I:L84I	1000	
VVD	**18000**	Zoltowski et al., 2009
I4V (I74V)	730	
C6A (C76A)	11000	
C6V (C76V)	21000	
T13V (T83V)	12000	
I15V (I85V)	780	
M54I (M135I)	24500	
M54L (M135L)	23000	
M84I (M165I)	20000	
M84L (M165L)	12500	
M84V (M165V)	16500	
I4V:I15V	28	
M54L:M84L	18000	
M54I:M84I	180000	
YtvA	**6240, 3600**	Zoltowski et al., 2009; Raffelberg et al., 2011
V4I (V28I)	16000	
I15V (I39V)	670	
N70A (N94A)	140	
N70D (N94D)	1250	
N70S (N94S)	300	
N80A (N104A)	2250	
N80D (N104D)	6890	
N80S (N104S)	1120	
Q101N (Q123N)	72	
EL222	**29**	Nash et al., 2011; Zoltowski et al., 2011
A42Q (A79Q)	227	
A42R (A79R)	2.7	
A42T (A79T)	8.9	
V4I:V84I	300	
V4I:L15I:A42Q:V48I	2000	

Red: Slow mutations; Green: Fast mutations; Black: Small effect.

chemistry provide mechanistic details important to tuning LOV photocycle kinetics. A landmark approach by Domratcheva et al. calculated transition states for adduct formation and adduct scission (Domratcheva et al., 2006). These transition states include a significant build up of electron density on the N5 position, exhibiting a partial charge of −0.275, −0.327, and −0.204 in the transition states for adduct formation, the light-state adduct and the transition state for adduct decay, respectively (Domratcheva et al., 2006). Notably, the largest localization of charge on N5 occurs in the light-state adduct. Based on these calculations, any factors that can aid in delocalization of electrons in the isoalloxazine ring will contribute to tuning the reaction landscape in LOV proteins. Moreover, the most significant effect of electron withdrawing agents will occur in stabilization of the light state adduct, where the largest buildup of charge exists. Due to these factors, delocalization of electrons through electron-withdrawing effects of H-bonding residues near N1, O2, N3, and O4 can have a pronounced effect on adduct stability (Raffelberg et al., 2011; Zoltowski et al., 2011). Several studies have examined the effect of H-bonding residues on attenuation of LOV chemistry.

In YtvA, Raffelberg et al. performed a detailed analysis of H-bonding residues on LOV reaction dynamics (Raffelberg et al., 2011). Variants of residues N70 (H-bonding to O2 and N3) and N80 (H-bonding to O4) were shown to have a large effect on the spectral and kinetic properties of the LOV photocycle (**Figure 2C**). Consistent with the reaction mechanism calculated by Domratcheva et al. variants at these sites tuned the ground and excited state absorption profiles, altered the quantum yields of adduct formation, and tuned the activation energies and lifetimes of the light-state adduct. Combined they were able to tune the half life of adduct decay within the range of 72–7000 s (Raffelberg et al., 2011).

A similar approach identified another location where H-bonding residues can tune reaction dynamics within the LOV active site. Whereas, most proteins contain a H-bonding residue near the flavin N1 position, EL222 does not (Zoltowski et al., 2011). The lack of an H-bonding residue at this site (position 42) enables increased solvent access to the active site and alteration of the electronic properties of the flavin (**Figure 2C**). NMR studies confirm an increase in electron withdrawing effects at the N1 position through introduction of H-bonding residues. Consistent with the Domratcheva mechanism, these electron withdrawing

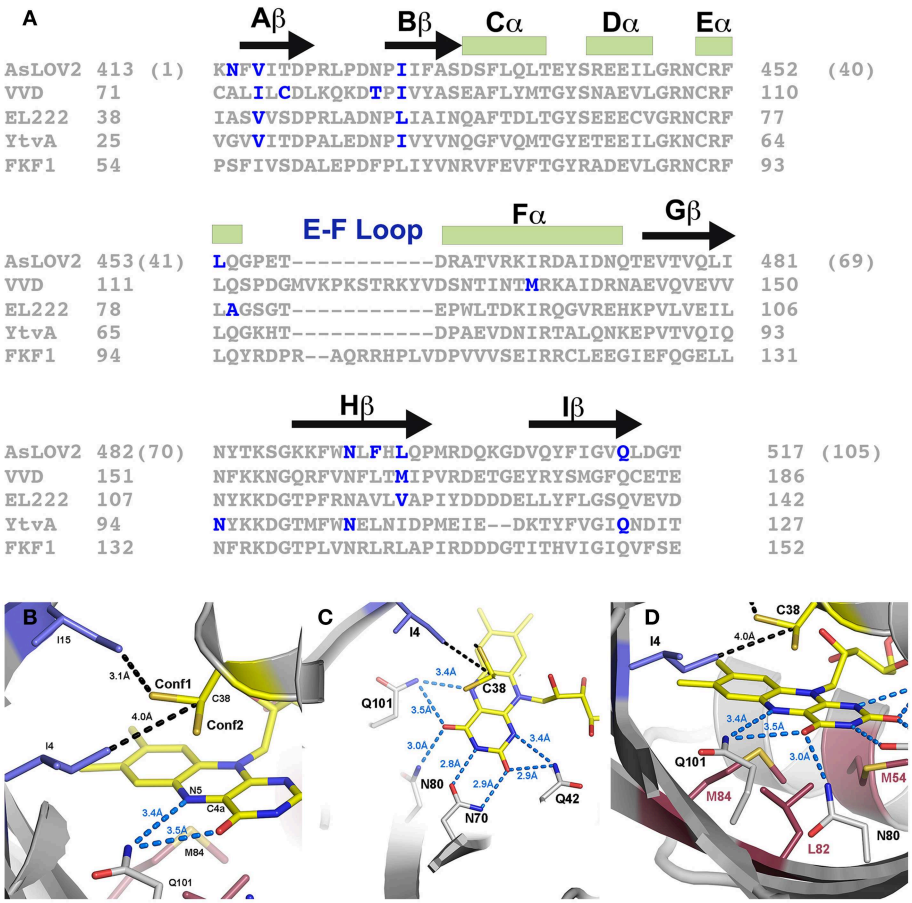

FIGURE 2 | Sites for rate altering variants. (A) Sequence alignment and universal numbering scheme for LOV proteins and optogenetic tools. The numbering scheme (in parentheses for AsLOV2) used in this review references K413 of AsLOV2 as residue 1 of the core LOV domain. All residues are then numbered in reference to the alignment provided, where residue inserts (E-F loop) or deletions (YtvA) are ignored in the universal numbering system. Residues that have been targeted for rate altering effects are depicted in blue. **(B)** Steric interactions (blue residues) select for alternative conformations of C38. Conf2 places the thiol directly above the C4a position, where it is poised for C4a adduct formation. I4 juts in between the two conformations placing its methyl group only 4.0 Å away from Cβ. Rotation between the two conformations would require movement of I4. **(C)** A network of H-bonds in the pyrimidine ring stabilize the C4a adduct through electron withdrawing effects. **(D)** Full active site containing residues attenuating Conf1/2 (blue), residues at the re-face (red) and H-bonding residues (gray). Three residues, M54, L82, and M84 attenuate adduct decay pathways through steric and electronic regulation of the flavin.

effects correlate with an increase in adduct stability. Through a combination of steric variants (position 4 and 15) and H-bonding at the N1 position (position 42), Zoltowski et al. were able to tune the EL222 lifetime over a range of 3–2000 s (Zoltowski et al., 2011, 2013). Importantly, these studies indicated that one cannot fully separate the effects of H-bonding and solvent access to the active site in affecting LOV kinetics as they impinge on the rate limiting N5 deprotonation.

N5 deprotonation can either be achieved through spontaneous deprotonation, proton abstraction by an unknown endogenous base or external bases such as imidazole (Kottke et al., 2003; Alexandre et al., 2007). Several studies have concluded that base catalysis is attenuated by solvent access to the flavin active site through a conserved solvent channel (Zoltowski et al., 2009, 2011; Purcell et al., 2010; Pudasaini and Zoltowski, 2013). In all known LOV structures, ordered water is present adjacent to C38. FTIR and *in vivo* approaches conclude that these ordered water molecules contribute to the native decay pathway and that dehydration of LOV proteins leads to large effects on adduct decay kinetics (Chan and Bogomolni, 2012; Pennacchietti et al., 2014). Further, studies of the fungal photoreceptor VVD, a bacterial LOV histidine kinase LOVK and a short LOV (sLOV) protein identify two main factors affecting solvent access (Zoltowski et al., 2009, 2011; Purcell et al., 2010; Pudasaini and Zoltowski, 2013; El-Arab et al., 2015). These include two residues (I4 and I15) that sterically interact with Conf1 to occlude solvent access to the LOV active site (Zoltowski et al., 2009). In addition, Ncap and Ccap elements adjacent to the β-scaffold regulate solvent accessibility, presumably through stabilization of the LOV core

(Purcell et al., 2010). Combined these sites can have up to a 1000-fold effect on solvent access as assayed by base catalysis efficiency (Zoltowski et al., 2009; Purcell et al., 2010; El-Arab et al., 2015).

The Flavin Re-face

Initial research into LOV proteins focused on the LOV1 and LOV2 domains of phototropins. The LOV1 and LOV2 domains were distinguished by differences in their photocycle properties and structural dynamics. Specifically, LOV1 domains offer longer photocycle lifetimes and dampened conformational responses as measured by FTIR (Iwata et al., 2005; Yamamoto et al., 2008; Alexandre et al., 2009b). In contrast, LOV2 domains had fast cycling photocycles and FTIR analysis indicated large-scale disruption of the LOV β-sheet following photoactivation. Research into the source of these differences in LOV domain function identified a Phe→Leu substitution between LOV2 and LOV1 domains that impart altered conformational landscapes and photocycle kinetics. Specifically, a F1010L (position 82) variant directly beneath the isoalloxazine ring of Neo1-LOV2 led to a 10-fold slower photocycle lifetime (90 s vs. 870 s) and led to LOV1 type conformational dynamics (Yamamoto et al., 2008). These studies were the first to identify the re-face of the flavin ring system as a key region regulating LOV structure and dynamics.

The ability to tune LOV reaction dynamics through alterations of residues near the re-face of the flavin draws on mechanistic analysis of the LOV photocycle. Similar to electron withdrawing effects stabilizing a build-up of charge in the isoalloxazine ring, the re-face of flavins is sensitive to the local electronic environment. Specifically, studies of flavoproteins indicates that diffuse electron containing amino acids such as Phe and Met can contribute electron density to the isoalloxazine ring (Ghisla and Massey, 1989). In LOV proteins, such interactions would promote increased conformational dynamics following light activation and destabilize the build up of charge following C4a bond formation.

These properties of the flavin re-face were exploited in a later study focusing on naturally varying residues that distinguish LOV photocycle properties. The study identified a cluster of residues within the re-face that tune LOV function over several orders of magnitude (Zoltowski et al., 2009) (**Figure 2D**). In the fungal photoreceptor VVD, two Methionine residues alter the steric and electronic environment of the active site flavin to promote adduct decay (M54 and M84). Introduction of branched chain aliphatic residues (I/L) leads to a stabilization of electron density within the isoalloxazine ring. The stabilization is confirmed by a long-lived light-state adduct and stabilization of reduced semiquinone species (Zoltowski et al., 2009; Vaidya et al., 2011). These sites allowed extension of the C4a adduct lifetime to the order of days, allowing for the first direct determination of a light-state structure (Vaidya et al., 2011). Combined, the studies indicate that the re-face can contribute to LOV kinetics and signaling through two interlocked manners. First, diffuse electron containing amino acids (M/F) destabilize the light state adduct and amplify conformational changes. In contrast, branched chain aliphatic residues promote steric constraints and charge stabilization on the active site flavin, thereby dampening conformational changes and promoting a stable light-state adduct.

Exploitation of the LOV Photocycle in Optogenetic Tools

Research into the divergent photocycle lifetimes of LOV proteins enables tuning of LOV kinetics by over four-orders of magnitude. These offer great potential in affording a tunable platform for optogenetic tools; however, exploitation of LOV photocycle properties in optogenetics has been fairly limited. Here we discuss some useful applications that result from altering LOV photocycle properties. In addition, we demonstrate current limitations to the above approach to alter LOV photocycle kinetics for tunable optogenetic tools.

Currently, two categories of optogenetic tools directly exploit properties of the LOV photocycle for an engineered cell biology tool. Both take advantage of fluorescent properties of LOV proteins to either develop new fluorescent imaging tools (iLOV, BsFbFP, and PpFbFP) or for possible implementation in super-resolution microscopy (Drepper et al., 2007; Chapman et al., 2008). A recent review of LOV proteins as fluorescent reporters provides detailed commentary on their development and improvement (Mukherjee and Schroeder, 2015), here we provide a brief synopsis of fluorescent LOV reporters and their utility. iLOV, BsFbFP, and PpFbFP take advantage of the fluorescent properties of dark-state LOV proteins (AsLOV2, YtvA, and a LOV protein from *Pseudomonas putida*, respectively) to allow the development of an oxygen independent fluorescent reporter (Drepper et al., 2007; Chapman et al., 2008; Gawthorne et al., 2012; Wingen et al., 2014). Initial work in fluorescent LOV reporters was conducted by Drepper et al. where they demonstrated oxygen-independent activity that for BsFbFP and PpFbFP that allowed anaerobic imaging. All these systems rely on swapping C38, required for adduct formation, with an inactive alanine to improve fluorescent properties of LOV proteins. Subsequent work by Chapman et al. used directed evolution approaches to improve the fluorescent properties of the iLOV system. The results of these studies were the development of a robust alternative to GFP reporter systems (Drepper et al., 2007; Chapman et al., 2008; Mukherjee and Schroeder, 2015). Additional studies have greatly improved the quality of fluorescent LOV reporters and extended their utility to additional approaches (i.e., metal sensing) (Drepper et al., 2010; Christie et al., 2012b; Ravikumar et al., 2015). These fluorescent LOV reporter systems exhibit brightness competitive with GFP, but with improved stability (reversible photobleaching) and functionality in low-oxygen or anaerobic conditions.

The second exploits both the UV-catalyzed adduct decay pathway that results in a steady-state light/dark photostationary state, and the fluorescent properties of dark-state LOV proteins. Specifically, researchers identified that violet/UV light can promote adduct scission, resulting in a photoswitchable

fluorescent reporter. They proposed that these systems can be exploited in YtvA for super-resolution microscopy approaches (Losi et al., 2013). The photoswitchable fluorescent properties make LOV proteins a possible template for fluorescence photoactivation localization microscopy (FPALM), however these systems are still currently being optimized for improved performance in cellular systems. Several factors, including the lifetime of the light-state adduct and differences in *in vitro* and *in vivo* photochemical properties limit these approaches (Pennacchietti et al., 2014).

Unfortunately initial attempts to incorporate rate-altering variants into optogenetic tool design have been hampered by unexpected effects on signal propagation. Rate altering variants have only been used in VVD (Wang et al., 2012; Chen et al., 2013; Ma et al., 2013; Kawano et al., 2015), and AsLOV2 (Strickland et al., 2008) platforms. Examination of variants in these and other systems indicates that they can often grossly affect signal propagation, thereby damaging the fidelity of the optogenetic tools (Gleichmann et al., 2013; Kawano et al., 2015). Specifically, a large random mutagenesis approach aimed at examining residue substitutions in an optogenetic device revealed that many of the sites targeted for affecting LOV photocycle lifetimes have deleterious effects on signal propagation (Gleichmann et al., 2013). These deleterious effects were significant in all variants that disrupt H-bonding contacts to the active site flavin (e.g., N70, N80, Q101). Only aliphatic sites showed minimal effect on signal propagation. Thus, in order to have greater control of optogenetic tools, we are forced to both consider chemical parameters and their structural consequences. Therefore, it is of keen interest to understand signal propagation in LOV systems to provide tunable LOV optogenetic devices.

Signal Transduction Mechanisms

LOV structures are distinguished by three general factors. All photoreactive elements are confined to a core PAS domain defined by the central β-scaffold and a helical interface that house the photoreactive flavin (Zoltowski and Gardner, 2011). Signal propagation, however, is isolated to Ncap and Ccap extensions to the PAS core that afford the capacity to inhibit signal transduction through sequestration or constrainment of a signaling motif (**Figure 3**) (Crosson et al., 2003; Halavaty and Moffat, 2007; Zoltowski et al., 2007; Zoltowski and Gardner, 2011; Diensthuber et al., 2013). These elements can exist alone in short LOV proteins (sLOV) or as a linker to signal transduction domains (e.g., histidine kinase, F-box, GAF domain, GGDEF domain etc…). Downstream signaling then focuses on several allosteric mechanisms of signal transduction stemming from C4a adduct formation and protonation of the N5 position. While initially hoped to function as a light switch between inactive (dark) and active (light) states, all characterized systems exist as more of a "dimmer-model," where all proteins retain some dark-state function that can be amplified by increasing light-intensities (Crosson and Moffat, 2001; Strickland et al., 2008, 2010; Pudasaini and Zoltowski, 2013). These aspects currently limit the fidelity of LOV optogenetic tools (**Table 1**). We begin by recapping key elements of the LOV photocycle that initiate signal transduction before focusing on mechanisms for each of the model optogenetic systems below.

Mechanistic studies of the LOV photocycle by numerous researchers identify two chemical elements that can initiate signal transduction in LOV systems. As noted above, these are inherently coupled to approaches to tune reaction dynamics and kinetics. First, adduct formation results in protonation of the flavin N5 position. N5 protonation in turn alters the H-bonding landscape near the flavin active site that has the capacity to induce allosteric conformational responses (Halavaty and Moffat, 2007; Zoltowski et al., 2007; Freddolino et al., 2013). Second, adduct formation results in a build up of electron density within the isoalloxazine ring, primarily centered on the N5 and C4a positions (Domratcheva et al., 2006). The build up of charge can be read out by nearby diffuse electron containing amino acids (F/M) that typically occupy positions near the re-face. As detailed by FTIR studies differentiating LOV1 and LOV2 domains of phototropins these residues can propagate conformational changes through disruption of the LOV β-sheet (Iwata et al., 2003, 2005; Yamamoto et al., 2008; Alexandre et al., 2009b). These aspects indicate that conformational changes initially propagate from residues within Aβ, Iβ and N/Ccap elements as detailed below (**Figure 4**).

AsLOV2

The LOV2 domains of plant phototropins are the most heavily studied of all LOV domains. Similarly, the AsLOV2 domain is the most commonly exploited LOV protein for optogenetic tools. Despite extensive characterization, the development of new robust tools based on an AsLOV2 platform remains challenging. These in part stem from residual dark-state activity of AsLOV2 proteins that limit the fold-amplification of light state signals (**Table 1**). We outline the current models of signal propagation in this system here, with specific emphasis on methods used to optimize LOV2 signaling in optogenetic tools.

Similar to many of the LOV domains, signal propagation in AsLOV2 is initiated by a combination of C4a adduct formation and N5 protonation (**Figure 4A**). Protonation of the N5 position alters H-bonding contacts to a glutamine residue (Q101) conserved in the majority of LOV proteins. FTIR, NMR, crystallographic and computational studies identify Q101 as the locus for signal transduction, albeit with slight deviations in the mechanisms of signal propagation (Harper et al., 2003, 2004; Iwata et al., 2003, 2005; Nozaki et al., 2004; Freddolino et al., 2006, 2013; Halavaty and Moffat, 2007; Nash et al., 2008; Yamamoto et al., 2008; Alexandre et al., 2009b). All models couple adduct formation to a marked reduction in the helical content of LOV2 proteins as well as a reduction in β-sheet contacts. These led to a model of signal propagation centered on the Hβ and Iβ (contains Q101) strands that allosterically regulate a C-terminal helix (Ccap; Jα). NMR studies indeed confirmed that adduct formation results in a weakening of the β-scaffold and light-driven unfolding of Jα (Harper et al., 2003, 2004).

Recent crystallographic structures of extended AsLOV2 structures indicate that the Ccap is not the only locus for structural regulation of effector proteins. Dark-state structures

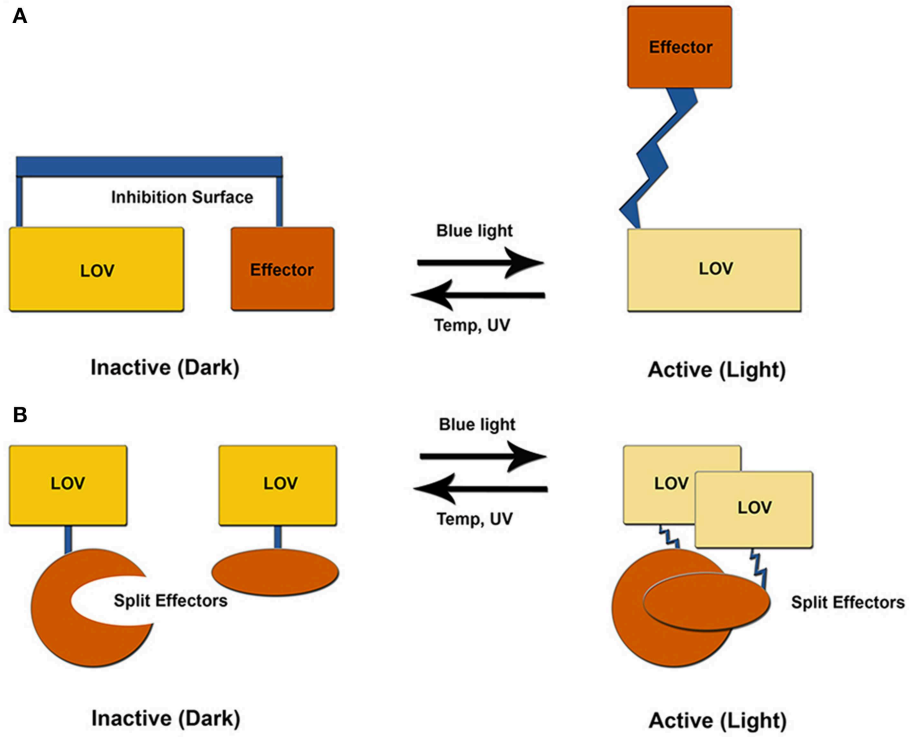

FIGURE 3 | LOV optogenetic tools. Existing LOV-based tools exploit one of two possible mechanisms. **(A)** LOV and effector are attached through a helical linker to create an inhibitory surface that is released following photoexcitation. **(B)** An effector molecule is split into two inactive components. Light activation induces LOV-mediated dimer formation to activate the effector molecule.

and dark-grown crystals exposed to blue-light provided a mechanism of signal propagation linking the flavin active site to both the Ncap and Ccap. N-terminally extended structures revealed an additional short helical element directly preceding the Aβ strand. The Ncap element also directly interacts with Jα, thereby linking Ncap and Ccap signaling elements (Halavaty and Moffat, 2007). These two helical elements are connected to the N5 position by Q101, which undergoes a light-driven switch following adduct formation. Briefly, the N5 proton alters H-bonding interactions between the flavin, Q101 and N2 in Aβ (Halavaty and Moffat, 2007). In light of previous NMR data, indicating unfolding of Jα, a consensus model of allosteric regulation was obtained. In the consensus model adduct formation alters H-bonds to Iβ and Aβ to favor dislodgement and unfolding of Jα. These in turn relieve inhibitory contacts between the LOV core and downstream signaling elements (**Figure 4A**).

At present, optogenetic tools exploit light-driven unfolding of a Ccap helical element to regulate an effector module through one of two possible pathways. These often rely on linking an effector protein through a compound helix coupled to Jα. Resulting unfolding of the Jα helix can then be used to relieve inhibition of the effector module through release of steric constraints, or to expose the Jα helix for light-driven interactions with an effector protein (**Figure 3**). These systems are best demonstrated by a LOV-Rac fusion (PA-Rac1) and a LOV based modification to the mammalian two-hybrid system, although several other platforms exist (**Table 1**) (Strickland et al., 2008, 2010; Wu et al., 2009; Lungu et al., 2012).

In PA-Rac1, the AsLOV2 domain is fused to Rac through a C-terminal compound helix composed of the Jα helix and N-terminus of Rac (Wu et al., 2009). Light activation leads to rotation of Q101, to unfold the compound helix, relieving steric constraints at an inhibitory surface between the LOV helical face and Rac. Although, PA-Rac1 is a robust optogenetic tool, crystallographic structures of the fusion protein highlight several complications in designing composite optogenetic devices. Namely, design of the compound helix must retain sufficient elements to maintain LOV-type signaling, but allow for close retention of the effector domain to develop an inhibition surface.

An alternative approach to AsLOV2 optogenetic tools is to couple allosteric regulation of the Jα helix to induce light driven dimerization. Two research groups have exploited this approach to induce gene transcription through modified yeast/mammalian 2-hybrid approaches or cellular colocalization. These systems attach a peptide-recognition element to the C-terminal end of the Jα helix. In the dark-state, binding of the Jα helix to the LOV core constrains the peptide recognition element rendering it incapable of binding to its cognate effector domain. Light activation disorders the Jα helix relieving constraints and leading to protein:protein interactions. Although conceptually based on the same principle, the approaches differ in their recognition element and cognate effector.

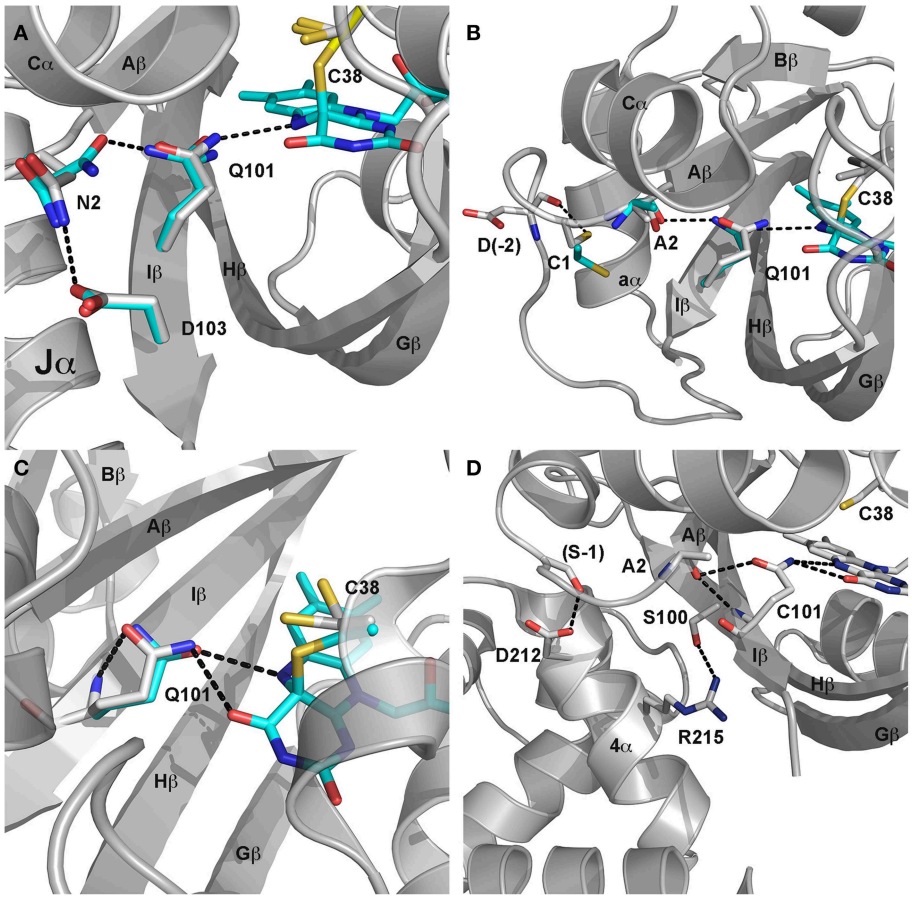

FIGURE 4 | LOV signaling mechanisms. (A) Dark (gray) and light (cyan) state structures of AsLOV2. Photoactivation leads to rotation of Q101 to alter H-bonding contacts to N2. N2 undergoes a light driven interchange involving contacts with D103 and Q101. The H-bond switch affects Ncap structure to disorder the Jα helix. **(B)** Dark (gray) and light (cyan) state structures of VVD. C4a adduct formation promotes rotation of Q101 to alter H-bonds to A2. Movement of the Ncap reorientates C1 to disrupt contacts with D-2, leading to rearrangement of the Ncap and dimer formation. **(C)** (YtvA) and **(D)** (EL222) mechanisms are less understood but likely involve Q101 and H-bonding contacts (black dotted line) to neighboring residues.

The first system, termed TULIPS (Tunable, Light-controlled Interaction Proteins), involved fusing a peptide designed to interact with PDZ domains (Strickland et al., 2012). These systems demonstrated remarkable ability to direct cellular localization of target proteins. Building upon previous attempts to optimize the fidelity of the light-dark switch (Strickland et al., 2010), Strickland et al. devised an optimal construct by coupling variants within the Ncap and Ccap helices to repress residual dark-state activity. A combined T406A, T407A (Ncap) and I532A (Ccap) (AsLOV2 numbering) triple variant abolished dark-state activity, but retained light-dark switching (Strickland et al., 2012). Further, they directly employed rate-altering variants (V4I) to demonstrate that *in vitro* approaches to alter LOV kinetics translated to *in vivo* function.

Kuhlman, Hahn and coworkers used an analogous approach, where they caged peptide elements recognized by Vinculin as modified Jα helices (ipaA and SsrA) (Lungu et al., 2012; Yi et al., 2014). Using molecular modeling they designed chimeric Jα helices that retained elements required for LOV docking and Vinculin binding. The resulting chimera protein demonstrated high affinity in the light and dark with 19-fold amplification in binding following blue-light exposure. Rational design of protein variants to repress dark-state binding identified two residues L514K and L531E (AsLOV2 numbering) that decrease dark-state binding, while having only minor effects on the light-state. The resulting system demonstrates a robust 49-fold amplification in affinity following light-treatment. A more recent study aimed at improving the SsrA system identified key structural elements that allow tuning of the light-dark binding affinity of LOV-SsrA and its cognate receptor (Guntas et al., 2015). A key highlight of the two approaches is that residues that attenuate signal amplification (L531E/I532A) do not necessarily apply to all systems, but rather key elements within the chimera proteins distinguish the conformational landscape.

VVD

VVD is a sLOV protein from *Neurospora crassa* involved in adaptation to increasing levels of blue light (Schwerdtfeger

and Linden, 2003; Elvin et al., 2005). VVD contains only the photoactive LOV domain fused to an Ncap required for signal transduction (Zoltowski et al., 2007). In contrast to AsLOV2, signal transduction in VVD does not require an effector domain, rather involves competitive light-driven formation of protein:protein complexes (Zoltowski and Crane, 2008). Structurally, VVD is one of only two LOV containing proteins that have been crystalized directly as dark-state and light-state proteins offering keen insight into signal propagation in sLOV proteins.

Initial crystal structures revealed a mechanism of signal transduction closely related to AsLOV2, but differing in its functional output. Briefly, direct rotation of Q101 was observed following N5 protonation (Zoltowski et al., 2007; Vaidya et al., 2011). Rotation of Q101 to favor H-bonds to the newly protonated N5 propagates out to the surface through interactions with A2 (position 72 VVD numbering) within Aβ (**Figure 4B**). These in turn lead to rearrangement of Ncap elements through a conserved hinge region (Zoltowski et al., 2007; Lamb et al., 2008, 2009; Vaidya et al., 2011; Lokhandwala et al., 2015). Essential to signal propagation is C1, which rotates from a buried position between the LOV core and Ncap. These movements expose a hydrophobic cleft to support homodimer formation through reorganization of Ncap elements. SAXS and light-state crystal structures confirm reorganization of the Ncap to favor a low affinity, rapidly dissociating dimer.

Light-driven dimer formation ideally suits VVD for optogenetic control of protein:protein interaction, however the low dimer affinity and long lifetime limit its fidelity. Several approaches have been used to both employ and optimize VVD as an optogenetic tool. An early approach was the VVD light-on system, which is a modification of yeast and mammalian 2-hybrid approaches (Chen et al., 2013; Ma et al., 2013). Several attempts to optimize the light-on system have been conducted that exploit photochemical and structural mechanisms of signal transduction (Ma et al., 2013). A more recent approach termed magnets, has further evolved the VVD system to maximize light-amplification of signal with desired on/off kinetics (Kawano et al., 2015). Since the two approaches are similar we focus on the more recent magnets system to highlight structure and chemical tuning of optogenetic tools.

The VVD-based magnet system focused on alleviating two limitations of VVD-based tools, namely slow on/off kinetics and weak dimerization. The magnet system examined the key Ncap signaling region to evolve a pair of VVD variants capable of hetero-dimerization, but incapable of homodimerization. Specifically, they introduced charged residues at key dimer contact regions (Ile52 and Met55; VVD numbering). By creating a VVD pair with negatively charged resides at Ile52/Met55 and a positively charged version, Kawano et al. were able to design a robust system with ∼40-fold activation upon light treatment (Kawano et al., 2015). By incorporating slow cycling variants in one component, paired with fast cycling elements in the other species, they were further able to amplify signal output and introduce improved on/off kinetics. The resulting system has not been employed widely, but affords tunable kinetics (four-orders of magnitude) and signal output (up to 1300% increase in signal intensity) (Kawano et al., 2015).

EL222

EL222 was initially discovered as one of four LOV domain containing signaling proteins in the marine bacterium *E. litoralis* (Swartz et al., 2007). The 222-amino acid protein contains an N-terminal LOV domain directly coupled to an HTH-DNA binding domain through a short C-terminal linker (Nash et al., 2011). The HTH domain acts in a manner analogous to Ncap and Ccap elements in VVD/AsLOV2, where the α4 dimerization helix of the HTH domain docks to the LOV β-scaffold. NMR and crystallographic studies confirm a signaling mechanism that incorporates both Ccap reorientation and dimerization (Nash et al., 2011; Zoltowski et al., 2013).

Adduct formation is believed to propagate to the C-terminal HTH domain through rotation of Q101 that leads to unfolding of the C-terminal linker and release of the α4 helix of the HTH domain (Nash et al., 2011) (**Figure 4D**). Release of steric constraints on the HTH domain facilitates dimerization of EL222 through both the N-terminal LOV domain and α4 (Zoltowski et al., 2013). EL222 dimerization is also facilitated by DNA binding to two copies of a 5 bp RGNCY consensus motif separated by 2 A/T base pairs (Y = C/T, R = A/G, N = any nucleotide) (Rivera-Cancel et al., 2012). DNA binding in turn can be harnessed for activation of gene transcription using methods analogous to VVD and AsLOV2 above (Motta-Mena et al., 2014).

Several attempts to optimize EL222 function through both chemical and structural tuning have been employed. Mechanism based tuning EL222 chemistry currently allow for lifetimes between 2 and 2000 s (Zoltowski et al., 2011, 2013). These variants have not been tested for fidelity in optogenetic tool function, however they reversibly bind DNA following light-dark cycles (Zoltowski et al., 2013). Further, signal propagation has been optimized through identification of a high affinity DNA binding site through both Chip-seq and SELEX approaches (Rivera-Cancel et al., 2012). Current iterations of the EL222 system afford over 100-fold signal amplification with rapid on/off kinetics (Motta-Mena et al., 2014). Mathematical modeling of DNA binding and photocycle properties has identified a substantial role of the LOV lifetime in dictating temporal control of gene transcription (Motta-Mena et al., 2014).

YtvA

YtvA regulates light-activated stress response pathways in *B. subtilis*. It is the best-characterized bacterial LOV protein, affording detailed knowledge of structural and chemical regulation of signaling mechanisms (Bednarz et al., 2004; Buttani et al., 2007; Avila-Perez et al., 2009; Mansurova et al., 2011; Raffelberg et al., 2011; Engelhard et al., 2013; Losi et al., 2013). These detailed studies enable widespread usage in optogenetic tools. Currently, these employ a general mechanism that bares homology to those present in AsLOV2. Namely, primary signaling mechanisms proceed through C4a adduct formation to regulate a C-terminal effector domain through

allosteric regulation of a Jα helix (Losi et al., 2005; Buttani et al., 2007; Engelhard et al., 2013) (**Figure 4C**). However, in contrast to AsLOV2, where unfolding of Jα mediates signaling, YtvA structural studies suggest signal propagation results from alteration of the Jα helical tilt (Tang et al., 2010; Engelhard et al., 2013). The helical tilt has been harnessed to regulate C-terminal effectors to regulate histidine kinases and gene transcription (Moglich et al., 2009; Ohlendorf et al., 2012; Diensthuber et al., 2013; Gleichmann et al., 2013).

The initial YtvA system was constructed by swapping the YtvA LOV domain, including the Jα helix with the PAS regulatory domain of the histidine kinase FixL (YF1). The resulting system imparted light-regulated control of kinase activity (Moglich et al., 2009). Through alteration of the length of the Jα-FixL helical linker, Möglich et al. were able to tune functionality to enable either light-state or dark-state kinase activity. In a novel extension to the YF1 system, they exploited the transcription activity of the cognate response regulator FixJ to enable light-activate gene regulation in bacterial species (Ohlendorf et al., 2012). The resulting Dusk/Dawn system allows for both light-activation and light-repression of gene transcription depending on the YF1 system employed. In both systems up to 460-fold induction of gene transcription is possible (Ohlendorf et al., 2012).

Several iterations of the YF1 system have been developed that optimize signal transduction as well as photochemical properties. Structural studies of a full-length YF1 chimera indicate that signal transduction impinges on both Ncap and Ccap elements, which undergo an alteration in helical pitch at N/C-terminal coiled-coil dimerization helices (Engelhard et al., 2013). These are coupled to LOV domain photochemistry through multiple H-bonding interactions. Mutational analysis of residues propagating signal transduction can tune the output and directionality of the Dusk/Dawn system. An analogous study examined the effect of residues lining the flavin active site (Gleichmann et al., 2013; Diensthuber et al., 2014). These indicated that residues employed to tune LOV photocycles could have deleterious effects on signal propagation, indicating that in some cases chemical and structural tuning cannot be separated.

FKF1

The plant photoreceptor FKF1 contains a single LOV domain, which binds to Gigantea (GI) following blue-light activation (Imaizumi et al., 2003; Sawa et al., 2007; Baudry et al., 2010). Biological studies indicate that only the N-terminal LOV domain of FKF1 is necessary for light-induced dimerization with GI (Sawa et al., 2007). Currently, two systems exploit the light driven FKF1-LOV:GI interaction for optogenetic tools (Yazawa et al., 2009; Polstein and Gersbach, 2012).

A recently reported system LITEZ utilizes blue light induced interaction between FKF1-LOV and GI to induce gene expression (Polstein and Gersbach, 2012). The design of this optogenetic tool resembles a 2-hybrid gene expression system, where one component (GI) binds DNA through inclusion of an N-terminal Zinc Finger domain. The photoreactive FKF1-LOV then activates gene transcription through recruitment of a C-terminal VP16 element to GI following light-activated LOV:GI complex formation.

The LITEZ system has been reported to be very efficient with up to 53-fold increase in gene activation (luciferase) following blue light treatment (Polstein and Gersbach, 2012). Due to the long-lived photocycle of FKF1-LOV ($100000\,s < \tau$), it is not necessary to continuously illuminate the live cells. However, the photocycle half-life of FKF1-LOV currently limits the system in regards to on/off kinetics. Due to a lack of detailed studies of FKF1 structure and kinetics, the system is the least characterized and is limited in the ability to fine tune signal amplification and on/off kinetics.

Concluding Remarks

LOV proteins afford a unique platform for coupling blue-light activation to a wide range of signal transduction elements. Although significant detail is known for chemical and structural mechanisms in these systems, there still remains a limitation to the design and fidelity of LOV-based tools. Further research into light-state crystal structures of LOV proteins as well as LOV optogenetic tools is needed to enable improved, robust design of optogenetic devices. Several key areas are noted here for future development.

Currently, structural studies of LOV proteins are, in most cases, limited to the isolated LOV domains. Few structures exist for full-length or multi-domain containing LOV proteins. These limit our understanding of allosteric mechanisms in LOV containing proteins and similarly optogenetic tools. Structural studies of LOV domains with extended N- and C-terminal regions indicate that these elements are essential to light-dark switching, even without the downstream effector domains. Subsequent studies have shown that targeting these elements for mutagenesis is a robust method for tuning optogenetic function. To further extend the utility of these tools it is essential for researchers to better understand the natural mechanisms coupling LOV dynamics to downstream effectors through the N- and C-terminal linkages.

Extension of our understanding of allosteric mechanisms of signal transduction in LOV proteins and optogenetic tools should leverage existing efforts to tune LOV domain chemistry. Direct determination of light-state structures has been facilitated by rate-altering variants. These structures afford snapshots of the light and dark-adapted states that facilitate understanding of optogenetic tools. Unfortunately, few studies have examined the effects of these variants on *in vivo* function or optogenetic tool utility. Going forward, it is recommended that studies of rate altering variants and corresponding light state structures be conducted in concert with their effect on *in vivo* function and optogenetic tool design. Such efforts may provide a global understanding of how LOV chemistry and structure regulate signal transduction and allostery.

Funding

Work was funded by the National Institutes of Health and the Herman Frasch Foundation (R15GM109282 and 739-HF12 to BZ).

References

Alexandre, M. T., Arents, J. C., van Grondelle, R., Hellingwerf, K. J., and Kennis, J. T. (2007). A base-catalyzed mechanism for dark state recovery in the *Avena sativa* phototropin-1 LOV2 domain. *Biochemistry* 46, 3129–3137. doi: 10.1021/bi062074e

Alexandre, M. T., Domratcheva, T., Bonetti, C., van Wilderen, L. J., van Grondelle, R., Groot, M. L., et al. (2009a). Primary reactions of the LOV2 domain of phototropin studied with ultrafast mid-infrared spectroscopy and quantum chemistry. *Biophys. J.* 97, 227–237. doi: 10.1016/j.bpj.2009.01.066

Alexandre, M. T. A., van Grondelle, R., Hellingwerf, K. J., and Kennis, J. T. M. (2009b). Conformational heterogeneity and propagation of structural changes in the LOV2/J alpha domain from *Avena sativa* phototropin 1 as recorded by temperature-dependent FTIR spectroscopy. *Biophys. J.* 97, 238–247. doi: 10.1016/j.bpj.2009.03.047

Avila-Perez, M., Vreede, J., Tang, Y. F., Bende, O., Losi, A., Gartner, W., et al. (2009). *In Vivo* mutational analysis of YtvA from *Bacillus subtilis* mechanism of light activation of the general stress response. *J. Biol. Chem.* 284, 24958–24964. doi: 10.1074/jbc.M109.033316

Baudry, A., Ito, S., Song, Y. H., Strait, A. A., Kiba, T., Lu, S., et al. (2010). F-box proteins FKF1 and LKP2 act in concert with ZEITLUPE to control arabidopsis clock progression. *Plant Cell* 22, 606–622. doi: 10.1105/tpc.109.072843

Bednarz, T., Losi, A., Gartner, W., Hegemann, P., and Heberle, J. (2004). Functional variations among LOV domains as revealed by FT-IR difference spectroscopy. *Photochem. Photobiol. Sci.* 3, 575–579. doi: 10.1039/b400976b

Bittl, R., Kay, C. W. M., Weber, S., and Hegemann, P. (2003). Characterization of a flavin radical product in a C57M mutant of a LOV1 domain by electron paramagnetic resonance. *Biochemistry* 42, 8506–8512. doi: 10.1021/bi034123i

Boyden, E. S. (2011). A history of optogenetics: the development of tools for controlling brain circuits with light. *F1000 Biol. Rep.* 3, 11. doi: 10.3410/B3-11

Buttani, V., Losi, A., Eggert, T., Krauss, U., Jaeger, K.-E., Cao, Z., et al. (2007). Conformational analysis of the blue-light sensing protein YtvA reveals a competitive interface for LOV-LOV dimerization and interdomain interactions. *Photochem. Photobiol. Sci.* 6, 41–49. doi: 10.1039/B610375H

Chan, R. H., and Bogomolni, R. A. (2012). Structural water cluster as a possible proton acceptor in the aduct decay reaction of oat phototropin 1 LOV2 domain. *J. Phys. Chem. B* 116, 10609–10616. doi: 10.1021/jp304934t

Chapman, S., Faulkner, C., Kaiserli, E., Garcia-Mata, C., Savenkov, E. I., Roberts, A. G., et al. (2008). The photoreversible fluorescent protein iLOV outperforms GFP as a reporter of plant virus infection. *Proc. Natl. Acad. Sci. U.S.A.* 105, 20038–20043. doi: 10.1073/pnas.0807551105

Chen, X., Wang, X., Du, Z., Ma, Z., and Yang, Y. (2013). Spatiotemporal control of gene expression in mammalian cells and in mice using the LightOn system. *Curr. Protoc. Chem. Biol.* 5, 111–129. doi: 10.1002/9780470559277.ch120267

Christie, J. M., Corchnoy, S. B., Swartz, T. E., Hokenson, M., Han, I.-S., Briggs, W. R., et al. (2007). Steric interactions stabilize the signaling state of the LOV2 domain of phototropin 1. *Biochemistry* 46, 9310–9319. doi: 10.1021/bi700852w

Christie, J. M., Gawthorne, J., Young, G., Fraser, N. J., and Roe, A. J. (2012a). LOV to BLUF: flavoprotein contributions to the optogenetic toolkit. *Mol. Plant* 5, 533–544. doi: 10.1093/mp/sss020

Christie, J. M., Hitomi, K., Arvai, A. S., Hartfield, K. A., Mettlen, M., Pratt, A. J., et al. (2012b). Structural tuning of the fluorescent protein iLOV for improved photostability. *J. Biol. Chem.* 287, 22295–22304. doi: 10.1074/jbc.M111.318881

Corchnoy, S. B., Swartz, T. E., Lewis, J. W., Szundi, I., Briggs, W. R., and Bogomolni, R. A. (2003). Intramolecular proton transfers and structural changes during the photocycle of the LOV2 domain of phototropin 1. *J. Biol. Chem.* 278, 724–731. doi: 10.1074/jbc.M209119200

Crosson, S., and Moffat, K. (2001). Structure of a flavin-binding plant photoreceptor domain: insights into light mediated signal transduction. *Proc. Natl. Acad. Sci. U.S.A.* 98, 2995–3000. doi: 10.1073/pnas.051520298

Crosson, S., Rajagopal, S., and Moffat, K. (2003). The LOV domain family: photoresponsive signaling modules coupled to diverse output domains. *Biochemistry* 42, 2–10. doi: 10.1021/bi026978l

Deisseroth, K. (2012). Optogenetics and psychiatry: applications, challenges, and opportunities. *Biol. Psychiatry* 71, 1030–1032. doi: 10.1016/j.biopsych.2011.12.021

Diensthuber, R. P., Bommer, M., Gleichmann, T., and Moglich, A. (2013). Full-length structure of a sensor histidine kinase pinpoints coaxial coiled coils as signal transducers and modulators. *Structure* 21, 1127–1136. doi: 10.1016/j.str.2013.04.024

Diensthuber, R. P., Engelhard, C., Lemke, N., Gleichmann, T., Ohlendorf, R., Bittl, R., et al. (2014). Biophysical, mutational, and functional investigation of the chromophore-binding pocket of light-oxygen-voltage photoreceptors. *ACS Synth. Biol.* 3, 811–819. doi: 10.1021/sb400205x

Dittrich, M., Freddolino, P. L., and Schulten, K. (2005). When light falls in LOV: a quantum mechanical/molecular mechanical study of photoexcitation in Phot-LOV1 of *Chlamydomonas reinhardtii*. *J. Phys. Chem. B* 109, 13006–13013. doi: 10.1021/jp050943o

Domratcheva, T., Fedorov, R., and Schlichting, I. (2006). Analysis of the primary photocycle reactions occurring in the light, oxygen, and voltage blue-light receptor by multiconfigurational quantum-chemical methods. *J. Chem. Theory Comput.* 2, 1565–1574. doi: 10.1021/ct0600114

Drepper, T., Eggert, T., Circolone, F., Heck, A., Krauss, U., Guterl, J. K., et al. (2007). Reporter proteins for *in vivo* fluorescence without oxygen. *Nat. Biotechnol.* 25, 443–445. doi: 10.1038/nbt1293

Drepper, T., Huber, R., Heck, A., Circolone, F., Hillmer, A. K., Buchs, J., et al. (2010). Flavin mononucleotide-based fluorescent reporter proteins outperform green fluorescent protein-like proteins as quantitative *in vivo* real-time reporters. *Appl. Environ. Microbiol.* 76, 5990–5994. doi: 10.1128/AEM.00701-10

El-Arab, K. K., Pudasaini, A., and Zoltowski, B. D. (2015). Short LOV proteins in methylocystis reveal insight into LOV domain photocycle mechanisms. *PLoS ONE* 10:e0124874. doi: 10.1371/journal.pone.0124874

Elvin, M., Loros, J. J., Dunlap, J. C., and Heintzen, C. (2005). The PAS/LOV protein VIVID supports a rapidly dampened daytime oscillator that facilitates entrainment of the Neurospora circadian clock. *Genes Dev.* 19, 2593–2605. doi: 10.1101/gad.349305

Engelhard, C., Raffelberg, S., Tang, Y., Diensthuber, R. P., Moglich, A., Losi, A., et al. (2013). A structural model for the full-length blue light-sensing protein YtvA from *Bacillus subtilis*, based on EPR spectroscopy. *Photochem. Photobiol. Sci.* 12, 1855–1863. doi: 10.1039/c3pp50128k

Fedorov, R., Schlichting, I., Hartmann, E., Domratcheva, T., Fuhrmann, M., and Hegemann, P. (2003). Crystal structures and molecular mechanism of a light-induced signaling switch: the Phot-LOV1 domain from *Chlamydomonas reinhardtii*. *Biophys. J.* 84, 2474–2482. doi: 10.1016/S0006-3495(03)75052-8

Fenno, L., Yizhar, O., and Deisseroth, K. (2011). The development and application of optogenetics. *Annu. Rev. Neurosci.* 34, 389–412. doi: 10.1146/annurev-neuro-061010-113817

Freddolino, P. L., Dittrich, M., and Schulten, K. (2006). Dynamic switching mechanisms in LOV1 and LOV2 domains of plant phototropins. *Biophys. J.* 91, 3630–3639. doi: 10.1529/biophysj.106.088609

Freddolino, P. L., Gardner, K. H., and Schulten, K. (2013). Signaling mechanisms of LOV domains: new insights from molecular dynamics studies. *Photochem. Photobiol. Sci.* 12, 1158–1170. doi: 10.1039/c3pp25400c

Gawthorne, J. A., Reddick, L. E., Akpunarlieva, S. N., Beckham, K. S., Christie, J. M., Alto, N. M., et al. (2012). Express your LOV: an engineered flavoprotein as a reporter for protein expression and purification. *PLoS ONE* 7:e52962. doi: 10.1371/journal.pone.0052962

Ghisla, S., and Massey, V. (1989). Mechanisms of flavoprotein-catalyzed reactions. *Eur. J. Biochem.* 181, 1–17. doi: 10.1111/j.1432-1033.1989.tb14688.x

Gleichmann, T., Diensthuber, R. P., and Moglich, A. (2013). Charting the signal trajectory in a light-oxygen-voltage photoreceptor by random mutagenesis and covariance analysis. *J. Biol. Chem.* 288, 29345–29355. doi: 10.1074/jbc.M113.506139

Grusch, M., Schelch, K., Riedler, R., Reichhart, E., Differ, C., Berger, W., et al. (2014). Spatio-temporally precise activation of engineered receptor tyrosine kinases by light. *EMBO J.* 33, 1713–1726. doi: 10.15252/embj.201387695

Guntas, G., Hallett, R. A., Zimmerman, S. P., Williams, T., Yumerefendi, H., Bear, J. E., et al. (2015). Engineering an improved light-induced dimer (iLID) for controlling the localization and activity of signaling proteins. *Proc. Natl. Acad. Sci. U.S.A.* 112, 112–117. doi: 10.1073/pnas.1417910112

Halavaty, A., and Moffat, K. (2007). N- and C-terminal flanking regions modulate light-induced signal transduction in the LOV2 domain of the blue light sensor phototropin 1 from *Avena Sativa*. *Biochemistry* 46, 14001–14009. doi: 10.1021/bi701543e

Harper, S. M., Christie, J. M., and Gardner, K. H. (2004). Disruption of the LOV-jalpha helix interaction activates phototropin kinase activity. *Biochemistry* 43, 16184–16192. doi: 10.1021/bi048092i

Harper, S. M., Neil, L. C., and Gardner, K. H. (2003). Structural basis of a phototropin light switch. *Science* 301, 1541–1544. doi: 10.1126/science.1086810

Holzer, W., Penzkofer, A., Fuhrmann, M., and Hegemann, P. (2002). Spectroscopic characterization of flavin mononucleotide bound to the LOV1 domain of Phot1 from *Chlamydomonas reinhardtii*. *Photochem. Photobiol.* 75, 479–487. doi: 10.1562/0031-8655(2002)075<0479:SCOFMB>2.0.CO;2

Huala, E., Oeller, P. W., Liscum, E., Han, I. S., Larsen, E., and Briggs, W. R. (1997). Arabidopsis NPH1: a protein kinase with a putative redox-sensing domain. *Science* 278, 2120–2123. doi: 10.1126/science.278.5346.2120

Imaizumi, T., Tran, H. G., Swartz, T. E., Briggs, W. R., and Kay, S. A. (2003). FKF1 is essential for photoperiodic-specific light signalling in Arabidopsis. *Nature* 426, 302–306. doi: 10.1038/nature02090

Iwata, T., Nozaki, D., Tokutomi, S., Kagawa, T., Wada, M., and Kandori, H. (2003). Light-induced structural changes in the LOV2 domain of Adiantum phytochrome3 studied by low-temperature FTIR and UV-visible spectroscopy. *Biochemistry* 42, 8183–8191. doi: 10.1021/bi0345135

Iwata, T., Nozaki, D., Tokutomi, S., and Kandori, H. (2005). Comparative investigation of the LOV1 and LOV2 domains in Adiantum phytochrome3. *Biochemistry* 44, 7427–7434. doi: 10.1021/bi047281y

Iwata, T., Tokutomi, S., and Kandori, H. (2002). Photoreaction of the cysteine S-H group in the LOV2 domain of Adiantum phytochrome3. *J. Am. Chem. Soc.* 124, 11840–11841. doi: 10.1021/ja020834c

Kawano, F., Aono, Y., Suzuki, H., and Sato, M. (2013). Fluorescence imaging-based high-throughput screening of fast- and slow-cycling LOV proteins. *PLoS ONE* 8:e82693. doi: 10.1371/journal.pone.0082693

Kawano, F., Suzuki, H., Furuya, A., and Sato, M. (2015). Engineered pairs of distinct photoswitches for optogenetic control of cellular proteins. *Nat. Commun.* 6, 6256. doi: 10.1038/ncomms7256

Kennis, J. T., Crosson, S., Gauden, M., van Stokkum, I. H., Moffat, K., and van Grondelle, R. (2003). Primary reactions of the LOV2 domain of phototropin, a plant blue-light photoreceptor. *Biochemistry* 42, 3385–3392. doi: 10.1021/bi034022k

Kennis, J. T., van Stokkum, I. H., Crosson, S., Gauden, M., Moffat, K., and van Grondelle, R. (2004a). The LOV2 domain of phototropin: a reversible photochromic switch. *J. Am. Chem. Soc.* 126, 4512–4513. doi: 10.1021/ja031840r

Kennis, J. T. M., van Stokkum, N. H. M., Crosson, S., Gauden, M., Moffat, K., and van Grondelle, R. (2004b). The LOV2 domain of phototropin: a reversible photochromic switch. *J. Am. Chem. Soc.* 126, 4512–4513. doi: 10.1021/ja031840r

Kottke, T., Heberle, J., Hehn, D., Dick, B., and Hegemann, P. (2003). Phot-LOV1: photocycle of a blue-light receptor domain from the green alga *Chlamydomonas reinhardtii*. *Biophys. J.* 84, 1192–1201. doi: 10.1016/S0006-3495(03)74933-9

Kottke, T., Hegemann, P., Dick, B., and Heberle, J. (2006). The photochemistry of the light-, oxygen-, and voltage- sensitive domains in the algal blue light receptor phot. *Biopolymers* 82, 373–378. doi: 10.1002/bip.20510

Lamb, J. S., Zoltowski, B. D., Pabit, S. A., Crane, B. R., and Pollack, L. (2008). Time-resolved dimerization of a PAS-LOV protein measured with photocoupled small angle X-ray scattering. *J. Am. Chem. Soc.* 130, 12226–12227. doi: 10.1021/ja804236f

Lamb, J. S., Zoltowski, B. D., Pabit, S. A., Li, L., Crane, B. R., and Pollack, L. (2009). Illuminating solution responses of a LOV domain protein with photocoupled small-angle X-ray scattering. *J. Mol. Biol.* 393, 909–919. doi: 10.1016/j.jmb.2009.08.045

Lokhandwala, J., Hopkins, H. C., Rodriguez-Iglesias, A., Dattenbock, C., Schmoll, M., and Zoltowski, B. D. (2015). Structural biochemistry of a fungal LOV domain photoreceptor reveals an evolutionarily conserved pathway integrating light and oxidative stress. *Structure* 23, 116–125. doi: 10.1016/j.str.2014.10.020

Losi, A., Gartner, W., Raffelberg, S., Cella Zanacchi, F., Bianchini, P., Diaspro, A., et al. (2013). A photochromic bacterial photoreceptor with potential for super-resolution microscopy. *Photochem. Photobiol. Sci.* 12, 231–235. doi: 10.1039/C2PP25254F

Losi, A., Ghiraldelli, E., Jansen, S., and Gartner, W. (2005). Mutational effects on protein structural changes and interdomain interactions in the blue-light sensing LOV protein YTvA. *Photochem. Photobiol.* 81, 1145–1152. doi: 10.1562/2005-05-25-RA-541

Lungu, O. I., Hallett, R. A., Choi, E. J., Aiken, M. J., Hahn, K. M., and Kuhlman, B. (2012). Designing photoswitchable peptides using the AsLOV2 domain. *Chem. Biol.* 19, 507–517. doi: 10.1016/j.chembiol.2012.02.006

Ma, Z., Du, Z., Chen, X., Wang, X., and Yang, Y. (2013). Fine tuning the LightOn light-switchable transgene expression system. *Biochem. Biophys. Res. Commun.* 440, 419–423. doi: 10.1016/j.bbrc.2013.09.092

Mansurova, M., Scheercousse, P., Simon, J., Kluth, M., and Gartner, W. (2011). Chromophore exchange in the blue light-sensitive photoreceptor YtvA from *Bacillus subtilis*. *Chembiochem* 12, 641–646. doi: 10.1002/cbic.201000515

Moglich, A., Ayers, R. A., and Moffat, K. (2009). Design and signaling mechanism of light-regulated histidine kinases. *J. Mol. Biol.* 385, 1433–1444. doi: 10.1016/j.jmb.2008.12.017

Moglich, A., and Moffat, K. (2010). Engineered photoreceptors as novel optogenetic tools. *Photochem. Photobiol. Sci.* 9, 1286–1300. doi: 10.1039/c0pp00167h

Moon, J., Gam, J., Lee, S. G., Suh, Y. G., and Lee, J. (2014). Light-regulated tetracycline binding to the Tet repressor. *Chemistry* 20, 2508–2514. doi: 10.1002/chem.201304027

Motta-Mena, L. B., Reade, A., Mallory, M. J., Glantz, S., Weiner, O. D., Lynch, K. W., et al. (2014). An optogenetic gene expression system with rapid activation and deactivation kinetics. *Nat. Chem. Biol.* 10, 196–202. doi: 10.1038/nchembio.1430

Mukherjee, A., and Schroeder, C. M. (2015). Flavin-based fluorescent proteins: emerging paradigms in biological imaging. *Curr. Opin. Biotechnol.* 31, 16–23. doi: 10.1016/j.copbio.2014.07.010

Nash, A. I., Ko, W. H., Harper, S. M., and Gardner, K. H. (2008). A conserved glutamine plays a central role in LOV domain signal transmission and its duration. *Biochemistry* 47, 13842–13849. doi: 10.1021/bi801430e

Nash, A. I., McNulty, R., Shillito, M. E., Swartz, T. E., Bogomolni, R. A., Luecke, H., et al. (2011). Structural basis of photosensitivity in a bacterial light-oxygen-voltage/helix-turn-helix (LOV-HTH) DNA-binding protein. *Proc. Natl. Acad. Sci. U.S.A.* 108, 9449–9454. doi: 10.1073/pnas.1100262108

Nihongaki, Y., Suzuki, H., Kawano, F., and Sato, M. (2014). Genetically engineered photoinducible homodimerization system with improved dimer-forming efficiency. *ACS Chem. Biol.* 9, 617–621. doi: 10.1021/cb400836k

Nozaki, D., Iwata, T., Ishikawa, T., Todo, T., Tokutomi, S., and Kandori, H. (2004). Role of Gln1029 in the photoactivation processes of the LOV2 domain in Adiantum phytochrome3. *Biochemistry* 43, 8373–8379. doi: 10.1021/bi0494727

Ohlendorf, R., Vidavski, R. R., Eldar, A., Moffat, K., and Moglich, A. (2012). From dusk till dawn: one-plasmid systems for light-regulated gene expression. *J. Mol. Biol.* 416, 534–542. doi: 10.1016/j.jmb.2012.01.001

Okajima, K., Kashojiya, S., and Tokutomi, S. (2012). Photosensitivity of kinase activation by blue light involves the lifetime of a cysteinyl-flavin adduct intermediate, S390, in the photoreaction cycle of the LOV2 domain in phototropin, a plant blue light receptor. *J. Biol. Chem.* 287, 40972–40981. doi: 10.1074/jbc.M112.406512

Pennacchietti, F., Abbruzzetti, S., Losi, A., Mandalari, C., Bedotti, R., Viappiani, C., et al. (2014). The dark recovery rate in the photocycle of the bacterial photoreceptor YtvA is affected by the cellular environment and by hydration. *PLoS ONE* 9:e107489. doi: 10.1371/journal.pone.0107489

Polstein, L. R., and Gersbach, C. A. (2012). Light-inducible spatiotemporal control of gene activation by customizable zinc finger transcription factors. *J. Am. Chem. Soc.* 134, 16480–16483. doi: 10.1021/ja3065667

Pudasaini, A., and Zoltowski, B. D. (2013). Zeitlupe senses blue-light fluence to mediate circadian timing in *Arabidopsis thaliana*. *Biochemistry* 52, 7150–7158. doi: 10.1021/bi401027n

Purcell, E. B., McDonald, C. A., Palfey, B. A., and Crosson, S. (2010). An analysis of the solution structure and signaling mechanism of LovK, a sensor histidine kinase integrating light and redox signals. *Biochemistry* 49, 6761–6770. doi: 10.1021/bi1006404

Raffelberg, S., Mansurova, M., Gartner, W., and Losi, A. (2011). Modulation of the photocycle of a LOV domain photoreceptor by the hydrogen-bonding network. *J. Am. Chem. Soc.* 133, 5346–5356. doi: 10.1021/ja1097379

Ravikumar, Y., Nadarajan, S. P., Lee, C. S., Rhee, J. K., and Yun, H. (2015). A new generation fluorescent based metal sensor - iLOV protein. *J. Microbiol. Biotechnol.* 25, 503–510. doi: 10.4014/jmb.1409.09035

Rivera-Cancel, G., Motta-Mena, L. B., and Gardner, K. H. (2012). Identification of natural and artificial DNA substrates for light-activated LOV-HTH transcription factor EL222. *Biochemistry* 51, 10024–10034. doi: 10.1021/bi301306t

Salomon, M., Christie, J. M., Knieb, E., Lempert, U., and Briggs, W. R. (2000). Photochemical and mutational analysis of the FMN-binding domains of the plant blue light receptor, phototropin. *Biochemistry* 39, 9401–9410. doi: 10.1021/bi000585+

Sato, Y., Iwata, T., Tokutomi, S., and Kandori, H. (2005). Reactive cysteine is protonated in the triplet excited state of the LOV2 domain in Adiantum phytochrome3. *J. Am. Chem. Soc.* 127, 1088–1089. doi: 10.1021/ja0436897

Sato, Y., Nabeno, M., Iwata, T., Tokutomi, S., Sakurai, M., and Kandori, H. (2007). Heterogeneous environment of the S-H group of Cys966 near the flavin chromophore in the LOV2 domain of Adiantum neochrome1. *Biochemistry* 46, 10258–10265. doi: 10.1021/bi701022v

Sawa, M., Nusinow, D. A., Kay, S. A., and Imaizumi, T. (2007). FKF1 and GIGANTEA complex formation is required for day-length measurement in Arabidopsis. *Science* 318, 261–265. doi: 10.1126/science.1146994

Schleicher, E., Kowalczyk, R. M., Kay, C. W., Hegemann, P., Bacher, A., Fischer, M., et al. (2004). On the reaction mechanism of adduct formation in LOV domains of the plant blue-light receptor phototropin. *J. Am. Chem. Soc.* 126, 11067–11076. doi: 10.1021/ja049553q

Schwerdtfeger, C., and Linden, H. (2003). VIVID is a flavoprotein and serves as a fungal blue light photoreceptor for photoadaptation. *EMBO J.* 22, 4846–4855. doi: 10.1093/emboj/cdg451

Song, S. H., Freddolino, P. L., Nash, A. I., Carroll, E. C., Schulten, K., Gardner, K. H., et al. (2011). Modulating LOV domain photodynamics with a residue alteration outside the chromophore binding site. *Biochemistry* 50, 2411–2423. doi: 10.1021/bi200198x

Strickland, D., Lin, Y., Wagner, E., Hope, C. M., Zayner, J., Antoniou, C., et al. (2012). TULIPs: tunable, light-controlled interacting protein tags for cell biology. *Nat. Methods* 9, 379–384. doi: 10.1038/nmeth.1904

Strickland, D., Moffat, K., and Sosnick, T. R. (2008). Light-activated DNA binding in a designed allosteric protein. *Proc. Natl. Acad. Sci. U.S.A.* 105, 10709–10714. doi: 10.1073/pnas.0709610105

Strickland, D., Yao, X., Gawlak, G., Rosen, M. K., Gardner, K. H., and Sosnick, T. R. (2010). Rationally improving LOV domain-based photoswitches. *Nat. Methods* 7, 623–626. doi: 10.1038/nmeth.1473

Swartz, T. E., Corchnoy, S. B., Christie, J. M., Lewis, J. W., Szundi, I., Briggs, W. R., et al. (2001). The photocycle of a flavin-binding domain of the blue light photoreceptor phototropin. *J. Biol. Chem.* 276, 36493–36500. doi: 10.1074/jbc.M103114200

Swartz, T. E., Tseng, T.-S., Frederickson, M. A., Paris, G., Comerci, D. J., Rajashekara, G., et al. (2007). Blue-light-activated histidine kinases: two component sensors in bacteria. *Science* 317, 1090–1093. doi: 10.1126/science.1144306

Tang, Y. F., Cao, Z., Livoti, E., Krauss, U., Jaeger, K. E., Gartner, W., et al. (2010). Interdomain signalling in the blue-light sensing and GTP-binding protein YtvA: a mutagenesis study uncovering the importance of specific protein sites. *Photochem. Photobiol. Sci.* 9, 47–56. doi: 10.1039/B9PP00075E

Taylor, B., and Zhulin, I. B. (1999). PAS domains: internal sensors of oxygen, redox potential, and light. *Microbiol. Mol. Biol. Rev.* 63, 479–506.

Vaidya, A. T., Chen, C. H., Dunlap, J. C., Loros, J. J., and Crane, B. R. (2011). Structure of a light-activated LOV protein dimer that regulates transcription. *Sci. Signal.* 4, ra50. doi: 10.1126/scisignal.2001945

Wang, X., Chen, X., and Yang, Y. (2012). Spatiotemporal control of gene expression by a light-switchable transgene system. *Nat. Methods* 9, 266–269. doi: 10.1038/nmeth.1892

Wingen, M., Potzkei, J., Endres, S., Casini, G., Rupprecht, C., Fahlke, C., et al. (2014). The photophysics of LOV-based fluorescent proteins–new tools for cell biology. *Photochem. Photobiol. Sci.* 13, 875–883. doi: 10.1039/c3pp50414j

Wu, Y. I., Frey, D., Lungu, O. I., Jaehrig, A., Schlichting, I., Kuhlman, B., et al. (2009). A genetically encoded photoactivatable Rac controls the motility of living cells. *Nature* 461, 104–108. doi: 10.1038/nature08241

Wu, Y. I., Wang, X., He, L., Montell, D., and Hahn, K. M. (2011). Spatiotemporal control of small GTPases with light using the LOV domain. *Meth. Enzymol.* 497, 393–407. doi: 10.1016/B978-0-12-385075-1.00016-0

Yamamoto, A., Iwata, T., Tokutomi, S., and Kandori, H. (2008). Role of Phe1010 in light-induced structural changes of the neo1-LOV2 domain of Adiantum. *Biochemistry* 47, 922–928. doi: 10.1021/bi701851v

Yazawa, M., Sadaghiani, A. M., Hsueh, B., and Dolmetsch, R. E. (2009). Induction of protein-protein interactions in live cells using light. *Nat. Biotechnol.* 27, 941–945. doi: 10.1038/nbt.1569

Yi, J. J., Wang, H., Vilela, M., Danuser, G., and Hahn, K. M. (2014). Manipulation of endogenous kinase activity in living cells using photoswitchable inhibitory peptides. *ACS Synth. Biol.* 3, 788–795. doi: 10.1021/sb5001356

Yin, T., and Wu, Y. I. (2015). Optogenetics: optical control of a photoactivatable Rac in living cells. *Methods Mol. Biol.* 1251, 277–289. doi: 10.1007/978-1-4939-2080-8_15

Zayner, J. P., and Sosnick, T. R. (2014). Factors that control the chemistry of the LOV domain photocycle. *PLoS ONE* 9:e87074. doi: 10.1371/journal.pone.0087074

Zoltowski, B. D., and Crane, B. R. (2008). Light activation of the LOV protein vivid generates a rapidly exchanging dimer. *Biochemistry* 47, 7012–7019. doi: 10.1021/bi8007017

Zoltowski, B. D., and Gardner, K. H. (2011). Tripping the light fantastic: blue-light photoreceptors as examples of environmentally modulated protein-protein interactions. *Biochemistry.* 50, 4–16. doi: 10.1021/bi101665s

Zoltowski, B. D., Motta-Mena, L. B., and Gardner, K. H. (2013). Blue light-induced dimerization of a bacterial LOV-HTH DNA-binding protein. *Biochemistry* 52, 6653–6661. doi: 10.1021/bi401040m

Zoltowski, B. D., Nash, A. I., and Gardner, K. H. (2011). Variations in protein-flavin hydrogen bonding in a light, oxygen, voltage domain produce non-Arrhenius kinetics of adduct decay. *Biochemistry* 50, 8771–8779. doi: 10.1021/bi200976a

Zoltowski, B. D., Schwerdtfeger, C., Widom, J., Loros, J. J., Bilwes, A. M., and Crane, B. R. (2007). Conformational Switching in the Fungal Light Sensor Vivid. *Science* 316, 1054–1057. doi: 10.1126/science.1137128

Zoltowski, B. D., Vaccaro, B., and Crane, B. R. (2009). Mechanism-based tuning of a LOV domain photoreceptor. *Nat. Chem. Biol.* 5, 827–834. doi: 10.1038/nchembio.210

Conflict of Interest Statement: The authors declare that the research was conducted in the absence of any commercial or financial relationships that could be construed as a potential conflict of interest.

frontiers in Molecular Biosciences

REVIEW
published: 01 September 2015
doi: 10.3389/fmolb.2015.00049

How can EPR spectroscopy help to unravel molecular mechanisms of flavin-dependent photoreceptors?

*Daniel Nohr, Ryan Rodriguez, Stefan Weber and Erik Schleicher**

Department of Physical Chemistry, Institut für Physikalische Chemie, Albert-Ludwigs-Universität Freiburg, Freiburg, Germany

Electron paramagnetic resonance (EPR) spectroscopy is a well-established spectroscopic method for the examination of paramagnetic molecules. Proteins can contain paramagnetic moieties in form of stable cofactors, transiently formed intermediates, or spin labels artificially introduced to cysteine sites. The focus of this review is to evaluate potential scopes of application of EPR to the emerging field of optogenetics. The main objective for EPR spectroscopy in this context is to unravel the complex mechanisms of light-active proteins, from their primary photoreaction to downstream signal transduction. An overview of recent results from the family of flavin-containing, blue-light dependent photoreceptors is given. In detail, mechanistic similarities and differences are condensed from the three classes of flavoproteins, the cryptochromes, LOV (Light-oxygen-voltage), and BLUF (blue-light using FAD) domains. Additionally, a concept that includes spin-labeled proteins and examination using modern pulsed EPR is introduced, which allows for a precise mapping of light-induced conformational changes.

Keywords: photoreceptor, EPR spectroscopy, distance determination, radicals, flavoproteins

OPEN ACCESS

Edited by:
Tilo Mathes,
Vrije Universiteit Amsterdam,
Netherlands

Reviewed by:
Litao Sun,
The Scripps Research Institute, USA
Johann P. Klare,
University of Osnabrueck, Germany

****Correspondence:***
Erik Schleicher,
Institut für Physikalische Chemie,
Albert-Ludwigs-Universität Freiburg,
Albertstr. 21, 79104 Freiburg,
Germany
erik.schleicher@
physchem.uni-freiburg.de

Specialty section:
This article was submitted to Biophysics, a section of the journal Frontiers in Molecular Biosciences

Received: *11 June 2015*
Accepted: *10 August 2015*
Published: *01 September 2015*

Citation:
Nohr D, Rodriguez R, Weber S and Schleicher E (2015) How can EPR spectroscopy help to unravel molecular mechanisms of flavin-dependent photoreceptors? Front. Mol. Biosci. 2:49. doi: 10.3389/fmolb.2015.00049

Introduction

Electron paramagnetic resonance (EPR) spectroscopy is a well-established spectroscopic method for the examination of the global as well as the local structure of paramagnetic molecules. Although only a minority of proteins is intrinsically paramagnetic, numerous proteins contain paramagnetic molecules in form of stable cofactors (e.g., organic molecules, transition-metal ions, or transition-metal clusters) (Jeschke, 2005). In addition, paramagnetic states can be generated transiently during the course of a reaction of a protein. In such a case, cofactor, amino acid and/or substrate radicals can be generated and thus characterized (Frey et al., 2006). Last, artificial paramagnetic labels (spin labels) can be attached to a specific site of the protein of interest. Among others, small and metastable nitroxide spin labels are commonly used, which can be covalently bound to cysteine residues (Klare and Steinhoff, 2009; Jeschke, 2012). As a consequence, cysteines (and afterwards radicals) can be introduced to virtually any position of interest (commonly named as site-directed spin labeling, SDSL) with the help of established molecular-biology techniques (Berliner et al., 2000; Hubbell et al., 2000; Fanucci and Cafiso, 2006).

EPR spectroscopy is not only helpful to characterize stable paramagnetic states, but is extremely powerful to analyze radical intermediates, which often occur in electron-transfer reactions. Here, EPR methods have one advantage as compared to other methods such as NMR: protein-size restrictions do not apply to EPR because the detection of EPR is limited to the paramagnetic

molecule itself and only those parts of a biomolecule that directly interact with it. As a non-invasive or minimally invasive method, EPR allows for the investigation of such systems in a functional state or even under in-cell conditions (Berliner, 2010; Hänsel et al., 2014). During the last decade, electron-electron double resonance (DEER or PELDOR) spectroscopy, a modern pulsed EPR method, became increasingly popular (Jeschke, 2002, 2012; Schiemann and Prisner, 2007; Reginsson and Schiemann, 2011; Hubbell et al., 2013). Here, the strength of the dipolar coupling between two radicals is determined, and from that, the distance between two radicals may be obtained with high accuracy. When combining this method with the aforementioned SDSL, distances (and even orientations) between any position in a protein may be obtained, which makes ELDOR spectroscopy similarly powerful as established methods, such as Förster resonance energy transfer (FRET) spectroscopy.

The focus of this review is to evaluate potential scopes of application of EPR to the emerging field of optogenetics—the genetic encoding of light-sensitive proteins that activate signaling pathways in response to light. The main objective for molecular spectroscopy in this context is to unravel the complex mechanisms of light-active proteins (photoreceptors), from their primary photoreaction to downstream signal transduction.

In principle, the mechanism of photoreceptors can be separated into three parts: (i) the response of the chromophore immediately after light excitation, (ii) signal propagation from the chromophore to the signaling domain (or very crudely expressed: from the center of the protein to its surface), and (iii) activation of the signaling domain. The time scales of these processes range from picoseconds for the first process down to (milli)seconds for the subsequent ones; therefore, various spectroscopic techniques are necessary to disentangle the entire mechanism. Only if all these facts are at hand, rational decisions can be made, which photoreceptor to choose for an optogenetic study, and more importantly, how the respective light-responsive proteins may be genetically encoded. Up to now, in most cases, small libraries of fusion variants with several tens of members were prepared and screened manually for optimized response (Möglich and Moffat, 2010). Additionally, many of these constructs show only partially activation/deactivation upon illumination, and thus, could be further optimized.

Although various other photoreceptors, in particular rhodopsins have been investigated using EPR spectroscopy (Van Eps et al., 2015), and have been successfully implemented as optogenetic transponders (Zhang et al., 2011), this review is focused to provide an overview of recent results from EPR spectroscopy on flavin-containing photoreceptors. The three up to now characterized flavin-based receptor classes can in principle be further divided into the large (∼60 kDa) cryptochrome/photolyase (CRY/PL) class, and the small (∼20 kDa) modular LOV (Light-oxygen-voltage) and BLUF (blue-light using FAD) domains. From the very beginning, flavin-containing photoreceptors have been identified as important tools for optogenetics, and several applications have been published to date (e.g., Wu et al., 2009; Kennedy et al., 2010; Möglich and Moffat, 2010; Christie et al., 2012). One should keep in mind that since their discovery, molecular spectroscopy of all flavors has been applied to these proteins (a number of recent reviews excellently summarize the results, e.g., Chaves et al., 2011; Zoltowski and Gardner, 2011; Losi and Gärtner, 2012), but only bringing the results of the application of various techniques together resulted in the wealth of knowledge on their (photo)chemistry that we have accumulated up to now.

Introduction to Selected EPR Techniques

It is beyond the aim of this review to comprehensively introduce the theory and all practical aspects of EPR spectroscopy; for this purpose, the reader is referred to a number of excellent and in-depth reviews and books (e.g., Weil et al., 1994; Schweiger and Jeschke, 2001; Jeschke, 2005). However, we would like to present a few special EPR techniques that have been proven very helpful when working with light-active flavoproteins. Specifically, continuous-wave EPR (cwEPR) is commonly applied for a first more rough characterization of a stable paramagnetic species; for a more detailed characterization of the local structure of a radical, advanced methods, such as pulsed electron-nuclear double resonance (ENDOR) spectroscopy, are preferably applied. For the characterization of meta-stable paramagnetic intermediates, transient EPR (trEPR) with its high time resolution is for sure the method of choice.

Steady-state EPR Spectroscopy

CwEPR spectroscopy is typically used to determine the **g**-tensor and large anisotropic hyperfine couplings (hfcs) of a stable paramagnetic species. In addition to the in general fast and technically simple measurement, one further advantage of cwEPR originates from the so-called lock-in detection. Here, a modulation of the magnetic-field strength with high frequency is applied, and a subsequent detection of the EPR signal at the same modulation frequency results in a significantly increased signal-to-noise ratio. The downside of this technique is its limitation in time resolution, which is restricted to time scale of several tens or hundreds of microseconds when the most common modulation frequency of 100 kHz is applied.

While the isotropic *g*-value of an organic radical can be easily measured at X-band microwave (mw) frequencies, the full resolutions of the **g**-tensor's anisotropy and hyperfine coupling (hfc) parameters typically require high mw frequencies, at least the commercially available Q− and W−band frequencies. **Figure 1** (left panel) shows a very high-magnetic-field cwEPR spectrum of *Xenopus laevis* (6-4) photolyase with its protonated $FADH^{\bullet}$ cofactor (dashed line). A least-squares best fit (drawn line) of the experimental data revealed the **g**-tensor principal values and some components of the anisotropic hfcs of N(5), N(10), and H(5). The spectrum was recorded with a laboratory-built EPR spectrometer operating at 360 GHz (Schnegg et al., 2006) because with lower (commercially available) mw frequencies it is impossible to fully resolve the **g**-tensor principal components of flavin radicals (Schleicher and Weber, 2012). Due to the very high magnetic field of 12.8 T, not only the **g**-tensor is fully resolved, but even a splitting of the g_y-component of the

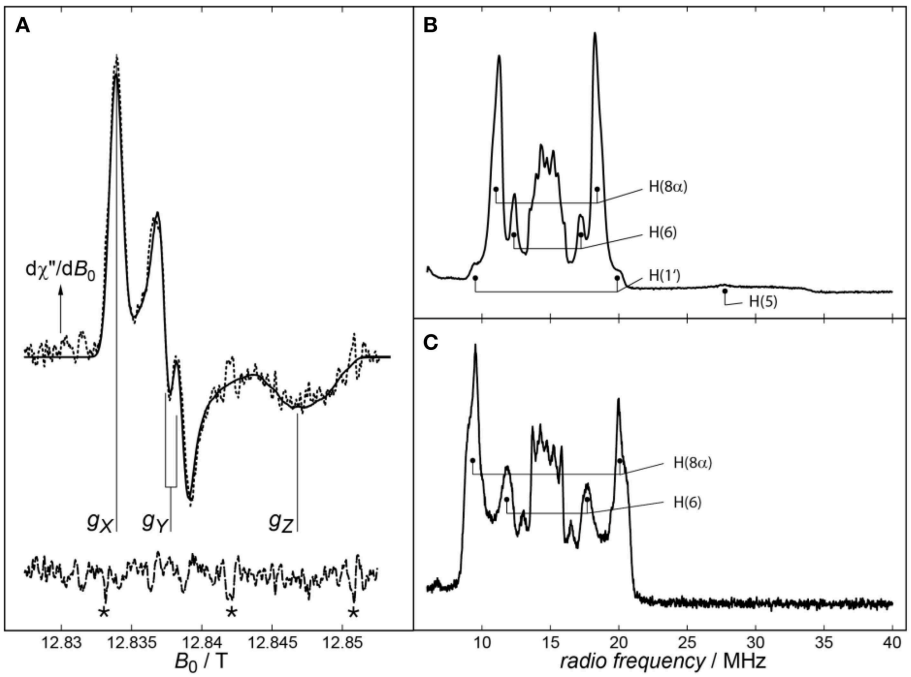

FIGURE 1 | (A) cwEPR spectrum of *Xenopus laevis* (6-4) photolyase recorded at 360 GHz. The experimental spectrum and its spectral simulation are depicted as dashed and solid lines, respectively. In addition to the well resolved principal values of the **g**-tensor, a splitting on the g_Y component of the spectrum can be observed, which is due to the projection of the H(5) hfc component A_y onto the *Y* principal axis of **g**. Signals arising from magnetic-field calibration are labeled by asterisks (*). Adapted from Schnegg et al. (2006). Right panel: Pulsed proton X-band (Davies) ENDOR spectra from *Synechocystis* sp. **(B)** and *Drosophila melanogaster* **(C)** cryptochromes recorded at 80 K. Assigned proton hfcs are marked. Adapted from Schleicher et al. (2010).

g-tensor is observed. It originates from the projection of the H(5) hfc component A_y onto the *Y* principal axis of **g**.

Pulsed (Davies-type) ENDOR spectroscopy (for in-depth reviews, see e.g., Prisner et al., 2001; Murphy and Farley, 2006) reveals hfcs of a sample by inducing NMR transitions within a paramagnetic species and surrounding hyperfine-coupled nuclei and detecting them via EPR. For this purpose, the EPR spectrometer is equipped with a radio-frequency (rf) source and amplifier. In comparison to cwEPR, a static magnetic field is applied; its optimal value has to be determined in advance. The Davies-ENDOR pulse sequence (see **Scheme 1**) then starts with a 180° (i.e., π) mw pulse to invert the magnetization of the electron-spin system, thus generating an "inverted" spin system, in which NMR transitions can be induced by application of a 180° (i.e., π) rf pulse of varying frequency following the mw pulse. In case of resonance, the rf pulse will again invert the magnetization, thus reducing the net magnetization. The pulse sequence is finished by a standard Hahn echo (π/2 – π) sequence. The final spectrum shows the inverted echo intensity as function of the radio frequency. This allows a direct readout of the type of coupling nucleus by its nuclear Larmor frequency. Some limitation of this technique is due to the relaxation time of the electron-spin system, which has to be long enough to apply the rf pulse that is relatively long as compared to the mw pulses; however, this is only a minor problem when working with organic radicals.

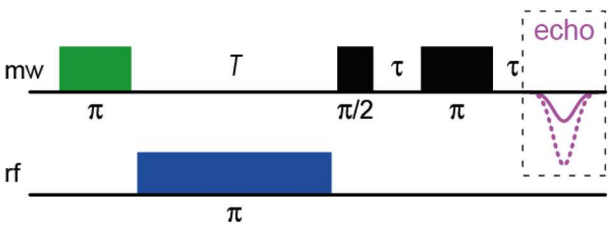

SCHEME 1 | The Davies-ENDOR pulse sequence.

Importantly, hfcs are, via the electron-spin density, quite sensitive to changes in their environment, and thus, altered hfcs can be used to gain structural information on the close surroundings of a paramagnetic molecule. In general, hfcs of a particular nucleus can be directly read out from ENDOR spectra as pairs of resonance lines that are, according to the condition $\nu_{ENDOR} = |\nu_N \pm A/2|$, either equally spaced about the magnetic-field dependent nuclear Larmor frequency ν_N and separated by the hfc constant *A* (for the case $\nu_N > |A/2|$), or centered around $A/2$ and separated by $2\nu_N$ (for $\nu_N < |A/2|$). A typical proton ENDOR spectrum of a flavin radical at X-band microwave frequency can be divided into five parts: (1) the strong central matrix-ENDOR signal reaching from around 13–16 MHz, originating from weakly coupled protons like backbone or water

protons close to the flavin, or those directly attached to the isoalloxazine ring, namely H(3), H(7α) and H(9). (2) Flanking the matrix-ENDOR signal couplings at around 12 and 17 MHz that are assigned to the proton H(6) can be observed. (3) The most intensive features in a flavin radical ENDOR spectrum arise from the protons of the methyl group at C(8), which can be detected at 10–12 MHz and 17–19 MHz. (4) In most published spectra, one of the two β-protons attached to C(1′) of the ribityl side chain is visible as small shoulders at 9–10 and 19–20 MHz (Schleicher et al., 2010). (5) In the neutral protonated state of the flavin radical, a broad rhombic feature can be observed reaching from 20 up to 34 MHz, which is assigned to the proton attached to N(5).

Two exemplary proton ENDOR spectra, one originating from the $FADH^{\bullet}$ of *Synechocystis* sp. CRY DASH, and the other from the $FAD^{\bullet-}$ of *Drosophila melanogaster* CRY, are shown in the right panel of **Figure 1**. As a first result, the protonation state of the flavin radical can be directly read out of the respective ENDOR spectrum: Depending on the presence or absence of a broad signal between 20 and 34 MHz originating from H(5), deprotonated anionic or protonated neutral flavin radical states, respectively, can be easily distinguished. Additionally, significantly different proton hfcs [in particular H(8α) and H(6)] can be observed upon transforming the anionic $FAD^{\bullet-}$ into the neutral $FADH^{\bullet}$ radical. This is because protonation at N(5) results in a significant redistribution of the unpaired electron-spin density from the less polar xylene ring of the isoalloxazine moiety toward the pyrazine and pyrimidine rings. In sum, proton ENDOR spectroscopy allows for an easy discrimination between the two protonation states, and gives access to the molecular wave function of a paramagnetic molecule via the determination of electron-spin densities (that are directly related to the respective hfcs).

Transient EPR Spectroscopy

Short-lived paramagnetic intermediates, such as triplet states or radical pairs (RP) generated in the course of photo-chemical reactions, can be favorably studied by measuring the EPR signal intensity as a function of time at a fixed magnetic field (Stehlik and Möbius, 1997; Bittl and Weber, 2005; van der Est, 2009). Typically, the best-possible time response of a commercial EPR spectrometer is in the order of about 20 μs (see chapter "Steady-State EPR Spectroscopy"). By removing the magnetic-field modulation, the time resolution can be pushed into the 10^{-8}–10^{-9} s range presupposed a suitably fast data acquisition system is present to directly record the transient EPR signal amplitude as a function of time. In transient EPR spectroscopy (trEPR), paramagnetic species are generated by a nanosecond laser flash, which also serves as a trigger signal. Spectral information can be obtained from a series of trEPR signals recorded at various magnetic-field points, thus yielding a two-dimensional variation of the signal intensity with respect to both the magnetic field and the time. Similar to e.g., transient absorption spectroscopy, trEPR spectra can be extracted at any fixed time after the laser pulse as slices parallel to the magnetic-field axis.

In **Figure 2A**, the one-dimensional representation of the trEPR signal from the photo-generated triplet state of FMN is shown (Kowalczyk et al., 2004; Schleicher et al., 2004). Due to signal detection in the absence of any source modulation, the sign of the resonances directly reflects the emissive (E) or enhanced absorptive (A) spin polarization of the EPR transitions, which arises due to the generation of the electron-spin state with an initial non-equilibrium energy-level population (Turro et al., 2000; Woodward, 2002; Hirota and Yamauchi, 2003). The spectral width of the signal reflects the strong mutual interaction of the unpaired electron spins in the triplet configuration. Because they are both localized on the same molecule (in this example on the isoalloxazine moiety of FMN), the spin–spin interactions are strong and hence, trEPR spectra of flavin triplet states are rather broad (Kowalczyk et al., 2004). The weak transition at low magnetic fields arises from the only weakly allowed "$\Delta M_S = \pm 2$"-transition.

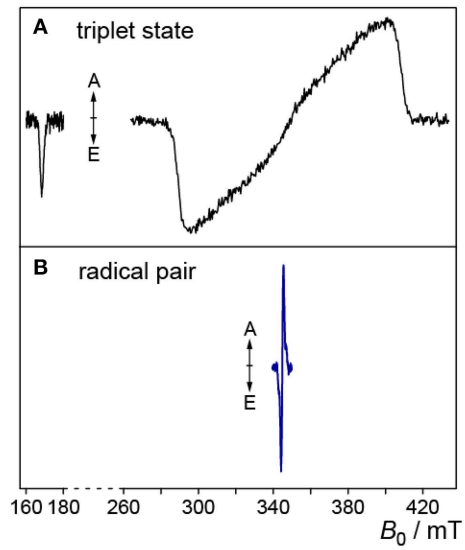

FIGURE 2 | Triplet and RP trEPR spectra of flavoproteins.
(A) Low-temperature (80 K) trEPR spectrum of the photoexcited triplet state of FMN extracted from a full 2D-plot, for details see Kowalczyk et al. (2004). The weak transition at ∼170 mT originates from the "$\Delta M_S = \pm 2$"-transition.
(B) trEPR spectrum of a photogenerated RP comprising a flavin and a tryptophan radical, measured at 274 K (Biskup et al., 2009).

In RPs, the average distance between the two unpaired electron spins is typically much larger. Hence, trEPR-spectra of photo-generated (and electron-spin polarized) RP states are narrower due to the reduced mutual dipolar and exchange interactions as compared to flavin triplet states (Schleicher et al., 2009). In **Figure 2B**, the trEPR signal of a flavin–tryptophan-based RP with a distance of ∼20 Å is depicted. The drastic influence of the strength of electron-electron interactions on the width of the spectra is obvious.

Analysis of the spectral shapes of trEPR-signals yields information on the chemical nature of the individual radicals composing the RP, and their interaction with each other and with their immediate surroundings. Spectral simulations based on the correlated-coupled RP mechanism are typically performed; these are outlined in more detail elsewhere (Closs

et al., 1987; Hore, 1989; Kothe et al., 1991; van der Est, 2009). Briefly, the signal of a single pair of coupled radicals consists of four resonance lines arranged in two antiphase doublets, each centered at the resonance magnetic-field position of the individual radical, respectively. The spacing between the lines within the antiphase signals is determined by the exchange and/or dipolar interactions. Each line pair may be further split by hyperfine interactions. In non-oriented frozen samples, interaction anisotropies will contribute to an inhomogeneous spectral broadening of some or all transitions.

State of the Art: Intermediates in Flavin-dependent Photoreceptors Probed by Modern EPR Spectroscopy

Cryptochromes

CRYs are blue-light photoreceptors with a wide range of regulatory functions in plants, animals and microorganisms. They are closely related to photolyases (PLs), with tight homologies in amino-acid sequence and spatial structure (Essen, 2006; Müller and Carell, 2009). PLs catalyze the light-driven, enzymatic cleavage of certain UV-induced lesions in DNA (Sancar, 2004; Weber, 2005; Essen and Klar, 2006). Except in mammals, PLs are very common in all three kingdoms of life (Essen and Klar, 2006). Both proteins use a flavin adenosin dinucleotide (FAD) as their primary redox-active chromophore/cofactor that is non-covalently bound in a cavity of the protein (Möglich et al., 2010; Chaves et al., 2011; Losi and Gärtner, 2012). Some of the characterized proteins carry an additional chromophore for light harvesting. In PLs, these second chromophores range from methenyltetrahydrofolate (Essen and Klar, 2006; Klar et al., 2006; Müller and Carell, 2009) via flavin derivatives to recently identified ribolumazine (Geisselbrecht et al., 2012; Zhang et al., 2013); however, the relevance for CRY photochemistry and function is still under debate (Selby and Sancar, 2012).

CRYs can function as classical photoreceptors or work as light-independent transcription factors (Lin and Todo, 2005). Examples are flower development and the entrainment of the circadian rhythm (Guo et al., 1998; van der Horst et al., 1999; Chaves et al., 2011). CRYs have also been suggested to play a major role in the magnetic orientation system of migratory birds, fruit flies and other animals (Gegear et al., 2008; Hore, 2012). Both classes of proteins show similarities in their basic structure, which are divided into an N-terminal domain and a C-terminal chromophore-binding domain where the FAD binding site is located. Additionally, CRYs contain an extended C-terminal region, the so-called C-terminal tail (CTT). Its length is rather variable; usually it is longer in plant CRYs than in animal CRYs, and it is supposedly involved in signal transduction. In the recently solved full-length structure of fruit fly CRY, the CTT forms an α-helix which occupies the FAD access cavity, at which the DNA lesion binds in PLs (Czarna et al., 2013).

After light excitation, PLs are able to engage in two light-dependent reactions: If the FAD cofactor is in its fully reduced $FADH^-$ state, an electron can be transferred to the DNA lesion, which results in splitting of the damaged DNA. Subsequent electron transfer back to the FAD renders this reaction net-zero with respect to the number of exchanged electrons. On the other hand, PLs and CRYs are able to react in the so-called photoreduction reaction: If the FAD is not in its fully reduced $FADH^-$ state, electrons can be transferred from the surface of the protein to the FAD by receiving an electron from a proximal tryptophan. Trp306 (*E. coli* PL numbering), which is located at the surface of the protein and is about 20 Å apart from the FAD, was first identified via a point-mutational study (Li et al., 1991). This distance is too large for an efficient direct electron transfer, and soon thereafter, two additional tryptophans (Trp359 and Trp382) were discovered as part of the so called "tryptophan triad" (Trp-triad) (Li et al., 1991). This triad represents a highly conserved electron-transport chain, which can be found in almost all members of the CRY/PL family. After the first electron transfer step, the electron hole is transported via well-defined intermediates from the proximal tryptophan to the surface-exposed (terminal) tryptophan, which in turn results in a transiently formed RP between the FAD and the terminal tryptophan. This intermediate state could either recombine back to the ground state, or is further stabilized via a subsequent deprotonation of the tryptophanyl cation radical involving solvent water molecules to form a neutral tryptophanyl radical (Aubert et al., 2000). The life time of the secondary RP comprising of $FAD^{\bullet -}$ (or $FADH^{\bullet -}$ in case of plant CRYs and PLs) and $Trp^{\bullet}$ is significantly prolonged up to the millisecond range. If the neutral tryptophanyl radical is reduced by an external electron donor, then the FAD remains in a one-electron reduced state. By substitution mutations it could be shown that both the surface-exposed tryptophan as well as the two bridging tryptophans are crucial for photoreduction ability. In PLs, however, the relevance of this intraprotein reaction for physiological DNA repair has been questioned (Kavakli and Sancar, 2004).

Despite the CTT region, CRY and PL structures are highly homologous, and although both harbor FAD as their redox-active chromophore, it seems that CRYs lost their ability to repair DNA damages. Earlier studies pointed out that the resting state *in vivo* in PLs is the fully reduced $FADH^-$ (Payne et al., 1987). To elucidate if the *in vivo* redox state is different in CRYs, insect cells overexpressing various CRYs were measured in the dark and after blue-light illumination using UV-vis and EPR spectroscopy. Oxidized FAD can in principle be detected in cells by fluorescence spectroscopy (by monitoring the emission at 525 nm, Galland and Tölle, 2003) or by UV-vis spectroscopy (by monitoring the absorbance at ∼450 nm). It could be shown that a light induced absorbance change matching the reduction of oxidized FAD occurs after a few minutes of blue-light illumination. The drawbacks of these optical methods are that (i) direct concentration measurements of the illuminated FAD states are not possible, and (ii) large experimental uncertainties arise from the intrinsic absorbance (and/or fluorescence) of cells. On the other hand, the use of EPR spectroscopy enabled direct measurements of the formation of the semiquinone radicals in living cells. Specifically, dark-grown intact cells overexpressing various CRYs were illuminated for defined time intervals with

blue light, and were subsequently shock-frozen in liquid nitrogen (Banerjee et al., 2007; Bouly et al., 2007; Hoang et al., 2008). The increase of an organic radical signal could be detected after a few minutes of illumination; control cells did not show any radical signal. Furthermore, a decrease of the signal back to a complete decay could be measured after dark incubation of the samples overnight (Engelhard et al., 2014).

To further characterize the detected radical signatures, and to assign the signal to a specific molecule, (Davis) ENDOR was applied at 80 K. Clearly, resonances could be obtained that are highly similar to those of purified protein-bound $FAD^{\bullet-}$ and $FADH^{\bullet}$ radicals found in plant and animal cryptochromes, respectively. With these results at hand, a novel mechanism of plant and animal CRYs could be proposed: In contrast to PLs, CRYs are activated via photoreduction of FAD starting from the oxidized FAD state (Banerjee et al., 2007; Bouly et al., 2007; Hoang et al., 2008). The formation of the fully-reduced $FADH^{-}$ state is strongly inhibited.

As a next logical step, the intermediate RPs that appear during the photoreduction reaction have been investigated in more detail. To this end, a trEPR study of wild-type CRY DASH of *X. laevis* (*X*Cry) was conducted to shed light on light-induced paramagnetic intermediates (Biskup et al., 2009). The obtained spectrum of wild-type *X*Cry resembles those published previously from trEPR on light-induced short-lived RP species in FAD photoreduction of PLs (Weber et al., 2002; Weber, 2005). The origin of the RP signature in *X*Cry could be unraveled by examination of a point mutant, Trp324Phe, which lacks the terminal tryptophan (equivalent to Trp306 in *E. coli* CPD photolyase) of the conserved electron-transfer cascade. This mutant did not show any trEPR signal. The conclusion, that Trp324 is indeed the terminal electron donor in electron-transfer reaction in *X*Cry was further supported by spectral simulations, which have been performed on the basis of the correlated coupled RP model. The calculations were performed using published **g**-tensor parameters for FAD and tryptophan neutral radicals. The relative orientations of the principal axes of both **g**-tensors and the dipole–dipole coupling tensor were taken from a *X*Cry homology model and kept fixed (Biskup et al., 2009).

After assigning the trEPR signal of the WT to the RP [FAD·· Trp324], the role of the first two tryptophans of the triad, namely Trp377 and Trp400 was explored in more detail (Biskup et al., 2013). For this purpose, two additional mutants, Trp377Phe and Trp400Phe, were produced and examined under otherwise identical experimental conditions. In contrast to the Trp324Phe sample, trEPR signals could be—most unexpectedly—observed in both mutants. At first glance, the obtained trEPR signal patterns are similar to the ones from the WT; however, slight differences could be detected upon closer inspection: Most importantly, the signals are shifted toward lower magnetic field, which corresponds to at least one paramagnetic species with **g**-tensor components larger than those of a tryptophan radical (Biskup et al., 2013). Published redox potentials and *g*-values lead to the conclusion that tyrosine is the only amino acid that is able to form such a RP (Bleifuss et al., 2001). A closer inspection of the *X*Cry structural model revealed two tyrosines, namely Tyr50 and Tyr397 to be ideal candidates to form a bridge between the FAD and the protein surface. In addition, these tyrosines are close to the Trp-triad and thus, are able to serve as a backup and function as an alternative electron transfer pathway. The assignment of the trEPR signals from the *X*Cry Trp377Phe and Trp400Phe mutants was again corroborated by spectral simulations, in which identical parameters as of the WT were used (Biskup et al., 2013). Only the **g**-tensor adjusted to be compatible with a tyrosine radical instead of a tryptophan radical. The resulting simulations showed signals shifted to lower magnetic fields, thus confirming a [Tyr···FAD] RP species. Another experimental way to prove this alternative electron transfer path was to investigate a Tyr50Phe/Trp400Phe double mutant, in which tyrosine and tryptophan were replaced by the redox-inert phenylalanine. Its weak trEPR signal was again shifted toward a higher magnetic field that closely resembles the WT signal, thus indicating a RP between Trp324 and the FAD.

In 2011, Biskup et al. expanded the concept of the highly conserved Trp-triad being the only electron-transfer pathway in the CRY/PL family even further (Biskup et al., 2011). **Figure 3** depicts results from a trEPR study of wild-type and point-mutated CRY DASH protein from *Synechocystis* sp. (*S*Cry). Here, an alternative ET pathway was revealed because a point mutation of the terminal tryptophan (Trp320Phe) showed the same trEPR spectrum as compared to the WT protein. An investigation of the protein structure identified an alternative tryptophan (Trp375) that could function as terminal electron donor. However, with 8.2 Å between Trp375 and the middle tryptophan (Trp373), the alternative terminal Trp' is nearly 5 Å further apart from Trp373 as the "expected" conserved terminal Trp. To probe this suggestion a second point mutant, Trp375Phe, was produced. No trEPR could be recorded, even with the conserved Trp-triad being fully intact, thus indicating that in *S*Cry an alternative pathway for electron transfer is used. The spectral evidence is supported by calculations based on Marcus' theory of charge transfer (Krapf et al., 2012). Here the

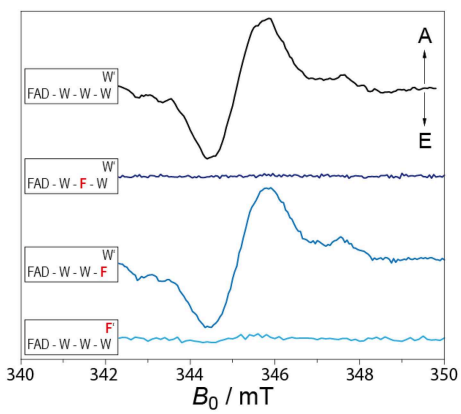

FIGURE 3 | TrEPR spectra of WT (solid black curve) and different Trp mutant proteins (solid blue curves) of *Synechocystis* Cry DASH. The spectra were scaled to a comparable signal-to-noise ratio. The three tryptophans correspond to (Trp396, Trp373, and Trp320, W′ correspond to Trp375). From top to bottom: WT, Trp373Phe, Trp320Phe, and Trp375Phe. Adapted from Biskup et al. (2011).

change in Gibb's free enthalpy for moving a positive charge along the conserved ($\Delta G =$ $-$ 62 kJ/mol) and alternative ($\Delta G = -81$ kJ/mol) pathways were computed, showing that the stabilization energy is about 20 kJ/mol higher for the alternative Trp'. This demonstrates that distance is not necessarily the decisive parameter to determine the electron-transfer pathways in CRYs and PLs, but solvent accessibility, and the stabilization of the charge-separated states, as well as the relative orientation of the involved molecules contribute substantially.

With the new results from the last years, the picture of a RP being formed upon photoexcitation in CRYs seems to be widely proven. But different from the early expectations the conserved Trp-triad is not the only pathway for electrons from the protein surface to the FAD chromophore. Different paths and also different types of amino acids can be used for electron transfer, even with the classic Trp-triad being fully intact. Why different types of CRYs use different routes for the electrons is a question, which needs to be answered in the future.

LOV Domains

First discovered as tandem sensor domains in the plant photoreceptor phototropin (Christie et al., 1998), "Light-oxygen-voltage" (LOV) domains have since been found in several plant, fungal, and bacterial proteins (Christie, 2007). LOV domains constitute a subclass of the Per-ARNT-Sim (PAS) family whose members serve as versatile sensor and interaction domains in diverse signaling proteins (Möglich et al., 2009); their identified responses range from phototropism (Briggs, 2007) via entrainment of the circadian clock (Kim et al., 2007) to regulation of morphogenesis (Möglich et al., 2010). The first structure of a LOV domain was that of the LOV2 domain of *Adiantum capillus-veneris* phototropin (Crosson and Moffat, 2001, 2002), and it confirmed the canonical PAS fold. Residues involved in FMN coordination and the photoreaction are largely conserved and define the flavin-binding pocket (Krauss et al., 2009).

LOV domains are distinguished from other flavoproteins by their characteristic photochemistry. After absorption of a photon in the blue spectral region by the dark-adapted LOV-450 state, the FMN cofactor undergoes efficient intersystem crossing within nanoseconds to yield a LOV-700 intermediate state with FMN in its triplet state (Swartz et al., 2001; Kennis et al., 2003). Within microseconds a covalent thioether bond between atom C(4a) of the flavin ring and a conserved nearby cysteine residue is formed (a so-called cysteinyl-4a-adduct), the LOV-390 state (Salomon et al., 2000, 2001). The photoreaction is fully reversible, and the signaling state thermally reverts to the ground (dark) state.

In principle, adduct formation can occur via three different molecular mechanisms: a concerted mechanism, an ionic mechanism following initial protonation of the excited ^{3}FMN triplet state, and a RP mechanism. To elucidate which leads to adduct formation, we designed a trEPR and optical study with various LOV domains at low-temperature: Triplet states of LOV domains were measured and compared to triplet states of flavins in solution (Kowalczyk et al., 2004; Schleicher et al., 2004). Specific protein-cofactor interactions that alter the electronic structure of LOV1 and LOV2 domains could be identified. In detail, a phenylalanine residue, which is highly conserved in LOV1 domains, alters the triplet-wavefunction (in particular the triplet "delocalization parameter" $|D|$) and is supposed to change the yield of adduct formation. Moreover, results from optical measurements clearly confirmed that adduct formation is possible at low temperatures, but the absorption spectra showed distinct changes as compared to spectra from frozen LOV domains with cysteinyl-4a-adduct. Additional triplet spectra were recorded at different pH values (in particular pH 2.8, which is well below the pK_a of 4.4 for the protonation of ^{3}FMN, Schreiner et al., 1975), both with FMN in aqueous solution and bound to LOV domains. If a protonation of the FMN triplet would have occurred in the LOV domains prior to adduct formation at 77 K, then the resulting ^{3}FMNH$^+$ would have been visible in the trEPR spectra, and could easily be distinguished from ^{3}FMN by its zero-field splitting parameters $|D|$ and $|E|$, and also by its triplet relaxation time (Kowalczyk et al., 2004). TrEPR experiments on protein-bound FMN and in frozen aqueous solution confirmed that proton transfer to ^{3}FMN does not occur at 77 K, which rules out the presence of ^{3}FMNH$^+$ as an intermediate at 77 K. These findings clearly demonstrated that adduct formation via an ionic mechanism can be excluded under these experimental conditions. Another possibility is that the thioadduct is formed via a concerted mechanism, directly from the triplet state. By the principle of conservation of angular momentum, however, the photoproduct is expected to be also formed in a triplet-spin configuration, and thus, should be detectable by trEPR; however, no such paramagnetic species was observed. This could be due to the fact that the triplet of the adduct species is hidden under the backdrop of an excess of triplets from unreacted LOV domains. It should be pointed out, however, that the triplet-state energy of the photoadduct is expected to be very high due to the formation of an sp^3-hybridized C(4a) from a formerly delocalized, and hence, stabilized π-electron system of the isoalloxazine ring. Therefore, we consider a concerted mechanism via such a transition state rather unlikely.

The only remaining plausible mechanism is the RP mechanism: After electron transfer from the functional cysteine to ^{3}FMN, a very short-lived and yet uncharacterized RP species is generated, which instantly forms a covalent bond after rapid triplet-to-singlet conversion. The generated protonated cysteinyl-4a-adduct deprotonates (an process inhibited at low temperature), and the signaling state is formed.

Despite closely similar sequence and almost identical structure, individual LOV domains differ markedly in their kinetics and quantum yields of the photocycles. Notably, dark-recovery times between a few seconds up to hours have been recorded (Kasahara et al., 2002; Zoltowski et al., 2009). One approach for understanding these phenomena is to assume that minor changes in the cofactor environment lead to subtle changes in protein conformation, which in turn could alter the stability of the carbon–sulfur bond, and thus, modulate the reaction speed of the ΔG-driven C–S bond splitting. A number of examples in the literature show significant modulation of adduct formation/bond breaking via point mutations at various sites of the phototropin protein (Christie et al., 2007; Jones et al., 2007; Raffelberg et al., 2011, 2013). Therefore, these findings support the idea that

minute changes in LOV domains can lead to significant changes in their reactivity. For a profound understanding of this unique photochemical reaction, information on the hydrogen-bonding situation and the close environment of the photo-labile center is crucial.

For this purpose, a study has been designed where parts of the micro-environment in the close vicinity of the flavin cofactor of a LOV domain was altered and, via ENDOR spectroscopy, the influence on the protein's reactivity was elucidated (Brosi et al., 2010). Resolving the micro-environment of cofactors in proteins and its influence on biological function is difficult as most of these structural changes are far beyond the typical resolution of protein X-ray crystallography: To increase structural information extractable from experimental data, its temperature dependence needs also to be taken into account. From these data, the internal energy of the system, and hence, the strength of interaction between the cofactor and its surrounding can be estimated. For this purpose, site-directed mutagenesis of LOV domains where the reactive cysteine residue is exchanged with either alanine or serine, were devised. This prevents the formation of the C4a adduct and instead leads to a meta-stable $FMNH^{\bullet}$, which has been identified to serve as a reaction intermediate analog.

In detail, it was possible to detect a unique spectral behavior of *Avena sativa* LOV2 (*As*LOV2) C450A samples as their 8α methyl-group rotational motion is slowed down starting at already rather elevated temperatures ($T < 110$ K) (Brosi et al., 2010). To identify responsible amino acids for altered protein-cofactor interaction, an extended mutagenesis study has been performed with modifications introduced to in the direct vicinity of the 8α methyl-group, where three amino acids, namely Leu496, Phe509, and Asn425, are located (see **Figure 4**). Mutations in these three amino acids clearly showed changed temperature behavior, which is in line with the predicted altered sterical interaction (see **Figure 4**, left panel). Moreover, the hfcs from the three arrested 8α protons shift as depending on the individual mutants (see **Figure 4**, right panel). Spectral assignment of these hfc tensors in combination with DFT calculations resulted in the precise determination of the orientation of the methyl group with respect to the isoalloxazine ring plane.

Finally, as an important link between molecular spectroscopy and protein photochemistry, Asn425 was identified as a central amino acid for the photochemistry of LOV domains (Brosi et al., 2010). Kinetic measurements demonstrated that the *As*LOV2 Asn425Cys sample has a seven-fold shorter adduct-state life time as compared to *As*LOV2 WT. This is most likely due to altered Asn425–FMN interaction, which in the end destabilizes the intrinsically weak C–S bond of the cysteinyl-4a-adduct.

This type of study was recently repeated with an engineered LOV photoreceptor YF1 using optical and EPR spectroscopy (Diensthuber et al., 2014). To probe for benign or adverse effects on receptor activity, all amino acids surrounding the FMN were mutated and their impact on light regulation was determined. While several mutations severely impaired the dynamic range of the receptor (e.g., Ile39Val, Arg63Lys, and Asn94Ala), residue substitutions in a second group were benign with little effect on regulation (e.g., Val28Thr, Asn37Cys, and Leu82Ile). Both detection methods identified correlated effects for certain of the latter mutations on chromophore environment and response kinetics in YF1 and the LOV2 domain from *Avena sativa* phototropin 1.

In sum, both studies concluded that mutations close to the FMN cofactor provide a powerful tool to adjust the light-responses of LOV photoreceptors as demanded for optogenetic applications. As outcome from low-temperature ENDOR studies, a slight reorientation of the FMN binding position and as a consequence, a (de)stabilization of the C(4a) adduct seems to be the most likely effect.

BLUF Domains

In 2000, the most recent member of blue-light percepting proteins, the flavin-containing blue-light receptors exemplified in the N-terminus of the AppA protein of the purple bacterium *Rhodobacter sphaeroides*, was first described in the literature (Masuda and Bauer, 2002). AppA acts here as a transcriptional antirepressor and interacts with the photosynthesis repressor protein PpsR to form a stable AppA–$(PpsR)_2$ complex in the dark. The blue-light activated form of AppA cannot associate with PpsR and thus, enables photosynthetic genes inhibition (Braatsch and Klug, 2004).

Via comparison of amino-acid sequences, a new class of blue-light photoreceptors, the so-called BLUF ("blue-light using FAD") domains (Gomelsky et al., 2000), were introduced. This class contains a series of proteins from proteobacteria, cyanobacteria and some eukaryotes (Gomelsky and Klug, 2002). Three-dimensional structures from X-ray crystallographic data are now available for a number of BLUF proteins. Their arrangement is unique among flavin-binding proteins and bears a more global similarity to a ferredoxin fold rather than to other photoreceptor molecules (Anderson et al., 2005; Kita et al., 2005; Grinstead et al., 2006; Jung et al., 2006; Yuan et al., 2006).

Some sort of photocycle has been assumed for BLUF proteins, however, no specific structural changes upon illumination have been observed so far. Illumination of BLUF domains induces a small but distinct red shift of about 10 nm of the FAD absorption in the UV-visible region (Laan et al., 2003), which is reversible in the dark. Lifetimes between a few seconds and up to several hours have been determined (Kraft et al., 2003; Masuda et al., 2004). The photocycle is unique compared to the LOV photoreceptors, in which light absorption induces relatively large spectroscopic changes of the chromophore. Although the molecular mechanism of BLUF photochemistry is still under significant discussion (see, e.g., Domratcheva et al., 2008; Wu and Gardner, 2009), three conserved amino acids are believed to be essential for this light-driven reaction: a tyrosine, a tryptophan and a glutamine, which are all located in direct proximity to N(5) of the FAD's isoalloxazine moiety. A reaction scheme was first proposed by Gauden and coworkers (Gauden et al., 2005; Laan et al., 2006): following blue-light illumination, a transient RP comprising of the FAD and a conserved tyrosine is formed, which drives the hydrogen-bonding network around the N(5) position to rearrange. In contrast to the triplet intermediate state in LOV domains, the BLUF reaction starts out mainly from the excited singlet state of the FAD (the complete reaction cycle is proposed to be completed within 1 ns) (Gauden et al., 2005). Nevertheless,

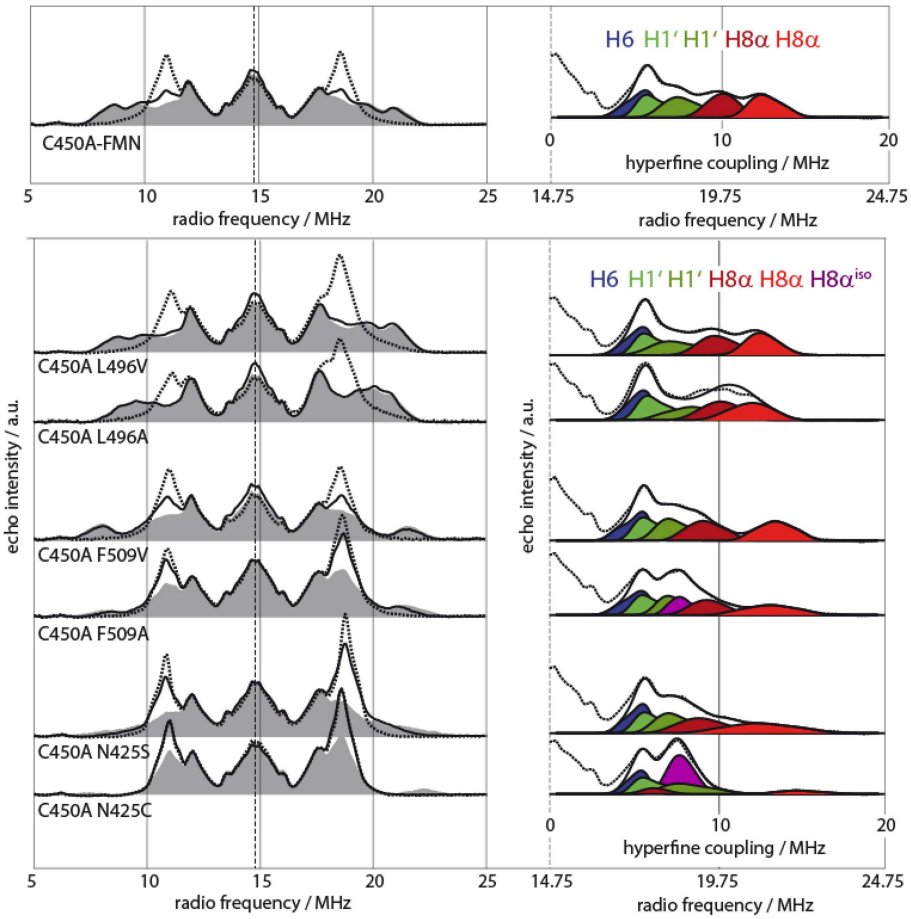

FIGURE 4 | Pulsed X-Band proton Davies-type ENDOR spectra of various *As*LOV2 single- and double mutants (adapted from Brosi et al., 2010). Left: Spectra were recorded at 120 K (dashed lines), 80 K (black lines), and 10 K (gray shaded) for all samples. **Right**: Sections of *As*LOV2 10-K spectra with accompanying spectral simulation of the outer wing of the spectrum (measured spectrum, dashed lines; single simulated hfcs, shades of blue, green, and red; envelope of simulated hfcs, black lines). Two protein samples, *As*LOV2 C450A/F509A and *As*LOV2 C450A/N425C, require another hyperfine component of axial symmetry for accurate spectral fitting. This feature represents hfcs from fast rotating 8α methyl group protons, is shown in purple and is denoted as $H8\alpha^{iso}$.

it has been demonstrated, that also triplet-state precursors are able to perform a hydrogen network rearrangement (Zirak et al., 2005).

As the primary light reaction is not accessible within the time scale of trEPR, light-activated intermediates of the FAD cofactor in three BLUF domains from *R. sphaeroides* (AppA-BLUF), *Synechocystis* sp. PCC 6803 (SlR-BLUF), and *Escherichia coli* (YcgF-BLUF) have been probed at low temperature (Weber et al., 2011). It was the goal of this study to shed some light on intermediate states, and to identify specific protein–cofactor interactions that modulate their electronic wave functions. As larger conformational changes are inhibited at these temperatures, the formation of intermediate states can be monitored; however, no final signaling state is formed thus rendering the reaction cyclic.

Photo-induced flavin triplet states and RP species have been detected on a microsecond time scale, but revealed a completely different behavior as compared to previously investigated LOV domains (Schleicher et al., 2004). Moreover, BLUF domains exhibit much higher spectral diversity. While the trEPR spectrum of the AppA-BLUF protein (see **Figure 5**, upper panel) is very similar to that of the LOV domains, triplet-state spectra obtained from the YgcF-BLUF protein show a completely different electron-spin polarization pattern (see **Figure 5**, middle panel). Moreover, spectra recorded from the Slr-BLUF protein exhibit an even more complex spectral shape around $g \sim 2$ (see **Figure 5**, lower panel). To rationalize these differences, spectral simulations of flavin-triplet state trEPR spectra have been performed (see dashed lines in **Figure 5**) (Weber et al., 2011). It is interesting to note that pre-illuminated BLUF domains did not show any signal assuming an efficient deactivation process that is completed within a ns-time scale (Mathes et al., 2012).

TrEPR spectra from YcgF-BLUF domains led us to the assumption that a nearby methionine can alter the wave function of the flavin triplet state, and thus, can be responsible for the unusual electron-spin polarization pattern (Weber et al., 2011).

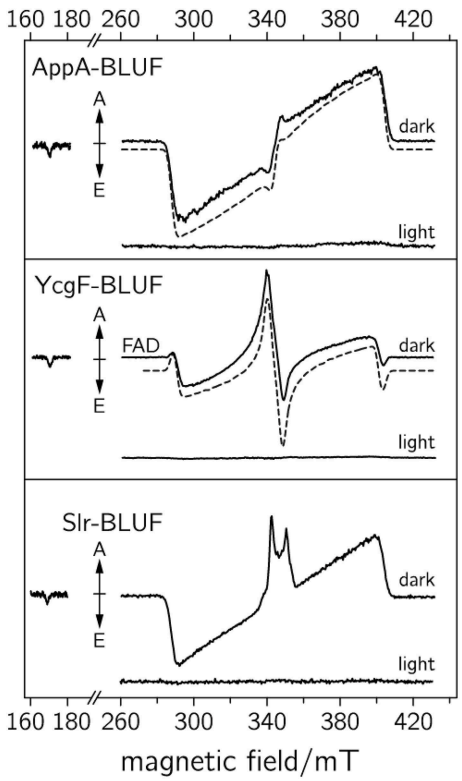

FIGURE 5 | TrEPR spectra of various BLUF domains recorded at 1 μs after pulsed laser excitation (adapted from Weber et al., 2011). Upper: dark-adapted and blue-light adapted AppA-BLUF protein. **Middle**: dark and blue-light illuminated YcgF-BLUF samples. **Lower**: dark and blue-light illuminated Slr-BLUF protein. The respective dashed curves represent spectral simulations of the dark-state sample.

Moreover, Slr-BLUF undergoes a competing electron-transfer reaction, which is tentatively assigned to a flavin-tyrosine RP, but deserves further investigation. Nevertheless, it remains unclear why only Slr-BLUF samples show light-induced electron transfer under the chosen experimental conditions. The answer to this question may be the key to correlating the electronic structure of light-induced excited states with biological signaling activity, which most likely depends on the stability of the light state. On the other hand, based on the rather broad trEPR RP signature, long-range electron transfer (over distances larger than 1 nm) can be excluded. Here, trEPR beautifully shows its potential for assigning electron-transfer partners even in molecules with several potential electron donors.

In a different approach, dark-state BLUF domains from *Thermosynechococcus elongatus* were illuminated at low temperature, and the resulting meta-stable radicals were characterized using steady-state EPR methods (Nagai et al., 2008; Kondo et al., 2011). The illumination at 5–200 K derived an EPR signal with a separation of 85 G between the main peaks around $g \sim 2$, showing a typical Pake powder pattern of magnetic dipole-dipole interaction between two nearby radicals. Extended illumination induced an EPR signal at $g = 2.0045$, which was assigned to a neutral flavosemiquinone $FADH^{\bullet}$. The Pake doublet was not detected in a mutant protein, in which the tyrosine residue was replaced with phenylalanine. Further analysis by pulsed-ENDOR spectroscopy revealed an assignment to an $FADH^{\bullet}$ and a tyrosine neutral radical by comparison with published ENDOR signals (Mino et al., 1997).

Very recently, a Gln50Ala mutant of Slr-BLUF was investigated (Fudim et al., 2015). Without the central glutamine, no red-shifted signaling state is formed, but light-induced proton-coupled electron transfer between the protein and flavin takes place, analogous as to the WT protein. Results from ultrafast optical spectroscopy demonstrated that the lifetime of the neutral flavin semiquinone–tyrosyl RP is greatly prolonged (from <100 ps in the wild-type protein) to several nanoseconds, which indicates that the formation of radical intermediates drives the hydrogen-bond rearrangement in BLUF photoactivation. This lifetime is now in a range suitable for detection by trEPR; therefore, this method was applied to investigate this Gln50Ala mutation at ambient temperatures (Fudim et al., 2015). The resulting trEPR spectrum consists of a point-symmetric E/A/E/A signal pattern spanning a width of 15.5 mT, without any resolved hyperfine structure. From the symmetric pattern of the signal and its signature, a spin-correlated RP species with a singlet excited-state precursor can be assumed. This is in contrast to the aforementioned low-temperature spectrum of WT Slr-BLUF, which has been assigned to a triplet-based spin correlated RP. A comparison between the RP observed in BLUF domains and cryptochromes, respectively, reveals major differences regarding signal pattern and width. For a quantitative analysis of the spectra obtained from the Slr-BLUF Gln50Ala sample, however, spectral simulations of this, for the first time in a protein observed strongly-coupled RP have to be performed to obtain exact distances and radical compositions.

Summary

The to date proposed and commonly accepted primary light reactions of the three examined flavin-dependent photoreceptors are summarized in **Figure 6**. Both differences as well as commonalities between each of the molecular mechanisms can be detected: Whereas all signaling states are in principle reversible, only the CRY reaction comprises of a redox reaction and thus, a yet unidentified electron donor is required in order to facilitate signaling-state formation *in vivo* (established electron donors like EDTA or DTT are used for *in vitro* measurements). This in turn demands an oxidizing agent (most likely molecular oxygen in case of *in vitro* measurements) for back reaction to the dark state. In contrast, no additional reagents could yet be identified for back reaction in BLUF and LOV domains. Their signaling states are intrinsically metastable and thus, back reactions are only dependent on the thermal energies of the system. Consequently, the back reaction of CRYs directly depends on the accessibility and on the concentration of the oxidizing agent, whereas the life times of the signaling states in LOV and BLUF domains can be significantly modulated by the amino acids surrounding the flavin cofactor.

On the other hand, all mechanisms unify an electron transfer reaction after light excitation, very likely because of the large oxidation potential of excited-state flavins, which is estimated to

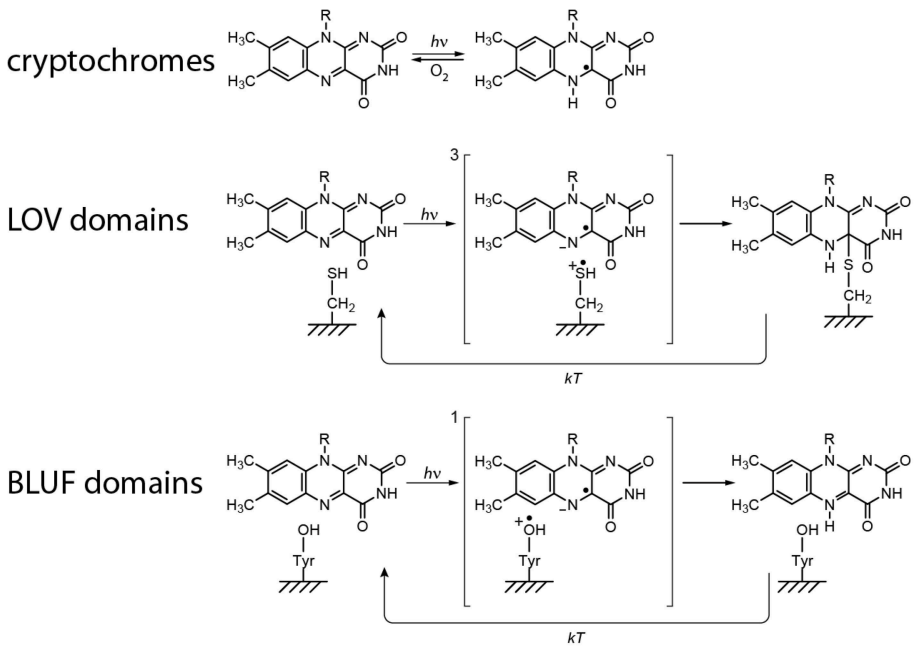

FIGURE 6 | Proposed primary light reactions of flavin-dependent photoreceptors.

be around 1.8 V (Heelis et al., 1990). However, clear differences of the life times and the distances between the three intermediate RPs are obtained. Whereas, CRY RPs are ∼20 Å apart, and hence, have millisecond life times, distances of ∼6 Å and correspondingly short life times are obtained in BLUF and LOV domains.

In sum, investigations with EPR spectroscopy are an obvious choice and indeed, played a substantial role for the elucidation of the primary reactions of these photoreceptors. In detail, first mechanistic proposals based on results from EPR (and optical) investigations were published for CRYs and LOV domains (Schleicher et al., 2004; Banerjee et al., 2007; Bouly et al., 2007). In addition, trEPR has been proven valuable for characterization of electron-transfer channels and the participating amino acids (Biskup et al., 2009, 2011, 2013; Weber et al., 2010). The signaling-state generation in BLUF domains, however, is generated within only a few nanoseconds, which inhibit direct results from EPR spectroscopy. In this case, either slowing down the reaction by decreasing the temperature or altering the reaction by selective mutations has been used.

How Can Secondary Events like Conformational Changes Be Investigated by Molecular Spectroscopy?

The signal-transduction events following the primary photoprocesses are far from being fully understood in all three photoreceptor classes, although some key results emerge to shed light onto the principal mechanisms: More than 10 years ago, ground-breaking results from NMR spectroscopy demonstrated a reordering or even an unfolding of the helix (named J_α) bridging a LOV2 domain and its signal-transduction module (Harper et al., 2004a,b; Herman et al., 2013), and thus, displayed a first molecular concept for signal propagation. Subsequent experiments with other LOV domains yielded evidence that also dimerization reactions can occur after light excitation (Buttani et al., 2007; Möglich and Moffat, 2007; Nakasako et al., 2008; Zayner et al., 2012; Herman et al., 2013). In *Arabidopsis* CRY2, a homo oligomerization and subsequent binding to its partner protein CIB1 has been identified (Hulsebosch et al., 1997; Kennedy et al., 2010), however, the variability of the CTT domain in CRYs implies that also other mechanisms are possible. In BLUF domains, also monomerization reactions have been identified (Prisner et al., 2001; Yuan et al., 2006; Wu and Gardner, 2009).

Despite these initial achievements in unraveling signal-transduction pathways, several major questions regarding these secondary steps in photoreception remain unanswered: Up to now, the interaction between individual multi-domain photoreceptors (e.g., LOV1 and LOV2) and how the two domains modulate the light-sensing signal are still unknown. Moreover, the slow dark-state recovery and the remarkable divergence of this reaction depending on the organism are still far from being understood. Furthermore, most amino acids that are responsible for conformational changes remain unidentified. Knowledge of these is in turn essential for application to optogenetics: exact control of the photoactivation and photoreversion rates, and optimized affinities between photoreceptor and signaling domain are highly desired and necessary.

In principle, photoreceptors are ideal for examining conformational changes as (i) both dark and signaling states can

be generated with almost 100% yield; subsequent temperature reduction enables freezing the light state and allows for steady-state spectroscopy on both states, (ii) all reactions are in principle reversible, which permits accumulation of signals from intermediate states, and (iii), short light pulses can be perfectly used as intrinsic trigger for time-resolved spectroscopy. The application of structure determination methods such as X-ray crystallography or NMR spectroscopy, however, are limited for the analysis of the signaling states because (i) dimerization reactions and/or reordering of domains "precludes" crystallization and (ii), most photoreceptors are too large for NMR spectroscopy. On the other hand, EPR spectroscopy in combination with SDSL may help to uncover conformational changes in photoreceptors. To examine structural changes upon light excitation, various EPR experiments are conceivable.

In general, the room temperature EPR-spectral shape of a nitroxide SL is sensitive to the reorientational motion of its side chain due to partial motional averaging of anisotropic components of the **g**− and hfc-tensors (Klare and Steinhoff, 2009; Hubbell et al., 2013). Therefore, changes in mobility, accessibility and polarity can be used to characterize the effects on the EPR signature due to the motional rate, amplitude, and anisotropy of the overall reorientational motion (Marsh, 2010; Klare, 2013). Changes in these parameters result in altered *g*-factors, spectral line widths, hf splittings, relaxation times, and rotational correlation times; all of them can be extracted from an EPR spectrum via spectral simulations (Klare and Steinhoff, 2009; Klare, 2013). This concept can be applied to all photoreceptors as changes in mobility of dark− and signaling state can be probed via cwEPR at ambient temperatures. To do so, a number of SDSL proteins have to be produced, and differences between the two states mapped. With the help of modern computational chemistry, changes of EPR parameters can nowadays be correlated to structural changes (Mchaourab et al., 2011; Polyhach et al., 2011). The drawback of this method is that only qualitative conclusions are possible.

For a quantitative analysis of conformational changes, the aforementioned concept has to be expanded to doubly-SL proteins. The basis for this approach is that the distance between the two SLs can be determined precisely through quantification of their mutual spin–spin interaction. Spin–spin interaction comprises static dipolar interaction, modulation of the dipolar interaction by the residual motion of the spin label side chains, and exchange interaction. The combination of static dipolar and exchange interaction in an unordered, immobilized sample leads to considerable broadening of the cwEPR spectrum if the interspin distance is less than 2 nm. In this case, interspin distances can then be determined by a detailed line-shape analysis of EPR spectra of frozen protein samples using spectra-deconvolution; however, this approach is still prone to various sources of errors (Hubbell and Altenbach, 1994; Hubbell et al., 2000; Steinhoff, 2004).

On the other hand, exchange interaction is typically negligible for interspin distances larger than 2 nm. Here, the direct measurement of the dipolar coupling is possible with the DEER/PELDOR pulse sequence, which separates the dipole–dipole interaction from other contributions to the spin Hamiltonian. DEER/PELDOR is based on the separate excitation of two groups of electron spins by applying 2 mw frequencies. The strength of the dipolar interaction is directly observed as modulated decay curves in the time domain (**Figure 7**). Via Fourier transformation, the frequency of the modulation can be extracted and directly correlated to the interspin distance (Polyhach et al., 2011; Jeschke, 2012). Comparison of distances between dark- and signaling states, performed with a number of differently doubly SL photoreceptors, results in a mapping of distance distributions that correspond to the extent of conformational changes. As a representative example, the expected alteration of the distance distribution in phototropins is depicted in **Figure 7**. The aforementioned reordering of the J_α-helix is expected to result in a displacement of the kinase domain. If SLs are attached to one of the LOV domains and to the kinase domain, these structural changes can be monitored and analyzed. Although the accessibility of full-length structural information is very helpful for the analysis of distance data, interpretation is still possible without this information at hand: A combination of structural information of the individual domains and modern structure modeling is able to bypass missing full-length structures. It has to be mentioned that this concept can be easily adapted to follow dimerization (monomerization) reactions: Here, the photoreceptor is labeled at one position, and DEER/ELDOR spectra of dark- and signaling states are recorded. Distances will only be obtained when the photoreceptor is in its dimeric state.

The only disadvantage of the concept is that for efficient and selective coupling of the SL to the protein, cysteine residues at defined positions are obviously prerequisite. In case of small LOV and BLUF domains, no or only a few cysteines are encoded in the WT proteins; however, a number of naturally occurring cysteine residues are found in large photoreceptors such as phototropins

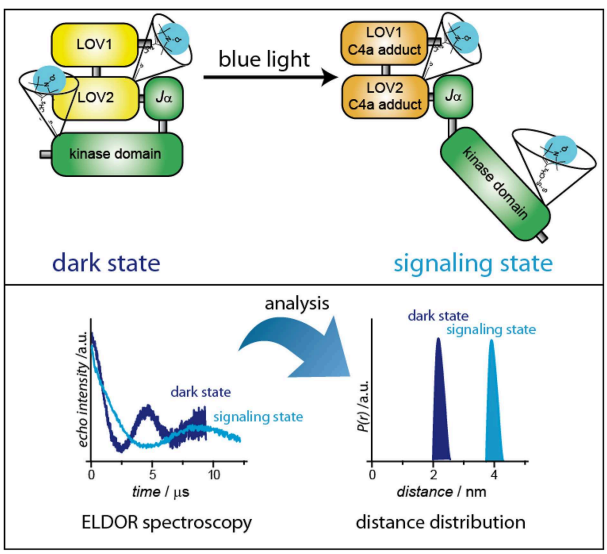

FIGURE 7 | Distance determination of dark- and signaling-states via pulsed ELDOR spectroscopy. As a representative example, plant phototropin has been chosen.

or plant cryptochromes. Here, "unwanted" cysteines need to be removed with the help of molecular-biology methods prior labeling to avoid attachment of more than two SL thereby complicating distance analysis. Although the general procedure is well established, mutating a number of amino acids in a protein may always lead to misfolded and/or non-functional protein. But such effects can in principle be controlled by a "clever" mutation scheme.

Additionally, various recently developed labeling techniques using click-chemistry and unnatural amino acids enable the possibilities to circumvent general labeling problems such as cysteine-rich proteins (Fleissner et al., 2009). Moreover, the usage of orthogonal labeling with two different SLs attached to the protein of interest provides additional information and clear advantages in performing ELDOR/DEER spectroscopy as modulation depths of the recorded time traces are significantly increased and selective mw excitation can be applied (Chen et al., 2011).

Clearly, bringing together modern pulsed EPR, ideally performed at various magnetic-field/microwave-frequency ranges to exploit orientation-selection effects, with other nowadays well established methods such as SDSL, freeze quenching, molecular quantum mechanics, molecular mechanics, and, last but not least, sophisticated frequency analysis to accurately extract SL distances, provides the means of unraveling the structure and structural changes of photoreceptors, isolated and in complex with other proteins. Although this global combined approach is challenging and not straightforward to apply, it may be the only means in cases where other more highly resolving techniques, such as X-ray diffraction, due to the lack of high-quality single crystals, or NMR, due to the too large size of a protein complex, do not lead to meaningful propositions for a full comprehension of the functioning of photoreceptors. While EPR and in particular trEPR have already demonstrated their value in unraveling the primary photochemistry of blue-light photoreceptors, DEER/PELDOR still needs to prove itself in the vibrant but challenging photoreceptor research field. Nevertheless, we are confident, that within the next decade significant insight in signal transduction will be presented based on pulse EPR distance analyses.

Funding

Deutsche Forschungsgemeinschaft, Research Training Group RTG 1976 (project 13).

References

Anderson, S., Dragnea, V., Masuda, S., Ybe, J., Moffat, K., and Bauer, C. (2005). Structure of a novel photoreceptor, the BLUF domain of AppA from *Rhodobacter sphaeroides*. *Biochemistry* 44, 7998–8005. doi: 10.1021/bi0502691

Aubert, C., Vos, M. H., Mathis, P., Eker, A. P. M., and Brettel, K. (2000). Intraprotein radical transfer during photoactivation of DNA photolyase. *Nature* 405, 586–590. doi: 10.1038/35014644

Banerjee, R., Schleicher, E., Meier, S., Viana, R. M., Pokorny, R., Ahmad, M., et al. (2007). The signaling state of *Arabidopsis* cryptochrome 2 contains flavin semiquinone. *J. Biol. Chem.* 282, 14916–14922. doi: 10.1074/jbc.M700616200

Berliner, L. J. (2010). From spin-labeled proteins to *in vivo* EPR applications. *Eur. Biophys. J.* 39, 579–588. doi: 10.1007/s00249-009-0534-x

Berliner, L. J., Eaton, G. R., and Eaton, S. S. (2000). *Distance Measurements in Biological Systems by EPR*. New York, NY: Kluwer Academic/Plenum Publishers.

Biskup, T., Hitomi, K., Getzoff, E. D., Krapf, S., Koslowski, T., Schleicher, E., et al. (2011). Unexpected electron transfer in cryptochrome identified by time-resolved EPR spectroscopy. *Angew. Chem. Int. Ed.* 50, 12647–12651. doi: 10.1002/anie.201104321

Biskup, T., Paulus, B., Okafuji, A., Hitomi, K., Getzoff, E. D., Weber, S., et al. (2013). Variable electron transfer pathways in an amphibian cryptochrome. Tryptophan versus tyrosine-based radical pairs. *J. Biol. Chem.* 288, 9249–9260. doi: 10.1074/jbc.M112.417725

Biskup, T., Schleicher, E., Okafuji, A., Link, G., Hitomi, K., Getzoff, E. D., et al. (2009). Direct observation of a photoinduced radical pair in a cryptochrome blue-light photoreceptor. *Angew. Chem. Int. Ed.* 48, 404–407. doi: 10.1002/anie.200803102

Bittl, R., and Weber, S. (2005). Transient radical pairs studied by time-resolved EPR. *Biochim. Biophys. Acta* 1707, 117–126. doi: 10.1016/j.bbabio.2004.03.012

Bleifuss, G., Kolberg, M., Pötsch, S., Hofbauer, W., Bittl, R., Lubitz, W., et al. (2001). Tryptophan and tyrosine radicals in ribonucleotide reductase: a comparative high-field EPR study at 94 GHz. *Biochemistry* 40, 15362–15368. doi: 10.1021/bi010707d

Bouly, J.-P., Schleicher, E., Dionisio-Sese, M., Vandenbussche, F., Van der Straeten, D., Bakrim, N., et al. (2007). Cryptochrome blue-light photoreceptors are activated through interconversion of flavin redox states. *J. Biol. Chem.* 282, 9383–9391. doi: 10.1074/jbc.M609842200

Braatsch, S., and Klug, G. (2004). Blue light perception in bacteria. *Photosynth. Res.* 79, 45–57. doi: 10.1023/B:PRES.0000011924.89742.f9

Briggs, W. R. (2007). The LOV domain: a chromophore module servicing multiple photoreceptors. *J. Biomed. Sci.* 14, 499–504. doi: 10.1007/s11373-007-9162-6

Brosi, R., Illarionov, B., Mathes, T., Fischer, M., Joshi, M., Bacher, A., et al. (2010). Hindered rotation of a cofactor methyl group as a probe for protein–cofactor interaction. *J. Am. Chem. Soc.* 132, 8935–8944. doi: 10.1021/ja910681z

Buttani, V., Losi, A., Eggert, T., Krauss, U., Jaeger, K.-E., Cao, Z., et al. (2007). Conformational analysis of the blue-light sensing protein YtvA reveals a competitive interface for LOV-LOV dimerization and interdomain interactions. *Photochem. Photobiol. Sci.* 6, 41–49. doi: 10.1039/B610375H

Chaves, I., Pokorny, R., Byrdin, M., Hoang, N., Ritz, T., Brettel, K., et al. (2011). The cryptochromes: blue light photoreceptors in plants and animals. *Annu. Rev. Plant Biol.* 62, 335–364. doi: 10.1146/annurev-arplant-042110-103759

Chen, Y.-X., Triola, G., and Waldmann, H. (2011). Bioorthogonal chemistry for site-specific labeling and surface immobilization of proteins. *Acc. Chem. Res.* 44, 762–773. doi: 10.1021/ar200046h

Christie, J. M. (2007). Phototropin blue-light receptors. *Annu. Rev. Plant Biol.* 58, 21–45. doi: 10.1146/annurev.arplant.58.032806.103951

Christie, J. M., Corchnoy, S. B., Swartz, T. E., Hokenson, M., Han, I.-S., Briggs, W. R., et al. (2007). Steric interactions stabilize the signaling state of the LOV2 domain of phototropin 1. *Biochemistry* 46, 9310–9319. doi: 10.1021/bi700852w

Christie, J. M., Gawthorne, J., Young, G., Fraser, N. J., and Roe, A. J. (2012). LOV to BLUF: flavoprotein contributions to the optogenetic toolkit. *Mol. Plant* 5, 533–544. doi: 10.1093/mp/sss020

Christie, J. M., Reymond, P., Powell, G. K., Bernasconi, P., Raibekas, A. A., Liscum, E., et al. (1998). *Arabidopsis* NPH1: a flavoprotein with the properties of a photoreceptor for phototropism. *Science* 282, 1698–1701. doi: 10.1126/science.282.5394.1698

Closs, G. L., Forbes, M. D. E., and Norris, J. R. (1987). Spin-polarized electron paramagnetic resonance spectra of radical pairs in micelles. Observation of electron spin-spin interactions. *J. Phys. Chem.* 91, 3592–3599. doi: 10.1021/j100297a026

Crosson, S., and Moffat, K. (2001). Structure of a flavin-binding plant photoreceptor domain: insights into light-mediated signal transduction. *Proc. Natl. Acad. Sci. U.S.A.* 98, 2995–3000. doi: 10.1073/pnas.051520298

Crosson, S., and Moffat, K. (2002). Photoexcited structure of a plant photoreceptor domain reveals a light-driven molecular switch. *Plant Cell* 14, 1067–1075. doi: 10.1105/tpc.010475

Czarna, A., Berndt, A., Singh, H. R., Grudziecki, A., Ladurner, A. G., Timinszky, G., et al. (2013). Structures of *Drosophila* cryptochrome and mouse cryptochrome1 provide insight into circadian function. *Cell* 153, 1394–1405. doi: 10.1016/j.cell.2013.05.011

Diensthuber, R. P., Engelhard, C., Lemke, N., Gleichmann, T., Ohlendorf, R., Bittl, R., et al. (2014). Biophysical, mutational, and functional investigation of the chromophore-binding pocket of light-oxygen-voltage photoreceptors. *ACS Synth. Biol.* 3, 811–819. doi: 10.1021/sb400205x

Domratcheva, T., Grigorenko, B. L., Schlichting, I., and Nemukhin, A. V. (2008). Molecular models predict light-induced glutamine tautomerization in BLUF photoreceptors. *Biophys. J.* 94, 3872–3879. doi: 10.1529/biophysj.107.124172

Engelhard, C., Wang, X., Robles, D., Moldt, J., Essen, L.-O., Batschauer, A., et al. (2014). Cellular metabolites enhance the light sensitivity of *Arabidopsis* cryptochrome through alternate electron transfer pathways. *Plant Cell* 26, 4519–4531. doi: 10.1105/tpc.114.129809

Essen, L.-O. (2006). Photolyases and cryptochromes: common mechanisms of DNA repair and light-driven signaling? *Curr. Opin. Struct. Biol.* 16, 51–59. doi: 10.1016/j.sbi.2006.01.004

Essen, L.-O., and Klar, T. (2006). Light-driven DNA repair by photolyases. *Cell Mol. Life Sci.* 63, 1266–1277. doi: 10.1007/s00018-005-5447-y

Fanucci, G. E., and Cafiso, D. S. (2006). Recent advances and applications of site-directed spin labeling. *Curr. Opin. Struct. Biol.* 16, 644–653. doi: 10.1016/j.sbi.2006.08.008

Fleissner, M. R., Brustad, E. M., Kálai, T., Altenbach, C., Cascio, D., Peters, F. B., et al. (2009). Site-directed spin labeling of a genetically encoded unnatural amino acid. *Proc. Natl. Acad. Sci. U.S.A.* 106, 21637–21642. doi: 10.1073/pnas.0912009106

Frey, P. A., Hegeman, A. D., and Reed, G. H. (2006). Free radical mechanisms in enzymology. *Chem. Rev.* 106, 3302–3316. doi: 10.1021/cr050292s

Fudim, R., Mehlhorn, J., Berthold, T., Weber, S., Schleicher, E., Kennis, J. T. M., et al. (2015). Photoinduced formation of flavin radicals in BLUF domains lacking the central glutamine. *FEBS J.* 282, 3161–3174. doi: 10.1111/febs.13297

Galland, P., and Tölle, N. (2003). Light-induced fluorescence changes in *Phycomyces*: evidence for blue light-receptor associated flavo-semiquinones. *Planta* 217, 971–982. doi: 10.1007/s00425-003-1068-6

Gauden, M., Yeremenko, S., Laan, W., van Stokkum, I. H. M., Ihalainen, J. A., van Grondelle, R., et al. (2005). Photocycle of the flavin-binding photoreceptor AppA, a bacterial transcriptional antirepressor of photosynthesis genes. *Biochemistry* 44, 3653–3662. doi: 10.1021/bi047359a

Gegear, R. J., Casselman, A., Waddell, S., and Reppert, S. M. (2008). Cryptochrome mediates light-dependent magnetosensitivity in *Drosophila*. *Nature* 454, 1014–1018. doi: 10.1038/nature07183

Geisselbrecht, Y., Frühwirth, S., Schroeder, C., Pierik, A. J., Klug, G., and Essen, L.-O. (2012). CryB from *Rhodobacter sphaeroides*: a unique class of cryptochromes with new cofactors. *EMBO Rep.* 13, 223–229. doi: 10.1038/embor.2012.2

Gomelsky, M., Horne, I. M., Lee, H.-J., Pemberton, J. M., McEwan, A. G., and Kaplan, S. (2000). Domain structure, oligomeric state, and mutational analysis of PpsR, the *Rhodobacter sphaeroides* repressor of photosystem gene expression. *J. Bacteriol.* 182, 2253–2261. doi: 10.1128/JB.182.8.2253-2261.2000

Gomelsky, M., and Klug, G. (2002). BLUF: a novel FAD-binding domain involved in sensory transduction in microorganisms. *Trends Biochem. Sci.* 27, 497–500. doi: 10.1016/S0968-0004(02)02181-3

Grinstead, J. S., Hsu, S.-T. D., Laan, W., Bonvin, A. M. J. J., Hellingwerf, K. J., Boelens, R., et al. (2006). The solution structure of the AppA BLUF domain: insight into the mechanism of light-induced signaling. *ChemBioChem* 7, 187–193. doi: 10.1002/cbic.200500270

Guo, H., Yang, H., Mockler, T. C., and Lin, C. (1998). Regulation of flowering time by *Arabidopsis* photoreceptors. *Science* 279, 1360–1363. doi: 10.1126/science.279.5355.1360

Hänsel, R., Luh, L. M., Corbeski, I., Trantirek, L., and Dötsch, V. (2014). In-cell NMR and EPR spectroscopy of biomacromolecules. *Angew. Chem. Int. Ed.* 53, 10300–10314. doi: 10.1002/anie.201311320

Harper, S. M., Christie, J. M., and Gardner, K. H. (2004a). Disruption of the LOV–Jα helix interaction activates phototropin kinase activity. *Biochemistry* 43, 16184–16192. doi: 10.1021/bi048092i

Harper, S. M., Neil, L. C., Day, I. J., Hore, P. J., and Gardner, K. H. (2004b). Conformational changes in a photosensory LOV domain monitored by time-resolved NMR spectroscopy. *J. Am. Chem. Soc.* 126, 3390–3391. doi: 10.1021/ja038224f

Heelis, P. F., Okamura, T., and Sancar, A. (1990). Excited-state properties of *Escherichia coli* DNA photolyase in the picosecond to millisecond time scale. *Biochemistry* 29, 5694–5698. doi: 10.1021/bi00476a008

Herman, E., Sachse, M., Kroth, P. G., and Kottke, T. (2013). Blue-light-induced unfolding of the Jα helix allows for the dimerization of Aureochrome-LOV from the diatom *Phaeodactylum tricornutum*. *Biochemistry* 52, 3094–3101. doi: 10.1021/bi400197u

Hirota, N., and Yamauchi, S. (2003). Short-lived excited triplet states studied by time-resolved EPR spectroscopy. *J. Photochem. Photobiol. C Photochem. Rev.* 4, 109–124. doi: 10.1016/S1389-5567(03)00024-8

Hoang, N., Schleicher, E., Kacprzak, S., Bouly, J.-P., Picot, M., Wu, W., et al. (2008). Human and Drosophila cryptochromes are light activated by flavin photoreduction in living cells. *PLoS Biol.* 6:e160. doi: 10.1371/journal.pbio.0060160

Hore, P. J. (1989). "Analysis of polarized EPR spectra," in *Advanced EPR in Biology and Biochemistry*, ed A. J. Hoff (Amsterdam: Elsevier), 405–440.

Hore, P. J. (2012). Are biochemical reactions affected by weak magnetic fields? *Proc. Natl. Acad. Sci. U.S.A.* 109, 1357–1358. doi: 10.1073/pnas.1120531109

Hubbell, W. L., and Altenbach, C. (1994). Investigation of structure and dynamics in membrane proteins using site-directed spin labeling. *Curr. Opin. Struct. Biol.* 4, 566–573. doi: 10.1016/S0959-440X(94)90219-4

Hubbell, W. L., Cafiso, D. S., and Altenbach, C. (2000). Identifying conformational changes with site-directed spin labeling. *Nat. Struct. Biol.* 7, 735–739. doi: 10.1038/78956

Hubbell, W. L., López, C. J., Altenbach, C., and Yang, Z. (2013). Technological advances in site-directed spin labeling of proteins. *Curr. Opin. Struct. Biol.* 23, 725–733. doi: 10.1016/j.sbi.2013.06.008

Hulsebosch, R. J., van den Brink, J. S., Nieuwenhuis, S. A. M., Gast, P., Raap, J., Lugtenburg, J., et al. (1997). Electronic structure of the neutral tyrosine radical in frozen solution. Selective 2H- 13C- und 17O-isotope labeling and EPR spectroscopy at 9 and 35 GHz. *J. Am. Chem. Soc.* 119, 8685–8694. doi: 10.1021/ja9707872

Jeschke, G. (2002). Distance measurements in the nanometer range by pulse EPR. *ChemPhysChem* 3, 927–932. doi: 10.1002/1439-7641(20021115)3:11<927::AID-CPHC927>3.0.CO;2-Q

Jeschke, G. (2005). EPR techniques for studying radical enzymes. *Biochim. Biophys. Acta* 1707, 91–102. doi: 10.1016/j.bbabio.2004.02.012

Jeschke, G. (2012). DEER distance measurements on proteins. *Annu. Rev. Phys. Chem.* 63, 419–446. doi: 10.1146/annurev-physchem-032511-143716

Jones, M. A., Feeney, K. A., Kelly, S. M., and Christie, J. M. (2007). Mutational analysis of phototropin 1 provides insights into the mechanism underlying LOV2 signal transmission. *J. Biol. Chem.* 282, 6405–6414. doi: 10.1074/jbc.M605969200

Jung, A., Reinstein, J., Domratcheva, T., Shoeman, R. L., and Schlichting, I. (2006). Crystal structures of the AppA BLUF domain photoreceptor provide insights into blue light-mediated signal transduction. *J. Mol. Biol.* 362, 717–732. doi: 10.1016/j.jmb.2006.07.024

Kasahara, M., Swartz, T. E., Olney, M. A., Onodera, A., Mochizuki, N., Fukuzawa, H., et al. (2002). Photochemical properties of the flavin mononucleotide-binding domains of the phototropins from Arabidopsis, rice, and *Chlamydomonas reinhardtii*. *Plant Physiol.* 129, 762–773. doi: 10.1104/pp.002410

Kavakli, I. H., and Sancar, A. (2004). Analysis of the role of intraprotein electron transfer in photoreactivation by DNA photolyase *in vivo*. *Biochemistry* 43, 15103–15110. doi: 10.1021/bi0478796

Kennedy, M. J., Hughes, R. M., Peteya, L. A., Schwartz, J. W., Ehlers, M. D., and Tucker, C. L. (2010). Rapid blue-light-mediated induction of protein interactions in living cells. *Nat. Methods* 7, 973–975. doi: 10.1038/nmeth.1524

Kennis, J. T. M., Crosson, S., Gauden, M., van Stokkum, I. H. M., Moffat, K., and van Grondelle, R. (2003). Primary reactions of the LOV2 domain of

phototropin, a plant blue-light photoreceptor. *Biochemistry* 42, 3385–3392. doi: 10.1021/bi034022k

Kim, W.-Y., Fujiwara, S., Suh, S.-S., Kim, J., Kim, Y., Han, L., et al. (2007). ZEITLUPE is a circadian photoreceptor stabilized by GIGANTEA in blue light. *Nature* 449, 356–360. doi: 10.1038/nature06132

Kita, A., Okajima, K., Morimoto, Y., Ikeuchi, M., and Miki, K. (2005). Structure of a cyanobacterial BLUF protein, Tll0078, containing a novel FAD-binding blue light sensor domain. *J. Mol. Biol.* 349, 1–9. doi: 10.1016/j.jmb.2005.03.067

Klar, T., Kaiser, G., Hennecke, U., Carell, T., Batschauer, A., and Essen, L.-O. (2006). Natural and non-natural antenna chromophores in the DNA photolyase from *Thermus thermophilus*. *ChemBioChem* 7, 1798–1806. doi: 10.1002/cbic.200600206

Klare, J. P. (2013). Site-directed spin labeling EPR spectroscopy in protein research. *Biol. Chem.* 394, 1281–1300. doi: 10.1515/hsz-2013-0155

Klare, J. P., and Steinhoff, H.-J. (2009). Spin labeling EPR. *Photosynth. Res.* 102, 377–390. doi: 10.1007/s11120-009-9490-7

Kondo, T., Masuda, S., Tsutsui, K., and Mino, H. (2011). Temperature dependence of relaxation time of a stable radical pair in SyPixD investigated by pulsed EPR. *Chem. Phys. Lett.* 501, 528–533. doi: 10.1016/j.cplett.2010.11.073

Kothe, G., Weber, S., Bittl, R., Ohmes, E., Thurnauer, M. C., and Norris, J. R. (1991). Transient EPR of light-induced radical pairs in plant photosystem I: observation of quantum beats. *Chem. Phys. Lett.* 186, 474–480. doi: 10.1016/0009-2614(91)90454-h

Kowalczyk, R. M., Schleicher, E., Bittl, R., and Weber, S. (2004). The photo-induced triplet of flavins and its protonation states. *J. Am. Chem. Soc.* 126, 11393–11399. doi: 10.1021/ja049554i

Kraft, B. J., Masuda, S., Kikuchi, J., Dragnea, V., Tollin, G., Zaleski, J. M., et al. (2003). Spectroscopic and mutational analysis of the blue-light photoreceptor AppA: a novel photocycle involving flavin stacking with an aromatic amino acid. *Biochemistry* 42, 6726–6734. doi: 10.1021/bi030055o

Krapf, S., Weber, S., and Koslowski, T. (2012). The road not taken: a theoretical view of an unexpected cryptochrome charge transfer path. *Phys. Chem. Chem. Phys.* 14, 11518–11524. doi: 10.1039/c2cp40793k

Krauss, U., Minh, B. Q., Losi, A., Gärtner, W., Eggert, T., von Haeseler, A., et al. (2009). Distribution and phylogeny of light-oxygen-voltage-blue-light-signaling proteins in the three kingdoms of life. *J. Bacteriol.* 191, 7234–7242. doi: 10.1128/JB.00923-09

Laan, W., Gauden, M., Yeremenko, S., van Grondelle, R., Kennis, J. T. M., and Hellingwerf, K. J. (2006). On the mechanism of activation of the BLUF domain of AppA. *Biochemistry* 45, 51–60. doi: 10.1021/bi051367p

Laan, W., van der Horst, M. A., van Stokkum, I. H., and Hellingwerf, K. J. (2003). Initial characterization of the primary photochemistry of AppA, a blue-light–using flavin adenine dinucleotide–domain containing transcriptional antirepressor protein from *Rhodobacter sphaeroides*: a key role for reversible intramolecular proton transfer from the flavin adenine dinucleotide chromophore to a conserved tyrosine? *Photochem. Photobiol.* 78, 290–297. doi: 10.1562/0031-8655(2003)078<0290:icotpp>2.0.co;2

Li, Y. F., Heelis, P. F., and Sancar, A. (1991). Active site of DNA photolyase: tryptophan-306 is the intrinsic hydrogen atom donor essential for flavin radical photoreduction and DNA repair *in vitro*. *Biochemistry* 30, 6322–6329. doi: 10.1021/bi00239a034

Lin, C., and Todo, T. (2005). The cryptochromes. *Genome Biol.* 6, 220. doi: 10.1186/gb-2005-6-5-220

Losi, A., and Gärtner, W. (2012). The evolution of flavin-binding photoreceptors: an ancient chromophore serving trendy blue-light sensors. *Annu. Rev. Plant Biol.* 63, 49–72. doi: 10.1146/annurev-arplant-042811-105538

Marsh, D. (2010). Spin-label EPR for determining polarity and proticity in biomolecular assemblies: transmembrane profiles. *Appl. Magn. Reson.* 37, 435–454. doi: 10.1007/s00723-009-0078-3

Masuda, S., and Bauer, C. E. (2002). AppA Is a blue light photoreceptor that antirepresses photosynthesis gene expression in *Rhodobacter sphaeroides*. *Cell* 110, 613–623. doi: 10.1016/S0092-8674(02)00876-0

Masuda, S., Hasegawa, K., Ishii, A., and Ono, T.-A. (2004). Light-induced structural changes in a putative blue-light receptor with a novel FAD binding fold sensor of blue-light using FAD (BLUF); Slr1694 of *Synechocystis* sp. PCC6803. *Biochemistry* 43, 5304–5313. doi: 10.1021/bi049836v

Mathes, T., Zhu, J., van Stokkum, I. H. M., Groot, M.-L., Hegemann, P., and Kennis, J. T. M. (2012). Hydrogen bond switching among flavin and amino acids determines the nature of proton-coupled electron transfer in BLUF photoreceptors. *J. Phys. Chem. Lett.* 3, 203–208. doi: 10.1021/jz201579y

Mchaourab, H. S., Steed, P. R., and Kazmier, K. (2011). Toward the fourth dimension of membrane protein structure: insight into dynamics from spin-labeling EPR spectroscopy. *Structure* 19, 1549–1561. doi: 10.1016/j.str.2011.10.009

Mino, H., Astashkin, A. V., and Kawamori, A. (1997). An EPR and pulsed ENDOR study of the structure of tyrosine $Z^{\bullet}$ in Tris-treated photosystem II. *Spectrochim. Acta A Mol. Biomol. Spectrosc.* 53, 1465–1483. doi: 10.1016/S1386-1425(97)00069-3

Möglich, A., Ayers, R. A., and Moffat, K. (2009). Structure and signaling mechanism of Per-ARNT-Sim domains. *Structure* 17, 1282–1294. doi: 10.1016/j.str.2009.08.011

Möglich, A., and Moffat, K. (2007). Structural basis for light-dependent signaling in the dimeric LOV domain of the photosensor YtvA. *J. Mol. Biol.* 373, 112–126. doi: 10.1016/j.jmb.2007.07.039

Möglich, A., and Moffat, K. (2010). Engineered photoreceptors as novel optogenetic tools. *Photochem. Photobiol. Sci.* 9, 1286–1300. doi: 10.1039/c0pp00167h

Möglich, A., Yang, X., Ayers, R. A., and Moffat, K. (2010). Structure and function of plant photoreceptors. *Annu. Rev. Plant Biol.* 61, 21–47. doi: 10.1146/annurev-arplant-042809-112259

Müller, M., and Carell, T. (2009). Structural biology of DNA photolyases and cryptochromes. *Curr. Opin. Struct. Biol.* 19, 277–285. doi: 10.1016/j.sbi.2009.05.003

Murphy, D. M., and Farley, R. D. (2006). Principles and applications of ENDOR spectroscopy for structure determination in solution and disordered matrices. *Chem. Soc. Rev.* 35, 249–268. doi: 10.1039/b500509b

Nagai, H., Fukushima, Y., Okajima, K., Ikeuchi, M., and Mino, H. (2008). Formation of interacting spins on flavosemiquinone and tyrosine radical in photoreaction of a blue light sensor BLUF protein TePixD. *Biochemistry* 47, 12574–12582. doi: 10.1021/bi8010187

Nakasako, M., Zikihara, K., Matsuoka, D., Katsura, H., and Tokutomi, S. (2008). Structural basis of the LOV1 dimerization of *Arabidopsis* phototropins 1 and 2. *J. Mol. Biol.* 381, 718–733. doi: 10.1016/j.jmb.2008.06.033

Payne, G., Heelis, P. F., Rohrs, B. R., and Sancar, A. (1987). The active form of *Escherichia coli* DNA photolyase contains a fully reduced flavin and not a flavin radical, both *in vivo* and *in vitro*. *Biochemistry* 26, 7121–7127. doi: 10.1021/bi00396a038

Polyhach, Y., Bordignon, E., and Jeschke, G. (2011). Rotamer libraries of spin labelled cysteines for protein studies. *Phys. Chem. Chem. Phys.* 13, 2356–2366. doi: 10.1039/C0CP01865A

Prisner, T., Rohrer, M., and MacMillan, F. (2001). Pulsed EPR spectroscopy: biological applications. *Annu. Rev. Phys. Chem.* 52, 279–313. doi: 10.1146/annurev.physchem.52.1.279

Raffelberg, S., Gutt, A., Gärtner, W., Mandalari, C., Abbruzzetti, S., Viappiani, C., et al. (2013). The amino acids surrounding the flavin 7a-methyl group determine the UVA spectral features of a LOV protein. *Biol. Chem.* 394, 1517–1528. doi: 10.1515/hsz-2013-0163

Raffelberg, S., Mansurova, M., Gärtner, W., and Losi, A. (2011). Modulation of the photocycle of a LOV domain photoreceptor by the hydrogen-bonding network. *J. Am. Chem. Soc.* 133, 5346–5356. doi: 10.1021/ja1097379

Reginsson, G. W., and Schiemann, O. (2011). Pulsed electron–electron double resonance: beyond nanometre distance measurements on biomacromolecules. *Biochem. J.* 434, 353–363. doi: 10.1042/bj20101871

Salomon, M., Christie, J. M., Knieb, E., Lempert, U., and Briggs, W. R. (2000). Photochemical and mutational analysis of the FMN-binding domain of the plant blue light receptor, phototropin. *Biochemistry* 39, 9401–9410. doi: 10.1021/bi000585+

Salomon, M., Eisenreich, W., Dürr, H., Schleicher, E., Knieb, E., Massey, V., et al. (2001). An optomechanical transducer in the blue light receptor phototropin from *Avena sativa*. *Proc. Natl. Acad. Sci. U.S.A.* 98, 12357–12361. doi: 10.1073/pnas.221455298

Sancar, A. (2004). Photolyase and cryptochrome blue-light photoreceptors. *Adv. Protein Chem.* 69, 73–100. doi: 10.1016/S0065-3233(04)69003-6

Schiemann, O., and Prisner, T. F. (2007). Long-range distance determinations in biomacromolecules by EPR spectroscopy. *Q. Rev. Biophys.* 40, 1–53. doi: 10.1017/S003358350700460X

Schleicher, E., Bittl, R., and Weber, S. (2009). New roles of flavoproteins in molecular cell biology: blue-light active flavoproteins studied by electron paramagnetic resonance. *FEBS J.* 276, 4290–4303. doi: 10.1111/j.1742-4658.2009.07141.x

Schleicher, E., Kowalczyk, R. M., Kay, C. W. M., Hegemann, P., Bacher, A., Fischer, M., et al. (2004). On the reaction mechanism of adduct formation in LOV domains of the plant blue-light receptor phototropin. *J. Am. Chem. Soc.* 126, 11067–11076. doi: 10.1021/ja049553q

Schleicher, E., and Weber, S. (2012). Radicals in flavoproteins. *Top. Curr. Chem.* 321, 41–66. doi: 10.1007/128_2011_301

Schleicher, E., Wenzel, R., Okafuji, A., Ahmad, M., Batschauer, A., Essen, L.-O., et al. (2010). The electronic structure of flavoproteins: investigations with proton electron–nuclear double resonance. *Appl. Magn. Reson.* 37, 339–352. doi: 10.1007/s00723-009-0101-8

Schnegg, A., Kay, C. W. M., Schleicher, E., Hitomi, K., Todo, T., Möbius, K., et al. (2006). The g-tensor of the flavin cofactor in (6–4) photolyase: a 360 GHz/12.8 T electron paramagnetic resonance study. *Mol. Phys.* 104, 1627–1633. doi: 10.1080/00268970600593108

Schreiner, S., Steiner, U., and Kramer, H. E. A. (1975). Determination of the p*K* values of the lumiflavin triplet state by flash photolysis. *Photochem. Photobiol.* 21, 81–84. doi: 10.1111/j.1751-1097.1975.tb06632.x

Schweiger, A., and Jeschke, G. (2001). *Principles of Pulse Electron Paramagnetic Resonance.* Oxford: Oxford University Press.

Selby, C. P., and Sancar, A. (2012). The second chromophore in *Drosophila* photolyase/cryptochrome family photoreceptors. *Biochemistry* 51, 167–171. doi: 10.1021/bi201536w

Stehlik, D., and Möbius, K. (1997). New EPR methods for investigating photoprocesses with paramagnetic intermediates. *Annu. Rev. Phys. Chem.* 48, 745–784. doi: 10.1146/annurev.physchem.48.1.745

Steinhoff, H.-J. (2004). Inter- and intra-molecular distances determined by EPR spectroscopy and site-directed spin labeling reveal protein-protein and protein-oligonucleotide interaction. *Biol. Chem.* 385, 913–920. doi: 10.1515/BC.2004.119

Swartz, T. E., Corchnoy, S. B., Christie, J. M., Lewis, J. W., Szundi, I., Briggs, W. R., et al. (2001). The photocycle of a flavin-binding domain of the blue light photoreceptor phototropin. *J. Biol. Chem.* 276, 36493–36500. doi: 10.1074/jbc.M103114200

Turro, N. J., Kleinman, M. H., and Karatekin, E. (2000). Electron spin polarization and time-resolved paramagnetic resonance: applications to the paradigms of molecular and supramolecular photochemistry. *Angew. Chem. Int. Ed.* 39, 4436–4461. doi: 10.1002/1521-3773(20001215)39:24<4436::AID-ANIE4436>3.0.CO;2-X

van der Est, A. (2009). Transient EPR: using spin polarization in sequential radical pairs to study electron transfer in photosynthesis. *Photosynth. Res.* 102, 335–347. doi: 10.1007/s11120-009-9411-9

van der Horst, G. T. J., Muijtjens, M., Kobayashi, K., Takano, R., Kanno, S.-I., Takao, M., et al. (1999). Mammalian Cry1 and Cry2 are essential for maintenance of circadian rhythms. *Nature* 398, 627–630. doi: 10.1038/19323

Van Eps, N., Caro, L. N., Morizumi, T., and Ernst, O. P. (2015). Characterizing rhodopsin signaling by EPR spectroscopy: from structure to dynamics. *Photochem. Photobiol. Sci.* doi: 10.1039/C5PP00191A. [Epub ahead of print].

Weber, S. (2005). Light-driven enzymatic catalysis of DNA repair: a review of recent biophysical studies on photolyase. *Biochim. Biophys. Acta* 1707, 1–23. doi: 10.1016/j.bbabio.2004.02.010

Weber, S., Biskup, T., Okafuji, A., Marino, A. R., Berthold, T., Link, G., et al. (2010). Origin of light-induced spin-correlated radical pairs in cryptochrome. *J. Phys. Chem. B* 114, 14745–14754. doi: 10.1021/jp103401u

Weber, S., Kay, C. W. M., Mögling, H., Möbius, K., Hitomi, K., and Todo, T. (2002). Photoactivation of the flavin cofactor in *Xenopus laevis* (6–4) photolyase: observation of a transient tyrosyl radical by time-resolved electron paramagnetic resonance. *Proc. Natl. Acad. Sci. U.S.A.* 99, 1319–1322. doi: 10.1073/pnas.032469399

Weber, S., Schroeder, C., Kacprzak, S., Mathes, T., Kowalczyk, R. M., Essen, L.-O., et al. (2011). Light-generated paramagnetic intermediates in BLUF domains. *Photochem. Photobiol.* 87, 574–583. doi: 10.1111/j.1751-1097.2010.00885.x

Weil, J. A., Bolton, J. R., and Wertz, J. E. (1994). *Electron Paramagnetic Resonance. Elementary Theory and Practical Applications*. New York, NY: John Wiley & Sons, Inc.

Woodward, J. R. (2002). Radical pairs in solution. *Prog. React. Kinet. Mec.* 27, 165–207. doi: 10.3184/007967402103165388

Wu, Q., and Gardner, K. H. (2009). Structure and insight into blue light-induced changes in the BlrP1 BLUF domain. *Biochemistry* 48, 2620–2629. doi: 10.1021/bi802237r

Wu, Y. I., Frey, D., Lungu, O. I., Jaehrig, A., Schlichting, I., Kuhlman, B., et al. (2009). A genetically encoded photoactivatable Rac controls the motility of living cells. *Nature* 461, 104–108. doi: 10.1038/nature08241

Yuan, H., Anderson, S., Masuda, S., Dragnea, V., Moffat, K., and Bauer, C. (2006). Crystal structures of the *Synechocystis* photoreceptor Slr1694 reveal distinct structural states related to signaling. *Biochemistry* 45, 12687–12694. doi: 10.1021/bi061435n

Zayner, J. P., Antoniou, C., and Sosnick, T. R. (2012). The amino-terminal helix modulates light-activated conformational changes in *As*LOV2. *J. Mol. Biol.* 419, 61–74. doi: 10.1016/j.jmb.2012.02.037

Zhang, F., Scheerer, P., Oberpichler, I., Lamparter, T., and Krauß, N. (2013). Crystal structure of a prokaryotic (6-4) photolyase with an Fe-S cluster and a 6,7-dimethyl-8-ribityllumazine antenna chromophore. *Proc. Natl. Acad. Sci. U.S.A.* 110, 7217–7222. doi: 10.1073/pnas.1302377110

Zhang, F., Vierock, J., Yizhar, O., Fenno, L. E., Tsunoda, S., Kianianmomeni, A., et al. (2011). The microbial opsin family of optogenetic tools. *Cell* 147, 1446–1457. doi: 10.1016/j.cell.2011.12.004

Zirak, P., Penzkofer, A., Schiereis, T., Hegemann, P., Jung, A., and Schlichting, I. (2005). Absorption and fluorescence spectroscopic characterization of BLUF domain of AppA from *Rhodobacter sphaeroides*. *Chem. Phys.* 315, 142–154. doi: 10.1016/j.chemphys.2005.04.008

Zoltowski, B. D., and Gardner, K. H. (2011). Tripping the light fantastic: blue-light photoreceptors as examples of environmentally modulated protein–protein interactions. *Biochemistry* 50, 4–16. doi: 10.1021/bi101665s

Zoltowski, B. D., Vaccaro, B., and Crane, B. R. (2009). Mechanism-based tuning of a LOV domain photoreceptor. *Nat. Chem. Biol.* 5, 827–834. doi: 10.1038/nchembio.210

Conflict of Interest Statement: The authors declare that the research was conducted in the absence of any commercial or financial relationships that could be construed as a potential conflict of interest.

frontiers in Molecular Biosciences

REVIEW
published: 23 June 2015
doi: 10.3389/fmolb.2015.00033

Applications of hydrogen deuterium exchange (HDX) for the characterization of conformational dynamics in light-activated photoreceptors

Robert Lindner[1†], *Udo Heintz*[1†] *and Andreas Winkler*[2*]

[1] *Department of Biomolecular Mechanisms, Max Planck Institute for Medical Research, Heidelberg, Germany,* [2] *Institute of Biochemistry, Graz University of Technology, Graz, Austria*

OPEN ACCESS

Edited by:
Tilo Mathes,
Vrije Universiteit Amsterdam, Netherlands

Reviewed by:
Kevin H. Gardner,
The City University of New York Advanced Science Research Center, USA
Tobin Roy Sosnick,
University of Chicago, USA

***Correspondence:**
Andreas Winkler,
Institute of Biochemistry, Graz University of Technology, Petersgasse 12/II, Graz 8010, Austria
andreas.winkler@tugraz.at

[†] *These authors have contributed equally to this work.*

Specialty section:
This article was submitted to Biophysics, a section of the journal Frontiers in Molecular Biosciences

Received: *31 March 2015*
Accepted: *26 May 2015*
Published: *23 June 2015*

Citation:
Lindner R, Heintz U and Winkler A (2015) Applications of hydrogen deuterium exchange (HDX) for the characterization of conformational dynamics in light-activated photoreceptors. Front. Mol. Biosci. 2:33. doi: 10.3389/fmolb.2015.00033

Rational design of optogenetic tools is inherently linked to the understanding of photoreceptor function. Structural analysis of elements involved in signal integration in individual sensor domains provides an initial idea of their mode of operation, but understanding how local structural rearrangements eventually affect signal transmission to output domains requires inclusion of the effector regions in the characterization. However, the dynamic nature of these assemblies renders their structural analysis challenging and therefore a combination of high- and low-resolution techniques is required to appreciate functional aspects of photoreceptors. This review focuses on the potential of hydrogen-deuterium exchange coupled to mass spectrometry (HDX-MS) for complementing the structural characterization of photoreceptors. In this respect, the ability of HDX-MS to provide information on conformational dynamics and the possibility to address multiple functionally relevant states in solution render this methodology ideally suitable. We highlight recent examples demonstrating the potential of HDX-MS and discuss how these results can help to improve existing optogenetic systems or guide the design of novel optogenetic tools.

Keywords: BLUF, LOV, PYP, mass spectrometry, light sensor, effector, optogenetics

Introduction

One prerequisite for rational modulation of biological assemblies or machines is their detailed structural characterization together with an appreciation of their inherent conformational dynamics. Major contributions toward improving our understanding of molecular and cellular function have been provided by X-ray crystallography, nuclear magnetic resonance (NMR) and electron microscopy (EM). However, in isolation these methods might not suffice to understand complex multi-protein assemblies or highly dynamic signaling complexes. To overcome this limitation a plethora of lower resolution techniques can be combined with high-resolution methods to create testable models of complex biomolecular assemblies. Such approaches, summarized under the term "integrative structural biology" [1, 2], are becoming the rule rather than the exception in the functional characterization of complex systems.

In the context of optogenetic tools that allow precise spatial and temporal control of cellular processes in living cells, one generally attempts to exploit intrinsic properties of naturally occurring photoreceptors. On the one hand, the light-dependent affinity of photoreceptor proteins to different interaction partners can be employed to control localization or dimerization of various effector proteins [3–10]. On the other hand, allosteric regulation of enzymatic functions or conformational substates by photoreceptor domains provides an interesting alternative due to the potentially more direct manipulation of cellular targets [11–19]. Some optogenetic tools make use of naturally occurring designs, but substantial effort has been made to expand the optogenetic toolbox with artificial light-responsive systems [20]. Although properties of individual photoreceptors have been studied extensively, a comprehensive description of how complex light-regulated proteins work on a molecular level is frequently missing.

Structural insight into molecular mechanisms of signal transduction in light-activated enzymes can provide important molecular details for guiding the rational design of novel light-regulated systems or improving existing optogenetic tools. Due to the inherent dynamic nature of photoreceptors, their structural characterization is frequently not straight-forward, especially in the presence of corresponding interaction partners or effector domains. Since many of the functionally relevant assemblies are beyond the current size limitations of standard NMR methodologies, additional in-solution methods are required to increase our understanding of structural dynamics in photoreceptor-effector interactions. Solution scattering studies, such as small- and wide-angle X-ray scattering, of dark- and light-activated states can provide important low-resolution information that is useful to estimate the extent of structural changes accompanying light activation. In addition, many other methods can be combined with high-resolution structural characterization of photoreceptors to improve our understanding of the underlying molecular mechanisms such as for example mutagenesis [21], limited proteolysis [22], chemical crosslinking [23], EM [24], analytical spectroscopy [25, 26], light scattering [27], atomic force microscopy [28] and others.

In this review we focus on an additional powerful method for addressing molecular details of light activation: hydrogen-deuterium exchange coupled to mass spectrometry (HDX-MS). Recent developments in mass spectrometry instrumentation and automated data processing have enabled the widespread application of HDX-MS to all areas of biomedical research [29]. Here we summarize recent examples of HDX-MS for extending the structural characterization of naturally occurring photoreceptors and synthetic optogenetic tools. We also highlight how the design of optogenetic tools can benefit from such integrative structural biology approaches.

The Potential of HDX-MS

Already during the early days of HDX in the 1960s, the capabilities of quantifying protein hydrogen exchange for improving our understanding of protein structure were appreciated [30]. According to the Linderstrøm-Lang model, amide hydrogen exchange requires opening-closing fluctuations of the protein that enable protected amide hydrogens to transition to an exchange-competent state for reacting with the solvent (Scheme 1 with k_{op} and k_{cl} corresponding to the rate constants of the opening and closing transitions, respectively. k_{ch} refers to the rate constant of the chemical exchange reaction of an amide hydrogen in the presence D_2O).

$$NH_{closed} \underset{k_{cl}}{\overset{k_{op}}{\rightleftharpoons}} NH_{open} \underset{(D_2O)}{\overset{k_{ch}}{\rightarrow}} ND_{open} \underset{k_{op}}{\overset{k_{cl}}{\rightleftharpoons}} ND_{closed}$$

The major factor limiting hydrogen exchange is the involvement of amides in hydrogen bonding, however, additional contributions such as solvent accessibility and electrostatic effects can also influence the observed exchange rates. Since amide hydrogens play a key role in the formation of secondary and tertiary structure elements, measurements of their exchange rates can be interpreted in terms of the conformational dynamics of individual higher-order structural elements as well as overall protein dynamics and stability. Challenges associated with measuring heavy hydrogen isotope incorporation, analyzing the data generated during typical HDX experiments and interpreting the obtained information in terms of protein structure and dynamics have initially hampered the wide application of HDX [31, 32]. The development of multi-dimensional NMR methods eventually allowed measurements of site specific amide proton exchange rates. This enabled the extraction of thermodynamic parameters that reflect the equilibrium between open and closed conformations in the native state as well as the kinetic characterization of protein folding pathways [33]. Real-time, native state NMR measurements have been applied to study secondary and tertiary structure stability and to identify amides involved in strong hydrogen bonds. Due to the limited time-resolution, conventional NMR readout of hydrogen exchange generally only provides information on highly protected amides that are typically observed in regions with stable secondary structure rather than dynamic signaling elements. However, changes in physical parameters that influence deuterium exchange (for example pH and temperature) can be used to slow down the exchange reaction and provide information on otherwise inaccessible amides. Also, improvements in NMR acquisition strategies and the use of rapid mixing devices for pulsed-quench HDX enable the measurement of hydrogen exchange in the ms to s regime [34]. Still, the requirement of high protein concentrations and incomplete assignments of amide hydrogens even for small proteins also limit the potential of HDX-NMR. Recent advances in mass spectrometric analysis of deuterium incorporation have enabled the characterization of larger proteins and complex supramolecular assemblies while at the same time monitoring exchange times on the order of seconds and less, which enables sampling of highly dynamic amides. Together with the development of automated data analysis tools, the requirement of relatively low protein quantities and the possibility to work at near physiological concentrations, these improvements have resulted in a renaissance of the HDX-MS methodology over the last two decades. Currently, applications of the method span diverse areas ranging from analysis of

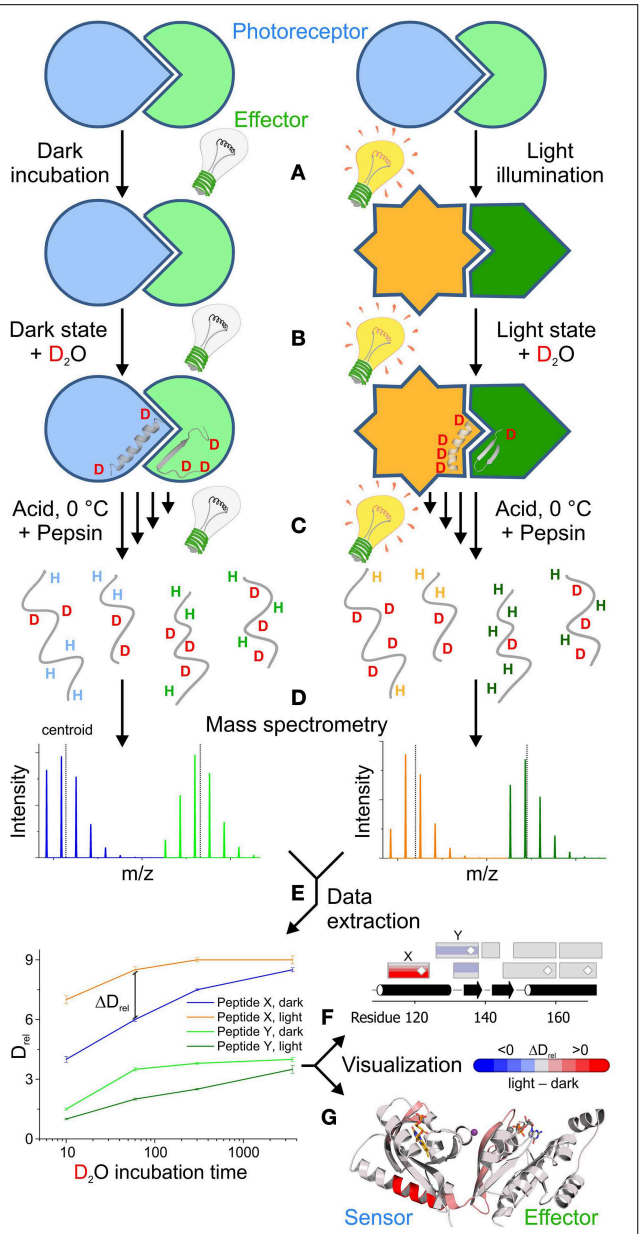

FIGURE 1 | Outline of a comparative HDX-MS experiment for the characterization of light activation in a photoreceptor-effector system. **(A)** Typically, the experiment starts with a pre-equilibration step, to obtain a well-defined population of the dark- as well as the light-state. **(B)** Dilution of the samples with deuterated buffer initiates the substitution of exchangeable hydrogens with deuterons. The exchange rate of specific amide hydrogens reflects the conformational dynamics of their corresponding secondary structure elements in the dark- and light-state conformation. **(C)** In order to address the rate of amide hydrogen exchange, the labeling reaction is stopped at different time points by quenching with buffer at pH 2.5 and lowering the temperature to 0°C. In order to quantify deuterium uptake at a higher spatial resolution than on the global protein level, the samples are generally treated with acid-tolerant proteases, for example pepsin, to obtain individual peptides that are subsequently separated in a liquid chromatography step and then directly infused into a mass spectrometer. **(D)** The characteristic increase in peptide mass due to the substitution of hydrogen with deuterium can be readily quantified using a mass spectrometer. Due to random back-exchange *(Continued)*

FIGURE 1 | Continued
of deuterons during the proteolysis and chromatography steps in aqueous media, unusually broad isotope distributions are observed for individual peptides. **(E)** Both the center of mass (centroid) and the characteristic isotope distribution are then extracted either manually or using automated software packages to identify regions with characteristic differences in deuterium uptake between the dark- and light-state. The increase of the mass centroid relative to an undeuterated reference measurement (denoted as D_{rel}) for all deuteration time points provides characteristic deuterium uptake curves that enable the identification of peptides with significant differences in D_{rel} between two functional states at various time points. In combination with the assignment to a specific peptide sequence these differences in relative deuteration levels (ΔD_{rel}) can be used for different visualization approaches that also provide information on overlapping peptides and corresponding secondary structure elements **(F)** or the three dimensional arrangement of the individual peptides **(G)**. In this scenario, blue colors correspond to less deuterium being incorporated in the light state due to a reduction of the conformational dynamics. In contrast, red colors reflect increased deuterium incorporation at a given time point corresponding to an increase in structural dynamics upon illumination. Results shown in **(E,F)** are not linked to **(G)**, which shows the photoreceptor architecture and HDX-MS results of PA-Rac1 [83] that are described in more detail in **Figure 5**.

protein interactions, characterization of individual protein conformations, protein folding studies, analysis of membrane proteins to research related to drug design [29, 35].

One reason for the broad application of HDX-MS is its ability to provide information on the global stability as well as on local conformational dynamics of proteins. Since proteins are dynamic entities that exhibit local and global conformational fluctuations, even the most stable secondary structure elements transiently break and re-form hydrogen bonds. According to the opening-closing model mentioned previously, deuterium exchange can only occur while loss of structural elements exposes hydrogens to the solvent. Depending on the rate constants of the opening (k_{op}) and closing (k_{cl}) reaction as well as the rate constant of chemical exchange (k_{ch}) under the specific conditions of the experiment, characteristic time dependent changes in the isotope distribution of individual peptides can be observed. An in depth discussion of the underlying mechanisms is beyond the scope of this article, however, details can be found elsewhere [31, 33, 36, 37]. Briefly, under conditions where k_{cl} is significantly faster than k_{ch}, there is only a low probability that a single opening event will lead to hydrogen exchange. This regime, termed EX2, is most frequently observed under native conditions and is characterized by a time-dependent, gradual increase of the isotopic distributions of individual peptides measured in a typical HDX-MS experiment (*cf.* **Figure 1**). The observed rate constant of hydrogen exchange (k_{ex}) under EX2 conditions reflects the thermodynamic equilibrium constant of closed and open states ($K_{op} = k_{op}/k_{cl}$) according to the expression $k_{ex} \approx K_{op} \cdot k_{ch}$. The other extreme, where $k_{ch} \gg k_{cl}$, is termed EX1 and corresponds to the situation where every opening event is accompanied by chemical exchange. The observed rate constant k_{ex} under EX1 conditions therefore directly corresponds to the structural opening rate constant k_{op} ($k_{ex} \approx k_{op}$) providing direct access to kinetic data. Provided that several amide positions within a peptide follow the EX1 exchange, characteristic bimodal

isotope distributions are observed, which are also referred to as correlated exchange patterns. Even though no clear distinction between sub-global unfolding or local fluctuations can be made based on the measured deuterium exchange rates of peptides, the ability to measure the time-dependent increase in deuterium incorporation and the characteristic peak shape of the isotopic distributions provides insight into the conformational dynamics of the studied system. Since dynamic properties of a system are tightly linked to protein function [38], it is obvious that a combination of HDX with crystallographic snapshots can substantially improve the understanding of system specific functions.

Another reason for the success of the methodology is the information content of comparative HDX experiments. Since the labeling reaction can be performed at low protein concentrations in solution, many different functionally relevant states, that might be difficult to address with other methods, can be characterized using HDX-MS. Although rich in information content, comparative analysis of multiple functional states entails increasing combinatorial complexity in data analysis; hence, development of automated data extraction and analysis software packages was essential to exploit the full potential of HDX-MS.

Typical Workflow for HDX-MS Characterization of a Photoreceptor

Due to the diversity of applications, different protocols for effectively using HDX-MS have been developed over the years [summarized in Konermann et al. [37]]. The most commonly used technique is "continuous labeling" where the native protein is exposed to deuterated buffer solutions and the incorporation of the deuterium label is monitored over time. A schematic workflow of this approach geared toward the characterization of a photoreceptor in its dark- and light-state is illustrated in **Figure 1**. In order to measure exchange characteristics representing the conformation of interest, it is important to pre-incubate the samples under conditions that provide high percentages of the protein in the respective state prior to the dilution in deuteration buffer (**Figure 1A**). Depending on the nature of the photoreceptor system, bi-stable light sensors might have to be switched to a specific functional state using appropriate light sources, whereas photoreceptors that exhibit a thermal dark state recovery can be incubated sufficiently long in the dark to ensure full population of the dark state. In order to obtain a significantly light-state biased steady-state population of the photoreceptor for the comparative measurement, the length of the pre-illumination step and the light intensity need to be adjusted depending on the rate of dark state recovery.

Dilution in D_2O-containing buffer then triggers hydrogen exchange under appropriate light conditions that maintain the steady state population of the dark- or light-state conformations (**Figure 1B**). In typical HDX-MS experiments hydrogen exchange is stopped after various time points ranging from seconds to hours and sometimes days by quenching the reaction in low pH buffer and lowering the temperature to 0°C (**Figure 1C**). In the case of photoreceptors, control experiments need to be performed to rule out any side reactions, such as cofactor bleaching, during prolonged incubation times; depending on the employed light intensities such effects generally limit the accessible time range to a few hours. Since the chemical exchange rate of amide hydrogens is slowest around pH 2.5 and due to the temperature dependence of any chemical reaction, the conditions used for quenching of the reaction, on the one hand, minimize the loss of deuterium label during the subsequent readout procedure in aqueous environment (termed back-exchange) and, on the other hand, favor the loss of deuterium incorporated at other exchangeable positions in polar side chains [33].

The increase in mass due to deuterium incorporation measured in the mass spectrometer is determined by the exchange characteristics of the backbone amide positions. While direct mass spectrometric analysis of the full-length protein after desalting can be used to estimate global changes in protein stability and dynamics upon illumination, more detailed information on how specific structural elements are affected can be obtained by proteolytic digestion. Immobilized acid tolerant proteases, such as pepsin, can be integrated into an automated liquid chromatography setup enabling rapid digestion, desalting and separation of the peptides prior to infusion into the mass spectrometer (**Figure 1D**). Due to the relatively unspecific cleavage properties of acid tolerant proteases, many overlapping peptides with variable abundance are measured during the mass spectrometric analysis. In combination with the unusually broad individual isotope distributions, due to random back-exchange events, this results in complex spectra that need to be evaluated.

Since manual data extraction and analysis is a tedious, time consuming task, automated software packages are generally used to extract the relative shift in mass centroids for given peptides in multiple time points and repetitive measurements (**Figure 1E**). As discussed previously, also the shape of the isotope distribution can provide important insight into molecular aspects of the exchange reaction and should be extracted for data analysis. Eventually, individual peptides need to be assigned to a specific sequence of the protein and can then be compared between different functional states. Characteristic deuterium uptake plots showing the time dependent increase in deuteration level relative to an undeuterated reference (D_{rel}, **Figure 1E**) provide information on the overall protection of structural elements and their conformational dynamics. More localized information might be obtained by correlating all peptides with the primary and secondary structure of the protein (**Figure 1F**) and extracting the information content available from overlapping peptides. If available, mapping onto the three-dimensional structure (**Figure 1G**) can ultimately help to identify potential signaling pathways due to the identification of structural elements that are affected by illumination in both the photoreceptor and effector domains. Since most of the routines required during data extraction and visualization are repetitive processes, automation of this workflow greatly helps to reduce the time required to interpret deuterium exchange experiments. In this context, the HDX-MS community benefits from the standardized instrumentation and data formats as well as from

powerful algorithms for signal processing, feature detection and peptide assignment [39, 40] originating from the widespread adaption of proteomics research.

Improvements in HDX-MS Data Evaluation

A major challenge in HDX data analysis is to identify and match signals originating from peptide species with unknown H/D compositions, and at the same time, to quantify the abundance of each deuterated species. A number of computational solutions have been proposed for individual parts of the HDX analysis workflow, for example quantification of deuterium incorporation [41–44], chromatogram alignment [45], or statistical evaluation of deuteration differences between different samples [46]. Hydra [47] was the first solution capable of providing a full analysis workflow and a number of web server based programs followed [48, 49]. ExMS [50] is a suite of MATLAB scripts which offer visualization for interactive parameterization. HDX-Workbench [51] is geared toward high-resolution HDX-MS data and offers a comprehensive graphical interface with visualization and manipulation capabilities. Hexicon 2 [52] adapted and extended the regularized feature detection and deuteration distribution estimation algorithms from its predecessor [53] for improved performance with high-resolution data. This recent generation of data analysis tools provides solutions for most data processing needs of a bottom-up HDX-MS experiment as described above and features rich graphical access to data, thus enabling on-line quality control and fast generation of conclusive results. Another advantage of modern software packages is their ability to identify and quantify differently deuterated subpopulations of individual peptides. A good estimate of the deuteration distribution provides insight into the dynamics of multi-state equilibria which may otherwise not be identified as such [54]. For some of the photoreceptor characterizations discussed below, where illumination modulates the equilibrium between dark- and light-states, robust deuteration distribution estimation was essential for valid interpretation of HDX-MS data.

The ease of data processing empowered the community to develop novel experimental protocols, for example, using electron transfer dissociation for resolution enhancement [55] or protease-free top-down fragmentation [56, 57]. Besides the continuous improvement of data processing algorithms, advancements in experimental technology and new applications of HDX-MS call for flexible solutions that let the user match data analysis to the experimental strategy. One development in this direction is Mass Spec Studio [58], featuring a modular architecture that allows users and developers to reuse core components and to tailor the workflow to their needs.

Challenges in the Characterization of Light-Sensitive Proteins

All photosensory modules used in optogenetics originate from natural photoreceptors that typically employ small molecule cofactors to sense light in specific regions of the electromagnetic spectrum. Cofactor-binding photoreceptors can be classified into six different families: Retinal binding rhodopsins [59], *p*-hydroxycinnamic acid binding xanthopsins [60], bilin binding phytochromes [61], as well as the group of flavin containing photoreceptors [23, 62] such as cryptochromes, light-oxygen-voltage sensing (LOV) domain containing proteins and sensor of blue light using FAD (BLUF) domain containing proteins. In addition to cofactor-binding photoreceptors, a UV-B sensitive plant photoreceptor termed UV resistance locus 8 (UVR8) has been shown to use tryptophan residues for light perception [63]. In all cases, photon absorption induces local structural changes near the cofactor which are then coupled to rearrangements of intra- or inter-protein contacts that result in channel opening, ion pump activation, regulation of various effector domain activities, or modulation of protein-protein interactions.

Structural studies of individual members of these photoreceptor families using X-ray crystallography have significantly contributed to a better understanding of molecular aspects of light-signaling. A variety of crystal structures of isolated photoreceptor domains in their dark states have been published, however, in many cases these structures are lacking the light-regulated output domains. In order to better appreciate potential signaling pathways to diverse effector domains and to identify similarities or differences in various members of the photoreceptor families, more crystal structures of full-length photoreceptors or light sensors in complex with their non-covalently linked effector domains would be helpful. In this respect, significant progress was recently made predominantly in the field of flavin containing BLUF and LOV proteins. Representative architectures are summarized in **Figure 2** and their comparison reveals intriguing insight into the coupling of sensors and effectors. Individual members of both families have very similar core photoreceptor structures, however, the N- and C-terminal extensions show characteristic differences between various systems. As illustrated in **Figure 2**, these flanking regions adopt different architectures tailored to the requirements of the specific effector system. From this it appears difficult to generalize signaling mechanisms even within a family of photoreceptors and additional functional studies addressing the coupling of sensor and effector will be required to better understand functioning of complex photoreceptors.

Another important aspect of the structural analysis of photoreceptors is the characterization of light-activated states. However, trapping photoreceptors in their light state conformation is a major obstacle for crystallographic studies and only few structures of crystals grown in the light-activated state are available. So far this has only been achieved for the single domain LOV proteins VIVID (VVD) [64] (**Figure 3A**) and PpsB1 [65] as well as for a truncated phytochrome construct [66], all of which revert slowly into their dark state conformation. For most photoreceptors, the increase in structural dynamics upon illumination makes crystallization and also NMR studies difficult. To circumvent the problems linked to the structural characterization of short-lived and highly dynamic light states, dark state crystals have been illuminated to study light-induced conformational changes [26, 67–76]. One of the best characterized photoreceptors using this approach is the xanthopsin member PYP that is shown for illustration

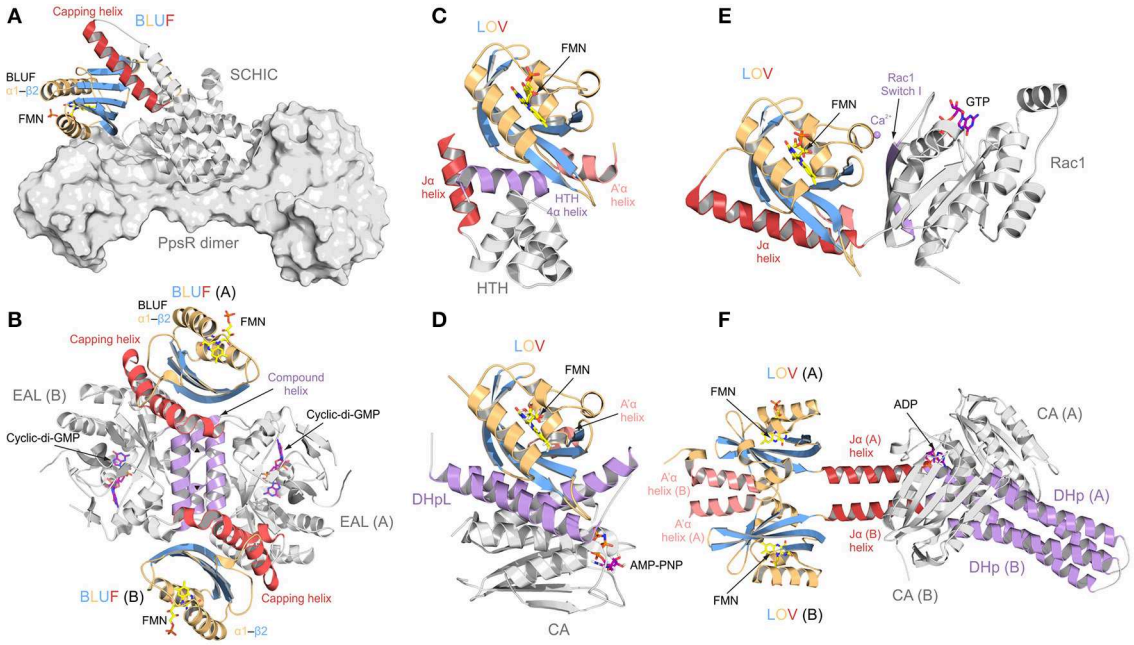

FIGURE 2 | Protein architectures of full length BLUF and LOV photoreceptor-effector systems. Photoreceptor domains are colored according to secondary structure: helices, orange; β-sheets, blue. N- and C-terminal helical domain extensions are colored in light and dark red, respectively, and elements important for signal transduction are colored in purple. **(A)** AppA-PpsR system from *Rhodobacter sphaeroides* [27]. AppA (shown as cartoon) senses blue light using a BLUF domain and, via its C-terminal SCHIC domain, binds to a dimer of the transcriptional repressor PpsR (a truncated construct is shown in surface representation). Illumination alters the DNA-binding ability of PpsR through allosteric modulation of its helix-turn-helix motif (HTH; not present in the AppA-PpsR$_2$ core complex structure—*cf.* **Figure 6**). **(B)** Blue-light regulated phosphodiesterase 1 (BlrP1) from *Klebsiella pneumonia* [86]. BlrP1 contains an N-terminal BLUF domain and a C-terminal EAL phosphodiesterase domain. The protein homo-dimerizes through a conserved interface made up of two dimerization helices and one compound helix formed by two short helices provided by each protomer (both shown in purple). Communication between the BLUF domains and the EAL active sites is bidirectional and mediated through the dimer interface [87]. **(C)** Light-activated transcription factor EL222 from *Erythrobacter litoralis* [14]. In contrast to the well-studied LOV2 from *Avena sativa* phototropin (shown in **(E)** as part of PA-Rac1), the C-terminal Jα helix (shown in red) does not pack against the LOV β-sheet. Instead it is replaced by a helix of the HTH DNA-binding motif. Illumination releases the HTH motif from the LOV β-sheet and thus enables DNA binding. **(D)** Light-activated monomeric histidine kinase EL346 from *Erythrobacter litoralis* [22]. Two α-helices of a dimerization/histidine phosphotransfer-like (DHpL) domain (shown in purple) pack against the LOV β-sheet and couple the photoreceptor to the catalytic/ATP-binding (CA) domain with bound adenosine 5′-(β,γ-imido)triphosphate (AMP-PNP, shown as stick model). Illumination is assumed to loosen the LOV-DHpL interactions, thus enabling CA domain activation. **(E)** Synthetic photoactivatable GTPase Rac1 (PA-Rac1) [19]. PA-Rac1 was generated by fusing the LOV2 domain from *Avena sativa* phototropin 1 to the small human Rac1 GTPase. A Ca^{2+} ion (purple sphere) bound in the interdomain interface restricts the dynamics of the Jα helix (dark red) packed against the LOV domain core. Illumination perturbs the Jα helical structure and renders the interface more dynamic, allowing the GTPase to engage in β-strand pairing with downstream effectors through its peripheral β-strand (purple) [83]. **(F)** Synthetic light-regulated histidine kinase YF1 [93]. The dimeric protein was generated by replacing the oxygen-sensing PAS domain of *Bradyrhizobium japonicum* FixL with structurally homologous LOV photoreceptor domain from *Bacillus subtilis* YtvA. The main part of the LOV dimer interface is formed by the N-terminal flanking helices (light red) that pack against the LOV β-sheet of the opposite subunit of the dimer. The C-terminal Jα helices (dark red) form a coiled coil structure extending away from the photoreceptor domains, connecting them to a dimerization/histidine phosphotransfer (DHp) domain (colored in purple) which forms an interaction platform for the CA domains. The activation mechanism is proposed to involve twisting of Jα upon illumination.

purposes in **Figure 3B**. Although illumination of dark-grown crystals provides insight into local structural rearrangements upon light activation, crystal lattice constraints prevent larger conformational changes and thus limit the analytical power of this technique. However, to understand signal propagation in photoreceptors on a structural and functional level, a detailed characterization of all functionally relevant signaling states is desirable. In this respect, HDX-MS is a powerful supplementary method for identifying structural elements affected by illumination as well as for the characterization of multiple functionally relevant photoreceptor states.

HDX-MS Applications in the Field of Photoreceptors

In the last decade, several studies have been performed that demonstrate the applicability of HDX-MS for the functional characterization of photoreceptors. The strategy common to most of these experiments is continuous labeling of the investigated proteins in the dark and under constant illumination, followed by bottom-up LC-MS analysis (*cf.* **Figure 1**). Photoactive Yellow Protein (PYP) from *Halorhodospira halophila* is the prototype of the xanthopsin

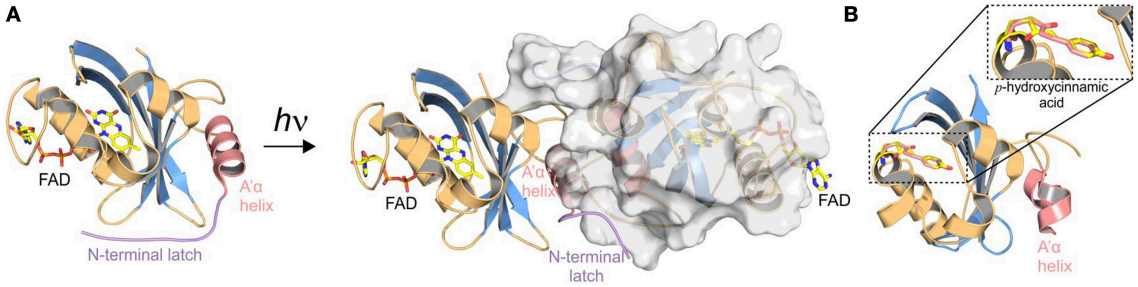

FIGURE 3 | Selected structures obtained from crystals grown in the dark and light-activated state vs. *in crystallo* light-activated photoreceptors. The PAS/LOV domains are shown in similar orientation and are colored according to **Figure 2**. **(A)** Crystal structures of dark- [76] and light-adapted [64] VIVID from *Neurospora crassa*. Blue light illumination of VIVID changes the oligomeric state from monomers to dimers. Dimerization is mediated by release of the N-terminal latch (shown in purple) from the protein core, enabling interaction with the acceptor pocket of another protomer. **(B)** PYP from *Halorhodospira halophile* in its light activated conformation [72]. Only one representative structure is shown, since no global structural rearrangements are observed upon illumination of dark-grown crystals. Modest structural changes that affect the hydrogen-bonding network around the cofactor are observed upon light activation of PYP. Illumination triggers a *trans-cis* isomerization of the *p*-hydroxycinnamic acid cofactor (yellow and light-red, respectively) that is covalently bound to a cysteine residue.

protein family and was the first photoreceptor to be studied using HDX-MS [77, 78]. PYP exhibits a PAS fold which comprises a five-stranded antiparallel β-sheet surrounded by α-helices and covalently binds a *p*-hydroxycinnamic acid cofactor via a cysteine residue. Upon blue light illumination, the cofactor undergoes a *trans-cis* isomerization that changes the hydrogen bond network around the ligand and induces receptor activation (**Figure 3B**). Structural differences between the dark- and light-states of PYP were localized to the direct vicinity of the *p*-hydroxycinnamic acid chromophore, where several residues form a characteristic hydrogen bond network around the *trans*-chromophore in the dark. HDX studies confirmed that photoisomerization of the chromophore destabilizes these interactions, as reflected in increased deuterium uptake and therefore increased conformational dynamics of elements flanking the chromophore binding site [77, 79]. While HDX-NMR experiments only identified elements in the direct vicinity of the cofactor [79], HDX-MS measurements revealed the propagation of the allosteric signal to helices flanking the PAS core and also to the β–sheet and the N-terminal capping region as shown in **Figure 4** [77].

Additional PAS photoreceptors that were studied by HDX belong to the family of LOV domains that, in contrast to PYP, contain a non-covalently bound flavin cofactor (FMN or FAD). In most LOV domains, the globular core is flanked by α-helical N- and C-terminal extensions that pack against the surface of the LOV β-sheet and play an important role in signal transduction [23]. Upon illumination with blue light, the flavin cofactor forms an adduct with a conserved cysteine residue, which initiates a cascade of structural changes propagating from the chromophore to the domain boundaries. Continuous labeling HDX-MS studies on the LOV domain protein VIVID that was shown to homodimerize in a light-dependent manner [76] showed that the intact photoreceptor reversibly unfolds and that the rate of unfolding decreases upon illumination [80]. Experiments on the peptide level revealed that stabilization of the PAS β-sheet and the central helical region close to the flavin cofactor explain the reduced unfolding upon illumination. In contrast, the high exchange rates of the N-terminal flanking helix that plays an important role in light induced dimerization [64], were hardly affected by illumination. Moderate protection of the crystallographic dimer interface upon illumination is in line with a rapid monomer-dimer interconversion [81]. These observations contrast with the above described studies on PYP, where illumination caused significantly increased amide proton exchange of helical PAS regions and slightly protected the N-terminus [77]. Therefore, different interactions of the flavin and the *p*-hydroxycinnamic acid chromophores as well as differences in the oligomerization state result in contrary effects with respect to conformational dynamics of two PAS-sensors and suggest that PAS signaling can operate via diverse mechanisms.

Even within the family of LOV photoreceptors, diverse effects on protein dynamics are observed in the lit state. NMR studies on the isolated LOV2 domain from *Avena sativa* phototropin 1 showed destabilization and undocking of the C-terminal helical extension (Jα) from the LOV β-sheet upon illumination [82]. In the isolated domain, the Jα helix is highly dynamic already in the dark such that deuterium exchange was too rapid to capture any differences between dark and lit states using either HDX-NMR or -MS methods [82, 83]. In contrast to VIVID, which does not contain a C-terminal helical extension, the core LOV2 domain showed no transient unfolding in HDX-MS experiments and only structural elements surrounding the flavin cofactor were affected by illumination [83]. Interestingly, HDX-NMR studies with isolated LOV2 indicate that the light state is destabilized sufficiently to undock the Jα helix without globally unfolding the PAS core [82]. Another remarkably different member of the LOV family that is small enough to be studied by NMR is the light-regulated transcription factor EL222 from *Erythrobacter litoralis*. It comprises an N-terminal LOV domain fused to a DNA-binding helix-turn-helix motif of which one helix is docked against the surface of the LOV β-sheet (**Figure 2C**) in a configuration resembling the C-terminal Jα helix of LOV2. A combination of HDX-NMR and chemical shift difference

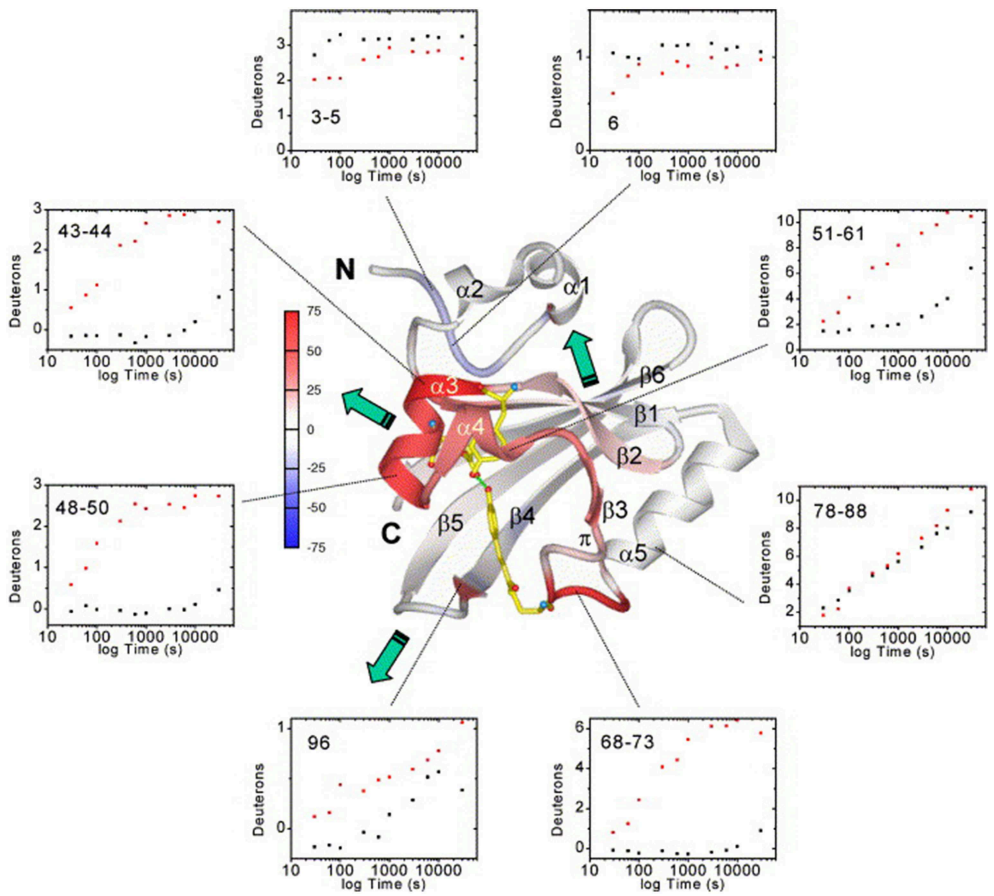

FIGURE 4 | Average deuteration changes upon illumination mapped on the PYP structure, H/D exchange kinetics and signal transduction pathways [77]. Average deuterium incorporation changes are mapped on the PYP dark-state ribbon diagram colored from −75 to +75% change according to the color bar. Secondary structure elements and the N- and C-termini are labeled. The chromophore and active-site residues Tyr42 and Glu46, which form hydrogen bonds (green dotted lines) to the phenolate oxygen atom of the chromophore in the dark state, are shown for better orientation. Green arrows indicate the three signal transduction pathways (through the PAS core helices, the β-hairpin, or the β-sheet interface). H/D exchange kinetics (black dots, dark state; red dots, I2 light state) are shown as examples of the data quality and the time-course of H/D exchange in representative PYP sequence segments. Reprinted from Brudler et al. [77] Copyright © 2006, with permission from Elsevier.

analysis showed that the helix undocks from the LOV domain upon illumination but at the same time remains protected from exchange on NMR timescales, indicating that illumination releases the domains from each other without perturbing any stable secondary structures [14].

In the context of multi-domain LOV-based photoreceptors, HDX-MS was used to study the effect of illumination for the synthetic photoactivatable GTPase Rac1 (PA-Rac1) [83] that had been proposed to function by release of the caged GTPase domain from the LOV photosensor upon illumination [19] (**Figure 2E**). Deconvolution of isotopically resolved MS spectra revealed the existence of two distinct conformational states of the Jα helix flanking the LOV core and connecting the photoreceptor with the GTPase. Blue-light illumination shifts the relative populations of these conformational states (**Figure 5A**) as previously described [84]. Of note, metal coordination at an inadvertently created binding site at the interdomain interface (**Figure 5B**) substantially increases the dynamic range by stabilization of the caged Jα conformation only in the dark (**Figures 5C,D**). In combination with solution scattering experiments, HDX-MS data suggested that illumination allosterically modulates GTPase dynamics rather than releasing the GTPase. These results highlight that, in addition to the considered photoreceptor activation mechanism, molecular details of engineered sensor-effector interfaces as well as structural dynamics of the dark-light transition are relevant for the successful design of artificial photoswitches.

Similar to LOV domains, also BLUF domains are small globular photoreceptor domains that bind a flavin cofactor, and exhibit a ferredoxin-like protein fold with two helices aligned parallel to a five stranded β-sheet. As observed for LOV proteins, also BLUF domains are frequently C-terminally flanked by a helix that packs against the surface of the central β-sheet and is likely involved in signal transduction. Light-activation causes a rearrangement of the hydrogen-bonding network around the cofactor, including tautomerization of an essential glutamine

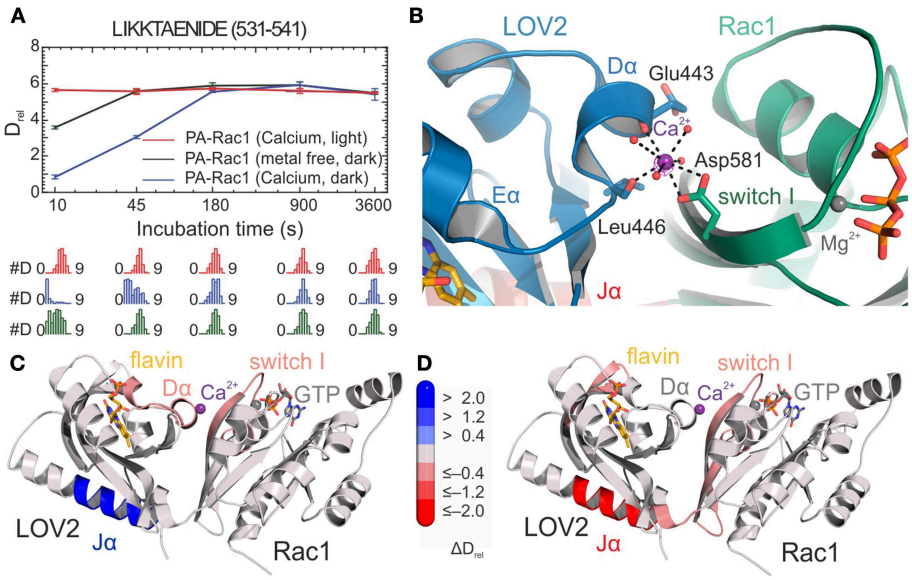

FIGURE 5 | HDX-results of the optogenetic tool PA-Rac1 [83]. (A) Deuterium uptake curves of a representative LOV2-Jα peptide with relative deuteration values (D_{rel}) plotted against deuteration time for three different functionally relevant states. D_{rel} values are shown as the mean of three independent measurements, and error bars correspond to the standard deviation. Lower panels show the Hexicon 2 estimated abundance distribution of individual deuterated species on a scale from undeuterated to all exchangeable amides deuterated [52]. The bimodal distributions indicate distinct conformational states of the Jα helix. **(B)** Calcium binding site at the LOV2–Rac1 interface. Coordinating residues from both LOV2 and the Rac1 domain providing four of the eight oxygen ligands are shown as stick models. The remaining water ligands are represented as spheres. **(C,D)** Structures of PA-Rac1 colored according to the differences in relative deuteration levels upon calcium coordination in the dark and illumination in the presence of calcium ions, respectively. Coloring corresponds to the differences in relative deuteration of individual peptides according to the bar legend [52] and highlights the effect of metal binding on the functionally relevant Jα helix and the LOV2-Rac1 interface. Shades of red or blue colors reflect an increased or decreased deuterium uptake, respectively. Reprinted with permission from Winkler et al. [83]. Copyright © 2015 American Chemical Society.

residue [85], which eventually alters the dynamics of the C-terminal β-strand and the adjacent helical extension. A multi-domain BLUF protein that was studied by HDX-MS is the blue-light regulated phosphodiesterase 1 (BlrP1) from *Klebsiella pneumoniae* that features a BLUF domain covalently linked to a metal-dependent EAL phosphodiesterase (**Figure 2B**). BlrP1 degrades the second messenger cyclic dimeric GMP in a light-stimulated fashion [86]. HDX-MS experiments addressing substrate and metal ion binding in the dark- and light-states of the characteristic BlrP1 dimer revealed a bidirectional communication between regions involved in light sensing in the BLUF domain and regions coordinating the catalytically relevant metal ions in the EAL domain [87]. The EAL dimer interface with its characteristic compound helix was shown to function as a central communication platform for the allosteric EAL-BLUF cross-talk, which is intensified upon illumination. Combination of all analyzed BlrP1 states allowed the mapping of a signaling pathway between the sensor and effector domains of the complex multi-domain protein and provided molecular details of regions involved in inter-domain communication.

Due to high-resolution mass spectrometers and sophisticated data evaluation tools, even more complex systems can nowadays be studied by HDX-MS. Experiments with the AppA-PpsR photoreceptor-effector system from *Rhodobacter sphaeroides* demonstrated that even mixtures of multi-domain proteins no longer pose a challenge for data processing and sequence assignment [27]. The AppA-PpsR system, which plays a role in photosynthesis-related gene expression, forms a non-covalent AppA-$PpsR_2$ heterotrimeric complex [88]. AppA is composed of a light-sensing BLUF domain and a SCHIC domain that was shown by HDX-MS analysis to be involved in complex formation with the transcriptional regulator PpsR (**Figure 6A**). Based on exchange data, crystallization constructs were designed and allowed structure determination of an AppA-$PpsR_2$ core complex [27]. Combination of functional, crystallographic [89] and HDX-MS experiments showed that illumination of the AppA-$PpsR_2$ complex influences the α1-β2 region of the AppA-BLUF domain and its C-terminal capping helix, which results in stabilization of the DNA-binding helix-turn-helix motif of PpsR and thus interferes with DNA-binding of the effector (**Figure 6B**). Together, the data suggest the involvement of a light-sensitive ternary AppA-PpsR-DNA complex in photosynthesis-gene regulation which had previously not been appreciated. In comparison to HDX-NMR experiments on the isolated AppA BLUF domain [90], it should be noted that the light-responsive elements identified by HDX-MS are highly dynamic with nearly complete deuterium exchange occurring within the dead time of a typical 2D NMR measurement.

Although complex soluble photoreceptor systems can be addressed by HDX-MS, the characterization of transmembrane proteins such as rhodopsin photoreceptors remains challenging. Based on their function three rhodopsin classes can be

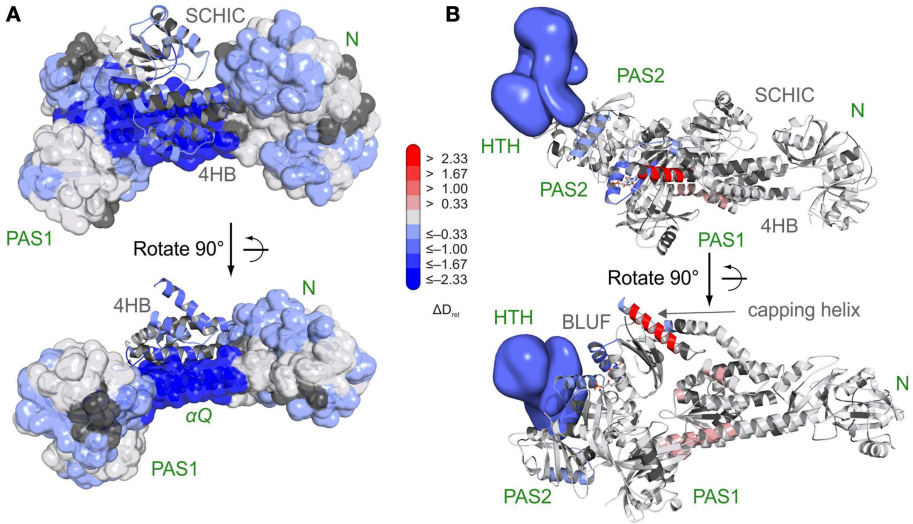

FIGURE 6 | Characterization of the AppA-PpsR$_2$ complex using HDX-MS [27]. (A) Superposition of HDX data addressing AppA-PpsR$_2$ complex formation of full length PpsR and C-terminally truncated AppA (AppA$_{\Delta C}$) with the crystallized AppA-PpsR$_2$core complex. HDX-MS data of the 15 s deuterium exchange time points are mapped onto the complex with the PpsR N–Q–PAS1 construct (N-terminal PAS domain—N; Q-linker—αQ; PAS1 domain) shown in transparent surface and the AppA domains (four helix bundle—4 HB; SCHIC) in cartoon representation. **(B)** Model of the AppA$_{\Delta C}$–PpsR$_2$ complex as described in Winkler et al. [27] colored with respect to the observed changes in deuterium incorporation between light- and dark-state measurements of the complex. The 15 s deuterium exchange time point is shown for visualization of protection (blue) or destabilization (red) upon complex illumination. Reprinted with permission from Winkler et al. [27], Nature Publishing Group.

distinguished: sensory rhodopsins, ion-pumps for H^+ and Cl^- as well as ion-channels. Although the different rhodopsins classes exhibit low sequence identity, they all comprise seven transmembrane helices and sense light using a retinal cofactor. The cofactor is bound to a conserved lysine forming a protonated Schiff base. Depending on the protein environment, rhodopsins can absorb photons of almost the entire visible range. Illumination results in photoisomerization of the retinal from an all-*trans* to a 13-*cis* configuration which triggers protein activation and initiates the photocycle. Bacteriorhodopsin (BR) is the simplest and one of the best studied rhodopsins and functions as a green light regulated proton pump that transports protons out of the cell. It is embedded into purple membranes where it naturally forms 2D crystals composed of BR trimers. In line with the tight packing of BR in purple membranes, HDX-MS studies showed nearly indistinguishable isotope exchange behavior under dark and light conditions [91]. Purple membranes exhibit a high degree of protection and even after extended labeling periods less than half of the amide protons of trimeric BR were exchanged. To circumvent this problem, HDX experiments on monomeric BR were performed in bicelles. Comparative experiments revealed pronounced destabilization of the protein upon illumination indicating that light-activated BR undergoes substantial structural changes [91]. Individual structural elements affected by illumination could not be identified because the presence of membranes or detergents impedes protease digestion and peptide separation and thus complicates spatially resolved bottom-up HDX-MS. In order to improve mechanistic interpretations, new and better strategies to detect deuteration of transmembrane proteins are currently being developed [29] and one such approach has recently been used in the context of photoreceptors for refolding studies with BR [92].

Conclusion

In summary, the studies described highlight HDX-MS as a powerful method for the detailed characterization of multiple functionally relevant signaling states of photoreceptors. In combination with additional functional or structural data, HDX-MS can significantly improve our understanding of signal integration in diverse light sensor domains, help in the identification of potential signaling pathways to various effector domains and also provide information on how the biological function of diverse output domains is regulated.

As far as the characterization of PAS/LOV and BLUF domains is concerned, HDX-MS analyses reveal that signaling state formation of different sensors within a family can be accompanied by diverse modes of conformational changes. Importantly, isolated sensory modules show different conformational dynamics compared to their analysis in the presence of the regulated effector domain. Depending upon the desired mode of action of novel optogenetic tools, a more detailed characterization of full-length members of different photoreceptor families in terms of light-induced structural rearrangements will be required to enable a more rational design of optogenetic systems that employ building blocks of naturally evolved sensor-effector couples. To improve the functionality of artificial tools, ultimately, also the specific requirements for regulation of different effector domains and the conformational

determinants that affect the dynamic range of the system need to be appreciated.

In the case of the established optogenetic tool PA-Rac1, HDX-MS analysis revealed that an inadvertently introduced metal ion binding site influences the dynamic range and potentially provides an explanation for the unsuccessful attempts to transfer the concept of PA-Rac1 to closely related GTPases [83]. In this respect, reengineering of the sensor-effector interfaces of similar LOV2-GTPase fusions to enable metal binding or to decrease the conformational dynamics of the corresponding effector regions by different means would be a promising rational approach to further expand the optogenetic toolbox. The observation that properties of newly generated interfaces can have pronounced effects for the functionality of optogenetic tools further emphasizes the need for a detailed characterization of existing tools to better understand their functionality *in vitro* and ultimately also *in vivo*.

Considering the variety of photoreceptor families and the modularity of naturally occurring systems with diverse effector domains, the application of HDX-MS in the field of light responsive proteins has so far only touched the tip of the iceberg. Recent developments in mass spectrometry instrumentation and data analysis automation are expected to increase the utility of HDX-MS in integrative structural biology and also in the field of photoreceptor research. This might provide interesting insight into signaling mechanisms of additional photoreceptor families such as cryptochromes and phytochromes, which are frequently employed modules in optogenetic tools.

Acknowledgments

We thank Ilme Schlichting for continuous support as well as Karl Gruber for critical reading of the manuscript. We acknowledge financial support by the Max Planck Society and the Hartmut Hoffmann-Berling International Graduate School of Molecular and Cellular Biology (HBIGS) to RL and UH as well as the Austrian Science Fund (FWF): P27124 to AW.

References

1. Karaca E, Bonvin AMJJ. Advances in integrative modeling of biomolecular complexes. *Methods* (2013) **59**:372–81. doi: 10.1016/j.ymeth.2012.12.004
2. Ward AB, Sali A, Wilson IA. Integrative structural biology. *Science* (2013) **339**:913–5. doi: 10.1126/science.1228565
3. Grusch M, Schelch K, Riedler R, Reichhart E, Differ C, Berger W, et al. Spatio-temporally precise activation of engineered receptor tyrosine kinases by light. *EMBO J.* (2014) **33**:1713–26. doi: 10.15252/embj.201387695
4. Guntas G, Hallett RA, Zimmerman SP, Williams T, Yumerefendi H, Bear JE, et al. Engineering an improved light-induced dimer (iLID) for controlling the localization and activity of signaling proteins. *Proc Natl Acad Sci USA.* (2015) **112**:112–7. doi: 10.1073/pnas.1417910112
5. Hughes RM, Vrana JD, Song J, Tucker CL. Light-dependent, dark-promoted interaction between Arabidopsis cryptochrome 1 and phytochrome B proteins. *J Biol Chem.* (2012) **287**:22165–72. doi: 10.1074/jbc.M112.360545
6. Kennedy MJ, Hughes RM, Peteya LA, Schwartz JW, Ehlers MD, Tucker CL. Rapid blue-light-mediated induction of protein interactions in living cells. *Nat Methods* (2010) **7**:973–5. doi: 10.1038/nmeth.1524
7. Niopek D, Benzinger D, Roensch J, Draebing T, Wehler P, Eils R, et al. Engineering light-inducible nuclear localization signals for precise spatiotemporal control of protein dynamics in living cells. *Nat Commun.* (2014) **5**:4404. doi: 10.1038/ncomms5404
8. Reis JM, Burns DC, Woolley GA. Optical control of protein-protein interactions via blue light-induced domain swapping. *Biochemistry* (2014) **53**:5008–16. doi: 10.1021/bi500622x
9. Shimizu-Sato S, Huq E, Tepperman JM, Quail PH. A light-switchable gene promoter system. *Nat Biotechnol.* (2002) **20**:1041–4. doi: 10.1038/nbt734
10. Yazawa M, Sadaghiani AM, Hsueh B, Dolmetsch RE. Induction of protein-protein interactions in live cells using light. *Nat Biotechnol.* (2009) **27**:941–5. doi: 10.1038/nbt.1569
11. Gasser C, Taiber S, Yeh C, Wittig CH, Hegemann P, Ryu S, et al. Engineering of a red-light–activated human cAMP/cGMP-specific phosphodiesterase. *Proc Natl Acad Sci USA.* (2014) **111**:8803–8. doi: 10.1073/pnas.1321600111
12. Motta-Mena L, Reade A, Mallory MJ, Glantz S, Weiner OD, Lynch KW, et al. An optogenetic gene expression system with rapid activation and deactivation kinetics. *Nat Chem Biol.* (2014) **10**:196–202. doi: 10.1038/nchembio.1430
13. Möglich A, Ayers RA, Moffat K. Design and signaling mechanism of light-regulated histidine kinases. *J Mol Biol.* (2009) **385**:1433–44. doi: 10.1016/j.jmb.2008.12.017
14. Nash AI, McNulty R, Shillito ME, Swartz TE, Bogomolni RA, Luecke H, et al. Structural basis of photosensitivity in a bacterial light-oxygen-voltage/helix-turn-helix (LOV-HTH) DNA-binding protein. *Proc Natl Acad Sci USA.* (2011) **108**:9449–54. doi: 10.1073/pnas.1100262108
15. Raffelberg S, Wang L, Gao S, Losi A, Gärtner W, Nagel G. A LOV-domain-mediated blue-light-activated adenylate (adenylyl) cyclase from the cyanobacterium *Microcoleus chthonoplastes* PCC 7420. *Biochem J.* (2013) **455**:359–65. doi: 10.1042/BJ20130637
16. Ryu M, Kang I, Nelson MD, Jensen TM, Lyuksyutova AI, Siltberg-Liberles J, et al. Engineering adenylate cyclases regulated by near-infrared window light. *Proc Natl Acad Sci USA.* (2014) **111**:10167–72. doi: 10.1073/pnas.1324301111
17. Stierl M, Stumpf P, Udwari D, Gueta R, Hagedorn R, Losi A, et al. Light modulation of cellular cAMP by a small bacterial photoactivated adenylyl cyclase, bPAC, of the soil bacterium *Beggiatoa*. *J Biol Chem.* (2011) **286**:1181–8. doi: 10.1074/jbc.M110.185496
18. Strickland D, Moffat K, Sosnick TR. Light-activated DNA binding in a designed allosteric protein. *Proc Natl Acad Sci USA.* (2008) **105**:10709–14. doi: 10.1073/pnas.0709610105
19. Wu YI, Frey D, Lungu OI, Jaehrig A, Schlichting I, Kuhlman B, et al. A genetically encoded photoactivatable Rac controls the motility of living cells. *Nature* (2009) **461**:104–8. doi: 10.1038/nature08241
20. Pathak GP, Vrana JD, Tucker CL. Optogenetic control of cell function using engineered photoreceptors. *Biol Cell* (2013) **105**:59–72. doi: 10.1111/boc.201200056
21. Zayner JP, Antoniou C, French AR, Hause RJJr, Sosnick TR. Investigating models of protein function and allostery with a widespread mutational analysis of a light-activated protein. *Biophys J.* (2013) **105**:1027–36. doi: 10.1016/j.bpj.2013.07.010
22. Rivera-Cancel G, Ko W, Tomchick DR, Correa F, Gardner KH. Full-length structure of a monomeric histidine kinase reveals basis for sensory regulation. *Proc Natl Acad Sci USA.* (2014) **111**:17839–44. doi: 10.1073/pnas.1413983111
23. Conrad KS, Bilwes AM, Crane BR. Light-induced subunit dissociation by a light-oxygen-voltage domain photoreceptor from *Rhodobacter sphaeroides*. *Biochemistry* (2013) **52**:378–91. doi: 10.1021/bi3015373
24. Burgie ES, Wang T, Bussell AN, Walker JM, Li H, Vierstra RD. Crystallographic and electron microscopic analyses of a bacterial phytochrome reveal local and global rearrangements during photoconversion. *J Biol Chem.* (2014) **289**:24573–87. doi: 10.1074/jbc.M114.571661
25. Diensthuber RP, Engelhard, C, Lemke, N, Gleichmann, T, Ohlendorf, R, Bittl, R, et al. Biophysical, mutational, and functional investigation of the chromophore-binding pocket of light-oxygen-voltage photoreceptors. *ACS Synth Biol.* (2014) **3**:811–9. doi: 10.1021/sb400205x

26. Mitra D, Yang X, Moffat K. Crystal structures of aureochrome1 LOV suggest new design strategies for optogenetics. *Structure* (2012) **20**:698–706. doi: 10.1016/j.str.2012.02.016
27. Winkler A, Heintz U, Lindner R, Reinstein J, Shoeman RL, Schlichting I. A ternary AppA–PpsR–DNA complex mediates light regulation of photosynthesis-related gene expression. *Nat Struct Mol Biol.* (2013) **20**:859–67. doi: 10.1038/nsmb.2597
28. Sorenson BA, Westcott DJ, Sakols AC, Thomas JS, Anderson P, Stojković, EA, et al. Domain structure of a unique bacterial red light photoreceptor as revealed by atomic force microscopy. *MRS Proc.* (2014) **1652**:mrsf13-1652-ll03-09. doi: 10.1557/opl.2014.259
29. Pirrone GF, Iacob RE, Engen JR. Applications of hydrogen/deuterium exchange MS from 2012 to 2014. *Anal Chem.* (2015) **87**:99–118. doi: 10.1021/ac5040242
30. Hvidt A, Nielsen SO. Hydrogen exchange in proteins. *Adv Protein Chem.* (1966) **21**:287–386.
31. Englander SW. Hydrogen exchange and mass spectrometry: a historical perspective. *J Am Soc Mass Spectrom.* (2006) **17**:1481–9. doi: 10.1016/j.jasms.2006.06.006
32. Iacob RE, Engen JR. Hydrogen exchange mass spectrometry: are we out of the quicksand? *J Am Soc Mass Spectrom.* (2012). **23**:1003–10. doi: 10.1007/s13361-012-0377-z
33. Dempsey CE. Hydrogen exchange in peptides and proteins using NMR spectroscopy. *Prog Nucl Magn Reson Spectrosc.* (2001) **39**:135–70. doi: 10.1016/S0079-6565(01)00032-2
34. Kleckner IR, Foster MP. An introduction to NMR-based approaches for measuring protein dynamics. *Biochim Biophys Acta* (2011) **1814**:942–68. doi: 10.1016/j.bbapap.2010.10.012
35. Engen JR. Analysis of protein conformation and dynamics by hydrogen/deuterium exchange MS. *Anal Chem.* (2009) **81**:7870–5. doi: 10.1021/ac901154s
36. Kaltashov IA, Bobst CE, Abzalimov RR. Hydrogen/Deuterium Exchange Mass Spectrometry (HDX MS) in the studies of architecture, dynamics, and interactions of biopharmaceutical products. In: Lee MS, editor. *Mass Spectrometry Handbook.* Hoboken, NJ: John Wiley & Sons, Inc. (2012). pp. 227–41. doi: 10.1002/9781118180730.ch10
37. Konermann L, Pan J, Liu Y. Hydrogen exchange mass spectrometry for studying protein structure and dynamics. *Chem Soc Rev.* (2011) **40**:1224–34. doi: 10.1039/C0CS00113A
38. Henzler-Wildman K, Kern D. Dynamic personalities of proteins. *Nature* (2007) **450**:964–72. doi: 10.1038/nature06522
39. Mueller LN, Brusniak M, Mani DR, Aebersold R. An assessment of software solutions for the analysis of mass spectrometry based quantitative proteomics data. *J Proteome Res.* (2008) **7**:51–61. doi: 10.1021/pr700758r
40. Perez-Riverol Y, Wang R, Hermjakob H, Müller M, Vesada V, Vizcaíno JA. Open source libraries and frameworks for mass spectrometry based proteomics: a developer's perspective. *Biochim Biophys Acta* (2014) **1844**:63–76. doi: 10.1016/j.bbapap.2013.02.032
41. Abzalimov RR, Kaltashov IA. Extraction of local hydrogen exchange data from HDX CAD MS measurements by deconvolution of isotopic distributions of fragment ions. *J Am Soc Mass Spectrom.* (2006) **17**:1543–51. doi: 10.1016/j.jasms.2006.07.017
42. Chik JK, Vande Graaf JL, Schriemer DC. Quantitating the statistical distribution of deuterium incorporation to extend the utility of H/D exchange MS data. *Anal Chem.* (2006) **78**:207–14. doi: 10.1021/ac050988l
43. Hotchko M, Anand GS, Komives EA, Ten Eyck LF. Automated extraction of backbone deuteration levels from amide H/^{2}H mass spectrometry experiments. *Protein Sci.* (2006) **15**:583–601. doi: 10.1110/ps.051774906
44. Weis DD, Engen JR, Kass IJ. Semi-automated data processing of hydrogen exchange mass spectra using HX-Express. *J Am Soc Mass Spectrom.* (2006) **17**:1700–3. doi: 10.1016/j.jasms.2006.07.025
45. Venable JD, Scuba W, Brock A. Feature based retention time alignment for improved HDX MS analysis. *J Am Soc Mass Spectrom.* (2013) **24**:642–5. doi: 10.1007/s13361-012-0566-9
46. Liu S, Liu L, Uzuner U, Zhou X, Gu M, Shi W, et al. HDX-analyzer: a novel package for statistical analysis of protein structure dynamics. *BMC Bioinformatics* (2011) **12**(Suppl. 1):S43. doi: 10.1186/1471-2105-12-s1-s43
47. Slysz GW, Baker CA, Bozsa BM, Dang A, Percy AJ, Bennett M, et al. Hydra: software for tailored processing of H/D exchange data from MS or tandem MS analyses. *BMC Bioinformatics* (2009) **10**:162. doi: 10.1186/1471-2105-10-162
48. Miller DE, Prasannan CB, Villar MT, Fenton AW, Artigues A. HDXFinder: automated analysis and data reporting of deuterium/hydrogen exchange mass spectrometry. *J Am Soc Mass Spectrom.* (2012) **23**:425–9. doi: 10.1007/s13361-011-0234-5
49. Pascal BD, Chalmers MJ, Busby SA, Mader CC, Southern MR, Tsinoremas NF, et al. The Deuterator: software for the determination of backbone amide deuterium levels from H/D exchange MS data. *BMC Bioinformatics* (2007) **8**:156. doi: 10.1186/1471-2105-8-156
50. Kan ZY, Mayne L, Chetty PS, Englander SW. ExMS: data analysis for HX-MS experiments. *J Am Soc Mass Spectrom.* (2011) **22**:1906–15. doi: 10.1007/s13361-011-0236-3
51. Pascal BD, Willis S, Lauer JL, Landgraf RR, West GM, Marciano D, et al. HDX workbench: software for the analysis of H/D exchange MS data. *J Am Soc Mass Spectrom.* (2012) **23**:1512–21. doi: 10.1007/s13361-012-0419-6
52. Lindner R, Lou X, Reinstein J, Shoeman RL, Hamprecht FA, Winkler A. Hexicon 2: automated processing of hydrogen-deuterium exchange mass spectrometry data with improved deuteration distribution estimation. *J Am Soc Mass Spectrom.* (2014) **25**:1018–28. doi: 10.1007/s13361-014-0850-y
53. Lou X, Kirchner M, Renard BY, Kothe U, Boppel S, Graf C, et al. Deuteration distribution estimation with improved sequence coverage for HX/MS experiments. *Bioinformatics* (2010) **26**:1535–41. doi: 10.1093/bioinformatics/btq165
54. Zhang J, Ramachandran P, Kumar R, Gross ML. H/D exchange centroid monitoring is insufficient to show differences in the behavior of protein states. *J Am Soc Mass Spectrom.* (2013) **24**:450–3. doi: 10.1007/s13361-012-0555-z
55. Zehl M, Rand KD, Jensen ON, Jorgensen TJ. Electron transfer dissociation facilitates the measurement of deuterium incorporation into selectively labeled peptides with single residue resolution. *J Am Chem Soc.* (2008) **130**:17453–9. doi: 10.1021/ja805573h
56. Abzalimov RR, Kaplan DA, Easterling ML, Kaltashov IA. Protein conformations can be probed in top-down HDX MS experiments utilizing electron transfer dissociation of protein ions without hydrogen scrambling. *J Am Soc Mass Spectrom.* (2009) **20**:1514–7. doi: 10.1016/j.jasms.2009.04.006
57. Amon S, Trelle MB, Jensen ON, Jorgensen TJ. Spatially resolved protein hydrogen exchange measured by subzero-cooled chip-based nanoelectrospray ionization tandem mass spectrometry. *Anal Chem.* (2012) **84**:4467–73. doi: 10.1021/ac300268r
58. Rey M, Sarpe V, Burns KM, Buse J, Baker CH, van Dijk, M, et al. Mass spec studio for integrative structural biology. *Structure* (2014) **22**:1538–48. doi: 10.1016/j.str.2014.08.013
59. Wickstrand C, Dods R, Royant A, Neutze R. Bacteriorhodopsin: would the real structural intermediates please stand up? *Biochim Biophy Acta* (2015) **1850**:536–53. doi: 10.1016/j.bbagen.2014.05.021
60. Meyer TE, Kyndt JA, Memmi S, Moser T, Colon-Acevedo B, Devreese B, et al. The growing family of photoactive yellow proteins and their presumed functional roles. *Photochem Photobiol Sci.* (2012) **11**:1495–514. doi: 10.1039/c2pp25090j
61. Vierstra RD, Zhang J. Phytochrome signaling: solving the Gordian knot with microbial relatives. *Trends Plant Sci.* (2011) **16**:417–26. doi: 10.1016/j.tplants.2011.05.011
62. Losi A, Gärtner W. Old chromophores, new photoactivation paradigms, trendy applications: flavins in blue light-sensing photoreceptors? *Photochem Photobiol.* (2011) **87**:491–510. doi: 10.1111/j.1751-1097.2011.00913.x
63. Jenkins GI. The UV-B photoreceptor UVR8: from structure to physiology. *Plant Cell* (2014) **26**:21–37. doi: 10.1105/tpc.113.119446
64. Vaidya AT, Chen CH, Dunlap JC, Loros JJ, Crane BR. Structure of a light-activated LOV protein dimer that regulates transcription. *Science Signal.* (2011) **4**:ra50. doi: 10.1126/scisignal.2001945
65. Circolone F, Granzin J, Jentzsch K, Drepper T, Jaeger K, Willbold D, et al. Structural basis for the slow dark recovery of a full-length LOV protein from *Pseudomonas putida*. *J Mol Biol.* (2012) **417**:362–74. doi: 10.1016/j.jmb.2012.01.056
66. Takala H, Bjorling A, Berntsson O, Lehtivuori H, Niebling S, Hoernke M, et al. Signal amplification and transduction in phytochrome photosensors. *Nature* (2014) **509**:245–8. doi: 10.1038/nature13310

67. Crosson S, Moffat K. Photoexcited structure of a plant photoreceptor domain reveals a light-driven molecular switch. *Plant Cell* (2002) **14**:1067–75. doi: 10.1105/tpc.010475
68. Endres S, Granzin J, Circolone F, Stadler A, Krauss U, Drepper T, et al. Structure and function of a short LOV protein from the marine phototrophic bacterium *Dinoroseobacter shibae*. *BMC Microbiol.* (2015) **15**:30, doi: 10.1186/s12866-015-0365-0
69. Fedorov R, Schlichting I, Hartmann E, Domratcheva T, Fuhrmann M, Hegemann P. Crystal structures and molecular mechanism of a light-induced signaling switch: the phot-LOV1 domain from *Chlamydomonas reinhardtii*. *Biophys J.* (2002) **84**:2474–82. doi: 10.1016/S0006-3495(03)75052-8
70. Jung A, Reinstein J, Domratcheva T, Shoeman RL, Schlichting I. Crystal structures of the AppA BLUF domain photoreceptor provide insights into blue light-mediated signal transduction. *J Mol Biol.* (2006) **362**:717–32. doi: 10.1016/j.jmb.2006.07.024
71. Jung YO, Lee JH, Kim J, Schmidt M, Moffat K, Srajer, V, et al. Volume-conserving trans–cis isomerization pathways in photoactive yellow protein visualized by picosecond X-ray crystallography. *Nat Chem.* (2013) **5**:212–20. doi: 10.1038/nchem.1565
72. Kort R, Hellingwerf KJ, Ravelli RBG. Initial events in the photocycle of photoactive yellow protein. *J Biol Chem.* (2004) **279**:26417–24. doi: 10.1074/jbc.M311961200
73. Möglich A, Moffat K. Structural basis for light-dependent signaling in the dimeric LOV domain of the photosensor YtvA. *J Mol Biol.* (2007) **373**:112–26. doi: 10.1016/j.jmb.2007.07.039
74. Salom D, Lodowski DT, Stenkamp RE, Trong IL, Golczak M, Jastrzebska B, et al. Crystal structure of a photoactivated deprotonated intermediate of rhodopsin. *Proc Natl Acad Sci USA.* (2006) **103**:16123–8. doi: 10.1073/pnas.0608022103
75. Zeng X, Ren Z, Wu Q, Fan J, Peng P, Tang K, et al. Dynamic crystallography reveals early signalling events in ultraviolet photoreceptor UVR8. *Nat Plants* (2015) **1**:14006. doi: 10.1038/nplants.2014.6
76. Zoltowski BD, Schwerdtfeger C, Widom J, Loros JJ, Bilwes AM, Dunlap JC, et al. Conformational switching in the fungal light sensor vivid. *Science* (2007) **316**:1054–7. doi: 10.1126/science.1137128
77. Brudler R, Gessner CR, Li S, Tyndall S, Getzoff ED, Woods JrVL. PAS domain allostery and light-induced conformational changes in photoactive yellow protein upon I2 intermediate formation, probed with enhanced hydrogen/deuterium exchange mass spectrometry. *J Mol Biol.* (2006) **363**:148–60. doi: 10.1016/j.jmb.2006.07.078
78. Hoff WD, Xie A, Van Stokkum IH, Tang X, Gural J, Kroon AR, et al. Global conformational changes upon receptor stimulation in photoactive yellow protein. *Biochemistry* (1999) **38**:1009–17. doi: 10.1021/bi980504y
79. Craven CJ, Derix NM, Hendriks J, Boelens R, Hellingwerf KJ, Kaptein, R. Probing the nature of the blue-shifted intermediate of photoactive yellow protein in solution by NMR: hydrogendeuterium exchange data and pH studies. *Biochemistry* (2000) **39**:14392–9. doi: 10.1021/bi001628p
80. Lee C, Malzahn E, Brunner M, Mayer MP. Light-induced differences in conformational dynamics of the circadian clock regulator VIVID. *J Mol Biol.* (2014) **426**:601–10. doi: 10.1016/j.jmb.2013.10.035
81. Zoltowski BD, Crane BR. Light activation of the LOV protein vivid generates a rapidly exchanging dimer. *Biochemistry* (2008) **47**:7012–9. doi: 10.1021/bi8007017
82. Harper SM, Neil LC, Gardner KH. Structural basis of a phototropin light switch. *Science* (2003) **301**:1541–4. doi: 10.1126/science.1086810
83. Winkler A, Barends TRM, Udvarhelyi A, Lenherr-Frey D, Lomb L, Menzel A, et al. Structural details of light activation of the LOV2-based photoswitch PA-Rac1. *ACS Chem Biol.* (2015) **10**:502–9. doi: 10.1021/cb500744m
84. Yao X, Rosen MK, Gardner KH. Estimation of the available free energy in a LOV2-J alpha photoswitch. *Nat Chem Biol.* (2008) **4**:491–7. doi: 10.1038/nchembio.99
85. Udvarhelyi A, Domratcheva T. Glutamine rotamers in BLUF photoreceptors: a mechanistic reappraisal. *J Phys Chem B* (2013) **117**:2888–97. doi: 10.1021/jp400437x
86. Barends TR, Hartmann E, Griese JJ, Beitlich T, Kirienko NV, Ryjenkov DA, et al. Structure and mechanism of a bacterial light-regulated cyclic nucleotide phosphodiesterase. *Nature* (2009) **459**:1015–8. doi: 10.1038/nature07966
87. Winkler A, Udvarhelyi A, Hartmann E, Reinstein J, Menzel A, Shoeman RL, et al. Characterization of elements involved in allosteric light regulation of phosphodiesterase activity by comparison of different functional BlrP1 states. *J Mol Biol.* (2014) **426**:853–68. doi: 10.1016/j.jmb.2013.11.018
88. Masuda S, Bauer CE. AppA is a blue light photoreceptor that antirepresses photosynthesis gene expression in *Rhodobacter sphaeroides*. *Cell* (2002) **110**:613–23. doi: 10.1016/S0092-8674(02)00876-0
89. Heintz U, Meinhart, A, Winkler A. Multi-PAS domain mediated protein oligomerisation of PpsR from *Rhodobacter sphaeroides*. *Acta Crystallogr D Biol Crystallogr.* (2014) **D70**:863–76. doi: 10.1107/S1399004713033634
90. Grinstead JS, Hsu SD, Laan W, Bonvin AMJJ, Hellingwerf KJ, Boelens R, et al. The solution structure of the AppA BLUF domain: insight into the mechanism of light-induced signaling. *Chembiochem* (2006) **7**:187–93. doi: 10.1002/cbic.200500270
91. Pan Y, Brown L, Konermann L. Hydrogen exchange mass spectrometry of bacteriorhodopsin reveals light-induced changes in the structural dynamics of a biomolecular machine. *J Am Chem Soc.* (2011) **133**:20237–44. doi: 10.1021/ja206197h
92. Khanal A, Pan Y, Brown LS, Konermann L. Pulsed hydrogen/deuterium exchange mass spectrometry for time-resolved membrane protein folding studies. *J Mass Spectrom.* (2012) **47**:1620–6. doi: 10.1002/jms.3127
93. Diensthuber RP, Bommer M, Gleichmann T, Möglich A. Full-length structure of a sensor histidine kinase pinpoints coaxial coiled coils as signal transducers and modulators. *Structure* (2013) **21**:1127–36. doi: 10.1016/j.str.2013.04.024

Conflict of Interest Statement: The authors declare that the research was conducted in the absence of any commercial or financial relationships that could be construed as a potential conflict of interest.

frontiers in Molecular Biosciences

HYPOTHESIS AND THEORY
published: 03 November 2015
doi: 10.3389/fmolb.2015.00062

A proposal for a dipole-generated BLUF domain mechanism

Tilo Mathes[1,2] *and Jan P. Götze*[3]*

[1] Biophysics Group, Department of Physics and Astronomy, Faculty of Sciences, Vrije Universiteit, Amsterdam, Netherlands, [2] Institut für Biologie/Experimentelle Biophysik, Humboldt Universität zu Berlin, Berlin, Germany, [3] School of Chemistry, University of St Andrews, St Andrews, UK

The resting and signaling structures of the blue-light sensing using flavin (BLUF) photoreceptor domains are still controversially debated due to differences in the molecular models obtained by crystal and NMR structures. Photocycles for the given preferred structural framework have been established, but a unifying picture combining experiment and theory remains elusive. We summarize present work on the AppA BLUF domain from both experiment and theory. We focus on IR and UV/vis spectra, and to what extent theory was able to reproduce experimental data and predict the structural changes upon formation of the signaling state. We find that the experimental observables can be theoretically reproduced employing any structural model, as long as the orientation of the signaling essential Gln63 and its tautomer state are a choice of the modeler. We also observe that few approaches are comparative, e.g., by considering all structures in the same context. Based on recent experimental findings and a few basic calculations, we suggest the possibility for a BLUF activation mechanism that only relies on electron transfer and its effect on the local electrostatics, not requiring an associated proton transfer. In this regard, we investigate the impact of dispersion correction on the interaction energies arising from weakly bound amino acids.

Keywords: BLUF, flavin, signal transduction, protein structure, electron transfer

OPEN ACCESS

Edited by:
Bela Mulder,
FOM Institute AMOLF, Netherlands

Reviewed by:
Litao Sun,
The Scripps Research Institute, USA
Shinji Masuda,
Tokyo Institute of Technology, Japan

***Correspondence:**
Jan P. Götze
jpg9@st-andrews.ac.uk

Specialty section:
This article was submitted to Biophysics, a section of the journal Frontiers in Molecular Biosciences

Received: *14 May 2015*
Accepted: *12 October 2015*
Published: *03 November 2015*

Citation:
Mathes T and Götze JP (2015) A proposal for a dipole-generated BLUF domain mechanism. Front. Mol. Biosci. 2:62. doi: 10.3389/fmolb.2015.00062

BLUF PHOTORECEPTORS

Flavins as Chromophores in Biological Photoreceptors

Most biological organisms depend on the ability to evaluate ambient light levels to face environmental challenges and to adjust their behavior and metabolism appropriately. These sensory mechanisms are especially crucial for plants or photosynthetically active bacteria. Various molecular solutions and mechanisms have been described over the years, which allow for a reaction to different light levels and qualities. A group of blue light receptor proteins employ flavin chromophores and are classified as cryptochromes (cry), light-oxygen-voltage (LOV), and blue light sensing using FAD (BLUF) photoreceptors. These proteins regulate gene expression and enzyme activities via a ubiquitously available cofactor, thus being interesting targets for the field of optogenetics; for corresponding reviews (see Losi, 2007; Hegemann, 2008; Möglich et al., 2010; Losi and Gärtner, 2012). The photoreceptor domains form a sheath around the flavin photosensor and translate light into biological information upon excitation of the chromophore. The flavin molecules used in these photoreceptors are riboflavin (RF, vitamin B_2) derived cofactors namely flavin-mononucleotide (FMN) and flavin-adenine-dinucleotide (FAD). A simpler flavin is lumiflavin (LF), which is the model compound primarily used in computational studies. The

photochemistry of all these compounds is almost exclusively determined by the isoalloxazine moiety and widely considered to be identical in BLUF domains (Laan et al., 2004).

As the employed chromophore is identical, any difference in photochemistry between the flavin-based photoreceptors (cry, LOV, and BLUF) must arise from the protein environment. Hence, the dynamic nature of chromophore-protein interaction is a matter of utmost interest, as insight into this relationship would allow scientists to rationally design and control sensitivity, quantum yield, and receptor-target interaction for optogenetic application and synthetic biology. As this information is sometimes problematic to obtain experimentally, computational methods provide very attractive approaches with molecular resolution to investigate the corresponding parts/modules of the given protein.

The general principle of a protein photoreceptor domain is rather simple: The chromophore/protein complex must be able to switch upon excitation of the chromophore from an equilibrium conformation, the resting state[1], to a metastable signaling state that is present for a certain amount of time before relaxing back to the resting state (**Figure 1A**). Depending on the photoreceptor domain at hand, the conformational change is facilitated by a different photochemical reaction. A common concept is light induced electron transfer (ET) from the protein environment to the flavin chromophore itself. Excited flavins either in the singlet or even more so in the triplet excited state represent efficient electron acceptors (Porcal et al., 2003) that receive electrons from aromatic amino acids like tyrosine and tryptophan (cry and BLUF; Gauden et al., 2007; Song et al., 2007) or the sulfur atom of cysteine side chains (LOV; Holzer et al., 2002). The photocycles of the different receptor domains diverge after this initial electron transfer: In cry radical states are stabilized; in BLUF domains, the hydrogen bond network is reordered without any chemical change of the flavin chromophore; and LOV domains form a covalent bond to the protein environment through a cysteinyl-flavin adduct. For more details, we point to Möglich et al. (2010) and references therein.

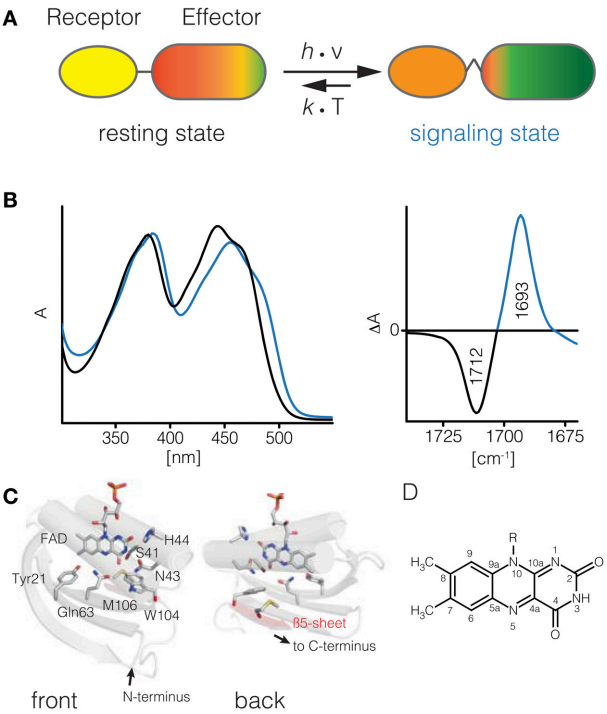

FIGURE 1 | BLUF photoreceptors. Upon illumination of the BLUF domain (receptor) structural changes are transmitted to its cognate effector domain and induce an increased activity **(A)**. These structural changes thermally relax into the resting state. The UV/vis spectrum of BLUF domains shifts by about 10–15 nm to red upon illumination **(B)**. In the signaling-minus-resting state FTIR difference spectrum a characteristic downshift of the C4 = O carbonyl signature is observed **(C)**. Structural model of the AppA BLUF domain and topology map (**D**, PDB ID 1YRX). Isoalloxazine moiety of flavin cofactors **(E)**.

Photoswitching in Bluf Domains

Here, we will focus on the modular blue light sensing using FAD (BLUF) photoreceptors. Their function has been first described in 2002 (Gomelsky and Klug, 2002; Iseki et al., 2002), and substantial progress has been made since then to elucidate the molecular events following flavin excitation and subsequent communication to the effector domain/protein. BLUF domains require a single flavin excitation event to form the signaling state conformation that has a half-life from few seconds up to tens of minutes. This signaling state conformation is represented by a subtle rearrangement of the hydrogen bonding network around the flavin. The redox state of the flavin in the signaling state remains identical to the resting state, making the BLUF domain possibly the chemically simplest and probably most intriguing blue light receptor domain. The signaling state differs from the resting state in several well-documented aspects consistent throughout the so far investigated BLUF domains (Kennis and Mathes, 2013): The UV/vis spectrum of the signaling state is shifted by 0.1–0.15 eV to lower energies, corresponding to a shift of 10–15 nm of the first bright $\pi \rightarrow \pi^*$ transition to longer wavelengths (**Figure 1B**). The most prominent feature of the IR spectrum is the downshift of the FMN(C4 = O4) stretch peak by about 20 cm^{-1} in the signaling state, indicating a strong change in hydrogen bonding to this particular functional group (**Figures 1C,E**). These observations are consistent throughout all investigated BLUF domains and have as such been used as a primary quality criterion for computational studies (see Computational Studies on BLUF). To accomplish this photochromic shift two conserved residues, Tyr21 and Gln63, are required.

Molecular Models of Bluf Domains

For BLUF domains several molecular models based on X-ray crystallographic and NMR spectroscopic data have been available since 2005 (Anderson et al., 2005; Jung et al., 2005, 2006; Kita et al., 2005; Grinstead et al., 2006; Yuan et al., 2006; Barends et al., 2009; Wu and Gardner, 2009; Winkler et al., 2013).

[1]Resting/signaling state is the notation which will be used throughout the article, in contrast to the commonly used "dark/light" terminology; we seek to avoid confusion with optically "dark" or "bright" electronic states.

Yet, for BLUF domains, the structural data sparked significant controversy as molecular models of even the same BLUF protein provided ambiguous geometries. The BLUF architecture comprises roughly 100–110 amino acids in size, up to 140 if the C-terminal capping α-helices are included. The common secondary structure motif is a Ferredoxin-like $\beta\alpha\beta\beta\alpha\beta\beta$ fold. The β-motifs form an anti-parallel β-sheet, which together with the two core α-helices encapsules the FMN chromophore via non-covalent interactions (see **Figure 1D**).

In the so far available crystal structures of the AppA BLUF domain significant differences have been observed for the conformation of the Trp104 residue, which was reported to be located either close/proximal (Trp-in; Anderson et al., 2005) to the FMN or located on the surface/distal to the chromophore (Trp-out; Jung et al., 2006) of the BLUF domains. The Trp-in conformation is found for the WT BLUF domain while the Trp-out conformation is present in an N-terminal mutant in the presence of high concentrations of β-mercaptoethanol and in the full-length protein (Winkler et al., 2013). Accordingly, the Trp side chain conformation is either in the range for formation of a N_ε-H hydrogen bond to Gln63(O), or it is found on the surface of the β-sheet, partially exposed to the surface. Note that "surface exposition" is not identical to "solvent exposition," the β-sheet is known to be either a dimerization interface (Anderson et al., 2005; Jung et al., 2005, 2006; Wu and Gardner, 2009) or protected from the solvent by the C-terminal capping helices (Kita et al., 2005; Yuan et al., 2006; Barends et al., 2009). Other BLUF domains like BlrB, TePixD, and SyPixD, which are present as dimeric (BlrB) or decameric (PixD) complexes in the crystal and solution show predominantly the Trp-out conformation. Despite the wide variety of available structures, most theoretical studies focus on the AppA BLUF domain as will be discussed below.

A more subtle yet crucial ambiguity is the side-chain conformation of Gln63. The resolution of the currently available crystal structures is not sufficient to distinguish between the amidic oxygen and nitrogen. Therefore, different conformations based on the proposed hydrogen bond pattern from Gln63 to Trp104 and from Tyr21 to Gln63 were proposed.

So far, no crystal or NMR structure prepared under light-adapted conditions has been reported. However, it is still conceivable that some of the reported dark-adapted structures contain features of the light-adapted state due to crystal packing, conformational selection by crystallization or photoactivation by synchrotron radiation. Some crystals were investigated by micro-UV-vis-spectrophotometry to demonstrate photoswitching functionality and dark state conformation (Jung et al., 2006). However, as the photochromic switch may be decoupled from the signal transduction (see discussion on signal transduction below), the UV/vis spectral properties may provide a misleading picture. Additionally, crystal structures recorded at cryogenic temperature may exhibit different side chain conformations than under RT conditions relevant for most spectroscopic investigations (Fraser et al., 2011).

In addition to studies involving the full protein, tryptophan, and tyrosine residues have been probed selectively by steady state NMR and UV resonance Raman spectroscopy corroborating the Trp-in position for the resting state in the truncated AppA BLUF domain (Grinstead et al., 2006; Unno et al., 2006, 2010). NMR spectroscopy, however, also showed that the region harboring Trp104 and Met106 is very flexible and generally influenced by the hydrogen bond network around the flavin (Grinstead et al., 2006; Wu et al., 2008; Yuan et al., 2011). Another commonly used approach for probing the conformation and environment of tryptophan residues in proteins is tryptophan fluorescence spectroscopy (Reshetnyak et al., 2001). These investigations showed that the environment of Trp104 depends on the length of the C-terminal truncation in AppA-BLUF constructs but does not change strongly upon formation of the signaling state and clearly does not become fully solvent exposed as suggested by some crystal structures (Toh et al., 2008; Dragnea et al., 2009). These studies, however, differ in their conclusions whether Trp104 is located in proximal Trp-in (Toh et al., 2008) or distal Trp-out location to the flavin (Dragnea et al., 2009). Similarly, no significant change in the tryptophan environment was observed for SyPixD (Yuan et al., 2011).

Selective isotope labeling of the tyrosine side chain in AppA and TePixD provided indirect information on the orientation of the hydrogen bonded glutamine residue. The presence of an unusually strong hydrogen bond donated from Tyr-21 in the signaling state of AppA was interpreted as incompatible with hydrogen bonding to the glutamine side chain amidic nitrogen (Iwata et al., 2011), while a previous study on TePixD concluded that both dark and light state properties of tyrosine are compatible with H-bonding to oxygen but could not fully exclude alternative orientations (Takahashi et al., 2007). A study on SyPixD with a different tyrosine isotope labeling pattern gave similar results and clearly showed that the structural changes are confined to the phenolic hydroxyl group without any changes to the aromatic nature of the phenyl ring (Mehlhorn et al., 2013).

Signal Transduction in Bluf Domains

On top of these apparent controversies on the tryptophan/methionine orientation also its relevance of for signal transduction remains to be considered. Biochemical and physiological experiments that investigate signal transduction of BLUF photoreceptors by using site-directed mutations provided inconsistent effects within the BLUF protein family. In AppA, the removal of Trp104 or Met106 each disrupt the signaling process *in vivo*, while the light-induced formation of the red shifted signaling state is not affected (Masuda et al., 2007). Similar results have been obtained for the bacterial photoactivated adenlylyl cyclase (bPAC), where signaling and photochemistry are also clearly decoupled by the corresponding mutations (Stierl et al., 2014). However, in other BLUF domains that also contain the semi-conserved tryptophan only the conserved Met106 is crucial for signaling (Masuda et al., 2008). Replacement of Trp104, however, has a significant effect on the structural dynamics and stability of the light-adapted state. In AppA, the Trp104Ala or Trp104Phe mutation reduces the stability of the signaling state, which is also witnessed by the absence of a secondary structure change involving the β5 sheet in light-minus-dark FTIR difference spectra (Masuda et al., 2005a; Majerus et al., 2007). Confusingly, the analogous mutations in SyPixD and

bPAC lead to stabilization, by exchange to Phe, or destabilization, by exchange to Ala, of the red shifted signaling state (Mathes, 2007; Bonetti et al., 2009; Stierl et al., 2014).

In this regard it should also be noted that even some variants lacking essential residues like the conserved glutamine or tyrosine still show light-induced signaling, however to significantly smaller extent (Metz et al., 2010; Stierl et al., 2014). These observations suggest that already the formation of radical intermediates in BLUF domains may be sufficient to drive signal transduction. Similar implications have been recently obtained by time resolved spectroscopic studies (Fujisawa et al., 2014; Fudim et al., 2015).

Photodynamics of Bluf Domains

Although steady state data are usually very robust and informative, they may be of very limited use for the elucidation of reaction mechanisms. The ultrafast hydrogen-bond rearrangement in BLUF domains in less than 1 ns (as indicated by the red shifted absorbance of the flavin) requires pump-probe spectroscopy and is limited to optical methods. A particular feature of the BLUF photodynamics is a highly multi-exponential excited state decay behavior (Dragnea et al., 2005; Gauden et al., 2005, 2006; Bonetti et al., 2008, 2009; Shibata et al., 2009; Mathes et al., 2011, 2012a), indicating a structural microheterogeneity in the resting state, which is most likely due to minor variations of the mutual flavin/tyrosine orientation. Depending on the BLUF domain at hand the observable excited state lifetimes range from few ps up to several ns and severely limit experimental access to reaction intermediates that are formed with faster (inverted) kinetics. So far in only two BLUF proteins, SyPixD and PapB, reaction intermediates have been identified (Gauden et al., 2006; Fujisawa et al., 2014). Both proteins show the formation of a neutral flavin semiquinone radical that decays into the red-shifted signaling state. For SyPixD also an anionic semiquinone radical intermediate preceding the formation of the neutral form has been observed that illustrates a strictly sequential electron transfer (ET) proton transfer (PT) process. In addition, a signature for the corresponding electron donor (Tyr21) has been obtained by transient IR spectroscopy (Bonetti et al., 2008). The significance for these intermediates for signaling state generation has been challenged recently (Lukacs et al., 2014) but is strongly supported by site-directed mutagenesis and redox tuning of the tyrosine electron donor, that directly affects the rate of electron transfer and the quantum yield of signaling state formation (Mathes et al., 2012a). Moreover, removal of the central glutamine residue leads to a two-orders of magnitude increase of the lifetime of the initially formed spin correlated radical pair, thus corroborating the importance of proton coupled electron transfer (PCET) in the BLUF photocycle (Fudim et al., 2015).

In addition to the resting state photodynamics, also the excited state dynamics and potential photochemical reactions of the signaling state provide information on the changed environment of the chromophore. BLUF domains form the same neutral tyrosyl/flavin radical from the red-shifted state, however with different reaction rates (Toh et al., 2008; Mathes et al., 2012b). In SyPixD the formation is significantly faster and takes place in a seemingly concerted manner. This indicates that the hydrogen bond network in the signaling state of SyPixD is preconfigured for efficient proton transfer to the flavin. Moreover, the initial excited state decay is less heterogeneous, thus indicating a more defined and tighter coordination of flavin and tyrosine in the light-adapted state (Shibata et al., 2009; Mathes et al., 2012b). Similar experiments have been carried out for PapB but tell a slightly different story (Fujisawa et al., 2014). Here, formation of the neutral radical intermediate appears equally fast for light- and dark-adapted states and suggests that the hydrogen bond rearrangement is already accomplished before the formation of the neutral radical. These results suggest that already the formation of a Tyr/FAD charge transfer state may be sufficient to drive the H-bond rearrangement in the flavin binding pocket.

So far, these insights into the dynamics of the photoreaction only provided indirect information on the structural changes involving Gln63 and Trp104. Implications on the Trp orientation have been found for AppA which shows a significant competing, yet signaling incapable ET reaction from Trp104 that leads to a decreased signaling state quantum yield (Laan et al., 2006; Gauden et al., 2007). In SyPixD no competing ET from the corresponding tryptophan has been observed unless the central glutamine is removed (Fudim et al., 2015). For AppA these results suggest that Trp104 is in a proximal position (Trp-in) to the flavin, thus allowing efficient ET. For SyPixD the situation is ambiguos since both Trp conformations (in/out) observed in the crystal structure, are more distant to the flavin than Trp104 in AppA. Moreover, ET from Tyr in SyPixD is significantly faster than in AppA and most likely outperforming Trp also in the Trp-in conformation.

The orientation of the glutamine residue is even more difficult to address based on the currently available spectroscopic data. Even though infrared spectroscopy is in principle capable of detecting the vibrational signature of the glutamine side chain, the strong overlap with the flavin signatures so far prevented any conclusive assignment (Stelling et al., 2007; Bonetti et al., 2008). In the discussion of an early time resolved spectroscopy study on AppA the idea of a tautomerized glutamine has been put forward (Stelling et al., 2007) as an alternative to the already existing rotation mechanism (Gauden et al., 2006) and has been picked up subsequently by computational approaches (Domratcheva et al., 2008; Sadeghian et al., 2008, 2010; Khrenova et al., 2013; Udvarhelyi and Domratcheva, 2013). While tautomeric intermediates are conceivable for the ultrafast reactions, especially in the light-adapted state (Mathes et al., 2012b), their relevance for the long living signaling state remains dubious due to the 10–15 kcal/mol relative instability over the amidic form. Any stabilizing effect of the protein environment for such a species has yet to be found and is an interesting matter for future computational studies.

Spectrally Silent Reactions

Although ultrafast spectroscopy showed that the prerequisites for the red-shifted state are already met in less than a nanosecond after excitation, further structural processes that are spectrally silent take place on longer timescale. These changes are likely important for maintaining the signaling relevant

conformation for ∼10 orders of magnitude longer than its formation. Unfortunately, very limited information is available on any relevant structural changes. In a time resolved FTIR study on the dark recovery of AppA a protonation change of an aspartate residue, most likely the conserved Asp82, was observed on the μs time scale (Majerus et al., 2007) and shows clearly that also peripheral structural changes other than those at the β5 sheet contribute to the stabilization of the signaling state (**Figure 1D**). Larger scale conformational and oligomeric changes, that have so far been often too challenging to be covered by computational approaches, were observed by transient grating (TG) spectroscopy. Using this technique dimerization or dissociation events were observed (Hazra et al., 2006, 2008; Nakasone et al., 2007, 2010; Tanaka et al., 2009, 2011a,b, 2012; Toyooka et al., 2011) that do not necessarily coincide temporally with the formation or decay of the red shifted signaling state but are dependent on the presence of the conserved methionine residue (Tanaka et al., 2011b).

COMPUTATIONAL STUDIES ON BLUF

Here, we summarize the computational approaches, which have addressed these open questions of BLUF domains. The topics covered by those articles are numerous: The Trp conformation is a leading theme for most theoretical studies, but many have ventured further, proposing photocycles (Sadeghian et al., 2008, 2010; Khrenova et al., 2010), structures of intermediates (Domratcheva et al., 2008; Khrenova et al., 2011b), conical intersections (Udvarhelyi and Domratcheva, 2011), and even signal transduction pathways (Khrenova et al., 2011a). These accomplishments have to be acknowledged in the light of the several different time scales on which BLUF events are occurring. The initial excitation process takes only femtoseconds (Frank Condon region), and thus needs treatment completely different from the conformational change of the domain as a whole, which requires up to several hundreds of picoseconds (see above). One has to find the appropriate trade-off between accuracy and computational cost for each of these time scales anew. The fact that we are dealing in several cases with excited state properties is another issue which should be kept in mind, as those properties are computationally much more expensive than ground state properties.

Computational Investigation of the Bluf Structure

In the past 10 years, several crystallographic, NMR- and vibrational spectroscopic studies have been reported, which aimed at elucidating the molecular details of resting and/or signaling state structure of BLUF domains (see above). However, the assignment to actual orientations of individual amino acids remains contradictory (**Figure 2**). At least three different (semi-)conserved and functionally relevant amino acids have undefined positions/conformations: Gln63, which is required for the photocycle; and the Trp104/Met106 pair, which is found at different positions in the reported structures (Anderson et al., 2005; Jung et al., 2006). Other amino acids, like Ser41 (Götze and Saalfrank, 2009) and Asn45 (Sadeghian et al., 2008) have been proposed to play a role as well, but those ideas and the associated mechanisms are not as established (and probably not as important) as the basic Gln63/Trp104/Met106 (QWM) triad outlined above. It should be noted that while there are no functional studies on Asn45 available, Ser41 in contrast has been demonstrated to affect ground state spectroscopic properties and dark activity of a BLUF regulated enzyme (Stierl et al., 2014). Interestingly, the quantum yield of signaling state formation is not affected (Bonetti et al., 2009).

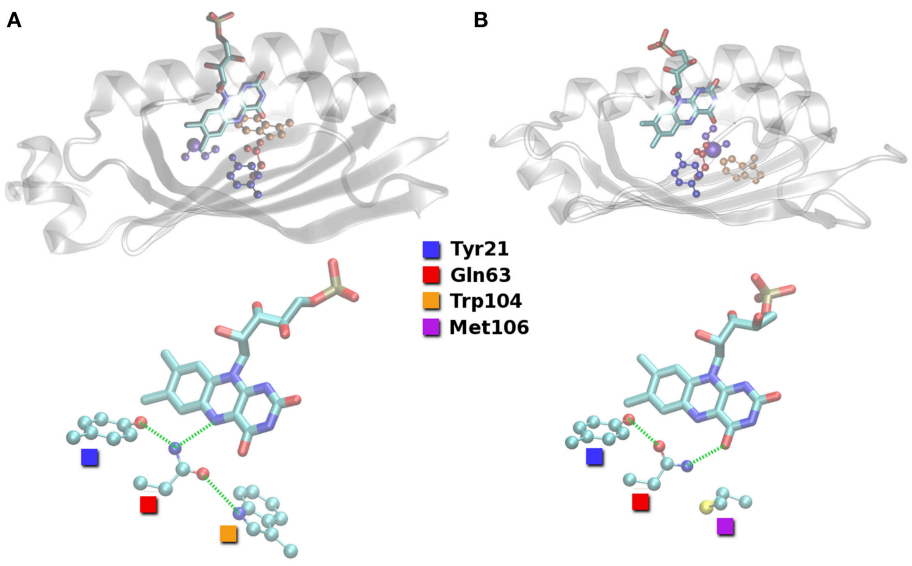

FIGURE 2 | Hydrogen bond arrangements close to the FMN compound as found in the putative resting state crystal structures of BLUF domains. (A) Structure of Anderson et al. (2005; PDB ID 1YRX). **(B)** Structure of Jung et al. (2006; PDB ID 2IYG). Hydrogen bond interactions indicated with green dashed lines.

The different orientations of the QWM triad are defined by the hydrogen bonding between the Trp104/Met106 pair and Gln63. It is easy to see from **Figure 2** that Gln63 is able to accept a hydrogen bond from Trp104 close to FMN (Trp-in). On the other hand, Gln63 is probably a hydrogen bond donor to Met106 inside the binding pocket (Trp-out). It is thus obvious that the region around Trp104/Met106 is flexible to some extent and relevant for signal transduction.

Although a variety of different computational studies have been performed, the comparability between these studies is unfortunately limited due to several reasons: First of all, the variation of BLUF amino acid sequences should be considered. This can be of minor concern, considering exchanges in the terminal or surface areas of the protein, but may also directly influence the comparability of the QM models (like His44 exchanged by arginine in, e.g., BlrB; Zirak et al., 2006, 2007). Hardly comparable to the other published BLUF domain models are studies based on BlrP BLUF (Tyagi et al., 2008; Barends et al., 2009; Wu and Gardner, 2009), since BlrP features a threonine residue instead of Trp104. In general, comparisons between systems with significant sequence deviations should be avoided, both theoretically and experimentally.

A related issue is the variance in the construct length/model size of the BLUF domain. The N-terminal ends are generally neglected, as they are very flexible, and hardly resolved in NMR or X-ray structures. Moreover, a recent experimental work reported the BLUF N-terminus to be of minor importance (Unno et al., 2012). The C-terminus, however, may differ with regards to the presence of the capping α-helices, which follow the β-sheet motif in the BLUF sequence. Those helices are found to be the linker element to the effector domain when applicable (Barends et al., 2009; Khrenova et al., 2011a; Winkler et al., 2013). If present in the BLUF domain crystal, those helices effectively shield the (usually more hydrophobic) β-sheet from the solvent. It should also be noted that the capping helices are differently oriented relative to the β-sheet depending on the BLUF domain at hand (Kita et al., 2005; Yuan et al., 2006; Barends et al., 2009; Wu and Gardner, 2009; Ren et al., 2012). Consequently, molecular dynamics simulations based on structures with those helices included can be expected to perform differently from those simulations which do not contain the C-terminal helices. Structurally resolved C-terminal helices are found in the crystal structures of TePixD (PDB ID 1X0P), SyPixD (PDB ID 2HFN), and all of the full length BlrP and AppA protein structures (Barends et al., 2009; Winkler et al., 2013). Some computational studies ignore the problem of varying sequence length by simply using the crystal structures as they are found in the PDB database (Domratcheva et al., 2008; Sadeghian et al., 2008; Hsiao et al., 2012); others cut the chains to analogous lengths to obtain constructs of equal size (Götze et al., 2012; Meier et al., 2012). As some BLUF domains occur in dimers or higher oligomers in solution (Hazra et al., 2006; Nakasone et al., 2007; Tanaka et al., 2009), another approach is to use dimeric models for those structures where the C-terminal helices are not reported and a dimerization interface is derived from the X-ray crystal structure (Rieff et al., 2011).

A possibly crucial, yet underappreciated issue is the amino acid protonation state. Crystal structures do not resolve hydrogen atoms, and NMR studies have been found to be contradictory in some regards (as discussed in Rieff et al., 2011). The resulting problem is two-fold: First, the signaling state Gln63 residue might be present in a tautomerized form (Stelling et al., 2007), which will be addressed below. Second, the histidine protonation state is undefined. Depending on the individual BLUF sequence, the reported structures contain up to five His residues (AppA: 5; BlrP: 4; BlrB, SyPixD, TePixD: 3). While the protonation state of buried residues may possibly be derived from the immediate environment, surface located His residues might either be fully protonated, depending on the pH, or vary between δ- or ε-protonated, neutral tautomers. Most modeling approaches in the past did not account for the possible variance in His protonation and assumed an arbitrary, static His protonation, with few exceptions (Rieff et al., 2011; Götze et al., 2012). The different His protonation schemes throughout the literature prevent for a direct 1:1 comparison of the individual results.

Finally, we would like to shift the focus away from the static atomic modeling problem to a dynamic view of the thermal BLUF movement. In the light of the MD studies conducted, which analyzed the hydrogen bonding probabilities inside the BLUF FMN binding pocket (Obanayama et al., 2008; Götze et al., 2012; Meier et al., 2012), the "on-off" picture of the QWM triad becomes more blurry, especially for the Trp-in conformations. In Götze et al. (2012), it was proposed that already the choice of the initial velocities can significantly influence the MD hydrogen bonding behavior of Gln63. While the results between the available MD studies are often not in line with each other (Obanayama et al., 2008; Meier et al., 2012), the diversity of results throughout the literature clearly indicates that a static, "zero Kelvin, QM only" view of the BLUF domain could be inappropriate for such a dynamic system. At least including temperature effects on a minimal level might be required in order to obtain meaningful results. For QM cluster models, a valid alternative would be to compare QM studies preferably to experimental low-temperature studies (see Fukushima et al., 2007, 2008).

Computational Approaches

From the previous section, it becomes clear that molecular models of BLUF domains are always associated with various assumptions. Despite these shortcomings, computational groups have made substantial progress regarding two core questions:

(i) *Photodynamics*: How are the different kinetic components of the photocycle related to physical processes in the protein matrix and the chromophore?
(ii) *Structure*: How are the different experimental characteristics combined to form a resting or signaling state conformation?

Since we focus below on the structural flexibility and spectroscopic properties of BLUF domains, there are some computational studies that we cannot take into account for our analysis. Those are the studies that do not provide explicit computations of hydrogen bonding probabilities and UV/vis or IR spectra (Ishikita, 2008; Nunthaboot et al., 2009, 2010).

The photodynamics research branch employs the Trp-out BLUF resting state conformation presented by Jung et al. (2005, 2006; PDB ID 2IYG). All models assume the Trp-in conformation as the signaling state. This assignment is supported by the full length structure of AppA, which displays a Trp-out conformation in the putative resting state (Winkler et al., 2013). However, there is a catch: Experimental evidence indicates a stronger hydrogen bond to FMN(O4) from the protein matrix in the signaling state, due to the drop of the FMN(C4)-FMN(O4) force constant upon signaling state formation (Masuda et al., 2005b). A stronger hydrogen bond cannot be explained by a chemically unaltered QWM triad, as Gln63 is required to present its oxygen atom toward Trp104 in a Trp-in-containing signaling state. Hence, the hydrogen bonding of Gln63(NH2) to FMN(O4) would be impossible.

To overcome this contradiction, Gln63 can be assumed to be a tautomer in the Trp-in signaling state (Stelling et al., 2007). This was first suggested by an experimental investigation (Stelling et al., 2007) with the caveat that the tautomer is expected to be about 10–15 kcal/mol less stable than the amide form. Imidic Gln63 is able to form (i) a donor hydrogen bond to FMN(O4) and (ii) an acceptor hydrogen bond to Trp104 at the same time. This would allow Gln63 in a Trp-in conformation to be a (possibly stronger) hydrogen bond donor to FMN(O4) than in the Trp-out resting state, consistent with the experiment. Yet, as tautomerized Gln63 is a possible hydrogen bond donor and acceptor on *both* the N and the O atoms, this feature is independent of the Gln63 rotational orientation. This rotation, which might or might not occur upon signaling state formation, is the central difference between the two models based on imidic Gln63 and a Trp-out resting state. The models presented by Domratcheva et al. include a Gln63 rotation during signaling state formation (Domratcheva et al., 2008; Khrenova et al., 2010, 2011b; Udvarhelyi and Domratcheva, 2011), while Sadeghian et al. assume a more rigid orientation of Gln63 at all times (Sadeghian et al., 2008, 2010). How this translates to differences in the proposed photocycles will be the topic of an individual section further below.

Structural Models

As a consequence from the QWM triad uncertainties, several groups tried to reproduce the experimental findings outlined above using calculated spectra and molecular dynamics. Since the observed shifts in UV/vis and IR signals are from a computational point of view rather small (about 0.1 eV or 20 cm^{-1}, respectively), only qualitative answers can be expected from these approaches. Concerning pure MD studies, which provide multiple ns trajectories of BLUF domains in different conformations, the reports by Khrenova and a study by Meier (Khrenova et al., 2011a; Meier and van Gunsteren, 2013) would fit into this group. However, there is no analysis of the hydrogen bonding patterns close to the flavin chromophore, as Khrenova et al. only feature hydrogen bonding patterns focused on the interaction of the BlrP BLUF domain and its target protein effector domain.

Unfortunately, the results of the remaining articles are hardly comparable. All other MD studies contain, possibly among others, the BLUF domains of PDB entries 1YRX and 2IYG (AppA Trp-in and Trp-out), but the reported hydrogen bonding patterns are very much different (see **Table 1**). The studies feature different force fields, equilibration protocols, run parameters, and histidine protonation states; it is therefore impossible to provide a convincing explanation for the strong disagreement of the data.

A second group of articles, partially overlapping with the first, is focusing on the generation of UV/vis and IR spectra from (post-processed) MD snapshots, X-ray or NMR data (Obanayama et al., 2008; Götze and Saalfrank, 2009; Rieff et al., 2011; Götze et al., 2012; Hsiao et al., 2012). Obanayama et al. (2008) belong to this group, although the presented spectra are based on a single structure, which is statistically problematic. Additionally, another study considers TD-DFT QM cluster spectra, based on NMR geometries, on manually

TABLE 1 | AppA BLUF hydrogen bonding patterns as displayed in Obanayama et al. (2008), Götze et al. (2012), and Meier et al. (2012).

Reference and year	Hydrogen bonding ratio/%							
	Tyr21(OH)–Gln63(O)		Gln63(NH)–FMN(O4)		Gln63(NH)–FMN(N5)			
	Trp-in	Trp-out	Trp-in	Trp-out	Trp-in	Trp-out		
Obanayama et al., 2008	80.0	62.7	33.8	10.0	16.1	28.0		
Meier et al., 2012[a]	0.0/0.0	4.5/92.8	81.4/45.2	50.4/76.9	44.7/56.4	53.1/17.8		
Götze et al., 2012[b]	25.0 ± 31.3	85.6 ± 6.2	5.0 ± 5.3	0.7 ± 0.6	1.2 ± 1.1	2.2 ± 1.2		
	Asn45(NH)–FMN(O4)		FMN(N3H)–Asn45(O)		Gln63(NH)–Tyr21(O)		Trp104(NH)–Gln63(O)	
	Trp-in	Trp-out	Trp-in	Trp-out	Trp-in	Trp-out	Trp-in	Trp-out
Meier et al., 2012[a]	84.7/94.0	2.0/15.8	86.6/86.8	77.5/94.1	93.0/99.2	0.1/0.0	54.0/90.1	0.0/0.0
Götze et al., 2012[b]	21.7 ± 6.7	16.1 ± 7.7	27.4 ± 7.7	34.9 ± 11.8	3.2 ± 7.9	0.0 ± 0.0	12.4 ± 20.2	0.0 ± 0.0

Hydrogen bond criteria, model construction and computational methodology may differ.

[a] *Two force fields (Gromos45A4/Gromos53A6) were used.*

[b] *Standard deviations from eight trajectories per model.*

created conformations and also MD snapshots (Götze and Saalfrank, 2009). A unique approach in structure generation is taken elsewhere, for which dynamic DFT/MM calculations are employed, obtaining IR spectra from protein dynamics (Rieff et al., 2011). Regarding the MD methodology, Rieff et al. (2011) is very close to the first group of articles; yet the authors do not present any hydrogen bonding patterns in their report. They do, however, find that the quality of the published NMR and X-ray structures is very heterogeneous, and conclude that the structures 1YRX and 2IYG represent the more reliable ones. Another article presents DFT/MRCI (Grimme and Waletzke, 1999) excitations on QM refined X-ray and artificial structures (Hsiao et al., 2012). Additionally to the trajectories discussed above for the data in **Table 1**, Götze et al. (2012) contains TD-DFT spectra on the basis of MD snapshots. A more recent member of this group contains data on both native and isomerized Gln63 (see next section) (Udvarhelyi and Domratcheva, 2013). Finally, the latest article trying to elucidate the structure of the BLUF resting state, features a simplified variant for reproducing exclusively the shifts of the UV/vis spectra upon changing the BLUF domain structure, e.g., by mutation (Collette et al., 2014).

Table 2 lists the calculated UV/vis and IR signals, for which a direct comparison between Trp-in and Trp-out is made within the same article. Experimental data are given for comparison, related to resting and signaling state. In Rieff et al. (2011), introduction of a polarizable force field essentially inverts the corresponding results for the IR spectrum, and the TD-DFT spectra of Götze et al. (2012) are non-conclusive. The results shown in (Götze and Saalfrank, 2009; Hsiao et al., 2012; Udvarhelyi and Domratcheva, 2013) agree that the Trp-in QWM triad displays a blue-shifted absorption spectrum compared to the Trp-out conformation. This notion is supported by Obanayama et al. (2008), although the data presented are based on a single structure only, as already indicated above. Note that the authors of Udvarhelyi and Domratcheva (2013) conclude that an imidic Gln63 residue is responsible for the signaling state (see below), and do not follow the assignment that we suggest here by the arrangement of **Table 2**.

The recent article by Collette et al. employs a different approach that does not lead to explicit values for the absorption wavelengths that could be compared to the other studies (Collette et al., 2014). Instead, they focus on the computation of the shifts that occur upon mutation, or the introduction of imidic Gln63 (iGln63) in different conformations. Their results unanimously prefer the Trp-in conformation to be the signaling state, due to the qualitative and quantitative comparability of the computed shifts to the experimental measurements. The authors have, however, not performed a thorough reoptimization of their structures before computing the shifts after insertion of the mutant/modified amino acid, thereby neglecting any influence that an exchange has on neighboring residues (or even further away from the point of exchange). As such, the data is drawn from a basis of BLUF domains in which the mutations have a strongly localized effect, and no effect on the overall protein or FMN conformation, which is not very likely.

Apart from this latest article in the field, it appears that the structural studies favor Trp-in to be the resting state; yet the hydrogen bonding patterns presented do not fully agree with each other and the calculated IR data are sparse. The computed UV/vis spectra are, however, consistent. In the following section we will discuss the influence of imidic Gln63.

TABLE 2 | AppA BLUF UV/vis and IR signals, as calculated throughout the literature from MD, NMR, or crystal structures.

Reference and Year	UV/vis maxima			
	First FMN $\pi \rightarrow \pi^*$		Second FMN $\pi \rightarrow \pi^*$	
	Trp-in	**Trp-out**	**Trp-in**	**Trp-out**
Obanayama et al., 2008	426 nm	435 nm	n/a	n/a
Götze and Saalfrank, 2009	448 nm	459 nm	339 nm	350 nm
Hsiao et al., 2012[a]	523 nm	575 nm	380 nm	405 nm
	441 nm	460 nm	355 nm	370 nm
Götze et al., 2012	438 nm	437 nm	347 nm	347 nm
Udvarhelyi and Domratcheva, 2013[b]	435 nm	(448 nm)	n/a	n/a
	443 nm	(444 nm)		
	432 nm	(437 nm)		
	Resting	**Signaling**	**Resting**	**Signaling**
Exp. Kraft et al., 2003	446 nm	458 nm	373 nm	378 nm

	IR FMN(C4 = O4) stretch	
	Trp-in	**Trp-out**
Obanayama et al., 2008	1700 cm^{-1}	1689 cm^{-1}
Rieff et al., 2011[c]	1750 cm^{-1}	1739 cm^{-1}
	1724 cm^{-1}	1733 cm^{-1}
	Resting	**Signaling**
Exp. Masuda et al., 2005b	1709 cm^{-1}	1695 cm^{-1}

Models with imidic Gln63 not included.

[a] *Hsiao et al. (2012) reports several other structures in qualitative agreement with the presented structures. MD structure reported here (second line) corresponds to QM refined X-ray structure with weighting factor $w_{xref} = 1$ (see reference, for details).*

[b] *Three different optimization restraint settings reported. No actual Trp-out structures, only rotated Gln63. In this study Trp-in is not considered to be the resting state.*

[c] *Reported values for static (upper line) and polarizable environment (lower line). Rieff et al. (2011) also reports rescaled values, about 20 cm^{-1} lower.*

Photocycle Models

Assuming Gln63 to form an imide (iGln63) upon FMN excitation provides an alternative to form hydrogen bonds to FMN(O4) in a Trp-in signaling state (see above). As no standard force field parameters for iGln63 are available, reported models of BLUF domains with iGln63 mostly rely on QM cluster or QM/MM approaches with iGln63 in the QM part (Domratcheva et al., 2008; Sadeghian et al., 2008, 2010; Khrenova et al., 2010, 2011b; Udvarhelyi and Domratcheva, 2011). Merz et al. (2011) technically belongs to that group as well, but investigates the effect of a FMN replacement by roseoflavin, and will therefore not be discussed further. Most photocycle studies discuss the Trp-in/Trp-out problem to some extent, but all presented models assume Trp-out (PDB ID 2IYG) to be the resting state, and

Trp-in is disregarded as a resting state candidate by initial comparison of structural and experimental data. Consequently, the focus of iGln63 models is not the Trp-in/Trp-out dilemma, but the photocycle of BLUF domains. A notable exception is reference (Udvarhelyi and Domratcheva, 2013), where the 1YRX Trp-in structure was used as the basis for a study involving iGln63.

Just as the structural articles of the last section, the reported excitation energies produce the required ∼10 nm shift in the UV/vis spectrum, despite the inverted conformation/state assignment. Furthermore, the calculated IR spectra display (for the most cases) the experimentally shown shift to lower energies in the FMN(C4 = O4) stretching vibration. On the downside, the second $\pi \rightarrow \pi^*$ excitation is rarely reported or discussed, and the computed UV/vis signals of the iGln63 models are overall shifted to higher energies. Extremely puzzling is that there is little overlap between **Table 2** and **Table 3** in the case of the Trp-out conformation although the chemical composition of the Trp-out cases is identical. Yet, the Trp-out values in **Table 3** are uniformly blue-shifted compared to the ones of **Table 2**. A probable reason is that QM methods differ significantly; in the articles summarized **Table 2**, mostly DFT based methods have been employed, while iGln63 models feature mostly CC2 or CASSCF-related calculations. As those are not the only differences, we again end up with the problem of comparability between the works of different groups, which already hampered our analysis before.

The greatest strength of the iGln63 models is that they provide possible photocycle mechanisms that relate to the experimentally observed PCET mechanism between Tyr21 and the flavin (see above). Computationally, a drop in energy is reported when following a Tyr21-Gln63 proton transfer in the lowest charge transfer state (CT) (Sadeghian et al., 2008). This CT may be populated by the bright $\pi \rightarrow \pi^*$ transition locally excited state (LE) of FMN. The proposed pathway involves the excitation of the LE state, crossing to the CT state and subsequent proton transfer from Tyr21(OH) to Gln63(O). The LE-CT conical intersection (CIn) close to the Franck-Condon (FC) region was structurally identified, having reduced Tyr21(OH)-Gln63(O) and Gln63(NH_2)-FMN(N5) hydrogen bond distances compared to the FC geometry (Udvarhelyi and Domratcheva, 2011). The initial proton transfer is followed by a second transfer from Gln63(NH_2) to FMN(N5), crossing back to a Tyr21$^{\bullet}$-iGln63-FMNH$^{\bullet}$ biradical ground state along the reaction coordinate. Here, the corresponding CIn was found to be structurally elusive.

Up to this point, the articles following the idea of an iGln63 are in agreement, afterwards the paths deviate: Sadeghian et al discard the possibility of Gln63 rotation, and they assume a Tyr21(O)-Gln63(O) hydrogen bond to be formed at all times. Assuming a *trans-cis*-isomerization of the iGln63(NH^-) group, the moiety is allowed to become a hydrogen bonding partner for FMN(O4). They find the *cis*-conformer of iGln63 to be more stable in a Trp-in conformation, and consequently assume conformational switching of Met106 and Trp104 upon formation of *cis*-iGln (Tanaka et al., 2009). They also investigated the possible conformations of a water molecule close to Tyr21, which was required for the Tyr21 conformation to remain stable (a possibly different reason is described in Rieff et al., 2011). Subsequently, a model for the events in the light-adapted state was proposed, explaining how the light-adapted conformation relaxes directly back to the ground state (Sadeghian et al., 2010). Two channels supposedly exist, based on either partial or complete, possibly concerted proton transfer involving Tyr21(OH), iGln63(OH^+), and FMN(N5). Both channels essentially recombine quickly to the ground state, explaining the photo-irreversibilty of the signaling state.

A different route was proposed by Domratcheva and coworkers. They proposed iGln63 rotation before or during the generation of the Trp-in conformation. This notion is based on structural arguments, supported by MD simulations and the corresponding QM/MM energies (Khrenova et al., 2011b). As already above, iGln63 essentially allows to form a hydrogen bond to FMN(O4) in both rotamers; therefore it might be very well possible that both mechanisms are taking place. Yet, it

TABLE 3 | BLUF UV/vis and IR signals, as calculated from imidic Gln63 models throughout the literature.

Reference and Year	UV/vis maxima			
	First FMN $\pi \rightarrow \pi^*$		Second FMN $\pi \rightarrow \pi^*$	
	Trp-out	**Trp-in**	**Trp-out**	**Trp-in**
Domratcheva et al., 2008	447 nm	454 nm	361 nm	356 nm
Sadeghian et al., 2008[a,b]	377 nm	390 nm	n/a	n/a
	414 nm	425 nm		
Khrenova et al., 2010	425–429 nm	441 nm	n/a	n/a
Khrenova et al., 2011b	424 nm	442 nm	n/a	n/a
Udvarhelyi and Domratcheva, 2013[c]	(444 nm)	461 nm	n/a	n/a
	(437 nm)	451 nm		
	Resting	**Signaling**	**Resting**	**Signaling**
Exp. AppA Kraft et al., 2003	446 nm	458 nm	373 nm	378 nm
Exp. BlrB Zirak et al., 2006	445 nm	457 nm	374 nm	379 nm

	IR FMN(C4 = O4) stretch	
	Trp-out	**Trp-in**
Domratcheva et al., 2008	1742 cm^{-1}	1748 cm^{-1}
Sadeghian et al., 2008[a]	1798 cm^{-1}	1791 cm^{-1}
Khrenova et al., 2010	1700 cm^{-1}	1675 cm^{-1}
	Resting	**Signaling**
Exp. AppA Masuda et al., 2005b	1709 cm^{-1}	1695 cm^{-1}
Exp. BlrB	n/a	n/a

*AppA BLUF if not noted otherwise. Note that Trp-in and Trp-out columns have been switched compared to **Table 2** as the consensus assignment of the resting and signaling state is different.*

[a] BlrB BLUF (PDB ID 2BYC).

[b] Reported values for BHLYP (upper line) and CC2 (lower line).

*[c] Two different optimization restraint settings for the iGln63 configurations reported. Trp-out values taken from **Table 2**; no actual Trp-out structures, only rotated Gln63.*

should be noted that the missing Tyr(OH)-Gln63(O) hydrogen bond in the signaling state may be in contrast to a recent experimental article (Iwata et al., 2011), and must possibly be replaced by a strong Tyr(OH)-iGln63(N) interaction. Recently, Domratcheva and coworkers have compared their mechanisms to the pathways proposed by the Schütz group; they concluded that a pathway including iGln63 rotation is favored (Khrenova et al., 2013).

So far, only one article provides insight in the actual Trp/Met exchange process on the basis of molecular dynamics and structural conversion form Trp-in to Trp-out and vice versa on the level of force fields (Meier and van Gunsteren, 2013). However, a viable explanation how the global BLUF conformation reacts on the relatively small changes close to the FMN chromophore is still missing (cf. Peter et al., 2012 for the LOV domain case). As this is an essential part of the photocycle and is expected to explain the relatively high stability of the hydrogen bond switched state, the questions regarding the BLUF photocycle are only partially answered. Furthermore, it would be required to test whether a reasonable photocycle can be constructed with the Trp-in conformation as well. So far two possible photocycles have been proposed for the Trp-out conformation, but especially due to the lack of calculations for a potential Trp-in based photocycle predictions that can be confirmed experimentally are not available from the computational studies.

A PHOTOCYCLE FOR THE TRP-IN RESTING STATE

In this section, we will present the results of basic density functional theory (DFT) calculations, serving as a preliminary framework for a potential photocycle for a Trp-in resting state. The calculations are based on small clusters taken from the 1YRX and 2IYG (AppA Trp-in/Trp-out) crystal structures, including lumiflavin, Tyr21, Ser41, Gln63, and Trp104/Met106. A detailed setup of the calculations can be found in the Supporting Information.

First, we tested the influence of Grimme's dispersion correction (Grimme et al., 2010) on the molecular interaction energies. This dispersion correction was recently introduced and refined over the years to remove the shortcomings of density functional theory when it comes to the interaction of weakly bound molecular clusters. The reason behind this is that DFT tends to underestimate the actual interaction between compounds that are not bound via covalent bonds or static Coulomb interactions (ions, dipoles). The presented values were calculated from a Counterpoise corrected optimization (Boys and Bernardi, 1970), including geometry restraints to keep the protein structure roughly resembled in our cluster models. Strikingly, the dispersion correction has a strong influence on the stability of Tyr-FMN and Ser-FMN interactions. In both cases, the interaction is quantitatively affected by up to 5 kcal/mol (see **Table 4**).

This shows that studies using DFT are limited in obtaining the correct binding energies and conformations for the BLUF domain when dispersion correction is not considered. This is particularly relevant for BLUF due to the large aromatic ring system of FMN and its potential π-interactions perpendicular to the isoalloxazin plane, which have still not found much attention in the literature.

TABLE 4 | Interaction energies (in kcal/mol) of Tyr21 and Ser41 with the rest of the investigated BLUF model.

Geometry	E_I(Tyr21)			E_I(Ser41)		
	w/D3BJ	w/o D3BJ	ΔE	w/D3BJ	w/o D3BJ	ΔE
A w/D3BJ	−7.16	−2.68	−4.48	−9.09	−4.26	−4.83
A w/o D3BJ	−7.09	−2.82	−4.27	−8.65	−4.19	−4.46
J w/D3BJ	−15.03	−10.09	−4.94	−5.21	−0.88	−4.33
J w/o D3BJ	−15.10	−10.25	−4.85	−5.36	−1.12	−4.24

A-values are based on the Anderson et al crystal structure (PDB ID 1YRX; Anderson et al., 2005) and J-values on the structure of Jung et al. (2006; PDB ID 2IYG). D3BJ indicates the presence or absence of the dispersion correction in the CAM-B3LYP calculations.

Second, we conducted an analysis of the change in dipole moment upon excitation using a long-range corrected density functional, CAM-B3LYP (Yanai et al., 2004). In the excited system, the change in dipole moment is between 2 and 33 Debye for the investigated states (local excited or charge transfer state, respectively, see **Table 5**). For comparison to **Table 2**, the TD-CAM-B3LYP vertical excitation energies for the bright state of the Anderson/Jung structures are 371/374 nm (regardless of dispersion correction), resulting in a small red shift of 0.03 eV. Given the nature and the physical meaning of vertical excitation energies (namely an upper limit to the range in which the photophysics take place, Götze and Thiel, 2013; Karasulu et al., 2014), the apparent "overestimation" resulting from the CAM-B3LYP calculations is indeed more realistic than the reproduction of a measured absorption maximum. While it is experimentally established that the electron transfer from Tyr21 to FMN leads to the formation of the red-shifted species, it has so far not been considered that the resulting change in local dipole moment might already strongly perturb the hydrogen bond network around the flavin. The MD simulations agree that the Gln63 conformation in the BLUF domain is very flexible (Obanayama et al., 2008; Götze et al., 2012; Meier et al., 2012). As such, transferring an electron to FMN and thus establishing a strong polarized electric field is likely to change the conformational distribution of Gln63. More precisely, the very initial effect of the electron relocation form Tyr21 to the polar part of FMN is the formation of a reversed electric field in the vicinity of the Gln63 side chain (**Figure 3**). Since the Gln63 side chain is a permanent dipole itself, a reaction of the Gln63 dynamics to the changed electric field can be expected, such as the proposed Gln63 flip.

In case of a flipped Gln63 anchor, there is no reason for the Trp104 to remain in the FMN binding pocket. There is no way for Gln63-NH_2 and Trp104-NH to interact in a binding fashion and even a slight steric repulsion can be inferred (see **Figure 4**). This might lead to a small preference for the Trp-out conformation, where Gln63 can form a hydrogen bond to the Met106 sulfur. This mechanism leaves the possibility for a post-rotation proton

TABLE 5 | Changes in dipole moment (in Debye) upon vertical excitation to the lowest bright local excitation (LE) or to the Tyr-FMN charge transfer (CT) state.

	A w/D3BJ		A w/o D3BJ		J w/D3BJ		J w/o D3BJ	
	$\lvert\mu_t\rvert-\lvert\mu_0\rvert$	$\lvert\mu_t-\mu_0\rvert$	$\lvert\mu_t\rvert-\lvert\mu_0\rvert$	$\lvert\mu_t-\mu_0\rvert$	$\lvert\mu_t\rvert-\lvert\mu_0\rvert$	$\lvert\mu_t-\mu_0\rvert$	$\lvert\mu_t\rvert-\lvert\mu_0\rvert$	$\lvert\mu_t-\mu_0\rvert$
LE, Gas phase	0.02	1.70	−0.05	4.18	0.44	1.98	0.39	1.98
LE, CPCM	0.96	2.03	1.15	2.28	1.05	2.38	0.95	2.36
CT, CPCM	28.00	33.15	27.56	33.10	24.20	31.73	24.21	31.85

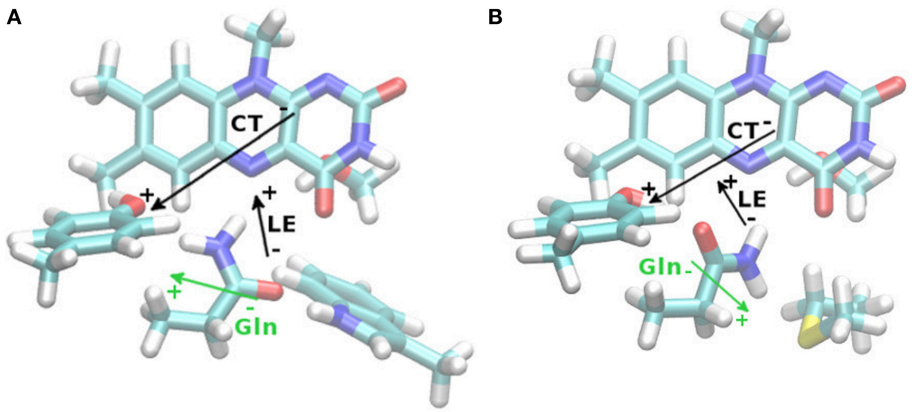

FIGURE 3 | TD-DFT difference dipole vectors ($\lvert\mu_t-\mu_0\rvert$, black arrows) based upon the Anderson (A) and Jung (B) CAM-B3LYP/6-31G(d,p) structures with D3BJ correction, for the lowest local excited state (LE) or the Tyr-FMN charge transfer (CT) state. Lengths of vectors are arbitrary, for actual size refer to **Table 5**. Gln63 permanent ground state dipole moment shown as well (green arrows).

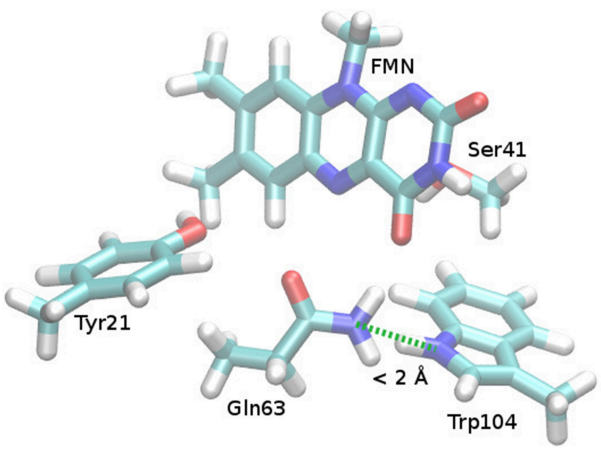

FIGURE 4 | Repulsive steric interaction between Gln63 and Trp104 after Gln63 rotation. Cut from the Anderson et al. AppA BLUF structure (PDB ID 1YRX, Anderson et al., 2005), missing hydrogen atoms added and optimized (see Supporting Information). After preparation, the Gln63 orientation was manually adapted to the torsional angles found in the structure of Jung et al. (2006; PDB ID 2IYG), yielding the presented structure.

transfer from Tyr21 to FMN, either via Gln63 or directly, and enables the formation of the red shifted state immediately after the formation of the CT state.

A PERSPECTIVE FOR BLUF RESEARCH

Although numerous experimental studies on BLUF photoactivation and its dynamics are available so far, a clear picture of the molecular processes in BLUF domain remains elusive. The commonly accepted features of BLUF photosensing consist of PCET driving a hydrogen bond rearrangement and that the structural properties of the $\beta5$ strand involving the conserved methionine and possibly also the semi-conserved tryptophan (where present) are essential for signal transduction. Orientation and photoinduced dynamics of the conserved glutamine, tryptophan and methionine side chains, however, are still far from understood. Moreover, secondary structural changes are most likely required for the high stability of the hydrogen bond switched state but this aspect has not been addressed sufficiently so far. To solve these fundamental questions in the future, experimental approaches sensitive and selective for individual chemical groups in the protein have to be applied. It also appears obvious that classical site-directed mutagenesis and the use of truncated proteins are very limited in providing a unifying picture of photoactivation and signal transduction of the wild type proteins. A promising approach in this regard is to use group/site-specific isotope labels in combination with time resolved vibrational spectroscopy methods like transient IR absorption, two-dimensional IR spectroscopy or stimulated Raman spectroscopy. The resulting data would furthermore provide a basis for theoreticians to

test/benchmark their calculations and to validate potential models.

The differences in the field of theory could be easily amended, but any attempt for consolidation has to take into account that the existing models already cover a wide variety of methods. A neutral point of view comparing Trp and Gln conformations and predicting observables that can be tested experimentally would be ideal. While several computational studies claim that they adopt a neutral point of view, they still present a specific model as their favorite as outcome. Given the usual error ranges of the employed theoretical methods (e.g., DFT methods 0.2–0.5 eV, Silva-Junior et al., 2008), these conclusions appear tentative at best. Further progress therefore can therefore only be made by advanced experimental approaches in combination with qualitative theoretical predictions.

ACKNOWLEDGMENTS

TM is grateful for support by John Kennis through a NWO-CW VICI grant, by the DFG (HE3824/24-1 to Peter Hegemann) and the DFG/NWO bilateral cooperation program (HE3824/25-1). JG appreciates funding from the EPSRC (grant ref. EP/J018139/1).

REFERENCES

Anderson, S., Dragnea, V., Masuda, S., Ybe, J., Moffat, K., and Bauer, C. (2005). Structure of a novel photoreceptor, the BLUF domain of AppA from *Rhodobacter sphaeroides*. *Biochemistry* 44, 7998–8005. doi: 10.1021/bi0502691

Barends, T. R. M., Hartmann, E., Griese, J. J., Beitlich, T., Kirienko, N. V., Ryjenkov, D. A., et al. (2009). Structure and mechanism of a bacterial light-regulated cyclic nucleotide phosphodiesterase. *Nature* 459, 1015–1018. doi: 10.1038/nature07966

Bonetti, C., Mathes, T., van Stokkum, I. H. M., Mullen, K. M., Groot, M. L., van Grondelle, R., et al. (2008). Hydrogen bond switching among flavin and amino acid side chains in the BLUF photoreceptor observed by ultrafast infrared spectroscopy. *Biophys. J.* 95, 4790–4802. doi: 10.1529/biophysj.108.139246

Bonetti, C., Stierl, M., Mathes, T., van Stokkum, I. H. M., Mullen, K. M., Cohen-Stuart, T. A., et al. (2009). The role of key amino acids in the photoactivation pathway of the synechocystis Slr1694 BLUF domain. *Biochemistry* 48, 11458–11469. doi: 10.1021/bi901196x

Boys, S. F., and Bernardi, F. (1970). Calculation of small molecular interactions by differences of separate total energies - some procedures with reduced errors. *Mol. Phys.* 19, 553–566. doi: 10.1080/00268977000101561

Collette, F., Renger, T., and Busch, M. S. A. (2014). Revealing the functional states in the active site of BLUF photoreceptors from electrochromic shift calculations. *J. Phys. Chem. B*. 118, 11109–11119. doi: 10.1021/jp506400y

Domratcheva, T., Grigorenko, B. L., Schlichting, I., and Nemukhin, A. V. (2008). Molecular models predict light-induced glutamine tautomerization in BLUF photoreceptors. *Biophys. J.* 94, 3872–3879. doi: 10.1529/biophysj.107.124172

Dragnea, V., Arunkumar, A. I., Yuan, H., Giedroc, D. P., and Bauer, C. E. (2009). Spectroscopic studies of the AppA BLUF domain from *Rhodobacter sphaeroides*: addressing movement of tryptophan 104 in the signaling state. *Biochemistry* 48, 9969–9979. doi: 10.1021/bi9009067

Dragnea, V., Waegele, M., Balascuta, S., Bauer, C., and Dragnea, B. (2005). Time-resolved spectroscopic studies of the AppA blue-light receptor BLUF domain from *Rhodobacter sphaeroides*. *Biochemistry* 44, 15978–15985. doi: 10.1021/bi050839x

Fraser, J. S., van den Bedem, H., Samelson, A. J., Lang, P. T., Holton, J. M., Echols, N., et al. (2011). Accessing protein conformational ensembles using room-temperature X-ray crystallography. *Proc. Natl. Acad. Sci. U.S.A.* 108, 16247–16252. doi: 10.1073/pnas.1111325108

Fudim, R., Mehlhorn, J., Berthold, T., Weber, S., Schleicher, E., Kennis, J. T. M., et al. (2015). Photoinduced formation of flavin radicals in BLUF domains lacking the central glutamine. *FEBS J.* 282, 3161–3174. doi: 10.1111/febs.13297

Fujisawa, T., Takeuchi, S., Masuda, S., and Tahara, T. (2014). Signaling-state formation mechanism of a BLUF protein PapB from the purple bacterium *Rhodopseudomonas palustris* studied by femtosecond time-resolved absorption spectroscopy. *J. Phys. Chem. B* 118, 14761–14773. doi: 10.1021/jp5076252

Fukushima, Y., Murai, Y., Okajima, K., Ikeuchi, M., and Itoh, S. (2008). Photoreactions of Tyr8- and Gln50-mutated BLUF domains of the PixD protein of Thermosynechococcus elongatus BP-1: photoconversion at low temperature without Tyr8. *Biochemistry* 47, 660–669. doi: 10.1021/bi700674w

Fukushima, Y., Okajima, K., Ikeuchi, M., and Itoh, S. (2007). Two intermediate states I and J trapped at low temperature in the photocycles of two BLUF domain proteins of cyanobacteria *Synechocystis* sp PCC6803 and Thermosynechococcus elongatus BP-1. *Photochem. Photobiol.* 83, 112–121. doi: 10.1562/2006-03-12-RA-845

Gauden, M., Grinstead, J. S., Laan, W., van Stokkum, I. H. M., Avila-Perez, M., Toh, K. C., et al. (2007). On the role of aromatic side chains in the photoactivation of BLUF domains. *Biochemistry* 46, 7405–7415. doi: 10.1021/bi7006433

Gauden, M., van Stokkum, I. H. M., Key, J. M., Lührs, D. C., van Grondelle, R., Hegemann, P., et al. (2006). Hydrogen-bond switching through a radical pair mechanism in a flavin-binding photoreceptor. *Proc. Natl. Acad. Sci. U.S.A.* 103, 10895–10900. doi: 10.1073/pnas.0600720103

Gauden, M., Yeremenko, S., Laan, W., van Stokkum, I. H. M., Ihalainen, J. A., van Grondelle, R., et al. (2005). Photocycle of the flavin-binding photoreceptor AppA, a bacterial transcriptional antirepressor of photosynthesis genes. *Biochemistry* 44, 3653–3662. doi: 10.1021/bi047359a

Gomelsky, M., and Klug, G. (2002). BLUF: a novel FAD-binding domain involved in sensory transduction in microorganisms. *Trends Biochem. Sci.* 27, 497–500. doi: 10.1016/S0968-0004(02)02181-3

Götze, J. P., Greco, C., Mitrić, R., Bonačić-Koutecký, V., and Saalfrank, P. (2012). BLUF Hydrogen network dynamics and UV/Vis spectra: a combined molecular dynamics and quantum chemical study. *J. Comp. Chem.* 33, 2233–2242. doi: 10.1002/jcc.23056

Götze, J., and Saalfrank, P. (2009). Serine in BLUF domains displays spectral importance in computational models. *J. Photochem. Photobiol. B* 94, 87–95. doi: 10.1016/j.jphotobiol.2008.10.003

Götze, J. P., and Thiel, W. (2013). TD-DFT and DFT/MRCI study of electronic excitations in Violaxanthin and Zeaxanthin. *Chem. Phys.* 415, 247–255. doi: 10.1016/j.chemphys.2013.01.030

Grimme, S., Antony, J., Ehrlich, S., and Krieg, H. (2010). A consistent and accurate ab initio parametrization of density functional dispersion correction (DFT-D) for the 94 elements H-Pu. *J. Chem. Phys.* 132, 154104. doi: 10.1063/1.3382344

Grimme, S., and Waletzke, M. (1999). A combination of Kohn-Sham density functional theory and multi-reference configuration interaction methods. *J. Chem. Phys.* 111, 5645–5655. doi: 10.1063/1.479866

Grinstead, J. S., Hsu, S. T. D., Laan, W., Bonvin, A. M., Hellingwerf, K. J., Boelens, R., et al. (2006). The solution structure of the AppA BLUF domain: insight into the mechanism of light-induced signaling. *ChemBioChem* 7, 187–193. doi: 10.1002/cbic.200500270

Hazra, P., Inoue, K., Laan, W., Hellingwerf, K. J., and Terazima, M. (2006). Tetramer formation kinetics in the signaling state of AppA monitored by time-resolved diffusion. *Biophys. J.* 91, 654–661. doi: 10.1529/biophysj.106.083915

Hazra, P., Inoue, K., Laan, W., Helfingwerf, K. J., and Terazima, M. (2008). Energetics and role of the hydrophobic interaction during photoreaction of the BLUF domain of AppA. *J. Phys. Chem. B* 112, 1494–1501. doi: 10.1021/jp0767314

Hegemann, P. (2008). Algal sensory photoreceptors. *Annu. Rev. Plant Biol.* 59, 167–189. doi: 10.1146/annurev.arplant.59.032607.092847

Holzer, W., Penzkofer, A., Fuhrmann, M., and Hegemann, P. (2002). Spectroscopic characterization of flavin mononucleotide bound to the LOV1 domain of Phot1

from *Chlamydomonas reinhardtii*. *Photochem. Photobiol.* 75, 479–487. doi: 10.1562/0031-8655(2002)0750479SCOFMB2.0.CO2

Hsiao, Y. W., Götze, J. P., and Thiel, W. (2012). The central role of Gln63 for the hydrogen Bonding network and UV-visible spectrum of the AppA BLUF domain. *J. Phys. Chem. B* 116, 8064–8073. doi: 10.1021/jp3028758

Iseki, M., Matsunaga, S., Murakami, A., Ohno, K., Shiga, K., Yoshida, K., et al. (2002). A blue-light-activated adenylyl cyclase mediates photoavoidance in Euglena gracilis. *Nature* 415, 1047–1051. doi: 10.1038/4151047a

Ishikita, H. (2008). Light-induced hydrogen bonding pattern and driving force of electron transfer in AppA BLUF domain photoreceptor. *J. Biol. Chem*. 283, 30618–30623. doi: 10.1074/jbc.M803864200

Iwata, T., Watanabe, A., Iseki, M., Watanabe, M., and Kandori, H. (2011). Strong donation of the hydrogen bond of tyrosine during photoactivation of the BLUF domain. *J. Phys. Chem. Lett*. 2, 1015–1019. doi: 10.1021/jz2003974

Jung, A., Domratcheva, T., Tarutina, M., Wu, Q., Ko, W. H., Shoeman, R. L., et al. (2005). Structure of a bacterial BLUF photoreceptor: insights into blue light-mediated signal transduction. *Proc. Natl. Acad. Sci. U.S.A*. 102, 12350–12355. doi: 10.1073/pnas.0500722102

Jung, A., Reinstein, J., Domratcheva, T., Shoeman, R. L., and Schlichting, I. (2006). Crystal structures of the AppA BLUF domain photoreceptor provide insights into blue light-mediated signal transduction. *J. Mol. Biol*. 362, 716–732. doi: 10.1016/j.jmb.2006.07.024

Karasulu, B., Götze, J. P., and Thiel, W. (2014). Assessment of Franck-Condon methods for computing vibrationally broadened UV-vis absorption spectra of flavin derivatives: Riboflavin, Roseoflavin, and 5-Thioflavin. *J. Chem. Theory Comput*. 10, 5549–5566. doi: 10.1021/ct500830a

Kennis, J. T. M., and Mathes, T. (2013). Molecular eyes: proteins that transform light into biological information. *Interface Focus* 3:20130005. doi: 10.1098/rsfs.2013.0005

Khrenova, M., Domratcheva, T., Grigorenko, B., and Nemukhin, A. (2011a). Coupling between the BLUF and EAL domains in the blue light-regulated phosphodiesterase BlrP1. *J. Mol. Model.* 17, 1579–1586. doi: 10.1007/s00894-010-0842-1

Khrenova, M. G., Domratcheva, T., Schlichting, I., Grigorenko, B. L., and Nemukhin, A. V. (2011b). Computational characterization of reaction intermediates in the photocycle of the sensory domain of the AppA blue light photoreceptor. *Photochem. Photobiol.* 87, 564–573. doi: 10.1111/j.1751-1097.2010.00861.x

Khrenova, M. G., Nemukhin, A. V., and Domratcheva, T. (2013). Photoinduced electron transfer facilitates tautomerization of the conserved signaling glutamine side chain in BLUF protein light sensors. *J. Phys. Chem. B* 117, 2369–2377. doi: 10.1021/jp312775x

Khrenova, M. G., Nemukhin, A. V., Grigorenko, B. L., Krylov, A. I., and Domratcheva, T. M. (2010). Quantum chemistry calculations provide support to the mechanism of the light-induced structural changes in the flavin-binding photoreceptor proteins. *J. Chem. Theory Comput*. 6, 2293–2302. doi: 10.1021/ct100179p

Kita, A., Okajima, K., Morimoto, Y., Ikeuchi, M., and Miki, K. (2005). Structure of a cyanobacterial BLUF protein, Tll0078, containing a novel FAD-binding blue light sensor domain. *J. Mol. Biol.* 349, 1–9. doi: 10.1016/j.jmb.2005.03.067

Kraft, B. J., Masuda, S., Kikuchi, J., Dragnea, V., Tollin, G., Zaleski, J. M., et al. (2003). Spectroscopic and mutational analysis of the blue-light photoreceptor AppA: a novel photocycle involving flavin stacking with an aromatic amino acid. *Biochemistry* 42, 6726–6734. doi: 10.1021/bi030055o

Laan, W., Bednarz, T., Heberle, J., and Hellingwerf, K. J. (2004). Chromophore composition of a heterologously expressed BLUF-domain. *Photochem. Photobiol. Sci*. 3, 1011–1016. doi: 10.1039/b410923f

Laan, W., Gauden, M., Yeremenko, S., van Grondelle, R., Kennis, J. T. M. and Hellingwerf, K. J. (2006). On the mechanism of activation of the BLUF domain of AppA. *Biochemistry* 45, 51–60. doi: 10.1021/bi051367p

Losi, A. (2007). Flavin-based blue-light photosensors: a photobiophysics update. *Photochem. Photobiol.* 83, 1283–1300. doi: 10.1111/j.1751-1097.2007.00196.x

Losi, A., and Gärtner, W. (2012). The evolution of flavin-binding photoreceptors: an ancient chromophore serving trendy blue-light sensors. *Annu. Rev. Plant Biol.* 63, 49–72. doi: 10.1146/annurev-arplant-042811-105538

Lukacs, A., Brust, R., Haigney, A., Laptenok, S. P., Addison, K., Gil, A., et al. (2014). BLUF domain function does not require a metastable radical intermediate state. *J. Am. Chem. Soc*. 136, 4605–4615. doi: 10.1021/ja4121082

Majerus, T., Kottke, T., Laan, W., Hellingwerf, K., and Heberle, J. (2007). Time-resolved FT-lR spectroscopy traces signal relay within the blue-light receptor AppA. *ChemPhysChem* 8, 1787–1789. doi: 10.1002/cphc.200700248

Masuda, S., Hasegawa, K., Ohta, H., and Ono, T. A. (2008). Crucial role in light signal transduction for the conserved Met93 of the BLUF protein PixD/Slr1694. *Plant Cell Physiol.* 49, 1600–1606. doi: 10.1093/pcp/pcn132

Masuda, S., Hasegawa, K., and Ono, T. A. (2005a). Tryptophan at position 104 is involved in transforming light signal into changes of β-sheet structure for the signaling state in the BLUF domain of AppA. *Plant Cell Physiol.* 46, 1894–1901. doi: 10.1093/pcp/pci208

Masuda, S., Hasegawa, K., and Ono, T. A. (2005b). Light-induced structural changes of apoprotein and chromophore in the sensor of blue light using FAD (BLUF) domain of AppA for a signaling state. *Biochemistry* 44, 1215–1224. doi: 10.1021/bi047876t

Masuda, S., Tomida, Y., Ohta, H., and Takamiya, K. (2007). The critical role of a hydrogen bond between Gln63 and Trp104 in the blue-light sensing BLUF domain that controls AppA activity. *J. Mol. Biol.* 368, 1223–1230. doi: 10.1016/j.jmb.2007.02.087

Mathes, T. (2007). *Photochemie und Signaltransduktion von Blaulichtrezeptorproteinen aus photosynthetisierenden Mikroorganismen*. Doctoral Thesis. Berlin: Humbold University Berlin.

Mathes, T., van Stokkum, I. H. M., Bonetti, C., Hegemann, P., and Kennis, J. T. M. (2011). The hydrogen-bond switch reaction of the Blrb BLUF domain of *Rhodobacter sphaeroides*. *J. Phys. Chem. B* 115, 7963–7971. doi: 10.1021/jp201296m

Mathes, T., van Stokkum, I. H. M., Stierl, M., and Kennis, J. T. M. (2012a). Redox modulation of flavin and tyrosine determines photoinduced proton-coupled electron transfer and photoactivation of BLUF photoreceptors. *J. Biol. Chem.* 287, 31725–31738. doi: 10.1074/jbc.M112.391896

Mathes, T., Zhu, J., van Stokkum, I. H. M., Groot, M. L., Hegemann, P., and Kennis, J. T. M. (2012b). Hydrogen bond switching among flavin and amino acids determines the nature of proton-coupled electron transfer in BLUF photoreceptors. *J. Phys. Chem. Lett*. 3, 203–208. doi: 10.1021/jz201579y

Mehlhorn, J., Steinocher, H., Beck, S., Kennis, J. T., Hegemann, P., and Mathes, T. (2013). A set of engineered *Escherichia coli* expression strains for selective isotope and reactivity labeling of amino acid side chains and flavin cofactors. *PLoS ONE* 8:e79006. doi: 10.1371/journal.pone.0079006

Meier, K., Thiel, W., and van Gunsteren, W. F. (2012). On the effect of a variation of the force field, spatial boundary condition and size of the QM region in QM/MM MD simulations. *J. Comp. Chem*. 33, 363–378. doi: 10.1002/jcc.21962

Meier, K., and van Gunsteren, W. F. (2013). On the use of advanced modelling techniques to investigate the conformational discrepancy between two X-ray structures of the AppA BLUF domain. *Mol. Simul*. 39, 472–486. doi: 10.1080/08927022.2012.743659

Merz, T., Sadeghian, K., and Schütz, M. (2011). Why BLUF photoreceptors with roseoflavin cofactors lose their biological functionality. *Phys. Chem. Chem. Phys.* 13, 14775–14783. doi: 10.1039/c1cp21386e

Metz, S., Hendriks, J., Jäger, A., Hellingwerf, K., and Klug, G. (2010). *In Vivo* effects on photosynthesis gene expression of base pair exchanges in the gene encoding the light-responsive BLUF domain of AppA in *Rhodobacter Sphaeroides*. *Photochem. Photobiol.* 86, 882–889. doi: 10.1111/j.1751-1097.2010.00749.x

Möglich, A., Yang, X., Ayers, R. A., and Moffat, K. (2010). Structure and function of plant photoreceptors. *Annu. Rev. Plant Biol.* 61, 21–47. doi: 10.1146/annurev-arplant-042809-112259

Nakasone, Y., Ono, T. A., Ishii, A., Masuda, S., and Terazima, M. (2007). Transient dimerization and conformational change of a BLUF protein: YcgF. *J. Am. Chem. Soc.* 129, 7028–7035. doi: 10.1021/ja065682q

Nakasone, Y., Ono, T. A., Ishii, A., Masuda, S., and Terazima, M. (2010). Temperature-sensitive reaction of a photosensor protein YcgF: possibility of a role of temperature sensor. *Biochemistry* 49, 2288–2296. doi: 10.1021/bi902121z

Nunthaboot, N., Tanaka, F., and Kokpol, S. (2009). Analysis of photoinduced electron transfer in AppA. *J. Photochem. Photobiol. A Chem*. 207, 274–281. doi: 10.1016/j.jphotochem.2009.07.020

Nunthaboot, N., Tanaka, F., and Kokpol, S. (2010). Simultaneous analysis of photoinduced electron transfer in wild type and mutated AppAs. *J. Photochem. Photobiol. A Chem*. 209, 79–87. doi: 10.1016/j.jphotochem.2009.10.013

Obanayama, K., Kobayashi, H., Fukushima, K., and Sakurai, M. (2008). Structures of the chromophore binding sites in BLUF domains as studied by molecular

dynamics and quatum chemical calculations. *Photochem. Photobiol.* 84, 1003–1010. doi: 10.1111/j.1751-1097.2008.00351.x

Peter, E., Dick, B., and Baeurle, S. A. (2012). Signals of LOV1: a computer simulation study on the wildtype LOV1-domain of *Chlamydomonas reinhardtii* and its mutants. *J. Mol. Model.* 18, 1375–1388. doi: 10.1007/s00894-011-1165-6

Porcal, G., Bertolotti, S. G., Previtali, C. M., and Encinas, M. V. (2003). Electron transfer quenching of singlet and triplet excited states of flavins and lumichrome by aromatic and aliphatic electron donors. *Phys. Chem. Chem. Phys.* 5, 4123–4128. doi: 10.1039/b306945a

Ren, S., Sawada, M., Hasegawa, K., Hayakawa, Y., Ohta, H., and Masuda, S. (2012). A PixD-PapB chimeric protein reveals the function of the BLUF domain C-terminal alpha-Helices for light signal transduction. *Plant Cell Physiol.* 53, 1638–1647. doi: 10.1093/pcp/pcs108

Reshetnyak, Y. K., Koshevnik, Y., and Burstein, E. A. (2001). Decomposition of protein tryptophan fluorescence spectra into log-normal components. III. Correlation between fluorescence and microenvironment parameters of individual tryptophan residues. *Biophys. J.* 81, 1735–1758. doi: 10.1016/S0006-3495(01)75825-0

Rieff, B., Bauer, S., Mathias, G., and Tavan, P. (2011). DFT/MM description of flavin IR spectra in BLUF domains. *J. Phys. Chem. B.* 115, 11239–11253. doi: 10.1021/jp2043637

Sadeghian, K., Bocola, M., and Schütz, M. (2008). A conclusive mechanism of the photoinduced reaction cascade in blue light using flavin photoreceptors. *J. Am. Chem. Soc.* 130, 12501–12513. doi: 10.1021/ja803726a

Sadeghian, K., Bocola, M., and Schütz, M. (2010). A QM/MM study on the fast photocycle of blue light using flavin photoreceptors in their light-adapted/active form. *Phys. Chem. Chem. Phys.* 12, 8840–8846. doi: 10.1039/b925908b

Shibata, Y., Murai, Y., Satoh, Y., Fukushima, Y., Okajima, K., Ikeuchi, M., et al. (2009). Acceleration of electron-transfer-induced fluorescence quenching upon conversion to the signaling state in the blue-light receptor, TePixD, from Thermosynechococcus elongatus. *J. Phys. Chem. B* 113, 8192–8198. doi: 10.1021/jp901631b

Silva-Junior, M. R., Schreiber, M., Sauer, S. P. A., and Thiel, W. (2008). Benchmarks for electronically excited states: time-dependent density functional theory and density functional theory based multireference configuration interaction. *J. Chem. Phys.* 129, 104103. doi: 10.1063/1.2973541

Song, S. H., Oztürk, N., Denaro, T. R., Arat, N. O., Kao, Y. T., Zhu, H., et al. (2007). Formation and function of flavin anion radical in cryptochrome 1 blue-light photoreceptor of monarch butterfly. *J. Biol. Chem.* 282, 17608–17612. doi: 10.1074/jbc.M702874200

Stelling, A. L., Ronayne, K. L., Nappa, J., Tonge, P. J., and Meech, S. R. (2007). Ultrafast structural dynamics in BLUF domains: transient infrared spectroscopy of AppA and its mutants. *J. Am. Chem. Soc.* 129, 15556–15564. doi: 10.1021/ja074074n

Stierl, M., Penzkofer, A., Kennis, J. T., Hegemann, P., and Mathes, T. (2014). Key residues for the light regulation of the blue light-activated adenylyl cyclase from *Beggiatoa* sp. *Biochemistry* 53, 5121–5130. doi: 10.1021/bi500479v

Takahashi, R., Okajima, K., Suzuki, H., Nakamura, H., Ikeuchi, M., and Noguchi, T. (2007). FTIR study on the hydrogen bond structure of a key tyrosine residue in the flavin-binding blue light sensor TePixD from Thermosynechococcus elongatus. *Biochemistry* 46, 6459–6467. doi: 10.1021/bi7004653

Tanaka, K., Nakasone, Y., Okajima, K., Ikeuchi, M., Tokutomi, S., and Terazima, M. (2009). Oligomeric-state-dependent conformational change of the BLUF protein TePixD (Tll0078). *J. Mol. Biol.* 386, 1290–1300. doi: 10.1016/j.jmb.2009.01.026

Tanaka, K., Nakasone, Y., Okajima, K., Ikeuchi, M., Tokutomi, S., and Terazima, M. (2011a). A way to sense light intensity: multiple-excitation of the BLUF photoreceptor TePixD suppresses conformational change. *FEBS Lett.* 585, 786–790. doi: 10.1016/j.febslet.2011.02.003

Tanaka, K., Nakasone, Y., Okajima, K., Ikeuchi, M., Tokutomi, S., and Terazima, M. (2011b). Light-induced conformational change and transient dissociation reaction of the BLUF photoreceptor synechocystis PixD (Slr1694). *J. Mol. Biol.* 409, 773–785. doi: 10.1016/j.jmb.2011.04.032

Tanaka, K., Nakasone, Y., Okajima, K., Ikeuchi, M., Tokutomi, S., and Terazima, M. (2012). Time-resolved tracking of interprotein signal transduction: synechocystis PixD-PixE complex as a sensor of light intensity. *J. Am. Chem. Soc.* 134, 8336–8339. doi: 10.1021/ja301540r

Toh, K. C., van Stokkum, I. H. M., Hendriks, J., Alexandre, M. T. A., Arents, J. C., Perez, M. A., et al. (2008). On the signaling mechanism and the absence of photoreversibility in the AppA BLUF domain. *Biophys. J.* 95, 312–321. doi: 10.1529/biophysj.107.117788

Toyooka, T., Tanaka, K., Okajima, K., Ikeuchi, M., Tokutomi, S., and Terazima, M. (2011). Macromolecular crowding effects on reactions of TePixD (TII0078). *Photochem. Photobiol.* 87, 584–589. doi: 10.1111/j.1751-1097.2010.00849.x

Tyagi, A., Penzkofer, A., Griese, J., Schlichting, I., Kirienko, N. V., and Gomelsky, M. (2008). Photodynamics of blue-light-regulated phosphodiesterase BlrP1 protein from *Klebsiella pneumoniae* and its photoreceptor BLUF domain. *Chem. Phys.* 354, 130–141. doi: 10.1016/j.chemphys.2008.10.003

Udvarhelyi, A., and Domratcheva, T. (2011). Photoreaction in BLUF receptors: proton-coupled electron transfer in the flavin-gln-tyr system. *Photochem. Photobiol.* 87, 554–563. doi: 10.1111/j.1751-1097.2010.00884.x

Udvarhelyi, A., and Domratcheva, T. (2013). Glutamine rotamers in BLUF photoreceptors: a mechanistic reappraisal. *J. Phys. Chem. B* 117, 2888–2897. doi: 10.1021/jp400437x

Unno, M., Kikuchi, S., and Masuda, S. (2010). Structural refinement of a key tryptophan residue in the BLUF photoreceptor AppA by ultraviolet resonance raman spectroscopy. *Biophys. J.* 98, 1949–1956. doi: 10.1016/j.bpj.2010.01.007

Unno, M., Masuda, S., Ono, T. A., and Yamauchi, S. (2006). Orientation of a key glutamine residue in the BLUF domain from AppA revealed by mutagenesis, spectroscopy, and quantum chemical calculations. *J. Am. Chem. Soc.* 128, 5638–5639. doi: 10.1021/ja060633z

Unno, M., Tsukiji, Y., Kubota, K., and Masuda, S. (2012). N-terminal truncation does not affect the location of a conserved tryptophan in the BLUF domain of AppA from *Rhodobacter sphaeroides*. *J. Phys. Chem. B* 116, 8974–8980. doi: 10.1021/jp305873z

Winkler, A., Heintz, U., Lindner, R., Reinstein, J., Shoeman, R. L., and Schlichting, I. (2013). A ternary AppA-PpsR-DNA complex mediates light regulation of photosynthesis-related gene expression. *Nat. Struct. Mol. Biol.* 20, 859–867. doi: 10.1038/nsmb.2597

Wu, Q., and Gardner, K. H. (2009). Structure and insight into blue light-induced changes in the BlrP1 BLUF domain. *Biochemistry* 48, 2620–2629. doi: 10.1021/bi802237r

Wu, Q., Ko, W. H., and Gardner, K. H. (2008). Structural requirements for key residues and auxiliary portions of a BLUF domain. *Biochemistry* 47, 10271–10280. doi: 10.1021/bi8011687

Yanai, T., Tew, D., and Handy, N. (2004). A new hybrid exchange-correlation functional using the coulomb-attenuating method (CAM-B3LYP). *Chem. Phys. Lett.* 393, 51–57. doi: 10.1016/j.cplett.2004.06.011

Yuan, H., Anderson, S., Masuda, S., Dragnea, V., Moffat, K., and Bauer, C. (2006). Crystal structures of the *Synechocystis* photoreceptor Slr1694 reveal distinct structural states related to signaling. *Biochemistry* 45, 12687–12694. doi: 10.1021/bi061435n

Yuan, H., Dragnea, V., Wu, Q., Gardner, K. H., and Bauer, C. E. (2011). Mutational and structural studies of the PixD BLUF output signal that affects light-regulated interactions with PixE. *Biochemistry* 50, 6365–6375. doi: 10.1021/bi200701d

Zirak, P., Penzkofer, A., Hegemann, P., and Mathes, T. (2007). Photo dynamics of BLUF domain mutant H44R of AppA from *Rhodobacter sphaeroides*. *Chem. Phys.* 335, 15–27. doi: 10.1016/j.chemphys.2007.03.013

Zirak, P., Penzkofer, A., Schiereis, T., Hegemann, P., Jung, A., and Schlichting, I. (2006). Photodynamics of the small BLUF protein BlrB from *Rhodobacter sphaeroides*. *J. Photochem. Photobiol. B* 83, 180–194. doi: 10.1016/j.jphotobiol.2005.12.015

Conflict of Interest Statement: The authors declare that the research was conducted in the absence of any commercial or financial relationships that could be construed as a potential conflict of interest.

frontiers in Molecular Biosciences

ORIGINAL RESEARCH
published: 01 October 2015
doi: 10.3389/fmolb.2015.00055

Light-induced structural changes in a short light, oxygen, voltage (LOV) protein revealed by molecular dynamics simulations—implications for the understanding of LOV photoactivation

Marco Bocola[1], Ulrich Schwaneberg[1], Karl-Erich Jaeger[2,3] and Ulrich Krauss[2]**

[1] Lehrstuhl für Biotechnologie, RWTH Aachen University, Aachen, Germany, [2] Forschungszentrum Jülich, Institut für Molekulare Enzymtechnologie, Heinrich Heine University Düsseldorf, Jülich, Germany, [3] Forschungszentrum Jülich, Institut für Bio- und Geowissenschaften, IBG-1: Biotechnologie, Jülich, Germany

The modularity of light, oxygen, voltage (LOV) blue-light photoreceptors has recently been exploited for the design of LOV-based optogenetic tools, which allow the light-dependent control of biological functions. For the understanding of LOV sensory function and hence the optimal design of LOV-based optogentic tools it is essential to gain an in depth atomic-level understanding of the underlying photoactivation and intramolecular signal-relay mechanisms. To address this question we performed molecular dynamics simulations on both the dark- and light-adapted state of PpSB1-LOV, a short dimeric bacterial LOV-photoreceptor protein, recently crystallized under constant illumination. While LOV dimers remained globally stable during the light-state simulation with regard to the Jα coiled-coil, distinct conformational changes for a glutamine in the vicinity of the FMN chromophore are observed. In contrast, multiple Jα-helix conformations are sampled in the dark-state. These changes coincide with a displacement of the Iβ and Hβ strands relative to the light-state structure and result in a correlated rotation of both LOV core domains in the dimer. These global changes are most likely initiated by the reorientation of the conserved glutamine Q116, whose side chain flips between the Aβ (dark state) and Hβ strand (light state), while maintaining two potential hydrogen bonds to FMN-N5 and FMN-O4, respectively. This local Q116-FMN reorientation impacts on an inter-subunit salt-bridge (K117-E96), which is stabilized in the light state, hence accounting for the observed decreased mobility. Based on these findings we propose an alternative mechanism for dimeric LOV photoactivation and intramolecular signal-relay, assigning a distinct structural role for the conserved "flipping" glutamine. The proposed mechanism is discussed in light of universal applicability and its implications for the understanding of LOV-based optogenetic tools.

Keywords: LOV domain, photoreceptor, molecular dynamics, signaling, optogenetics

OPEN ACCESS

Edited by:
Tilo Mathes, Vrije Universiteit Amsterdam, Netherlands

Reviewed by:
Josiah Zayner, NASA, USA
Peter Freddolino, University of Michigan, USA

****Correspondence:***
Marco Bocola, Lehrstuhl für Biotechnologie, RWTH Aachen University, Worringerweg 3, D-52074 Aachen, Germany m.bocola@biotec.rwth-aachen.de; Ulrich Krauss, Forschungszentrum Jülich, Institut für Molekulare Enzymtechnologie, Heinrich Heine University Düsseldorf, Wilhelm Johnen Strasse, D-52428 Jülich, Germany u.krauss@fz-juelich.de

Specialty section:
This article was submitted to Biophysics, a section of the journal Frontiers in Molecular Biosciences

Received: *01 May 2015*
Accepted: *05 September 2015*
Published: *01 October 2015*

Citation:
Bocola M, Schwaneberg U, Jaeger K-E and Krauss U (2015) Light-induced structural changes in a short light, oxygen, voltage (LOV) protein revealed by molecular dynamics simulations—implications for the understanding of LOV photoactivation. Front. Mol. Biosci. 2:55. doi: 10.3389/fmolb.2015.00055

Introduction

Blue-light photoreceptors containing light-oxygen-voltage (LOV) domains regulate a variety of different physiological responses in both eukaryotes and prokaryotes (Demarsy and Fankhauser, 2009; Krauss et al., 2009; Herrou and Crosson, 2011). Their light sensitivity is directly dependent on the photochemistry of a non-covalently bound flavin mononucleotide (FMN) chromophore. Upon illumination with blue light a covalent adduct is formed between the FMN-C4a atom and a strictly conserved cysteine residue in the LOV domain (Swartz et al., 2001). Concomitantly, the FMN-N5 atom becomes protonated with the conserved cysteine likely representing the proton donor (Kennis et al., 2003). In the dark, the FMN-cysteinyl thiol adduct is broken and the FMN-N5 atom deprotonated thus concluding the photocycle. Whereas, adduct formation occurs on a faster (microseconds) timescale (Swartz et al., 2001), adduct decay can take seconds to hours depending on the LOV protein (Zikihara et al., 2006; Jentzsch et al., 2009; Rani et al., 2013; Endres et al., 2015). Most LOV photoreceptors are oligomeric multi-domain sensory systems, consisting of a light-perceiving LOV domain and fused effector domains such as kinases, anti-sigma factors, helix-turn-helix DNA binding domains, phosphodiesterases and cyclases (Möglich et al., 2010; Herrou and Crosson, 2011). Those in turn influence a multitude of different cellular light responses in plants (Möglich et al., 2010), bacteria (Herrou and Crosson, 2011), and fungi (Idnurm et al., 2010). In recent years, it became apparent, that adduct formation leads to small-scale structural changes in the vicinity of the FMN chromophore, which are in many cases relayed to the fused effector domains via helical interdomain linkers (termed N-terminal cap or A'α-helix and C-terminal Jα-helix) (Harper et al., 2003, 2004; Halavaty and Moffat, 2007, 2013; Nash et al., 2011; Diensthuber et al., 2013; Herman et al., 2013; Endres et al., 2015; Herman and Kottke, 2015). There is growing experimental evidence that those structural changes in turn result in altered LOV photoreceptor biological activities (Harper et al., 2004; Vaidya et al., 2011; Aihara et al., 2012; Okajima et al., 2014; Kashojiya et al., 2015).

Based on the modularity of LOV photoreceptors various artificial LOV "photoreceptor" proteins have been constructed in recent years, where light-induced structural changes in the LOV domain have been exploited to allow the control of the biological activity of fused protein domains (for an extensive recent review see Shcherbakova et al., 2015). In most cases, the LOV2 domain of *Avena sativa* phototropin 1 (AsLOV2) was utilized as sensory module in those so-called LOV-based optogenetic tools (Shcherbakova et al., 2015). AsLOV2 represents the best studied and understood LOV domain system. Various complementary biophysical (nuclear magnetic resonance (NMR) and X-ray crystallographic) (Harper et al., 2003, 2004; Halavaty and Moffat, 2007; Yao et al., 2008), mutational (Nash et al., 2008; Zoltowski et al., 2009; Zayner et al., 2012; Zayner and Sosnick, 2014) and functional studies (Harper et al., 2004; Jones et al., 2007; Aihara et al., 2012; Zayner et al., 2012) hint toward A'α and Jα-helix dissociation and/or unfolding as the consequence of light-dependent adduct formation in the protein. In contrast, for the dimeric LOV photoreceptor YtvA of *Bacillus subtilis* and the artificial LOV histidine kinase YF1, constructed using the YtvA LOV domain as sensory domain, a rotational movement of the protruding Jα-helix constituting a coiled-coil like interaction in the dimeric protein, was suggested to cause the observed alteration of effector domain "activity" (Möglich and Moffat, 2007; Möglich et al., 2009; Diensthuber et al., 2013; Engelhard et al., 2013). While the structural consequences of adduct formation are rather well-understood for monomeric AsLOV2, the atomic-level structural rearrangements in the LOV core domain that cause Jα dissociation and unfolding and thus the mode of information flow throughout the protein after photon capture, are not. For dimeric natural and artificial LOV photoreceptors such as YtvA and YF1, the situation is even worse. While several mutational and functional studies support the Jα-helix rotation model (Möglich et al., 2009; Diensthuber et al., 2013; Gleichmann et al., 2013), the associated structural changes have so far not been resolved at the atomic level, due to the lack of X-ray crystallographic data for the full-length proteins in both the light- and dark state. Like for AsLOV2, the mode of information flow between the site of photon capture and the A'α/Jα-helix or even more importantly, to the fused effector domains, remains largely elusive. For the understanding of LOV photoactivation and signaling as well as for the rational design and mutational optimization of recently constructed LOV-based optogentic tools such an atomic level understanding is essential.

This required atomic-resolution information could experimentally be provided by either high-resolution NMR structures of both the dark and light states which are inherently difficult to obtain, or by crystallization of the respective protein under constant illumination, which so far has only been successful in few cases (Vaidya et al., 2011; Circolone et al., 2012). Alternatively, information about transition between the different structural states and allosteric information flow can be obtained by molecular dynamics (MD) simulations (Karplus and McCammon, 2002). In recent years a number of MD simulations have been conducted on various LOV domains and full-length LOV photoreceptors (Dittrich et al., 2005; Freddolino et al., 2006; Peter et al., 2010, 2012a,b; Song et al., 2011; Freddolino et al., 2013). However, the issue as to how photon absorption by the FMN molecule and subsequent adduct formation results in a signal relay to fused effector domains remains far from resolved. The common feature, that evolved from those simulations on LOV domain systems from different organisms, which is corroborated by experimental evidence, is the role of a highly conserved glutamine residue (Q513 in AsLOV2, Q123 in YtvA and YF1), whose conformation is directly linked to photoreceptor activation (Nash et al., 2008; Avila-Perez et al., 2009). The question thus arises whether the mode of information flow from the photon absorbing FMN molecule to structurally conserved N- and C-terminal helical extensions (A'α and Jα) and consequently to fused effector domains is at atomic level conserved between plant and bacterial LOV photoreceptors, especially as the latter ones have so far not been studied by MD methods, i.e., how do small-scale conformational changes in the vicinity of FMN chromophore impact on the conformation of N- and C-terminally located structural elements.

We recently reported the X-ray crystal structure of a so-called short LOV protein PpSB1-LOV from *Pseudomonas putida*, obtained from crystals grown under constant low-light illumination (**Figure 1A**) (Circolone et al., 2012). Like other LOV domains, PpSB1-LOV possesses a typical mixed α/β Per-ARNT-SIM (PAS) fold in the topological order Aβ-Bβ-Cα-Dα-Eα-Gβ-Hβ-Iβ (**Figure 1B**). The FMN binding pocket is constituted by the β-scaffold surrounded by the three helices with the FMN molecule anchored above the central Iβ sheet. Outside of the canonical LOV-core domains the N-terminal A'α helix and the C-terminal Jα-helix protrude from the LOV core, largely constituting the LOV-LOV dimer interface (**Figure 1**). In contrast to fast-cycling phototropin LOV sensor domains, such as the LOV2 domain of *Avena sativa* phototropin 2 (Swartz et al., 2001), PpSB1-LOV possesses a very slow dark recovery with a long lived light state (light-state lifetime: approx. 2500 min; at 20°C) (Jentzsch et al., 2009). Unlike other LOV photoreceptors, PpSB1-LOV lacks a fused effector domain (Krauss et al., 2005; Jentzsch et al., 2009; Circolone et al., 2012; Rani et al., 2013). Similar architectures are found widespread throughout the bacterial world (Losi and Gärtner, 2008; Möglich et al., 2009; Rani et al., 2013), with short (effector-less) LOV proteins representing the third largest group of bacterial LOV photoreceptors (Losi and Gärtner, 2008). With respect to the observed dimeric arrangement, PpSB1-LOV strongly resembles the arrangement seen in the recently obtained dark-state structure of YF1 (Diensthuber et al., 2013) and probably YtvA (Ogata et al., 2009; Engelhard et al., 2013). Given this similar structural arrangement, i.e., parallel arrangement of the LOV-core domains in the homodimeric protein with protruding N- and C-terminal coaxial coiled-coil extensions, it is tempting to speculate that PpSB1-LOV and YtvA-LOV in YF1 undergo grossly similar light-dependent structural changes. Unfortunately, no dark-state crystal structure of PpSB1-LOV is yet available. Therefore, the structural basis of PpSB1-LOV photoactivation and intramolecular signal relay remains elusive. Moreover, with regard to the FMN-cysteinyl-thiol adduct the PpSB1-LOV light-state structure represents a "mixed state" as no clear evidence for the presence of the Cys53-SG FMN-C4a covalent linkage in the electron density map was observed (Circolone et al., 2012). Upon close inspection of the electron density around the FMN-C4a atom *sp3* hybridization of the 4a carbon atom can be inferred, which is in contrast to a planar conformation seen in LOV dark-state structures (Circolone et al., 2012). Moreover, in the PpSB1-LOV light-state structure, Q116 (corresponding to Q123 and Q513 of YtvA-LOV and AsLOV2) depicts two possible hydrogen bonds with the FMN isoalloxazine ring, namely FMN-O4 ... NE2-Q116 (2.75 Å) and FMN-N5 ... NE2-Q116 (2.87 Å); (Circolone et al., 2012). This is in contrast to previously reported photoexcited state structures of LOV domains, where a flipping of the Gln side chain oxygen (OE1) and amide (NE2) atoms was proposed as a consequence of illumination (Crosson and Moffat, 2002; Fedorov et al., 2003; Möglich and Moffat, 2007; Zoltowski et al., 2007; Vaidya et al., 2011). Please note, that none of the presently solved LOV X-ray structures does allow an unambiguous assignment of the respective side-chain atom positions solely based on electron density due to a too low resolution and high side chain disorder. Due to those structural features, it is currently not clear whether the reported PpSB1-LOV light-state structure correctly depicts all structural consequences of light-state formation. Therefore, since no PpSB1-LOV dark-state structure is available, no conclusion can be drawn about structural differences between the dark- and light state.

In order to address those open questions we performed molecular dynamics simulations on both the dark and

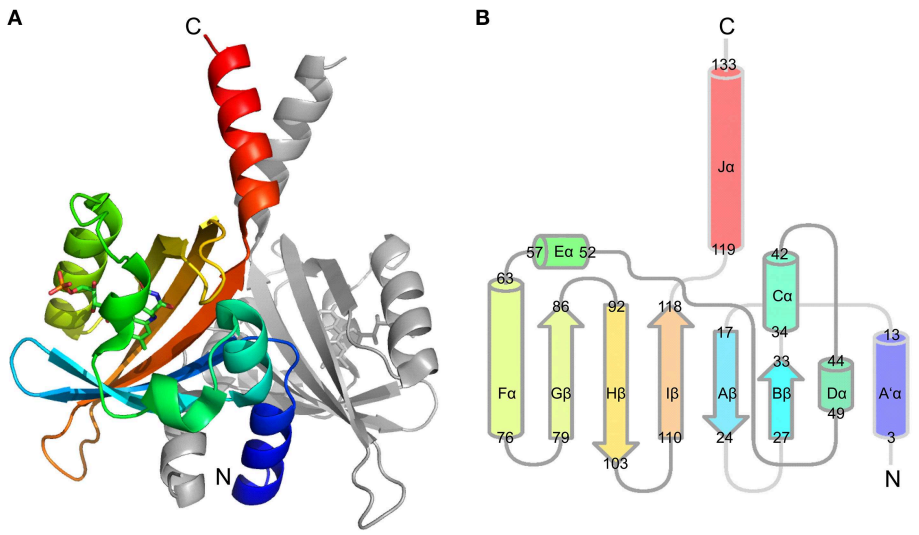

FIGURE 1 | PpSB1-LOV dimer structure (PDB-ID: 3SW1) (A) and conserved topology of LOV secondary structural elements (B). Chain A is colored using rainbow coloring from the N- to the C-terminus The FMN chromophore is shown in stick representation. **(B)** Depicts the LOV/PAS topology of PpSB1-LOV with α-helices shown as cylinders and β-sheets drawn as arrows. The non-canonical A'α- and Jα-helical extensions protrude from the LOV core. Numbers refer to amino acids at the boundaries of the respective secondary structural element.

light-adapted (adduct) state of PpSB1-LOV, by either introducing or omitting the FMN-C4a Cys53-SG adduct in the PpSB1-LOV (light-state) starting structure of the respective simulations. Based on those simulations we investigate the stability of the proposed PpSB1-LOV light-state X-ray structure and probe the conformational space the protein can sample after breaking the adduct, thus analyzing the early structural consequences of adduct breakage for PpSB1-LOV. Our simulations show that the presented PpSB1-LOV light-state X-ray structure remains globally stable during the simulation, i.e., with regard to the orientation of the C-terminal Jα coiled-coil interaction in the dimer, but reveals distinct conformational changes for side chains in the vicinity of the FMN chromophore. The direct comparison of light- and dark-state simulations, suggest different Jα-helix orientations as well as variable mobility between the two states. These changes coincide with a tilting of the Iβ and Hβ strands relative to the light-state starting structure and result in a correlated movement of both LOV core domains in the dimer. The observed global changes are most likely initiated by the reorientation of the conserved glutamine Q116 which flips its side chain oxygen atom position between Aβ (V19) in the dark state, and the Hβ strand (S98) in the light state, while enabling two potential hydrogen bonds to FMN-N5 and -O4, respectively. This local Q116 reorientation impacts on a salt-bridge network constituted by K117 and E96, which is stabilized in the light state, hence accounting for the observed decreased mobility. Based on these findings we propose a new signal-relay mechanism for dimeric LOV photoactivation and intramolecular signal-relay, assigning an alternative structural role for the conserved "flipping" glutamine. The proposed mechanism is discussed in light of universal applicability and its implications for the understanding and the design of LOV-based optogenetic tools.

Materials and Methods

Simulation Setup

The X-ray crystal structure of the short LOV protein PpSB1-LOV (Circolone et al., 2012) from *Pseudomonas putida* (PDB-ID: 3SW1) solved under constant illumination was used as basis for the modeling of the light- and dark-adapted state and subsequent molecular dynamics calculations using YASARA Structure (Krieger et al., 2004; Krieger and Vriend, 2014) (Ver. 14.7.17) software. The dark adapted structure was constructed by omitting the covalent bond between C53 and FMN. In the light-state starting structure the covalent bond between the C53-SG atom and the FMN-C4a atom was computationally introduced. The starting structures were protonated using the implemented pka-prediction and hydrogen bond network optimization algorithm (Krieger et al., 2012) and solvated in a periodic box (Krieger et al., 2006) using constrained TIP3P (Miyamoto and Kollman, 1992) water molecules. The box was neutralized at pH 7.4 using 0.9% NaCl solution and the water density was equilibrated to a final water density of 0.997 g/ml at 298 K. All simulations were performed utilizing the AMBER03 and the AMBER99 (see Supplementary Figure 8) (Wang et al., 2000; Duan et al., 2003; Krieger et al., 2004) force field for the protein residues and the general AMBER force field (Wang et al., 2004) (GAFF) using AM1-BCC (Jakalian et al., 2002) charges for the cofactor (parameters for the covalent Cys-FMN adduct are listed in Supplementary Table 2) and the default value for electrostatic cutoff (7.86 Å) was used with Particle Mesh Ewald algorithm (Essmann et al., 1995) for long range electrostatics utilizing 128 gridpoints on a 0.7 Å grid. The structure was initially minimized (Krieger et al., 2002) using first steepest descent without electrostatics to remove steric clashes and subsequently relaxed by steepest descent minimization and simulated annealing from 298 K (timestep 2 fs, atom velocities scaled down by 0.9 every 10th step) until convergence was reached, i.e., the energy improved by less than 0.05 kJ/mol per atom during 200 steps. Molecular dynamics calculations in an NPT ensemble using constrained bond length to all hydrogen atoms (Hess et al., 1997; Miyamoto and Kollman, 1992) were performed at 298 K and a solvent density of 0.997 g/ml using temperature rescaling the atom velocities using a modified Berendsen thermostat to slowly heat up the minimized system during an equilibration phase until the target temperature and density was reached. The simulation time step was 1.33 fs for intermolecular and 4 fs for intramolecular interactions to speed up the simulation and snapshots were saved every 25 ps. The MD-simulations were performed in three independent runs with different initial velocities for each system over 25, 45, and 95 ns and the trajectories were analyzed using YASARA (Krieger and Vriend, 2014) Structure and VMD (Humphrey et al., 1996).

H-Bonding and Salt-bridge Analysis

To obtain information about interactions in the vicinity of FMN chromophore distances and angles between relevant donor-acceptor pairs was obtained from the trajectories by using VMD. The corresponding distance and angle data was analyzed by using a custom Perl script employing moderate donor-acceptor distance (D-A) and angle (D-H ··· A) cutoff values of 3.2 Å and 130–180°, respectively (Jeffrey, 1997; Steiner, 2002). The script returns percent occupancy for the respective interaction for the trajectory. The corresponding values for all trajectories are listed in Supplementary Table 1. For the identification of salt-bridges the distance between the K117-NZ and E96-CD was measured and a distance cut-off of 5 Å was used for identification of a salt-bridge. This larger distance measure was chosen to avoid ambiguity due to E96-OE1/OE2 rotation (Barlow and Thornton, 1983; Xu et al., 1997).

Jα-Crossing Angle Analysis

The crossing angle of the Jα helices and A'α helices between the two subunits was calculated over the trajectories using YASARA by plotting a normal vector along the backbone atoms of the respective residues constituting the helix (Jα: residues 120–132; A'α: residues 3–13) and analysing the angle between the two normal vectors. The corresponding helix-crossing angle data was plotted as frequency distribution by using GraphPad Prism (GraphPad Software Inc. La Jolla, CA, USA). The average (mean) helix-crossing angles as well as the associated standard deviations were derived from the corresponding frequency distribution analyses.

Dynamic Cross-correlation Analyses

Dynamic cross correlation analysis of all residue RMSD were performed using YASARA to deduce correlated movements of all residue pairs. The values in the DCCM range from −1 (perfectly anti-correlated) to +1 (perfectly correlated). The values along the diagonal are +1 (selfcorrelation). The DCC between a residue pair i and j is obtained with the following formula, where d is the displacement between the current position and the average position, and the angle brackets indicate the average over all sample snapshots.

$$DCCM_{i,j} = \frac{\left\langle \vec{d}_i \cdot \vec{d}_j \right\rangle}{\sqrt{\left\langle \vec{d}_i^{\,2} \right\rangle \cdot \left\langle \vec{d}_j^{\,2} \right\rangle}}$$

All corresponding dark- and light-state dynamic cross-correlation matrices were combined into average dark- and light-state matrices and a light-dark plot was generated by subtracting the averaged light- and dark-state matrices to identify changes in correlated motions between the two states. All matrix operations were carried out with Matlab R2014b (Mathworks GmbH, Ismaning, Germany).

Results

The question as to how the light signal is relayed from the site of photon capture in the LOV domain active site to N- and C-terminal helical linker elements and consequently to fused effector domains in full-length oligomeric multi-domain LOV photoreceptors remains, despite extensive experimental efforts, still largely unresolved. This is due to the fact that all photoexcited state X-ray structures, i.e., for LOV proteins crystallized in the dark and illuminated immediately before data collection, show only small structural changes compared to the corresponding dark-state structures (Crosson and Moffat, 2002; Fedorov et al., 2003; Halavaty and Moffat, 2007; Möglich and Moffat, 2007; Zoltowski et al., 2007; Endres et al., 2015). Here, the crystal-lattice probably impedes larger scale structural changes. Moreover, no atomic resolution dark or light-state NMR structures, which would resolve this issue, have been reported for a LOV protein in solution. Thus, MD simulations represent the ideal technique to reveal possible structural consequences of photoactivation as the covalent adduct, i.e., the most salient feature of the LOV domain light state, can easily be introduced or omitted in the corresponding light- or dark-state simulations.

The Previously Published PpSB1-LOV Light-state Structure Remains Globally Stable over the Simulation Trajectory

Given the structural features of the recently solved PpSB1-LOV light-state X-ray structure, i.e., lack of clear electron density for the covalent FMN-cysteinyl-thiol adduct and the orientation Q116 side chain forming two possible hydrogen bonds with the FMN molecule, it is not clear if the structure depicts all structural features of a fully populated light state. To address this issue we computationally introduced a covalent linkage between the FMN-C4a atom and C53-SG atom. For simulation of the dark state, this covalent bond was omitted. We performed three independent simulations for the dimer of PpSB1-LOV in the dark state and three simulations for the light state (**Table 1**).

When the resulting trajectories are superimposed globally over the backbone atoms of the dimer, an average RMSD over the backbone atoms of 1.84 Å (dark) 1.66 Å (light) can be calculated, suggesting that larger structural changes do occur during the dark-state simulation compared to the light-state simulation. In order to better visualize potential inter-domain movements, the dark- and light-state trajectories were superimposed over all backbone atoms of chain A (**Figures 2A,B**). Potential domain rearrangements become then more apparent for chain B of the dimer. Especially, the N- and C-terminal A'α and Jα helices show increased RMSDs in the dark-state simulation. The corresponding RMSD values for the Jα helix (residues 120–132) are 2.75 Å (dark state) and 2.18 (light state). Likewise, for the A'α helix higher RMSD values are observed (dark state: 2.38, light state: 1.82). A residue-resolved RMSD plot (**Figure 2C**), as

TABLE 1 | Summary of the performed simulations.

Name	State	Duration (ns)	RMSD (full)[$] (Å)	RMSD (core)[§] (Å)	RMSD (A'α)[§] (Å)	RMSD (Jα)[§] (Å)
1D	Dark	25	1.84	2.87	2.60	2.31
2D	Dark	45	1.86	2.66	2.37	3.25
3D	Dark	95	1.82	2.42	2.17	2.70
Average	Dark		1.84	2.65	2.38	2.75
1L	Light	25	1.82	3.04	1.87	3.01
2L	Light	45	1.61	2.37	1.97	2.21
3L	Light	95	1.64	2.32	1.74	1.94
Average	Light		1.66	2.44	1.82	2.18

The trajectories were superimposed over the backbone atoms of both chains[$] or over chain A[§]. RMSD values were calculated for the full length dimer (including Jα and A'α helix), the respective core domain (residues 17–117), the A'α helix (residues 3–13) and the Jα helix (residues 120–132) of chain B, relative to the starting structure. The reported average values were weighted for the duration of the respective trajectory.

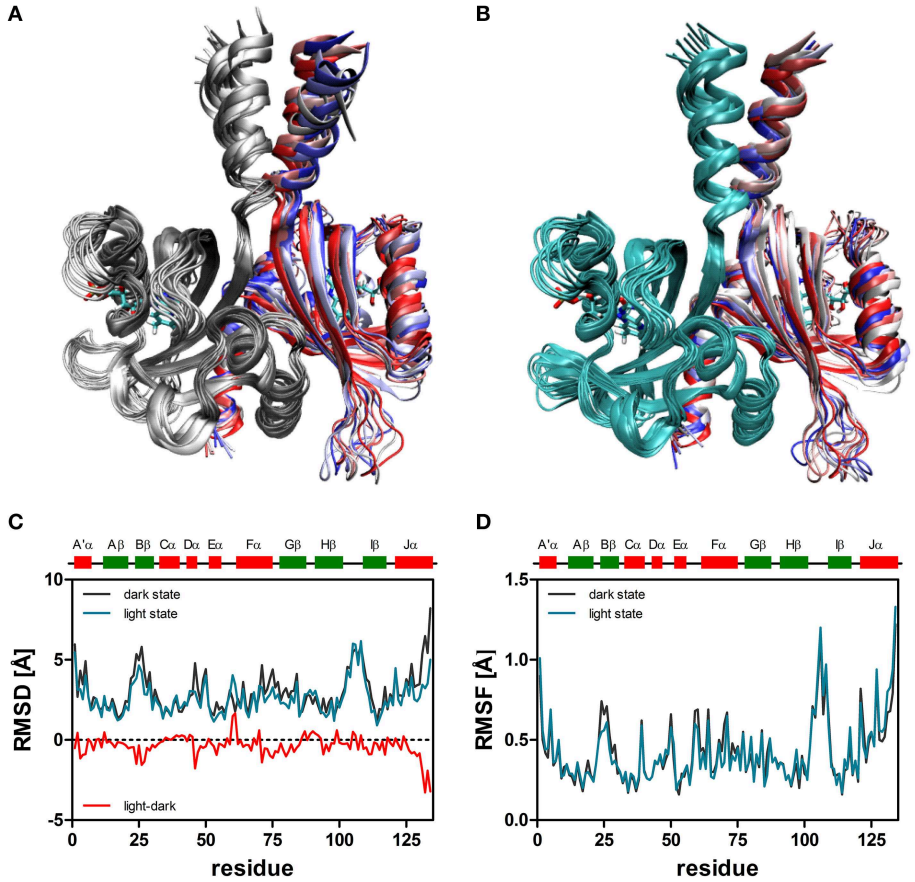

FIGURE 2 | Superimposition of 10 snapshots (Δt = 5 ns) of representative (2D, 2L) dark-state (A) and light-state trajectories (B). The snapshots were superimposed with VMD over all backbone atoms of chain A, colored in gray (dark-state) and cyan (light state). In both panels chain B is color coded by simulation time (t = 0: dark red; t = 45 ns: dark blue). The FMN cofactor is shown in stick representation in both subunits. **(C)** Per residue RMSD of the backbone atoms derived for chain B of the dark-state (dark gray) and the light-state (cyan) trajectories. The red line depicts light-dark RMSD values, with negative values indicating larger changes in the dark state. **(D)** Residue-resolved RMSF values for the dark-state (dark gray) and light-state (cyan) trajectories. Above the graph, LOV domain secondary structure elements are shown with α-helices in red and β-strands in green.

well as the corresponding heatmaps (Supplementary Figures 1, 2) pinpoint regions showing increased structural changes in the dark-state (**Figure 2C**; negative values in the light-dark plot). Those regions are (i) the N-terminal A'α helix, (ii) the Aβ-Bβ loop, (iii) parts of the Fα helix and the adjacent Gβ strand as well as the C-terminal Jα-helix. In the corresponding RMSF plot (**Figure 2D**) the N- and C-terminal A'α and Jα helices, Aβ-Bβ loop as well as the Hβ-Iβ loop show increased fluctuations. The Hβ-Iβ loop shows similar fluctuations in both the dark- and light-state simulations (**Figure 2D**).

Local Structural Changes in the PpSB1-LOV Active Site Induced by Adduct Formation

In order to address details of the structural changes that occur between the transition from dark- to light state we superimposed both trajectories over all backbone atoms of chain A. Potential consequences of photoactivation were analyzed for residues in the immediate vicinity of the FMN chromophore, i.e., the conserved glutamine Q116 as well as neighboring residues on the Aβ, Hβ, and Iβ strand (**Figure 3**). In the PpSB1-LOV light-state structure (PDB-ID: 3SW1) the Q116 side chain orientation facilitates two hydrogen bonds to the FMN chromophore (Q116-NE2 … FMN-N5, 2.87 Å; Q116-NE2 … FMN-O4, 2.75 Å). The Q116 side chain oxygen atom (OE1) faces toward the Aβ strand with a distance of 3.84 Å to the backbone amide of V19. To obtain information about the H-bonding interactions in the FMN binding pocket we analyzed all trajectories for the above outlined interactions (Supplementary Table 1). As criteria for the presence of an H-bond we used moderate cut-off values for distance (D…A; 3.2 Å) and angle (D-H…A; 130–180°) (Jeffrey, 1997; Steiner, 2002). For all trajectories H-bond occupancy was calculated as described in the Materials and Methods Section.

Applying those criteria, in the dark state (1D, 2D, 3D), only the H-bond between Q116-NE2 and the FMN-O4 atom (via 2HE) is retained (present in about 49% of the trajectory time steps), while no H-bond is formed to FMN-N5 (occupancy below 5%) (Supplementary Table 1; **Figures 3**, **4A**; Supplementary Figures 3, 4A). The Q116 side chain oxygen (OE1) is facing toward

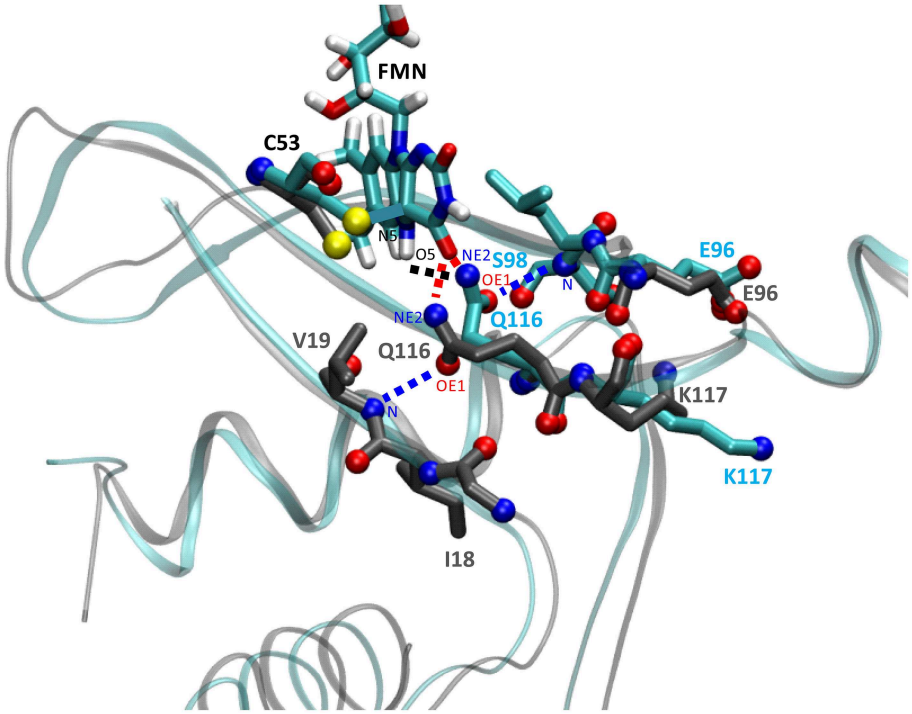

FIGURE 3 | Illustration of the structural differences between dark- and light-state simulations in the vicinity of the FMN chromophore. The figure shows a representative state (averaged over 100 simulation frames) at a later time of the dark-state and light-state trajectory (2D, 2L). Relevant side chains are shown in stick representation with side chain nitrogen and oxygen atoms as CPK spheres. Residue carbon atoms are color-coded representing the dark-state (carbon atoms in dark gray) and light-state (carbon atoms in cyan). Potential H-bonds or electrostatic interactions are depicted as dashed lines (for details see the main text). The light-state Q116-NE2 … FMN-N5-H5 H-bond is shown in black, the dark- and light-state Q116-NE2 … FMN-O4 H-bonds are depicted in red and the Q116-OE1 … V19-N interaction (dark-state) or the Q116-OE1 … S98-N H-bond (light state) is drawn in blue. For orientation and clarity the photoactive cysteine (C53), the FMN chromophore (in the light state) as well as parts of the protein backbone are shown in gray (dark state) and cyan (light state). Besides Q116, the side chains of K117 (Iβ) and E96 (Hβ) experience a correlated reorientation (for details see the main text).

the backbone amide of V19 in the dark state, with an average distance above the 3.2 Å cut-off set for a hydrogen bond, but nevertheless establishing a weak electrostatic interaction (**Figure 4B**, Supplementary Figures 3, 4B). The corresponding interaction is absent in all the light-state trajectories (**Figures 3**, **4E**; Supplementary Figures 3, 4E).

In the light-state trajectories (1L, 2L, 3L) the FMN-Q116 the H-bond between the Q116-NE2 atom and the FMN-O4 (via 2HE and 1HE) is retained (present in about 39 and 9% of all trajectory time steps; Supplementary Table 1; **Figures 3**, **4D**, Supplementary Figures 3, 4D). Additionally H-bonding interactions are possible between Q116-NE2 and the FMN-N5 atom (via the newly protonated FMN-N5 H5-atom) (present in about 9% of all trajectory time steps; Supplementary Table 1, **Figure 3**). At the same time the FMN-OE1 atom flips toward the backbone amide of S98 on Hβ in the light state, establishing a new electrostatic interaction (**Figures 3**, **4F**; Supplementary Figures 3, 4F). Applying the above described H-bonding selection criteria an H-bond is detected in about 23% of all trajectory time steps (Supplementary Table 1). In the dark state, this conformation is only present in about 10% of all trajectory time steps (Supplementary Table 1). Thus, while the overall dimer arrangement seen in the PpSB1-LOV light-state X-ray structure remained stable over the light-state simulation time (**Figure 2**) pronounced side chain rearrangements in the vicinity of the FMN chromophore occur, corroborating the "mixed" state nature of the recently solved PpSB1-LOV X-ray structure.

Adduct Formation Induces the Displacement of the Hβ and Iβ Strands Impacting an Inter-subunit Salt-bridge Network

In the PpSB1-LOV light-state X-ray structure, the LOV-LOV dimer interface is largely constituted, by hydrophobic interactions of the A'α helices, the Jα-helices and interfacial residues of the Hβ and Iβ strands (Circolone et al., 2012).

To illustrate the observed effects, an early representative state (averaged over the first 100 frames) and a late representative state (averaged over the last 100 frames) of the dark state (2D) trajectory is shown (**Figure 5A**). Here, the trajectory snapshots were superimposed over the backbone of chain A and chain B was colored according to simulation time. A displacement of the whole domain is visible from $t = 0$ (chain B colored in red) to $t = 45$ ns (chain B colored in blue). A similar overlay of early and late frames of the light-state trajectory did not reveal a similar subunit reorientation (**Figure 5D**). Over the trajectories this trend in displacement can be quantified e.g., for the Hβ and

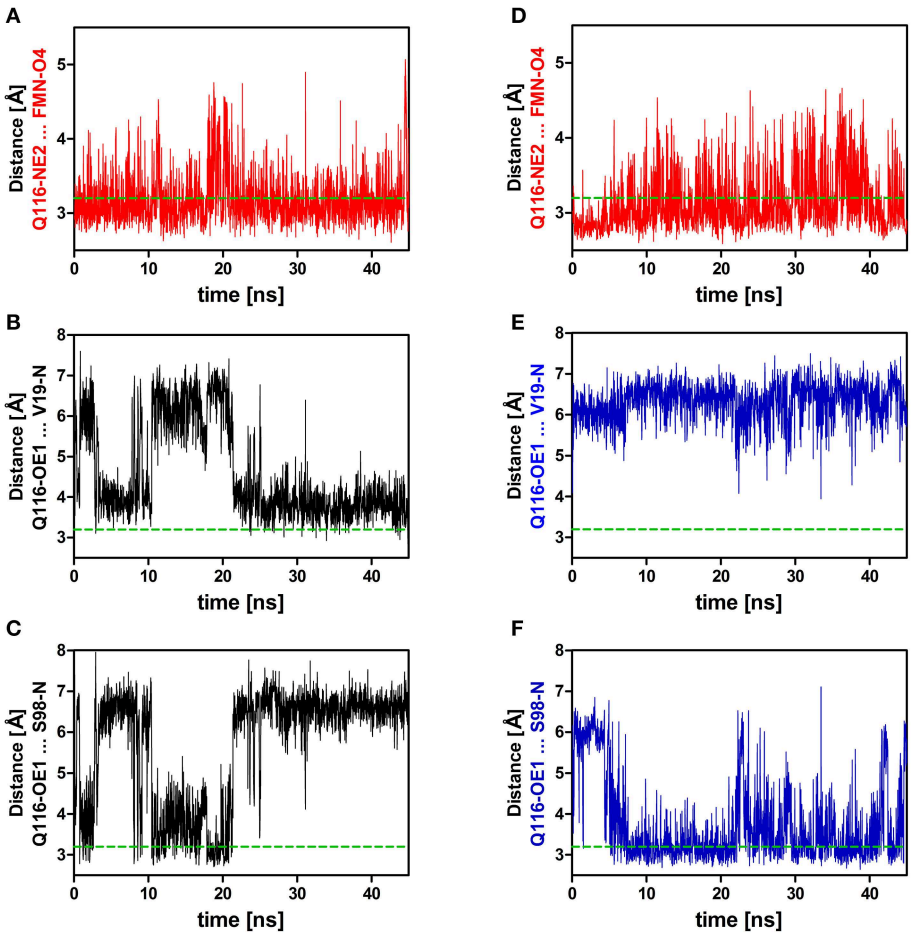

FIGURE 4 | Relevant distances between the side chain nitrogen (NE2) and oxygen (OE1) atoms of Q116 and the FMN chromophore (A,D) as well as to the backbone amide atoms of V19 and S98 (B,C,E,F). On the left side **(A–C)** distances derived from the dark-state trajectory are shown, while on the right side **(D–F)** distances derived from the light-state trajectory are depicted. The dashed green line represents the 3.2 Å hydrogen bonding distance cut-off (Jeffrey, 1997; Steiner, 2002).

Iβ strands (RMSD Hβ (residues 94–104): dark state: 1.11 Å, light state: 0.99 Å; RMSD Iβ (residues 109–117): dark state: 0.93 Å, light state: 0.75 Å). Additionally, tilting of the C-terminal end of the Iβ strand toward the dimer interface and hence away from the respective core domain can be observed in the light-state simulations relative to the dark-state simulations (Supplementary Figure 9).

Additionally, a salt-bridge network between Hβ and Iβ can be identified in the PpSB1-LOV light-state X-ray structure which is constituted by the residues K117 and E96 of opposing subunits (**Figures 5A,D**). In both the dark- (**Figure 5A**) and light-state simulation (**Figure 5D**) different E96-K117 salt-bridge arrangements are observed. For all trajectories salt-bridge occupancy was calculated as described in the Materials and Methods Section. In both states E96 and K117 can form both an inter-subunit salt-bridge as well as an intra-subunit salt-bridge. In all dark-state simulations at least one inter-subunit salt-bridge is present, but the occupancy is on average below 50% (**Figure 5B**; Supplementary Figures 5, 6). In all three light-state simulations the occupancy for the same inter-subunit salt-bridge is increased to above 75% (**Figure 5E**, Supplementary Figures 5, 6). In all light- and dark-state simulations an intra-subunit salt-bridge between the same residues can be formed (if one of the inter-subunit salt-bridges is absent) (**Figures 5C,F**; Supplementary Figures 5, 6). This switching behavior suggests, that adduct formation may shift a pre-existing equilibrium toward the stabilization of the inter-subunit salt-bridge network.

The Orientation of Protruding Jα and A'α Helices is Influenced by Adduct Formation

The comparison of light- and dark-state simulations reveals different Jα-helix orientations as well as variable Jα mobility between the two states in both the short and the longer trajectories (**Figure 6**). The depicted helix crossing-angle distribution plots were obtained from the crossing angle of the normal vector as described in the Materials and Methods Section. The light-state conformation seems to be stable with average crossing angles of 38° ± 5° (1L), 41° ± 5° (2L), and

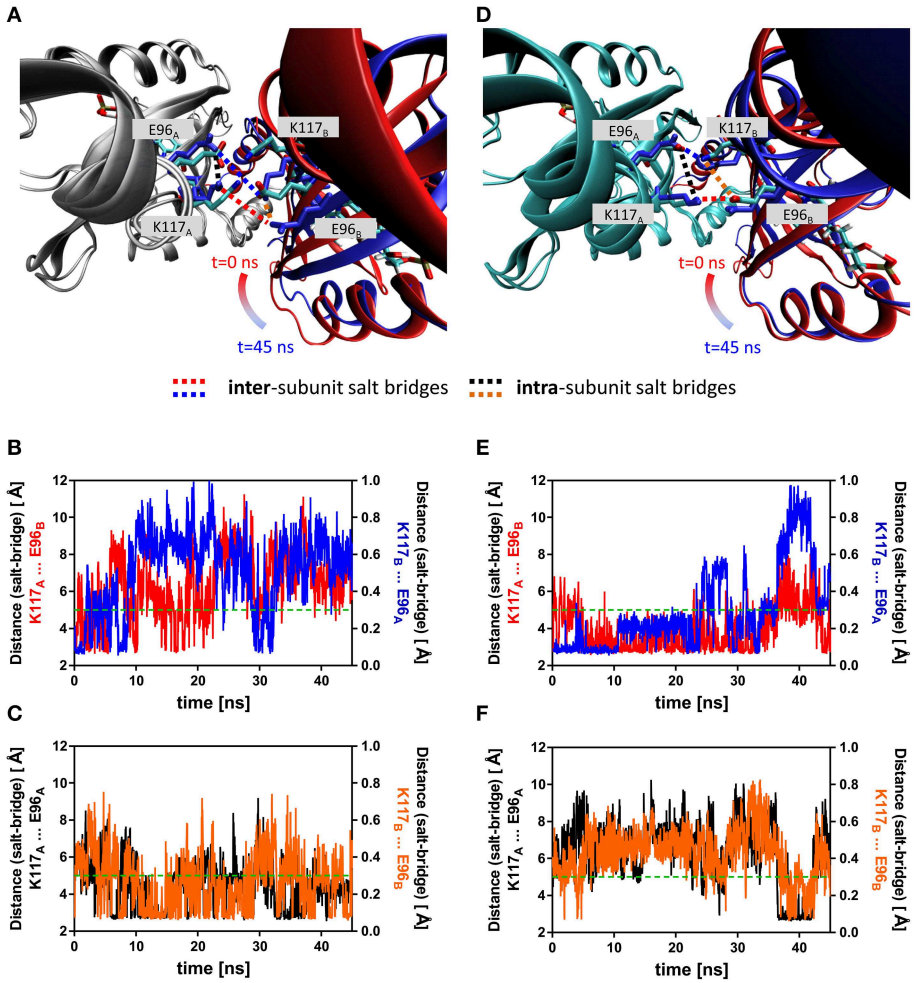

FIGURE 5 | Overlay of early and late representative snapshots from of the dark- and light-state trajectories (A,D). The presented snapshots were averaged over 100 frames to illustrate a representative state rather than single snapshot. The snapshots of representative simulations (2D, 2L) were superimposed over chain A of the dimer, colored in gray (dark state) and cyan (light-state). Chain B is shown in cartoon representation with the snapshots color-coded according to simulation time (t = 0 ns; red, t = 45 ns; blue). The K117 and E96 side chains, which can form an intra-subunit salt-bridge in the dark- and light state and an inter-subunit salt-bridge in the light-state are shown in stick representation with early snapshot (t = 0 ns) colored according to element (nitrogen in blue, oxygen in red and carbon in cyan). The K117 and E96 side chains of the late snapshot are shown in blue to illustrate the observed structural change. Inter-subunit salt-bridges are highlighted by blue and red dashed lines and intra-subunit salt-bridges by black and orange dashed lines. **(B)** Distance between atoms that would constitute the inter-subunit K117-*E96*' salt-bridge (labeled in **(A)** with red and blue dashed lines) in the dark state. **(C)** Distance between atoms constituting the intra-subunit K117-E96 salt-bridge (labeled in **(A)** with black and orange dashed lines) in the dark state. **(E)** Distance between atoms that constitute the inter-subunit K117-*E96*' salt-bridge (labeled in **(D)** with red and blue dashed lines) in the light state. **(F)** Distance between atoms that constitute the intra-subunit K117-E96 salt-bridge (labeled in **(A)** with black and orange dashed lines) in the light state. The dashed green line represents the 5 Å distance cut-off used for assignment of a salt-bridge (see Materials and Methods Section for details).

46° ± 6° (3L), respectively (**Figures 6B,D,F**; cyan line). The corresponding dark-state simulation reveals an increased overall Jα conformational mobility sampling multiple helix angles between 24° and 96° degree over the short trajectories (1D, 2D) (**Figures 6B,D**, dark gray line). In the longer trajectory a sharper angle distribution, with an average value of 39° ± 6°, is found for the dark-state trajectory (**Figure 6F**).

For the A'α helix similar angle distributions are observed for all trajectories revealing a broader angle distribution between 50° and 90° in the respective dark-state simulations (**Figures 6A,C,E**; dark gray line) and a sharper angle distribution in the light state (**Figures 6A,C,E**; cyan line).

Correlated Motions

To evaluate correlation of the above outlined intra- and inter- subunit interactions and characterize structural differences between the two states we analyzed the correlated motions of all residue pairs along the dark- and light state trajectories. Dynamic cross-correlation matrices (DCCMs) were calculated as described in the Materials and Methods Section. The obtained dark- and light state DCCMs show typical intra-subunit correlation patterns, e.g., blocks along the main diagonal for consecutive helical motifs and lines perpendicular to the main diagonal indicating correlated motions of neighboring β-strands (Supplementary Figures 7A,C). To better characterize the

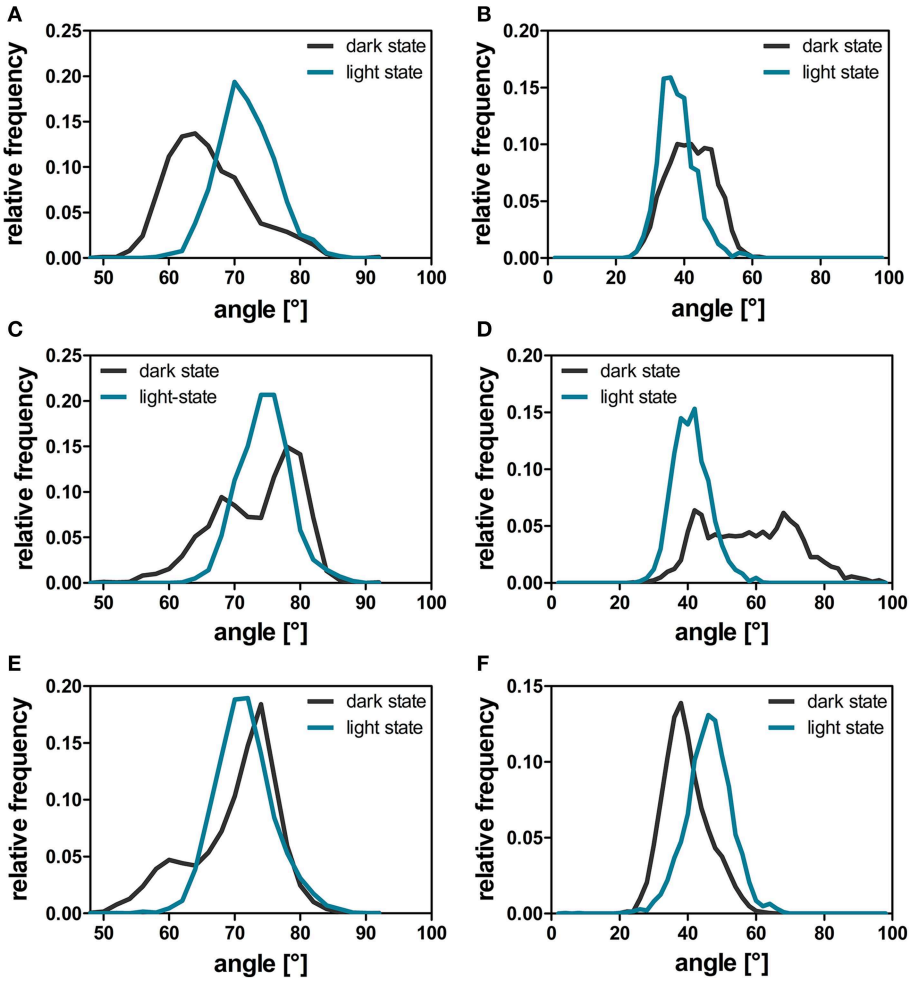

FIGURE 6 | A'α and Jα-crossing angles over the dark-state (dark gray line) and light-state (cyan line) trajectories. The helix angle between the A'α **(A,C,E)** and Jα helices **(B,D,F)** between chain A and chain B was calculated with YASARA for each time step by plotting a normal vector along the backbone atoms of the respective residues constituting the helix (A'α: residues 119–133; Jα: residues 3–13). The respective angles were analyzed for all dark- and light-state trajectories as described in the Materials and Methods Section. The panels depict the data derived from the three different simulation runs: 1D, 1L **(A,B)**; 2D, 2L **(C,D)**, and 3D, 3L **(E,F)**.

differences in correlated motions between the light- and dark-state simulations we generated a light-dark difference DCCM (Supplementary Figure 7B). No major differences between the dark- and light-state correlations along the main diagonal are observed indicating no major structural rearrangements within the monomer. In **Figure 7A** the light-dark differences in cross correlations between residues 90–134 on the Hβ, Iβ, and Jα (X-Axis) and chain A (Y-Axis) are highlighted, showing increased correlated motions along the main diagonal for the Hβ-Iβ loop region (residues 100–110) in the light state. Additionally changes off the diagonal, indicating long-range interactions, are observed for Hβ/Iβ and Jα/A'α, visible as yellow region in the upper left corner of **Figure 7A** and red region in the lower part of **Figure 7A**. The residues E96, S98, Q116, and K117 are all showing increased correlated motions in the light state, within the monomer. In **Figure 7B** the light-dark differences in cross-correlation between chain A (X-axis) and chain B (Y-axis) are shown. Surprisingly, the differences between dark- and light state become more evident compared to the intramolecular correlations (Supplementary Figure 7B). This can be seen for example in the region of Gβ-Hβ (chain A) which shows a change in correlated motions together with the N-terminal region from A'α to Eα on chain B. The largest increase in correlated motions is observed between the Jα helices of chain A and B (**Figure 7B**; Supplementary Figures 7A,C).

Discussion

Photoactivation and Signal-relay Mechanism of PpSB1-LOV Inferred from MD Simulations

Based on the presented simulations, the following photoactivation and signal relay mechanism can be inferred (illustrated in **Figure 8**). The recently solved crystal structure of PpSB1-LOV, obtained under illumination, can be assigned

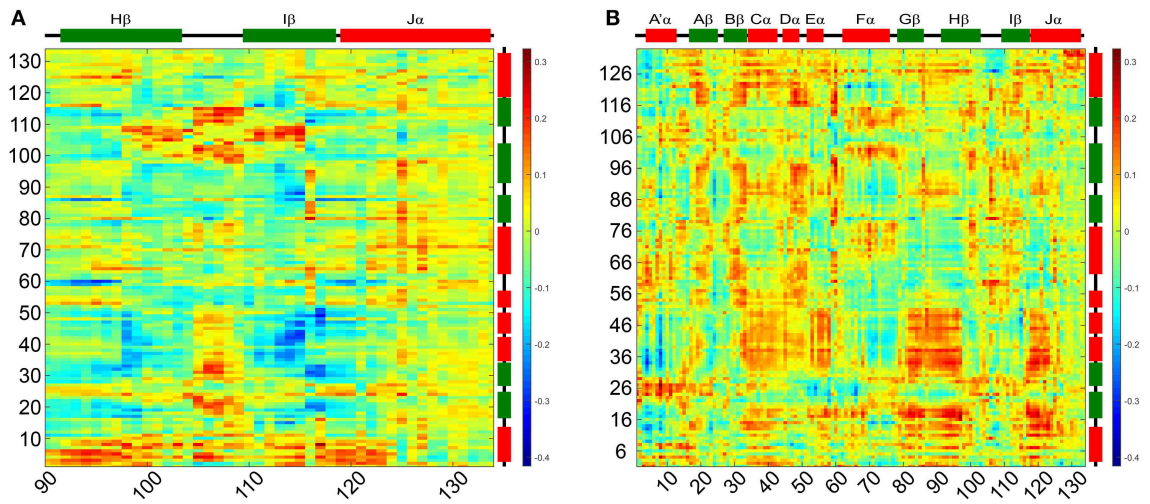

FIGURE 7 | Light-dark dynamic cross-correlation matrices (DCCMs) illustrating differences in pairwise correlated motions. (A) Differences in cross correlations between residues 90–134 on the Hβ, Iβ, and Jα and chain A. **(B)** Differences in cross correlation between chain A and chain B of the dimer. Positive values (red) can result from two scenarios: (i) increase in residue pair correlation in the light state and (ii) increased anti-correlated motions in the dark state. All correlations discussed in the manuscripts are of the first category.

according to our simulations with high confidence to a metastable light-state. In the light state FMN-N5 protonation enables two potential H-bonds between the FMN molecule and Q116 (FMN-N5···Q116-NE2 (with the FMN-N5-H5 being the H-bond donor) and FMN-O4···Q116-NE2 (with Q116-NE2-2HE/1HE being the H-bond donor) (See Local Structural Changes in the PpSB1-LOV Active site Induced by Adduct Formation; Supplementary Table 1; **Figure 8B**). In contrast to the crystal structure a rotation of the Q116 side chain is observed. The Q116-OE1 atom flips toward S98 on the Hβ strand (compare **Figures 8A,B**; Q116 flipping indicated by green arrow). The Q116 side chain oxygen atom (OE1) is hereby most of the time oriented toward the S98 backbone amide (**Figure 4F**), thus "locking" the Q116 side chain at the back-face of the FMN molecule (**Figure 8B**).

This structural signal could be relayed via the Iβ backbone to K117 and via the Hβ backbone (Fenwick et al., 2014) to E96 as indicated by DCCM analyses (**Figure 7A**). As consequence, tilting of the C-terminal end of the Iβ strand (Supplementary Figure 9) toward the dimer interface influences the conformation of K117 which together with E96 on Hβ reorient to form an inter-subunit salt-bridge in the light state (See Adduct Formation Induces the Displacement of the Hβ and Iβ Strands Impacting an Inter-subunitsalt-bridge Network, **Figure 5**). This likely "locks" the two LOV subunits in a stable relative position as observed in the PpSB1-LOV light-state X-ray structure, with lower average RMSD values for the core domain, A'α and Jα (**Table 1**). This is also reflected in increased inter-subunit correlated motions in the light state (**Figure 7B**).

In contrast, in the dark state (**Figure 8A**), the Q116 side chain is oriented toward the FMN molecule, with one potential H-bond being formed between the Q116-NE2 atom and the FMN-O4 atom (see Local Structural Changes in the PpSB1-LOV Active Site Induced by Adduct Formation, Supplementary Table 1). The Q116 side chain oxygen (OE1) is mainly oriented toward V19 (**Figure 4B**) on the Aβ strand (**Figure 8A**). Due to this reorientation of Q116 toward Aβ compared to the light state (Q116 oriented toward S98 on Hβ), the stabilizing inter-subunit K117…*E96′* – E96…*K117′* salt-bridge breaks, enabling an increased mobility in the relative orientation of the two subunits (**Figure 5A**). This is reflected by higher average RMSD values for the core domain, A'α and Jα (**Table 1**). In addition, all light-state simulations reveal relatively narrow Jα and A'α crossing angle distributions, while multiple conformations are sampled in the corresponding dark-state simulations, indicating, that no stable dark-state equilibrium is reached on the employed simulation time scales. This is not surprising, since the experimentally determined light-state lifetime of PpSB1-LOV is with about 2500 min (Jentzsch et al., 2009) at 20°C far outside of achievable simulation time scales. Therefore, we cannot conclude on the equilibrium structure of the PpSB1-LOV dark state, as conformational changes which might not be observed on our simulation timescale, i.e., further subunit rotation, increased A'α displacement and or subunit dissociation could occur. Those issues, as well as the feasibility of our mechanistic proposal, can only be unambiguously resolved if a dark-state X-ray structure or NMR data for the PpSB1-LOV protein becomes available.

The here proposed mechanism is globally similar to previous hypotheses, i.e., brought forward based on the dark-state X-ray structure of YF1 (Diensthuber et al., 2013), a recently engineered artificial photoreceptor containing the YtvA-LOV domain as sensory module (Möglich et al., 2009). This structure suggested decreased helix-crossing angles for the A'α-helix (29°) and Jα-helix (33°) in the dark state compared to the light-adapted state, which was modeled based on the PpSB1-LOV X-ray structure (A'α-helix: 70°; Jα-helix: 49°) (Diensthuber et al., 2013),

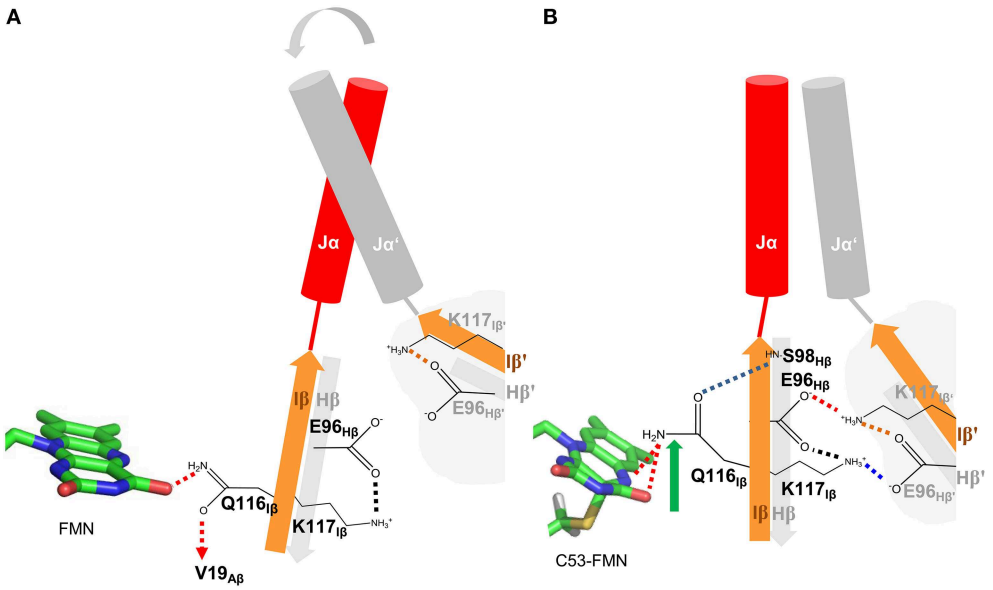

FIGURE 8 | Illustration of the signal relay mechanism proposed for PpSB1-LOV. The Hβ (gray) and Iβ (orange) strands of both subunits, harboring the here identified mechanistically relevant amino acid residues (Q116, E96, S98) are shown. In the dark state **(A)**, Q116 is facing toward V19 on Aβ (indicated by a dashed arrow), while enabling one H-bond to the FMN molecule (red dashed lines). The respective Hβ-Iβ orientation facilitates the destabilization of an inter-subunit K117-*E96′* salt-bridge which shows increased occupancy in all light-state simulations (red and blue dashed lines in **B**) resulting in meta-stable subunit interactions and increased Jα mobility in the dark state. In the light state **(B)**, Q116 flips toward S98 on Hβ (flipping indicated by green arrow) establishing a new H-bond between Q116-OE1 and S98-NH (blue dashed line). This results in a correlated displacement of the Hβ and Iβ strands, stabilizing the inter-subunit salt-bridge network (red and blue dashed lines) between K117 and E96 of opposing subunits. This stabilizing interaction "locks" the two subunits (including Jα and A'α) in an orientation as observed in the light-state X-ray structure.

which is corroborated by our simulations (See The Orientation of Protruding Jα and A'α Helices is Influenced by Adduct Formation, **Figure 6F**). NMR relaxation data for full-length YtvA in the dark state revealed a low order parameter (S^2); (calculated from relaxation rates and heteronuclear NOEs) for the Jα-helix indicating a high degree of mobility (Jurk et al., 2011). This effect can also be observed in our simulations (see The Orientation of Protruding Jα and A'α Helices is Influenced by Adduct Formation, **Figures 6B,D**). Without either a dark state structure of PpSB1-LOV, a light-state structure of YF1 or full-length dark and light-state structures of YtvA it is impossible to delineate between the two scenarios.

For monomeric AsLOV2 Freddolino et al. (2013) recently presented a mechanistic proposal based on MD simulations, as to how photon capture by the FMN chromophore initiates the displacement of the Jα helix. The authors suggested that structural changes to the Iβ strand and the Hβ-Iβ loop lead to a tilting of the Iβ strand that forces a corresponding movement of the Jα helix, eventually resulting in a disruption of the native interface between the respective secondary structure elements. Those structural changes are globally similar to the structural changes which we suggest to occur in photoactivation of dimeric PpSB1-LOV, although in our case occurring in the dark-state simulation and not the light-state trajectory as observed by Freddolino and co-workers. However, this discrepancy and the apparent reversal of the reaction in PpSB1-LOV compared to AsLOV2 is most likely related to the fact that the here presented simulations start from a light-state structure obtained from crystals grown under constant illumination. In contrast, the AsLOV2 light-state structure is obtained by illuminating a dark grown crystal and hence larger-scale structural changes are most probably impeded by the crystal lattice. Thus, globally, the AsLOV2 light-state structure resembles the dark state. This assumption is corroborated by a small all-atom RMSD value of 0.608 Å between the dark- and light-state AsLOV2 X-ray structures. It is thus not surprising, that larger structural perturbations are observed in the dark-state simulation of dimeric PpSB1-LOV. Freddolino co-workers and Peter et al. (2010) noted that the Q513 sidechain samples several conformations in the light state. However, no correlation was found between the Q513 rotamerization state and larger-scale changes in the LOV domain structure except in cases where the Q513-FMN interaction was lost. It thus seems that in both PpSB1-LOV and AsLOV2 Q116/Q513 rearrangement is the trigger to initiate a structural relay mechanism most likely via Hβ/Iβ displacement/tilting. For monomeric AsLOV2 this could result in the dissociation of the C-terminal Jα helix from the core. For dimeric PpSB1-LOV increased inter-domain correlations (**Figure 7B**), strengthened inter-domain salt-bridge interactions (**Figure 5**) as well as a more defined A'α and Jα angle distribution (**Figure 6**) are observed, hinting at an essential functional role for residues in the dimer interface, which is constituted by Hβ/Iβ and the two terminal α-helices.

Evidence for the Conservation of the Identified Signaling Mechanism in Other LOV Systems

We here identified a possible alternative mode of signal-relay in PpSB1-LOV from the site of photon capture, involving a conserved glutamine in the LOV domain FMN-binding site, to the N- and C-terminal helical extensions (A'α-helix and Jα-helix) outside the canonical LOV-core domain. In the corresponding light-state trajectory, Q116-OE1 reorients toward the backbone amide of S98, which is accompanied by a movement of the Iβ-strand and consequently a movement of the K117 toward *E96′* (of the opposite subunit) hence stabilizing an inter-subunit salt-bridge, which connects the two LOV domains of the dimer, locking the dimer arrangement as well as the Jα and A'α interactions. As outlined above, the proposed photoswitching mechanism, is globally similar to the one proposed previously based on simulations of other LOV domains (Neiss and Saalfrank, 2004; Peter et al., 2012a,b; Freddolino et al., 2013) using a monomeric model setup, but differs with regard to certain aspects, i.e., the nature of the Q513 displacement in the light-state simulations and the impact of those changes on the structural regions neighboring the displaced/tilted Iβ strand.

The question thus immediately arises if this mode of signaling could be conserved in other LOV sensory systems, which possess similar structural elements. If the outlined signal-relay mechanism of PpSB1-LOV would be conserved in other LOV systems, one would expect to identify conserved residues at the respective key positions or at least find functional mutation data for the respective regions that would support their importance for signaling.

Figure 9 shows a close-up view of the LOV domain active site of different LOV sensory systems, with the residues corresponding to the key residues identified for the PpSB1-LOV signal relay shown in stick representation. Additionally, residues, for which functional mutation data is available, displaying an altered signaling phenotype (either observed for the full-length photoreceptor in the biological context Harper et al., 2004; Jones et al., 2007; Avila-Perez et al., 2009; Gleichmann et al., 2013, or *in vitro* for the isolated LOV domain by biophysical means, Zayner et al., 2012), are depicted in stick representation and are labeled in green. In **Figure 9A**, the FMN binding site of PpSB1-LOV along with the here identified key amino acids in the vicinity of the chromophore, is shown. Additionally, the K117-E96 salt-bridge network which stabilizes the LOV-LOV interaction in the light-state is highlighted. In YF1 (**Figure 9B**) the position of K117 is occupied by asparagine (N124) and E96 is conserved (E105 in YF1). In the YF1 dimer structure E105 and N124 do not form a hydrogen-bond. Please note, that YF1 was crystallized in the dark, hence according to our here described model, a potential N124-E105 inter-subunit interaction would be expected to be broken. Given the overall structural similarity between PpSB1-LOV, YtvA, and YF1, it is tempting to speculate that in YF1 and YtvA, like in PpSB1-LOV a light triggered rotation of the two subunits relative to each other results in altered Jα and A'α interactions which are stabilized by an interaction between E105 and N124 of opposing subunits. *In vitro* and *in vivo* functional data for YtvA (Avila-Perez et al., 2009) and YF1 (Gleichmann et al., 2013) highlight the importance of both residues for the signal-relay since their mutation results in an altered signaling behavior. In analogy, **Figures 9C,D** depict the LOV domain active site of the phototropin 1 LOV2 domain of *Arabidopsis thaliana* (**Figure 9C**) and *Avena sativa* (**Figure 9D**). Like for PpSB1-LOV and YF1, the key residues for the proposed signal-relay mechanism are shown in stick representation. The positions of K117 and E96 of PpSB1-LOV are occupied by hydrophobic residues in AsLOV2 (L493 and L514) and AtLOV2 (I555 and L576). Those hydrophobic residues seem to "lock" the Jα-helix in place as observed in the respective dark-state X-ray structures. In light of the proposed signaling mechanism, reorientation of the active-site glutamine (AsLOV2: Q513; AtLOV2: Q575) would result in concomitant displacement of neighboring L515 (AsLOV2) or L576 (AtLOV2) which could trigger the release of the Jα-helix from the LOV core. Moreover, mutation of some of those residues (e.g., L493 and L514 in AsLOV2) resulted to a certain degree in altered structural changes *in vitro* (Harper et al., 2004; Jones et al., 2007; Zayner et al., 2013). While the here described hypothesis is certainly not mutually exclusive, as the respective mutational data can also be explained by other mechanistic proposals, such as the one brought forward for monomeric phototropin LOV sensor domains by Freddolino et al. (2013); (Outlined in Photoactivation and Signal-relay Mechanism of PpSB1-LOV Inferred from MD Simulations), it nevertheless provides an alternative scenario which could account for the observed signal relay especially for dimeric LOV photoreceptors. Further studies of site-directed mutants, both *in vitro* and in the biological context are needed to unequivocally delineate between the hypotheses described to date.

Conclusions

Taken together, our simulations stress the importance of the conserved LOV domain glutamine for the overall signaling process and identify new key residues which might be involved in the signal relay from the site of photon capture to N- and C-terminally located effector domains via the A'α and Jα helical connectors. As outlined above, in light of functional mutation data, the proposed signal-relay mechanism might be universally applicable, but certainly not mutually exclusive, in the explanation of the signaling behavior of bacterial short LOV proteins, YtvA and homologous proteins as well as for the phototropin LOV system.

The proposed mechanism is elegant in two ways. First of all, it can explain available functional mutation data and, secondly, accounts for the observation that functionally dissimilar mutations can be introduced at presumed key positions without completely abolishing LOV functionality in terms of photocycling and conformational changes. From mutational studies of AsLOV2 it became apparent, that the only residue required for photocycling is the conserved photoactive cysteine and that many mutations even though intended to be disruptive only attenuated or even increased the light-dependent conformational change, i.e., Jα displacement and/or unfolding (Zayner et al., 2012; Zayner and Sosnick, 2014). In light of our mechanistic proposal, this can be explained, because the major atom partners involved the primary conformational switch, apart

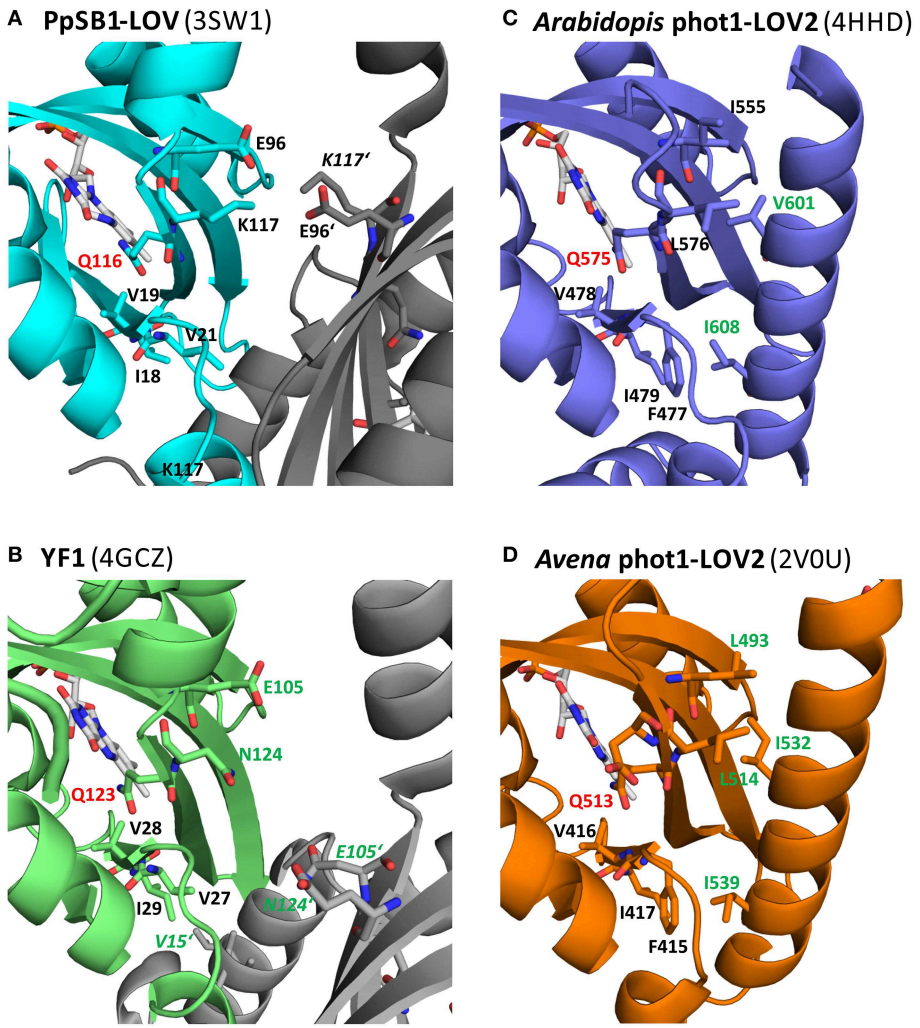

FIGURE 9 | Amino acid positions in three different LOV systems corresponding to the here identified key amino acids of PpSB1-LOV. The conserved "flipping" glutamine is highlighted in red (Q116 PpSB1-LOV; Q123 YF1; Q575: At-phot1-LOV2; Q513: As-phot1-LOV2). The residues corresponding to the PpSB1-LOV E96-K117 salt-bridge network **(A)** are E105, N124 (YF1; **B**), I555, L576 (At-phot1-LOV2; **C**) and L514, L493 (As-phot1-LOV2; **D**). The position of V19, whose backbone amide group forms a weak electrostatic interaction with Q116-OE1 in the dark-state trajectories of PpSB1-LOV corresponds to V28 (YF1), V478 (At-phot1-LOV), and V416 (As-phot1-LOV2). Additionally neighboring residues, which protrude into the LOV-core / A'α interface, are shown in stick representation. Residues which upon mutation showed an altered signaling phenotype are highlighted in green.

from the conserved glutamine, are backbone amide positions on Hβ and Aβ, which cannot be altered by mutation. Likewise the structural signal is proposed to be propagated *via* a displacement of the protein backbone from e.g., Q116 to K117 and S98 to E96 in PpSB1-LOV, which most probably cannot be directly influenced by mutation. Moreover, the proposed mechanism can account for the evolutionary plasticity of the LOV sensor domain, i.e., revealed by the multitude of different sensor-effector domain combinations in different LOV photoreceptors. According to our mechanistic proposal, the primary signaling event (glutamine displacement between Aβ and Hβ) can still be accommodated even if key functional amino acids (e.g., S98 and E96 on Hβ, K117 on Iβ and V19 on Aβ of PpSB1-LOV) are mutated, since the glutamine only switches the interaction between backbone amides of those residues. Hence mutation of those residues can in evolutionary terms be used to accommodate different interaction partners, i.e., the Jα-helix packing against the β-scaffold in the phototropin LOV system or LOV dimer stabilization via a salt-bridge (PpSB1-LOV) or hydrogen-bonding (YtvA, YF1) network.

At the same time, the presented mechanistic proposal has implications for the design and understanding of LOV-based optogenetic tools such as YF1 (based on YtvA) and those based on AsLOV2. If the general signal-relay mechanism is conserved between those systems, they represent an ideal testing ground for our proposal, as the here identified key residues can be easily mutated and screened for altered signaling phenotypes, which is not always so easy for the parent natural photoreceptor system. Currently, the design of LOV-based optogenetic switches is still a trial and error process, also due to the lack of an in-depth understanding of the mode of information flow from the site

of photon capture to the fused effector domain *via* N- and C-terminal helical linker elements which proofed to be functionally important for the signal relay. Thus, the information gained in the here presented simulations can in the future contribute to the rational understanding and design of novel LOV-based optogenetic switches.

Author Contributions

US, KEJ, MB, and UK conceived the study. MB and UK designed the experiments. MB performed the simulations. MB and UK analyzed and interpreted the data. MB and UK drafted the manuscript. All authors critically revised and approved the final version of the manuscript.

Acknowledgments

We gratefully acknowledge funding by the German Research Foundation (DFG) within the Research Training Group GK1166/2 "Biocatalysis in Non-Conventional Media—BioNoCo." UK and KEJ also acknowledge funding by the Federal Ministry of Education and Research (BMBF) in the framework of the collaborative research project "OptoSys" (FKZ 031A16).

Supplementary Material

The Supplementary Material for this article can be found online at: http://journal.frontiersin.org/article/10.3389/fmolb.2015.00055

References

Aihara, Y., Yamamoto, T., Okajima, K., Yamamoto, K., Suzuki, T., Tokutomi, S., et al. (2012). Mutations in N-terminal flanking region of blue light-sensing light-oxygen and voltage 2 (LOV2) domain disrupt its repressive activity on kinase domain in the Chlamydomonas phototropin. *J. Biol. Chem.* 287, 9901–9909. doi: 10.1074/jbc.M111.324723

Avila-Perez, M., Vreede, J., Tang, Y., Bende, O., Losi, A., Gärtner, W., et al. (2009). *In vivo* mutational analysis of YtvA from Bacillus subtilis: mechanism of light activation of the general stress response. *J. Biol. Chem.* 284, 24958–24964. doi: 10.1074/jbc.M109.033316

Barlow, D. J., and Thornton, J. M. (1983). Ion-pairs in proteins. *J. Mol. Biol.* 168, 867–885. doi: 10.1016/S0022-2836(83)80079-5

Circolone, F., Granzin, J., Jentzsch, K., Drepper, T., Jaeger, K. E., Willbold, D., et al. (2012). Structural basis for the slow dark recovery of a full-length LOV protein from *Pseudomonas putida*. *J. Mol. Biol.* 417, 362–374. doi: 10.1016/j.jmb.2012.01.056

Crosson, S., and Moffat, K. (2002). Photoexcited structure of a plant photoreceptor domain reveals a light-driven molecular switch. *Plant Cell.* 14, 1067–1075. doi: 10.1105/tpc.010475

Demarsy, E., and Fankhauser, C. (2009). Higher plants use LOV to perceive blue light. *Curr. Opin. Plant Biol.* 12, 69–74. doi: 10.1016/j.pbi.2008.09.002

Diensthuber, R. P., Bommer, M., Gleichmann, T., and Möglich, A. (2013). Full-length structure of a sensor histidine kinase pinpoints coaxial coiled coils as signal transducers and modulators. *Structure* 21, 1127–1136. doi: 10.1016/j.str.2013.04.024

Dittrich, M., Freddolino, P. L., and Schulten, K. (2005). When light falls in LOV: a quantum mechanical/molecular mechanical study of photoexcitation in Phot-LOV1 of *Chlamydomonas reinhardtii*. *J. Phys. Chem. B* 109, 13006–13013. doi: 10.1021/jp050943o

Duan, Y., Wu, C., Chowdhury, S., Lee, M. C., Xiong, G. M., Zhang, W., et al. (2003). A point-charge force field for molecular mechanics simulations of proteins based on condensed-phase quantum mechanical calculations. *J. Comput. Chem.* 24, 1999–2012. doi: 10.1002/jcc.10349

Endres, S., Granzin, J., Circolone, F., Stadler, A., Krauss, U., Drepper, T., et al. (2015). Structure and function of a short LOV protein from the marine phototrophic bacterium *Dinoroseobacter shibae*. *BMC Microbiol.* 15:365. doi: 10.1186/s12866-015-0365-0

Engelhard, C., Raffelberg, S., Tang, Y., Diensthuber, R. P., Möglich, A., Losi, A., et al. (2013). A structural model for the full-length blue light-sensing protein YtvA from *Bacillus subtilis*, based on EPR spectroscopy. *Photochem. Photobiol. Sci.* 12, 1855–1863. doi: 10.1039/c3pp50128k

Essmann, U., Perera, L., Berkowitz, M. L., Darden, T., Lee, H., and Pedersen, L. G. (1995). A smooth particle mesh Ewald method. *J. Chem. Phys.* 103, 8577–8593. doi: 10.1063/1.470117

Fedorov, R., Schlichting, I., Hartmann, E., Domratcheva, T., Fuhrmann, M., and Hegemann, P. (2003). Crystal structures and molecular mechanism of a light-induced signaling switch: the Phot-LOV1 domain from *Chlamydomonas reinhardtii*. *Biophys. J.* 84, 2474–2482. doi: 10.1016/S0006-3495(03)75052-8

Fenwick, R. B., Orellana, L., Esteban-Martín, S., Orozco, M., and Salvatella, X. (2014). Correlated motions are a fundamental property of beta-sheets. *Nat. Commun.* 5, 4070. doi: 10.1038/ncomms5070

Freddolino, P. L., Dittrich, M., and Schulten, K. (2006). Dynamic switching mechanisms in LOV1 and LOV2 domains of plant phototropins. *Biophys. J.* 91, 3630–3639. doi: 10.1529/biophysj.106.088609

Freddolino, P. L., Gardner, K. H., and Schulten, K. (2013). Signaling mechanisms of LOV domains: new insights from molecular dynamics studies. *Photochem. Photobiol. Sci.* 12, 1158–1170. doi: 10.1039/c3pp25400c

Gleichmann, T., Diensthuber, R. P., and Möglich, A. (2013). Charting the signal trajectory in a light-oxygen-voltage photoreceptor by random mutagenesis and covariance analysis. *J. Biol. Chem.* 288, 29345–29355. doi: 10.1074/jbc.M113.506139

Halavaty, A. S., and Moffat, K. (2007). N- and C-terminal flanking regions modulate light-induced signal transduction in the LOV2 domain of the blue light sensor phototropin 1 from *Avena sativa*. *Biochemistry* 46, 14001–14009. doi: 10.1021/bi701543e

Halavaty, A. S., and Moffat, K. (2013). Coiled-coil dimerization of the LOV2 domain of the blue-light photoreceptor phototropin 1 from *Arabidopsis thaliana*. *Acta Crystallogr. F* 69, 1316–1321. doi: 10.1107/S1744309113029199

Harper, S. M., Christie, J. M., and Gardner, K. H. (2004). Disruption of the LOV-Jalpha helix interaction activates phototropin kinase activity. *Biochemistry* 43, 16184–16192. doi: 10.1021/bi048092i

Harper, S. M., Neil, L. C., and Gardner, K. H. (2003). Structural basis of a phototropin light switch. *Science* 301, 1541–1544. doi: 10.1126/science.1086810

Herman, E., and Kottke, T. (2015). Allosterically regulated unfolding of the a'alpha helix exposes the dimerization site of the blue-light-sensing aureochrome-LOV domain. *Biochemistry* 54, 1484–1492. doi: 10.1021/bi501509z

Herman, E., Sachse, M., Kroth, P. G., and Kottke, T. (2013). Blue-light-induced unfolding of the j alpha helix allows for the dimerization of aureochrome-LOV from the diatom *Phaeodactylum tricornutum*. *Biochemistry* 52, 3094–3101. doi: 10.1021/bi400197u

Herrou, J., and Crosson, S. (2011). Function, structure and mechanism of bacterial photosensory LOV proteins. *Nat. Rev. Microbiol.* 9, 713–723. doi: 10.1038/nrmicro2622

Hess, B., Bekker, H., Berendsen, H. J. C., and Fraaije, J. G. E. M. (1997). LINCS: a linear constraint solver for molecular simulations. *J. Comput. Chem.* 18, 1463–1472.

Humphrey, W., Dalke, A., and Schulten, K. (1996). VMD: visual molecular dynamics. *J. Mol. Graph.* 14, 33–38. doi: 10.1016/0263-7855(96)00018-5

Idnurm, A., Verma, S., and Corrochano, L. M. (2010). A glimpse into the basis of vision in the kingdom *Mycota*. *Fungal Genet. Biol.* 47, 881–892. doi: 10.1016/j.fgb.2010.04.009

Jakalian, A., Jack, D. B., and Bayly, C. I. (2002). Fast, efficient generation of high-quality atomic charges. AM1-BCC model: II. Parameterization and validation. *J. Comput. Chem.* 23, 1623–1641. doi: 10.1002/jcc.10128

Jeffrey, G. A. (1997). "An introduction to hydrogen bonding," in *Topics in Physical Chemistry* (New York, NY: Oxford University Press), 11–96

Jentzsch, K., Wirtz, A., Circolone, F., Drepper, T., Losi, A., Gärtner, W., et al. (2009). Mutual exchange of kinetic properties by extended mutagenesis in two short LOV domain proteins from *Pseudomonas putida*. *Biochemistry* 48, 10321–10333. doi: 10.1021/bi901115z

Jones, M. A., Feeney, K. A., Kelly, S. M., and Christie, J. M. (2007). Mutational analysis of phototropin 1 provides insights into the mechanism underlying LOV2 signal transmission. *J. Biol. Chem.* 282, 6405–6414. doi: 10.1074/jbc.M605969200

Jurk, M., Dorn, M., and Schmieder, P. (2011). Blue flickers of hope: secondary structure, dynamics, and putative dimerization interface of the blue-light receptor YtvA from *Bacillus subtilis*. *Biochemistry*. 50, 8163–8171. doi: 10.1021/bi200782j

Karplus, M., and McCammon, J. A. (2002). Molecular dynamics simulations of biomolecules. *Nat. Struct. Biol.* 9, 646–652. doi: 10.1038/nsb0902-646

Kashojiya, S., Okajima, K., Shimada, T., and Tokutomi, S. (2015). Essential role of the a 'alpha/a beta gap in the n-terminal upstream of LOV2 for the blue light signaling from LOV2 to kinase in Arabidopsis phototototropin1, a plant blue light receptor. *PLoS ONE* 10:e124284. doi: 10.1371/journal.pone.0124284

Kennis, J. T., Crosson, S., Gauden, M., van Stokkum, I. H., Moffat, K., and van Grondelle, R. (2003). Primary reactions of the LOV2 domain of phototropin, a plant blue-light photoreceptor. *Biochemistry* 42, 3385–3392. doi: 10.1021/bi034022k

Krauss, U., Losi, A., Gärtner, W., Jaeger, K. E., and Eggert, T. (2005). Initial characterization of a blue-light sensing, phototropin-related protein from *Pseudomonas putida*: a paradigm for an extended LOV construct. *Phys. Chem. Chem. Phys.* 7, 2804–2811. doi: 10.1039/b504554a

Krauss, U., Minh, B. Q., Losi, A., Gärtner, W., Eggert, T., von Haeseler, A., et al. (2009). Distribution and phylogeny of light-oxygen-voltage-blue-light-signaling proteins in the three kingdoms of life. *J. Bacteriol.* 191, 7234–7242. doi: 10.1128/JB.00923-09

Krieger, E., Darden, T., Nabuurs, S. B., Finkelstein, A., and Vriend, G. (2004). Making optimal use of empirical energy functions: force-field parameterization in crystal space. *Proteins* 57, 678–683. doi: 10.1002/prot.20251

Krieger, E., Dunbrack, R. L. Jr., Hooft, R. W., and Krieger, B. (2012). Assignment of protonation states in proteins and ligands: combining pKa prediction with hydrogen bonding network optimization. *Methods Mol. Biol.* 819, 405–421. doi: 10.1007/978-1-61779-465-0_25

Krieger, E., Koraimann, G., and Vriend, G. (2002). Increasing the precision of comparative models with YASARA NOVA–a self-parameterizing force field. *Proteins* 47, 393–402. doi: 10.1002/prot.10104

Krieger, E., Nielsen, J. E., Spronk, C. A., and Vriend, G. (2006). Fast empirical pKa prediction by Ewald summation. *J. Mol. Graph. Model.* 25, 481–486. doi: 10.1016/j.jmgm.2006.02.009

Krieger, E., and Vriend, G. (2014). YASARA View-molecular graphics for all devices-from smartphones to workstations. *Bioinformatics* 30, 2981–2982. doi: 10.1093/bioinformatics/btu426

Losi, A., and Gärtner, W. (2008). Bacterial bilin- and flavin-binding photoreceptors. *Photochem. Photobiol. Sci.* 7, 1168–1178. doi: 10.1039/b802472c

Miyamoto, S., and Kollman, P. A. (1992). Settle - an analytical version of the shake and rattle algorithm for rigid water models. *J. Comput. Chem.* 13, 952–962. doi: 10.1002/jcc.540130805

Möglich, A., Ayers, R. A., and Moffat, K. (2009). Design and signaling mechanism of light-regulated histidine kinases. *J. Mol. Biol.* 385, 1433–1444. doi: 10.1016/j.jmb.2008.12.017

Möglich, A., and Moffat, K. (2007). Structural basis for light-dependent signaling in the dimeric LOV domain of the photosensor YtvA. *J. Mol. Biol.* 373, 112–126. doi: 10.1016/j.jmb.2007.07.039

Möglich, A., Yang, X., Ayers, R. A., and Moffat, K. (2010). Structure and function of plant photoreceptors. *Annu. Rev. Plant Biol.* 61, 21–47. doi: 10.1146/annurev-arplant-042809-112259

Nash, A. I., Ko, W. H., Harper, S. M., and Gardner, K. H. (2008). A conserved glutamine plays a central role in LOV domain signal transmission and its duration. *Biochemistry* 47, 13842–13849. doi: 10.1021/bi801430e

Nash, A. I., McNulty, R., Shillito, M. E., Swartz, T. E., Bogomolni, R. A., Luecke, H., et al. (2011). Structural basis of photosensitivity in a bacterial light-oxygen-voltage/helix-turn-helix (LOV-HTH) DNA-binding protein. *Proc. Natl. Acad. Sci. U.S.A.* 108, 9449–9454. doi: 10.1073/pnas.1100262108

Neiss, C., and Saalfrank, P. (2004). Molecular dynamics simulation of the LOV2 domain from *Adiantum capillus-veneris*. *J. Chem. Inf. Comp. Sci.* 44, 1788–1793. doi: 10.1021/ci049883u

Ogata, H., Cao, Z., Losi, A., and Gärtner, W. (2009). Crystallization and preliminary X-ray analysis of the LOV domain of the blue-light receptor YtvA from *Bacillus amyloliquefaciens* FZB42. *Acta Crystallogr. F* 65, 853–855. doi: 10.1107/S1744309109026670

Okajima, K., Aihara, Y., Takayama, Y., Nakajima, M., Kashojiya, S., Hikima, T., et al. (2014). Light-induced conformational changes of LOV1 (Light Oxygen Voltage-sensing Domain 1) and LOV2 relative to the kinase domain and regulation of kinase activity in chlamydomonas phototropin. *J. Biol. Chem.* 289, 413–422. doi: 10.1074/jbc.M113.515403

Peter, E., Dick, B., and Baeurle, S. A. (2010). Mechanism of signal transduction of the LOV2-Jalpha photosensor from *Avena sativa*. *Nat. Commun.* 1:122. doi: 10.1038/ncomms1121

Peter, E., Dick, B., and Baeurle, S. A. (2012a). Illuminating the early signaling pathway of a fungal light-oxygen-voltage photoreceptor. *Proteins* 80, 471–481. doi: 10.1002/prot.23213

Peter, E., Dick, B., and Baeurle, S. A. (2012b). Signals of LOV1: a computer simulation study on the wildtype LOV1-domain of *Chlamydomonas reinhardtii* and its mutants. *J. Mol. Model.* 18, 1375–1388. doi: 10.1007/s00894-011-1165-6

Rani, R., Jentzsch, K., Lecher, J., Hartmann, R., Willbold, D., Jaeger, K. E., et al. (2013). Conservation of dark recovery kinetic parameters and structural features in the *pseudomonadaceae* "short" light, oxygen, voltage (LOV) protein family: implications for the design of LOV-based optogenetic tools. *Biochemistry* 52, 4460–4473. doi: 10.1021/bi400311r

Shcherbakova, D. M., Shemetov, A. A., Kaberniuk, A. A., and Verkhusha, V. V. (2015). Natural photoreceptors as a source of fluorescent proteins, biosensors, and optogenetic tools. *Annu. Rev. Biochem.* 84, 519–550. doi: 10.1146/annurev-biochem-060614-034411

Song, S. H., Freddolino, P. L., Nash, A. I., Carroll, E. C., Schulten, K., Gardner, K. H., et al. (2011). Modulating LOV domain photodynamics with a residue alteration outside the chromophore binding site. *Biochemistry* 50, 2411–2423. doi: 10.1021/bi200198x

Steiner, T. (2002). The hydrogen bond in the solid state. *Angew. Chem. Int. Edit.* 41, 49–76. doi: 10.1002/1521-3773(20020104)41:1<48::AID-ANIE48>3.0.CO;2-U

Swartz, T. E., Corchnoy, S. B., Christie, J. M., Lewis, J. W., Szundi, I., Briggs, W. R., et al. (2001). The photocycle of a flavin-binding domain of the blue light photoreceptor phototropin. *J. Biol. Chem.* 276, 36493–36500. doi: 10.1074/jbc.M103114200

Vaidya, A. T., Chen, C. H., Dunlap, J. C., Loros, J. J., and Crane, B. R. (2011). Structure of a light-activated LOV protein dimer that regulates transcription. *Sci. Signal.* 4, ra50. doi: 10.1126/scisignal.2001945

Wang, J., Cieplak, P., and Kollman, P. A. (2000). How well does a restrained electrostatic potential (RESP) model perform in calculating conformational energies of organic and biological molecules? *J. Comput. Chem.* 21, 1049–1074. doi: 10.1002/1096-987X(200009)21:12<1049::AID-JCC3>3.0.CO;2-F

Wang, J. M., Wolf, R. M., Caldwell, J. W., Kollman, P. A. and Case, D. A. (2004). Development and testing of a general amber force field. *J. Comput. Chem.* 25, 1157–1174. doi: 10.1002/jcc.20035

Xu, D., Tsai, C. J., and Nussinov, R. (1997). Hydrogen bonds and salt bridges across protein-protein interfaces. *Protein Eng.* 10, 999–1012. doi: 10.1093/protein/10.9.999

Yao, X., Rosen, M. K., and Gardner, K. H. (2008). Estimation of the available free energy in a LOV2-J alpha photoswitch. *Nat. Chem. Biol.* 4, 491–497. doi: 10.1038/nchembio.99

Zayner, J. P., Antoniou, C., French, A. R., Hause, R. J., and Sosnick, T. R. (2013). Investigating models of protein function and allostery with a widespread mutational analysis of a light-activated protein. *Biophys. J.* 105, 1027–1036. doi: 10.1016/j.bpj.2013.07.010

Zayner, J. P., Antoniou, C., and Sosnick, T. R. (2012). The amino-terminal helix modulates light-activated conformational changes in AsLOV2. *J. Mol. Biol.* 419, 61–74. doi: 10.1016/j.jmb.2012.02.037

Zayner, J. P., and Sosnick, T. R. (2014). Factors that control the chemistry of the LOV domain photocycle. *PLoS ONE.* 9:e87074. doi: 10.1371/journal.pone.0087074

Zikihara, K., Iwata, T., Matsuoka, D., Kandori, H., Todo, T., and Tokutomi, S. (2006). Photoreaction cycle of the light, oxygen, and voltage domain in FKF1 determined by low-temperature absorption spectroscopy. *Biochemistry* 45, 10828–10837. doi: 10.1021/bi0607857

Zoltowski, B. D., Schwerdtfeger, C., Widom, J., Loros, J. J., Bilwes, A. M., Dunlap, J. C., et al. (2007). Conformational switching in the fungal light sensor Vivid. *Science* 316, 1054–1057. doi: 10.1126/science.1137128

Zoltowski, B. D., Vaccaro, B., and Crane, B. R. (2009). Mechanism-based tuning of a LOV domain photoreceptor. *Nat. Chem. Biol.* 5, 827–834. doi: 10.1038/nchembio.210

Conflict of Interest Statement: The authors declare that the research was conducted in the absence of any commercial or financial relationships that could be construed as a potential conflict of interest.

Advantages of publishing in Frontiers

OPEN ACCESS
Articles are free to read, for greatest visibility

COLLABORATIVE PEER-REVIEW
Designed to be rigorous – yet also collaborative, fair and constructive

FAST PUBLICATION
Average 85 days from submission to publication (across all journals)

COPYRIGHT TO AUTHORS
No limit to article distribution and re-use

TRANSPARENT
Editors and reviewers acknowledged by name on published articles

SUPPORT
By our Swiss-based editorial team

IMPACT METRICS
Advanced metrics track your article's impact

GLOBAL SPREAD
5'100'000+ monthly article views and downloads

LOOP RESEARCH NETWORK
Our network increases readership for your article

Frontiers
EPFL Innovation Park, Building I • 1015 Lausanne • Switzerland
Tel +41 21 510 17 00 • Fax +41 21 510 17 01 • info@frontiersin.org
www.frontiersin.org

Find us on